Technische Universität München
Fakultät für Chemie
Lehrstuhl für Anorganische und Metallorganische Chemie

Contributions to Multi-Photon Absorption in Metal-Organic Frameworks

David Christian Mayer

Vollständiger Abdruck der von der Fakultät für Chemie der Technischen Universität München zur Erlangung des akademischen Grades eines

Doktors der Naturwissenschaften (Dr. rer. nat.)

genehmigten Dissertation.

Vorsitzender: Prof. Dr. Klaus Köhler

Prüfer der Dissertation:
1. Prof. Dr. Dr. h.c. Roland A. Fischer
2. Prof. Dr. Jürgen Hauer
3. Prof. Dr. Christof Wöll

Die Dissertation wurde am 01.07.2020 bei der technischen Universität München eingereicht und durch die Fakultät für Chemie am 13.10.2020 angenommen.

Die vorliegende Arbeit wurde am Lehrstuhl für Anorganische und Metallorganische Chemie der Technischen Universität München im Zeitraum von November 2016 bis Juni 2020 erstellt.

„Nothing exists except atoms and empty space;

everything else is opinion”

Democritus

„In steter Veränderung ist diese Welt.

Wachstum und Verfall sind ihre wahre Natur.

Die Dinge erscheinen und lösen sich wieder auf.

Glücklich, wer sie friedvoll einfach nur betrachtet.“

Buddha

Für Moritz und Jule

Danksagung

In erster Linie gilt mein ganz besonderer Dank

Prof. Dr. rer. nat. Dr. phil. h.c. Roland A. Fischer

für die Möglichkeit, in einer fachlich und menschlich herausragenden Umgebung an einem hochgradig faszinierenden wissenschaftlichen Thema zu arbeiten. Ich verdanke Ihnen nicht nur auf wissenschaftlicher Ebene ihren Einsatz aller Art, sondern bin Ihnen auch für das mir gegenüber gebrachte Vertrauen und Ihre Unterstützung auf privater Ebene von Herzen dankbar. Die Gelegenheit, Hintergründe in der Projektassistenz von Wissenschaftsarbeit zu erfahren und mich dadurch in diesen Belangen neuen Herausforderungen zu stellen und mich weiterentwickeln zu können verdanke ich ebenfalls Ihnen.

Meiner Prüfungskommission danke ich für die bereitwillige und freundliche Übernahme des Koreferats.

Wie so oft, haben an der Entwicklung dieser Arbeit zahlreiche Menschen mitgewirkt, deren mein herzliches **Dankeschön** gilt!

Insbesondere möchte ich mich bedanken bei…/ I am particular thankful to…

…**Dr. Alexander Pöthig** dem ich hier zu größten Dank verpflichtet bin und dessen Wirken auf mein Vorrankommen im Studium und während der Promotion nicht in Worte zu fassen ist. Alex, ich danke dir für die Einführung in die spannende Welt der Kristallographie, deine Zuversicht, deine stete Unterstützung in den vielen kleinen und großen Herausforderungen und vor allem Dingen für deine Freundschaft!

…**Dr. Gregor Kieslich** für seine Einführung in die Pulverdiffraktometrie, seine Unterstützung bei kleineren und größeren kristallographischen Problemen, sein immer offenes Ohr bei Fragestellungen aller Art und seine sehr hilfreichen, immer auf das Wesentlich fokussierte, wissenschaftlichen Hilfestellungen.

…**Prof. Raghavender Medishetty** to guide me during the beginning of my PhD, to introduce me to the topics of non-linear optics and metal-organic frameworks and to pave the way for the success of this thrilling topic.

…**Prof. Marek Samoc** and **Dr. Jan Zareba** for providing their far-reaching expertise in the field of non-linear optics and a lot of non-linear optical measurements on divers compounds of this thesis, which finally ended in two successful co-shared publications.

…**Prof. Robert Zalesny** and **Dr. Marta Choluj** for the quantum chemical calculations in the second chapter of this thesis. Their theoretical work considerable contributed to the success of this work.

…**Prof. Jochen Feldmann** und **Dr. Aurora Manzi** für die linear und nicht-linear optischen Charakterisierungen im dritten Kapitel dieser Arbeit, welche in einer erfolgreichen gemeinsam Publikation mündeten. Vielen Dank für das entgegenbrachte Vertrauen, der Hilfe in der Interpretation der Daten und dem Eifer in den durchgeführten Messungen.

…**Prof. Jürgen Hauer** und **Dr. Erling Thyhaug** für die hervorragende Zusammenarbeit, der unvoreingenommenen Interesse an diesem Thema und der immer zeitnahen und schnellen Hilfe in allerlei messrelevanten Fragestellungen. In particular, I am very thankful to Dr. Erling Thyrhaug, whose discussion with me were always very amusing and pushed my photophysical knowledge a lot!

…**Dr. Christian Gemel, Dr. Eliza Gemel** und **Dr. Mirza Cokoja**, für eine stets offene Tür bei Fragestellungen aller Art und Enthusiasmus sowie Kreativität in der Lösung ebenjener.

…**Dr. Markus Drees,** für die Einführung in das quantenchemische Rechnen schon während meines Studiums und seine große Hilfe in allen Belangen und Problemen der Quantenchemie sowie darüber hinaus.

…**Dr. Gabriele Raudschl-Sieber,** für Ihre Unterstützung bei der Festkörper-NMR Spektroskopie und ihr großes Engagement bei manchmal doch kleinen Probemengen.

…dem AMC Sekretariat, **Martin Schellerer** und **Dana Weiß**. Ohne eure Ansprechbarkeit und Unterstützung in administrativen Dingen wäre der Uni-Alltag deutlich anstrengender. Vielen Dank für eure Arbeit „im Verborgenen“. Mein besonderer Dank gilt **Martin**, mit dem ich über zwei Jahre hinweg diverse kleine und größere Projekte im Rahmen von COORNETs stemmen durfte.

…den hilfsbereiten Techniker und Angestellten an der TUM, **Rodica Dumitrescu, Maria Weindl, Jürgen Krudermann, Tobias Kubo, Peter Richter, Ulrike Ammari, Petra Ankenbauer, Bircan Dilki**, für ihre tatkräftige Unterstützung im Laboralltag, bei den Analysen und der Vorbereitung zweier Showvorlesungen.

…den Studenten die ich im Rahmen von Forschungspraktika und Abschlussarbeiten begleiten durfte: **Benedikt Winkler, Sebastian Weishäupl, Xiaoyu Zhou, Elyha Petro** und allen Studenten im Rahmen von PRODEF und HYMAT.

…der **Gesellschaft deutscher Chemiker** für die finanzielle Unterstützung im Form zweier Reisestipendien.

Neben allen fachlichem ist doch das Zwischenmenschliche ausschlaggebend und eine Arbeit tun zu dürfen die dich erfüllt. Ich möchte daher allen Menschen danken die mich neben dem Labor und dem Laboralltag begleitet haben und somit das Leben lebenswerter machten.

Daher danke ich meinen jetzigen und ehemaligen Kollegen der **AMC**, insbesondere **Alexander Pöthig, Philipp Altmann, Jana Weßing, Daniel Peeters, Stefan Burger, Gregor Kieslich, Konstantin Epp, Christian Schneider, Julius Hornung, Lena Staiger, Kathrin Kratzl, Anna-Lisa Semrau, Pia Vervoorts, Fabian Schmidt** und **Sebastian Weishäupl** für eine großartige, teils ausgelassene Gruppenatmosphäre und dem Zusammenhalt in und außerhalb der Arbeitsgruppe, sowie diverse gemeinsame Aktivitäten in und außerhalb der Uni. Hervorzuheben sind hier unsere alljährlichen Weihnachtskonzerte, die mir doch jedes Jahr wieder aufs Neue Spaß bereiteten.

Mein herzlicher Dank gilt weiterhin meinen ehemaligen Studentenkollegen, ohne deren gemeinsame Zeit das Studium nur halb so viel Spaß bereitet hätte,

Mara, Kathrin, Bruno, Stefan, Ines, Jonas, Michael, Fabian, Lorenz und **Sebastian.**

Ohne meiner **Eltern** wäre das hier alles wohl nicht möglich gewesen. Ich danke von Herzen **meiner Mutter**, dass sie mich zu jeder Zeit von Kräften unterstützt hat, vor während und nach meiner universitären Laufbahn. Des Weiteren gilt mein Dank **Oswald** der mir in den letzten 21 Jahren stets zur Seite gestanden ist.

Zu guter Letzt möchte ich mich bei der wohl wichtigsten Person in meinem Leben bedanken: **Edith**. Ich kann hier kaum in Worte fassen, wie unglaublich dankbar ich dir für deine Unterstützung in den letzten 11 Jahren bin. Ohne deinen Beistand, deiner unermüdlichen Toleranz, deiner Bereitschaft zurückzutreten und mich mal lassen zu machen, wäre es wohl nie so weit gekommen. Ich bin dir zutiefst dankbar, dass du immer für mich da bist und freue mich auf alles, was auf uns Vier noch zukommen wird.

Zusammenfassung

Die vorliegende Arbeit befasst sich mit Koordinationspolymeren als neue multiphotonen-absorbierende Materialklasse. Diese junge Klasse von porösen Materialien, bestehend aus einem organischen und einem anorganischen Baustein, wurde intensiv beforscht bezüglich einer Vielzahl von unterschiedlichen Materialeigenschaften mit herausragenden Ergebnissen in Gasadsorption, Speicherung und Trennung. Optische Eigenschaften wurden vor allem untersucht mit Hinblick auf Lumineszenz und Frequenzverdoppelung (sogenannte Second Harmonic Generation = SHG). Allerdings wurden nicht-linear optische Eigenschaften höherer Ordnung, wie z.B. Multiphotonenabsorption, in Koordinationspolymeren bisher nur unzureichend beforscht. Koordinationspolymere sind supramolekulare Verbindungen, die sich aus einem anorganischen Grundbaustein und einem organischen Liganden zusammensetzen. Basierend auf dem modularen Aufbauprinzip dieser Verbindungsklasse kann eine Vielzahl von unterschiedlichen Materialen synthetisiert werden, welche eine große Zahl unterschiedlicher Materialeigenschaften zur Verfügung stellen. Optische Eigenschaften von Koordinationspolymeren sind determiniert durch die Eigenschaften der aufbauenden Einheiten (organischer Ligand, anorganischer Metallcluster) und die Wechselwirkung derselbigen. Die Möglichkeit die jeweiligen Aufbaueinheiten chemisch einzustellen und somit die inhärenten optischen Eigenschaften auf einer molekularen Ebene abzustimmen, stellt Koordinationspolymere als eine hochinteressante Materialklasse in nicht-linear optischen Anwendungen dar. Allerdings sind Designprinzipien, welche besagte Eigenschaften adressieren, bisher nur unzureichend verstanden. Das zugrundeliegende Konzept besteht in der Assemblage von kleinen, multiphotonen-absorbierenden organischen Verbindungen zu kristallinen (porösen) Materialien. Intra -und intermolekulare Wechselwirkungen zwischen den aufbauenden Liganden gelten als treibende Kraft in der Verstärkung der optischen Antwort nach Anregung mit Licht und zeigen eine potentielle Multiparameterabhängigkeit.

Das Ziel der vorliegenden Arbeit besteht in der Synthese, der strukturellen sowie nicht-linear optischen Charakterisierung neuer multiphotonenaktiver Koordinationspolymere, um die obig genannten verschiedenen Aspekte sowie deren Koabhängigkeiten genauer zu beleuchten. Die hier vorgestellten, neuen Materialien basieren auf vierbindigen Ligandenstrukturen und prototypischen Zink, Cadmium sowie Zirconium basierten Knotenpunkten. Die organischen Linker wurden mit Hilfe von etablierten Syntheserouten für multiphotonen-absorbierende Moleküle, dargestellt. Neue Koordinationspolymere wurden strukturell charakterisiert und Ergebnisse von Multiphotonenabsorptionsmessungen wurden im Rahmen des Einflusses von intermolekularen Wechselwirkungen mit der Hilfe von etablierten Theorien vergleichbarer Materialklassen diskutiert. Weiterhin wurden die Messergebnisse versucht mit strukturellen Eigenschaften der Koordinationspolymere zu korrelieren mit dem allgemeinem Ziel, Struktur-Eigenschaftsbeziehungen abzuleiten. Zugrundeliegende Mechanismen der Multiphotonenabsorption in Koordinationspolymeren sind bisher nur unzureichend verstanden. Die wohl interessanteste Frage in diesem Zusammenhang lässt sich folgendermaßen darstellen: „Lassen sich strukturelle Aspekte in Koordinationspolymeren so einstellen, dass eine gezielte Steuerung der nicht-linear optischen Antwort der Verbindung möglich ist, bzw. kann man gezielt Strukturen vorhersagen die große Multiphotonenabsorptionsquerschnitte zeigen?“

Abstract

The present work focusses on coordination polymers as a new, potential multi-photon absorbing material class. This young class of hybrid inorganic-organic (porous) materials have been intensively investigated towards a multitude of different properties, with outstanding performances in e.g. gas adsorption, storage and separation. Optical properties seem to be well explored for luminescence and second-harmonic generation phenomena, however, coordination polymers as optical media in higher-order non-linear optical processes, such as multi-photon absorption, have rarely been investigated. Coordination polymers are supramolecular compounds, which are constructed from inorganic building blocks and organic linkers. Based on modular construction principles, the so-called modular building block approach, a plethora of materials can be obtained, yielding a vast array of material properties. Optical properties are particular predetermined by the character of the structuring unit and by the interplay between them. The ability to fine-tune the individual building blocks, and therefore the inherent underlying optical properties on a molecular level, makes coordination polymers a highly promising material class in non-linear optical applications. However, design principles which shape the non-linear optical properties of coordination polymers are sparsely understood. The underlying concept herein, is to assemble crystalline (porous) materials from small, multi-photon absorbing organic compounds. Intra- and intermolecular interactions are thought to enhance the optical response via differing multi-photon absorption channels, with potential multiparameter dependencies.

In order to address the different aspects in the above introduced correlations, the main aim of this thesis is the synthesis, structural and non-linear optical characterization of multi-photon absorbing coordination polymers. These novel materials are based on tetratopic linker molecules and prototypic zinc, cadmium and zirconium based carboxylic nodes. The organic linker molecules are synthesized following well established routes for multi-photon absorbing molecules. New coordination polymers were intensively characterized towards their structural composition. Results of measurements of multi-photon

absorption efficiencies were interpreted in terms of either intramolecular or intermolecular effects using established theories for similar material classes. Furthermore, correlations with the structural situation were anticipated to be deduced with the overall aim to derive structure-property relations of multi-photon absorbing coordination polymers. Underlying mechanisms are only partly understood leaving many questions unanswered. Most importantly, can structural aspects be precisely fine-tuned to access high multi-photon absorption efficiencies?

Table of Contents

List of Abbreviations

A	Acceptor
ACQ	Aggregation caused quenching
AIE	Aggregation induced emission
azpy	4,4-Azopyridine
BET	Brunauer, Emmett, Teller
bpea	1,2-Bis(4-pyridyl)ethane
bpee	1,2-Bis(4-pyridyl)ethene
bpy	4,4-Bipyridine
CA	Closed aperture
CCN	Crystalline coordination network
CIE	Crystallization induced emission
CP	Coordination polymer
CPMAS	Cross polarization magic angle spinning
CT	Charge transfer
D	Donor
DEF	Diethylformamide
DOS	Density of states
DMF	Dimethylformamide
DMAc	Dimethylacetamide
EA	Elemental analysis
EEM	Emission-excitation mapping
ESG	Excited state geometry
ET	Energy transfer
EtOH	Ethanol
EQY	External quantum yield
FRET	Förster resonance energy transfer
GGA	Generalized gradient approximation
HOMO	Highest occupied molecular orbital
HLCT	Hybridized local and charge transfer
IR	Infrared
ISC	Intersystem crossing
KS-DFT	Kohn-Sham density functional theory
LIFM	Lehn institute of functional materials
LLCT	Ligand-to-ligand charge transfer
LMCT	Ligand-to-metal charge transfer
LUMO	Lowest unoccupied molecular orbital
MeOH	Methanol
MLCT	Metal-to-ligand charge transfer
MO	Molecular orbital
MOF	Metal-organic framework
MPA	Multi-photon absorption
NLO	Non-linear optics
NTO	Natural transition orbital
NU	Northwestern university
OA	Open aperture
OSM	Optically smart materials
PAW	Projected augmented wave

PCN	Porous coordination network
PDOS	Projected density of states
PES	Potential energy surface
PL	Photoluminescence
PLE	Photoluminescence excitation
PXRD	Powder X-ray diffraction
Ry	Rydberg
SBU	Secondary building unit
SCXRD	Single crystal X-ray diffraction
SHG	Second harmonic generation
SOS	Sum-over-state
SSMPEF	Solid-state multi-photon excited fluorescence
SSTPEF	Solid-state two-photon excited fluorescence
TBAPy	Free base of (pyrene-1,3,6,8-tetrayl)tetrabenzoic acid
TCSPC	Time correlated single photon counting
TCPE	Free base of ethene-1,1,2,2-tetrayl)tetrakis(([1,1'-biphenyl]-4-carboxylic acid
TCPE-F	Free base of ethene-1,1,2,2-tetrayl)tetrakis(3-fluoro-[1,1'-biphenyl]-4-carboxylic acid
TD-DFT	Time-dependent density functional theory
TDM	transition density matrix
TFA	Trifluoro acetic acid
TGA	Thermogravimetric analysis
THG	Third harmonic generation
TPA	Two-photon absorption
TPBD	Free base of tetrakis[(1,1‘-biphenyl)-4-carboxylic acid]-1,4-benzene diamine
TPE	Tetraphenylethylene
TRES	Time resolved emission spectroscopy
ZIF	Zeolitic imidazolate framework

List of Figures

List of Tables

List of Schemes

1 Introduction

Photo active materials are materials, which interactively react with light and subsequently respond to optical radiation in a multitude of different ways, such as luminescence, charge transport, photoinduced switching etc.[1] The utilization of photons as a chemical reagent in order to do something meaningful and to accomplish a desired function needs materials which are capable of controlling luminous radiation.[2] Such materials are not only subject of research, but have already found diverse applications in our daily lives (e.g. photovoltaics, medicine, optical communication and imaging etc.). In particular, photo active materials include huge technological importance in the field of clean energy production and will have an enormous influence on future technologies in that direction. Photo active materials are the basis of many cutting-edge technologies, including light-emitting displays, photovoltaic cells, LEDs, photomultipliers and resistors, to name a view. The above mentioned effects share a common feature, that is the interaction of a material with light.

Optical nonlinearities are exhibited from photo active materials due to interaction of the latter with intensive laser fields.[3] The research field of non-linear optics (NLO) is only a year younger than lasers and a large number of laser applications owe their existence to NLO.[4] Furthermore, NLO plays a major role in many optical applications, among others optical signal processing, optical communication, ultrafast switching, ultra-short pulsed lasers, sensor etc. Future applications for NLO include quantum optics, quantum computing, plasma physics or particle accelerators. The importance of NLO active materials is hardly noticed in everyday life. They, however, hold a profound indirect influence as NLO has made a diversity of advanced applications possible, which directly affect modern technology (state-of-the-art analysis and medicinal techniques, high-capacity telecommunications, micromachinig, high-resolution spectroscopy).[4] Due to the numerous successful applications of NLO to science, many different material classes were investigated towards their NLO activity. Among others, inorganic materials (nanocrystals, nanocomposites, quantum dots, nanowires, metal clusters, nanoparticles, organometallic complexes), organic materials (divers organic chromophores, porphyrins and

related macrocycles, phthalocyanines and related macrocycles, cyanine dyes, dendrimers), carbon-based materials (fullerenes, carbon nanotubes) or polymeric materials.[2]

Multi-photon absorption (MPA) is the simultaneous absorption of a number of photons in one single process (within a time window 10^{-8} s). MPA was first hypothesized by Göppert-Mayer in 1932[5] and experimentally shown in 1961 by Kaiser and Garrett.[6] It is the most straight forward and consequently also the most studied NLO process, so far.[7, 8] MPA has important advantages over conventional single photon absorption (focus and penetration depth), which has led to a multitude of applications, such as microscopy, micromachining and microfabrication, three-dimensional data storage, optical power limiting, up-converted lasing, photodynamic therapy and the local release of bio-active species.[7] Thus, the importance of the MPA process can be rationalized on the basis of the latter points and further provides an understanding of the need of MPA active materials. Because of the MPA process, low energy photons delivered in a short pulse can produce an equivalent effect as single photon absorption. Therefore, MPA can be regarded as a non-linear up-conversion process, opening the way for efficient frequency modulation. So far, an extensive amount of different materials was investigated for their MPA properties, among others a multitude of organic chromophores of different sizes, organometallic complexes or inorganic semiconductor materials (ZnO nanostructures, quantum dots, transition metal chalcogenide), to name a few.[8] For organic chromophores theoretical considerations alongside with extensive experimental investigations enabled to develop a straight forward theory of structure-property relationships in MPA active organic molecules. However, the synthesis of MPA active materials is either massively complicated by multiple-steps procedures or by a limited optical performance of the obtained materials.

The latter facts bring inorganic-organic hybrid materials, such as coordination polymers (CPs) and metal-organic frameworks (MOFs) to the foreground. So far MPA studies concentrated on layered organic-inorganic hybrid perovskite materials[9-11] and on CPs constructed from small organic ligands.[12] MPA studies on CPs and MOFs incorporating larger linker molecules are gradually increasing, at the moment.[13-20]

The underlying conceptual thinking of a MOF based approach for the synthesis of multi-photon absorbing materials is that by appropriate functionalization and subsequent coordination to a metal or metal-oxo center, small MPA active chromophores can be converted to stable and crystalline frameworks. Using topological considerations, the alignment of MPA linkers can be rationalized. The concept operates at different levels, however, has the overwhelming aim to increase and control the NLO response of small, MPA active units by targeted molecular assembly. The first level is located at the linker itself. Coordination to a metal node alongside with the enhanced strain by framework forces is minimizing radiationless decay pathways and can create linker geometries, which enhances charge transfer pathways in the organic scaffold (e.g. via planarization), thus increasing the MPA properties. Furthermore, polarization of the ligand electron density and introduction of metal-ligand interactions by push-pull effects of the metal can render NLO effects, which would not be found in the sole linker molecule. The last and probably most important point is found in intermolecular electrostatic interactions between specifically aligned molecules, which are the driving force for energy delocalization and have been shown to hold a tremendous effect on the non-linear absorption. Collective excited states in the framework of exciton theory are consistently used to describe the optical response of molecular aggregates or organic crystals and similar effects are thought to arise in CPs and MOFs, depending on the respective linker distances and alignment. Since the latter can be controlled in crystalline coordination networks (CCNs) via topological considerations, intermolecular interactions can be specifically targeted, potentially leading to enhanced MPA performance. The self-assembly process gives the opportunity to fix the position of the ligand and to determine, which structural factors have the biggest influence.[12]

From the above summarized facts, a couple of leading questions can be deduced, which might guide future work in the area of MPA active CPs and MOFs:

Q1: How can one design "small" ligand molecules with high MPA activity?

- What are possible synthons for the assembly of MPA ligands under MOF synthesis considerations?
- How does the connectors (carboxylic acids, pyridine, etc.) for incorporation in CCNs contribute to the push-pull characteristics of ligand motifs?
- Can we design MPA ligands with high rigidity of the molecular scaffold while holding expense π-electron systems with charge transfer characteristics?

Q2: Can chromophore aggregation in CPs and MOFs be controlled with topological tools?

- How can we specifically target the synthesis of polymorphic CPs and understand their formation?
- Can one deduce synthetic protocols for the targeted preparation of specific topological isomers?
- What is the grade of control in the materials design CPs and MOFs can offer to target a specific design of chromophore arrays?

Q3: How does the structure of CPs and MOFs influence their electronic structure, and what are the consequences for the non-linear optical properties?

- Can we understand the photo-response of CPs? Which models are suitable to describe the spectroscopic features? What is the nature of the excited state?
- What is the origin of potentially enhanced non-linear absorptivity in MPA-CPs? What aspects of the structure and composition controls size-enhancement? Can one correlate structure information and spectroscopic information?

In the following paragraphs, some of the above mentioned questions will be targeted and recent work on MPA active CPs and MOFs will be presented. The work starts with MPA ligand design and presents the synthesis of the used chromophore linkers throughout this thesis. The following chapter is concerning

with the synthesis and structural characterization of a series of pillar-layered MOFs incorporating aggregation enhanced emission dyes. This work is mainly focusing on local ligand effects. Chapter 2.3 investigates excitonic effects on two-photon absorption (TPA), and how the electronic structure of CPs, chromophore packing as well as the NLO properties are correlated to each other. Finally, chapter 2.4 investigates synthesis and structural aspects of polymorphic zirconium based MOFs incorporating push-pull chromophores.

The theory, which lays behind the presented work is extensive and spreads over a couple of different scientific areas. For an overview, the reader is referred to chapter 3, which should work as a theoretical background section, providing a more in depth discussion of reoccurring subjects and serving as an introduction to the respective topics. It further provides an up to date summary of MPA in CPs and MOFs.

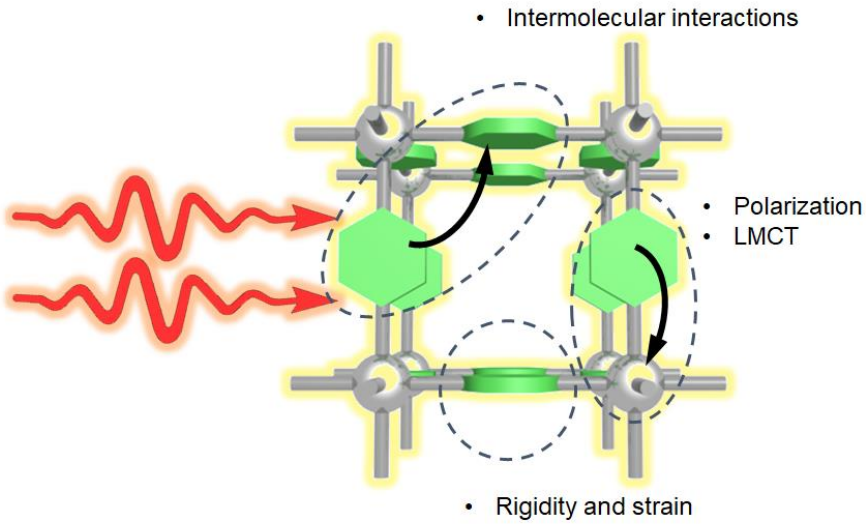

Figure 1. The different photophysical levels in CPs and MOF, adding functionality to the material: Ligand-metal interactions (right side), intermolecular interactions between ligands (upper left corner) and framework forces generating rigidity and strain to the linker (bottom centre).

2 Results and Discussion

2.1 Synthesis and characterization of tetratopic ligand structures for potential MPA active MOFs and CPs

2.1.1 Introductory remarks

The work presented in the following chapter is concerned with the synthesis and characterization of partially literature known and/or new potentially MPA active tetratopic ligands for the further incorporation in MOFs. In the course of the study, the synthesis and characterization of the organic ligands H_4TCPE[21] (tetrakis[4-((4-carboxylato)phenyl)phenyl]ethylene), H_4TBAPy [22](4,4',4'',4'''-(pyrene-1,3,6,8-tetrayl)tetrabenzoic acid) and H_4TPBD[20] (tetrakis(1,1′-biphenyl-4-carboxylic acid)-1,4-benzenediamine) are introduced. These ligands were used in the subsequent CP synthesis as (1) they fulfill the specifications for potential high non-linear response (extended π-electron systems, donor-acceptor groups, polarizable π-cores or AIE effects), (2) all molecules showed good fluorescence quantum-yields (prerequisite for measuring MPEF) and (3) were already been used in the construction of MOFs (H_4TCPE, H_4TCPE-F, H_4TBAPy). Another aspect are the topological properties of these ligand class. Tetratopic ligands are an interesting type of linkers, due to the topological diversity of the built networks and the fact that the MOF formation is largely depending on the geometry of the linkers (very pronounced for Zr^{IV}-MOFs). This opens the possibility to rationalize the MOF synthesis on the basis of ligand geometries (e.g. in the targeted synthesis of polymorphic structures). Finally, a couple of interesting molecular building blocks have been synthesized, which are also presented.

Tetratopic ligands can be rationalized on a common synthesis strategy (Figure 2). A tetra-halogenated organic building block (either bromo or iodo-functionalized) is subjected to cross-coupling reactions (Suzuki-coupling, Negishi-coupling, Stille cross-coupling, Buchwald-Hartwig coupling, Ullmann-reaction etc.).[23] These types of reactions normally proceed very smoothly with

tolerable to high yields. The challenge, however, lays in the separation of the byproducts, as often the mono, di or tri-substituted analogues are formed. The presented structures have been synthesized using literature known Suzuki cross-coupling procedures.[24] Separation from byproducts were performed by either column chromatography or recrystallization procedures. All organic compounds synthesized within this thesis were characterized by NMR, Raman and IR spectroscopy, mass spectrometry as well as elemental analysis. Please compare the experimental part for further details. Optical studies are presented in the pursuing chapters. Furthermore, single crystal structure analysis was conducted on all unknown compounds. For the case of the organic ligands in this work, the structure of H_4TCPE and H_4TBAPy are already documented.[21, 25] Attempts for the crystallization of H_4TCPE-F failed, however, Me_4TPBD could be successfully crystallized. A discussion of the respective structure can be found in the following paragraph.

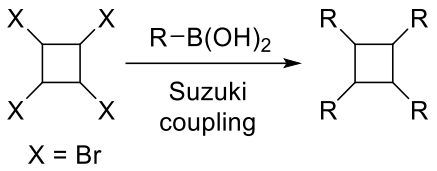

Figure 2. The general synthesis strategy for the implementation of tetratopic ligands pursued within this thesis. A suitable tetrabrominated building block, depicted by the square is reacted with a boronic acid using Suzuki cross-coupling procedures.

2.1.2 Synthesis of H_4TBAPy

The synthesis of the pyrene based ligand motif H_4TBAPy (4,4',4'',4'''-(pyrene-1,3,6,8-tetrayl)tetrabenzoic acid) was conducted following a procedure by Farha and Hupp et. al. (Scheme 1).[26] The Suzuki-Miyaura reaction between 1,3,6,8-tetrabromopyrene (from commercial suppliers) and (4-(ethoxycarbonyl)phenyl)boronic acid gave the ethyl ester variant, Et_4TBAPy. Subsequent Soxhlet extraction with chloroform over the course of 24 h was used to separate from byproducts. The clean Et_4TBAPy was basic hydrolyzed, filtered and thoroughly washed with excess water to give the ligand H_4TBAPy (~ 55 % yield over three steps). In the published procedure, the authors claim that the use of the (ethoxycarbonyl)phenylboronic acid is of importance, as the ethyl substituent slows down the kinetic rate of the formation of Et_4TBAPy,

leading to less formation of side-products. However, changing to the methoxy-variant of the boronic acid did not reveal any distinct differences in the reaction behavior. Furthermore, the use of a Soxhlet apparatus for the separation procedure is an elegant way in the purification of Et_4TBAPy (or Me_4TBAPy), as it circumvents the hot filtration with boiling chloroform (as suggested initially by Hupp et. al.).

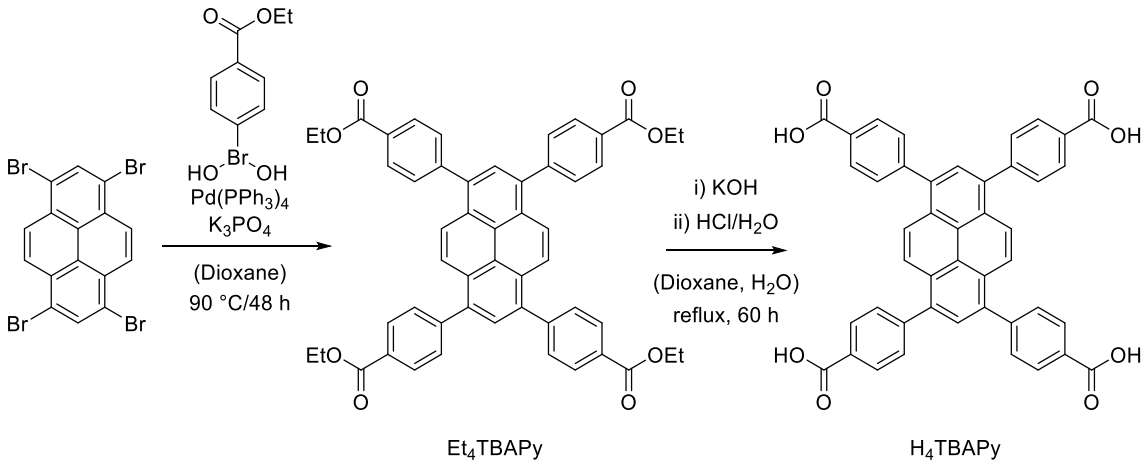

Scheme 1. Synthesis procedure of H_4TBAPy in a two-step synthesis starting from tetrabromoperylene.

2.1.3 Synthesis of H_4TCPE and H_4TCPE-F

The synthesis of H_4TCPE and its fluorinated analogue H_4TCPE-F was conducted for studying the influence of the fluorine substituent in the peripheral phenyl groups of the H_4TCPE moiety. The ligand synthesis starts with the synthesis of tetrakis(4-bromophenyl)ethene, which can be conducted as a solid-state reaction of tetrakisphenylethylene in a brome atmosphere (scheme 2).

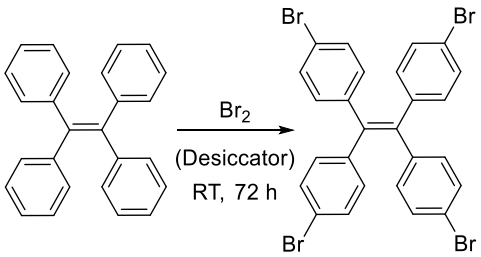

Scheme 2. Synthesis procedure for 1,1,2,2-tetrakis(4-bromophenyl)ethene.

Subsequent recrystallization of the raw product from acetone yields the tetrabromo-building block in high purity and very good yield (~ 95 %). The Suzuki-Miyaura coupling reaction of tetrakis(4-bromophenyl)ethene with (4-(methoxycarbonyl)phenyl)boronic acid under standard reaction conditions gave the methylester Me_4TCPE.[21] The reaction procedure uses cesium fluoride as a base. This fact seems to be important for the reaction. Exchanging CsF to other bases (K_3PO_4, K_2CO_3, Cs_2CO_3) showed a pronounced influence on the overall yield, with reaction losses of about 25 %. Me_4TCPE was purified by column chromatography, using dichloromethane/hexane mixtures (1:9). This step is important in obtaining very clean product. Similar level of purities can be obtained via several recrystallization steps using acetone, however, with lower overall yields. Subsequent basic hydrolysis of Me_4TCPE and acidification gave the final product, H_4TCPE in good yields (~ 55 %, scheme 3).

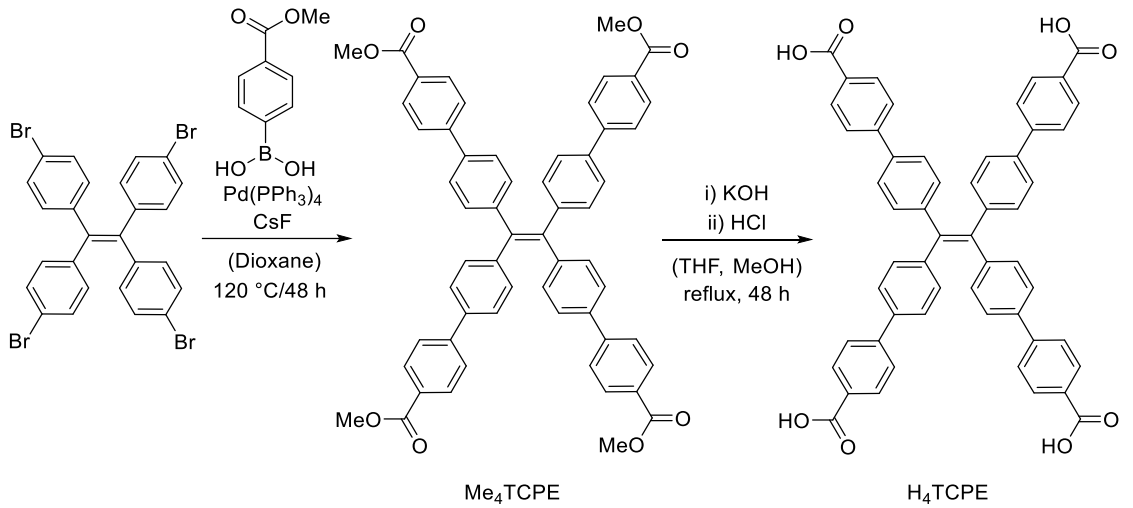

Scheme 3. Synthesis procedure of H_4TCPE via the tetrabromo building block tetrakis(4-bromophenyl)ethene.

The fluorinated analogue of H_4TCPE, H_4TCPE-F, was synthesized following the same procedure as describe above.[27] Suzuki-Miyaura coupling of tetrakis(4-bromophenyl)ethene with (3-fluoro-(4-methoxycarbonyl)phenyl)boronic acid yields Me_4TCPE-F. Subsequent basic hydrolysis followed by acidification gives the final product, H_4TCPE-F (~ 45 % over three steps). Separation from byproducts was accomplished by column chromatography (dichloromethane/hexane 1:9). Recrystallization of Me_4TCPE-F from acetone is also possible. However, due the slightly more polar character of Me_4TCPE-F

compared with Me_4TCPE, recrystallization even more negatively influences the overall yield.

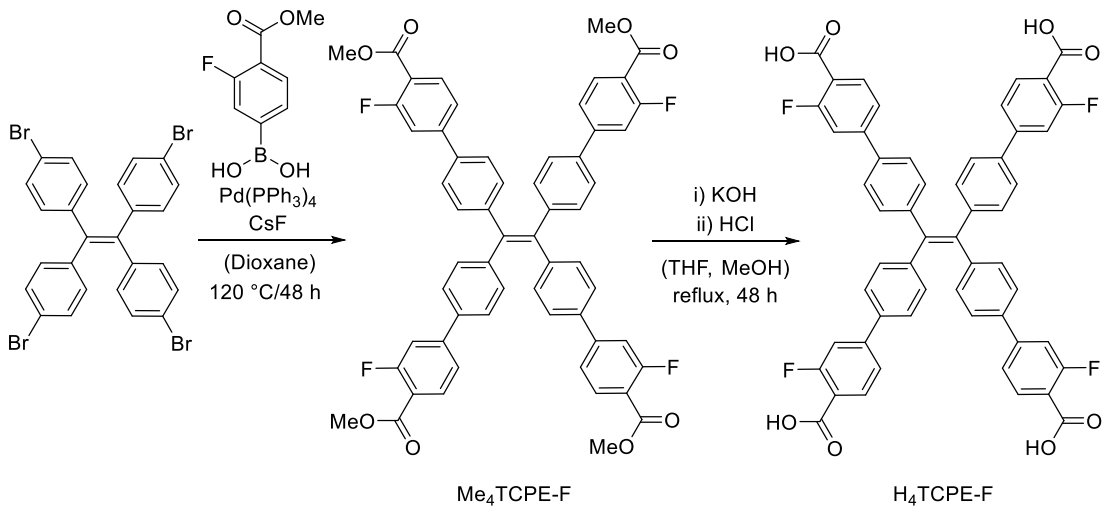

Scheme 4. Synthesis procedure of H_4TCPE-F via the tetrabromo building block tetrakis(4-bromophenyl)ethene.

2.1.4 Synthesis of H_4TPBD

The development of push-pull type MOF ligands in accordance with molecular design principles under MOF practicability clearly puts triphenylamine or carbazole based building units in the focus. The target compound, H_4TPBD, combines two V-shaped A-π-D-π-A quadrupolar building units, branched by a phenyl group thought to enable electronic communication between the quadrupolar units. This fact should enhance the charge-transfer network upon photo-excitation. H_4TPBD can be regarded as a moderate push-pull type ligand, where the acceptor group (the carboxylic acid group), as part of the molecular charge-transfer network, coordinates to the MOF SBU. Consequently, the acceptor ability is expected to become even more enhanced upon metal coordination.

The synthesis of H_4TPBD follows the same retrosynthetic strategy as introduced above. Tetraphenylbenzene-1,4-diamine is brominated using N-bromosuccinimide in dimethylformamide to yield the tetrabromo building block tetrakis(4-bromophenyl)-benzene-1,4-diamine. The latter is further coupled with (4-(methoxycarbonyl)phenyl)boronic acid under Suzuki-Miyaura cross-coupling conditions to give Me_4TPBD. The methylester actually is very soluble in

chloroform and partly soluble in dichloromethane (solubility test showed very good solubility in chloroform and ethylacetate, moderate solubility in acetone, dichloromethane and alcohols). Basic hydrolysis and subsequent acidification gave the target compound, H_4TPBD, in an overall yield of ~ 35%. Purification of Me_4TPBD was accomplished by hot washing with dichloromethane and subsequent cooling to -30°C. This procedure gave the product in very good purity, however, with rather low yields. The main problem in the synthesis of H_4TPBD thus was found to be the purification of the methylester. Attempts for column chromatography were impeded by the high chemical similarity of the side-products (single, double and triple substituted moieties), expressed by similar R_f values of the compounds in different solvent combinations (strongly pronounced smearing behavior). The best combination was found to be ethylacetate/toluene (2:8, R_f = 0.2), however, several attempts for purification of Me_4TPBD via column chromatography using the above solvent combination failed, due to pronounced smearing and merging of different fractions. Consequently, recrystallization cycles in dichloromethane and consequent recapturing of mother liquors enabled the synthesis of the ligand in a ~ 300 mg scale (scheme 5, 6 and 7).

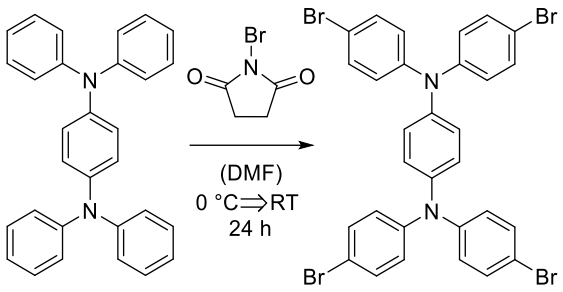

Scheme 5. Synthesis of N^1,N^1,N^4,N^4-tetrakis(4-bromophenyl)benzene-1,4-diamine from tetraphenylbenzene-1,4-diamine using N-bromosuccinimide as a mild bromination agent.

Single crystals suitable for single-crystal structure analysis were grown via slow evaporation of pentane into a chloroform solution of Me_4TPBD. The compound crystallizes as small and thin clear yellow plates in the triclinic space group $P\bar{1}$ with Z = 2 (R_1 = 0.049, wR_2 = 0.121, R_{int} = 0.0674). The asymmetric unit consist of one molecule Me_4TPBD. The distances of C-C, C-N C-O bonds lay in ranges as expected for organic molecules. The torsional angles of the triphenylamine moieties is found to be ~ 34°. The torsional angles of the

biphenyl groups show values of ~ 19° and ~ 37°. The ligand shows an overall rectangular shape with distances of the carboxylic C-atoms of ~ 14 Å and ~ 17 Å. The packing of the compound is dominated by a high amount of dispersive interactions between the neighbored biphenyl arms, mainly $C_{arom}H\cdots\pi$ and $C_{arom}HO$ type interactions (characteristic distances of ~ 2.62 – 2.89 Å). The Me_4TPBD molecules show side-slipped coplanar packing along the crystallographic c-axis forming molecular stacks (compare Figure 3).

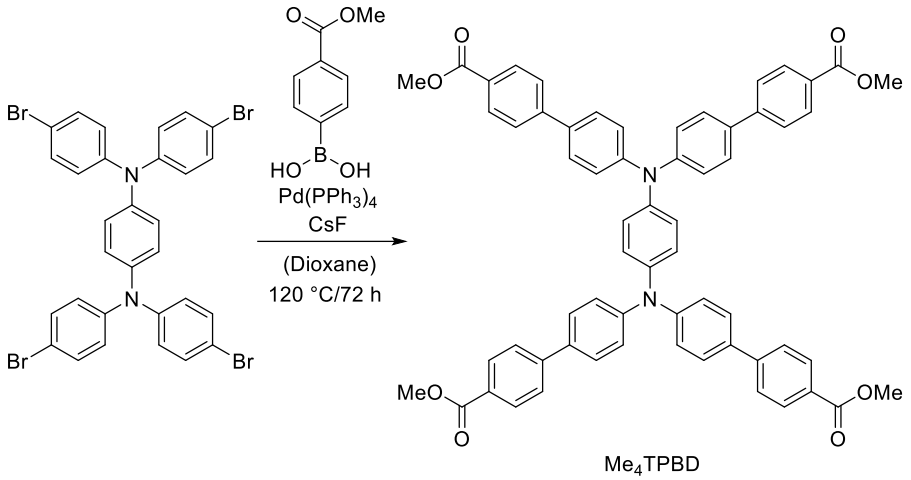

Scheme 6. Synthesis of Me_4TPBD starting from tetraphenylbenzene-1,4-diamine applying classical Suzuki cross-coupling conditions.

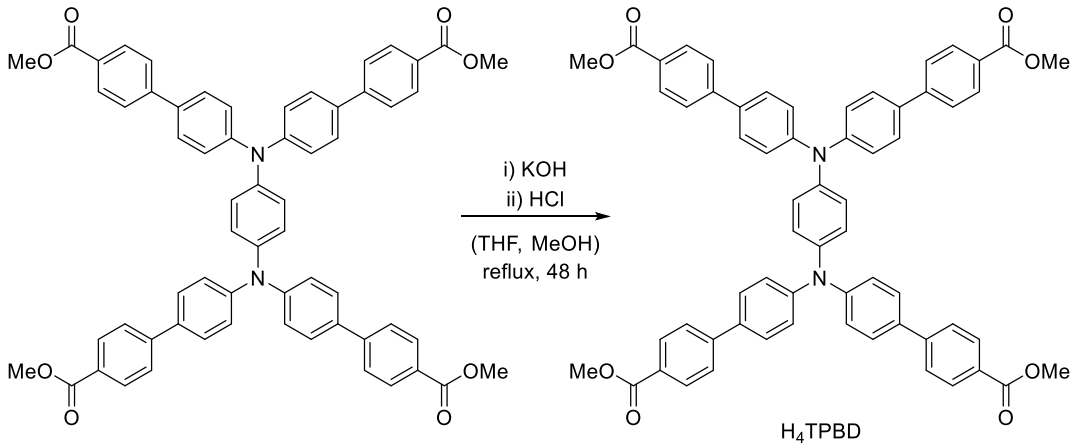

Scheme 7. Synthesis of H_4TPBD via basic hydrolysis of the methylester Me_4TPBD and subsequent acidification.

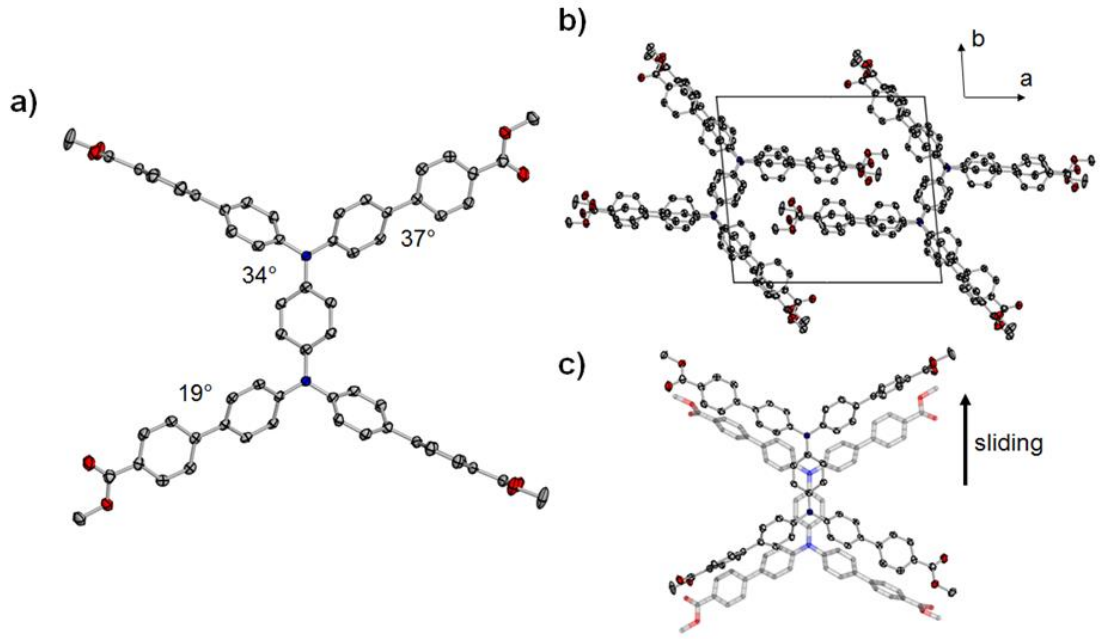

Figure 3. Single crystal structure of Me_4TPBD. All ellipsoids are at the 50% probability, H-atoms have been omitted for clarity. a) The molecular structure of Me_4TPBD with the important torsional angles. b) The packing along the crystallographic c-axis. The figure shows two Me_4TPBD stacks with interacting biphenyl side arms holding the overall structure together c) The molecular sliding of a Me_4TPBD dimer within a stack. The arrow shows the sliding direction. Grey: carbon; red: oxygen; blue: nitrogen.

2.1.5 Synthesis of carbazole based building units for further attempts of MPA ligands

As has already been stated in the introduction part of this chapter, phenylamine or carbazole based units constitute interesting building units for MPA ligand synthesis in MOF chemistry. Consequently, the successful synthesis of H_4TPBD was tried to pursue in accessing a new tetratopic carbazole based ligand, namely (1,4-phenylenebis(9H-carbazole-9,3,6-triyl))tetrabenzoic acid. The initial idea was that by using carbazoles in the synthesis of this ligand, the π-electron system should be stronger delocalized, as the phenyl rings are forced to be more planar. Figure 4 shows the anticipated molecule and retrosynthetic steps, which were followed in the synthesis attempts. Even though the targeted linker molecule could not be successfully synthesized, two interesting building blocks for further studies could be prepared, namely 1,4-bis(3,6-dibromo-9H-carbazol-9-yl)benzene and dimethyl 4,4'-(9H-carbazole-3,6-diyl)dibenzoate. For the synthesis of 1,4-bis(3,6-dibromo-9H-carbazol-9-yl)benzene, 1,4-di(9H-carbazol-9-yl)benzene was

synthesized from carbazole and 1,4-diiodobenzene by Ullmann coupling. Subsequent bromination of 1,4-di(9H-carbazol-9-yl)benzene yielded the tetrabromo building block in excellent yields. Attempts for Suzuki-Miyaura cross-coupling using (4-(methoxycarbonyl)phenyl)boronic acid and 1,4-bis(3,6-dibromo-9H-carbazol-9-yl)benzene failed due to the very low solubility of the potential target compound in almost all tested solvents. Because of the latter fact, the molecule deprived from any purification procedure as well as analytics.

The second retrosynthetic attempt comprised of the initial synthesis of the A-π-D-π-A “side-arm” dimethyl 4,4'-(9H-carbazole-3,6-diyl)dibenzoate following Suzuki-Miyaura cross-coupling procedures of 3,6-dibromocarbazole and (4-(methoxycarbonyl)phenyl)boronic acid to give dimethyl 4,4'-(9H-carbazole-3,6-diyl)dibenzoate in moderate yields. Subsequent Ullmann-coupling with 1,4-diiodobenzene showed similar problems as found for the Suzuki-coupling reaction pathways, which could be assigned to the potential low solubility of the targeted compound.

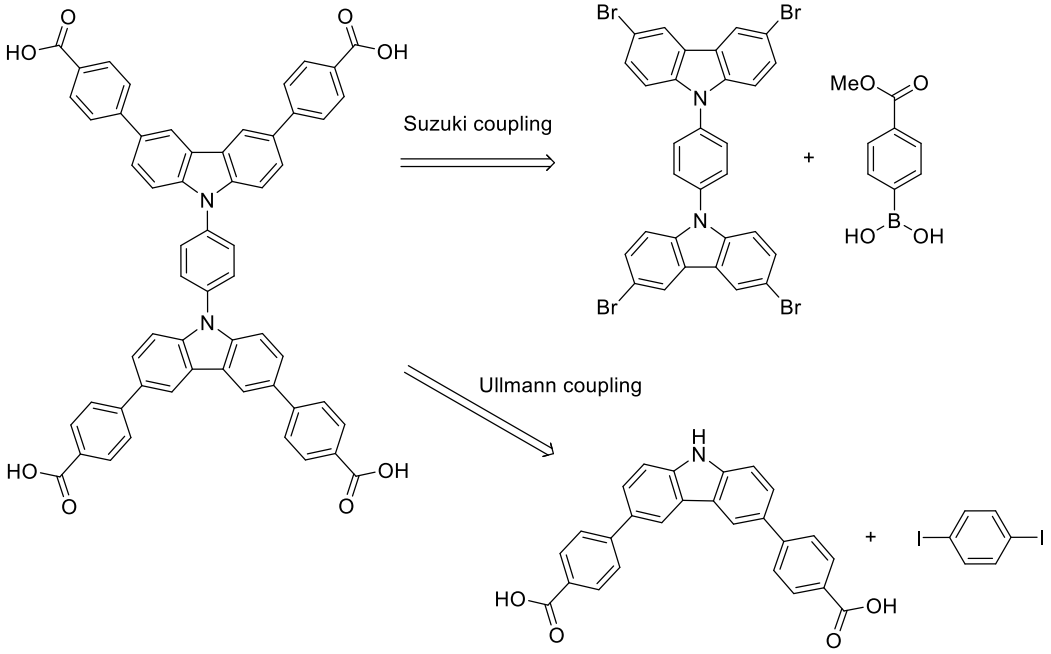

Figure 4. Retrosynthetic steps followed in the synthesis attempts of (1,4-phenylenebis(9H-carbazole-9,3,6-triyl))tetrabenzoic acid by either Suzuki coupling using 1,4-bis(3,6-dibromo-9H-carbazol-9-yl)benzene (Suzuki coupling route) or dimethyl 4,4'-(9H-carbazole-3,6-diyl)dibenzoate (Ullmann coupling route).

2.1.6 Closing remarks

The presented successful synthesis approaches for H_4TBAPy, H_4TCPE, H_4TCPE-F and H_4TPBD enabled the further incorporation of these ligands in MOF materials. These types of linkers were chosen for MPA studies due to the already indicated reasons in the beginning of this chapter. Since H_4TPBD is a new developed ligand type without any implementation in CPs or MOFs, synthetic approaches for new CNN materials were focusing on this ligand. Furthermore, H_4TPBD constitutes a linker type within the push-pull terminology. H_4TCPE and H_4TCPE-F were chosen due to the already successful work of H_4TCPE based MPA-MOFs in our group extending over a couple of TCPE based framework materials.[19, 28] The aim was to expand the number of MPA studies on AIE-MOFs, as well as looking into induced effects (sterically or electronically) by ligand modification (H_4TCPE and H_4TCPE-F). Finally, H_4TBAPy was initially chosen due to the great number of interesting MOFs with this ligand. Among TBAPy based CPs, the MOFs NU-901 and NU-1000 are a very interesting platform for studying structure-property relationship, as these compounds are polymorphic structures and thus contain the same stoichiometry but hold differing ligand orientations.[29, 30] Within this thesis, different literature known synthesis attempts for NU-1000 and NU-901 were followed with the aim to provide a synthetic protocol for the phase-pure synthesis of the two polymorphic structures for potentially further NLO characterizations. Since so far no MPA studies could be performed on these materials and the linear photophysical properties of NU-901 and NU-1000 are already sufficient described, there will be no further discussion about non-linear optical properties of that materials. The modified synthetic protocols and special characteristics concerning the synthesis of NU-901/NU-1000 are given in the experimental part (see chapter 5.1.19). In closing this chapter, the molecular building units successfully synthesized within the synthesis attempts for carbazole based push-pull ligands constitute an interesting starting point for further ligand development.

2.2 Aggregation induced emission dyes as potential ligand class for multi-photon absorbing CPs and MOFs

2.2.1 Introductory remarks

Aggregation of molecules into a dense phase will change the underlying optical properties in a manifold of ways. Often, aggregated molecules will feature lower quantum yields and deteriorate emission properties in the solid state, due to the formation of non-emissive (dark) states. This behavior is typically called aggregation caused quenching (ACQ). Undoubtedly, this effect is a major impediment to a number of applications of organic aggregates and related materials and also an obstacle when applications of CPs or MOFs are considered relying on multi-photon induced emission. Tang and co-workers where the first to reveal some class of organic molecules, which show the invers effect of ACQ, so called aggregation induced emission (AIE) or sometimes referred to as crystallization induced emission (CIE).[31] The AIE effect has sparked enormous interest due to its great potential in a wide area of photophysical applications.[32-34] The fundamental mechanism that underlies the AIE effect was found to originate from a restriction of nonradiative relaxation pathways (intramolecular vibrations and rotational motions).[35] The tetraphenylethylene (TPE) unit has been shown to be a highly interesting AIE-active molecule.[36] The incorporation of TPE based ligands as a scaffold in CPs relying on the AIE effect, has further been shown to be a prospective strategy to suppress intermolecular motions similar to self-aggregation.[37, 38] Indeed, a great number of studies on this type of ligands as structuring unit of CPs have been published and a detailed analysis of the underlying mechanisms of fluorescence enhancement was conducted. For example, a number of luminescent MOFs as potential light phosphors or chemical sensor have been investigated.[39] As has already been elucidated in the introduction of this thesis, our group was among the first to study non-linear optical properties of highly-emissive MOFs comprised of AIE ligands.[19, 28] MOFs based on the H_4TCPE ligand (see also chapter 4.6.2) were shown to hold extremely high values of two-photon brightness, compared to the parent linker molecule. This work impressively showed that the incorporation of ligands featuring AIE characteristic into CPs

can significantly enhance the non-linear absorption response. Furthermore, a comprehensive electronic structure calculation study revealed that the local ligand conformation is responsible for the differences in the non-linear absorption found in these materials.

Despite the collected data on two-photon absorption of AIE-based MOFs so far (our group and other works), open questions such as the limitation of this approach in terms of self-confining ligand structures etc. remain poorly addressed. The presented work in this paragraph deals with the TPA properties of two porous isostructural pillar-layered MOFs based on the already introduced H_4TCPE and H_4TCPE-F ligands. These type of MOFs are not capable of strong self-confining the ligands intramolecular vibrational and rotational motions (according to SXCRD analysis) and thus demonstrate an interesting platform for studying the non-linear optical response as a function of linker confinement. The key point of the presented study is to further investigated AIE ligands as structuring units in the construction of MPA active CPs and MOFs. The work is structured as follows. The synthesis and structural characterizations of a series of TCPE based pillar-layered MOFs is introduced. Upcoming difficulties in the synthesis of the MOFs are discussed and rationalized on structural arguments within the pillar-layered MOF series. The non-linear optical characterization of two isostructural MOFs is presented. Furthermore, it is shown that thermal activation of the materials leads to a collapsed framework, which holds its connectivity as proven by IR and Raman spectroscopic analysis. The low-crystalline material formed upon structure transformation of the pillar-layered MOFs is further characterized in terms of non-linear absorption and the measured values are shown to be considerable increased by a contraction process. The enhanced non-linear response of the contracted framework materials is discussed in terms of structural arguments accompanied by a potentially enhanced self-confining of the TPE based ligands in the collapsed frameworks.

2.2.2 Synthesis attempts and structural characterization of pillar-layered MOFs [Zn_2(TCPE)(X)]

The solvothermal reaction of H_4TCPE with $Zn(NO_3)_2 \cdot 4\ H_2O$ and a series of bipyridine pillar molecules (bpy = 4,4-bipyridine, bpee = 1,2-bis(4-pyridyl)ethene, bpea = 1,2-bis(4-pyridyl)ethane and azpy = 4,4-azopyridine) in different formamides (DMF, DMAc, DEF) water/alcohol (MeOH, EtOH) mixtures achieved pillar-layered MOFs with the formal composition of [Zn_2(TCPE)(X)] (X = bpy, bpee, bpea, azpy) as bright, yellow (red for the azpy compound) powders following literature protocols.[39] All pillar-layered MOFs could be characterized by SCXRD analysis, which revealed a similar structural situation within the compounds. However, bulk characterization of the materials proved to be very difficult, as the collected PXRD data showed several deviations in expected reflex positions and intensities, compared to the theoretical pattern based on the structural model by SCXRD analysis. Consequently, the initial synthesis conditions were systematically varied to access higher crystalline materials. The following table gives an overview about the synthesis attempts.

Table 1. Synthesis conditions for the reaction screening of pillar-layered MOFs [Zn_2(TCPE)(X)]. Different target temperatures were accessed either via heating (cooling) rates or direct heating of the reaction mixtures within a programmable oven. The overall reaction time was limited to 24 (48) hours. Different reaction mixtures in differing ratios were used, in which MeOH, EtOH and water were applied as modulators (main component is the formamide). The overall amount of solvent was limited to 4 mL.

Temperature	**80 °C, 100 °C, 120 °C**		
Time	24 h, 48 h		
Heating rate	none, 0.5 – 0.8 °C/min		
Cooling rate	none, 0.1 – 0.2 °C/min		
Equivalents	$Zn(NO_3)_2 \cdot 4\ H_2O$ 2 eq.	bis-pyridine 2 eq.	H_4TCPE 1 eq.
	DMF	*DMAc*	*DEF*
MeOH	0.1-0.25	0.1-0.25	0.1-0.25
EtOH	0.1-0.25	0.1-0.25	0.1-0.25
MeOH/H_2O	0.1-0.25/0.05	0.1-0.25/0.05	0.1-0.25/0.05
EtOH/H_2O	0.1-0.25/0.05	0.1-0.25/0.05	0.1-0.25/0.05

The majority of the conducted experiments showed the formation of either amorphous, low- crystalline materials or the formation of impurities (intermediate phases). In principle, the synthesis of the materials proofed to be sensitive against high amounts of water and long reaction times. Furthermore,

possibly differing amounts of incorporated reaction solvent (ca. 40 % accessible void as determined by PLATON squeeze for the compounds) influenced the position and intensity of PXRD reflexes, which affected the analysis of PXRD data. In summary, reaction condition screening enabled the synthesis of a phase-pure bulk material for the pillar-layered MOF [Zn_2(TCPE)(bpy)]. However, the other compounds could not be synthesized to a satisfactory grade of purity (compare the given PXRD data). It should be noted that the provided literature protocol of [Zn_2(TCPE)(bpy)] did not led to a satisfactory quality of MOF material.[39] The most successful approach is summarized as follows. A bipyridine solution of MeOH was slowly layered over a H_4TCPE/ $Zn(NO_3)_2$·4 H_2O solution in DMF. The reaction mixture was allowed to react at a temperature of 100 °C for 24 h and further cooled to RT outside the oven. The quality of the so-obtained MOF materials is shown in figure 5 as depicted by PXRD studies.

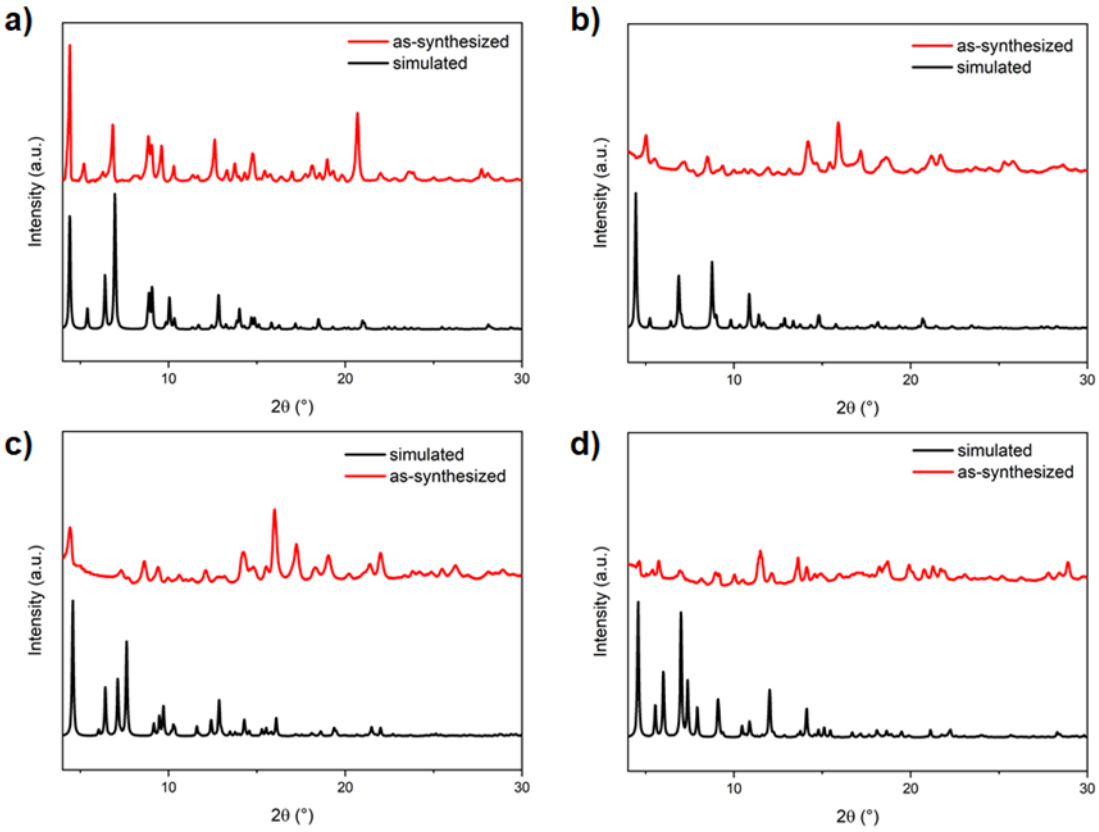

Figure 5. PXRD data of the several pillar-layered MOFs in a range from 4 to 30°. a) [Zn_2(TCPE)(bpy)] b) [Zn_2(TCPE)(bpee)] c) [Zn_2(TCPE)(bpea)] d) [Zn_2(TCPE)(azpy)]. Note that the deviation in intensity found for (a) is ascribable to preferred crystal orientations and probably due to solvent incorporation.

As has been stated above, SCXRD analysis revealed a similar structural situation in all compounds. Although the MOFs [Zn_2(TCPE)(X)] (X = bpee, bpea, azpy) could not be synthesized as bulk materials, SCXRD analysis was possible. All materials showed the formation of yellow respectively red polycrystalline powders, which were permeated by cubic blocks. The analysis of the structures can give some insight about possible reasonings, why [Zn_2(TCPE)(X)] (X = bpee, bpea, azpy) withdraws from satisfactory synthesis as bulk materials. Very recently, Maspoch and Guillerm presented an extensive analysis about geometry mismatch in the topological guided synthesis of MOFs and CPs.[40] They claimed that the connection of apparently incompatible building blocks in assembly of CPs can induce structural irregularity. The structural analysis of [Zn_2(TCPE)(X)] (X = bpee, bpea, azpy) suggest a similar mechanism for these materials, which could provide an option to understand the synthesis problems.

All MOFs crystallize in the triclinic space group $P\bar{1}$ besides [Zn_2(TCPE)(bpee)], which crystallizes in the monoclinic space group $P2_1/n$. The MOFs are isoreticular and comprise of zinc based secondary building units in paddlewheel geometry which are connected by TCPE ligands to form rectangular grids $[Zn_2(TCPE)]_\infty$. Such grids are further connected by the bipyridine pillars to form a pillar-layered structure in **fsc** topology. The $[Zn_2(TCPE)]_\infty$ grids hold a dimension of ~16 x 20 Å and the layers are separated by ~14 Å. All MOFs are twofold interpenetrated, with the zinc paddlewheel SBU of a sub-framework located near the edge of the second sub-framework. Furthermore, the $[Zn_2(TCPE)]_\infty$ grids of each sub-framework are separated by distances of ~ 6 Å. Despite the interpenetration, the MOFs still contain ~40 % accessible void per unit cell, according to PLATON.[41] Figure 6 exemplarily reveals the structure situation for [Zn_2(TCPE)(bpy)], which also holds for the other compounds. Figure 22 b shows the **fsc** frameworks for the remaining MOFs. Structural details are further given in the experimental section.

As can already been seen by visual inspection of figure 7, the incorporation of bpee, bpea and azpy indeed introduces a structural distortion in the pillar-layered MOFs which leads to a deformation of the Zn^{II} based paddlewheel complexes as well as a shearing of the $[Zn_2(TCPE)]_\infty$ grids with respect to each

other, which is most pronounced for the bpea ligand. The perfectly arranged **fsc** topology would request, however, a linear pillar molecule (please note that the symmetry embedding of a **fsc** topology follows the $P4/mmm$ space group).

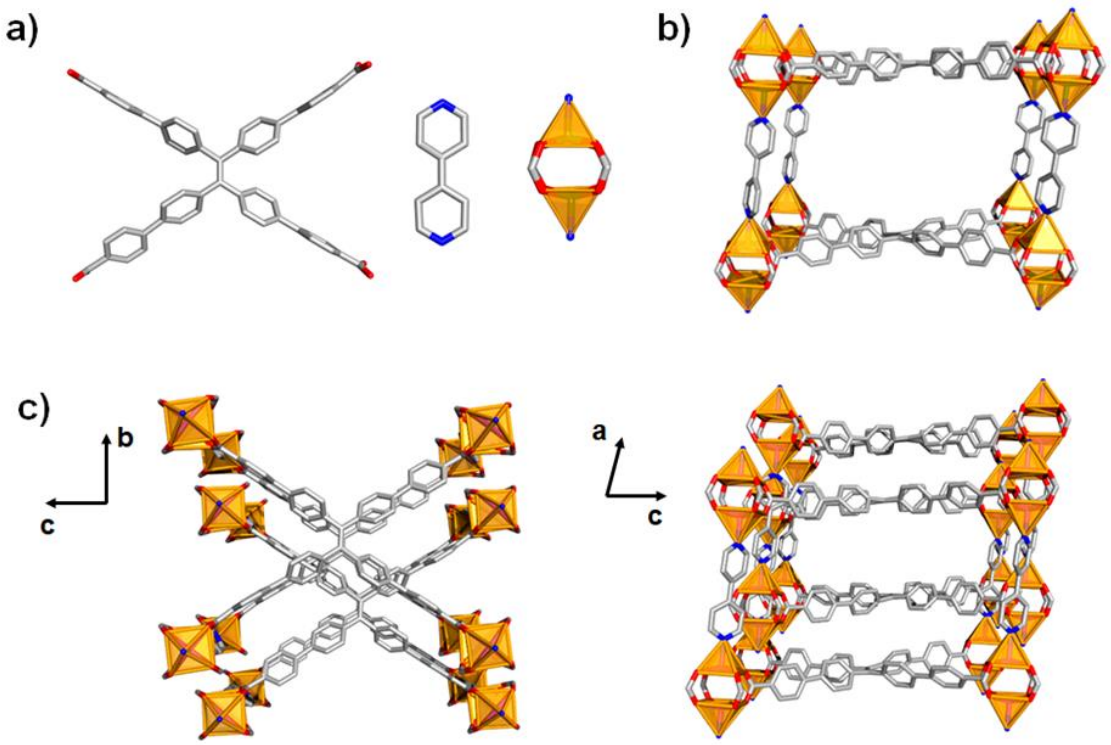

Figure 6. a) Depiction of the building blocks to assembly [Zn_2(TCPE)(bpy)]. b) A sub-framework shown as **fsc** network as found in the interpenetrated structure. c) The structure of [Zn_2(TCPE)(bpy)] along the crystallographic *a* and *b* axis depicting the twofold interpenetration in the pillar-layered MOFs.

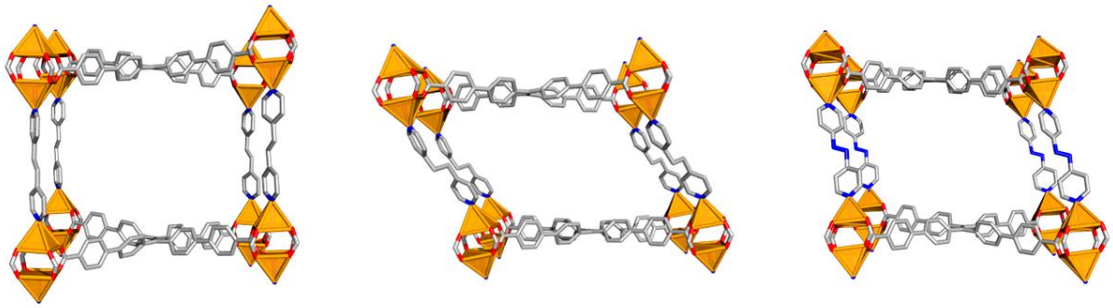

Figure 7. The **fsc** sub-frameworks as found in [Zn_2(TCPE)(bpee)], [Zn_2(TCPE)(bpea)] and [Zn_2(TCPE)(azpy) with an sideview along the TPE core of TCPE.

Interestingly, the bpy ligand does match this prerequisite best. Also, the synthesis procedure as described above showed to deliver the highest quality material of pillar-layered MOFs for the bpy compound [Zn_2(TCPE)(bpy)]. Figure 8 summarizes the introduced distortion in the paddlewheel complexes. Figure 9 shows the introduced geometry mismatch from a linear geometry (as needed for **fsc** topology) to a zigzag mode.

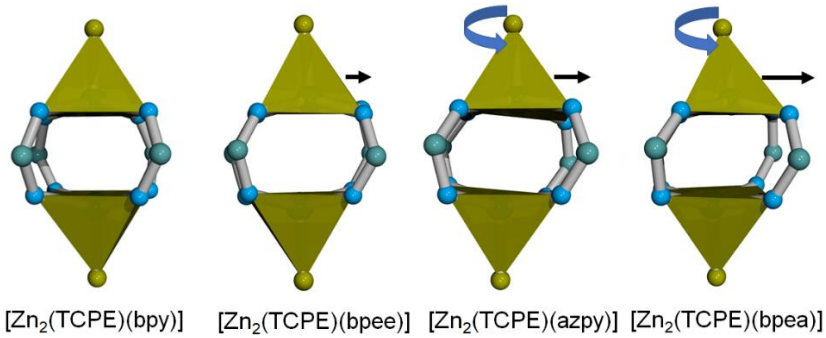

Figure 8. Zn^{II} paddlewheel complexes as found in the pillar-layered MOF series and the distortion introduced by the geometry mismatch of the bpee, azpy and bpea ligands. The distortion can be described by two parameters, the shearing of the pentagonal pyramids (depicted by the black arrows) as well as the introduced twist (blue arrow). Grey: carbon; Light blue: oxygen; Green: nitrogen.

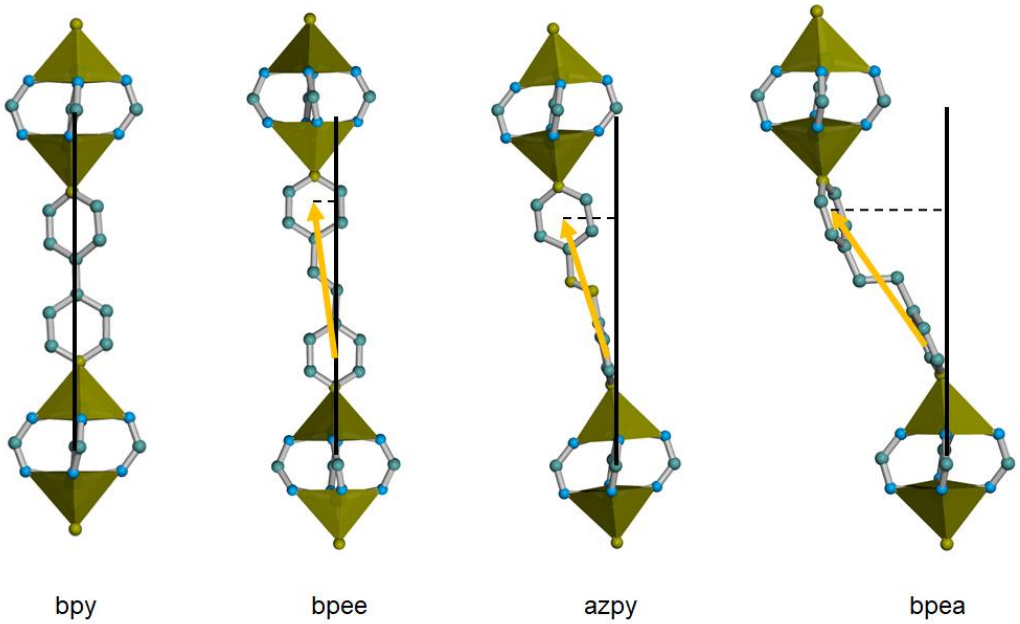

Figure 9. A schematic representation of the induced geometry mismatch in the series of pillar-layered MOFs under investigation. When going from bpy to bpea the angle of the “perfect” default orientation (linear) as required in the **fsc** topology enhances (black line as orientation for the eye, orange arrow shows the connection of the phenyl centroids, dashed lines reveal the angle of deviation). Grey: carbon; Light blue: oxygen; Green: nitrogen.

The structural analysis therefore suggest that the reason for problems in the bulk synthesis of the pillar-layered MOFs incorporating bpee, bpea and azpy co-ligands might be due to a induced deviation from the default **fsc** topology. To be more precise, the greater twist in the bipyridine co-ligand when going from bpy to bpea alters the direction of the paddlewheel complexes in the MOFs and with that induces distortion in the Zn^{II} SBUs alongside with a shearing of the $[Zn_2(TCPE)]_\infty$ grids, according to the structure analytics. Consequently, the inclination of the paddlewheel complexes from their perfect orientation seems to influence the crystallization process, as it introduces differing binding modes in the coordination of the carboxylic acids (rotation along the Ph-COOH axis). Indeed, it could be shown that combining, for example, paddle wheel complexes with bent ditopic ligands favors the formation of isolated metal-organic polyhedra (MOPs).[40]

Finally, induced geometry mismatch in the series of pillar-layered MOFs seems to have an influence on the synthetic outcome, when analyzing the single crystal structure results. However, the extent of such effects is still under debate and a topic of ongoing research in the MOF community (compare the work by Maspoch and Guillerm or Kieslich and Cheetham).[40, 42] The presented analysis, nevertheless, can provide an approach to rationalize the found synthetic problems on a structural level, but it should be pointed out that the crystallization processes in the formation of MOFs and related materials is a multi-parameter process and far from being understood in detail.

At this point, literature screening of further H_4TCPE based pillar-layered frameworks revealed another MOF of similar stoichiometry and structure as the presented materials, $[Zn_2(TCPE)(bib)]$.[39] This MOF, however, does not incorporate a bipyridine based pillar motif, but a pillar constructed from *bis*-imidazole (bib = 1,4-di(1H-imidazol-1-yl)benzene). Interestingly, the bib ligand shows a pronounced deviation from a linear arrangement, with a strong zig-zag distortion. However, an analysis of the N-donor unit reveals that the imidazole ring enables a linear coordination of the zinc paddlewheel complex, whereas in the case of $[Zn_2(TCPE)(bpee)]$, $[Zn_2(TCPE)(bpea)]$ and $[Zn_2(TCPE)(azpy)]$, the N-donating pyridine is stronger turned outwards with higher zig-zag deviation. This fact also points towards a difficile dependence on the strength of the N-

donor type and the coordination possibilities, which are ultimately defined by the pillar geometry. Note that imidazole N-donors are stronger (up to factors of 2-3) then pyridine N-donors with similar pK_a-values.

2.2.3 Post-synthetic framework construction of $[Zn_2(TCPE)(bpy)]$ and $[Zn_2(TCPE\text{-}F)(bpy)]$

Based on the synthetic findings and with access to the new TPE-AIE MOF $[Zn_2(TCPE)(bpy)]$ the spectrally-resolved TPA properties of two isostructural and isoreticular MOFs, namely $[Zn_2(TCPE)(bpy)]$ and $[Zn_2(TCPE\text{-}F)(bpy)]$ could be investigated. The latter is the fluorinated analogue of $[Zn_2(TCPE)(bpy)]$, was initially synthesized by Li et. al. and is also referred to as LMOF-301. $[Zn_2(TCPE\text{-}F)(bpy)]$ is based on the $H_4TCPE\text{-}F$ ligand, as introduced in chapter 2.1.3 of this thesis. The two MOFs are an interesting class for studying structure-property relationships of AIE based CPs, due to several reasons. First, the fact that both materials are isostructural will diminish structural related effects on the TPA properties, when the results are compared to each other (to a first order). Secondly, the crystal structure analysis reveals that the TPE cores in the TCPE/TCPE-F ligands of the MOF hold deserve disordering, which suggest that the confinement of the AIE ligands induces less steric forces on the TPE cores, which directly influences the optical properties of the compounds. It should be noted that phenyl ring flipping primarily contributes to enhance the radiationless decay rate of the excited state of TPE. Thirdly, the effect of the fluorine is not thought to affect the electronic properties of the ligands, but rather is thought to influence the structural and sterical aspects in this material class. The materials are shown to undergo a framework collapse upon thermal activation. The so formed materials are analyzed among others using Raman and IR spectroscopic techniques and it is revealed that the collapsed MOFs retain their network connectivity but loose crystallinity. The contracted frameworks interestingly show higher TPA efficiencies than their crystalline counterparts, which underpins the initial assumption that the ligand confinement induced by the framework forces among others dictate the non-linear absorption properties of that material class.

The synthesis of [Zn_2(TCPE)(bpy)] followed the protocol as given above and in the experimental section. The synthesis of [Zn_2(TCPE-F)(bpy)] followed the literature protocol, with partially improvements based on the experiences as gained in the synthesis of [Zn_2(TCPE)(bpy)].[27] The MOFs were thoroughly characterized using PXRD, TGA, Raman and IR spectroscopy and solid-state ^{13}C CPMAS NMR spectroscopy (also compare the experimental part). The provided structure for [Zn_2(TCPE-F)(bpy)] from the literature source shows a triclinic space group $P\bar{1}$ with one ligand TCPE, two Zn^{2+} ions and one 4,4-bipyridine ligand in the asymmetric unit (Z=2). The single crystal structure of [Zn_2(TCPE-F)(bpy)] follows the description of [Zn_2(TCPE)(bpy)] almost identically. The MOF comprises of zinc based secondary building units in paddlewheel geometry which are connected by TCPE-F ligands to form rectangular grids [Zn_2(TCPE-F)]$_\infty$. These grids are connected by the 4,4-bipyridine pillar motif to form a network in **fsc** topology. The [Zn_2(TCPE-F)]$_\infty$ grids hold similar dimensions as found in [Zn_2(TCPE)(bpy)] . [Zn_2(TCPE-F)(bpy)] is twofold interpenetrated, with the zinc paddlewheel SBU of a sub-framework located near the edge of the second sub-framework. The sub-frameworks are separated by similar distances as found in the TCPE-variant. Both MOFs show a considerable amount of incorporated solvent, which was treated as diffusive contribution to the electron density by the PLATON squeeze procedure. The PXRD patterns of [Zn_2(TCPE)(bpy)] and [Zn_2(TCPE-F)(bpy)] were proven by Pawley refinement and were shown to be in good accordance with the results from SCXRD data (Figures 10 and 11).

Solvent exchange of the as-synthesized materials and subsequent thermal activation revealed a structural transformation of the pillar-layered MOFs with a loss of crystallinity, as evident in the PXRD patterns. The solvent exchanged MOFs showed the formation of a semi-crystalline phase, which did not allow for satisfactory indexing of unit-cell parameters (Figures 12 and 13). The structural composition of the activated materials was further analyzed by IR and Raman spectroscopy and N_2 adsorption measurements.

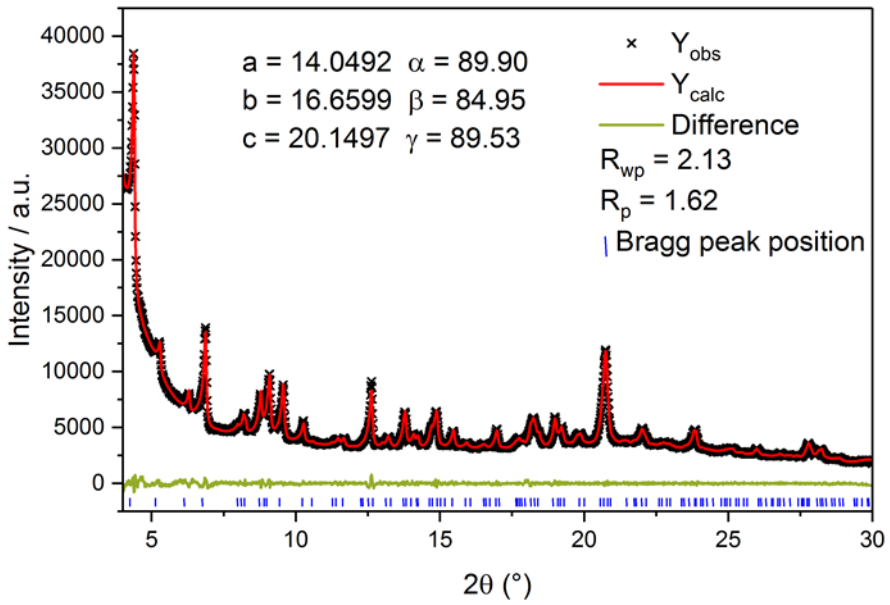

Figure 10. Pawley refinement data of [Zn_2(TCPE)(bpy)] and the corresponding fit parameters at a range of 3-30°. The obtained crystal parameters are in good agreement with the single crystal X-ray data (a = 13.9758(7), b = 16.3474(8), c = 20.2980(10), α = 89.948(5), β = 83.096(5), γ = 89.209(5)). Blue ticks mark the allowed Bragg reflection in the corresponding space group ($P\bar{1}$).

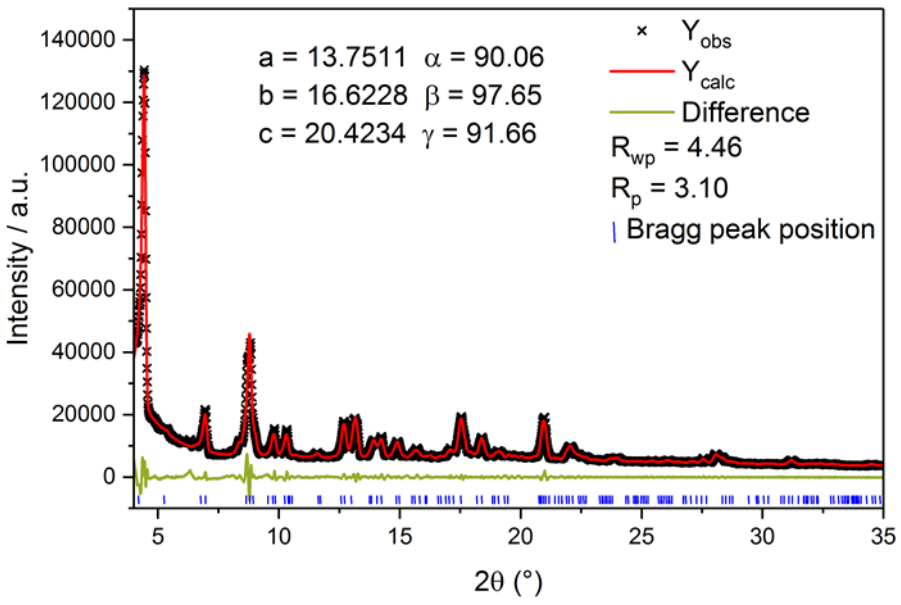

Figure 11. Pawley refinement data of [Zn_2(TCPE-F)(bpy)] and the corresponding fit parameters at a range of 3-30°. The obtained crystal parameters are in good agreement with the single crystal X-ray data (a = 13.967(5), b = 15.480(5), c = 20.893(5), α = 90.064(2), β = 99.260(2), γ = 91.46782)). Blue ticks mark the allowed Bragg reflection in the corresponding spacegroup ($P\bar{1}$).

The vibrational spectroscopy data of [Zn_2(TCPE)(bpy)] and [Zn_2(TCPE-F)(bpy)] show the expected bands. The spectra are dominated by signals corresponding to incorporated linkers. Strikingly, the Raman spectra of all compounds, as-synthesized and activated forms, show no characteristic ring breathing vibration mode (995 cm^{-1}) of the pyridine pillar in the Raman spectrum, which supports the coordination of the bpy to the paddle wheel complex in the as-synthesized forms and the remaining connectivity of the activated/contracted network. The IR spectroscopic data proof the formation of the Zn^{II} paddlewheel complex (characteristic broad band of $\upsilon_{C=O}$ at ~ 1400 cm^{-1}), which stays intact upon activation. The IR spectra shows no formation of free acid as well as signs for uncoordinated bipyridine after activation induced framework contraction.

N_2 adsorption isotherms measured on the activated materials at 77 K indicate a modest BET surface area, which falls far below theoretical values based on the pristine MOFs ([Zn_2(TCPE)(bpy)]: experimental, 22 m^2/g; theoretical, 2332 m^2/g; [Zn_2(TCPE-F)(bpy)]: experimental, 76 m^2/g; theoretical, 2330 m^2/g). Note that the BET surface areas were calculated based on the solvent accessible surface area from crystal structures using the Materials 5.0 software suite as well as crystal density and unit cell volume from crystal structure data by equation 2.1.

$$Surface\ Area\ (m^2\ g^{-1}) = \frac{Surface\ Area\ per\ Cell\ (\text{Å}^2)}{Density\ (g\ cm^{-3})\ \times Cell\ Volume\ (\text{Å}^3)} \times 10^4 \qquad (2.1)$$

Altogether, the evaluation of the spectroscopic and adsorption data suggest that the MOFs undergo structural deformation upon solvent exchange such as that the MOF structures experience a partial framework contraction with received network connectivity. Interestingly, the MOFs were not reforming after extensive resuspensions in DMF solvent. Solid-state absorbance spectroscopy supports the notion of a contracted framework, as the absorbance spectra show a pronounced redshift for both compounds, which is indicative for a change in the local environment of the ligands and shows that the ligand geometries

approach a more ligand like structure (compare the experimental section for the optical spectra and further details). Similar behavior was also found for the emission spectra of the compounds. Figure 12 and figure 13 summarize the important characterization details.

Exploring the crystal structure of the compounds in terms of ligand dynamics, [Zn_2(TCPE)(bpy)] and Zn_2(TCPE-F)(bpy)] show a pronounced disorder of the TPE cores of TCPE and TCPE-F inside the MOFs. The split layers of the disorder measured at 100 K reflect two parts with an occupancy ratio of approximately 60 : 40 in both compounds. Interestingly, such a behavior cannot be found in the single crystal structure of H_4TCPE, where the tight packing of the molecule and intermolecular interactions of the form O···H-C_{arom} between co-crystallized DMF and the TPE core prevent phenyl ring rotation. Furthermore, looking into the type of intermolecular interactions between the sub-frameworks in the two MOFs, small numbers of slightly weak intermolecular interactions of the type π···H-C_{arom} and F···H-C_{arom} are found, with characteristic distances of 2.09 to 2.84 Å. The crystallographic models therefore indicate that in [Zn_2(TCPE)(bpy)] and Zn_2(TCPE-F)(bpy)] the phenylene rings of the TPE core in TCPE and TCPE-F are rotationally disordered around their local C_2 axes over two positions, enabling liberation/rotation modes between these positions. Thus, according to the above analysis the conformational strain acting on the ligands inside the pillar-layered MOFs is low, meaning that the framework forces do not exert great mechanical stress to the AIE active ligands. Furthermore, intermolecular effects between sub-frameworks do not impact the ligand geometries to a large extent. Consequently and from a photophysical point of view, the emission properties of the MOFs should behave more ligand like (in its free form), however, contraction of the frameworks should act similar to the formation of TPE aggregates, with enhanced quantum yield and emission efficiency.

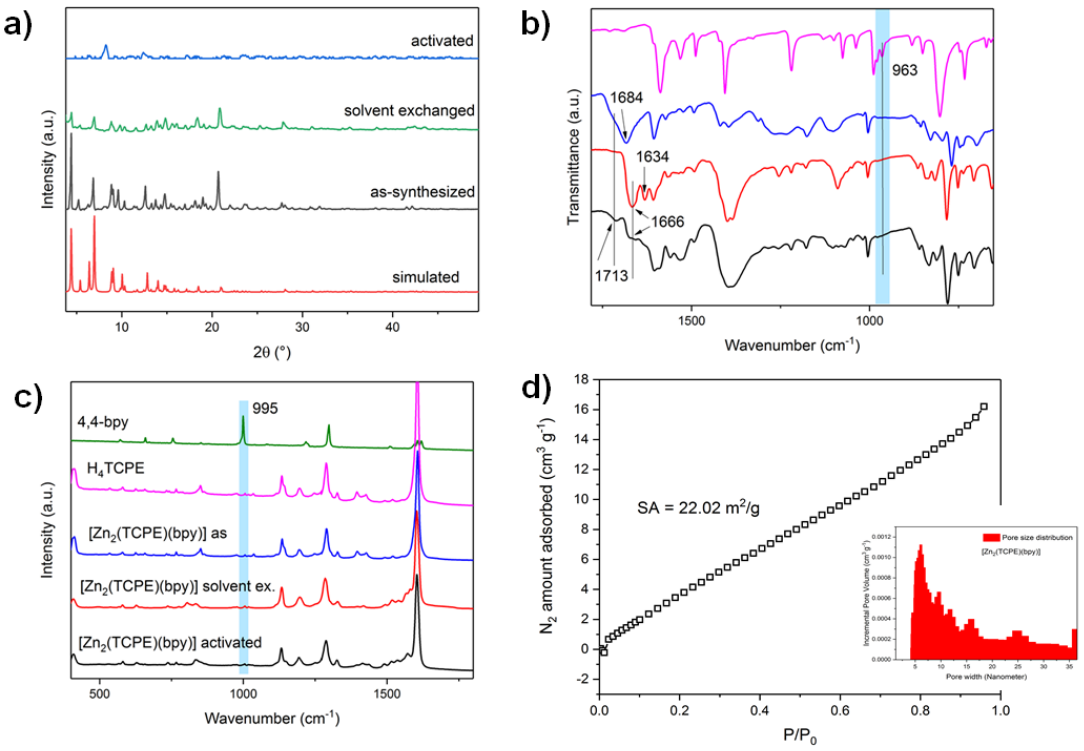

Figure 12. a) PXRD data of $[Zn_2(TCPE)(bpy)]$ in its solvated (as-synthesized), solvent-exchanged (to acetone) and activated form, representing the structure transformation of the pillar-layered MOFs upon activation (Note that the data is background corrected). b) IR-spectroscopic data in important ranges for bpy, free H_4TCPE, $[Zn_2(TCPE)(bpy)]$ and the contracted framework $[Zn_2(TCPE)(bpy)]$-contr (from top to bottom). The data show the expected signals: 1713 cm^{-1} (s C=O, free acid) 1684 cm^{-1} (as C=O, free acid), 1666/1634 cm^{-1} (as C=O of DMF), 1400 cm^{-1} (as C=O Zn^{II} paddlewheel) 963 cm^{-1} (ring breathing pyridine). c) Raman spectra showing no formation of a characteristic pyridine ring breathing mode at 995 cm^{-1} for the activated MOF. d) The N_2 adsorption isotherm of $[Zn_2(TCPE)(bpy)]$-contr and the pore size distribution (inlet) demonstrating the loss of porosity due to framework collapse.

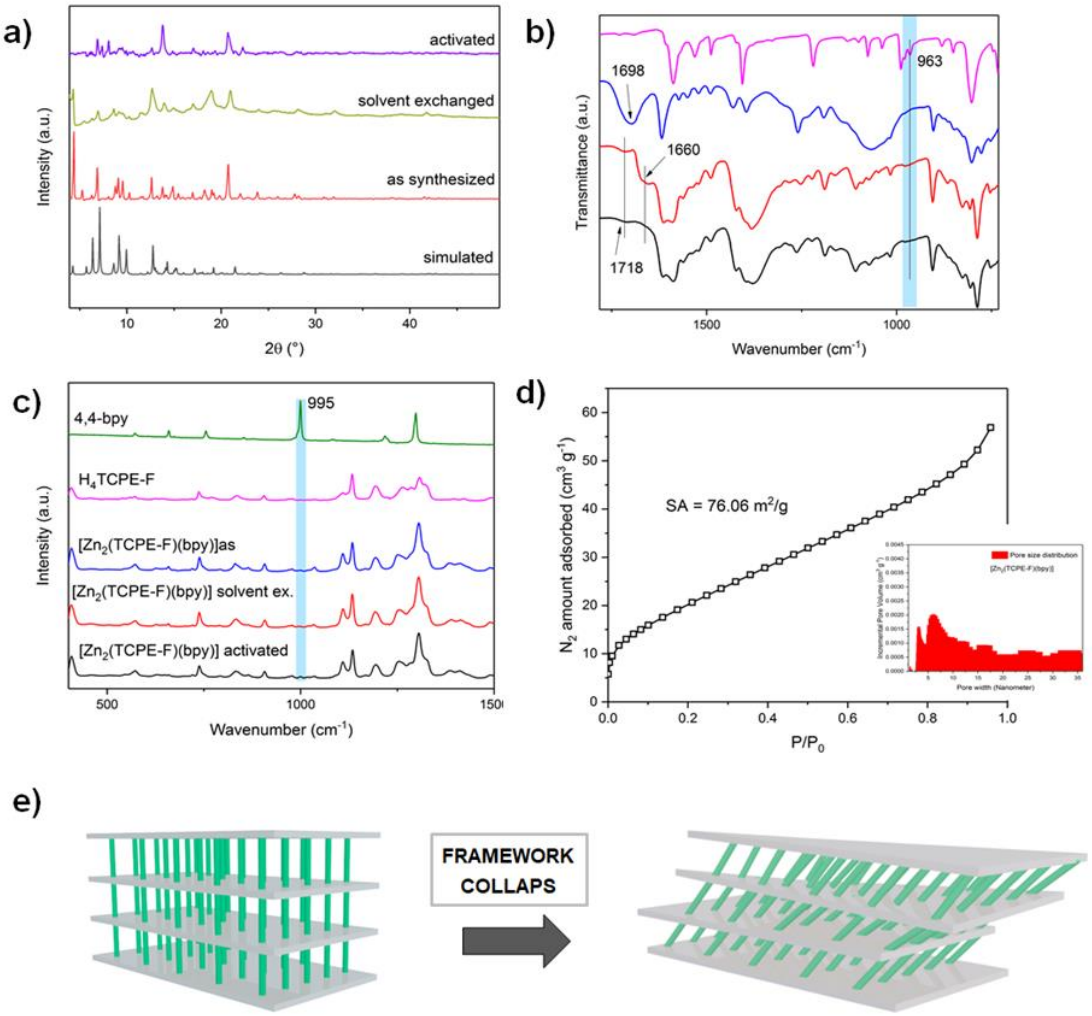

Figure 13. a) PXRD data of [Zn_2(TCPE-F)(bpy)] in its solvated (as-synthesized), solvent-exchanged (to acetone) and activated form, representing the structure transformation of the pillar-layered MOFs upon activation (Note that the data is background corrected). b) IR-spectroscopic data in important ranges for bpy, free H_4TCPE-F, [Zn_2(TCPE-F)(bpy)] and the contracted framework [Zn_2(TCPE-F)(bpy)]-contr (from top to bottom). The data show the expected signals: 1718 cm^{-1} (s C=O, free acid) 1698 cm^{-1} (as C=O, free acid), 1660 cm^{-1} (as C=O of DMF and Zn^{II} paddlewheel), 1400 cm^{-1} (as C=O Zn^{II} paddlewheel) 963 cm^{-1} (ring breathing pyridine). c) Raman spectra showing no formation of a characteristic pyridine ring breathing mode at 995 cm^{-1} for the activated MOF. d) The N_2 adsorption isotherm of [Zn_2(TCPE-F)(bpy)]-contr and the pore size distribution (inlet) demonstrating the loss of porosity due to framework collapse. e) A schematic sketch for the demonstration of the framework collapse after thermal activation.

2.2.4 Excursus: Mechanistic aspects of the photophysics in TPE based MOFs

Comprehensive work about photophysical aspects of TPE based ligands in MOFs have been conducted by Dincă and Shustova et. al.[37, 38] They showed that the incorporation of a TPE based chromophore into a MOF enforces similar confinement effects to the rotational barriers of phenyl ring flipping as aggregation of the TPE molecules does. Consequently, rotation-induced excitation-energy dissipation is suppressed, and emission properties are enhanced. They further showed that steric strain acting on the TPE core can be addressed by the linker design as well as the type of the underlying network.[43] This work laid the basics for an understanding of the linear photophysical properties of TPE based luminescent MOFs. However, non-linear absorption channels will intrinsically differ from linear absorption and the effects of aggregation in AIE based chromophores onto the MPA properties has rarely been investigated. Nevertheless, from a structural point of view, possible parameters for the tuning of non-linear absorption in TPE-AIE MOFs will follow structural aspects as unraveled for their linear optical properties. Briefly, inter - and intramolecular effects such as conformational strain, intermolecular forces (H-bonding, π···H-C_{arom} interaction etc.) or incorporated solvents, which suppress phenyl ring flipping or liberation of the TPE core will diminish the radiationless decay rate and with that enhance the multi-photon induced brightness. Despite these aspects still many questions remain unaddressed regarding the limitation of this approach in the non-linear absorption properties of MOFs. Although the collected data indicate that incorporation of AIE-based ligands improves the MPA properties, is it really always the case?

2.2.5 Linear and non-linear optical characterization of [Zn_2(TCPE)(bpy)] and [Zn_2(TCPE-F)(bpy)]

Linear and non-linear optical characterizations on H_4TCPE, H_4TCPE-F, [Zn_2(TCPE)(bpy)], [Zn_2(TCPE-F)(bpy)], [Zn_2(TCPE)(bpy)]-contr and [Zn_2(TCPE-F)(bpy)]-contr were performed by the group of Prof. Samoć, in particular by J. K. Zareba from the Advanced Materials and Engineering and Modelling Group, Faculty of Chemistry, Wroclaw University of Science and Technology, Poland.

The following paragraph presents the results of the investigations. Discussion and interpretation of the data was conducted in cooperation with the author of this thesis. For further information on photophysical details please refer to J. K. Zareba (email: jan.zareba@pwr.edu.pl).

Linear optical characterization of the MOF compounds and the ligands (as solid-state materials) was performed by single-photon absorbance and emission measurements. Moreover, fluorescence lifetimes of the H_4TCPE, H_4TCPE-F, [Zn_2(TCPE)(bpy)] and [Zn_2(TCPE-F)(bpy)] were collected. Table 3 summarizes the important photophysical data. The determination of absolute quantum yield (φ) measurements using an integration sphere showed φ values of 24.7 %, 20.0 %, 9.1 % and 6.9 % for H_4TCPE, H_4TCPE-F, [Zn_2(TCPE)(bpy)] and [Zn_2(TCPE-F)(bpy)]. Consequently, the incorporation of the ligands into the respective MOFs renders over a 50 % drop in the absolute quantum yields. The contracted networks, however, feature values of 11.8 % and 27.3 % (for [Zn_2(TCPE)(bpy)] and [Zn_2(TCPE-F)(bpy)]). Note the nearly 4-fold enhancement in the case of [Zn_2(TCPE-F)(bpy)]-contr and the negligible enhancement in the case of [Zn_2(TCPE)(bpy)]-contr.

Table 2. Photophysical data of the investigated compounds. Note that all fluorescence lifetimes were collected on the solid materials by TCSPC measurements (377 nm excitation, 530 nm emission). Global fitting procedure show a biexponential decay for the acids and a three-exponent decay for the MOFs. The table gives averaged lifetimes and the corresponding proportion. [a]Solution measurements in DMF, [b]Solid-state measurements. The collected data demonstrate that fluorinated compounds feature shorter decay lifetimes and the MOFs show significantly shorter decay lifetimes than the corresponding ligands.

	$\lambda_{abs}[nm]$	$\lambda_{em}[nm]$	φ [%]	τ [ns]
H_4TCPE	303[a], 365[a] 488[b]	523[a] 528[b]	24.7	2.91 (4.45, 44.9%; 1.66, 55.1%)
H_4TCPE-F	291[a], 313[a], 361[a], 517[b]	523[a] 528[b]	20.0	2.77 (4.38, 42.3%; 1.59, 57.7%)
[Zn_2(TCPE)(bpy)]	440[b]	517[b]	9.1	2.30 (5.88, 16.7%; 2.14, 53.3%; 0.584, 30.0 %)
[Zn_2(TCPE-F)(bpy)]	455[b]	517[b]	6.9	2.17 (6.08, 13.7%; 2.10, 54.4%; 0.624, 31.9 %)

Comparing table 3 the decay lifetimes of the MOFs are shown to hold significantly lower values than the corresponding acids. All optical

measurements attest to the fact, that there is indeed a common structural feature in the pillar-layered MOFs that has a negative impact on their single photon spectroscopic properties. Regarding what has been introduced in the structural discussion above, the hypothesis of a low conformational locking of the phenyl rings rotation (or liberation) is transported to the photophysical properties of the MOF compounds, as seen in a lower emissivity with shorter fluorescence lifetimes. The comparison between the emission properties of the ligands and the MOFs support this argument, as for both solid organic acids, H_4TCPE and H_4TCPE-F, the emission properties are higher. Altogether the structural analysis expressed by the great disordering of TPE cores alongside with the results of single-photon characterization implies that the MOF materials experience rotation-induced excitation-energy dissipation similar to the free ligands in solution. Figure 14 shows the two disordered parts of TCPE and TCPE-F inside the MOFs.

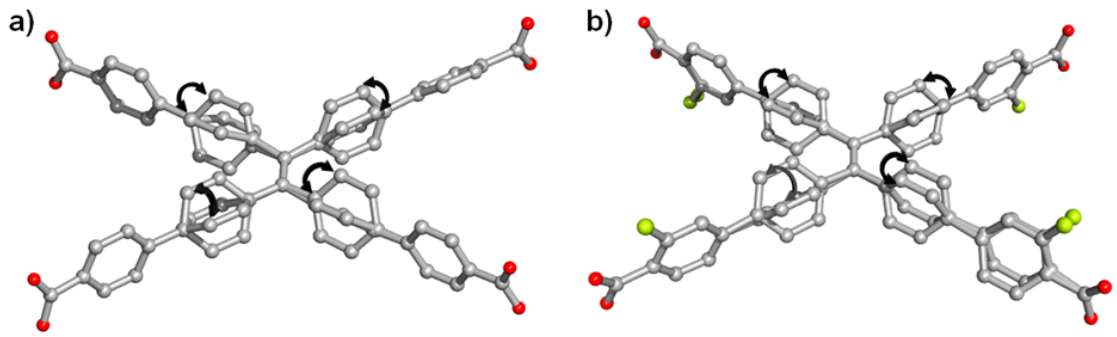

Figure 14. The rotational disorder of the TCPE (a) TCPE-F (b) ligands according to single-crystal structures as found in the MOFs. The black arrows illustrate the possible liberation/rotational degrees of freedom in the TPE cores which probably cause the low single-photon emission properties. Grey: carbon, red: oxygen, yellow: fluorine.

The non-linear optical response was measured as spectrally-resolved TPA cross-sections with the use of the SSTPEF (solid-state two-photon excited fluorescence) method.[12] In summary, H_4TCPE, H_4TCPE-F, [Zn_2(TCPE)(bpy)], [Zn_2(TCPE-F)(bpy)], [Zn_2(TCPE)(bpy)]-contr and [Zn_2(TCPE-F)(bpy)]-contr were characterized in a wavelength range from 650 to 950 nm. Figure 15 summarizes the measured values. The followed approach allows to get an insight in the effects of TCPE/TCPE-F confinement within the MOFs as a framework contraction is thought to lower the rotational degrees of freedoms of

the TPE cores and with that should diminish radiationless decay pathways. The same effect can be studied by comparison of the MOF materials with the solid organic acids. Similar to the single-photon emission characterizations, the TPA cross-section of the compounds reveal that the pillar-layered MOFs, in their as-synthesized forms, hold a structural feature that negatively affect the TPA efficiency. [Zn_2(TCPE)(bpy)] (145 GM @ 700nm) and [Zn_2(TCPE-F)(bpy)] (165 GM @ 690 nm) feature much lower TPA cross-section values than there corresponding acids in the solid state (H_4TCPE: 476 GM @ 670 nm; H_4TCPE-F: 474 GM @ 670 nm). Interestingly, the observed experimental relationship contrast the initial findings on previously investigated TCPE-based MOFs however, goes along with the underlying conceptual understanding, that an enhanced conformational locking of AIE based ligands can enhance not only the linear optical but also the non-linear optical properties. The difference between the non-fluorinated and fluorinated analogues remain with the experimental errors, which shows that in the system the fluorine substituent has a minor effect on the TPA process. The same results is found for the single ligands.

The SSTPEF measurements on the contracted frameworks [Zn_2(TCPE)(bpy)]-contr and [Zn_2(TCPE-F)(bpy)]-contr shows an large TPA enhancement in the case of [Zn_2(TCPE-F)(bpy)]-contr (409 GM @ 660 nm vs. 165 GM @ 690 nm for non-contracted framework), whereas little enhancement in the case of [Zn_2(TCPE)(bpy)]-contr (171 GM @ 690 nm vs. 145 GM @ 700 nm). Apparently, the fluorine substituent does not influence the electronic structure in the MOFs and ligands (to a great extent), but rather provides large benefit as an additional tool for the suppression of ligand dynamics in the contracted networks. Evidently, the steric bulk imparted by the fluorine substituent improves the single and TPA properties of [Zn_2(TCPE-F)(bpy)]-contr as evident from higher absolute quantum yields and greater TPA cross-sections. Such a combination of photophysical effects is advantageous in applications relying on TPA induced fluorescence. Taking both effects into account, the enhancement factor for the two-photon brightness (product of absorption cross-section and quantum yield) is over 6-fold for [Zn_2(TCPE-F)(bpy)]-contr in comparison with the non-contracted MOF [Zn_2(TCPE-F)(bpy)].

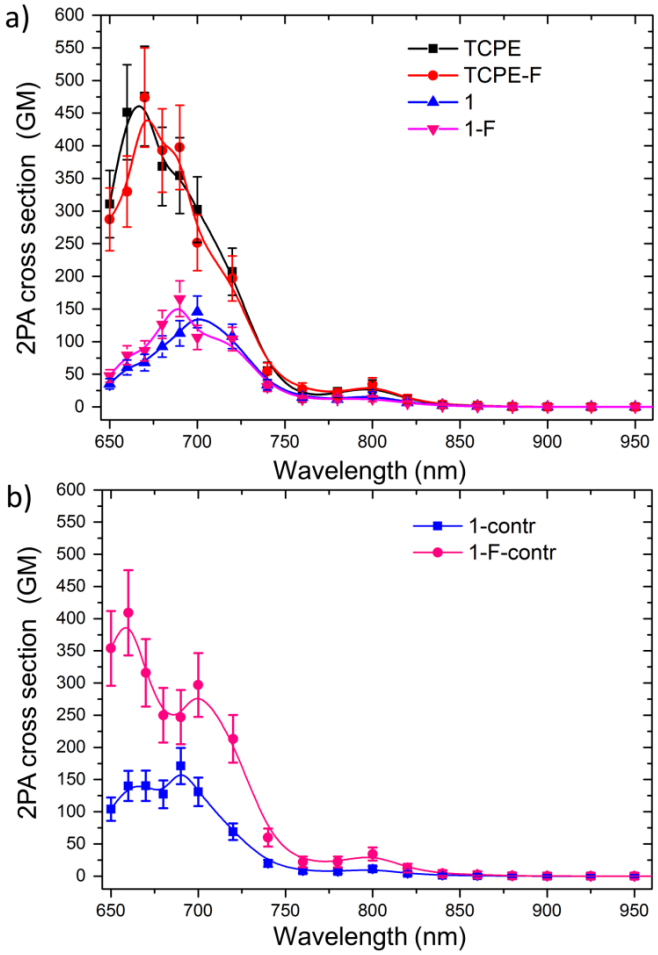

Figure 15. (a,b) Two-photon absorption spectrum in Göppert-Mayer for the compounds H_4TCPE, H_4TCPE-F, [Zn_2(TCPE)(bpy)] (= 1), [Zn_2(TCPE-F)(bpy)] (= 1-F), [Zn_2(TCPE)(bpy)]-contr (1-contr) and [Zn_2(TCPE-F)(bpy)]-contr (1-F-contr) in a range of 650 to 950 nm.

2.2.6 Simulation of the conformational TPA dependency in [Zn_2(TCPE)(bpy)] and [Zn_2(TCPE-F)(bpy)]: A SOS-TD-DFT study

Quantum chemical calculations on H_4TCPE, H_4TCPE-F, [Zn_2(TCPE)(bpy)] and [Zn_2(TCPE-F)(bpy)] were performed by the group of Prof. R. Zaleśny, in particular by M. Cholui from the Department of Physical and Quantum Chemisty, Faculty of Chemistry, Wroclaw University of Science and Technology, Poland. The following paragraph presents a short summary of the results. For more detailed information, please refer to R. Zaleśny directly (email: robert.zalesny@pwr.edu.pl).

To unveil the experimental findings, that the ligand conformation of the investigated systems has a large impact on the TPA properties, electronic

structure calculations on the level of TD-DFT (cam-B3LYP/6-31+G(d))[44, 45] were conducted. To simulate the conformational dependency the following approach was followed. Several geometries of the organic ligands were extracted from the available crystallographic data. The latter provides well-defined conformations of the TCPE/TCPE-F molecules in the solid-state forms of the MOFs and the acids. TPA cross-sections were calculated using the sum-over-state formalism (SOS-approach) within quadratic response theory on optimized geometries.[46, 47] As has already been said above, the crystal structure of H_4TCPE-F is not literature known, consequently to enable a comparison between H_4TCPE and H_4TCPE-F the structure of the latter was assumed to be analogues to that of H_4TCPE and the hydrogen atoms at the meta position were replaced by fluorine atoms. The results of the electronic structure calculations corroborate the experimental findings, namely that the fluorine atom does not affect the TPA cross-sections (109 GM @ 580 nm for both ligands). The calculations further show that the $S_0 \rightarrow S_1$ transition is two-photon forbidden (but with very high one-photon oscillator strength) and the $S_0 \rightarrow S_2$ transition is two-photon allowed, corresponding to the experimental feature at 660 nm (compare Figure 15).

To understand the influence of the dynamics of the phenyl ring flipping in the two-photon response of the MOFs, TPA cross-sections were calculated for the found limiting conformations from crystal structures (Figure 14). Moreover, intermediate structures obtained by linear transformation between the single conformations (phenyl ring rotation in the TPE groups) were computationally investigated and it was shown that the crystallography derived geometries indeed show the highest values (for both MOFs A and B rotamer; [Zn_2(TCPE)(bpy)]: 42(52) GM @ 560 nm; [Zn_2(TCPE-F)(bpy)]: 38(38) GM @ 560 nm; Note literature for conversion procedure[48]), whereas the intermediate structures are less two-photon active at the long-wavelength transition (Figure 32). The comparison with the calculations for the solid-state ligand conformation reveals a drop in the TPA cross-section by a factor of 2-3, which can directly be attributed to the conformational change of the ligand, when incorporated into the pillar-layered MOFs.

To model the TPA enhancement process upon framework collapse of the porous materials, an obstacle to overcome is the missing knowledge about the local ligand conformation. However, as has already been proposed above, the single-photon spectroscopic similarities between the contracted MOF materials and the solid acids suggest that the local ligand geometries might be similar. Therefore, again a linear transformation procedure between the H_4TCPE conformation and the ligand conformations as found in [Zn_2(TCPE)(bpy)] was conducted. Calculations of TPA cross-sections showed that on passing from the MOF conformations to the [Zn_2(TCPE)(bpy)] there is a rise in the TPA long-wavelength feature, indeed supporting a picture in which framework contraction leads to an increase in the TPA activity (further computational details are given in the experimental section).

The theoretical approach as introduced above allowed to confirm the observed experimental relationships and furthermore underpin the assumption about the importance of the local ligand structures. However, insights into the specific electronic parameters, which is at the core of the observed changes can be conducted by an analysis of the TPA active channels using the three-state model.[49] This allows to decompose the electronic contribution of the two-photon active $S_0 \rightarrow S_2$ transition in its participating channels. The three-state model reveals that the bright $S_0 \rightarrow S_1$ and $S_0 \rightarrow S_3$ single-photon excitations influence the strength of the $S_0 \rightarrow S_2$ transition in the case of the solid organic ligands H_4TCPE and H_4TCPE-F. However, in the case of the excited state contribution for the two limiting conformations found in [Zn_2(TCPE)(bpy)], in the one case (rotamer A) the $S_0 \rightarrow S_1$ excitation influences the TPA allowed $S_0 \rightarrow S_2$ transition, whereas in the other case (rotamer B) higher-lying states (S_3, S_4 and S_5) become more important.

Finally, the large contribution for the bright $S_0 \rightarrow S_1$ and $S_0 \rightarrow S_3$ one-photon excitation to the two-photon $S_0 \rightarrow S_2$ transition allows for accessing a more general ligand design principle in the case of TPE based ligands, as ligand changes which access the increase of $S_0 \rightarrow S_1$ and $S_0 \rightarrow S_3$ single-photon excitation should directly influence the TPA properties. Practically, this could be accessed by an extension of the H_4TCPE core.

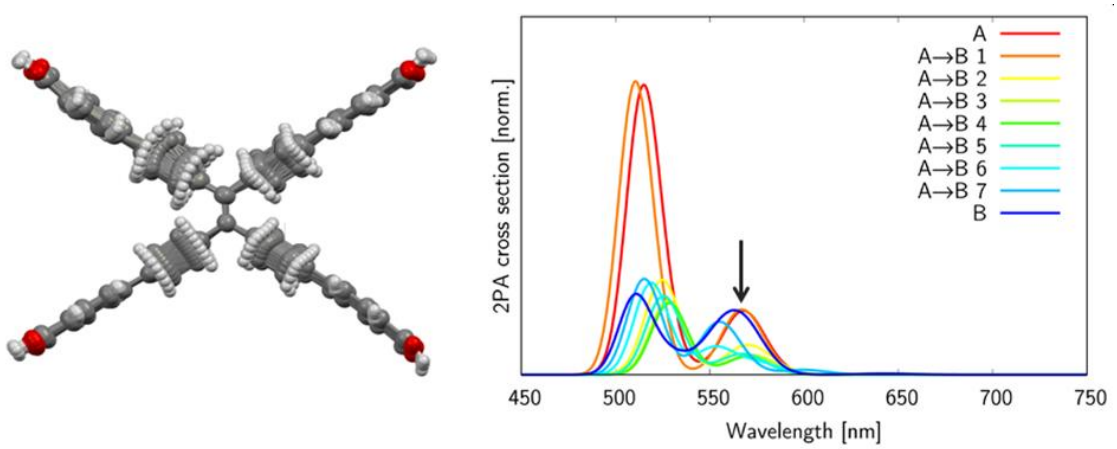

Figure 16. Simulated TPA spectra for [Zn_2(TCPE)(bpy)]. A and B depict the two rotamer structures found in the SCXRD analysis due to rotational disorder (compare Figure 14 as well). 1 to 7 depict the artificially formed structures by rotation of the TPE phenyl groups between structures A and B. For all molecular confomers, wavelength depend TPA cross-sections were calculated. The arrow shows the important section and reveals the drop in TPA performance when the phenyl groups are rotates. Highest values are indeed predicted for the two limiting structures A and B. Note that the calculated band at longer wavelength (black arrow) corresponds to the experimental feature at 690 nm (Figure 15).

2.2.7 Discussion and conclusion

The presented study revealed further information about how the local conformation and geometrical situation of an AIE chromophore in a MOF, specifically based on TPE units, influences the linear and non-linear optical properties of such a material. Therefore, approaches to synthesize a series of pillar-layered MOFs based on the H_4TCPE ligand and its fluorinated analogues, as well as a number of geometrically different, but topologically similar bipyridine pillars were conducted. It was shown that within the [Zn_2(TCPE)(X)] (X = bpy, bpee, bpea, azpy) series all pillar-layered MOFs, which substantially derive from the **fsc** topology by geometrical mismatch of the bipyridine pillar (linear to zig-zag), could not be synthesized as bulk materials on a satisfactory level. The highest crystallinity and purity among these materials was indeed shown to be educible for the bpy based MOF, which is the framework material reflecting the geometry of **fsc** topology the most. Analyzing stability issues of pillar-layered MOFs by using the concept of geometrical mismatch of factual ligand geometries vs. topological required geometries has rarely been done for pillar-layered MOF materials. The presented results point towards induced framework distortion by incorporation of zig-zag bipyridine pillars alongside with

crystallinity issues and could serve as a starting point for the understanding of the influence of geometry mismatch on the framework stability of pillar-layered MOFs.

Based on the synthetic results, two isostructural and isoreticular MOFs with the composition [Zn_2(TCPE)(bpy)] and [Zn_2(TCPE-F)(bpy)] were further synthesized and structurally characterized. The two pillar-layered MOFs were shown to be sensitive against thermal activation procedure and solvent exchange, as evident from PXRD and BET studies. The MOFs showed a framework collapse with remaining network connectivity leading to a contracted framework material, proven by IR and Raman spectroscopy. By doing so, a conceptual series of optical active materials could be derived with intrinsically increased ligand distortion due to a multiple of effects (intermolecular Van-der-Waals interactions of different types, ligand confinement through framework strain, steric bulk by fluorine substituent) going from the porous pillar-layered MOFs to the contracted framework materials with or without fluorine substitution. Along state-of-the-art results of similar systems, the linear optical characterization for the as-synthesized MOFs, [Zn_2(TCPE)(bpy)] and [Zn_2(TCPE-F)(bpy)] showed a structural feature which negatively affect the AIE properties of that materials. Analysis of the underlying structure situation revealed rotational disorder of the TPE phenyl rings in both compounds at 100 K. Consequently, the low emission properties of [Zn_2(TCPE)(bpy)] and [Zn_2(TCPE-F)(bpy)] were assigned to potential rotation-induced-excitation-energy dissipation, due to low conformational locking of the TPE phenyl ring rotation. Alongside with this fact, the solid ligands and the contracted framework indeed showed greater emission efficiencies, as evident form enhanced quantum yields and single-photon fluorescence lifetimes. The non-linear optical characterization in the form of TPA and TPEF showed a similar behavior. The measured TPA cross-section revealed a factor 3 lower TPA efficiency for the as-synthesized MOFs, but an enhancement for the solid ligands and the contracted frameworks. Consequently, the adopted ligand conformations within the contracted frameworks and the solid acids indeed proved feature-increased TPA activities. Such an effect was most pronounced for the fluorinated MOF [Zn_2(TCPE-F)(bpy)], which point towards the direction that the steric bulk of the fluorine substituent positively affects the TPE phenyl ring locking in the

contracted material. The experimental found results were supported by theoretical calculations on a multitude of rotamer structures of TCPE and TCPE-F following the crystal conformation of [Zn_2(TCPE)(bpy)] and [Zn_2(TCPE-F)(bpy)]. The results of the theoretical calculations were in good accordance to the measured values and reflect the influence of the TPE dynamics on the TPA properties. It needs to be stated that the non-linear response of the MOFs is affected by two interlocked effects. First, the intrinsic influences by the local molecular geometry. Secondly, by non-radiative relaxation pathways through ligand dynamics. Contraction of the frameworks can therefore affect both effects, as linker compression will enhance the radiative decay rate and might result in a local structure with good TPA performance.

In summary, the presented work demonstrates that the porosity of a CP can negatively influence the crystal engineering of AIE based MPA-MOFs, when it comes to the question about maximizing TPA and TPEF properties of MOFs. Nevertheless, the presented results go alongside with recent work of our group and support the initial conceptual idea that conformational locking of an AIE ligand within a CP or MOF will enhance the non-linear optical response. Interestingly, in this work the enhancement of conformational strain has been conducted not by incorporation of an organic molecule into a framework, but by subsequent framework contraction, which opens further pathways for post-synthetic “engineering” of TPA properties (note that most chromophores in bioimaging e.g. suffer from aggregation caused quenching with low TPEF behavior). Finally, the presented work show that the concept of conformational locking of an AIE based chromophore in MOFs for enhanced TPA efficiency can be accessed by a multiple of suitable concepts such as interpenetration, targeted ligand substitution which would suppress molecular motion modes, or the use of sterically pronounced and strong binding SBUs (e.g. Zr^{IV}-oxo cluster[19]), which show a higher ligand deformation potential (see e.g. the work by Shustova et. al).[43] In this regard, the TPA response of CPs and MOFs as a function of external stimuli emerge as a highly interesting research area.

2.3 Insights in the control of TPA efficiency by chromophore packing in CPs and MOFs

2.3.1 Introductory remarks

As it is extensively explained in the introduction of the present thesis and in the theoretical background chapter, electronic excitations in molecular assemblies are of fundamental interest in the field of optical applications (optoelectronics, photonics, photocatalysis, non-linear optics to name just a view) and constitute a highly interesting research field. Intermolecular electrostatic interactions are the driving force of two key phenomena of optical active materials, energy transfer and energy delocalization.[50] The latter has been shown to hold a tremendous potential on optical non-linearities.[46, 51, 52] The key point of the presented study is to deepen the understanding of the MPA properties of CPs and to further reveal possible influences of intermolecular interactions on MPA in CPs and MOFs by an interplay of organic synthesis, crystal engineering, linear and non-linear optical spectroscopic characterizations and electronic structure calculations on the level of TD-DFT. Within this chapter, the synthesis of two new coordination polymers is introduced, incorporating the same MPA active ligand motif, H_4TPBD, which was designed using the presented synthesis concepts (see chapter 2.1.4 and 4.6.3).

The work is structured as follows. The linear optical characterization of H_4TPBD is presented. TD-DFT calculations are conducted on the ligand molecule to substantiate the spectroscopic findings. Furthermore, the synthesis of two new Zn^{II} and Cd^{II} CPs is presented. The structure and topological situation of the CPs is discussed. The linear and non-linear optical characterizations of the MOF materials are introduced, and the measured optical response is rationalized using the exciton theory.[53] Finally, TD-DFT calculations on molecular cluster aggregates are presented, to support the spectroscopic findings. In the end, the presented work will show that intermolecular interactions in CPs and MOFs seem to account for a non-negligible contribution on the non-linear response of the investigated systems. The intermolecular interactions are shown to be addressable by structural

aspects. Note that the difference of the presented study to the work in chapter 2.2 can be found in two aspects. The used ligand motif H_4TPBD is decorated with nitrogen donor atoms in the molecular scaffold to enhance the charge transfer characteristics and thus H_4TPBD can be regarded as a moderate push-pull chromophore, in contrast to often used linker molecules in MOF chemistry. Secondly, while the work on AIE-dyes as potential TPA absorbing linker units was completely focusing on local ligand effects, the presented work of this chapter is dealing with intermolecular effects on the non-linear response of CPs.

Linear and non-linear optical characterization on compounds H_4TPBD, [Zn_2(TPBD)(DMAc)$_2$] and [Cd_2(TPBD)(H_2O)$_4$] as well as data interpretation were conducted by the author of this thesis in cooperation with Dr. A. Manzi from the Chair of Photonics and Optoelectronics, Nano-Institute Munich, Department of Physics and CeNS, Ludwigs-Maximilians-Universität, Munich. Furthermore, optical characterization of H_4TPBD and aggregates at higher concentrations were conducted by Dr. Thyrhaug from the Chair of Dynamic Spectroscopy, Department of Chemistry, Technical University of Munich. Dr. Thyrhaug did the data analysis and helped with the interpretation. All electronic structure calculations presented within the following chapters were conducted by the author of this thesis.

2.3.2 H_4TPBD, a multibranched push-pull ligand

H_4TPBD (= tetrakis(1,1′-biphenyl-4-carboxylic acid)-1,4-benzenediamine), is a tetratopic ligand motif, which was initially constructed using design principles for high MPA efficiency under MOF synthesis perspectives.[7] The compound comprises of triphenylamine donor units connected with carboxylic acid groups as electron acceptors. The carboxylic acid groups simultaneously act as coordinating donor groups to the metal nodes in the construction of potential new MOF structures. Coordination to a metal center is thought to enhance the acceptor tendencies of the carboxylic acid groups via simple bond polarization and thus should enhance the intermolecular charge transfer between triphenylamine and carboxylic acid groups to a greater extent.

H_4TPBD is a tetratopic, rectangular (4-c) ligand, from a topological point of view, and holds C_2 symmetry (highest possible point group suitable is C_{2h}

symmetry). From a photophysical point of view, H_4TPBD can be classified as a multibranched chromophore, comprised of four donor-acceptor push-pull biphenyl arms (4'-(diphenylamino)-[1,1'-biphenyl]-4-carboxylic acid). Considering the acceptor-donor arrangement in H_4TPBD, the molecule is composed of two interlinked quadrupolar A-π-D-π-A units. Regarding the given Hammett and Pytela constants of the acceptor/donor groups[54], H_4TPBD falls into the range of existing push-pull multibranched structures, as for example 4-((E)-2-(benzo[d]thiazol-4-yl)vinyl)-N,N-bis(4-((E)-2-(benzo[d]thiazol-7-yl)vinyl)phenyl)aniline.[55, 56] The photoresponse of such multibranched chromophore systems has been described to be governed by an intersystem charge-transfer (ICT) state localized on the push-pull sidearms with potential energy delocalization between the sidearms. The excited state properties of biphenyl based push-pull chromophores (as in this case the 4'-(diphenylamino)-[1,1'-biphenyl]-4-carboxylic acid branch) show a subtle interplay between locally-excited (LE) and charge-transfer (CT) states. The extent of π-electron overlap affects the extent of electronic delocalization, which will be varied by the torsional angle of the phenyl groups (affected by solvent, thermal motion and substituents) and in the end defines the molecular photophysics.[57] The lowest lying transition dipole moment of a biphenyl push-pull chromophore will lay along the long axis of the chromophores (compare the blue arrows in Figure 17). In multibranched chromophoric systems (in H_4TPBD four biphenyl push-pull branches), the single branches may be subject of potential excitonic interactions between the single arms (this approach is applicable for chromophores with an electrostatic interaction between the sidearms small compared to the typical transition energy).[55, 58-60]

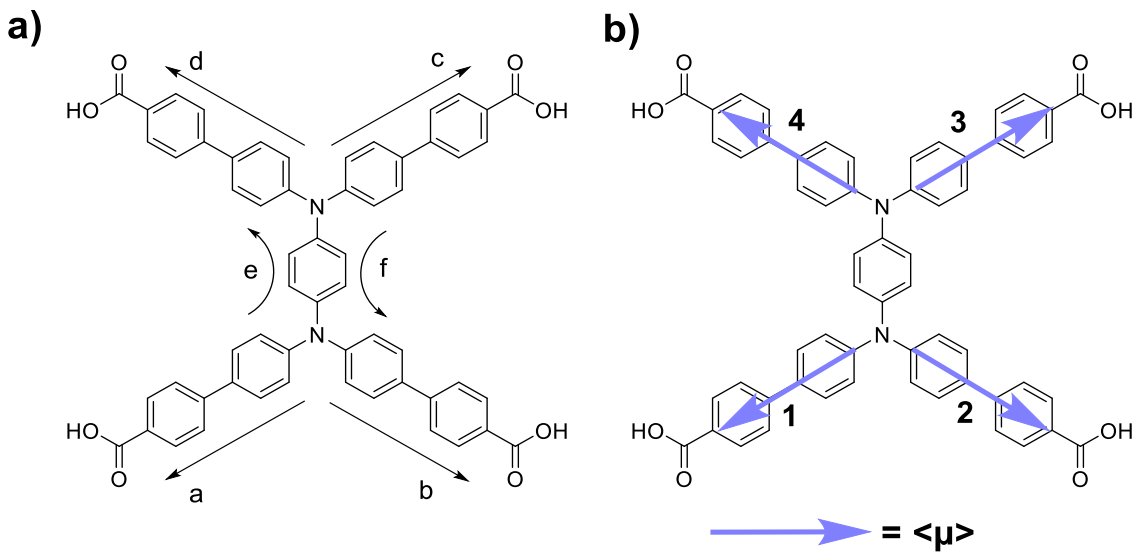

Figure 17. a) Charge transfer pathways present in H_4TPBD. b) The single transition dipole moments μ of locally excited side-arms in H_4TPBD. The numbering corresponds to the single excited wavefunction used in the formation of symmetry adapted linear-combinations (C_{2h}) for the description of the excitonic states.

H_4TPBD is an intensively yellow colored powder, which forms a yellow/bright green solution upon solvation in different organic solvents. The stead-state absorption spectrum shows one strong absorption band centered at 375 nm (ε = 66000 L mol^{-1} cm^{-1}), which has no obvious solvatochromic shift. Steady state emission spectroscopy reveals a single emission band with an asymmetric shape centered at 525 nm. Similar to the absorption spectra, the PL also shows no solvatochromic shift. H_4TPBD holds a strong Stokes shift of ~ 160 nm (measured in DMF), which implies a pronounced excited state distortion pointing towards a broad and shallow potential energy surface for both the ground and excited states. Measurements of the external quantum yield (EQY, φ) reveal a value of φ (DMF) ~ 10 %. Excitation-emission mapping of H_4TPBD (DMF, 20 μM) shows no wavelength dependency for both the emission and excitation spectra, suggesting the presence of a single species. By plotting the emission spectrum on an energy scale, the signal loses its asymmetry, showing a symmetric spectra, which can be fitted with a single gaussian distribution. Calculation of the reorganization energy based on the fitting parameters reveals a value of ~ 0.5 eV. Comparison to the experimental Stokes shift shows an difference by a factor of ~ 2. This fact implies an deviation of the simple displaced harmonic oscillator picture and furthermore suggest pronounced

anharmonicity in the PES (e.g. by charge-transfer mechanisms or a tendency to enhance conjugation during photoexcitation). The collected excitation spectra resemble the absorption spectra to a first order. They further imply several overlapping transitions in the regarded spectral range. The red edge of the excitation spectra can be fitted with a Gaussian distribution. Since there is no wavelength dependency of the emission spectra, the emitting state will always be the same and can be related to the fitted red edge state in the excitation spectrum. Finally, time-resolved fluorescence spectra reveal very fast fluorescence decays for the chromophores in DMF solution. Actually, the measured decays are close to the instrument response, which complicated the determination of life time values. However, a global fitting procedure shows a dominating decay component with a life time of approximately 850 ps and a second minor contribution of ~ 3.5 ns. The relative complex decay requires three exponential functions to be fitted at every wavelength with relative amplitudes changing over the wavelength range. Table 3 summarizes the collected photophysical data of H_4TPBD. Figure 18 shows the absorption and PL spectra of the chromophore in different solvents, alongside with the EEM, extracted PLE spectra as well as TRES traces.

Table 3. Photophysical data of H_4TPBD.

H_4TPBD:	λ_{abs}^{max} **[nm]**	λ_{em}^{max} **[nm]**	ε **[L mol^{-1} cm^{-1}]**	λ_h **[nm]**	$\tau\,[ps]$	φ **[%]**
	371	525	66000	160	850	10

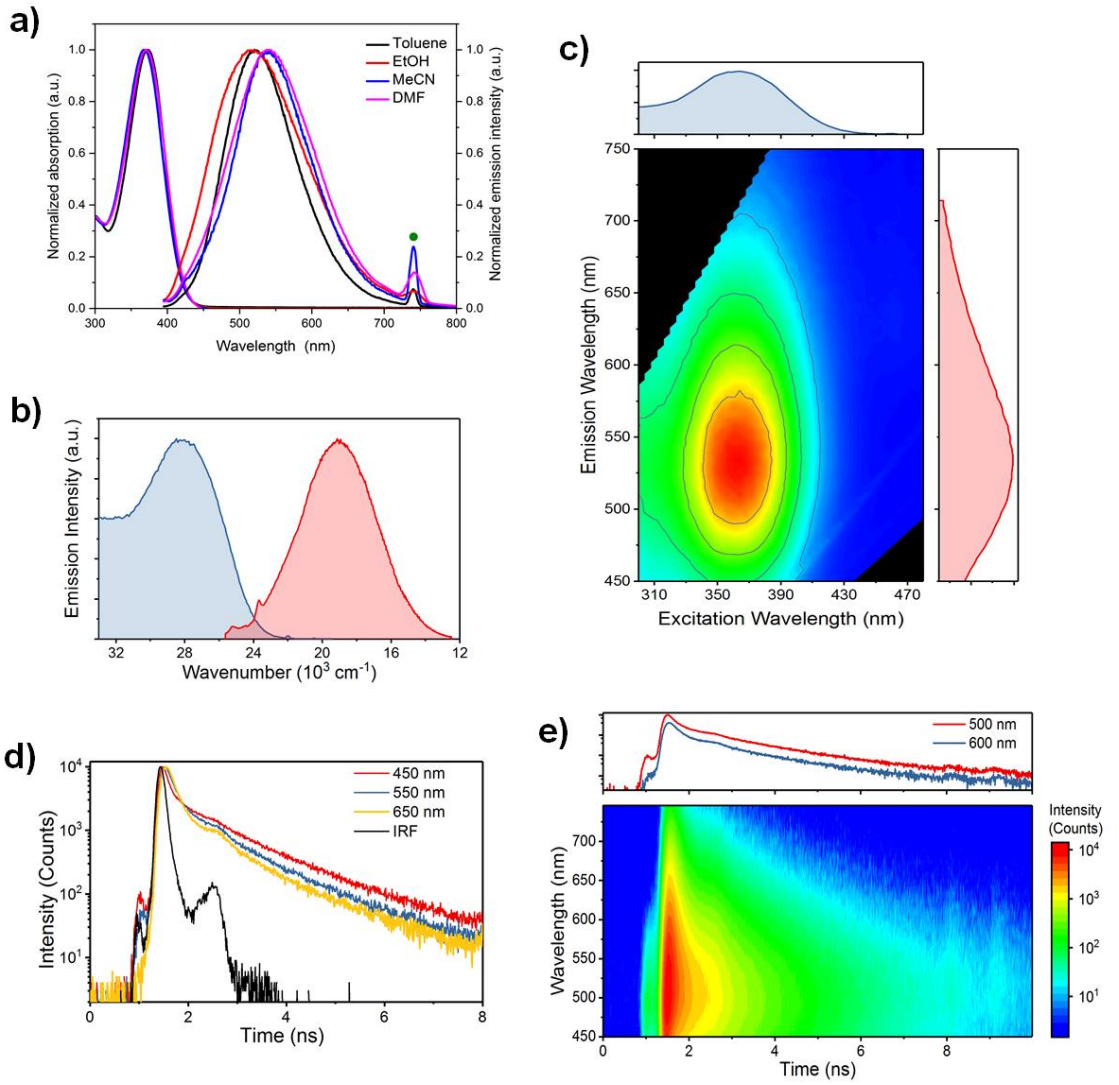

Figure 18. a) Absorption and emission spectrum of H_4TPBD in differing organic solvents. Please note that the green dot shows the second harmonic of the laser excitation. b) PLE and emission spectra of H_4TPBD plotted on an energy scale. c) EEM of H_4TPBD. d) Fluorescence decays at different emission wavelength. e) TRES trace of H_4TPBD.

Based on the molecular structure, the photophysical properties of the chromophore shall be describable in the context of a multibranched push-pull chromophore, as introduced above. The molecular structure of H_4TPBD possess donor (nitrogen groups) and acceptor (carboxylic acid groups) moieties, coupled by an extensive π-electron system. Consequently, the absorption band at 375 nm should be dominated by a mixture of locally excited $\pi \rightarrow \pi^*$ transitions (phenyl rings) alongside with delocalized charge-transfer states (between the nitrogen donor and carboxylic acid acceptors within the context of HLCT = hybridized local and charge-transfer states).[61] The weak solvatochromic absorption behavior of H_4TPBD can be rationalized on the non-

polar ground state of H_4TPBD, due to symmetry reasons (vertical excited states maintain the symmetry of the ground state).[50, 62, 63] The huge Stokes shift of the chromophore implies a large structural reorganization in the excited state, which is probably accompanied by a torsion of the biphenyl rings to ensure a higher planarity during photo excitation (symmetry breaking). The latter is inherently connected with rather broad potential energy landscapes. The almost missing solvatochromic emission behavior in the PL spectra shows that the emissive state holds a non-polar character. The EEM reveals a single emissive channel over the whole PL range.

To gain an insight into the photophysics of H_4TPBD, two approaches were followed in modelling the excited state properties of the chromophore. First, the compound was investigated in the framework of exciton theory. This has widely been done on multibranched chromophores and was shown to work well for this chromophore class.[59, 64-66] The excited states of H_4TPBD were modelled in the basis of single excitations located at the respective biphenyl branches (compare the blue arrows in Figure 17) supposing C_{2h} symmetry. The results provide a first overview about the excited state situation and can be compared to the measured absorption spectrum.

Subsequently, the molecule was further investigated using TD-DFT calculations. The vertical excitations were analyzed by their corresponding molecular orbitals as well as fragmented transition density matrix analysis. Furthermore, the relaxed excited state geometry of the first excited state was computed to get an insight to the excited state distortion and the charge redistribution upon photoexcitation as well as the origin of the high Stokes shift.

Within the Frenkel exciton picture, the results predict four exciton eigenstates holding A_g, B_g, A_u and B_u symmetry (for each irreducible representation of the C_{2h} point group) with an overall splitting of $4V$. The low-lying bright states hold A_u and B_u symmetry with the transition dipole moment along the two molecular axis (compare Figure 19). Table 5 summarizes the excited wavefunction and the reducible representation Γ_{red}. Figure 19 shows the excited states diagram with the expected excitonic eigenstates and their orientation of the transition dipole moments. Accordingly, the excitonic representation predicts two bright states accessible by single-photon absorption. The separation of these states

will be smaller than the typical excitation frequency of H_4TPBD and thus gives rise of one single broad band in the absorption spectrum, which indeed is found in the experimental spectrum. Note, that a description in the exciton theory takes a complete delocalization of the excited state over all contributing branches as a basis.

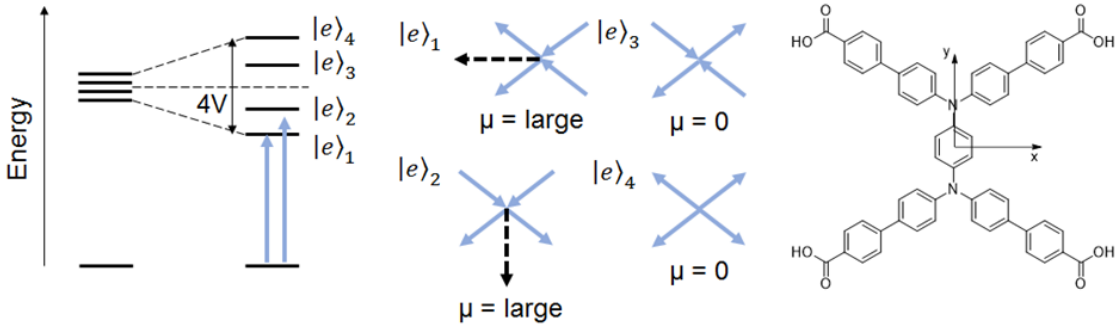

Figure 19. An energy diagram of the excitonic eigenstates in the basis of single excited states of the molecular branches. The blue arrows represent the phase relation of the localized transition dipole moments. The lengths are proportional to their magnitudes. The black dashed arrows correspond to the resulting sums. The $|e\rangle_1$ and $|e\rangle_2$ are predicted to hold oscillator strength, where as the $|e\rangle_3$ and $|e\rangle_4$ are dark states. The right picture shows the molecular axis system used for the construction of SALCs.

Table 4. Exciton eigenstates $|e\rangle$ in the basis of the transition dipole moments of the side arms of H_4TPBD.

Exciton eigenstates of H_4TPBD in C_{2h}	
Basis	$\{\phi_1, \phi_2, \phi_3, \phi_4\}$
Reducible representation	$\Gamma_{red} = A_g + B_g + B_u + A_u$
A_u wavefunction	$\|e\rangle_1 = 1/\sqrt{2}\,(\phi_1 + \phi_2 - \phi_3 - \phi_4)$
B_u wavefunction	$\|e\rangle_2 = 1/\sqrt{2}\,(\phi_1 - \phi_2 - \phi_3 + \phi_4)$
B_g wavefunction	$\|e\rangle_3 = 1/\sqrt{2}\,(\phi_1 - \phi_2 + \phi_3 - \phi_4)$
A_g wavefunction	$\|e\rangle_4 = 1/\sqrt{2}\,(\phi_1 + \phi_2 + \phi_3 + \phi_4)$

To get a more complete picture of the absorption properties of H_4TPBD, TD-DFT calculations were conducted on DFT optimized geometries using crystal structure data as molecular input structure. All calculations were conducted on the level of cam-B3LYP/def2TZVP.[44, 67] The gas-phase TD-DFT results predict three narrow states (two bright and one dark state; S_1, S_2 and S_3, within $\Delta\lambda$ = 4.2 nm) in the visible range with oscillator strengths of 1.11, 0.01 and 2.01 (the

S_2 state is predicted to be dark due to symmetry reasons) centered at 325 nm, giving rise of one single absorption band (Figure 20). The transition dipole moments of these states are found to lay along the molecular axis. Analysis of the natural transition orbitals (NTOs) of the S_1 and S_3 states show that the most contributing Kohn-Sham molecular orbitals (KS-MO) for the S_1 state are a HOMO → LUMO+1 (87%) excitation and a HOMO → LUMO+2 (67%) for the S_3 state. The S_2 state is the HOMO → LUMO (90%) excitation. The inspection of the NTOs further suggest that both bright absorption bands (S_1, A_u symmetry, 12.42 D; S_3, B_u symmetry, 21.78 D) can be assigned to a $\pi \rightarrow \pi^*$ transition, located at the tetraphenylbenzene-1,4-diamine core and the biphenyl side arms (similar for the S_2 state). Furthermore, electron density is also shifted from the triphenylamine moieties to the carboxylic acid groups during photo excitation. This fact is supported by the analysis of fragmented transition density matrices (TDMs), which reveal in the case of the S_1 state mainly a localized excitation on the central diaminophenyl group. For the S_3 state, however, the fragmented TDM shows considerable diagonal matrix contributions suggesting local excitonic interactions between the single branches, alongside with a considerable amount of outer diagonal matrix contributions, revealing CT participation between the respective fragments. Interestingly, the latter is exclusively located at the V-shaped A-π-D-π-A moiety of H_4TPBD (e.g. CT from fragment 3 to 1, Figure 19, and a,b respectively c,d pathways in Figure 16) and highly symmetric! Note that a detailed explanation of the concept of TDMs is given in chapter 2.3.5. The small energy difference of the bright states can be understood on the respective difference of the participating orbitals, as the LUMO+1 and LUMO+2 (Figure 20) lie close in energy.

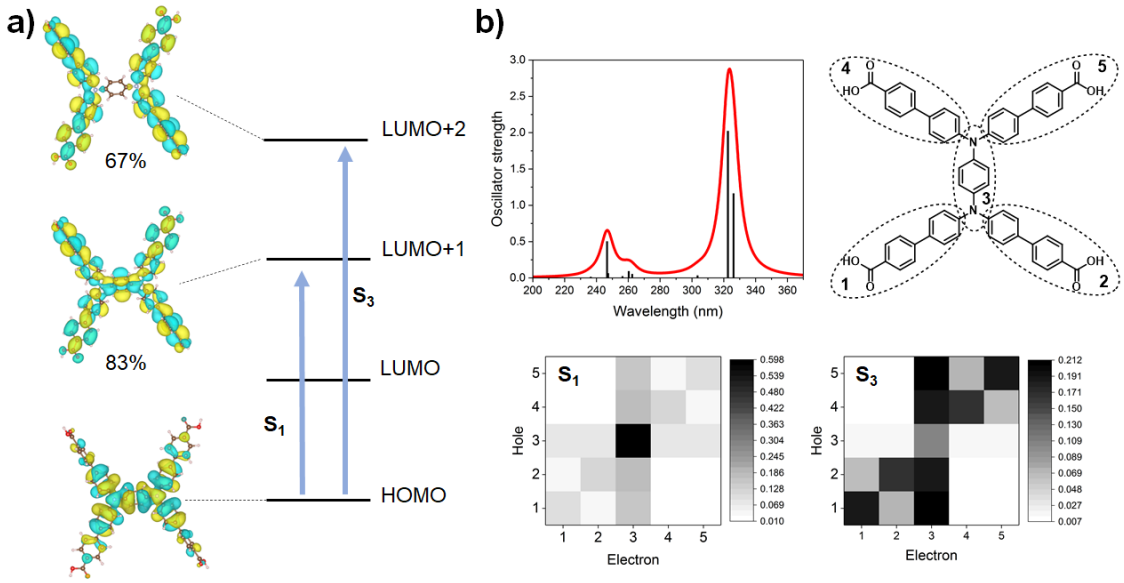

Figure 20. a) Natural transition orbitals of the low energy excited states S_1 and S_3 (gas phase calculations, major contributions shown). b) Theoretical UV/Vis spectra of H_4TPBD (Lorentzian broadening), the fragmented TDMs and the fragmentation scheme. The S_1 state is predicted at 325 nm, the S_3 state at 320 nm (~ 50 nm deviation to experimental value). The TDMs reveal the charge transfer characteristics for the S_3 state (HLCT state).

To get an insight in the excited state geometry (ESG) of H_4TPBD, the first electronic excited state S_1 was fully geometry optimized. Subsequent calculation of vibrational frequency revealed no negative eigenfrequencies, proofing the obtained geometry to be a local minima of the excited state PES. As expected, the ESG of H_4TPBD shows a strong distortion from the ground state structure, expressed by smaller torsional angles in the biphenyl groups and the N-Ph-N groups and a decrease in the Ph-Ph as well as the N-Ph bond lengths (the molecule tends to enhance the resonance energy of the π-electron systems upon photo excitation). Interestingly, the rather strong distortion is expressed in a relatively low induced dipole moment (0.00 D → 1.352 D), which is consistent with the non-solvatochromic emission behavior of H_4TPBD. The calculated ESG reveals that the biphenyl groups become planarized during photo excitation, which is found to be very pronounced for one sidearm (torsional angle of only 3.6°). The latter induced rotation provides an basis for the understanding of the high Stokes shift found in the measurements. The difference of the computed S_1 ESG and the S_0 ground state energy amounts to 0.452 eV (380 nm). Taking the up-shift of the S_0 state into account (e.g. by coupling to a high frequency vibration of 1400 – 1600 cm^{-1}), the computed

Stokes shift is found to be 210 nm, which comes close to the experimental value. In general, the TD-DFT calculations show two addressable excited states (S_1, irrep. A_u; S_3, irrep. B_u) at close proximity. Therefore, the excited state calculations imply that higher electronic states contribute in the photo absorption of H_4TPBD.[68] Furthermore, the small energy difference of the respective states suggest possible state mixing of S_1 ($\pi\pi^*$ character) and S_3 (HLCT character). In the context of the missing emission-solvatochromism, the experimental and calculated data both suggest further that the emissive state is the S_1 state.

The presented models for the photo response of H_4TPBD show an interesting absorption behavior and provide a first basis to understand the photophysical properties via a mixture of different by far non-trivial effects, which are correlated to each other and need further investigations (e.g. energy transfer between side arms, charge transfer between the nitrogen donor and the carboxylic acid acceptor, resonance effects and amount of π-conjugation in the network, locally excited states at the phenyl rings, strong ESG distortion via torsion of the biphenyl groups, potential mixing of excited states).

To investigate the TPA behavior of H_4TPBD, excited-to-excited state transition dipole moments were calculated using quadratic response theory as implemented in the GAMESS-US software (cam-B3LYP/6-31G(d) level of theory). By using an essential three-state model (as introduced in the background section) different TPA active channels of the NLO chromophore were investigated. Calculation of TPA strengths δ for the first two-photon allowed S_2 state within the theoretical framework predicted a two-photon absorption strength of 23832 a.u. corresponding to a TPA cross-section of 97 GM. Note that the essential three-state model has been proven to cover the important physics of TPA in centrosymmetric and pseudo-centrosymmetric molecules within an error of $\sim$ 15 %, compared to higher level theory. The analysis of the contributing TPA channels for the S_2 state revealed the $|\mu_{01}^{12}|$ and the $|\mu_{02}|$ channels as main TPA active channels, due to the strong transition dipole moments of the $S_0 \rightarrow S_2$ and the $S_1 \rightarrow S_2$ excitations and the specific energy order of the respective states. Note that the S_2 state holds an HLCT character similar to the S_3 state introduced above (based on visual investigation of the

NTOs) and corresponds to the HOMO → LUMO transition of H_4TPBD. To sum up, the quadratic response theoretical calculations predict a strong optical non-linearity of H_4TPBD, which corroborates the initial idea of push-pull ligand design by incorporation of nitrogen donor moieties in the scaffold of the organic linker and support this approach for future work.

Finally, the aggregation behavior of H_4TPBD in DMF solution upon photoexcitation was investigated. DMF solutions of the chromophore at different concentrations (1 mmol/L and 0.1 mmol/L) were subjected to excitation-emission mapping (EEM) and time-resolved fluorescence lifetime measurements. The spectroscopic analysis at high concentrations reveal substantial changes in the spectra depending on excitation/emission wavelengths. The high concentration PLE spectra always show a redshifted and much broader signal compared to the monomer. This effect was accounted to a number of distinct species (possibly a broad molecular distribution), which cannot interconvert between each other during the excited state lifetime. Given the fact, that this behavior comes with increasing concentration, the spectral changes point towards formation of aggregates with non-trivial alignment. Interestingly, in the PLE spectra, the lowest energy absorption band is redshifted, however, the emission band is similar to the monomer emission. This fact might be interpreted in a sense, that the conformer structure of the formed aggregate is relatively similar to the excited state monomer structure and significant different to the ground-state conformation of the isolated molecule. Emission spectra show a redshift of ~ 70 nm between the monomer and the higher concentration species. The excitation spectra of the latter show a considerable dependency of the emission wavelength, with a feature at 400 – 430 nm contributing much more stronger at longer emission wavelengths. Table 5 summarizes important photophysical data. The measured fluorescence lifetimes of the high concentrated solutions showed two components at similar lifetimes found for the monomer (~ 800 ps and 2 – 4 ns), however, the shorter component dominates to a higher degree.

Table 5. A short summary of collected photophysical data of H_4TPBD (1 mM). Note that the Stokes shift is given with regard to the low-energy PLE band.

$H_4TPBD_{aggr.}$:	λ_{abs}^{max} [nm]	λ_{em}^{max} [nm]	λ_{PLE} [nm]	λ_h [nm]	$\tau\,[ps]$	φ [%]
	371	600-610	430	170	800	---

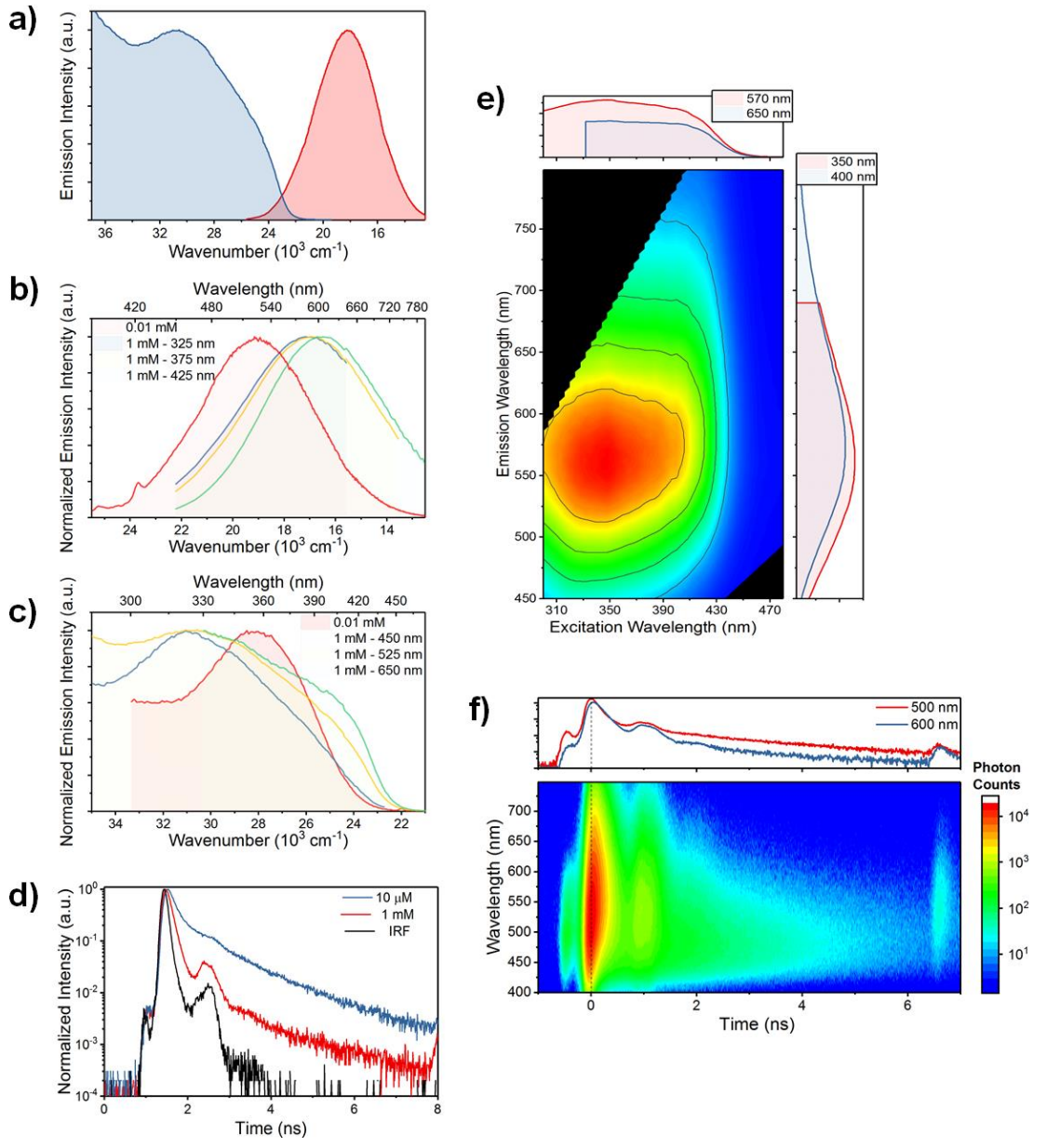

Figure 21. An overview of the photo-characterization of concentration dependent H_4TPBD. a) Emission and PLE spectra. b) A comparison of emission spectra of low and high concentration H_4TPBD solutions showing the redshifted emission signal. c) A comparison of concentration dependent PLE spectra of H_4TPBD showing the redshifted PLE signal, and the emission dependency with the rising contribution at 430 nm. d) A comparison of fluorescence lifetime at different concentrations showing the higher contribution of the faster component for the higher concentrated solutions. e) EEM of H_4TPBD in DMF (1 mM) and f) TRES of the latter.

The concentration depended behavior as introduced above is complex and very interesting. The fact that the PLE spectra and the PL signal red-shifts with higher concentrations and that the emission lifetimes relocates to lower values implies that the measured phenomena are of intermolecular origin. The difference in the PLE spectra between high and low concentration solutions, suggest that intermolecular interactions already exist in the ground state. The collected data point toward the formation of aggregates at higher concentration with non-trivial alignment. According to the spectral shifts (UV-Vis, PL and PLE), interactions are not strongly pronounced (weak coupling limit).

2.3.3 Synthesis and structural characterization of H_4TPBD based Zn^{II} and Cd^{II} CPs

Having the new potential ligand H_4TPBD in hand, the synthesis of Zn^{II} and Cd^{II} based CPs were approached. Zinc and cadmium were chosen, as they are so-called optical innocent metals, due to their closed-shell configuration (d^{10} metal ions). Consequently, no d-d transitions in the optically considered region (300 – 800 nm) can be expected.[12, 69] Furthermore, the Zn^{II} and Cd^{II} metal ions have excessively been used in the construction of luminescent MOFs.[39] Depending on the size of the π-electron system of the used ligands, metal-ligand interactions (LMCT or MLCT) have been shown to be present or absent. For extended ligands such as H_4TPBD, the frontier orbitals of the organic ligand are energetically below the frontier orbitals of the metal nodes, excluding any L-M interaction.[70, 71] Consequently, Zn^{II} and Cd^{II} metal ions where considered to be a good starting point for further studies.

The solvothermal reaction of H_4TPBD with zinc nitrate in dimethylacetamide (DMAc)/H_2O mixtures yielded a fluorescent two-dimensional CP of the composition $[Zn_2(TPBD)(DMAc)_2]$.[20] The framework compound was characterized using IR and Raman spectroscopy, PXRD, TGA, EA and SCXRD. The results can be found in the experimental part of this thesis. $[Zn_2(TPBD)(DMAc)_2]$ crystallizes in the monoclinic space group $P2_1/c$ and is composed of a four connecting (4-c) Zn^{II} node and the ligand TPBD (deprotonated form). The SBU contains two Zn^{II} ions, which are connected by four TPBD ligand motifs and two DMAc molecules. Each zinc atom is positioned

in a square pyramidal coordination environment, consisting of three carboxylate groups and one DMAc molecule. One carboxylate group coordinates in a bidentate asymmetrical chelating fashion, whereas the other two carboxylate groups bridge the two zinc atoms in a $\kappa^1:\kappa^1$ mode, leading to a rhombic node structure. Topology analysis using the ToposPro software package[72] classified $[Zn_2(TPBD)(DMAc)_2]$ as a twofold interpenetrated uninodal (4,4)-network with **sql** topology. However, considering the TPBD ligand as a two triangular vertex, the underlying topology can be better described as **bex** topology. The twofold network interpenetration leads to a Herringbone type packing of TPBD ligand within the crystallographic *bc* plane with stacking along the *b* and *c* axes, respectively. The molecule stacking shows a side-slipped planar ordering with center-to-center distances of the TPBD cores of 10.0 and 15.1 Å (compare Figure 24).

The solvothermal reaction of H_4TPBD with cadmium nitrate in DMF/H_2O/EtOH mixtures yielded a fluorescent three-dimensional framework with the composition $[Cd_2(TPBD)(H_2O)_4]$.[20] The framework compound was also analyzed using IR/Raman spectroscopy, TGA, EA, PXRD and SCXRD. $[Cd_2(TPBD)(H_2O)_4]$ crystallizes in the triclinic space group $P\bar{1}$. It is built up by a four-connecting (4-c) node unit and the ligand TPBD. The node contains two cadmium atoms, which are coordinated by four carboxylate groups and four water molecules. One Cd^{II} metal ion is hexacoordinated in a bidentate fashion by two carboxylates and two water molecules. The cadmium atoms are bridged by two carboxylates ($\kappa^1:\kappa^1$ mode). The rhombic node as found in $[Zn_2(TPBD)(DMAc)_2]$ resembles the node in $[Cd_2(TPBD)(H_2O)_4]$. Topology analysis revealed a 3-fold interpenetrated uninodal (4,4)-network of **cds** topology regarding the TPBD ligand as a four-connecting vertex. Attempts to consider TPBD as a two triangular vertex artificially complicated the topology analysis, as a new, unknown topology was found. Since the **cds** topology describes the network in a proper way, attempts to further extend the description by a binodal (3,4)-network were dropped. Please note that ToposPro revealed a net network with $\{8^3\}2\{8^5,10\}$ point symbol in the latter case. Interestingly, $[Cd_2(TPBD)(H_2O)_4]$ also adopts a Herringbone type packing motif within the crystallographic *ab* plane with stacking along the *a* and *b* axis. The chromophores show a side slipped planar packing with center-to-center

distances of 11.5 and 10.9 Å. Compared to [Zn_2(TPBD)($DMAc)_2$], the TPBD chromophores in [Cd_2(TPBD)($H_2O)_4$] experience a mean reduction in distances by 24%, which leads to a denser packed framework along the *a* axis (Figure 25).

The reaction of the (4-c) linker H_4TPBD with group 12 metal ions yields structurally related uninodal (4,4)-networks, but of different dimensionality (**sql** = 2D network, **cds** = 3D rod network). Also, the symmetry and shape of the formed metal nodes are quite similar, both with a rhombic-planar symmetry containing two metal ions. The different grade of interpenetration in the two CPs has a profound influence on the packing density, however, not on the overall packing motif! It should be noted, that the synthesis of [Zn_2(TPBD)($DMAc)_2$] and [Cd_2(TPBD)($H_2O)_4$] is significantly affected by the amount of water and the purity of the ligand. Reaction condition screening revealed that great amounts of water negatively influence the crystallinity of the obtained material. Furthermore, reaction temperatures higher than 100 °C should be avoided. Please also compare the experimental part for the synthesis procedure. Structural evidence of the as-synthesized CPs was proven by Pawley refinement, which are in excellent accordance with the results from SCXRD (Figure 22 and 23).

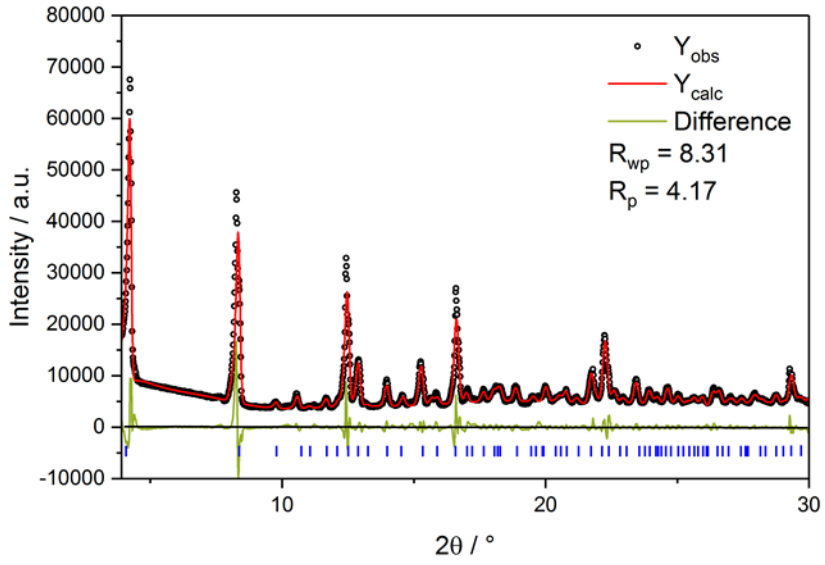

Figure 22. Pawley refinement data of [Zn_2(TPBD)(DMAc)$_2$] and the corresponding fit parameters. The Pawley refinement proofs the absence of any side phases. The obtained crystal parameters are in great accordance with single crystal X-ray data ($P21/c$, a = 21.6930(5); b = 10.0915(5); c = 15.5219(7); β = 98.6755(5)). The blue tick marks indicate the allowed Bragg reflections in the space group $P21/c$.

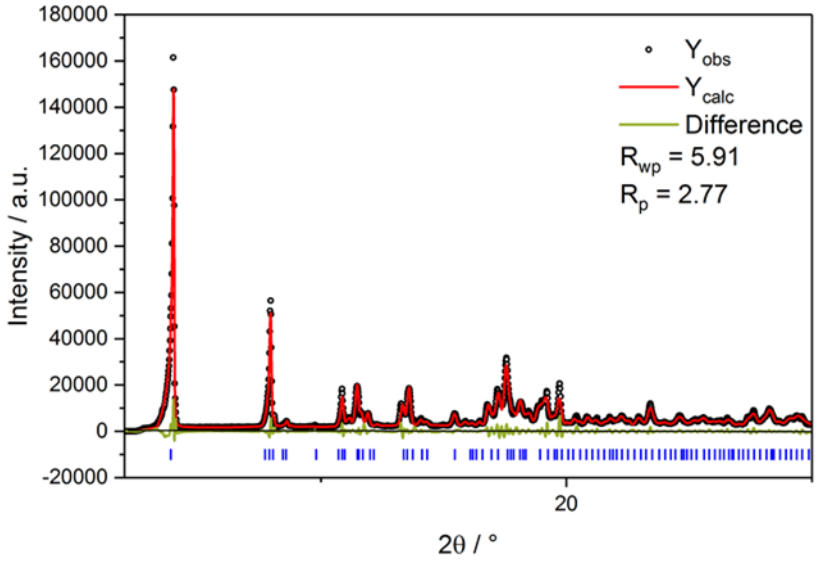

Figure 23. Pawley refinement data of [Cd_2(TPBD)(H_2O)$_4$] and the corresponding fit parameters. The Pawley refinement proofs the absence of any side phases. The obtained crystal parameters are in great accordance with single crystal X-ray data ($P\bar{1}$, a = 11.0174(1); b = 11.5188(0); c = 22.3942(0); α = 90.9720(7); β = 92.5800(6); γ = 93.1064(2)). The blue tick marks indicate the allowed Bragg reflections in the space group $P\bar{1}$.

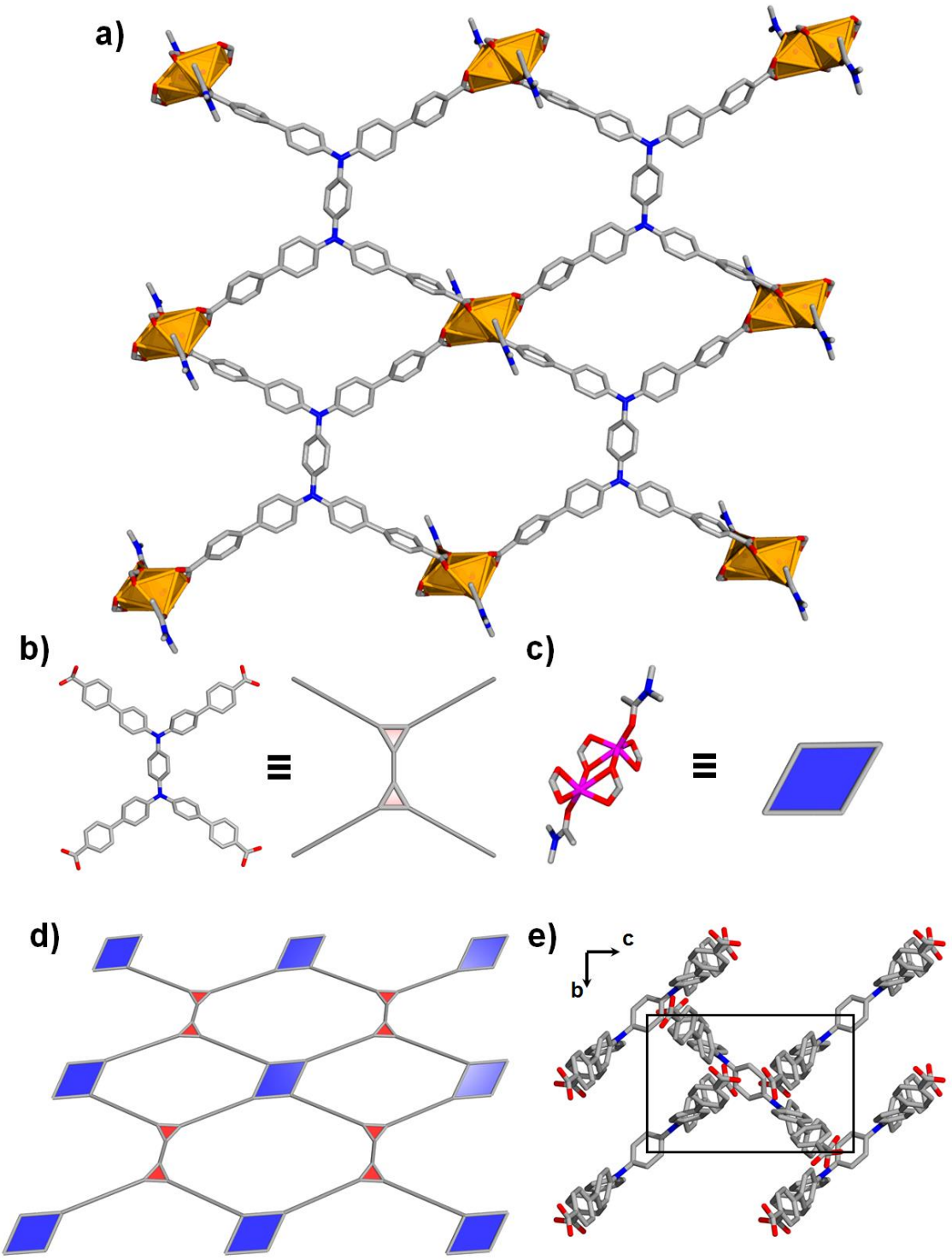

Figure 24. a) A portion of the single crystal structure of $[Zn_2(TPBD)(DMAc)_2]$. b) Representation of the TPBD ligand as a two triangular vertex. c) The Zn^{II} containing SBU. d) the underlying **bex** (or **sql**) topology of $[Zn_2(TPBD)(DMAc)_2]$. d) The Herringbone packing in $[Zn_2(TPBD)(DMAc)_2]$.

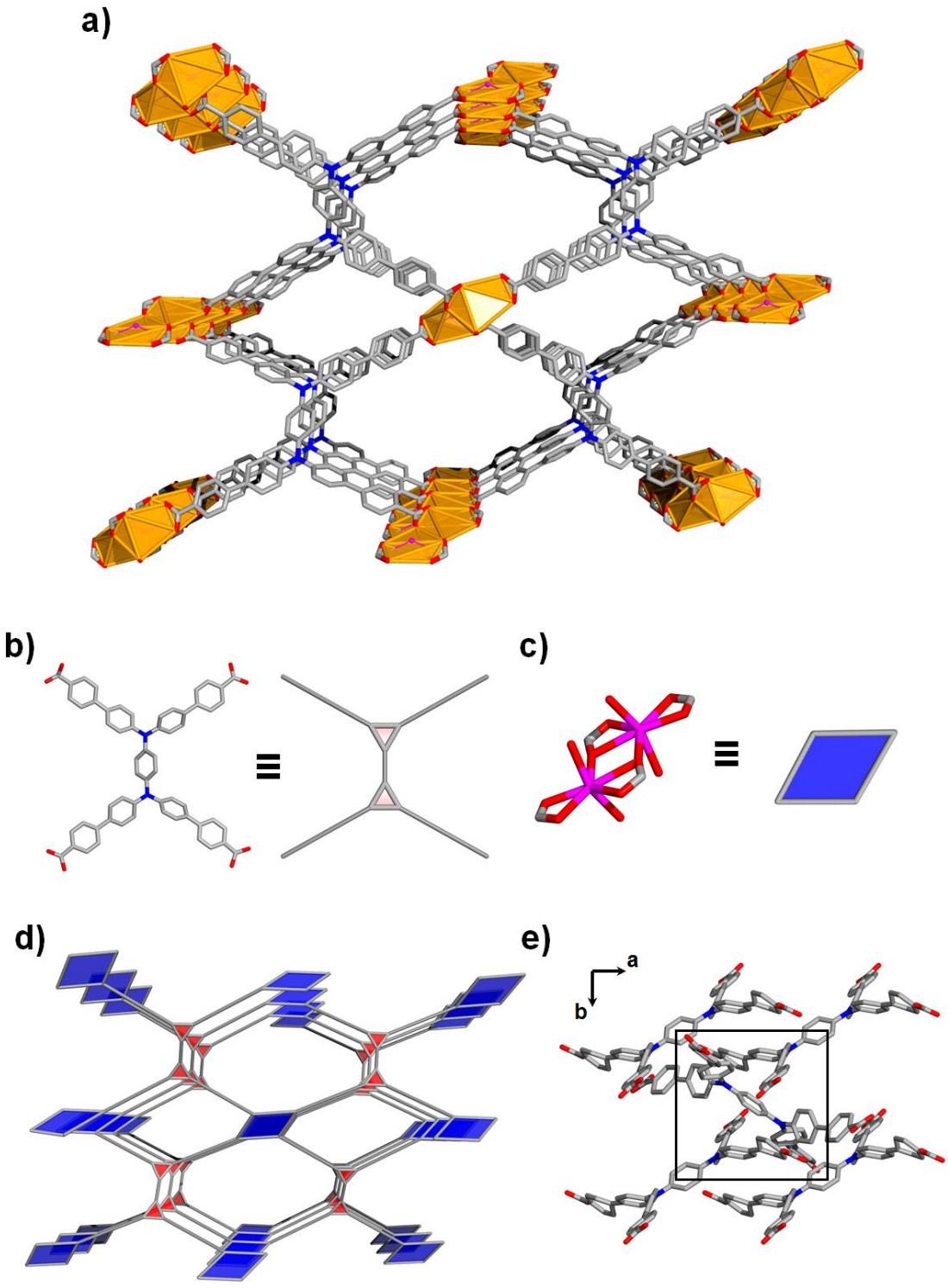

Figure 25. a) A portion of the single crystal structure of $[Cd_2(TPBD)(H_2O)_4]$. b) Representation of the TPBD ligand as a two triangular vertex. c) The Cd^{II} containing SBU. d) The underlying **cds** topology of $[Cd_2(TPBD)(H_2O)_4]$. d) The Herringbone packing in $[Cd_2(TPBD)(H_2O)_4]$.

2.3.4 Linear and non-linear optical characterization of $[Zn_2(TPBD)(DMAc)_2]$ and $[Cd_2(TPBD)(H_2O)_4]$

The linear optical characterization of the two CPs was conducted using reflectance, fluorescence and excitation spectroscopy as well as EQY measurements. The CPs hold a distinct gas-to-crystal shift compared to H_4TPBD, with the absorption edge located at ~ 486 nm for $[Zn_2(TPBD)(DMAc)_2]$ and ~ 506 nm for $[Cd_2(TPBD)(H_2O)_4]$. The PL spectra show emission centered at ~ 520 nm for both compounds similar to free H_4TPBD (525 nm). The external quantum yield amount to $\varphi([Zn_2(TPBD)(DMAc)_2])$ = 0.24 and $\varphi([Cd_2(TPBD)(H_2O)_4])$ = 0.52, revealing a twofold enhanced EQY for the Cd^{II} based MOF compared to $[Zn_2(TPBD)(DMAc)_2]$. To investigate the origin of the PL, the compounds were analyzed by PLE spectroscopy similar to H_4TPBD. Like in the case of the concentration dependent PLE investigations of H_4TPBD, the excitation spectra of $[Zn_2(TPBD)(DMAc)_2]$ and $[Cd_2(TPBD)(H_2O)_4]$ reveal multiple channels contributing to the emission of the coordination networks, expressed in a broad PLE spectrum for both compounds. For $[Zn_2(TPBD)(DMAc)_2]$ one finds signals at 424, 361 and 340 nm, whereas for $[Cd_2(TPBD)(H_2O)_4]$ the PLE spectra show the existence of three bands centered at 444, 361 and 336 nm over the whole emission range (Figure 26). It needs to be noted that the assignment of the above mentioned bands should be considered with care, as the intensities of PLE measurements on solid samples is heavily influenced by the experimental conditions (e.g. thickness of single crystals, size and shape of the laser focus, scattered light and so on). Nevertheless, one finds a pronounced redshifted PLE signal for the CPs, very similar to the high concentration excitation spectra of H_4TPBD. This fact suggest that intermolecular interactions in H_4TPBD aggregates and CPs are of the same nature and that the emissive states are located at the linker. Excitation at 400 nm will mainly populate low energy near band-gap states. The measured PL at 400 nm excitation shows values of 525 nm for $[Cd_2(TPBD)(H_2O)_4]$ and 514 nm for $[Zn_2(TPBD)(DMAc)_2]$.

In summary, the static spectroscopic characterization point towards the formation of near band edge states with $\pi \rightarrow \pi^*$ character and small-sized intermolecular interactions between neighboring TPBD units, probably strongly

bound excitons. Calculations of absorption spectra within Frenkel exciton theory (chapter 5.4.2) are in satisfactory agreement with the experimental PLE spectra, at least are able to predict the found red-shift. To further unravel the nature of the intermolecular interactions, a study in the framework of TD-DFT on TPBD clusters, excerpt from SCXRD structures, was conducted (compare the following section). Figure 26 summarizes the linear optical characterizations.

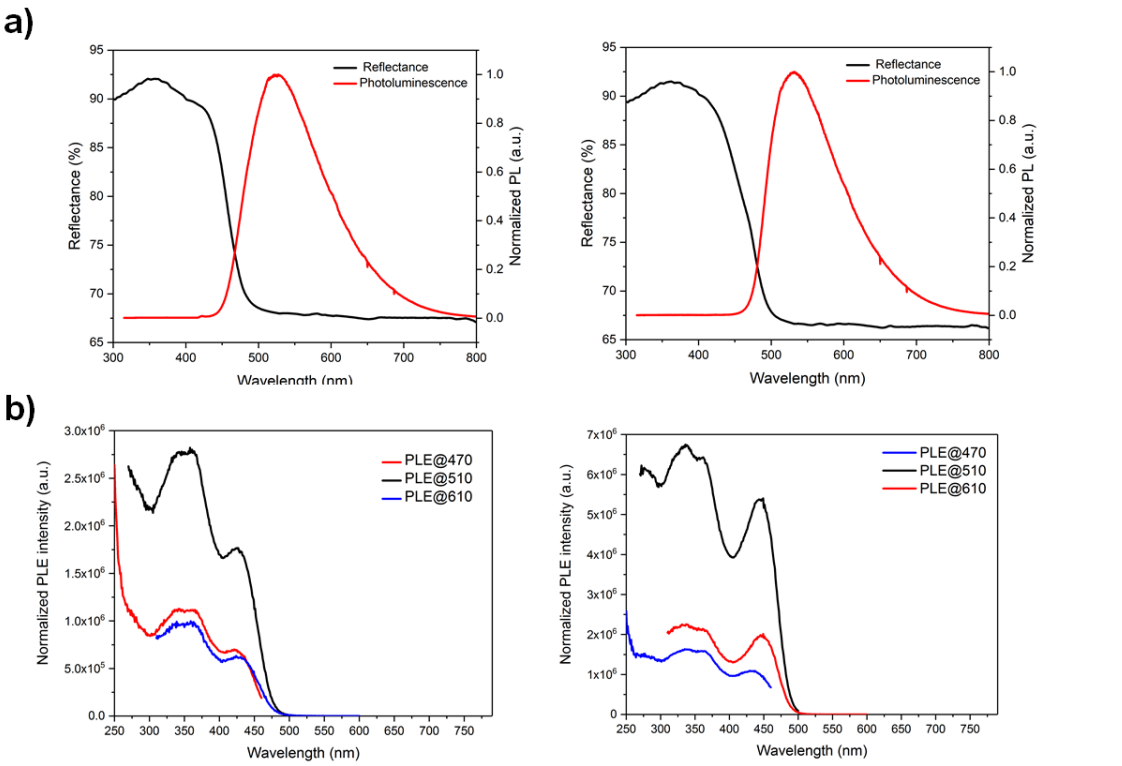

Figure 26. a) Solid-state reflectance and photoluminescence spectra of $[Zn_2(TPBD)(DMAc)_2]$ (left) and $[Cd_2(TPBD)(H_2O)_4]$ (right). b) PLE spectra of $[Zn_2(TPBD)(DMAc)_2]$ (left) and $[Cd_2(TPBD)(H_2O)_4]$ (right).

Intermolecular interactions in chromophore assemblies have been discussed as an enhancement mechanism to strong cooperative NLO response (the basis of size scaling of MPA is extensively discussed in the background section of this thesis, compare chapter 4.3.2). The presented spectroscopic analysis above suggest a structure relation towards the TPA response of $[Zn_2(TPBD)(DMAc)_2]$ and $[Cd_2(TPBD)(H_2O)_4]$. To proof this hypothesis, the non-linear absorption of the framework compounds were studied by below-band gap excitation using an excitation source at λ_{ex} = 800 nm. Excitation energy for the non-linear optical studies was provided by a femtosecond laser with a pulse width of 100 fs at a

repetition rate of 1 kHz. Upon excitation at 800 nm, a PL signal is observed centered around 520 nm, with no shift compared to the one-photon excited PL, which shows that the nonlinear absorption proceeds via similar states as the one-photon excitation.[18] Since linear absorption at the excitation wavelength is negligible, the absorption process is of nonlinear origin, indicating a TPA process. The absence of a real accessible energy level at 800 nm (compare the PLE and reflectance data in the experimental section), shows that the absorption process must proceed via a virtual state, which excludes resonance enhancement effects in the TPA process.[7] To proof the order of the nonlinear optical absorption, power-dependent studies were carried out similar to the above presented experiments. Since the probability of a non-linear absorption is a power function of the excitation fluence, the intensity of the luminescence follows a power law. Thus, by measuring the PL intensity as a function of excitation intensity, one can obtain the order of the NLO process. The analysis of the compounds by global fitting procedures of the power dependent PL data to a square function shows an order-two process. This identifies TPA as the underlying NLO process. Non-linear absorption of $[Zn_2(TPBD)(DMAc)_2]$ and $[Cd_2(TPBD)(H_2O)_4]$ at 800 nm excitation will populate near band gap states. Consequently, the non-linear response of the framework compounds will be influenced by intermolecular interactions between the chromophores.

The TPA properties of the CPs were quantified by a modified SSTPEF procedure in the $\mu J/cm^2$ area. Since solid TPA references (e.g. perylene) showed no measurable TPA signal at the regarded power range in our setup, a comparison to reference values was not possible. Thus the CPs withdraw from the determination of relative TPA cross-section values using the SSTPEF method.[12] Changing to a power region (mJ/cm^2) suitable for the solid TPA references, however, led to photosaturation effects in the CPs. Indeed, this shows that $[Zn_2(TPBD)(DMAc)_2]$ and $[Cd_2(TPBD)(H_2O)_4]$ are stronger two-photon absorber then, for example, crystalline perylene. The TPA efficiencies were estimated by direct comparison of the integrated TPEF areas at similar wavelengths. As has been said, this did not enable the determination of absolute cross-section values, however, the approach allows for the determination of a structure related relative enhancement factor ξ and circumvents uncertainties in the measurements of solid TPA standards.[20]

Equation 2.2 summarizes the important quantities, compare also the background section of this thesis for insights in the SSTPEF method.

$$\frac{\sigma_{CdTPBD}}{\sigma_{ZnTPBD}} = \xi = \frac{A_{CdTPBD} d_{ZnTPBD} \varphi_{ZnTPBD}}{A_{ZnTPBD} d_{CdTPBD} \varphi_{CdTPBD}} \quad (2.2)$$

Where ξ is defined as the ratio of TPA cross-sections σ, A is the TPEF area, d is the chromophore density (number of linkers per unit cell) and φ is the quantum efficiency. Following this analysis approach, a relative enhancement of a factor of 9 was found for the Cd^{II} based network in comparison to $[Zn_2(TPBD)(DMAc)_2]$. This enhancement can be rationalized by a subsequent analysis of the included quantities in equation 2.2. Key elements for the enhancement of TPA efficiencies have been described to origin from an increase in the number of active centers or by coherent interactions via conjugation (“through bond”) or between chromophores (“through-space”, collective and cooperative interactions). Since $[Zn_2(TPBD)(DMAc)_2]$ and $[Cd_2(TPBD)(H_2O)_4]$ exhibit slightly different chromophore densities ($[Zn_2(TPBD)(DMAc)_2]$: 1.00 mol/dm^3; $[Cd_2(TPBD)(H_2O)_4]$: 1.19 mol/dm^3), one would expect slightly higher TPEF areas for $[Cd_2(TPBD)(H_2O)_4]$, provided that no intermolecular interactions exist and the NLO response is only limited by the number of active centers. Consequently, the enhanced TPA efficiency in $[Cd_2(TPBD)(H_2O)_4]$ cannot be deduced to a simple additive behavior.[51] Apparently, the difference in the electronic structure of the two CPs being a function of the local chromophore arrangement alters the NLO response. Population of below band gap states holding different character in $[Cd_2(TPBD)(H_2O)_4]$ most probably will lead to the enhanced non-linear absorptivity. On the contrary, even though $[Zn_2(TPBD)(DMAc)_2]$ exhibit the same principal packing motif, the latter seems to negatively affect the TPA properties, at least in comparison with the Cd^{II} based framework.

Finally, higher chromophore density, denser packing and intermolecular interactions cooperatively seem to achieve a stronger TPA efficiency in $[Cd_2(TPBD)(H_2O)_4]$. The observed increase in the two-photon response can be related to a predominantly “through-space” interaction mechanism[51], induced by tighter and denser packed chromophores as a direct consequence of higher network interpenetration in $[Cd_2(TPBD)(H_2O)_4]$. The presented results, even

though not fully conclusive, consolidate that intermolecular interactions in CCNs can constitute an active mechanism for the enhancement of third-order NLO effects, in accordance with recent literature.[73-78] Figure 27 summarizes the non-linear optical characterization.

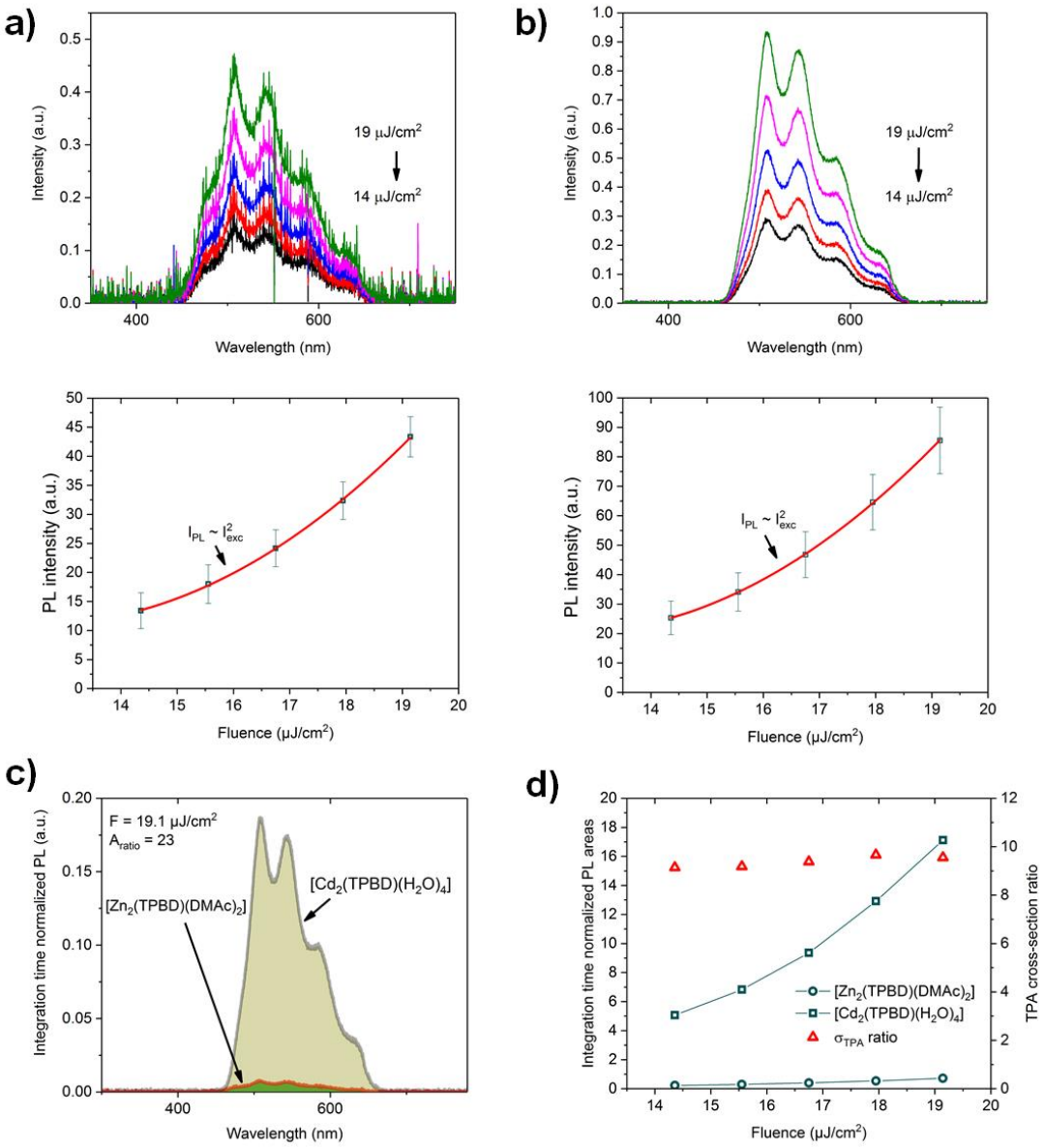

Figure 27. a,b) (from top to down) TPEF signal of $[Zn_2(TPBD)(DMAc)_2]$ (a) and $[Cd_2(TPBD)(H_2O)_4]$ (b) and the integrated PL intensity as a function of laser power. c) A graphical representation of the TPEF enhancement. d) The normalized TPEF areas and the respective enhancement factors.

Note that the measured TPEF signals showed the formation of a structured contribution in the spectra (compare Figure 27). The TPEF signals were

collected with a fiber-coupled CCD spectrometer as a detector. The modulation of the PL signals therefore is contributable to an interference signal from the used optical fiber, which is strongly expressed due to the broad emission wavelength range of the CPs.[79] However, since all measurements were conducted using the same experimental conditions (same setup, same detector, same type of sample preparation), the influence of signal modulation will not greatly affect the above presented analysis, also because the determination of an enhancement factor ξ relies on a relative manner (one can assume that the experimental condition factor is cancelled out).[12] Initially, the single fractions in the PL were assigned to vibronic contributions.[20] This fact cannot fully be ruled out. Nevertheless, further linear optical measurements on the systems and the linker H_4TPBD revealed no structured emission signal.

2.3.5 Calculations of excited-state properties of $[Zn_2(TPBD)(DMAc)_2]$ and $[Cd_2(TPBD)(H_2O)_4]$

To understand the photo absorption of $[Zn_2(TPBD)(DMAc)_2]$ and $[Cd_2(TPBD)(H_2O)_4]$ and to further access information about the type of intermolecular interactions between neighboring TPBD units in the CPs the photo response was modelled using periodic DFT calculations as well as TD-DFT calculations on small molecular clusters. The photo response of aggregates and molecular crystals is commonly been described within the exciton theory.[53, 80, 81] Since in CPs large and extensive organic linker molecules are periodically arranged, the description in terms of exciton theory is reasonable.[82, 83] The exciton picture originates from solid state physics, where an exciton is described as a quasiparticle consisting of a positively electron-hole and an excited electron (compare the background section about excited states theory in molecular aggregates and crystals). The modelling of exciton properties quite naturally originates from the GW + Bethe-Salpeter equation.[84] However, for computationally demanding systems (such as CPs or MOFs), the solution of these approaches is limited or almost impossible. Consequently, for getting an insight in the processes upon photoexcitation of $[Zn_2(TPBD)(DMAc)_2]$ and $[Cd_2(TPBD)(H_2O)_4]$ a approach by Ciofini[85] or Coudert et. al.[86] was followed, where small-sized molecular clusters extracted from the crystal structures were subject to TD-DFT calculations. Furthermore, to get an idea

about potentially excitonic properties, an analysis of the theoretical data was conducted following work of Plasser[87-89] as well as Dreuw and co-workers.[87, 90-92] The central idea of this approach is the identification of an exciton wavefunction as the one-particle transition density matrix (TDM) between the ground state and an excited state as well as the recognition of the ground state part as the hole coordinate, while the excited state part corresponds to the electron coordinate. The authors developed a number of density-based descriptors for excited state calculations, which enables to deduce the character of an excited state in the excitonic picture and to distinguish between Frenkel excitonic character or charge-transfer excitons.[89] A similar approach has in parts be conducted by Deria et. al. in the description of excited states of the two MOFs NU-901 and NU-1000.[30] Within the presented work, the electron-hole correlation plots and related charge-transfer numbers are used for the analysis of the excited states of cluster fragments deduced from $[Zn_2(TPBD)(DMAc)_2]$ and $[Cd_2(TPBD)(H_2O)_4]$.[87] The followed theoretical approach is subsequently described.

Starting from the available crystallographic information, the structures of $[Zn_2(TPBD)(DMAc)_2]$ and $[Cd_2(TPBD)(H_2O)_4]$ were periodically optimized using the Quantum Espresso software package (plane-wave DFT) at the GGA approximation using periodic boundary conditions. The Kohn-Sham states were expanded in projected-augmented wave (PAW) pseudopotentials with a kinetic cut-off energy of 60 Ry (480 Ry for the density). The Γ-point was used for Brillouin zone sampling. The atomic positions of the crystal structures (no cell parameter optimization) were geometry optimized using the PBE functional and a Grimme D3 dispersion correction (as implemented in the software). Convergence criteria for the calculations were set to 0.0001 Ry (for the forces) and 0.0038 Ry (for the total energy). Geometry optimization was conducted only on the Γ-point. The k-point sampling for calculations of density of states (DOS) and projected density of states (PDOS) was done on a 3x3x3 k-point mesh centered at the Γ-point.

Excited state properties were investigated using TD-DFT calculations (20 states) on TPBD clusters comprised of 3 molecules along the different crystallographic axis (Figure 29), which were extracted from the optimized

structures. The metal ions (Zn^{2+} and Cd^{2+}) were replaced by hydrogen atoms on each carboxylate groups, to ensure charge neutrality. This approximation can be rationalized by two facts. First, recent theoretical work has shown that the optical properties of Zn^{II} and Cd^{II} based MOFs are mostly defined by ligand centered $\pi \rightarrow \pi^*$ excitations, due to the lower lying frontier orbital of extended π-electron ligands compared to the zinc and cadmium frontier orbitals.[70, 71] Secondly, analysis of the PDOS calculations of $[Zn_2(TPBD)(DMAc)_2]$ and $[Cd_2(TPBD)(H_2O)_4]$ revealed, that the electronic states localized around the band-gap are composed of only ligand centered states (Figure 28). Thus, band-gap and below band-gap excitation of $[Zn_2(TPBD)(DMAc)_2]$ and $[Cd_2(TPBD)(H_2O)_4]$ will happen between occupied and unoccupied TPBD centered orbitals.

The analysis of the TD-DFT calculations is conducted by fragmented TDMs, as already presented in the excited state part of H_4TPBD. The matrix representation of the single particle TDM in a basis set of spin atomic orbitals $\{\chi_\mu(r)\}$ is constructed as:[87, 89]

$$D_{\mu\upsilon}^{0I} = \langle \phi^0 | \hat{a}_\mu^\dagger \hat{a}_\upsilon | \phi^I \rangle \tag{2.3}$$

$$\gamma^{0I}(r_h, r_e) = \sum_{\mu\upsilon} D_{\mu\upsilon}^{0I} \chi_\mu(r_h) \chi_\upsilon(r_e) \tag{2.4}$$

Where $\hat{a}_\mu^\dagger \hat{a}_\upsilon$ are the creation and annihilation operators. ϕ^0 respectively ϕ^I are the ground state and excited state wavefunctions. $D_{\mu\upsilon}^{0I}$ is the one electron TDM with respect to the ground state and $\gamma^{0I}(r_h, r_e)$ is the TDM in the spin atomic orbitals.

$$\Omega_{CT} = \frac{\sum_{AB} \Omega_{AB}}{\Omega} \tag{2.5}$$

Ω_{CT} represents the charge-transfer number, a descriptor of the transported charge upon photo absorption between the fragments A and B. $\sum_{AB} \Omega_{AB}$ is the summation over all outer diagonal contributions ($A \neq B$) and Ω is the complete sum of all matrix entries.

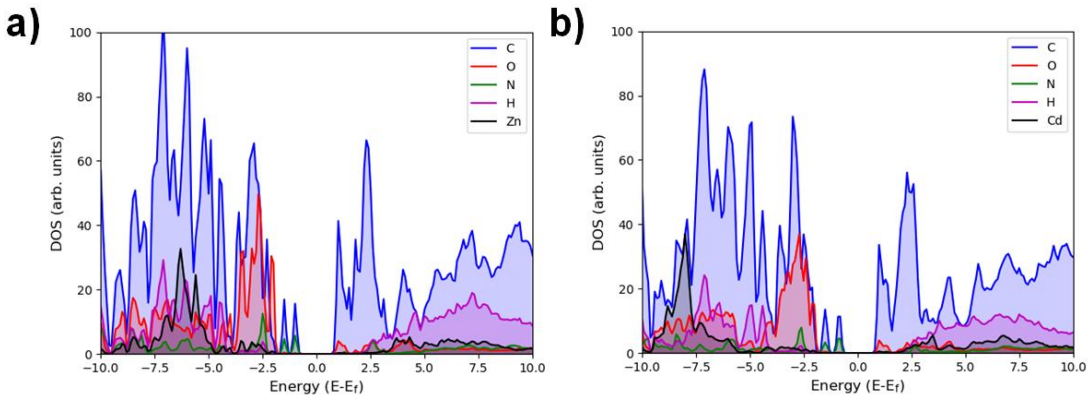

Figure 28. (a,b) Projected density of states of $[Zn_2(TPBD)(DMAc)_2]$ (a) and $[Cd_2(TPBD)(H_2O)_4]$ (b). The energy of the HOMO is assigned to zero. The major contribution to the lowest part of the optical absorption will be ligand centered, as the narrow peaks near the conduction and the valence band correspond to the organic ligand.

For a detailed explanation of the underlying physics of the concepts of TDMs, the reader is referred to excellent literature.[88] Within the presented analysis, two approaches were followed, which will be explained in the following part. Electron-hole correlation plots are used to get access to electron and hole positions, e.g. from where to where electron density is promoted during excitation. Therefore, the molecule or the molecular aggregate is split into functional groups or fragments under study. The shift in electron density between these fragments (= fragmented TDM) is presented by a heatmap, where the intensity of electron transition between two fragments is marked in grey. Local excitations at each group are displayed at the diagonal, whereas charge transfer between different groups appear as off-diagonal contributions. The hole (electron) distribution is displayed along the x-axis (y-axis). This analysis enables to distinguish between Frenkel excitonic states (main contribution in the fragmented TDM on the diagonal part) and charge resonance states (off-diagonal contribution in the fragmented TDM). Summation over all contributions on the respective fragments gives access to so-called charge

transfer numbers, which represent the weight of a charge transfer between different molecular units. This charge transfer ratio will range from 0 to 1, where 0 corresponds to a local excitation and 1 denotes a complete charge-separated state.[93]

$[Zn_2(TPBD)(DMAc)_2]$ and $[Cd_2(TPBD)(H_2O)_4]$ occupy Herringbone type packing motifs along the *c*(*b*) axis (for $[Zn_2(TPBD)(DMAc)_2]$), respectively *a*(*b*) axis (for $[Cd_2(TPBD)(H_2O)_4]$). The difference between the packing motifs is found in the fact, that in the Zn^{II} based CP, the *b* axis is elongated by almost 25 % compared to $[Cd_2(TPBD)(H_2O)_4]$, which finally leads to a more planar aligned TPBD ligand. In the Cd^{II} based MOF, however, the denser packing along the *a* axis leads to a small twist of the TPBD ligand, which brings the side-arms of the TPBD ligand closer together. To depict the structural situation as close as possible and to enable computational feasibility along with good accuracy, the maximum number of chromophores used for the construction of cluster aggregates was restricted to 3 TPBD units (at the cam-B3LYP/def2SVP level of theory). Please note that the input geometries for the TD-DFT calculations display all suitable dimeric forms of TPBD in the Herringbone packing motif. Figure 29 shows the regarded molecular clusters. Figure 30 gives the calculated UV-Vis spectra.

The analysis of the respective excited states was performed in the frame of fragmented TDMs. For the fragmentation, each TPBD molecule was regarded as a single contributing entity, which gives access to charge transfer between single molecular moieties. This approach was conducted on the first 10 excited states for each molecular cluster.

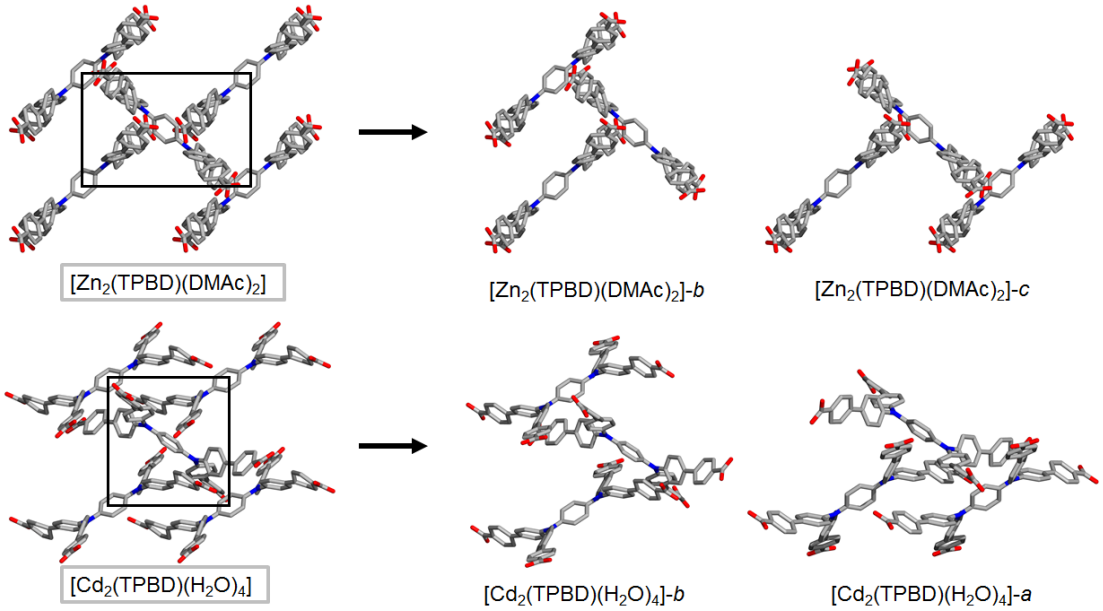

Figure 29. The input structures for TD-DFT calculations and the corresponding packing motifs.

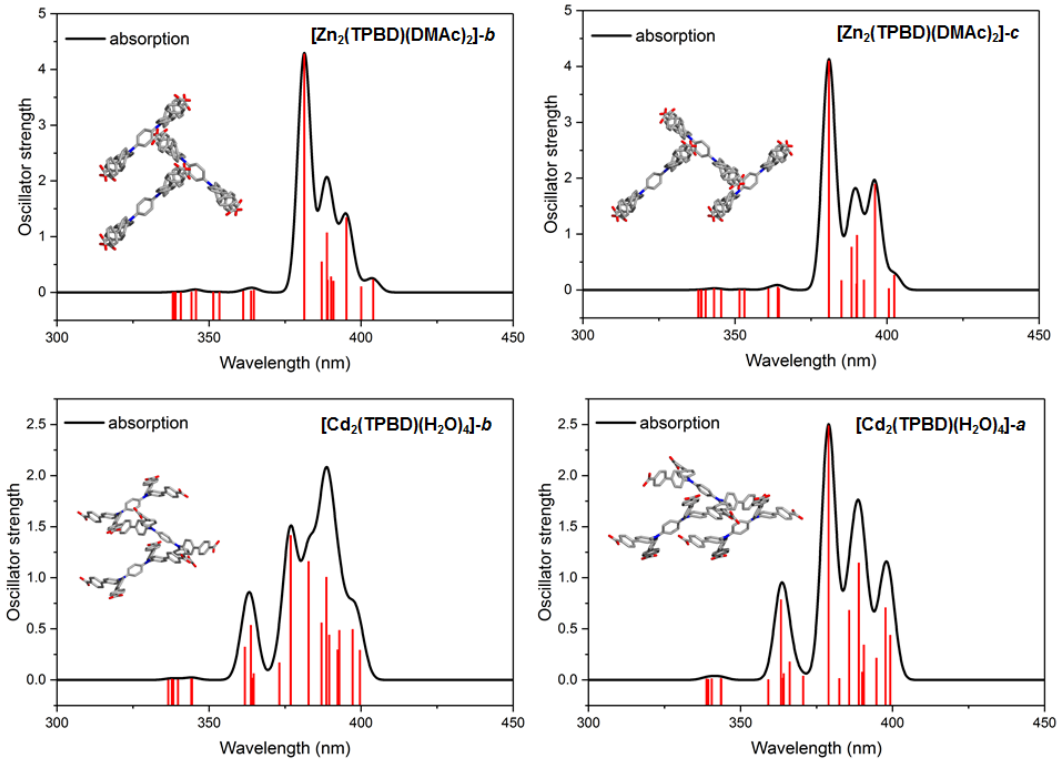

Figure 30. Theoretical UV-Vis spectra of the respective TPBD-clusters (assignment see inlets).

The analysis of the electron-hole correlation plots given in figure 31 and figure 32 for the first 10 excited states shows that the electron and hole in the case of $[Zn_2(TPBD)(DMAc)_2]$-*c* is mostly localized on single respectively two TPBD molecules. In parts, the excited state is distributed over three TPBD units. The charge-transfer numbers (~ 0.30) of each excited state reveal moderate CT contributions. The state with the highest oscillator strength is the S_9 state. The TDM of the S_9 state shows a strong hole-electron delocalization over three single TPBD molecules located at the diagonal entries, giving rise of a Frenkel type exciton (moderate CT of ~ 0.30).

Going now to the $[Zn_2(TPBD)(DMAc)_2]$-*b* case, the distance of planar arranged TPBD molecules diminished by roughly 5 Å. This fact is directly depicted in the TDMs of the respective excited states. In all states the electron-hole correlation plots reveal a stronger delocalization, as more TPBD moieties contribute to the excited state, a direct consequence of the smaller distances (two, respectively three molecules, black squares at the matrix diagonals). Again, the S_9 state holds the highest oscillator strength and shows a Frenkel type excitonic character spread over three TPBD molecules according to the underlying TDM.

Altogether, the analysis of the fragmented TDMs based on TD-DFT calculations suggest that in $[Zn_2(TPBD)(DMAc)_2]$ intermolecular interactions are of Frenkel type excitonic character with a propagation over two or three molecules. Furthermore, all states show a moderate amount of CT character (CT numbers between 0.27 and 0.38), where charge is exclusively transported between two neighbored TPBD molecules.

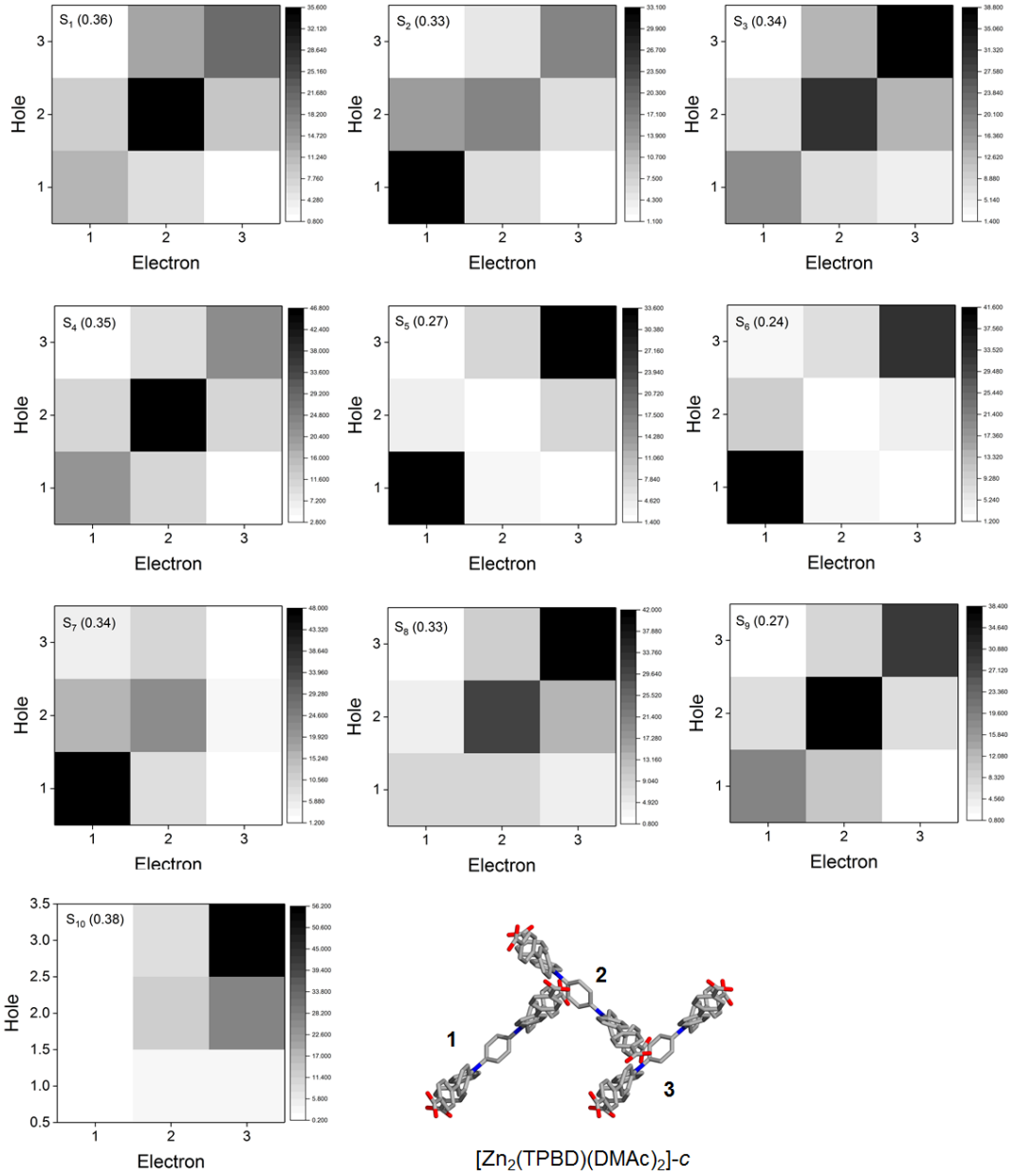

Figure 31. The fragmented TDMs for the first 10 excited states of $[Zn_2(TPBD)(DMAc)_2]$-*c* and the charge transfer numbers. The sketch at the bottom shows the fragmentation scheme used in the analysis of the TDMs. Note the individual scale for each plot.

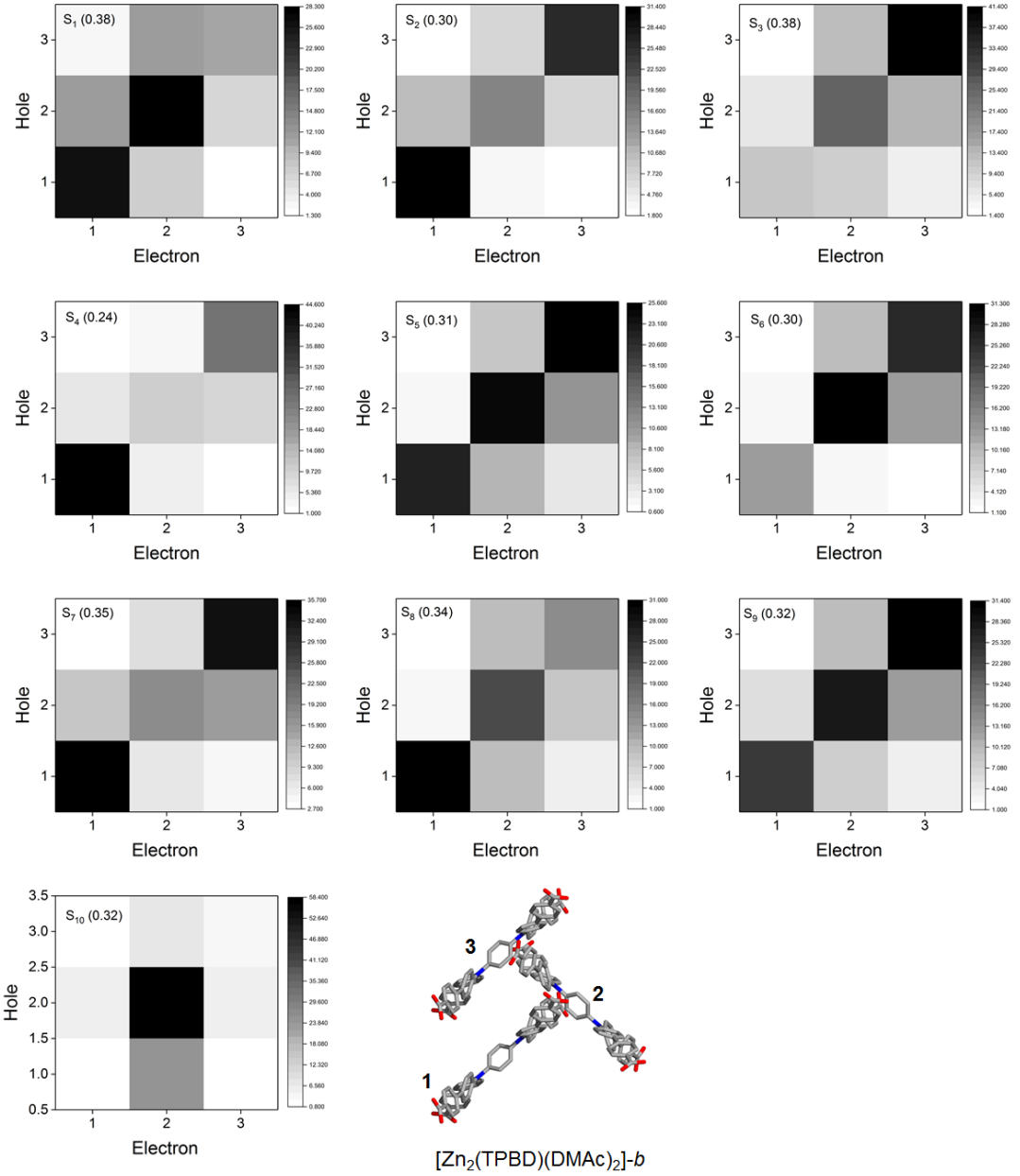

Figure 32. The fragmented TDMs for the first 10 excited states of $[Zn_2(TPBD)(DMAc)_2]$-*b* and the charge transfer numbers. The sketch at the bottom shows the fragmentation scheme used in the analysis of the TDMs. Note the individual scale for each plot.

The fragmented TDMs for $[Cd_2(TPBD)(H_2O)_4]$-*a* reveal a somewhat different trend, when compared to $[Zn_2(TPBD)(DMAc)_2]$-*b(c)*. The electron-hole correlation plots show greatly enhanced outer diagonal contributions illustrated by the increased CT numbers (between 0.38 and 0.76). The electron-hole interactions are spread over two, respectively three chromophores giving rise of a short-range localized exciton with CT character. The high-lying states S_{10} (CT number: 0.76) or S_{13} (CT number: 0.53) can be regarded as almost charge-seperated states between fragment 1 and 2 (or 1 and 3 for S_{13}, Figure 33). For $[Cd_2(TPBD)(H_2O)_4]$-*b* one finds a similar picture, with enhanced outer diagonal contributions and CT numbers. The low-lying states S_1, S_2 and S_3 for example, depict charge-transfer states between chromophores 1, 2 and 3, where upon photo excitation charge is shifted from chromophore 1 to 3 and vice versa. Whereas in the case of $[Zn_2(TPBD)(DMAc)_2]$-*b(c)* the low lying states show the formation of excitons mainly distributed over two TPBD chromophores, holding Frenkel character.

In summing up, within the presented theory the photophysics of $[Zn_2(TPBD)(DMAc)_2]$ and $[Cd_2(TPBD)(H_2O)_4]$ can be described as follows. In $[Zn_2(TPBD)(DMAc)_2]$ the calculations predict the formation of short-range Frenkel type excitons distributed over two, respectively three chromophores. In $[Cd_2(TPBD)(H_2O)_4]$ excitonic interactions are mostly of short-range charge transfer character, where photoexcitation shifts charge between two or three chromophores. The existence of net charge transfer in $[Cd_2(TPBD)(H_2O)_4]$ upon photo excitation and the fact that CT character is larger pronounced in the latter than in $[Zn_2(TPBD)(DMAc)_2]$ can be rationalized on structural arguments. The slightly distorted TPBD ligand in the Cd^{II}-based framework, due to higher network interpenetration, leads to closer arranged biphenyl sidearms, which produce a pathway for the photoexcited charge. However, in $[Zn_2(TPBD)(DMAc)_2]$ the TPBD chromophores are more planar aligned at greater distances, which will prevent orbital overlap and gives rise to Frenkel type resonance interactions with small charge transfer character. In both compounds the formed exciton is not exceeding three chromophores (according to the calculations), and thus will stay within the unit cell of both compounds.

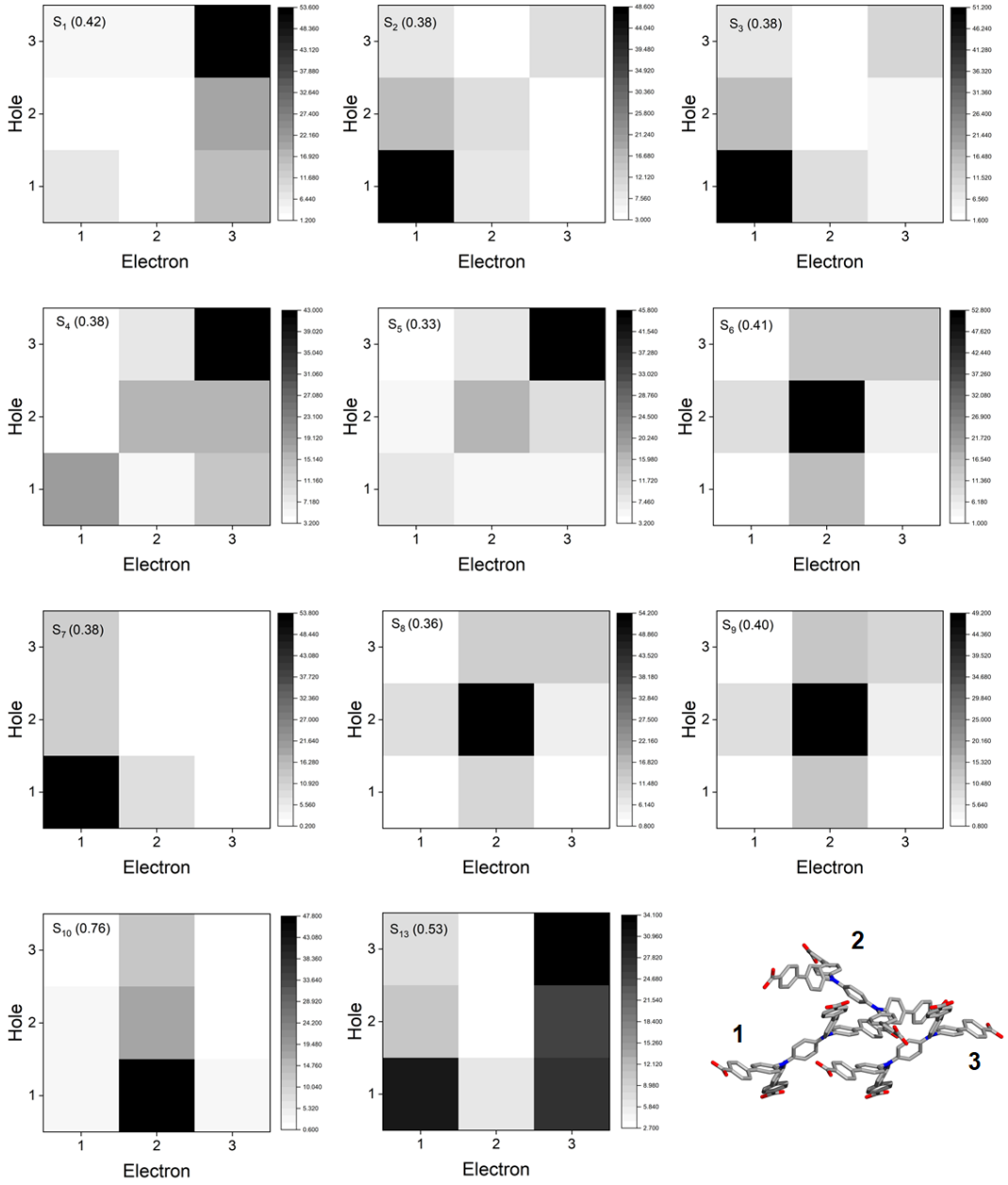

Figure 33. The fragmented TDMs for the first 10 excited states of $[Cd_2(TPBD)(H_2O)_4]$-*a* and the charge transfer numbers. The sketch at the bottom shows the fragmentation scheme used in the analysis of the TDMs. Note the individual scale for each plot.

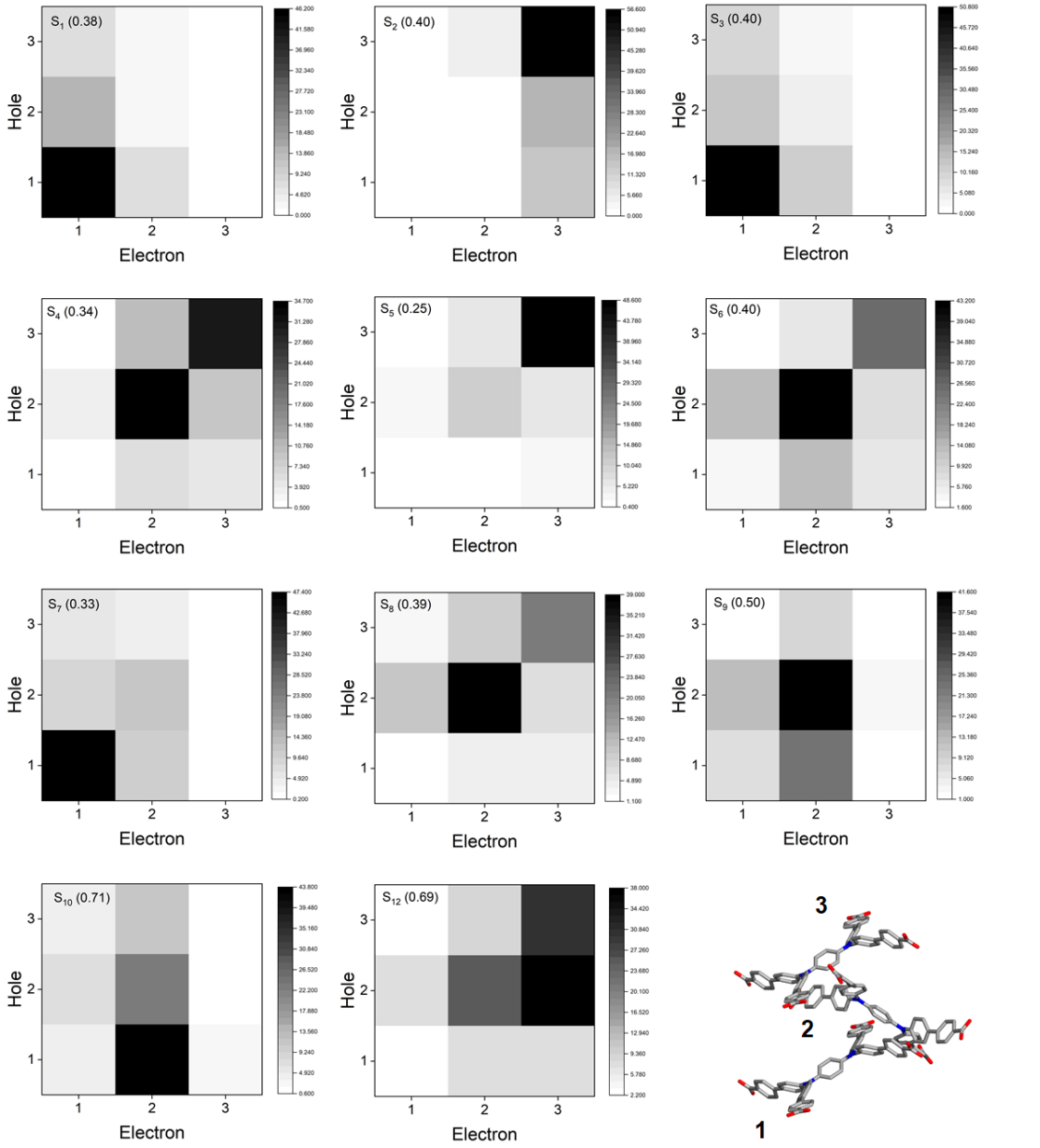

Figure 34. The fragmented TDMs for the first 10 excited states of $[Cd_2(TPBD)(H_2O)_4]$-*b* and the charge transfer numbers. The sketch at the bottom shows the fragmentation scheme used in the analysis of the TDMs. Note the individual scale for each plot.

2.3.6 Discussion and conclusion

Within the presented study, information about the influence of packing density and chromophore arrangement on TPA properties of photoactive CPs could be established. Two fluorescent CPs, $[Zn_2(TPBD)(DMAc)_2]$ and $[Cd_2(TPBD)(H_2O)_4]$, incorporating a multibranched push-pull chromophore were successfully synthesized and subsequently structurally characterized. The materials possess different uninodal network topologies and dimensionalities but show a similar herringbone type packing motif. Due to different grades of interpenetration, the chromophore arrangement in one of the CPs, namely $[Cd_2(TPBD)(H_2O)_4]$, shows a denser packing with decreasing chromophore distances of 25 % along one crystallographic axis, compared to $[Zn_2(TPBD)(DMAc)_2]$. Furthermore, the smaller distances lead to a less planar orientation within the herringbone packing as reflected by slightly twisted chromophores. Spectroscopic analysis using reflectance, PL and in particular PLE spectroscopy reveal potential intermolecular interactions between the TPBD chromophores in both CPs. The excited state properties of the latter were simulated using TD-DFT in a cluster approach and subsequent analyzed by fragmented TDMs. According to the results, the excited state of $[Zn_2(TPBD)(DMAc)_2]$ can be described as a localized Frenkel exciton, however, in $[Cd_2(TPBD)(H_2O)_4]$ the deviation from a more planar alignment opens charge transfer pathways and thus dramatically enhances the CT character. In both compounds, the formed exciton is localized within one unit cell. Comparison of PLE spectra of TPBD aggregates (formed by high concentrations in DMF solution) and the both CPs imply that the type of intermolecular interactions are of similar character. The spectroscopic characterizations, alongside with the theoretical modelling predict a suggestion for the excited state mechanism of the two CPs. Upon absorption of a photon, short-range, strongly bound excitons will be formed, located within one unit cell. The exciton holds different character depending on the regarded compound (in $[Zn_2(TPBD)(DMAc)_2]$ a neutral Frenkel type exciton, in $[Cd_2(TPBD)(H_2O)_4]$ a charged CT type exciton). The formed exciton, however, will rapidly relax and localize on a single TPBD chromophore, which is subject of emission. Due to the latter, the measured PL signal of the CPs corresponds to the single molecule PL measured at ~ 520 nm.

The non-linear response of the CPs was investigated by TPA in the potentially excitonic states centered at 425 to 450 nm (excitation of two photon with 800 nm corresponds to a single photon excitation at 400 nm). It was found that in $[Cd_2(TPBD)(H_2O)_4]$ the TPEF areas were dramatically enhanced in comparison with $[Zn_2(TPBD)(DMAc)_2]$ under similar experimental conditions. Taken the chromophore density and the EQYs of the two materials into account, an enhancement factor of ~ 9 was detected for the Cd^{II} based framework with regard to $[Zn_2(TPBD)(DMAc)_2]$. The TPA enhancement in $[Cd_2(TPBD)(H_2O)_4]$ might be rationalized on the enhanced charge-transfer character of the initially formed exciton as well as the potential stronger coupling between the single TPBD molecules due to smaller distances.

In the presented work concepts for the description of excited states of organic aggregates and organic crystals has been used to analyze the photophysics of two CPs. This has rarely been done on CPs and MOFs and a systematic approach for the limits of the presented ansatz is or should be subject of further research.[94] In general, the excited state properties of CCNs have scarcely been investigated systematically and there is still a great lack in the understanding of these properties, experimentally and theoretically.[94] Since non-linear optical properties are inherently connected to the electronic structure of the investigated material, the excited state properties of the CPs are also of immense importance, when one wants to derive structure-property relationship for MPA in CPs. The building unit principle of CPs and MOFs opens the possibility to access unusual chromophore alignments by design, which could otherwise not been achieved. The presented work already demonstrates that a specific design of chromophore assemblies in CCNs bears a potential to control the MPA properties of this material class. Furthermore, intermolecular interactions needs to be taken into account, when the non-linear response is analyzed. Based on the findings, such collective interactions seem to have a pronounced influence on the TPA behavior and can be specifically targeted by crystal engineering. In the two CPs at the center of investigations of this chapter, different grades of network interpenetration have a substantial effect on the spectroscopic fingerprint. Enhanced CT character alongside with a potentially stronger delocalization of the excited state is induced by another

entwinning layer which increases the network interpenetration and opens further channels for TPA enhancement.

Finally, it needs to be stated that the presented work does not purport to be complete. It rather represents a first approach to rationalize the young research field of multi-photon absorbing CCNs. The complex mechanism ruling the optical properties of CPs cannot be unveiled based solely on the relatively simple models and measurements presented within this work. Further studies extending the scope and numbers of investigated systems will be required to get a comprehensive picture of the ongoing phenomena.

2.3.7 *Appendix: Structural characterization and topological analysis of further Cd^{II} and Zn^{II} based CPs incorporating TPBD.*

During the synthesis and characterization procedure of $[Cd_2(TPBD)(H_2O)_4]$, single-crystal structure analysis revealed the formation of a possible side phase with the stoichiometry $[Cd_2(TPBD)(DMF)]$. This CP could not be reproduced by a number of synthesis attempts. For the sake of completeness, the single crystal structure of that compound will be discussed here, as it represents a very interesting topological situation. It needs to be noted, that $[Cd_2(TPBD)(DMF)]$ and $[Cd_2(TPBD)(H_2O)_4]$ can be regarded as pseudo polymorphic structures, since the obey similar space groups and stoichiometries, besides the type and amount of incorporated solvent (two Cd^{II}-ions and one TPBD unit).[95, 96] Please note that the term pseudo-polymorphism describes a phenomena, wherein compounds crystallize in forms, which differ in the stochiometry and type of included solvent molecules. This fact quite nicely illustrates the strength of the building block approach of MOFs, as the structure formation is mainly determined by the formation of ionic bonds between the organic ligands and the inorganic nodes. In the case of $[Cd_2(TPBD)(H_2O)_4]$, one finds single metal nodes containing two Cd^{2+} ions, whereas in $[Cd_2(TPBD)(DMF)]$ one finds a metal-oxo rod in which Cd^{2+} ions are coordinated by oxygen atoms in a distorted octahedrally and a distorted pentagonal bipyramidally fashion. These polyhedra are connected by sharing edges and vertices to form a non-trivial rod-type SBU. However, this fact leads to a chromophore arrangement obeying a herringbone packing motif in the case of $[Cd_2(TPBD)(H_2O)_4]$ and an almost co-planar stacking along the crystallographic *a* axis in the case of the solvate $[Cd_2(TPBD)(DMF)]$.

SCXRD analysis of $[Cd_2(TPBD)(DMF)]$ reveals a crystal in the triclinic space group $P\bar{1}$ with one molecule TPBD, two Cd^{2+} ions and one molecule DMF in the unit cell (Z = 2). The two symmetry inequivalent Cd^{II} atoms show a distorted octahedrally coordination environment for Cd1 and a distorted pentagonal bipyramidally coordination environment for Cd2, as has already been stated above. The polyhedra are connected among each other by three edges to form a sub-unit of four edge-sharing polyhedra. This motif is further connected to

form a rod structure, in which the sub-units are connected by vertices of the respective polyhedra. The structuring of the building unit can be more easily understood, when looking only at the point of extensions of the rod SBU (the carbon atoms of the carboxylic acid groups, linked by black lines in Figure 35), which gives edge-shared rhombohedrons propagating along the crystallographic *a*-axis. Figure 35 gives an overview of the structure.

The topological situation of the compound is complex and necessitates some explanation. Following the PE&M approach[97] the underlying network found in $[Cd_2(TPBD)(DMF)]$ is indeed a new 7-nodal (3,3,3,4,4,4,5-c) network with the stoichiometry (3-c)(3-c)(3-c)(4-c)(4-c)(4-c)(5-c) and can be described by point symbol $\{4.7.8\}\{4^2.6.7^2.8\}\{4^3.6.7.8\}\{4^3.6^2.8\}\{4^3.6^3.7^2.8^2\}\{6.8.9\}\{7.8.9\}$. However, this rod-MOF approach might not be expedient for the structure situation, as it is quite difficult. A possible more suitable way is to interpret the structure as an AA-stacking of 3D **bex** layers (Figure 35 c). For this approach, the rod SBU needs to be seperated finally ending at a **sqc27** topology (3,4-c nodal network).

Approaches to access another Zn^{II} CP incorporating H_4TPBD by using room temperature based synthesis methods gave a new compound with the stoichiometry $[Zn_2(TPBD)(DMF)_2(Tol)]$ (Tol = toluene). This CP was synthesized by an overlaying approach of a $Zn(NO_3)_2$ solution in a mixture of toluene/MeOH (1:1) and a H_4TPBD solution (DMF). After a long-term crystallization experiment ($t \sim 1$ a), crystals of $[Zn_2(TPBD)(DMF)_2(Tol)]$ formed, suitable for SCXRD analysis. However, the total amount of the product was too low for further analysis methods. Consequently, only the structure will be discussed in the following section. For a detailed synthesis procedure, please see the experimental section.

$[Zn_2(TPBD)(DMF)_2(Tol)]$ crystallizes in the monoclinic space group $P2_1/c$ with two molecules TPBD, four Zn^{2+} ions, 12 DMF and two toluene molecules in the unit cell (Z = 4). Formerly, $[Zn_2(TPBD)(DMF)_2(Tol)]$ is a pseudo polymorphic structure in comparison with $[Zn_2(TPBD)(DMAc)_2]$ (actually another solvate structure). In $[Zn_2(TPBD)(DMF)_2(Tol)]$ the Zn^{2+} ions are pseudo tetrahedrally coordinated by two chelating carboxylate group as well as two DMF solvent molecules. The structure can best be described by a ladder type arrangement regarding the TPBD as a four connecting ligand. These 1D ladders show an

intercatenation, in which the ladder structure packs in a herringbone type arrangement. Interestingly, the herringbone packing in $[Zn_2(TPBD)(DMF)_2(Tol)]$ shows similar distances along coplanar packed TPBD moieties compared to $[Zn_2(TPBD)(DMAc)_2]$, however, with a lowered herringbone angle (compare Figure 36).

In summing up, the reaction of the four-connecting ligand H_4TPBD shows a broad topological variety in the underlying analyzed structure motifs, ranging from 1D ladder type arrangements over 2D networks to 3D structures, with different grades of interpenetrations or rod type arrangements. This fact unambiguously illustrates how the underlying chemistry concepts of MOFs open up the possibility to address differing chromophore arrangements and consequently could define the photophysical properties of this material class. In other words, the structural modifiability, which can be rationalized by topological approaches, can provide a certain toolkit to engineer the photophysical properties of a material.

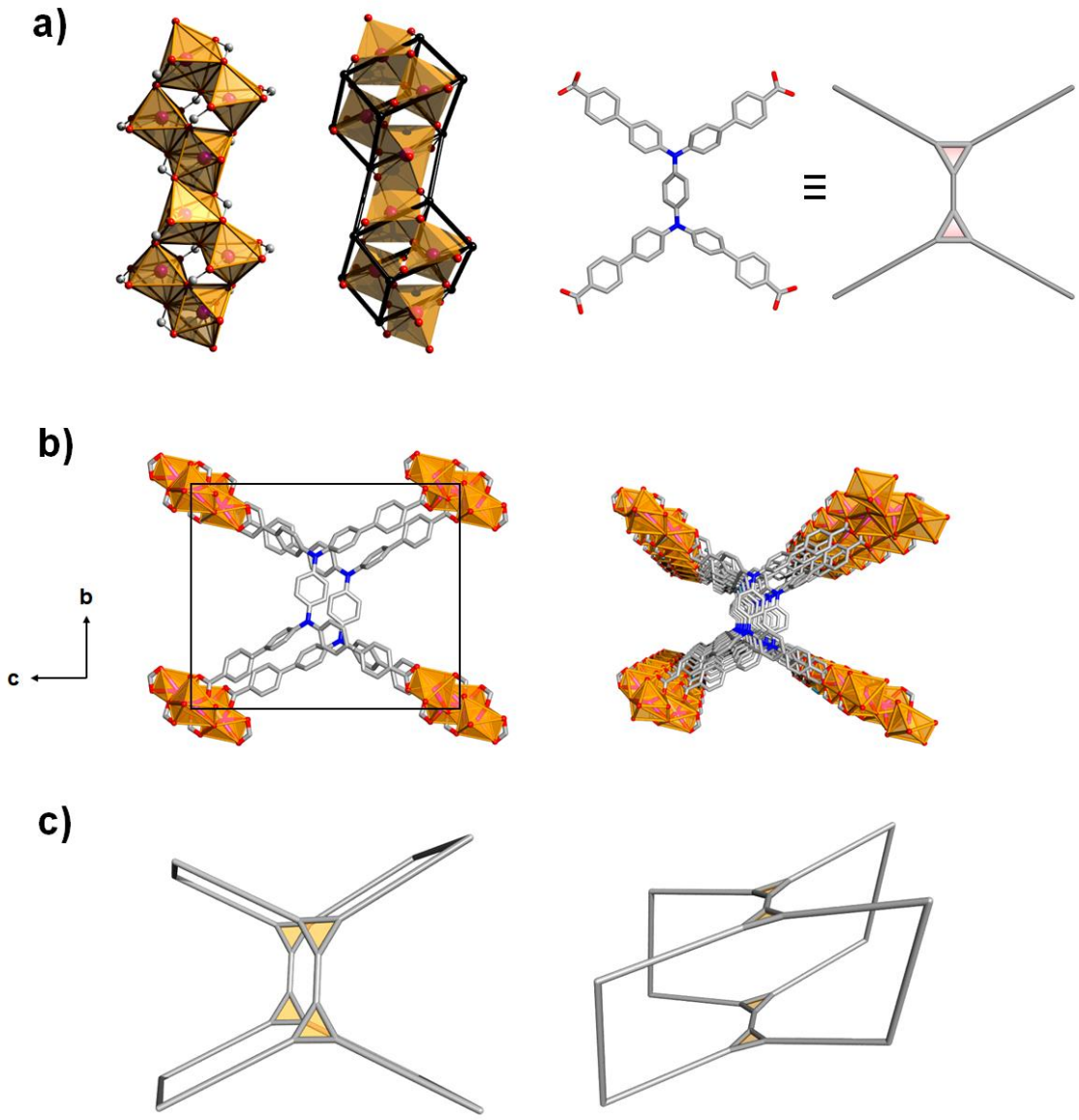

Figure 35. a) The rod SBU as found in [Cd_2(TPBD)(DMF)] with and without the connected point of extensions (black lines) and the TPBD chromophoric linker depicted as two triangular vertex. b) The structure of the CP along the *a*-axis. c) The **sqc127** network topology as found in [Cd_2(TPBD)(DMF)] from differing views.

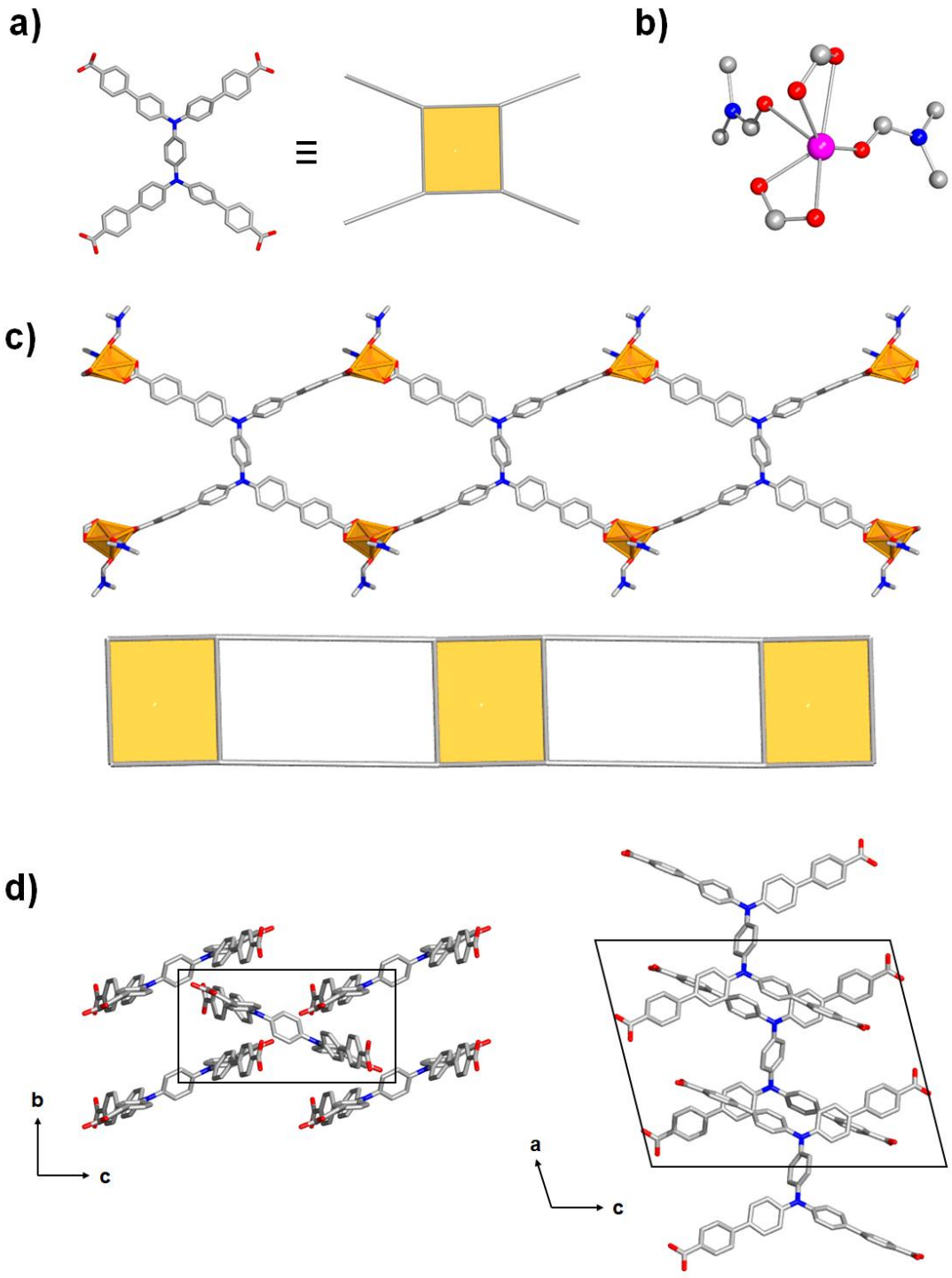

Figure 36. a) TPBD depicted as a (4-c) ligand b) The coordination environment of Zn^{2+} ions in $[Zn_2(TPBD)(DMF)_2(Tol)]$. c) A portion of the single crystal structure of $[Zn_2(TPBD)(DMF)_2(Tol)]$ and 1D ladder type arrangement. d) The herringbone packing of TPBD along the *a* and the *b*-axis.

2.4 Structural and synthetic aspects in H_4TPBD based Zr^{IV}-MOFs

2.4.1 Introductory remarks

The importance of polymorphism in the photophysical properties of organic solid-state materials directly relates to the impact of different packing modes of the building units and with that to the type and strength of intermolecular interactions between neighbored molecules. The different chromophore alignments in polymorphic phases will differently redistribute the excitonic oscillator strength among the interacting molecules within the polymorphic structures and defines the absorption behavior of the material. In view of these facts, MOFs and CPs represent a highly promising class of inorganic-organic hybrid materials, as the topological diversity of these materials gives the unique possibility to target specific local chromophore arrangements, which would otherwise only be reachable with great synthetic difficulties. The pore size and geometry of MOFs brings chromophores into diverse positions relative to one another thereby creating various possibilities for localized intermolecular interactions in interesting cluster geometries. In this context, polymorphism is a prospective material property, as a diverse phase system gives access to a number of materials with similar chemical composition, but different structure. For example, Deria and co-workers systematically interrogated the topological influence on the excited state properties of two polymorphic Zr^{IV}-MOFs comprised of pyrene based ligands (NU-901 and NU-1000, see the theoretical background section for structural composition).[29, 30, 98]

Topological complexity and polymorphism are at their height for Zr^{IV}-oxo-based MOFs, as the hexanuclear oxozirconium cluster gives access to a number of differing coordination modes (6, 8, 12 connecting).[99] This behavior is strongly pronounced for the class of Zr^{IV}-MOFs with tetratopic ligand motifs.[100-102] Among others, crystal topologies exhibit the **ftw**, **scu**, **csq**, **shp she** and **sqc** topologies.[103] Please note that {**ftw**, **shp**} and {**scu**, **csq**, **sqc**} topologies are topological isomers. MOFs incorporating these topologies are all different in their node connectivity and linker conformation. Furthermore, their embedded structures span different underlying pore geometries, which vary in size and

pore diameters (e.g. **shp** = narrow triangular channels, **scu** = rhomboid microchannels, **ftw** = cubic pores, **csq** = triangular microchannels and hexagonal mesochannels). Interesting binodal Zr^{IV}-MOFs are NU-901, NU-1000, MOF-525, NU-902, PCN-222/MOF-545, PCN-223, PCN-224, PCN-225, PCN-128, PCN-94, PCN-600, to name just a few.[101] With the structural diversity of Zr^{IV}-MOFs comes the challenge in synthesis of a single polymorphic structure, as the high grade of identity of the underlying MOFs often gives side-phases in the synthesis, dictated by experimental parameters (reaction temperature, pH-value, identity and concentration of modulators, substrate identities, metals salt/solvent ratio, precursor and ligand concentrations).[99, 104-107]

Based on reaction screening studies for the two polymorphic structures NU-901 and NU-1000 following literature protocols (see the experimental part and chapter 1 of this thesis), the synthesis of new Zr^{IV}-MOFs with the push-pull ligand H_4TPBD was approached. The aim of the work was to investigate reaction conditions for the specific synthesis of polymorphic structures in the phase system $Zr_6O_4(OH)_4$/TPBD. Systematic reaction screening gave access to only one, but crystalline phase $[Zr_6O_6(OH)_4(TPBD)_3]$, which was characterized by SCXRD, PXRD, TGA, BET, IR and Raman spectroscopy. Structural solution of the underlying crystal structure was complicated due to the low diffraction quality in the SCXRD analysis. Furthermore, potentially merohedral twinning of the collected structure data further considerable complicated the structure solution procedure. A structure model was derived by a combinatorial approach of *in silico* modelling of the structures, information gained from SCXRD analysis and Rietveld refinement of in-house PXRD data.

2.4.2 *In silico* prediction of $Zr_6O_4(OH)_4$ based TPBD structures using a reverse topological approach

Using the reverse topological approach[108] and common underlying network topologies for binodal Zr^{IV}-MOFs of (4,6-c); (4,8-c) and (4,12-c) connectivities, different crystal-structure of TPBD MOFs were predicted in **shp**, **scu**, **csq** and **ftw** topology, using the Material Studios 5.0 software suite and archetypical MOF structures (MOF-525 for **ftw** topology, PCN-222 for **csq** topology, PCN-

223 for **shp** topology and NU-902 for **scu** topology). Therefore, the symmetry of the respective single crystal structures of the MOFs were artificially reduced to $P\bar{1}$ symmetry. The organic ligands were deleted and subsequently replaced by TPBD units. The cell-parameters and ligand geometry were slightly adjusted to suite the size of the TPBD molecule. The so obtained structures were returned back to higher symmetry taking the respective high symmetry positions of the ligand and the $Zr_6O_4(OH)_4$ nodes into account. Note that the space groups were chosen somewhat artificial to approach the actual structure situation as near as possible ($P23$ for the **ftw** derived MOF, $Zr_6O_4(OH)_4$ center of gravity in Wyckoff position 1a; $P6/mmm$ for **csq** derived MOF, $Zr_6O_4(OH)_4$ center of gravity in Wyckoff position 1a; $P2/m$ for **scu** derived MOF, $Zr_6O_4(OH)_4$ center of gravity in Wyckoff position 1b; $P6/mmm$ for **shp** derived MOF, $Zr_6O_4(OH)_4$ center of gravity in Wyckoff position 1a). The input structures were allowed to fully relax (unit cell parameters as well as atomic positions) under space group symmetry restraints using the forcite module as implemented in Material Studios software (UFF, smart algorithm, force-field settings as implemented, ultra-fine quality, energy convergence criteria 2.0e-5 kcal/mol, force convergence criteria 0.001 kcal/mol, displacement criteria 1.0e-5 kcal/mol). The optimized geometries are shown in figure 37. The *in silico* prediction of accessible structures for $Zr_6O_4(OH)_4$ /TPBD together with the synthesis screening of potentially new Zr^{IV}-TPBD-MOFs opened the possibility to access underlying structure motifs in the outcome of the synthesis experiments by comparison of theoretical PXRD patterns with experimental data (Figure 39). In turn, the approach provided a first direction of an underlying structure model, without extensive structure elucidation techniques (Results: **ftw** MOF, a = 22.98; **csq** MOF, a = b = 50.47, c = 19.28, γ = 120°; **scu** MOF, a = b = 24.86, c = 20.28, $\alpha = \beta$ = 90 γ = 60°; **shp** MOF, a = b = 22.12, c = 24.25 , γ = 120°).

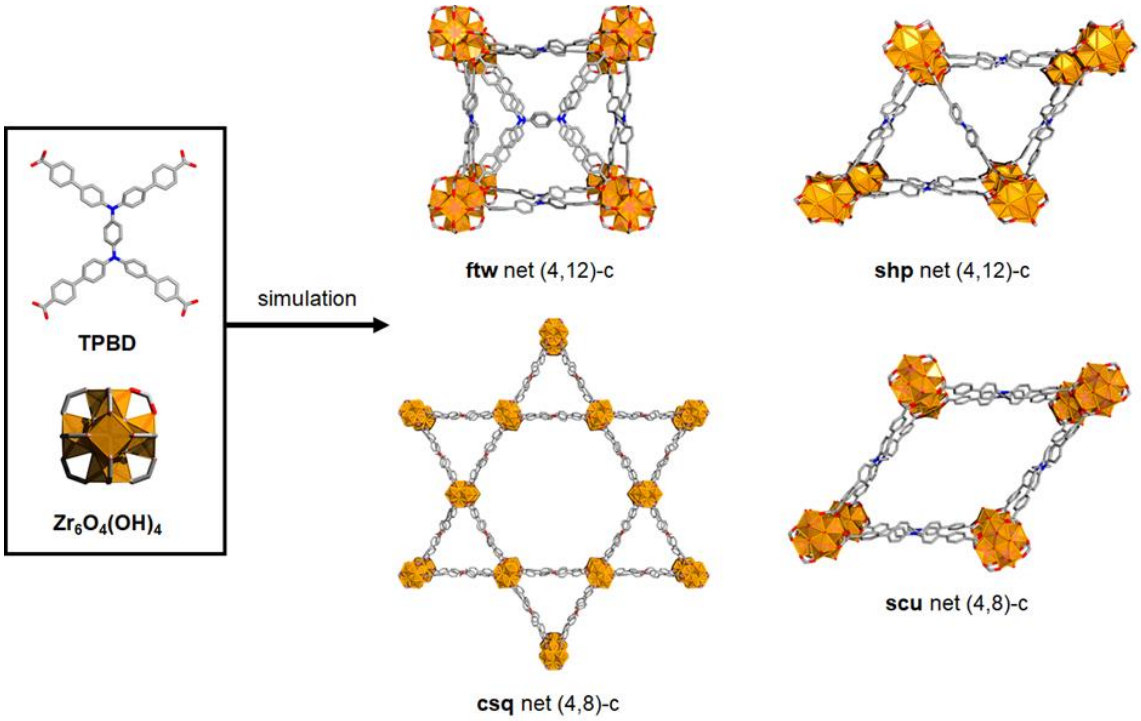

Figure 37. Results of the UFF simulations using the reverse topological approach, TPBD and $Zr_6O_6(OH)_4$ as input for geometry optimizations. The structures follow underlying topologies as regularly found in Zr^{IV}-MOFs.

2.4.3 Synthesis screening approaches in the $Zr_6O_4(OH)_4$/TPBD phase system

The synthesis of Zr^{IV} based MOFs is following a classical solvothermal approach. It involves two steps, (1) the crystallization of modulator capped Zr_6-oxo cluster nodes followed by (2) the addition of free base $TPBD^{4-}$ ligand at elevated temperatures to the solvated Zr_6-oxo cluster in formamide solutions. The synthesis of Zr^{IV}-MOFs presents itself as a multiparameter space, where the type of Zr^{IV} precursors, the amount of water, the type of modulator, the used solvent, the temperature as well as the concentration and temperature will be mutually dependent regarding the experimental conditions.[104] Factors that are known to influence the outcome of polymorphic structures are:

(1) The type of of Zr^{IV} salts (e.g. $ZrCl_4$, $ZrOCl_2$, $Zr(acac)_2$, $Zr(O^{iso}Pr)_4$ or $Zr(OPr)_4$).[109] It was shown that differing Zr^{IV} precursors affects the crystallinity and morphology of Zr^{IV}-MOFs to a great extent. First results point towards the influences of crystal water in the respective Zr^{IV} salts and with that the kinetics of Zr_6O_8-clusters formation.[101]

(2) The choice of modulator. Classical modulators are organic acids, such as benzoic acid, propionic acid, acetic acid, formic acid or methacrylic acid. The influence of the modulator is characterized by its acidity (strong or weak), the steric demand (small or steric demanding molecules) and the miscibility of the modulator with the reaction solvent. The selective formation of different polymorphs has been shown to be dependent on modulator concentration, where the quantity of $[Mod^-]/[Base^{4-}]$ (Mod^- = concentration of free modulator, $Base^{4-}$ = concentration of free ligand base) showed to considerable influence the reaction outcome.[99, 104, 110]

Beside these aspects, the geometrical constitution of the ligand in binodal (4,X-c) with X = 6, 8, 12 Zr^{IV}-MOFs has shown to hold a great influence on the type of formed polymorphs.[111-113] Briefly, planar and square type ligands tend to form the **ftw** topology.[103] Deviations in the aspect ratio (= relation between the long and short axis of the tetratopic ligand) to a more rectangular ligand favors the formation of other topologies e.g. **scu**.

It should be noted that the ligand aspect ratio is not a necessary requirement for the formation of **ftw** type structures (there are **ftw** type MOFs with ligand aspect ratios of 1.45), however, there will be an upper limit in the aspect ratio, in which the formation of **ftw** type structures is thermodynamically not favored. Furthermore, the different embeddings of the structures following the underlying topologies will distort the local ligand geometries inside the MOFs. As it has been shown for porphyrin Zr^{IV}-MOF structures, in a **ftw** type MOF the local structure of the ligand is very planar. However, in **scu** type structures the phenylcarboxylic groups rotate by an angle of 60° forming an energetically more favorable intermediate. Based on such analysis, the groups of Farha et. al. or Morris et. al. propose that the **ftw** type MOF is the kinetic product and will predominantly be formed at lower temperatures.[99, 104-106] In contrast, the **csq** net is the thermodynamic product and will predominantly be formed at elevated temperatures.

The synthetic screening of the above presented parameters in the system $Zr_6O_4(OH)_4$/TPBD were limited to the following conditions. As modulator benzoic acid and acetic acid were used. Furthermore, $ZrCl_4$ was used throughout in all conducted reactions. Dry DMF (8 mL) was used as solvent.

The concentration of $ZrCl_4$ and H_4TPBD were fixed to constant values (23 mmol H_4TPBD and 0.12 mmol $ZrCl_4$). With this approach the effect of modulator was screened in the synthesis of potentially new Zr^{IV}-MOFs. Thus, different equivalents of benzoic acid and acetic acid were applied, using different equivalents with regard to the used $ZrCl_4$ ([$ZrCl_4$]/[Mod] = 15 – 225 in steps of 15). Furthermore, in each single reaction the amount of water was screened, by enhancing the H_2O content through substitution of deionized H_2O ([$ZrCl_4$]/[H_2O] = 0, 5, 10). Finally, the reactions were conducted at temperatures of 100 °C and 120 °C for either 24 or 48 h. Figure 38 gives an overview of the conducted reactions with a graphical outline of the reaction success. After all, an amount of 360 reactions were performed. The outcome of the experiments were evaluated by visual inspections (with and without a microscope) and subsequent PXRD studies of the obtained powders. Please note, that such an approach consumes a considerable amount of ligand. The presented synthesis screening consumed almost 8 g of H_4TPBD. Regarding the fact that the synthesis and clean-up procedure of H_4TPBD takes at least one week (three step synthesis) and the average yield is 300 – 500 mg, the shaping factor of Zr^{IV}-MOF screening turned out to be the synthesis of the organic ligand. The reaction procedure was similar for all conducted reactions. The modulator and the zirconium salt were dissolved in 5 mL of dry DMF and reacted at 100 °C for 2 h to pre-form the capped $Zr_6O_4(OH)_4(Mod)_{12}$ SBU. Subsequently, a H_4TPBD/DMF solution was smoothly added to the Zr^{IV} SBU and the reaction was put in a pre-warmed oven at the respective temperature and time. During all reactions, ultrasonification procedure was waved, as the local heat input of ultrasonification can render unintended reactions and with that might negatively affect the interpretation of the reaction screening outcome. After all, the evaluation of the latter revealed the formation of a very crystalline material in the case of benzoic acid as modulator (45 equiv. with regard to $ZrCl_4$), dry DMF, $ZrCl_4$ as precursor and a reaction time of 24 h at 100 °C. The outcome of the remaining reactions revealed formation of amorphous powder products to a great extent or clear solution with no formation of any solid material. Using acetic acid as a modulator consistently showed the formation of non-crystalline powders at all considered reaction conditions. Changing to benzoic acid revealed that at higher modulator concentrations, the solvothermal reactions

showed no formation of product (clear reaction solutions), but at lower modulator equivalents the conducted reactions gave access to bright yellow powders. Analysis of these powders by PXRD revealed amorphous material for 4 out of 5 reaction solutions and a highly crystalline material for exactly one single batch.

Interestingly, the slightly more acidic benzoic acid in the above reactions showed to be the better modulator for the MOF formation (note the pK_a value of benzoic acid in DMF is 12.1 whereas the pK_a value of acetic acid in DMF is 13.4). Furthermore, in all conducted reactions water turned out to negatively affect the crystallinity of the material, which points towards the importance of the kinetics of the Zr_6O_8-cluster. Figure 39 shows the measured PXRD data of the resulting material. By comparison with the simulated PXRD data based on the computationally derived structures, one immediately recognizes that the **ftw** based structure almost perfectly fits the position of the experimental reflections, giving rise of the formation of a **ftw**-Zr^{IV}-MOF.

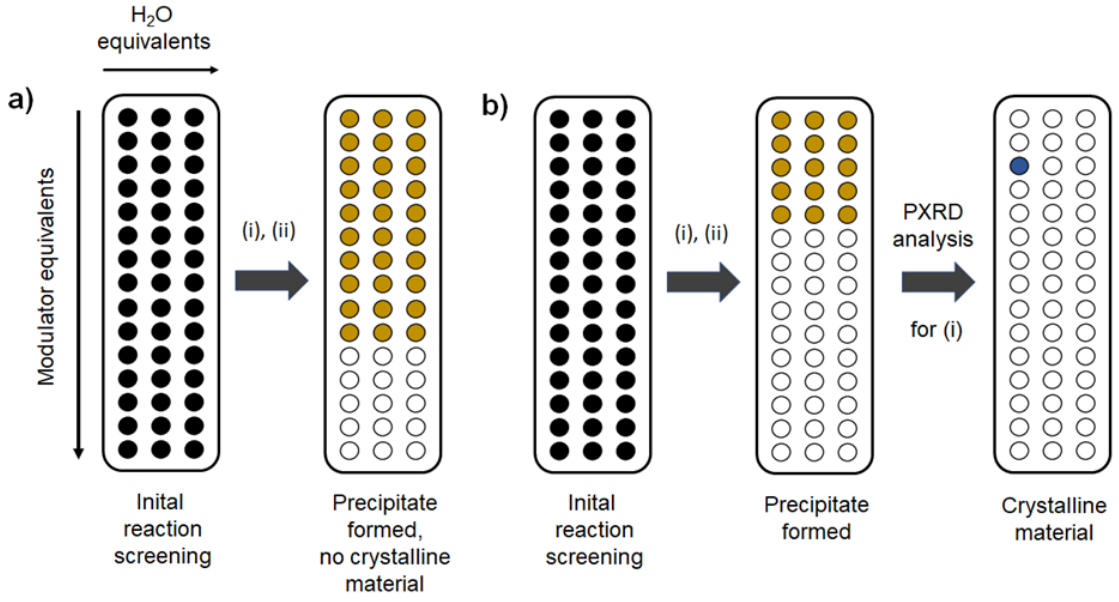

Figure 38. Schematic of the synthetic screening approach. Note that (i) corresponds to 100 °C at 24 h and 48 h and (ii) corresponds to 120 °C and 24 h respectively 48 h. a) Reaction outcome for acetic acid as modulator. All reaction conditions showed the formation of amorphous powder for low to intermediated modulator concentrations. b) Benzoic acid as modulator. Reaction conditions (i) and (ii) in all cases showed the formation of product for low modulator concentrations from low to high water contents. However PXRD analysis revealed only crystalline material in the case of a single reaction conditions (i).

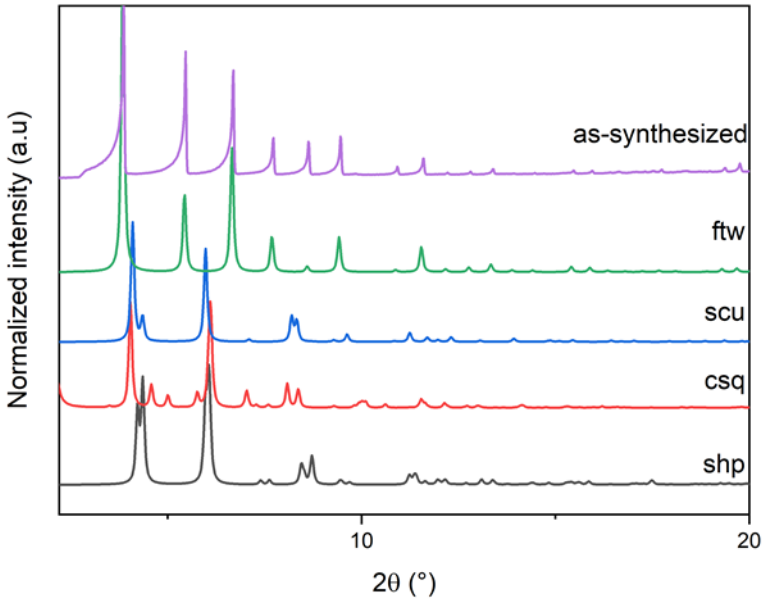

Figure 39. A comparison of theoretical PXRD spectra for the different structures simulated on the basis of differing underlying network topologies in a range of 2 – 20°, with the PXRD data of the as-synthesized material resulting from the above introduced reaction screening procedure.

2.4.4 Single crystal structure analysis of $[Zr_6O_4(OH)_4(TPBD)_3]$

The synthesis of $[Zr_6O_4(OH)_4(TPBD)_3]$ as described above revealed the formation of small, cubic bright yellowish single crystals. So far, several single crystals of different batches were tried to be characterized by SCXRD analysis, however, no complete structure could be solved or refined to a satisfactory level based on the collected data. The reason for that is rooted in a quite complex crystal structure combined with a limited SCXRD data quality. The diffraction of the measured single crystals was consistently yielding weak signals, likely due to the highly porous nature of the framework compound, the small sizes of the crystals and their stability issues (it turned out that cooling to 100 K destroys the single crystals after a short period of time. However, measurements at elevated temperatures up to RT worsened the diffraction quality even more, possibly due to loss of co-crystallized DMF and substantial signal overlap). The maximum resolution achieved in the measurements was 1.1 Å. The majority of the tested single crystals showed resolutions between 1.5 and 1.1 Å. Please note that already these resolutions were only accessed at a long exposure time of 60 s per frame using a high X-ray intensity of 20 kW/mm^2 (Mo-K_α radiation, in-house

SC diffractometer equipped with a microfocus rotating anode source). After checking several single crystals for their measurability, one crystal showed a satisfactory data quality. Indexing of the obtained diffraction data revealed a cubic crystal lattice in $m\bar{3}m$ point group. Depending on the number of considered reflections in the unit cell determination procedure, either a primitive setting (a = 22.8 Å, I/sigma ratio of 20) or a body centered setting (a = 44.6 Å, I/sigma ratio of 10) was determined. The analysis of the diffraction data using the body centered setting initially revealed a $Im\bar{3}m$ space group. By further pursuing, however, no solution of the crystal structure was possible. This fact together with the consideration of the E^2-1 value suggested occurring twinning phenomena in the MOF compound. A more precise analysis of the data indeed revealed a possible merohedral twinning with a two-fold rotation along the face diagonal of the unit cell leading to a $Im\bar{3}$ space group (checking for twinning by merohedry using Xprep revealed a twin law of 0 1 0 1 0 0 0 0 -1, BASF = 0.43, in a $m\bar{3}$ Laue class, R_{int} = 0.030, compare the experimental part for the Xprep output). However, using the $Im\bar{3}$ space group (a = 44.6 Å) for structure solution, the procedure also yielded no successful solution. Therefore, returning to the initial primitive setting, space group determination based in Xprep resulted in the possible space groups $P23$ and $Pm\bar{3}m$. E-value statistics also point towards possible twinning. However, since most **ftw** based MOFs follow the archetypical $Pm\bar{3}m$ space group the former was used in the structure solution procedure. The structure could be partly solved by intrinsic phasing (SHELXT), and the positions of the zirconium atoms and the oxygen atoms were identified. Consequently, the local coordination situation of the Zr_6-oxo cluster was resolved, which revealed a twelve-fold coordinated cluster, as required for a **ftw** topology (Figure 40). However, the positions of the ligand atoms could not properly be assigned and refined to a satisfactory level, due to possible ligand disordering alongside with the low diffraction quality of the compound (most likely due to missing intensity data at higher angles). The difficulties towards the determined space group and the possibly occurring twinning as described above suggest that the material might be highly affected by pseudo symmetry, which could be induced through flexible orientations of the pseudo-symmetric ligand H_4TPBD. Note that twinning arising from pseudo-symmetry can be particular difficult to describe and is quite abundant in high symmetric structures

of Zr-MOFs (compare the excursus and the work by Lillerud et. al.).[114] Consequently, the occurrence of different assignable space groups, implies that the structure can consists of domains with regular alternations (described e.g. by $Im\bar{3}$ or the $P23$ space group, note that $Im\bar{3}$ here is a superstructure of the cubic primitive setting) between the neighboring linkers alongside with domains occupying randomly disordered ligands (best described by $Pm\bar{3}m$ space group). These single domains consequently would appear in the diffraction pattern, which is very likely the case for our structure determination. This fact considerably complicates the crystal structure solution and refinement and prevent from a complete assignment of all atom positions in the structure. Nevertheless, the SCXRD analysis revealed the existence and the arrangement of the Zr_6-oxo cluster, which opened the possibility to deduce a structure model on the basis of PXRD data. Finally, the SCXRD results support the formation of a **ftw** based MOF with the formal composition $[Zr_6O_4(OH)_4(TPBD)_3]$ as initially supposed by the reverse topological approach and the comparison with *in silico* simulated structures to PXRD data (see above).

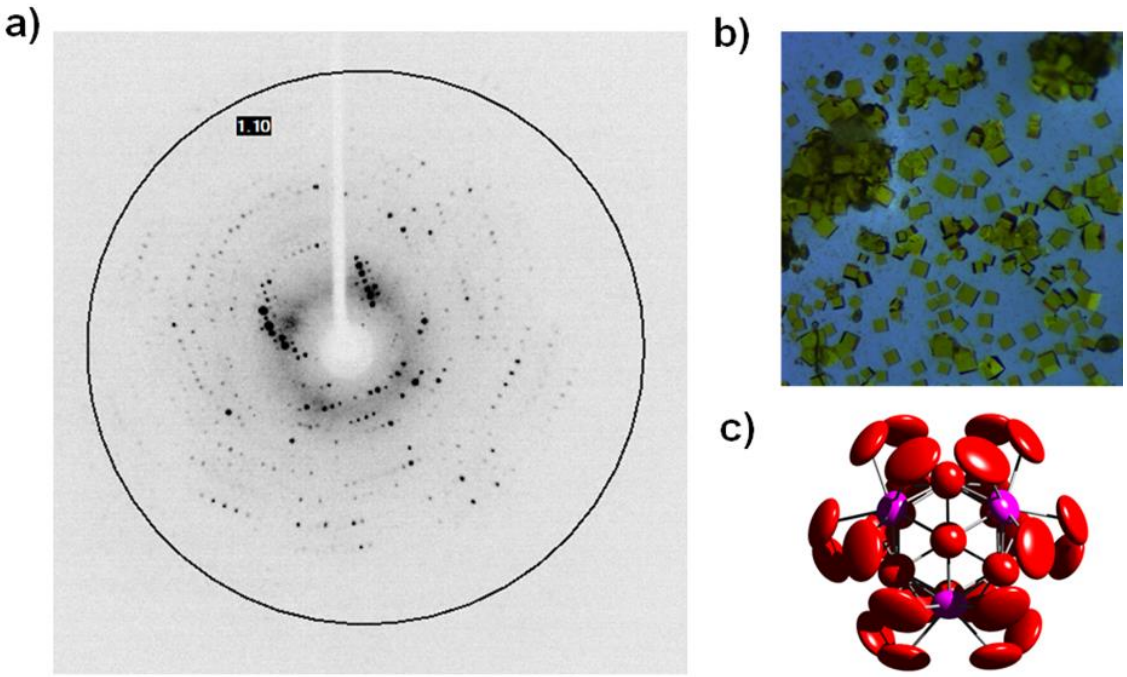

Figure 40. a) A diffraction pattern of $[Zr_6O_4(OH)_4(TPBD)_3]$ showing the limited diffraction quality as depicted by the low resolution. b) Single crystals of $[Zr_6O_4(OH)_4(TPBD)_3]$ used in the SCXRD showing nicely cubic crystals at an average size of 30 µm. c) The $Zr_6O_4(OH)_4$ SBU revealing the coordination environment of the Zr_6 cluster in the MOF from structure solution in $Pm\bar{3}m$ space group. Ellipsoids are at the 50 % probability level; Oxygen = red, zirconium = purple.

2.4.5 Excursus: Twinning from pseudo-symmetry arising by flexible orientations of pseudo-symmetric ligands in MOFs

Twinning in MOFs, especially those with high symmetry, can arise from the flexible rotation of pseudo-symmetric ligands. H_4TPBD is belonging to such a class, as although the linker is a rectangular ligand, it is close enough to square planar and can be disordered by rotation (inducing a pseudo C_4 rotation, Figure 40). Another occurring phenomenon could be e.g. MOFs with special metrics emulating cubic symmetry but actual corresponding to a tetragonal structure. Such phenomena arise frequently in the crystal structure analysis of MOFs and have been described in detail by Lillerud et. al. or by Matzger et. al.[112, 114] A very similar case as it is been found in the above discussed crystal structure analysis of [$Zr_6O_4(OH)_4(TPBD)_3$] has been described for NU-1100, a cubic pyrene based ***ftw*** *MOF by Farha et. al. and Rosseinsky et. al. (compare there).[115, 116] It has already been stated that twinning by pseudo-symmetric ligands due to rotational disorder in* ***ftw*** *Zr^{IV}-MOFs can be particular difficult to describe. Figure 41 summarizes the background and gives insight into possible reasons using [$Zr_6O_4(OH)_4(TPBD)_3$] as an example. H_4TPBD possesses a two-fold rotation axis. However, the overall shape of the ligand (almost square planar) allows for a pseudo-4-fold rotation axis. Incorporation of such a ligand in a MOF can occur randomly throughout the structure, leading to a cubic symmetry in $Pm\bar{3}m$ space group (Figure 41 right top corner). This setting implies a statistically distributed ordering of the ligand within one unit cell. However, may be induced by small differences in the crystallization conditions, the incorporation of the ligand can follow a certain ordering implying e.g. domains in $P23$ symmetry (Figure 41 lower corner), or an superstructure in $Im\bar{3}$ space group (Figure 41 right section), as was found in the single crystal data above. Such a phenomenon will lead to single crystal material with certain amount of disordered and ordered domains, which may lead to considerable (pseudo)-merohedral twinning in the diffraction data. These details give an idea about the complexity of the structure situation found in [$Zr_6O_4(OH)_4(TPBD)_3$] and might illustrate, why solution of the collected SCXRD is non-trivial. The low diffraction quality, furthermore, prevents from applying alternative techniques in the solution of twinned structures, as diffraction data at higher angles is missing.*

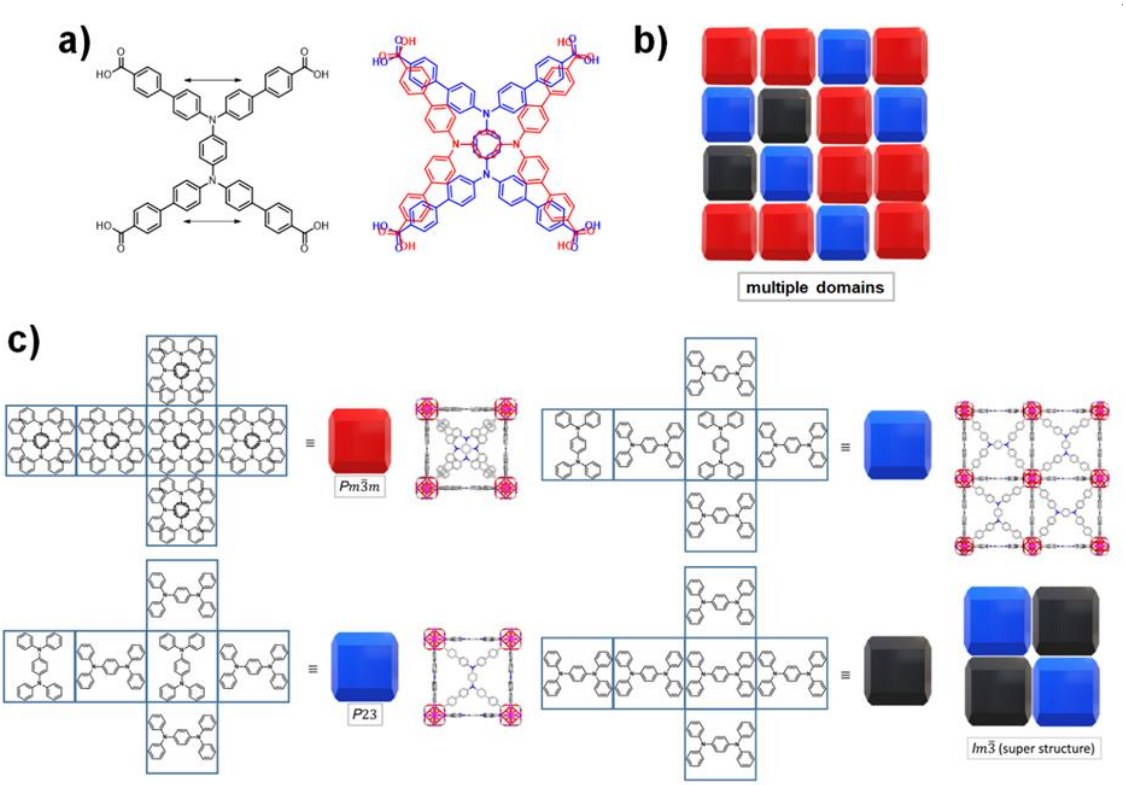

Figure 41. a) Induced pseudo 4-fold rotation of H_4TPBD. Note that the Ph-N-Ph angle needs to be bend (black arrows) which results in an enhanced distance between vertical carboxyl groups (15.4 to 17.7 Å). b) A sketch of possible multiple twin domains in a single crystal of $[Zr_6O_4(OH)_4(TPBD)_3]$ due to pseudo-symmetry of the ligand. c) Statistical disorder of TPBD in $[Zr_6O_4(OH)_4(TPBD)_3]$ described by $Pm\bar{3}m$ space group (occupancy of 0.5 for each ligand position suspected). Organization of TPBD in $[Zr_6O_4(OH)_4(TPBD)_3]$, which leads to domains with superordinate symmetry, e.g. $P23$ or $Im\bar{3}$. The resulting lattice is a super structure of the primitive setting.

2.4.6 Rietveld refinement of $[Zr_6O_4(OH)_4(TPBD)_3]$

The results from the SCXRD analysis (structure solution in $Pm\bar{3}m$ revealed a 12-fold coordinated octahedral Zr_6O_8 cluster, Figure 39) together with the *ab initio* structure optimization and the comparison of the simulated with the experimental PXRD strongly suggested a ftw-type structure for the new Zr^{IV}-MOF compound. Furthermore, the high similarities of the experimental PXRD data to published PXRD data of already known MOFs in ftw topology, e.g. MOF-525,[117] NU-1101-1104[118] or PCN-94[21] supported the ftw arrangement. Consequently, a starting model for Rietveld refinement of $[Zr_6O_4(OH)_4(TPBD)_3]$ was developed by modelling the ligand motif TPBD and the Zr_6O_8 clusters as rigid bodies with refineable translational and rotationally degrees of freedom. A PXRD pattern was recorded on a laboratory powder diffractometer STOE

STADI P, using $CuK_{\alpha 1}$ monochromatic radiation and a detector in transmission geometry. The data were collected in a 2θ range of 2 – 50° with 0.0015° steps. The diffraction shape was modeled with a pseudo-Voigt function and the background was modelled by a 15th order polynomial function. Atomic vibrational motion was modeled isotopically. Indexing of the powder pattern suggested a primitive cubic cell (a = 22.6 Å) based on systematic absences. Taking the possibility of random disordering of the TPBD into account, the model for Rietveld analysis was set up in $Pm\bar{3}m$ space group (the prototypical space group for ftw MOFs), which also goes along with the results from indexing of the SCXRD analysis. Pawley refinement in $Pm\bar{3}m$ space group showed good agreement with similar cell parameters as found in the indexing procedure. The resulting model could successfully be refined using rigid bodies by Rietveld refinement to a satisfying quality (R_{wp} = 9.81). Occupancies of the final atoms were manually set to meet the chemical stoichiometry of $[Zr_6O_8(TPBD)_3]$. Residual electron density in the cavities of the MOF (note that the PXRD data were collected on as-synthesized, solvated material) was modelled as dimethylformamide molecules as rigid bodies with refineable translationally degrees of freedom and occupancy.

The final structure is shown in figure 45. Rietveld plots and Pawley refinement are given in figures 42, 43 and 44. It should be noted that, similar to the SCXRD data, the collected PXRD data shows indications for the occurrence of multiple domains, as evident from super structure reflections at higher angles (asterisk in Figure 43). Taking the possibility of a super structure in $Pm\bar{3}m$, respectively in $Im\bar{3}$ (merohedral twin found in the analysis of SCXRD data) into account, these reflexes could be fitted very well by Pawley refinement, which supports the assumption of a disordered system with short-range correlations in $[Zr_6O_4(OH)_4(TPBD)_3]$. As can be seen from figure 44, reflection intensity at higher angles (> 20°) is only satisfactory reproduced in the refined structure model. This 2θ region mainly contains information of the linker molecules. The atom positions of the latter will, however, be strongly influenced by the high disordered nature of TPBD in $[Zr_6O_4(OH)_4(TPBD)_3]$ and the formation of ordered domains within the structure, ultimately leading to the found intensity deviations.

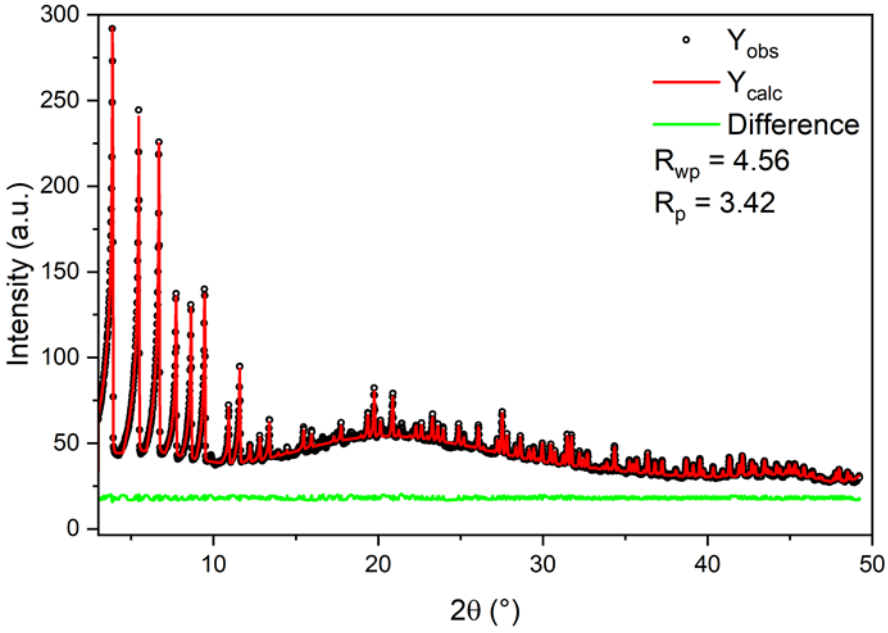

Figure 42. Pawley refinement of the collected PXRD data in a 2θ range from 3° to 50° showing good agreement between observed and calculated reflexes ($Pm\bar{3}m$, a = 22.8934 Å).

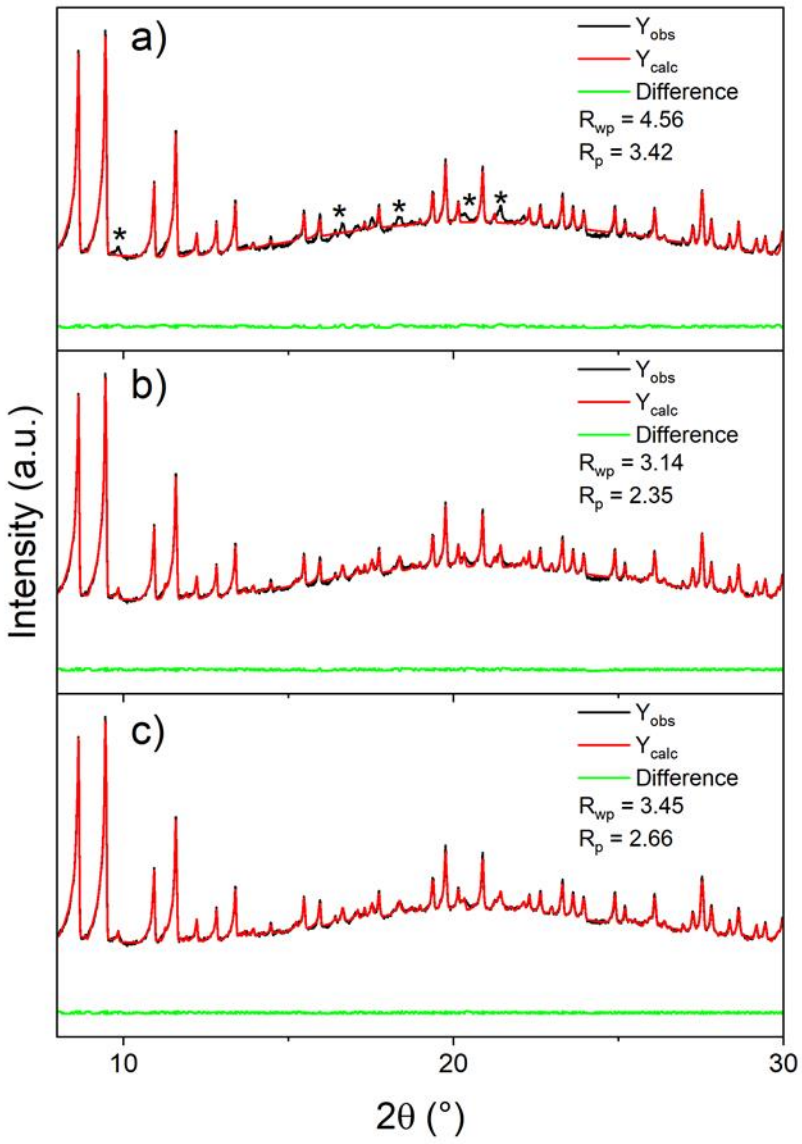

Figure 43. Pawley refinement of as-synthesized $[Zr_6O_4(OH)_4(TPBD)_3]$ in $Pm\bar{3}m$ (a), $Pm\bar{3}m$ with doubled axis (a = 45.7908 Å, b) and $Im\bar{3}$ super structure (a = 45.7872 Å, c). The reflections marked with an asterisk can therefore be assigned to potential super structure domains similar to the SCXRD analysis.

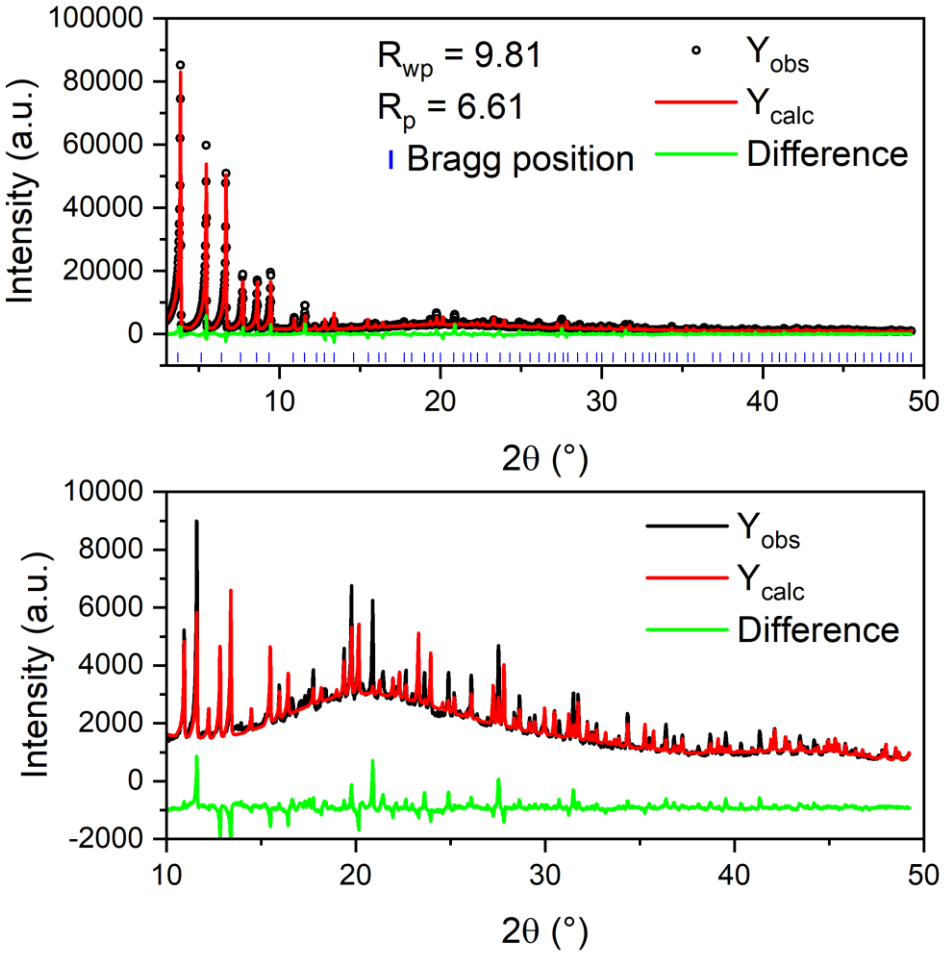

Figure 44. Results of Rietveld refinement in $Pm\bar{3}m$ (a = 22.8934 Å) space group in a range of 3-50° (top) and a zoom to the 10-50° region (down).

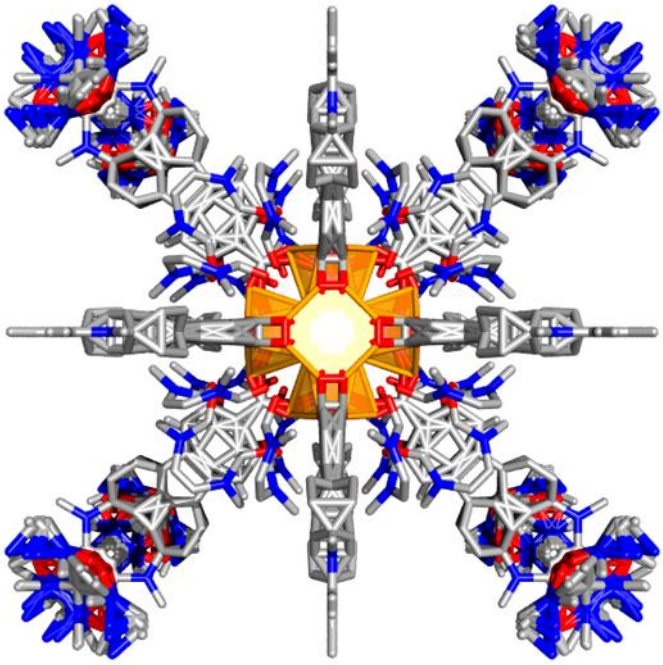

Figure 45. Results of the Rietveld refinement of $[Zr_6O_4(OH)_4(TPBD)_3]$. Note the highly disordered nature of TPBD and the solvent DMF molecules at (0, 0, 0) and (0, 0.3, 0.5) positions.

2.4.7 Basic characterization of $[Zr_6O_4(OH)_4(TPBD)_3]$

The new Zr^{IV}-MOF $[Zr_6O_4(OH)_4(TPBD)_3]$ was characterized by PXRD studies, IR and Raman spectroscopy, BET measurements (N_2 and CO_2 adsorption) and thermogravimetric analysis (for further details, please compare the experimental section). PXRD patterned showed the formation of pure-phase compound following the experimental procedures as outlined in the experimental part of this thesis. Investigations of long-term stabilities (fresh as-synthesized material held in an open laboratory environment for 4 weeks) showed the formation of impurities (asterisk in Figure 46), suggesting a phase-transition of the initial material or a partial degradation. The comparison of the PXRD data of DCM exchanged, activated and as-synthesized MOF revealed a considerable dependency of the reflex intensities for the solvated and the exchanged MOF. The affected reflexes can be indexed to the [110] and the [210] Miller indices. The respective crystal planes contain linker carbon atoms as well as carboxylic oxygen atoms in the affected crystal planes, which implies that the pore solvent DMF is preferentially located at the $Zr_6O_4(OH)_4$ cluster and in the surrounding of the ligands, as also supported by Rietveld refinement (compare Figure 45).

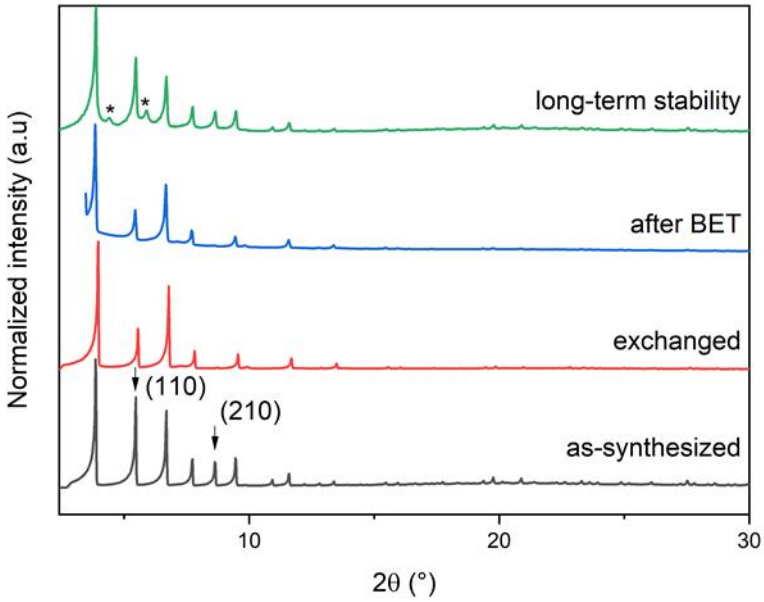

Figure 46. PXRD data of $[Zr_6O_4(OH)_4(TPBD)_3]$ as-synthesized (solvated), exchanged to DCM, after thermal activation at 120 °C for 48 h and subsequent BET characterization and long-term stability on air. The black arrows show the affected reflexes by solvent incorporation. The asterisks show the impurities dues to partly degradation or formation of side phases.

IR and Raman spectroscopic studies support the formation of the new MOF. The spectra are dominated by linker localized excitation bands. Starting with the results from IR spectroscopy, the spectra show the characteristic bands and prove the coordination of the carboxylic group of TPBD to the Zr_6-oxo cluster. The symmetric (s) and anti-symmetric (as) C=O carboxylic stretch vibrations of the free linker (1728 and 1684 cm^{-1}) almost completely decrease in intensity. Note a characteristic band for free DMF at 1670 cm^{-1} further proof the incorporation of reaction solvent in the porous MOF material. Furthermore, characteristic phenyl ring vibrations of the biphenyl groups and the benzene diamine group (1593, 1521 and 1489 cm^{-1}) decrease in intensity revealing the framework strain acting on the ligand when incorporated in the MOF. Asymmetric C=O stretching modes of the carboxylic groups are centered at 1401 cm^{-1}. These bands are characteristic for the formation of the octahedral Zr_6-oxo cluster. Finally, the spectrum shows C-H in plane bending bands located at 1089, 1173 and 1254 cm^{-1}.

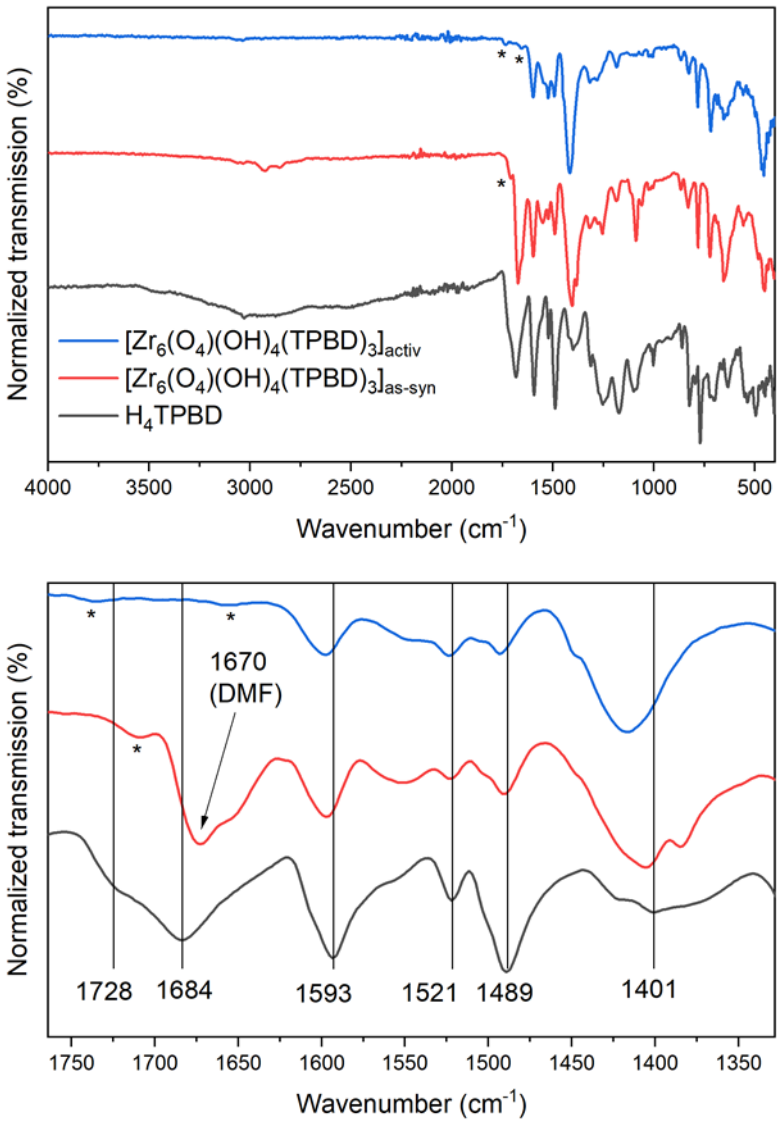

Figure 47. ATR-FTIR-spectra of as-synthesized, activated $[Zr_6O_4(OH)_4(TPBD)_3]$ and powdered H_4TPBD and the assignments of characteristic bands. Upper graph shows the complete range, lower graph shows a zoom in the 1300 to 1700 cm^{-1} region. The asterisk belongs to potentially non-coordinated carboxylic acid groups of modulator, free TPBD, water or DMF impurities.

The result of the Raman spectroscopy accompanies the IR spectroscopic investigation. The Raman spectrum shows characteristic bands at 822, 841 and 846 cm^{-1} belonging to CH-deformation vibrations (out-of-plane dangling) of the phenyl ring groups. Furthermore, a phenyl ring vibration at 1001 cm^{-1} and C-H in plane bending vibrations at 1147, 1181, 1246 and 1289 cm^{-1}. The increase in the anti-symmetric C=O vibrations at 1403 cm^{-1} proof the formation of the Zr_6-oxo node. Finally, a very strong band at 1593 cm^{-1} can be assigned to characteristic C=C stretch vibration (phenyl rings).

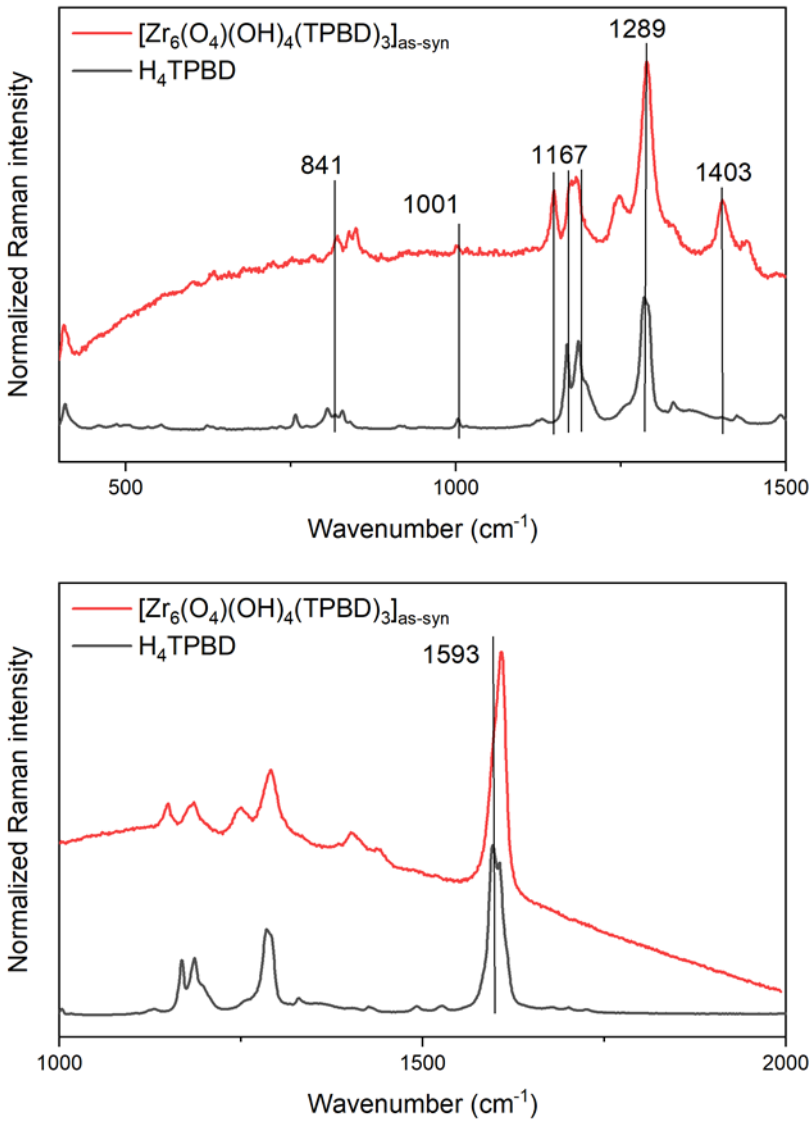

Figure 48. Raman spectra of H_4TPBD and [$Zr_6O_4(OH)_4(TPBD)_3$] (as-synthesized) with characteristic bands.

Thermogravimetric analysis of the material revealed a thermal stability of up to 486 °C. Measurements of TGA traces of as-synthesized and activated material showed the incorporation of ~ 40 % of DMF in the as-synthesized MOF, supporting the porous nature of the compound and proofing the successful activation procedure. Both measurements (Figure 49) reveal a thermal deconstruction process, which start at 400 °C and proceeds via multiple steps. The fact that the TGA trace does not reach into a stable plateau at 1200 °C suggest that a full degradation of the compound would apparently

require higher temperatures. Note that the TGA measurements were conducted in synthetic air with a rate of 10 K/min.

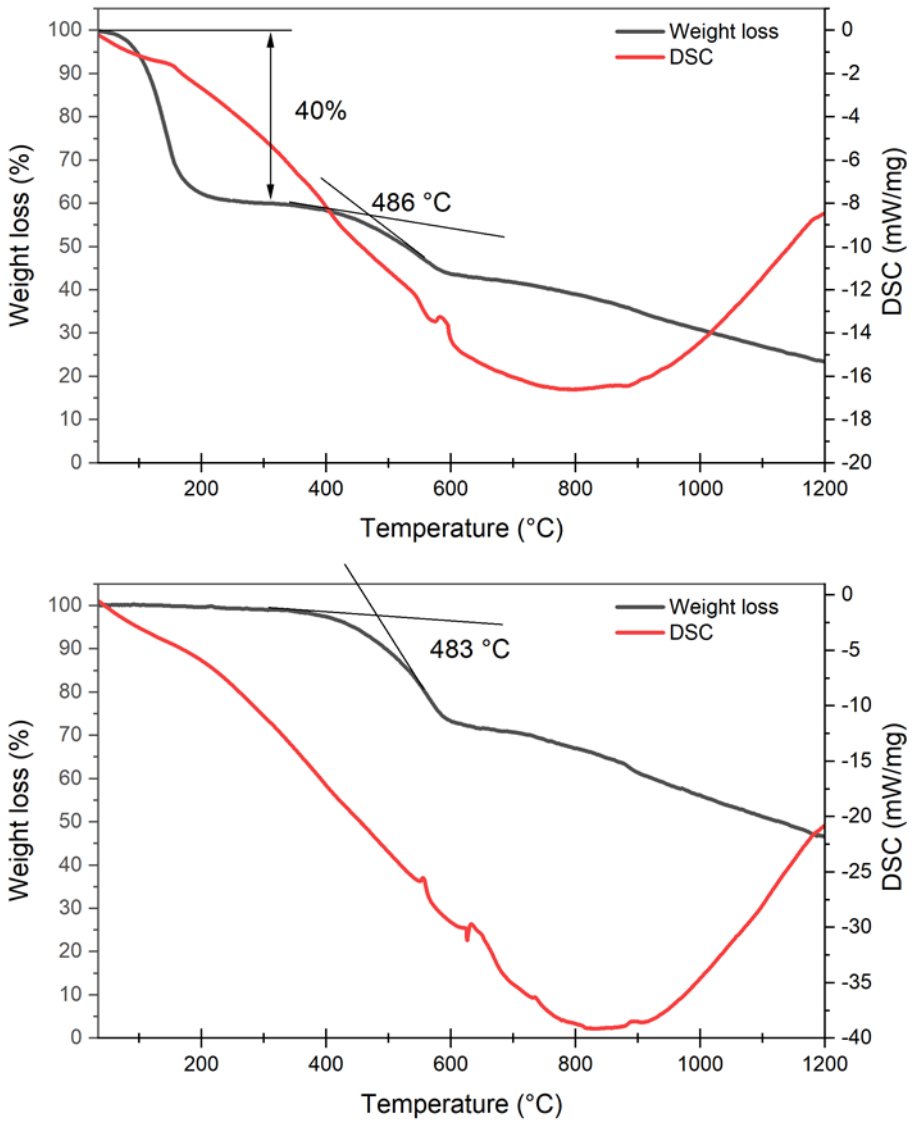

Figure 49. TGA traces and DSC signals for as-synthesized and activated $[Zr_6O_4(OH)_4(TPBD)_3]$.

BET characterizations of the material by measurement of N_2 (77 K) and CO_2 (195 K) adsorption isotherms reveal a high BET area of ~ 3000 m^2/g (for both gases, CO_2 isotherms are given in the experimental part). Note that the adsorption curves reveal a type I isotherm, as expected for a **ftw** type MOF. Comparable systems from literature (such as MOF-525 or the NU-1100 series) show BET areas at ~ 2600 – 4000 m^2/g.[117, 118] Analysis of the pore size distribution and the cumulative pore volume show the existence of two type of

pores at a pore diameter of 10 Å respectively 20 Å. The pore sizes are in very good agreement with crystallographic data, which also reveal two type of pores in the similar size centered at (0, 0, 0) and (0.5, 0.5, 0), as expected for a **ftw** topology. According to the cumulative pore volume, the 10 Å pore accounts for roughly 56 % of the total adsorbed volume, whereas the bigger pore accounts for the remaining 44 %. Figure 50 summarizes the BET analysis. Note that PXRD measurements of the material directly after BET characterization revealed no apparent signs for MOF destruction during the BET measurements, however, with a loss of long range ordering (Figure 46).

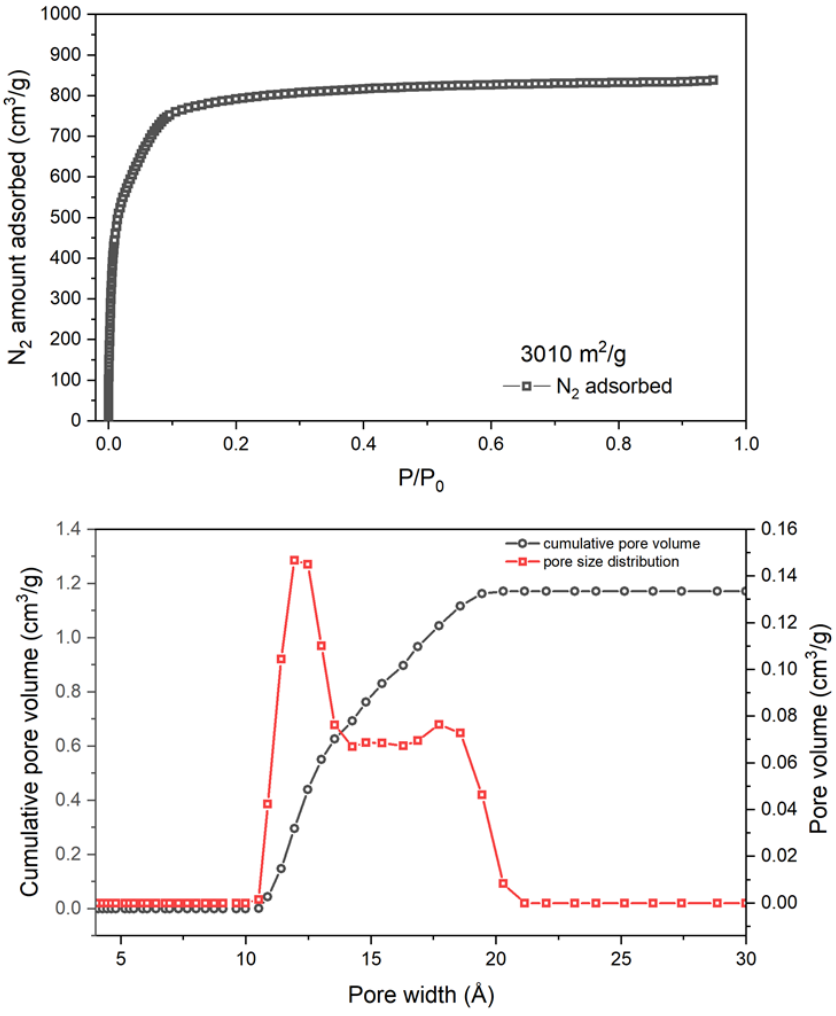

Figure 50. N_2 adsorption isotherm (77 K) of $[Zr_6O_4(OH)_4(TPBD)_3]$ and the corresponding pore sized distribution as well as the cumulative pore volume.

2.4.8 Discussion and conclusion

In the presented work, experimental investigations of the phase system $Zr_6O_4(OH_4)$/TPBD were conducted, with the aim to synthesize new Zr^{IV}-MOFs based on the ligand H_4TPBD. The formation of polymorphic structures in the deviation of structure-property relationship of optical properties of MOFs is of great importance, as such studies allows to purely target the relations of optical response with the underlying materials structure. The effect of modulator and Zr^{IV}-precursor has rarely been investigated in tetratopic Zr^{IV}-MOFs, compared, for example, to the UiO series.[104] The experimental procedure followed a reaction screening in the $ZrCl_4$, H_4TPBD system (DMF as solvent, benzoic and acetic acid as modulators). The systematic variation of different underlying reaction conditions (temperature, reaction time, water content and modulator/Zr/H_4TPBD ratio) showed a considerable effect of water content, Mod^-/$TPBD^{4-}$ and Zr^{4+}/$TPBD^{4-}$ ratios. It was shown that high concentrations of modulator and water, greater reaction temperatures and longer reaction times negatively affect the reaction outcome. On the contrary, very low water contents, less acidic modulators with low concentrations and low reaction temperatures as well as smaller reaction times showed a positive effect on the synthesis results. The negative influence on the reaction outcome when different equivalents of water were put to the reaction mixtures points towards an influence of the SBU formation kinetics. In principle, for Zr^{IV}-MOFs, higher water contents in the system speed up the SBU formation. This effect is also thought to affect the MOF formation in the acetic acid series, as the latter can carry high quantities of water in particular when aged batches are used (note that using acetic acid as modulators revealed the formation of amorphous powders for every reaction). By using the ratio of [Mod^-/$TPBD^{4-}$] as a descriptor, within the benzoic acid series, low [Mod^-/$TPBD^{4-}$] ratios throughout showed the best reaction outcome. Furthermore, consistently at higher modulator concentrations for both cases (acetic and benzoic acid) no formation of any material was found. The fact that [$Zr_6O_4(OH)_4(TPBD)_3$] forms at low [Mod^-/$TPBD^{4-}$] ratios with rather weakly acidic modulators, suggest that the synthesis favors a high concentration of deprotonated H_4TPBD. Note that low concentrations of weak acidic modulators hold a high concentration of free ligand, as the modulator extent to dissociate weaker and thus shift the

equilibrium on the side of $TPBD^{4-}$. At lower [Mod^{-}/$TPBD^{4-}$] ratios, the MOF assembly is expected to proceed faster suggesting that $[Zr_6O_4(OH)_4(TPBD)_3]$ might be the kinetically product. Looking onto geometrical aspects of ligand deformation upon incorporation in the MOF, $TPBD^{4-}$ needs to undergo a structural transformation to adopt a pseudo-4-fold symmetry, which ultimately leads to a lower Ph-N-Ph angle and a rotation of the phenyl carboxylate groups to lay in a single plane. The aspect ratio of H_4TPBD allows for the formation of a **ftw** structure.

In summary, the recent experimental results reveal the formation of a new **ftw** type Zr^{IV}-MOF $[Zr_6O_4(OH)_4(TPBD)_3]$. By changing the concentration of the applied modulator and water concentrations two main driving forces in the formation of the MOF could be found, which manifest in the kinetics of SBU formation as well as in the [Mod^{-}/$TPBD^{4-}$] ratio. However, crystallization is a complex combination of thermodynamics and kinetics and thus certain other parameters will contribute to the formation of the final structure of $[Zr_6O_4(OH)_4(TPBD)_3]$.

Structure analytics of the compound was considerably complicated by pseudo-symmetry of the TPBD ligand, leading to (pseudo)-merohedral twinning. Based on initial results from SCXRD and *ab initio* structure modelling, a model could be set up which was further Rietveld refined using rigid body approach to yield a final structure model. The latter was supported by IR/Raman spectroscopic investigations, BET analysis and TGA. It needs to be noted, that the presented model of $[Zr_6O_4(OH)_4(TPBD)_3]$ follows topological considerations and will not account for the real structure situation in an absolute manner. The model takes statistical disordering of the TPBD linker as a basis. The real situation will, however, show such a behavior only to a certain amount, besides the formation of more ordered domains in the material. The proportion of the different accounting domains in such situations can be deduced (e.g. from intensity ratios of respective reflexes in PXRD data). However, a full elucidation of the ongoing phenomena needs more sophisticated techniques (e.g. state-of-the-art diffraction techniques using synchrotron radiation).

Finally, control in polymorph formation in Zr^{IV}-MOFs is of fundamental importance in unraveling structure-property relations of optical active materials.

Gaining control over the preparation of a specific topology by defined experimental reaction conditions is at the center of Zr^{IV}-MOF chemistry. The presented analysis shows that by systematically fixing certain reaction parameters, indeed the preparation of certain topologies is suitable. Furthermore, it reveals that in the phase system $Zr_6O_4(OH)_4$/TPBD an interplay of different parameters defines structure formation. Suggesting that the concentration of free H_4TPBD is crucial for the latter, stronger acidic modulators could therefore be a good starting point of further investigations.

3 Conclusion and Outlook

As already pointed out in the introduction of this thesis, NLO active materials are an important material class, mainly due to their great impact on laser based technologies and pursuing applications. The latter fact results in a great interest on high-performing, new NLO active materials from an academic and commercial point of view. In this regard, MPA as a NLO process is important in a variety of different applications, such as microscopy, micromachining and microfabrication, three-dimensional data storage, optical power limiting, up-converted lasing, photodynamic therapy and more. At the current stage, systematic investigations of higher order (> 2^{nd} order) NLO processes in CPs and MOFs is just at the beginning and there is not much known about a mechanistic understanding of NLO processes. However, due to the ability to generate materials at will on the basis of clear geometrical design concepts, in principal a targeted access to a materials NLO property by means of reticular chemistry should be feasible. The declared object of this thesis goes along that line of thought and aimed at the expansion of MPA active CPs, with a trial to understand mechanistic concepts of MPA enhancement in crystalline network compounds. By doing so, different levels of investigations were pursued, starting at a local, intramolecular level and proceeding further to intermolecular interactions between linkers in a CP. The underlying conceptual strategy consists in the fact that with coordination of a linker to a metal node, the organic molecule is restrained in the framework, reducing molecular degrees of freedom, enhancing the electronic polarization by push-pull effects of coordinating metals and improving charge-transfer characteristics in the organic scaffold by potential planarization of the latter. At a further stage, different degrees of intermolecular electrostatic interactions between neighboring chromophores, which are pinned in room by the rules of the framework topology, can be accessed. The different chromophore alignments will differently redistribute the excitonic oscillator strength among the interacting molecules, giving rise of possible MPA enhancement effects.

In the first part of this thesis, AIE dyes based on the tetraphenylethylene unit were incorporated in pillar-layered MOFs, [Zn_2(TCPE)(bpy)] and [Zn_2(TCPE-

F)(bpy)]. The conducted work was a follow up study of recent investigations of our group with such linker motifs. The findings point toward the direction, that conformational locking of phenyl ring dynamics in the MOFs is key to enhance the two-photon brightness of the materials, as a post-synthetic contraction of the framework compounds by a thermal activation procedure showed an enhancement of the TPA efficiency in [Zn_2(TCPE)(bpy)]-contr and [Zn_2(TCPE-F)(bpy)]-contr. Electronic structure calculations on the level of TD-DFT and quadratic response theory revealed that besides restriction of intermolecular movements of the tetraphenylethylene core specific molecular geometries of the TCPE/TCPE-F ligands are responsible for a TPA enhancement, respectively, attenuation. The results of the work indicate different levels of further tuning options. Firstly, linker motifs holding AIE characteristics are an interesting class of MPA active structuring units for coordination networks. In the specific case of TCPE based linkers, the electronic structure calculations predicted a higher TPA performance by an elongation of the tetraphenylethylene scaffold. Secondly, conformational locking of intramolecular movements responsible for radiationless decay pathways in AIE linkers is an key factor for enhanced two-photon brightness. Such molecular restrictions can be accessed by different approaches, for example, targeted linker substitution increasing the steric bulk in the molecule surrounding, usage of specific topologies enhancing the operative framework strain (expressed by the difference in free molecule geometry vs. incorporated molecule geometry) or influences of external stimuli (e.g. pressure dependent TPA; targeted framework collapse etc.). Furthermore, a highly prospective fact is that with amorphization of the MOF material, the TPA efficiency is not lost rather enhanced (at least for the special material class of pillar-layered MOFs investigated in this thesis), as it disengages from possible drawbacks of post-synthetic treatment (e.g. when MOFs should be used as two-photon probes in cellular environment). The data on the pillar-layered MOFs obtained here, show that the nonlinear absorption of AIE-MOFs is remarkably controlled by the local ligand conformation of the incorporated AIE dye. The latter fact provides an unique possibility to specifically target ligand design, when it comes for the search of maximized NLO response.

The excited-state electronic structure of CPs and MOFs is a hot topic at the current research in the field of crystalline network compounds, due to its

inherent importance in areas like photocatalysis, photovoltaics, upconversion, photoswitching solid state lightning and so forth. However, experimentally as well as theoretically investigations are still in the beginning. In case of MPA and NLO, the excited state properties of a material are inherently connected with the NLO response, clarifying the importance of the excited-state electronic structure for MPA processes. In inorganic-organic hybrid materials like CPs or MOFs, the band structures are formed of several discrete sub-bands, showing fairly flat dispersion curves. Therefore, often the excited state properties of CPs and MOFs are described using a MO formalism of organometallic complexes (e.g. a linker connected to a metal-oxo cluster). Such an approach, however, disregards intermolecular, excitonic interactions between precisely ordered chromophores in a crystalline array. Excited state properties of molecular assemblies or organic crystals are commonly described using exciton theory. In CPs or MOFs these concepts are used to characterize energy transfer phenomena, mainly by incoherent hopping of molecular excitons between chromophores in the network. However, excited states, which are delocalized over more than one organic linker have rarely been described. The origin of multi-photon response enhancement can be attributed to such excitonic interactions and are thought to arise also in CPs or MOFs. Following that line of thought, the second part of this thesis investigated the origin of excitonic intermolecular interactions in two densely packed CPs and the effect of such interactions to the TPA response. Therefore, a new symmetric multibranched MPA ligand was synthesized, based on triphenylamine donors and phenylcarboxylic acid acceptors, following design criteria of push-pull chromophores. The ligand was successfully incorporated in two densely packed CPs, $[Zn_2(TPBD)(DMAc)_2]$ and $[Cd_2(TPBD)(H_2O)_4]$, comprising of optically innocent metal units. The two new framework materials were characterized by reflectance, PL and PLE spectroscopy and measurements of quantum efficiency (EQY). Especially, PLE spectroscopy showed the contribution of near band-edge states to the emission properties over the whole PL range, strongly red-shifted compared to the sole ligand motif. By spectroscopic comparison with chromophore aggregates of the used linker formed by artificial high concentrations, the results implied $\pi \rightarrow \pi^*$ transitions within the organic molecule as well as small range excitonic interactions between the

chromophores as optical relevant excited states in the CPs. The latter was further investigated by an electronic structure study using a mixture of periodic DFT and TD-DFT methods on small chromophore clusters following the arrangement as found in the crystal structure analysis. The calculations corroborated the delocalized excited states in the linker assemblies and revealed that the nature of the underlying excitonic interaction is more Frenkel type in $[Zn_2(TPBD)(DMAc)_2]$, respectively, more polar in $[Cd_2(TPBD)(H_2O)_4]$. All excited state interactions showed small ranges (within one unit cell, delocalized over two, respectively three chromophores) and thus could be regarded as strongly bound excitons, as expected for such type of materials. Two-photon excitation in the near band-edge region showed a dramatically enhanced TPA response for $[Cd_2(TPBD)(H_2O)_4]$ (factor of ~ 9) compared to $[Zn_2(TPBD)(DMAc)_2]$. These results implied, even though not fully conclusive, that intermolecular interactions between specifically packed chromophores opens new channels for the enhancement of MPA properties. Such type of interactions, however, can be targeted by the versatile tailorability of reticular chemistry concepts in CPs and MOFs. The impartment of intermolecular phenomena on specific structures and the control may open further opportunities to contribute to the overall third-order nonlinearity and the notion needs to be extended to other MOF systems. The recent work indicates that concepts of excitonic interactions in CPs and MOFs needs to be pursued providing a thorough understanding of the limits of such concepts. From a synthetic point of view, polymorphic structures constitute a highly interesting platform for the study of excited-state properties, also with regard to MPA processes. Furthermore, rather densely packed CPs (interpenetration, intercalation, etc.) seem to benefit from the lower linker distances, imparting excitonic interactions on the structures. Consequently, highly porous framework compounds may not be the best choice, when one wants to target enhancement mechanisms based on the intermolecular approach.

As has been said above, the importance of structural polymorphism in the light-matter interaction of organic solid-state materials relates to the impact of different packing modes of the building units. The different chromophore alignments will differently redistribute the excitonic oscillator strength among the interacting molecules within the polymorphic structures and ultimately define the

absorption behavior of the investigated material. Zirconium based MOFs are at the forefront, when it comes to polymorphism in CPs and MOFs. However, the targeted synthesis of a unique phase is still a challenge in zirconium MOF chemistry. Furthermore, a specific analysis of the influences of synthesis parameters on the outcome of polytopic Zr-MOFs has received limited attention. The last chapter of the presented work therefore is dealing with a synthetic screening of new Zr^{IV}-MOF phases incorporating the push-pull ligand H_4TPBD introduced above. The work revealed the formation of a phase pure **ftw** Zr^{IV}-MOF as a function of modulator concentration. Structural analysis was impeded by a couple of factors (merohedral twinning, low diffraction quality, extensive linker disorder), however, could be solved by an interplay of *in silico* modelling in a reverse topological approach and Rietfeld refinements using a rigid body ansatz. The work demonstrated that high-throughput reaction screening of different reaction conditions together with simulation of structure models using topological considerations is a prospective approach in the synthesis of new Zr^{IV}-MOF phases. By doing so, a new potential MPA active MOF could be synthesized and structurally characterized. Furthermore, the dependency of MOF synthesis on modulator concentration and acidity showed again the importance of the latter in general Zr^{IV}-MOF synthesis and in particular provides solution to further reaction approaches in the considered Zr^{IV}/H_4TPBD systems.

Each reported study of this work investigated different affecting levels (intramolecular, intermolecular, synthetically, structurally, …) existing in CPs and MOFs on the higher-order NLO performance (in particular TPA) of hybrid inorganic-organic framework materials. Strikingly, at every investigated level a profound influence was found, which again illustrates that many basic parameters govern the TPA properties in these materials. In order to close the cycle, the presented work in parts approached the questions *Q1, Q2* and *Q3* raised in the introduction. A transfer of the derived methodology to other prototypic ligand structures, MOFs and CPs will provide more information on the general applicability of the underlying concepts. To accomplish this, substantiate theoretical work is needed to understand the results and postulate basic principles. Also, more sophisticated spectroscopic techniques together with sample preparation (for incorporation of MOFs in NLO devices, SURMOF techniques are highly required) will be needed. The work presented so far, by

our group and others, shows that CPs and MOFs are attractive candidates for solid-state non-linear optical applications.

4 Theoretical background

In the following parts, a selection of methods and important theoretical backgrounds of the applied theory and methodology of the above chapters will be discussed. The formalism introduced here should serve as a starting point for enabling the reader an understanding of the used reoccurring concepts. The first part is therefore dealing with excited state theory of molecules and molecular aggregates, as well as organic crystals. Furthermore, theoretical methods used within this work, such as Kohn-Sham density functional theory (KS-DFT) and its time-dependent version (TD-DFT) will shortly be summarized. Furthermore, the physical basis of non-linear optics (NLO) will shortly be discussed, and the basis of the multi-photon absorption (MPA) process will be summarized, with an emphasize on size-enhancement effects.

The second part of the theoretical background will give a brief overview about coordination polymers (CPs) and their photophysical properties. The discussion will be limited to important aspects of reticular chemistry, excited state theory of CPs and concepts therein. Finally, NLO properties of CPs and metal-organic frameworks (MOFs) will be summarized, introduced and shortly reviewed.

4.1 Excited state theory

Molecules can interact with light in many ways. Depending on the energy of the incoming photon and the presence of resonant transitions in the molecule, either elastic processes (e.g. scattering) or inelastic processes (e.g. absorption of the photon and transfer to an excited state) can occur. The latter is what is called an excitation. Molecular transitions susceptible to electromagnetic radiation (light) can be categorized by the excitation energy. This fact coincides with degrees of freedom of the molecule, which are excited by the energy of the photon. These degrees of freedoms are of, from low to higher energy, translational, rotational and vibrational as well as of electronic nature. While translational, rotational and vibrational degrees of freedom exclusively involve nuclear movements and occur below energies that of visible light (< 1.5 eV), above that energy electronic excitations will occur (excitation of outer valence

electrons). Any excitation of a resonant, high-lying transition usually causes all low lying states to be excited, too. For example, electronic absorption spectra can show “vibronic” contributions (vibronic progressions), indicating that vibrational transitions take also part. In general, the processes after photo-excitation can be categorized as photochemical or photophysical. Photochemical reactions include rearrangement of bonds, whereas photophysical properties do not involve the cleavage or formation of bonds (e.g. internal conversion, intersystem-crossing, non-radiative and radiative decay). The light-induced reactivity of molecules is strongly depending on the character of the involved orbitals as well as on the structure of the molecules. Light-induced processes are usually depicted using so-called Jablonski-diagrams.[119] After initial excitation into a bright state, the fastest process will usually be internal conversion to the lowest excited state via canonical intersections. The latter are ubiquitous in the potential-energy surface (PES) of polyatomic molecules. Internal conversion is usually fast and completes in few vibrational periods (less ps). This fact is the origin of Kasha’s rule, which is derived from the observation that fluorescence usually originates from the lowest excited state. Emission normally occurs on time-scales of 0.5 – 20 ns.[120-122]

Excited states can be described in terms of the involved molecular orbitals (MOs). The low lying excited states of a molecule can be well described by a single or a few one-electron transitions from an occupied to a virtual orbital. As the zeroth-order approximation of an excitation energy is orbital-energy difference, the transition of an electron of the highest-occupied MO (HOMO) to the lowest-unoccupied MO (LUMO) will mainly contribute to the lowest excited state of the molecule (MO picture). In the adiabatic picture, excited states are described on the basis of excitation energy (S_1, S_2, S_3… for singlet excited states and T_1, T_2, T_3… for triplet excited states). Besides energy-based characterization, one can categorize the excited states also according to the character of the participating orbitals. This leads to a picture of combination of local symmetry, (e.g. π, σ) and bonding (i.e. anti-bonding, non-bonding) properties. In terms of large molecules and aggregates these pictures reach their interpretive powers, as MOs can be spatially delocalized and excitations

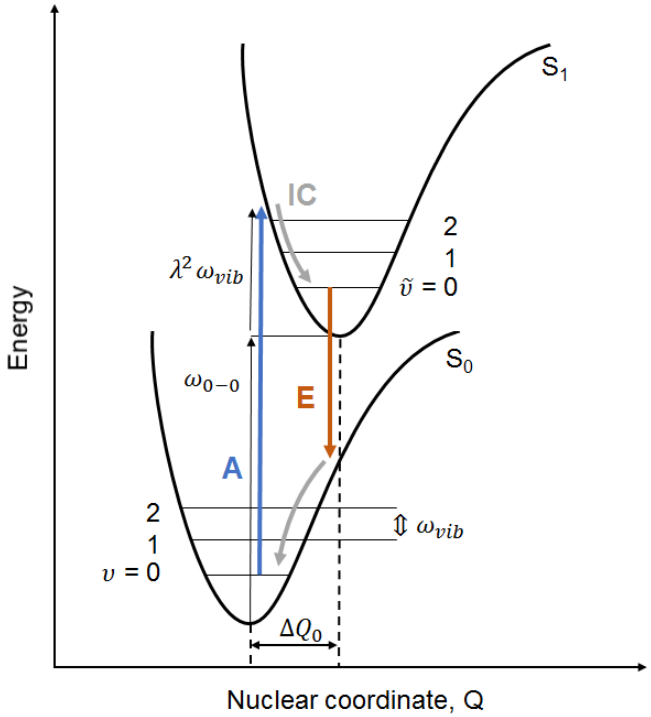

Figure 51. Energy-level diagram showing the potential wells for a ground state (S_0) and an excited state (S_1) of a molecule. The excited state potential is shifted along the nuclear reaction coordinate Q. The vibrational energy is denoted by ω_{vib}, the 0-0 transition energy ω_{0-0}. The quantity $\lambda^2\omega_{vib}$ is the nuclear relaxation energy, the amount of energy being released when the molecule is relaxed to the lowest state of the excited state potential. The blue arrow indicate absorption from the lowest vibrational level, followed by internal conversion and emission (red arrow).

can involve many orbital excitations with differing weights. On the contrary, in solid-state physics, excited states are described as so-called excitons, which can be understood as correlated electron-hole pairs (quasi-particles), which arise from transitions between bands in extended periodic systems. Interestingly, it can be shown that the quasi-particle picture of excitons and the MO pictures is inherently connected via the one-electron transition density matrix (in turn to the natural transition orbital picture) and that molecular excitations can be rationalized in both pictures.[87, 90-93, 123]

The first descriptions of excited states in molecular aggregates are rather old (over 60 years ago), but have not lost their importance, nowadays. Still theoreticians and experimentalist work on the understanding of the nature of the excited states in molecular aggregates, crystals and related compounds, due to the great scientific and socially significance. M. Kasha was the first to introduce models describing the photophysical properties in aggregates based entirely on

the coulomb coupling between neighboring chromophores which derives upon the interaction of the single transition dipole moments.[53, 81, 124] Employing the exciton theory of Davydov[53] and Frenkel[125], Kasha surmised that in certain aggregates the coulomb coupling is becoming positive (later to be known as H-aggregates) in which the highest energy states consumes all oscillator strength.[126] As fluorescence normally proceeds via the lowest excited state, in such systems fluorescence is suppressed. On the other side, when the coulomb coupling is negative (later to be known as J-aggregates), the oscillator strength is focused on the lowest excited state and no suppression of fluorescence occurs. It is important to be aware of the fact, that the difference in photoluminescence of H- and J-aggregates derives from the differences in radiative decay rates and not the emission quantum yield.[80] The latter depends on how large the radiative decay rate is in contrast to the non-radiative decay rate and thus one can have H-aggregates showing strong emission when the weak radiative decay rate dominates. Finally, they already recognized that in J-aggregates, the emitting states has a transition dipole moment, that scales with a $N^{1/2}$ behavior, with N is the number of chromophores in the aggregate.[127] This later turned out to be the reason for coherence enhancement of the radiative decay rate, the physical reason for super-radiance[128] and size-scaling in NLO.[52, 129] The treatment of the excited stated interactions via coulomb coupling has two inherent drawbacks, as it does not account for electron-vibrational coupling as well as the incorporation of wave function overlap and charge transfer interactions between aggregates. The existing theory, however, can be extend to incorporate such phenomena. There are a couple of excellent review articles, which summarizes the massive field of exciton theory (formation, transport, annihilation etc.).[80, 127, 130]

In the following section, I will shortly summarize the Kasha-Model and introduce the Frenkel exciton Hamiltonian[127], the basis for the description of aggregated chromophoric systems. As many optically active CPs are built from ligands with extended π-electron structure and due to the fact that in such systems the optical response will mainly be determined by those ligands, the description of the excited state of a CP using concepts established for weak Van-der-Waals bonded organic crystals or molecular aggregates is reasonable.

Nevertheless, further effects like metal ligand interactions (or vice versa) needs be considered in case of CPs.

In concluding this introduction part, I would like to take the focus again on the description of excited states from the quantum chemical and solid-state physics point of view. As has been said, the solid-state physics method is formulated in terms of a correlated quasi-particle electron-hole wavefunction.[131] This possess the advantage of a direct connection to the picture of charge carriers (electrons and holes), which are invoked for the understanding of physical properties (conductivity, photovoltaics etc.) and quite naturally emerge from the GW + Bethe-Salpeter method.[93, 132] However, this is a simplification which is based on the one-electron approximation.[80] On the contrary, the molecular orbital quantum chemical point of view has the inherent advantage to take all molecular details into account, but lack the direct connection to charge carriers (an excited wavefunction is formed by a linear-combination of single, double triple etc. excited ground-state slater-determinants formed from atomic orbitals).[133] The theory for excited states in molecular aggregates and crystals, as it will be introduced in the following chapter, however, is a phenomenological theory which describes excited states of aggregates and crystals in the framework of a state interaction theory.[124] An exciton thus can be regarded as a solution of the underlying Hamiltonian and its corresponding wavefunctions. Even though the wavefunction formalism is rather similar to molecular orbital theory, the underlying physical interpretation is completely different, as exciton wavefunctions in this approach describe a change in the phase relation of the transition dipole moment (again, there is no description of an quasi-particle, with hole and electron coordinates, when only neutral states are considered).

4.1.1 Exciton theory in molecular aggregates and crystals

The electronic states of a molecule will undoubtedly change when assembled into a molecular aggregate or a crystal. An isolated molecule in its ground state will have two spin-paired electrons residing in its HOMO. The promotion of an electron into the LUMO will leave a hole in the HOMO, resulting in an excited single or triplet state, depending on the electron’s spin state. In a molecular aggregate or crystal, the electron can be promoted into the LUMO on the same

site as the hole (Frenkel excitonic state) or onto a neighboring site (charge transfer excitonic state). Furthermore, the electron or hole can travel from site to site via intersite electronic coupling. This very general case can be summarized in an electronic Hamiltonian of the following form (position representation using annihilation and creation operators).[130]

$$\begin{aligned}\widehat{H}_{el} = & -U(0)\sum_{n} c_n^{+}c_n d_n^{+}d_n - \sum_{n}\sum_{r\geq 1} U(r)c_n^{+}c_{n+r}d_n^{+}d_{n+r} \\ & + \sum_{n}[t_e c_n^{+}c_{n+1} + t_h d_n^{+}d_{n+1} + H.C.] \\ & + \sum_{n}[V c_n^{+}d_n^{+}d_{n+1}c_{n+1} + H.C.]\end{aligned} \qquad (4.1)$$

c_n^{+} (c_n) are the electron creation (annihilation) operators for site n, d_n^{+} (d_n) are the hole creation (annihilation) operators for site n. $U(0)$ is the coulomb energy of an electron-hole pair, located on a single site, $U(r)$ denotes the coulomb energy when the electron and hole are located at different sites. The transfer element matrix element for nearest-neighbor electron (hole) transfer is given by t_e (t_h), whereas the dipole-dipole interaction term V transfers an electron-hole pair from site $n+1$ to n. $H.C.$ depicts the Hermitian conjugate. The given site-basis Hamiltonian is quite general and can be used to describe excitons in the Frenkel and Wannier limit.[130, 134] Considering nearest neighbour interactions ($r = 1$) reduces to the consideration of only charge transfer excitations (no charge separated states between greater spatially separated molecules). The $U(0)$ term is described in a neutral basis (the hole and electron remain at the same site) consisting of a monomer wavefunction excited in the first electronically state with all other molecules in the ground state (the monomer molecule is considered as a two-level system, the asterisk denotes an excited state).

$$\Phi_{Frenkel} = \phi_1\phi_2\phi_3 \ldots \phi_n^{*} \ldots \phi_N \qquad (4.1)$$

The $U(1)$ term is described in a charge separated basis, where the electrons of one monomer are excited to the LUMO of a neighboring molecule (site separated).

$$\Phi_{CT} = \phi_1\phi_2\phi_3 \dots \phi_n^+\phi_{n+1}^- \dots \phi_N \tag{4.2}$$

Without any interaction between the molecules, these product based wavefunctions would lead to N degenerated eigenstates with the energy difference of $U(1) - U(0)$ (corresponding to the exciton binding energy, compare equation 4.1). When the latter is much greater than the molecular interactions, the Frenkel and charge transfer terms can be separated, which finally leads to the following equations:

$$\widehat{H}_{Frenkel} = U(0)\sum_n B_n^+ B_n + \sum_n [V\, B_n^+ B_{n+1} + H.C.] \tag{4.3}$$

where the Frenkel creation and annihilation operator are defined as $B_n^+ = c_n^+ d_n^+$ and $B_n = c_n d_n$

The dipolar interaction V couples the Frenkel states with each other. For the charge transfer part one finds:

$$\widehat{H}_{CT} = \sum_n U(1) c_n^+ c_n d_{n+1}^+ d_{n+1} + \sum_n [t_e c_n^+ c_{n+1} + t_b d_n^+ d_{n+1} + H.C.] \tag{4.4}$$

Solving the above Hamiltonians gives a set of N eigenfunctions which are linear combinations of the respective functions 4.2 and 4.3 and are enumerated by a factor k.

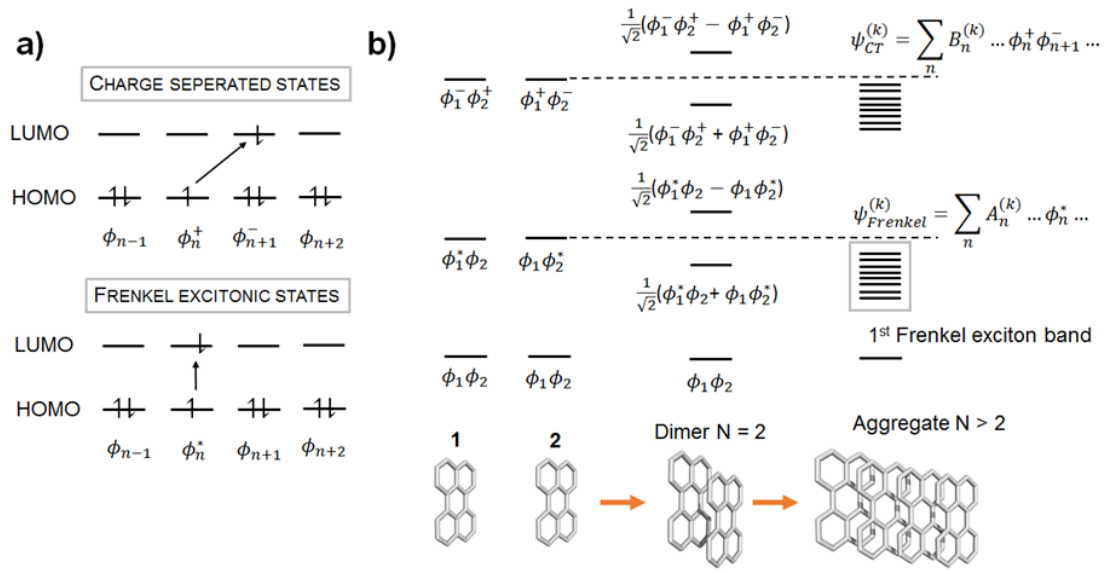

Figure 52. a) A schematic illustration of the product basis states of a molecular aggregate assembled from similar chromophores. Frenkel excitonic states are characterized by single molecule excitations where the excited electron occupies the LUMO of the initial molecule. Charge separated states form so-called charge transfer excitons. In the above picture, the basis state for such a type of interaction is described by one electron promoted to the LUMO of a neighboring molecule. b) At large separations, there is no interaction between molecules 1 and 2. When the molecules start to approach each other, interactions mix the neutral excited Frenkel states to form superposition states. The same happens to the ionic separated states, which form delocalized charge resonance states. When an aggregate is formed and the number of interacting molecules expands, an exciton band is formed for both types of interactions, the neutral Frenkel exciton band and the CT exciton band.

I will further concentrate on the Frenkel Hamiltonian as depicted in equation 4.4 and change to a different setting, waving a description using creation and annihilation operators in the basis of interacting molecules $|n\rangle$:

$$\hat{H}_{Frenkel} = \sum_n E_0 |n\rangle\langle n| + \frac{1}{2}\sum_n \sum_{n\neq m} V_{nm} |n\rangle\langle m| \qquad (4.5)$$

with $|n\rangle = \phi_1\phi_2\phi_3 \dots \phi_n^* \dots \phi_N$ and V_{nm} is the dipole-dipole interaction matrix element. This type of description does not explicitly account for charge-separated interactions as described above (equation 4.1) The classical exemplary system for the solution of the Frenkel Hamiltonian is a string (or ring)

of equidistantly arranged molecules. The linear combinations representing the exciton states of this aggregate are given by (using bra-ket notation):

$$|k\rangle = \sum_{n} e^{i2\pi k\frac{n}{N}} |n\rangle \tag{4.6}$$

Here k runs from $k = 1,2,3, \dots, N-1$, which is equivalent to use symmetric boundary conditions (for even N: $-0.5N < k \leq 0.5N$, for odd N: $-0.5(N-1) < k \leq 0.5(N-1)$). The energy of an exciton is fully delocalized over the entire aggregate and can be obtained by incorporation of equation 4.7 in equation 4.6. The probability to find an exciton on a molecule n is given by $|\langle n|k\rangle|^2 = \frac{1}{N}$.

$$E(k) = \langle k|\hat{H}|k\rangle = E_0 + \frac{1}{2}\sum_{n}\sum_{n\neq m} V_{nm} e^{i2\pi k\frac{(n-m)}{N}} \tag{4.7}$$

Applying again the nearest neighbor approximation (tight-binding Hamiltonian) and assuming an aggregate with even numbers of molecules this would lead to:

$$E(k) = E_0 + 2V_0 \cos k\frac{2\pi}{N} \tag{4.8}$$

Using equation 4.9 and the given boundary conditions one finds the energy dispersion of an exciton state as

$$E(0) = E_0 + 2V_0 \; to \; E\left(\frac{N}{2}\right) = E_0 - 2V_0 \tag{4.9}$$

forming the exciton band with a band-with of $4V_0$. For optical spectroscopy, the single molecules hold a transition dipole moment and one immediately recognizes that for the $|k = 0\rangle$ case, all single transition dipole moments interfere constructively, whereas for $\left|k = \frac{N}{2}\right\rangle$ all single transition dipole moments show deconstructive interference (for an even numbered aggregate). Thus, the $|k = 0\rangle$ is a bright state and the $\left|k = \frac{N}{2}\right\rangle$ a dark state. The position of the bright state is dependent on the sign of the coupling V_0 and therefore on the mutual spatial position of the single molecules with regard to each other. For electrical neutral monomers, the leading coupling term is the point dipole-dipole interaction. It features a non-trivial dependence on the position of the transition dipole moments of the respective molecules.[80]

$$V_{nm} = \frac{|\vec{\mu}_n||\vec{\mu}_m|}{{R_{nm}}^3}(cos\alpha_{nm} - 3cos\beta_n cos\beta_m) = \frac{|\vec{\mu}_n||\vec{\mu}_m|}{{R_{nm}}^3}\kappa \qquad (4.10)$$

Here, $\left|\vec{\mu}_{n(m)}\right|$ denotes the respective transition dipole moments, R_{nm} is the distance between the single monomers, α_{nm} and β_n, β_m depict the relative orientations of each dipole moments according to figure 53. The angular dependence is summarized in the κ factor and can take positive or negative values, leading to distinct differences in the exciton band structure. If the monomers of the aggregate are assembled in a cofacial manner, the transition dipole moments are oriented parallel and consequently κ is becoming positive. This yields $V_0 > 0$ with an exciton band structure which has an optical bright state at $|k = 0\rangle$ and an energy of $E_0 + 2V_0$ (blueshift in the absorbance spectra). On the contrary, if κ is negative (head-to-tail configuration), this follows in $V_0 < 0$ with an energy of $E_0 - 2V_0$ and a redshifted absorbance spectra. The former is what is called a H-aggregate, whereas the latter is called J-aggregate,[135, 136] as has already been referred to in the introductory part of this paragraph.[127] The emissive behaviour of these aggregate types can also be rationalized by exciton theory. For H-aggregates, the emission from the lowest exciton state $\left|k = \frac{N}{2}\right\rangle$ (Kasha's rule) to the ground-state is dipole forbidden and thus perfectly

arranged H-aggregates are not emissive. In J-aggregates, the lowest excited state ($|k = 0\rangle$) is dipole allowed and features a radiative decay rate that is N-fold enhanced with respect to the decay rates of the monomers. The classification of J -and H-aggregates as well as the description of their photophysics within the dipole-dipole approximation was initially introduced by M. Kasha and turned out to be very strong for a big class of chromophore molecules.[81, 126] Generally, there are several deviations (structural defects in the local surroundings of chromophores, intermolecular vibrations leading to time-dependent fluctuations) from the ideal situation described above. These deviations tend to localize the excitation energy on a smaller part of the aggregate. In a perfect organic crystal, for example, the theory predicts a $N \rightarrow \infty$ behavior to form a continuous band. However, in practice N is at the order of 1-100 monomers and one will find aggregate states that exist within the larger crystal.[80, 130] The structural defects result in a deviation of the site energy E_0, (= ΔE_{nm}) and consequently in a change of the exciton coupling term V. The grade of disorder defines the extension of the excited state, which can be expresses by the ratio of ΔE_{nm} and V. For $\left|\frac{V}{\Delta E_{nm}}\right| \gg 1$, the interaction is larger than the difference in site energy and the transfer of exciton energy will occur in a wavelike manner. If $\left|\frac{V}{\Delta E_{nm}}\right| \ll 1$, the interaction is smaller then the site energy difference (weak coupling limit), the excitation energy transfer between molecules will occur via a diffusive hopping process (incoherent energy transfer, this is usually called the Förster limit).[80] In CPs, the governing parameters for the formation of (extended) exciton states will be the strength of the transition dipole moments and its respective direction (dependent on the used linker for CP synthesis), the mutual spatial orientation of the ligands and its distances (expressed by R_{nm} and κ) as well as the number of defect sites (controllable by the synthesis procedure).

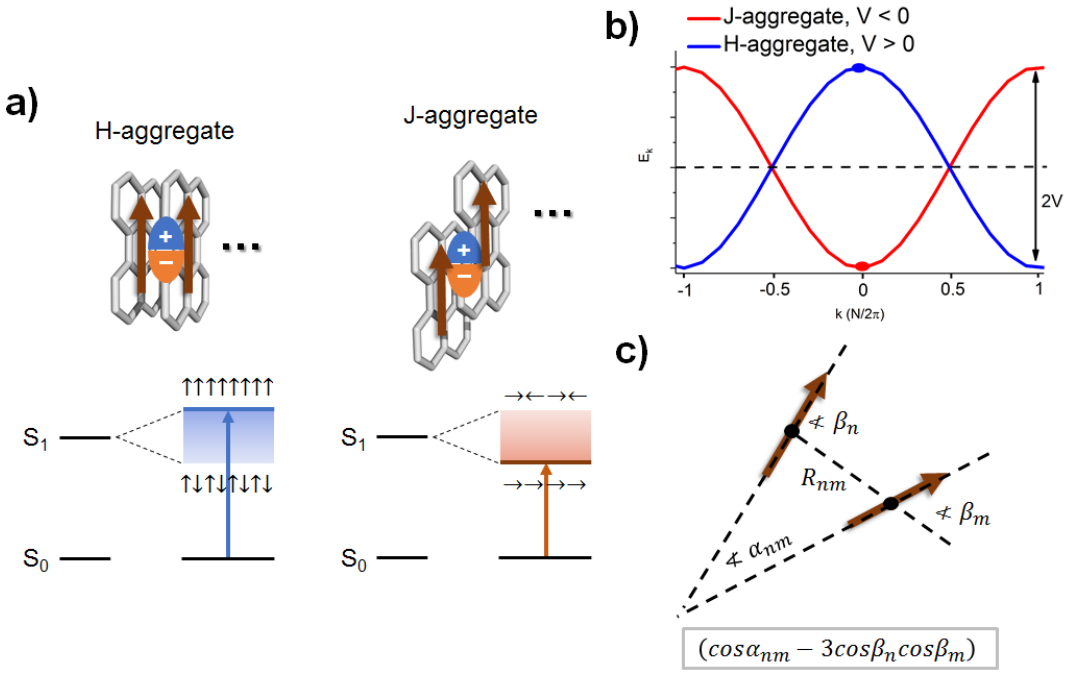

Figure 53. The exciton band structure as a mutual function of chromophore arrangement. A chromophore here is depicted as a perylene molecule carrying a transition dipole moment (red arrow). a) H -and J-aggregate: Cofacial arrangement of transition dipole moments (H-aggregate) gives rise to a positive dipole-dipole interaction (V > 0), the symmetric state features the highest energy, is centered at the top of the exciton band structure and holds the highest oscillator strength (all transition dipole moments are up); Head-to-tail arrangement of transition dipole moments (J-aggregate) show negative dipole-dipole coupling (V < 0), the symmetric state features the lowest energy and is centred at the bottom of the exciton band structure (highest oscillator strength, all transition dipole moments are aligned in one direction. d) The energy dispersion in the exciton band structure (energies of the exciton states as a function of k) in the nearest neighbour approximation. c) Angular dependency of the dipole-dipole interaction of the respective transition dipole moments.

4.2 Computational models in excited state theory

In this chapter I will shortly introduce the methods applied for quantum chemical calculations done in this work (ground state and excited state calculations). They rely on Kohn-Sham Density Functional Theory (KS-DFT)[137] and its time dependent variant (TD-DFT).[138] Besides these methods, there are also other prominent quantum chemical methods available for the modelling of excited states, which will not be treated in-detail here, but are listed for the sake of completeness. These methods are Hartree-Fock Configuration Interaction, many-body perturbation theory (Møller-Plesset PT), coupled-cluster (CC) theory and the whole class of multi-configurational self-consistent field (SCF) and complete-active space SCF methods.[139] The calculations of non-linear optical

properties can be divided in methods related to static or frequency dependent quantities. In particular, response theory in combination with electronic structure methods is been used to derive so called response functions, which describe the non-linear optical answer of a system as a function of an external field in a perturbative manner. This approach allows for determination of frequency dependent quantities. Other methods, for example, are finite-field methods which gives access to static polarizabilities.[3, 46] These methods will not be discussed here, as they out of scope of this thesis but are mentioned for the interested reader.

4.2.1 DFT and TD-DFT

Kohn-Sham Density functional theory (KS-DFT) is a computational quantum mechanical method to describe the ground state structure of many-body systems. KS-DFT or DFT has become very popular since the 1970's and is nowadays used in many disciplines (physics, chemistry and material science).[140] In DFT, the idea is to determine the energy and related properties of a system based on the three-dimensional electron density, rather than solving the complex many-body wave function problem of the Schrödinger equation. The Hohenberg-Kohn theorems provide the basis for this approach.[137] The first Hohenberg-Kohn theorem proves that there is a one-to-one mapping between the exact electron density and the exact external potential. The second Hohenberg-Kohn theorem ensures a variational principle, that the energy of a trial density (derived from a known wave function) is always higher than the energy of the exact density. So far, this approach is exact, however, does not describe how to access the exact electron density directly. A solution to that problem was given by Kohn and Sham, which suggested to describe the density of a system by the density of a non-interacting system. Such a system could be described by a single Slater determinant and consequently the density could be constructed from a set of orbitals, the Kohn-Sham (KS) orbitals.[141] The latter can be obtained by solving the Kohn-Sham equations, a set of n coupled differential equations. For KS-DFT, the energy of a system transforms into:

$$E[\{\psi_{KS}\},\rho]^{KS} = T[\{\psi_{KS}\}] + J[\rho] + v_{ext}[\rho](r) + f_{xc}[\rho](r) \qquad (4.11)$$

The term $f_{xc}[\rho](r)$ is the so-called exchange-correlation functional, which structure is unknown. However, there are approximate solution to the exchange-correlation (xc) functional used in practice and state-of-the-art xc-functionals often yield accuracies comparable to *ab-initio* methods at a fraction of the computational cost.[142] This fact makes KS-DFT a very strong and widely used methods to quantum mechanically treat big system (> 50 atoms) within a reasonable amount of time. Nevertheless, the empirical character of the xc-functionals undermines the reliability of DFT and thus DFT shows weaknesses in the correct treatment of e.g. charge transfer transitions, Van-der-Waals interactions, band-gap energies etc.[143]

The time-dependent variant of DFT is the so-called TD-DFT. This is a density-based approach for the computation of excited states. For TD-DFT the same accounts as for DFT, that due to the computational efficiency, it allows for the description of excited states of large systems (compared to other *ab-initio* methods). TD-DFT relies on a set of theorems and approximations, similar to DFT. The Runge-Gross theorem ensures a one-to-one mapping between time-dependent density and the time-dependent potential of an interacting system evolving from an initial state.[138] This time-dependent non-interacting system (similar to DFT) can be represented as a Slater determinant consisting of singe-electron orbitals. In practice, this leads to the time-dependent Kohn-Sham equations, which can be reduced to a linear-response formulation giving an eigenvalue problem (Casida's equation).

$$\begin{pmatrix} A & B \\ B^* & A^* \end{pmatrix}\begin{pmatrix} X \\ Y \end{pmatrix} = \omega \begin{pmatrix} 1 & 0 \\ 0 & -1 \end{pmatrix}\begin{pmatrix} X \\ Y \end{pmatrix} \qquad (4.12)$$

$\boldsymbol{X}$ and $\boldsymbol{Y}$ are the excitation amplitudes and ω is the excitation energy. The elements of the $\boldsymbol{A}$ and $\boldsymbol{B}$ matrices depend on the type of xc-functional and contain the occupied and unoccupied KS-orbitals, their corresponding energies, the Hartree Fock non-local orbital exchange as well as the xc-kernel. TD-DFT is

a very strong method, as it enables the calculation of excited states of computational demanding systems, and at the same time access to physical interesting properties such as, absorption, emission and adiabatic energies, excited state geometries, vibronic couplings, oscillator strengths, dipoles and atomic point charges as well as environmental effects.[144] However, again the use of empirical fitted xc-functionals is a source of significant error and consequently, TD-DFT calculations are strongly dependent on the used functional.[133]

4.3 Non-linear optics

The field of non-linear optics has constantly been growing since the first prediction of NLO processes and has experienced a tremendous experimental boost since the development of the first lasers.[8] The latter provided scientist with a source of high-intensity fields needed for NLO processes to be studied in detail. NLO effects today are important for a wide variety of applications, which range from photonics to biomedicine.[2]

The purpose of this chapter is to introduce the fundamentals of the theory of non-linear optics, starting with a molecular description of the theory and further expanding it to solids. Focus will be laid on the general features of this theory. Furthermore, I will in more detail treat the MPA process, as this is the main process of interest within this work. Also size-scaling effects in MPA processes will shortly be discussed. Please note that part of the following discussion has already been published in a recent review paper by our group.[12]

In the following, I will concern with light-matter interaction in the visible and infrared spectral region. Consequently, the light will carry energy in the range required for electronical and vibrational excitation of e.g. a molecule. For such energies, the light-matter interaction can be regarded as scattering of photons by the electrons.[46] Each photon carries a momentum, which will partially be transferred to the molecule since the electron remains bound, however, the great mass of the molecules will prohibit energy transfer so that the scattered photons will have the same frequency as the incoming ones. This elastic scattering process can be regarded as an “absorption” process of a virtual

excited state, intermediate in energy to the stationary states of the system. The lifetime of this virtual state will be short enough not to violate the uncertainty principle ($\tau\Delta E \sim \frac{\hbar}{2}$, with ΔE as the difference of the virtual state and the nearest electronically excited state, τ lifetime of the process). The de-excitation of the virtual state back to the ground state, is associated with the emission of a scattered photon, a linear process. The high intensity radiation of the incident light now enhances the probability for multi-photon interactions, where two or more photons are simultaneously absorbed in one quantum mechanical process. The frequency of the scattered photon does not have to be equal to the absorbed photons, a non-linear process. These basic principles envisage a large number of multi-photon interactions, to be used to accomplish frequency conversion of light. When laser detuning decreases, which leads to a smaller difference of the virtual state and the stationary state ΔE, the interaction process can no longer be described as an instantaneous scattering. The molecule state will become absorbing. With a high density of photons, MPA processes in molecule states are possible, which is an incoherent process.[8] In optics, the laser field can be described as an oscillating electro-magnetic wave, in which the optical active system resides. The interaction between them is to a first approximation the electric-dipole coupling. In a semi-classical sense, all charged particles in the light field (electrons, atomic nuclei) will experience a force following the time oscillations of the electro-magnetic wave and thereby acting as small antennas from which electro-magnetic radiation is transmitted. The oscillating charges in the considered system give rise to an induced dipole moment. The degree, to which the external electromagnetic field manages to set the charges in motion is, to a first order, expressed in terms of a linear polarizability α.[3] The response of the induced dipole moment is dependent on the frequency of the light field and consequently α is also frequency dependent.

$$\mu(t) = \mu^0 + \alpha E(t) \qquad (4.14)$$

With μ^0 being the permanent dipole moment of the optical active system. Now, one immediate question arises, how to understand non-linear light-matter

interactions? The answer of this question is found in a non-trivial generalization of equation 4.14, which lets the polarization be expanded in a Taylor series to introduce higher order terms.[12]

$$\mu(t) = \mu^0 + \alpha E(t) + \frac{1}{2!}\beta E(t)^2 + \frac{1}{3!}\gamma E(t)^3 + \cdots \qquad (4.15)$$

Equation 4.15 introduces β as the first-order non-linear hyperpolarizabiliy, γ as the second-order non-linear hyperpolarizability and so forth. It should be said, that these quantities are molecular quantities and when going to solid materials on a macroscopic level, further transformations need to be done. As in the linear case, the non-linear hyperpolarizabilities are frequency dependent. In non-linear optics, equation 4.15 describes the fundamental origin of nonlinearity at a microscopic level that governs the NLO performance of a material (here e.g. a molecule). The electric field of the incoming light can be described vectorial, comprising of a static and one or more oscillating terms.

$$E_\alpha(t) = \sum_\omega E_\alpha^\omega e^{-i\omega t} \qquad (4.16)$$

The E_α^ω are the oscillating Fourier amplitudes of the electric field along the axis α. Furthermore, the introduction of the electric field as a vectorial quantity, implies that the non-linear hyperpolarizabilities are tensor quantities (α is a first-rank tensor, β is a second-rank tensor and γ a third-rank tensor). Inserting the equation of the time dependent field into the Taylor expansion of μ yields:

$$\mu_\alpha(t) = \mu_\alpha^0 + \sum_\omega \alpha_{\alpha\beta}(-\omega;\omega)\, E_\beta^\omega e^{-i\omega t} + \frac{1}{2}\sum_{\omega_1,\omega_2} \beta_{\alpha\beta\gamma}(-\omega_\sigma;\omega_1,\omega_2) E_\beta^{\omega_1} E_\gamma^{\omega_2} e^{-i\omega_\sigma t} + \frac{1}{6}\sum_{\omega_1,\omega_2,\omega_3} \gamma_{\alpha\beta\gamma\delta}(\omega_\sigma;\omega_1,\omega_2,\omega_3) E_\beta^{\omega_1} E_\gamma^{\omega_2} E_\delta^{\omega_3} e^{-i\omega_\sigma t} \quad (4.17)$$

The ω_σ depicts the sum of the respective frequencies and the generated molecular polarization along the molecular axis α. As the single frequency components can be positive or negative the above equation involves both sum-frequency as well as difference-frequency generated polarization. This approach can be generalized to interactions with more than one electric field component (corresponding for example to two lasers A and B, working at the frequencies ω_A and ω_B). As these derivations are rather lengthy, I here refer to the literature. In principle, molecular properties in non-linear optics are defined by the expansion of the molecular polarization in orders of the external electric field. The same accounts for the number of involved photons in the non-linear processes, higher-order processes request multi-numbered photons and thus in non-linear optical processes a high density of photons is required.[3, 8, 46]

A quantum-mechanical treatment of non-linear optical processes can be conducted by time-dependent perturbation theory. This approach gives analytical expressions which then can be parametrized using quantum chemical methods or directly been solved, to access the molecular hyperpolarizability tensor elements. A short sketch of the time-dependent perturbation theory is given below. Everything starts with the time-dependent Schrödinger equation (SE).[145]

$$i\hbar \frac{\delta}{\delta t}|\psi(t)\rangle = \hat{H}|\psi(t)\rangle \quad (4.18)$$

Assuming a small time-dependent time perturbation, the Hamilton operator can be separated in a time-independent term and a time-dependent potential.

$$\hat{H} = \hat{H}_0 + V(t) \tag{4.19}$$

The next steps involve to express the $|\psi(t)\rangle$ in the basis of $\hat{H}_0$ and rewrite the time-dependent coefficients $d(t)$ of $|\psi(t)\rangle = \sum_n d_n(t)e^{-iE_n t/\hbar}|n\rangle$ in a power series of the external perturbation $V(t)$. The determination of $d(t)$ gives access to the perturbed wavefunction. With the latter important operators can be calculated, where in the case of optics the expectation values of the dipole operator are of highly interest, since it corresponds to the molecular polarization and thus to the polarizability and hyperpolarizabilities. By consequently following this approach, one finds e.g. for the linear polarizability:[46]

$$\alpha_{\alpha\beta}(-\omega;\omega) = \frac{1}{\hbar}\sum_n \left[\frac{\langle 0|\hat{\mu}_\alpha|n\rangle\langle n|\hat{\mu}_\beta|0\rangle}{\omega_{n0} - \omega - i\epsilon} + \frac{\langle 0|\hat{\mu}_\beta|n\rangle\langle n|\hat{\mu}_\alpha|0\rangle}{\omega_{n0} + \omega + i\epsilon}\right] \tag{4.20}$$

Equation 4.20 can be used for direct computation of the linear polarizability once the excitations energies and the transition dipole moments are known. Furthermore, it elucidates the dependence of the linear polarizability on the quantum mechanical properties of the system.

Such equations are also called sum-over-state (SOS) expressions, as they contain the summation over all intermediate states until the final state is reached (compare the sum over n in equation 4.20). Similar types of SOS expressions can also be derived for higher-order hyperpolarizabilities and thus give rise for the calculation of NLO properties. Besides the time-dependent perturbation theory, there are also other methods to derive expressions for the hyperpolarizabilities, which are the main quantity for the description of a NLO response. For further reading the reader should be referred to e.g. work by Kuzyk.[145-147]

The description so far assumes a single quantum system in an external field, a microscopic response. However, the major experimental measurements are

conducted either in liquids or in the solid-state. Consequently, in the macroscopic case one will consider the polarization $P(t)$ in an external field.[8]

$$P(t) = P_{\alpha}^{0}(t) + P^{(1)}(t) + P^{(2)}(t) + \cdots \tag{4.21}$$

Using the Fourier transformation of the time-dependent electric field and defining $\chi^{(n)}$ as a macroscopic susceptibility tensor of rank $n+1$, one can rewrite equation 4.21 as:

$$P(t) = P_{\alpha}^{0}(t) + \varepsilon_0 \sum_{\omega} \chi_{\alpha\beta}^{(1)}(-\omega;\omega) E_{\beta}^{\omega} + \varepsilon_0 \sum_{\omega_{1,}\omega_2} \chi_{\alpha\beta\gamma}^{(2)}(-\omega;\omega_{1,}\omega_2) E_{\beta}^{\omega_1} E_{\gamma}^{\omega_2} + \cdots \tag{4.22}$$

One immediately recognized the similarity between equation 4.17 and 4.22. By comparison, the macromolecular susceptibility can be derived from the molecular hyperpolarizabilities (assuming the electric field to be the same).

$$\chi^{(1)} = \frac{\alpha}{\varepsilon_0};\ \chi^{(2)} = \frac{\beta}{2\varepsilon_0};\ \chi^{(3)} = \frac{\gamma}{6\varepsilon_0} \tag{4.23}$$

These non-linear optical susceptibilities will still not be related to the experimentally observed values, as the electric field experienced by the individual molecule in a macroscopic sample is not the same as the applied external field. Instead, a molecule in solution or in a crystal will experience a local electric field, E_{loc}^{ω}, which is different from the macroscopic applied field due to a first approximation by the surrounding molecules. The determination of the local field effects is a non-trivial question and there are approaches based on differing theories. Furthermore, the local field effects a molecule experiences in solution will strongly differ from the local field effects a molecule experiences in

a crystal. In solution, the orientations of the molecules are random, so orientationally averaging over the single molecular contributions of the microscopic hyperpolarizabilities can be conducted. However, in solids the polarizability tensors transform according to the macroscopic coordinate system of the material and the different contributions sum up according to the respective molecular orientations.[12, 148, 149]

In this context, the advent of CPs in non-linear optics brings several interesting issues. First, the above presented theory for the description of NLO effects only accounts for effects, that are due to electric dipoles. This approach excludes important material properties, which could be present in CPs, e.g. chiro-optical properties, or properties that are related to the magnetic component of the interacting light field. Furthermore, a molecular approach, as implemented in the above equations 4.17 and 4.22 may not be fully suitable for the description of the electro-magnetic field interaction with a material class, which is formed by interactions that are much stronger than van-der-Waals forces.[12]

4.3.1 Multi-photon absorption

The concept of MPA, the instantaneous absorption of a number (≥ 2) of photons by an optical active system to change between the ground state and an excited state, was initially proposed by M. Göppert-Mayer in here doctoral dissertation in 1931. The prediction was based only on theoretical considerations and the key issue to support her theory was the introduction of a virtual state. The experimental implementation of her prediction lasted until the development of laser radiation, when Kaiser and Garrett reported two-photon excited fluorescence in $CaF_2:Eu^{2+}$ crystals.[5, 6]

Multi-photon related studies include the fundamental research on MPA, multi-photon excitation and multi-photon active materials. They have greatly enriched and deepen our understanding of light-matter interactions since the first experimental proof of the underlying theory. Among others, e.g. in areas like the multi-photon induced surface photoelectric effect, multi-photon induced photochemical reactions, further knowledge about selection rules and pathway for molecular transitions and the in-depth understanding what makes a material

a good multi-photon absorber. Today, there are several major areas, which include multi-photon excitation based applications: (1) multi-photon pumped frequency upconversion lasing, (2) MPA based optical limiting, stabilization and reshaping, (3) MPA based stimulated scattering, (4) multi-photon excitation based frequency upconversion imaging and scanning microscopy, (5) multi-photon excitation based three-dimensional data-storage and microfabrication. This growing use of MPA based applications imposed the development of smart optical NLO active materials, which lead to the synthesis and characterization of a vast variety of interesting multi-photon absorbing material classes (from small organic chromophores to dendrimers, polymers, metal-containing compounds and other advanced materials). The parallel development of theoretical methods alongside with improved non-linear optical characterization techniques allowed for an increasing understanding of important governing parameters in MPA. As a result, the development of an extensive structure-property relation was implemented for mainly multi-photon absorbing organic dyes, which enabled the deviation of molecular design principles.[7, 8, 51]

The attenuation of light passing through an optical medium can be expresses using a phenomenological approach similar to the Lambert-Beer law.

$$\frac{\delta I(z)}{\delta z} = -\alpha I(z) - \beta I^2(z) - \gamma I^3(z) - \cdots \qquad (4.24)$$

$I(z)$ is the intensity of the incident light beam along the propagation direction z. α, β and γ are the one, two and three-photon absorption coefficients. Focussing on two-photon absorption (TPA), meaning that there is no linear absorption ($\alpha = 0$) and higher order processes at a given wavelength λ can be excluded, equation 4.24 gives a second order differential equation in $I(z)$, which can be solved as:

$$I(z,\lambda) = \frac{I_0(\lambda)}{1 + \beta(\lambda) I_0(\lambda) z} \qquad (4.25)$$

z is the propagation length in the medium and $\beta(\lambda)$ is the TPA coefficient of the medium, which depends on the wavelength. Furthermore, $\beta(\lambda)$ [cm/GW] is a macroscopic parameter, which is also depending on the concentration of the two-photon absorbing molecules, further expressed as:

$$\beta(\lambda) = \sigma_2'(\lambda) N_A d_0 \times 10^{-3} \qquad (4.26)$$

with $\sigma_2'(\lambda)$ as average two-photon absorbability [cm^4/GW], N_A is the Avogadro constant and d_0 as the molar concentration of the absorbing molecules. Equation 4.25 is only valid for small TPA efficiencies. When the TPA is strong enough that ground state depletion is no longer be negligible, the TPA coefficient is no longer a material constant but will depend on the laser intensity. Expanding the definition of $\sigma_2'(\lambda)$ by the photon energy of the input light beam, $\sigma_2(\lambda) = \sigma_2'(\lambda) \cdot h\upsilon$ gives the two-photon cross-section in units of cm^4/photon/s. In practise most of the measured values are in a range of 10^{-51} to 10^{-42} cm^4/s, hence an informal unit was introduced defined as 1 GM = 10^{-50} cm^4/s, where GM stands for Göppert-Mayer. Similar expressions as for TPA can also be derived for higher-order absorption processes. To experimentally derive the MPA cross-section one simply has to measure the non-linear transmission as a function of the input laser intensity. If the laser intensity can be tuned over a wide wavelength range, a complete MPA spectrum of the active compound can be obtained. It should be noted, that the above formulations imply, that the incident light intensity has a uniform intensity distribution and is not dependent on time. In practice, the used laser source is usually pulsed and focused, thus depending on time and space. To obtain more valid MPA cross-sections from measurements, the above derived equation would needs to be modified, respectively.[8, 150]

Referring to equation 4.17 and 4.22, the non-linear hyperpolarizability tensors are complex quantities. It can be shown, that the real part of $\chi^{(3)}$(or γ), for example, describes the induced change in refractive index, while the imaginary part describes non-linear absorption. Similarly, the imaginary part of $\chi^{(5)}$ describes the three-photon absorption process and so on. Interestingly, non-

linear absorption is an odd-ordered process, and thus not dependent on the absence of inversion symmetry (note that $\chi^{(m)}; m = 2n$ vanishes under inversion symmetry).[3]

The treatment of non-linear absorption in the semi-classical NLO theory as has been introduced above, is not rigorous, however, a complete treatment can be accessed by the quantum theory of radiation.[46] The time-dependent perturbation theory leads to so-called SOS expressions, which describe the quantity of interest, the non-linear hyperpolarizabilities, in a complete quantum mechanical manner (the light field as well as the system) by implementation of intermediate virtual states.[145] These states are occupied by the light field and the optical active system and allow for a consistent treatment of the non-linear optical effects. In the following we will restrict to TPA in molecular systems with a single laser beam of a given frequency ω. Similar to equation 4.20, one can derive a SOS-expression for the molecular second-order hyperpolarizability $\gamma(-\omega;\ \omega, -\omega, \omega)$. The simultaneous and purely resonant process of absorption of two quanta is accordingly described by $Im[\gamma(-\omega;\ \omega, -\omega, \omega)]$. This leads to the following equation, which will act as the main equation in describing TPA from here on.[47, 151, 152]

$$S_{\alpha\beta}^{gf} = \sum_{i} \frac{\langle g|\hat{\mu}_\alpha|i\rangle\langle i|\hat{\mu}_\beta|f\rangle}{\omega_i - \omega_1} + \frac{\langle g|\hat{\mu}_\alpha|i\rangle\langle i|\hat{\mu}_\beta|f\rangle}{\omega_i - \omega_2} \qquad (4.27)$$

The TPA tensor elements $S_{\alpha\beta}^{gf}$ are the quantities which are associated with the two-photon absorption process. The averaging procedure of the TPA tensor elements give access to the measurable TPA cross-section via equation 4.27.

$$\delta^{gf} = \langle \left| S_{\alpha\beta}^{gf} \right|^2 \rangle = \frac{1}{15} \sum_{\alpha\beta} \left\{ S_{\alpha\alpha}^{gf} \left(S_{\beta\beta}^{gf} \right)^* + 2 S_{\alpha\beta}^{gf} \left(S_{\alpha\beta}^{gf} \right)^* \right\} \qquad (4.28)$$

$$\sigma_2 = \frac{8\pi^3 a_0^5 \alpha^2}{c} \frac{\omega^2}{\Gamma_f} \delta^{gf} \qquad (4.29)$$

a_0 is the Bohr-radius, c is the speed of light, α is the fine structure constant, ω is the photon energy and Γ_f is the lifetime broadening. In the simplest case for a TPA process where the input radiation is a single linearly polarized light beam the equation simplifies to (ω_1 and ω_2 in equation 4.27 simplify to 0.5ω) :

$$\sigma_2 = \left(\frac{2\pi}{c}\right)^2 \frac{\omega^2}{6\epsilon_0^2 h^2} \left| \sum_i 2 \frac{\mu_{gi}\mu_{if}}{\omega_i - \omega} \right|^2 \qquad (4.30)$$

where μ_{gi} are the transition dipole moment matrix elements along the propagation of the light wave. Equation 4.27 runs over all intermediate eigenstates of the quantum system under observation. However, the TPA is often dominated by the interaction of the ground state with a few excited states. Regarding only a number of important states leads to the so-called few-state models, respectively. For two excited states, one has three essential states and equation 4.30 reduces to:[49]

$$\sigma_2 \approx C \frac{\mu_{gi}^2 \mu_{if}^2}{(\frac{\omega_i}{\omega} - 1)^2 \Gamma} \qquad (4.31)$$

The three states in the “three-state” model of TPA have alternating symmetry assuming a centrosymmetric point group: both the ground and final state wavefunction have *gerade* symmetry, whereas the intermediate state has *ungerade* symmetry. With regard to the selection rules for TPA, the first two-photon allowed excitation will be the $S_0 \rightarrow S_2$ excitation (assuming e.g. D_{2h} symmetry for a linear push-pull molecule, these states are the $1A_g$, the $1B_u$ and the $2A_g$ states). A straight-forward analysis of equation 4.31 gives input about the requirement of the NLO system to enhance the TPA properties:[7]

(1) Large π-electron chains with enforced coplanarity that ensure large conjugation lengths that lead to high values of $\mu_{gi}, \mu_{if}, \mu_{gf}$

(2) Electron donor and acceptor groups at the end and at the center of the molecule to enhance the $\mu_{gi}, \mu_{if}, \mu_{gf}$ (→ low lying charge transfer states)

(3) Centrosymmetric molecules that possess a strong one-photon absorption transition close to the two-photon active laser wavelength, consequently minimizing the $\Delta = \omega_i - \omega$ term while enhancing σ_2. The occurrence of a one-photon absorption close to the virtual state is also called resonance enhancement

(4) Chromophores with narrow one-photon and TPA bands. A narrow TPA band will automatically lead to a high σ_2, as the area of the band is fixed by the $S_{\alpha\beta}^{gf}$ and thus will lead to a small Γ value

The above points (1) to (4) describe design concepts for two-photon active molecules. However, the deviated rules can also be generalized to other systems. To summarize the main points from theory, TPA efficiency can be controlled by geometrical parameters, such as the dimensionality of the charge-transfer network, its length of conjugation and grade of planarity, and the strength and places of donor-acceptor groups. As the SOS approach for the calculation of TPA cross-sections in principle includes the summation over all eigenstates of the NLO system, interference between different optical active molecular channels are also included.[153] The fact that in non-centrosymmetric molecules the TPA efficiency will be lower compared to centrosymmetric molecules is because in centrosymmetric molecules there is the probability for resonance with an two-photon forbidden intermediate state (point 3), and furthermore, the transition dipole moment μ_{gi} will be larger, cause the molecule will be effectively polarized by the complete part of the optical field cycle.

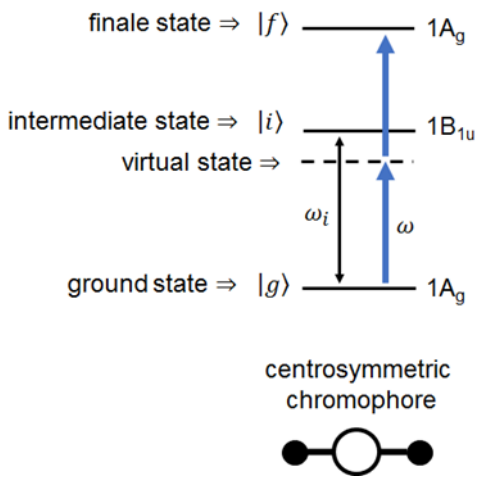

Figure 54. General energy level diagram for the essential states in a centrosymmetric push-pull chromophore with D_{2h} symmetry (three-state model) to familiarize with the concept of resonance enhancement in such chromophores. The important quantity is the detuning of the intermediate state (single-photon allowed S_1 state) from the laser wavelength ω.

The analysis of few states equations, together with the immense amount of experimental studies on two-photon absorber has led to a fundamental understanding of molecular structure-property relationships. As there is strong correlation between an intermolecular charge-transfer and TPA, the initial design of two-photon absorbing organic molecules is rooted at the synthesis of push-pull chromophores (push: electron donating group, pull: electron accepting group). Several systematic studies showed that geometric considerations indeed can enhance the TPA efficiency.[154-160] Molecular design strategies started with symmetrical chromophores (type Ia) holding either donor (D) or acceptor (A) groups at each side of the molecules separated by π – sytems (A-π-A = pull-pull, D-π-D = push-push). Compared to the linear asymmetric analogues (A-π-D, type II), it could be shown that type II chromophores appeared to be more efficient. The important benefit of multidimensional conjugation was quickly recognized and the use of molecular branching to enhance σ_2 was quickly demonstrated, which led to the type Ib quadrupolar structures (D-π-A-π-D, or A-π-D-π-A). These structures where shown to be 4-fold more effective than their dipolar analogues. Refining the concepts finally led to the development of multibranched structures, in which two or more A-π-D units are connected with an extended conjugation (dendrimers, oligomeric structures etc.). Note, that the structures are octupolar when they belong to one

of the following symmetry classifications: O_h, T_d, D_{nh} (n = 3, 4, …) and C_{3h}. These types of organics have been shown to be highly efficient and superior two-photon absorbers, which could be attributed to cooperative effects of interactions between the different branches: (1) increase in the number density of active sub-units (2) synergistic interactions between the sub-units either via enhanced conjugation (“through bond) (3) or “through space but close proximity” interactions (excitonic or electronic nature). The multidimensionality concept has also been successfully applied to coordination and organo-metallic compounds.[7, 8, 51]

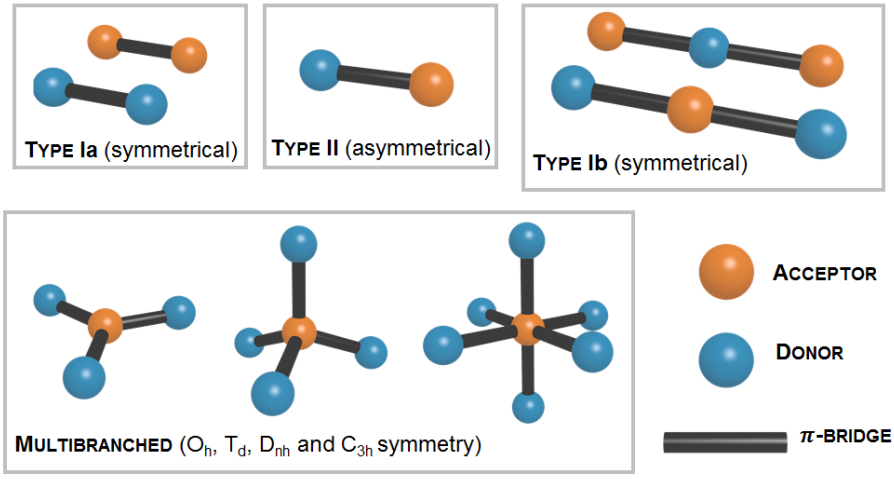

Figure 55. Classification of push-pull structure motifs. Please note that for the multibranched systems only a small variety of possible structures are shown. Type Ia and Ib are quadrupolar structure motifs. Type II are a dipolar push-pull structures and the multibranched systems hold a octupolar electrical moment.

It should be noted that a quantitative description of structure-property relationship in TPA of organic molecules is derived in an atomistic theory (an intrinsic microscopic quantity), however, the macroscopic measured value is the TPA coefficient β, which is the product of the cross-section and the number density of the active absorbers. Thus there are at least three extrinsic factors that will influence the measurements: (1) the timescale involved in the absorption measurement and the response speed limited by the measurement technique, (2) the perturbation of the state structure by the surroundings (local field effect), (3) the intensity limit at which other non-linear absorptions will induce permanent changes in the molecular structure. In order to report the microscopic, intrinsic quantity σ_2 the concentration of the two-photon active

species in the system needs to be known, which is in the case of solution measurements of a discrete species (organic molecule, metalorganic complex) straight forward, it becomes not so obvious in the case of a polymeric systems. In such cases, a structural unit as the asymmetric unit, its multiplication comprising one ligand molecule, or even the complete unit cell (in case of a CP) could be used and it is always important to exactly define the structural unit, which was used for calculation of σ_2. In order to avoid ambiguities in reporting of TPA cross-section values, various merit factors have been implemented in literature, to normalize the measured NLO response, molar mass (σ_2/M), number of delocalized electrons (σ_2/N), square number of delocalized electrons (σ_2/N^2), molecular volume (σ_2/V_m). A comparison between different materials is only meaningful, if the data is valid normalized. The reported values will change, depending on the type of normalization.[12, 161] In the framework of the SOS formalism, Kuzyk reported about the existence of a fundamental limit of the σ_2 of organic molecules, σ_2^{max}. According to the SOS theory, σ_2 can be calculated to be proportional to N (N is the number of electrons in the molecule). Unexpectedly, the molecules with the highest number of electrons showed the lowest σ_2/σ_2^{max} ratio. Based on these findings, Kuzyk concluded that the model established for molecular structure-property relations in TPA is not well optimized, as it does not take advantage of all electrons in the system. To overcome such limitations, a possible strategy is to use intermolecular interactions and exploit excitonic interactions in molecular assemblies of two-photon absorbers, which could lead to distinct size-enhancement effects.[51, 146, 147, 162]

4.3.2 Size enhancement in MPA

In contrast to the massive investigation undertaken in the structure-property relationships of TPA and organic molecules, the effect of intermolecular interactions on TPA properties has not been fully elucidated. Theoretical considerations predict the occurrence of an intense NLO response promoted by the large oscillator strength of a few electronic states with size-enhanced nonlinearities, proportional to N^2 with N is the number of coupled monomers.[46, 52, 129] Seminal work on semiconductor materials, both theoretically as well as

experimentally, indeed show that excitonic interactions needs to be taken into account, when the nonlinearities should be described correctly.[163, 164] Similar effects are thought to arise also in organic semiconductors or molecular aggregates.[165-168]

The underlying problems of size enhancement in MPA will shortly be sketched in the following paragraph. I will, again, concentrate on TPA.

The interest in this approach arises from the fact to circumvent complicated synthesis strategies in accessing efficient two-photon absorbers, but rather use simple molecular building units.[51] By targeted assembly of this SBUs based on design criteria, one could exploit *specific* intermolecular interactions to cooperatively enhance the TPA response. Cooperative effects in TPA need to be separated from size-enhancement effects based on simple additive behaviour. If the measured two-photon response is linearly dependent on the density of absorber, the different sub-units behave nearly independent (additive behaviour). On the contrary, if a variation in the measured two-photon response for the assembly is found, either an increase or a decrease, there will be some “kind of coupling” between the structuring units. The response of the whole system is not simply the sum of the responses of the single components. Such a behaviour was first described with molecular dendrimers (e.g. on substituted triarylamines), where interactions between the different branches lead to enhanced TPA based e.g. on excitonic interactions between the different sidearms (the so called “branching” effect).[59, 64, 169]

A direct approach for size-enhancement via cooperative effects in TPA based on excitonic interactions can be derived from the Frenkel exciton theory. The latter approximately predicts an enhanced transition dipole moment scaling according to $\sqrt{N}\mu_{mon}$, where μ_{mon} is the monomer transition moment. Assuming total cooperativity, dipole-dipole coupling in molecular aggregates can lead to an overall scaling factor with a N^2 dependency (N is the number of coupled molecules). Please note that the cooperative effects in TPA within the exciton model is either related to the two-exciton transition, which occurs at resonances almost twice of the one-photon absorption (enhancement via a double resonance effect), or via population of TPA allowed states in the first exciton manifold holding gerade symmetry (depending on the coupling, these states will

be at the bottom or at the top of the one-exciton band).[170] The cooperative enhancement within the exciton theory can be fully treated by the calculation of the molecular second-order hyperpolarizability γ using the dipole-dipole approximation and expressions for the respective transition dipole moments of the participating bands.[51] In the following approach, I will introduce how excitonic coupling effects σ_2 by deriving some phenomenological equation within the essential three-states model of TPA and excitonically coupled chromophores arranged in a linear chain. I will assume that the non-linear absorption takes place between the ground state of the manifold and the two-exciton band (Figure 56, blue arrows). To summarize, in the one-exciton band with a width of two times the interaction energy, N molecules on the aggregate share one molecule excitation, which is localized over the complete manifold. On the contrary, the two-exciton manifold holds two-molecule excitations, where the single molecule excitations are located at different molecules (due to Pauli repulsions) and the two-exciton manifold holds a width of four times the interaction energy. For the transition dipole moment of the one-exciton band from the ground state one finds:[49, 170]

$$\mu_{gf} = \mu_{mon} \sqrt{\frac{2}{N+1}} \frac{1-(-1)^k}{2} cot\left[\frac{\pi k}{2(N+1)}\right] \qquad (4.32)$$

Where k runs again over all coupled monomers N. A similar quantity can be analytically derived for the transition dipole moment between the one- and the two-exciton band. Since the equations are rather long, I here refer to [170]. Now, within the essential three-state model the TPA cross-section can be written as:[49]

$$\sigma_2 \sim C \frac{\mu_{gn}^2 \mu_{nf}^2}{(\omega_{gn} - \omega)^2 \Gamma} \qquad (4.33)$$

The most important quantities here are the squared transition dipole moment between the ground-state and the one-exciton band, respectively between the one- and two-exciton bands. Squaring equation 4.32 exemplarily demonstrates, how an expression can be derived, showing the N dependency of the transition dipole moments:

$$\mu_{gf}{}^2 = \mu_{mon}{}^2 \left(\frac{2}{N+1}\right)\left(\frac{1-(-1)^k}{2}\right)^2 cot^2\left(\frac{\pi k}{2(N+1)}\right)$$

$$\mu_{gf}{}^2 \approx \mu_{mon}{}^2 \left(\frac{1-(-1)^k}{2}\right)^2 \left[\frac{8}{\pi^2}(N+1) + \frac{4}{3}(N+1)^{-1} - \frac{\pi^2}{2}(N+1)^{-3}\right] \quad (4.34)$$

$\mu_{gf}{}^2$ has been simplified using the Laurent-expansion for the cotangents function with a truncation after the second term. Equation 4.34 shows that only uneven states in the exciton manifold contribute to $\mu_{gf}{}^2$ and that the $k = 1$ state contains by far the most oscillator strength (up to $0.81(N+1)\mu_{mon}{}^2$). When the dipole-dipole interaction V is negative (e.g. in J-aggregates), this state will be found on the bottom of the one-exciton band. Finally, the simplification of the squared transition dipole moment using an expansion expression shows that the μ^2 's will scale with an $N+1$ behavior, which is valid for both, excitations from the ground state to the one-exciton band and in between the respective manifolds.[170] A combination of equation 4.34 with 4.33 now shows, that the non-linear population of the two-exciton band by using TPA will lead to an overall scaling with a $(N+1)^2$ dependency, taken only the respective transition dipole moments into account. Furthermore, the dephasing of the laser frequency with regard to the excitation frequency (the $(\omega_{gn} - \omega)^2$ factor) will introduce a dramatic resonance enhancement, when the excitation energy approaches the OPA energy. Finally, population of the first exciton manifold via TPA is possible, when the symmetry of the aggregate or crystal obeys centro-symmetry by vanishing transition dipole moments in the ground and excited states of the array. The N-dependency then will lie between an additive behavior (linear) and a N^2 behavior (due to similar arguments as introduced above). A more precise

and complete treatment of scaling behavior in TPA can be found, for example, in [51] and references therein.

Besides intermolecular interactions based on dipole-dipole interactions, there has been other mechanism discussed for cooperative enhancement effects in TPA. These mechanisms mainly rely on enhanced electronically coupling in more planarized π electron systems or vibrational contributions to nonlinearity.[171, 172] Finally, it should be stated that enhancements of non-linear responses in crystalline or aggregated states is non-trivial and often many phenomena superimpose, especially in solid systems. A clear deviation of the single contributions is often not possible, as the regarded optical systems are influenced on a microscopic (excited states) as well as a mesoscopic to macroscopic level (local field enhancement, waveguiding, crystal size distribution, diffraction and scattering etc.) To properly distinguish between the particular contributions, experiments and sample preparation needs to be conducted carefully.[12]

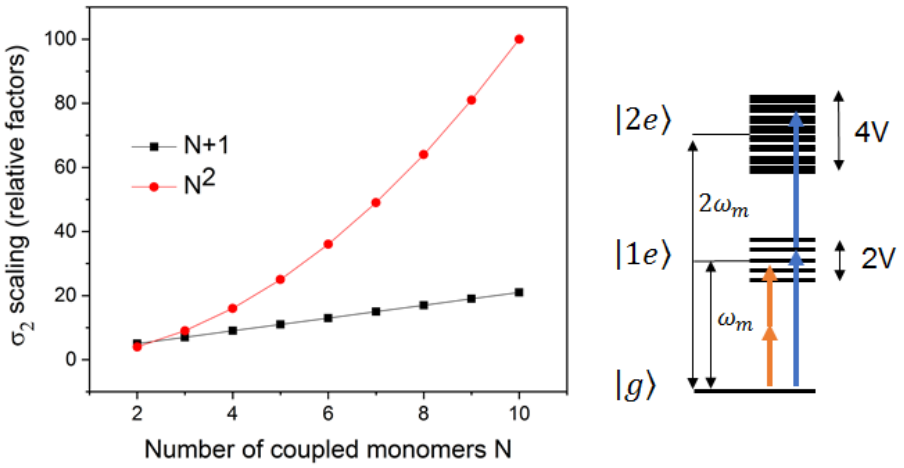

Figure 56. Predicted size scaling of σ_2 due to excitonic coupling in molecular assemblies (the σ_2 scaling originate from the size enhancement of the transition dipole moments from the ground state to the first exciton manifold $|1e\rangle$ with roughly $\sqrt{N}\mu_{mon}$). TPA into $|1e\rangle$ (left side) will show a trend, laying between the two lines, whereas TPA in the two-exciton band $|2e\rangle$ will non-linearly scale with N^2 (Analysis exclusively on scaling of μ_{mon}). The right side shows the one -and two-exciton bands, centered at roughly the monomer frequency ω_m and a bandwidth of $2V$, respectively at twice the monomer frequency $2\omega_m$ and a bandwidth of $4V$.

4.4 Coordination polymers

In the following chapter, basics of CPs will be discussed. For this purpose, CPs will be defined and the synthesis, structural elucidation, general properties, reticular chemistry as well as topological concepts will be discussed. After introducing CPs and the underlying chemistry concepts, the photophysical properties of this material class will be summarized. The chemistry of CPs has a long history and emerges from coordination chemistry. Early attempts for the synthesis of CPs dates to the discovery of the pigment “Prussian Blue”. Therefore, the following discussion does not claim to be exhaustive, rather the intention is to give a global picture of the development in the field of CPs, especially focused on photophysical properties. Please note that part of the following discussion has mainly been extracted from a very recent and detailed book about MOFs published by O. M. Yaghi and co-workers, which gives a great overview about recent parts of reticular chemistry.[173] Further information can be found in several review papers, please compare [174-184].

The knowledge about how atoms are linked in space to make molecules and how these molecules react and behave has reached a sophisticated level nowadays. Chemistry plays an essential role in material science, not only in understanding material properties, but rather on the targeted synthesis of new materials. Interestingly, the science of making extended chemical structures has remained relatively untouched, compared to the progress of molecular chemistry, regarding the predictability of the described material. This can be traced back to the fact, that inorganic solid-state compounds are often synthesized at high temperatures and that the structure formation is influenced by many correlative effects, which are hard to predict.[42] The possibility of the translation of inorganic complex chemistry to the realm of solid-state chemistry was successfully shown with the synthesis and crystallization of MOFs. These materials were shown to be architectural stable and permanent porous. The fact, that the reaction of mainly carboxylates with metals or metal-oxo clusters forming strong, directed bonds under mild conditions, which preserved the reactivity and structure of the building blocks gave rise of the development of new concepts in solid-state chemistry. Knowing the geometry of the building units it now becomes possible to expand their metrics and specifically

synthesize materials, which hold function, by design. This is a new concept in solid-state materials, as the outcome of a synthesis can be predicted to a certain extent. The framework fixes the molecule in a specific orientation and spatial alignment, like the molecule fixes the atom in a specific orientation. This term is called reticular chemistry and can be rationally described by tools of topology.[173, 185-188]

4.4.1 MOFs and CCNs

Based on the 2013 IUPAC recommendations, the terminology of CPs and MOFs are defined in a hierarchically manner in which the most general term is coordination polymer. Coordination networks are therefore a subset of CPs and MOFs are a further subset of coordination networks. The exact wording is given below with some comments.[189]

A CP is “a coordination compound with repeating coordination entities extending in 1,2, or 3 dimensions.”. A CP does not need to be crystalline, consequently the term 1-periodic, 2-periodic or 3-periodic cannot be used throughout, rather the term 1,2, or 3 dimensions only indicate the degree of extension of the CP.[190]

A coordination network (CN) is “a coordination compound, extending, through repeating coordination entities, in 1 dimension, but with cross-links between two or more individual chains, loops, or spiro-links, or a coordination compound extending through repeating coordination entities in 2, or 3 dimensions.”. A preferred and widely used term will likely be CP. From the above definitions, it should however be clear that these two terms are not synonymous. They differ in the definitions of crystallinity, as coordination networks are crystalline solid state materials and require periodicity within their definition (compare “…a coordination compound with repeating coordination entities…” to “…a coordination compound, *extending, though* repeating coordination entities…”).[190]

Finally, a metal-organic framework (MOF) is “…a coordination network, with organic ligands containing potential voids.”.[190] The wording of the former definition accounts for the fact that many MOF systems are dynamic and will

potentially show changes in porosity, or guest filled voids upon external stimuli like temperature, pressure etc.[191-193] For these reasons, it is also not required, that a MOF be crystalline, although commonly used characterization techniques of MOFs are often based on X-ray diffraction.[194] MOFs are also described as soft porous crystals, which summarize the fact that MOFs possess structural transformability accompanied with a highly ordered network. Consequently, MOFs have been classified into three categories, 1st, 2nd and 3rd generation MOFs. First generation MOFs have frameworks, whose porosity collapse irreversible upon guest removal. Second generation MOFs show stable and robust frameworks, which maintain porosity after guest removal. Third generation MOFs show flexible or dynamic pores, which reversible response to external stimuli in the sense that two types of transformation are possible.[195] Transformations can occur while retaining crystallinity (crystal-to-crystal) or while crystallinity is lost (crystal-to-amorphous). These transformations are essentially phase transitions. Breathing MOFs are a state-of-the-art example of crystal-to-crystal phase transitions with a large unit cell change provoked by external stimuli.[193] The word “organic ligands” in the definition of MOFs can be controversial in the context of coordination networks, as arguments can be found that classify ligands such as oxalates, cyanides, etc. as either organic or inorganic compounds.[189] In general, MOFs can be regarded as supramolecular 2 or 3 dimensional frameworks which contain voids, assembled from organic ligands and metal ions or clusters.

The conceptual foundation of coordination chemistry was initially laid by the swiss Nobel laureate and chemist Alfred Werner.[196] Very early attempts for the synthesis of coordination compounds were based on serendipity, which for example lead to the finding of the famous “Prussian Blue”.[173] Gaining insight into the molecular structure of transition metal coordination compounds based on work by Alfred Werner, served as an example to extend the practice of coordination chemistry to higher dimensions. The slow diffusion of benzene to a solution of $Ni(CN)_2$ in NH_3 yielded a crystalline material with the formal composition of $[Ni(CN)_2(NH_3)](C_6H_6)$, the so called Hofmann clathrate.[197] Single crystal X-ray diffraction analysis revealed an extended crystalline coordination compound built from 2D layers of alternating octahedrally and square planar coordinated Ni^{2+} ions. The field of synthetic metal-organic chemistry as it is

conducted today emerged from these early ground-laying work. Linking metal ions entirely by organic ligands to form coordination networks was first reported by Saito and coworkers, which made use of well-established Cu^+ chemistry, synthesizing a series of α,ω-dinitrile based coordination networks of differing dimensionality, grade of interpenetration and network topology.[198-200] In further work, R. Robson and B. Hoskins realized that geometrical principles for the simplification of crystal structures as outlined by A. F. Wells[201] using nodes and links can be applied to predict structures by linking from suitable building blocks of a given geometry and connectivity. They linked Cu^+ ions with a tetrahedrally shaped ligand TCTPM (=4,4',4'',4'''-tetracyanotetraphenylmethylene), which ultimately yielded in a diamond network. Furthermore, the combination of tetrahedral and square planar building units, by reaction of Cu^+ and $Pt(CN)_4^{2-}$ units, gave a structure based on the platinum sulfide network as predicted by theory.[202, 203] The term metal-organic framework was first coined in work by O. M. Yaghi about coordination networks of the form $[Cu(BPY)_{1.5}](NO_3)$ (BPY = 4,4'-bipyridine).[204] To increase stability of the obtained coordination networks, charged chelating ligands were introduced. This approach is rooted in the fact, that these types of linkers can balance the charge on the metals which circumvents the formation of charged networks with counterions sitting in the potential voids. Furthermore, the increasing bond strength enhances the thermal and chemical stability of this framework compounds. This approach finally led to the introduction of secondary building units (SBUs) and permanent porosity in metal-organic extended structures. The reaction of $Zn(NO_3)_2 \cdot 6H_2O$ and benzene dicarboxylic acid (H_2BDC) in DMF/toluene by slow vapor diffusion of triethylamine/toluene revealed the first Metal-Organic framework, MOF-2 ($Zn(BDC)H_2O$) as a neutral framework, constructed from interlinked $Zn_2(\text{-}COO)_4$ paddle wheel SBUs linked by BDC struts (**sql** network).[205] The increased stability of this compound enabled the removement of solvent molecules from the pores without collapse of the structure. This work was the basis for the synthesis of the next MOF structure by O. M. Yaghi and coworkers in 1999, implementing metal-oxo SBUs, the famous MOF-5.[206] This MOF is composed of octahedral $Zn_4O(\text{-}COO)_6$ SBUs and BDC to give a 3D framework structure of **pcu** topology. MOF-5 provides an open porous structure of great thermal and

architectural stability, which finally leads to permanent porosity, as shown by nitrogen adsorption characterization.

This work laid the basis for a rapid development in the field of MOFs with ~ 75000 coordination network structures in the CSD database (based on a MOF subset search on metal centers in 1,2 and 3D periodic structures that cover the bonding motifs of all common MOFs, 9% of CSD, 2016 release) and annually ~ 6000 new coordination network structures.[207, 208] The key points in making robust and stable framework compounds consequently was found to origin from the use of charged chelating ligands (mostly carboxylates) and the SBU approach.

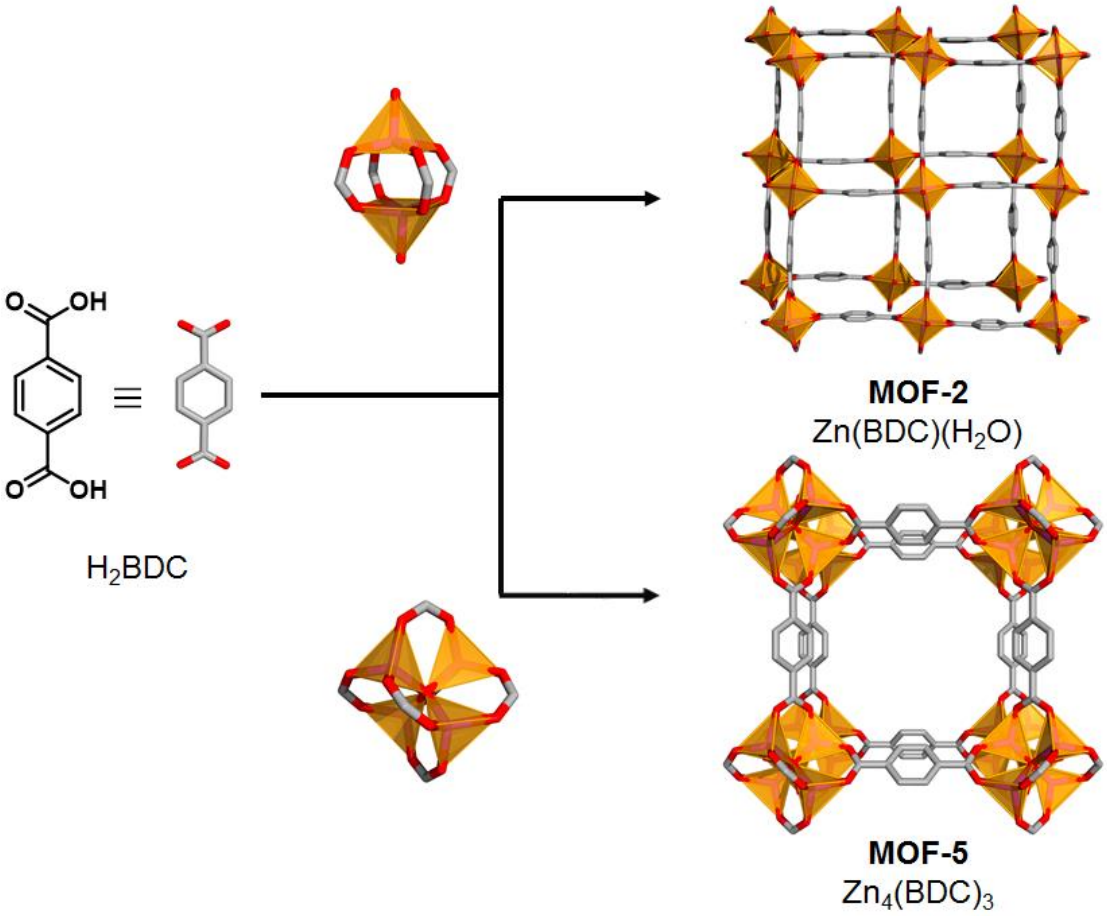

Figure 57. Crystal structures of MOF-2 and MOF-5 and their respective building units ($Zn_2(COO^-)_4$ paddlewheel complex in the case of MOF-2 and basic zinc carboxylate $Zn_4O(COO^-)_6$).

Synthesis procedures of MOFs are as manifold as this material class is itself. Basically, one can distinguish between solvothermal and non-solvothermal synthesis methods. Solvothermal reactions are defined as reactions taking place in closed vessels under autogenous pressure above the boiling point of the used solvent. Non-solvothermal reactions are normally classical approaches for the crystallization of molecules or inorganic salts and rely on methods like slow evaporation of the used solvent, or gradual temperature changes to exceed the critical nucleation concentration of a material. In general, the synthesis of MOFs has shown be dependent on many parameters, such as compositional (molar ratio of starting materials, solvent, pH value, modulator etc.) and process parameters (time, temperature, pressure, heating rates, type of vessels etc.).[209] Furthermore, inherent material properties (thermodynamic and kinetic parameters) also play a crucial role in the nucleation and crystal growth processes of MOFs.[42] So far, finding the right parameter for a given system in MOF synthesis is still an empirical task and the parameter space has to be screened by carefully executed experiments.[210] There are high-throughput methods available, which allow for the systematic investigations of experimental parameters, however, these synthetic approaches do not allow for gaining detailed information about the formation and crystallization mechanisms of MOFs and related compounds. The kinetic and thermodynamic effects of crystallizing porous frameworks under typical solvothermal conditions are poorly understood. The autogenous pressure generated in solvothermal reactions or the incorporation of solvent in open voids (solvent effect) may affect the relative phase stabilities. Solvation effects are difficult to track in the synthesis of MOFs, as it is problematic to compare the energetics of a large-pore system with greater amount of solvent in the cavities to a smaller-pore system, incorporating less solvent. This fact is of particular importance in the case of mixed-solvent synthetic approaches.[42] In order to reliably create new MOF materials, with improved physical properties there is still a need to enhance the understanding of how the different synthesis parameters can be chosen to target specific MOF phases.[211]

The crystal structures of MOFs are unambiguously determined using crystallographic techniques, such as X-ray diffraction. Single-crystal X-ray diffraction (SCXRD) and powder X-ray diffraction (PXRD) techniques are the

method of choice for crystallographic characterization of MOF materials and are general used within the MOF community.[114, 212] These techniques are widely employed and well understood, however, the structure elucidation of MOFs as highly porous materials (low-density materials) is not always a straightforward process. Porous MOFs contain a lot of available void spaces, which in some cases constitute up to 90% of the crystal volume. These voids are initially occupied by solvent molecules from the synthesis. Structure elucidation is therefore impeded by a couple of challenges, which can be related to the impact of pore contents or symmetry. Summarizing the important factors one can find (1) highly disordered pore solvent amounts, (2) guest molecules with long range structures (3) guest induces distortion of the framework structure (4) twinning and (5) pseudo symmetry as governing factors.[114] Other factors are diffusive scattering and X-ray absorption. In contrast to molecular crystals, where recrystallization from solution until a suitable crystal quality is found, is possible, MOF crystal growth takes place during synthesis. Thus, one has to optimize the synthesis procedures to get better quality single crystals (keep in mind that the quality of a diffraction experiment almost always depends on the quality of the studied specimen). Another approach, if the synthetic conditions do not allow for the growth of SCXRD suitable crystals, is the solution of the structure from power X-ray diffraction data. However, this is usually a more challenging task. In principle, *ab initio* structure solution of MOFs using power data is possible and has been shown on MOFs like the famous UiO-66 using high quality synchrotron data.[213] The process is similar to what is carried out with other materials and includes pattern indexing, intensity integration, structure solution and final Rietveld refinement. Note, that it could be shown that the charge-flipping method greatly improves the structure elucidation.[194] A unique characteristic of MOFs is the structural descriptiveness by the topological approach. Combining the topological approach with structure solution from powder data greatly enhances the success, as the number of possible structures can be reduced.[214] According to reticular chemistry, some networks can preferentially be formed with the use of specific building units.[187] When combining two different type of nodes, edge-transitive networks are the most frequently observed nets. Crystal structure models are produced by means of computer simulation according to the most feasible topology and consequently

used as input structures for Rietveld refinement.[214] Another approach is to model organic ligands and metal clusters as rigid bodies and follow a global optimization procedure using Monte-Carlo based optimization algorithms e.g. simulated annealing techniques.

In concluding, since the synthesis and characterization of MOF-5[206] and HKUST-1[215] in 1999 (surely the two most-known and most-studied MOF structures in the field), a manifold of new MOFs covering very interesting physical properties have been realized. Férey and co-workers reported on flexible porous MOFs (MIL-47, MIL-53, MIL-88) starting in 2002.[216-218] The concept of isoreticular chemistry was made famous and mixed-linker compounds of the general form [M_2(dicarboxylate)(L)] (M = Zn, Cu, L = diaza compounds, dipyridines, pyrazines etc.) were shown to be a versatile compound class.[219] Further in 2002 the famous imidazolate-based MOF platform of zeolitic imidazole frameworks (ZIFs) was introduced.[220] Today, there is definitely a larger amount of interesting frameworks as could have been mentioned here,[173] however, among the most studied compounds in the field of MOFs due to their high thermal stability, relatively easy synthetic approach and good crystallinity are HKUST-1, UiO-66, Cr-MIL-100, Cr-MIL-101, NU-901/NU-1000, MIL-125, CAU-1 and ZIF-8.[209]

Application-oriented research done on MOFs has obviously been focusing on topics related to porous materials. Classically, MOFs have been investigated towards gas storage and separation, carbon sequestration, catalysis and biomedical applications. Despite their enormous high internal surface areas (7800 m^2/g)[221] compared to 1000 m^2/g for zeolites and mesoporous silica, the main challenges for MOFs in industrial applications is still their relatively low thermal stability (~ 300 °C), limited chemical stability (most MOF structure are water sensitive) and reactivation in multiuse industrial environments.[208] Recently, research on MOFs is systematically been extended to further potential research areas, where MOFs are thought to be of highly interest. The areas include e.g. electronics and optoelectronics (low-K materials, photo switching),[222, 223] magnetism (qbits and single molecule magnets),[224] conductivity,[225] sensing,[226] data storage[227] and non-linear optics.[12, 228]

4.4.2 Topology and reticular chemistry

“Reticular chemistry is the study of linking discrete chemical entities (molecules and clusters) by strong bonds to make extended structures…”. The term reticular derives from “reticulum” and means “*having the form of a net*” or “*netlike*”.[186] The field of reticular chemistry deals with the synthetic control of extended framework structures such as MOFs, where organic molecules are joined together with polynuclear metal clusters. The vast geometrical and compositional variation by using inorganic units needs a complete theoretical description of all possible combinations, which can be achieved by tools of topology (from Greek τόπος meaning “place” and λόγος meaning “study”). The concept of topology allows to simplify structures, by only considering the connections between the formative constituents, not their chemical structure.[173]

This approach significantly reduces the amount of information and complexity of a structure, which can give a more detailed understanding of structural conditions and simultaneously allows for the “reverse engineering” of solid state materials.[229] The simplification of crystal structures (atomic positions, connectivity, spatial arrangement and symmetry) by a description in terms of atom packings or connected polyhedrons is common practice in inorganic chemistry.

The topological description of structures indeed dates to A. F. Wells.[201] This concept is frequently used nowadays to describe extended framework structures and was introduced in zeolite chemistry before been transferred to MOFs. The underlying basics of the simplified description of a crystal structure by means of topology is to consider only the connection and not the chemical information or metrics of a crystal structure.[173] The inherent connection is invariant to bending, stretching and collapsing but not to the formation nor deconstruction of connections.

The topology of a network underlying a crystal structures is derived by deconstruction into vertices and edges (nodes). The nodes are distinguished by the number of points of extension (= the number of connections to other building blocks). An edge has two points of extension and a vertex has three or more point of extensions (a metal ion with coordination number 4, an organic MOF ligand with 3 or 4 donor groups etc.).[177, 182] The nomenclature of networks

with a given topology uses three letter codes and is summarized in the reticular chemistry resource (RCSR) database. The names are assigned arbitrarily or are related to already existing structure types, minerals etc.[230] The definition of nodes enables the synthetic chemist to simplify any given crystal structure to a net of vertices which are linked by edges.

Networks are a collection of nodes that can be described using graph theory. The underlying networks of a crystal structure are special nets, so called infinite 2- or 3-peridodic graphs (no loops, multiple connections, directionality or loose ends).[231] The deconstruction of a crystal structures into its underlying net is an approach to identify the graph that describes it (Figure 58). The steps of deconstruction comprise of finding the building blocks that represent the nodes. To decide, which geometrical units are representing the building blocks of a given MOF structure, the number of points of extensions for each node need to be found. Typically for MOF structures are carboxyl groups as donating groups of ligands and a point of extension of such a group could be for example the carboxy C-atom. Building blocks with two point of extensions typically refer to edges, whereas building block with 3,4… point of extensions are vertices. To find the topology it is not only important to know the point of extensions, but also the connections between them and the spatial arrangement of the nodes with regard to each other. Note that a network of edges and vertices is only unique, if it cannot be transformed into another net by bending and stretching but only by breaking and forming connections.[181] For example, three connecting 3-c nodes can be connected to form 2D layers with different structures, which are all described by the same topology.

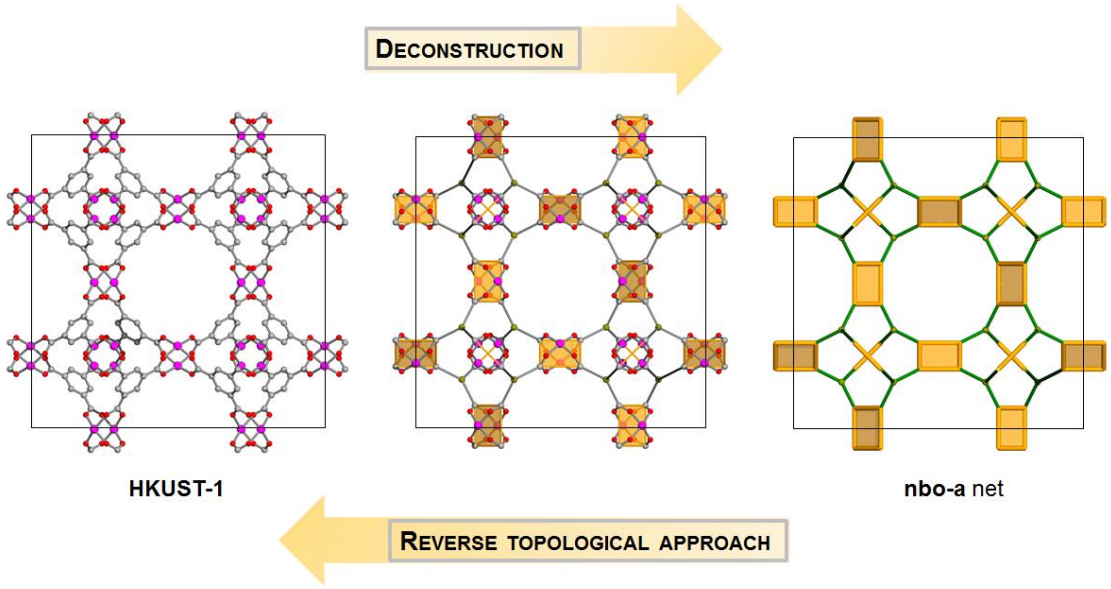

Figure 58. The deconstruction of $Cu_3(BTC)_2(H_2O)_3$ (left picture) into its underlying network of **nbo** topology (right picture). The picture in the middle represents the reduction of the H_3BTC ligand to its point of extension (3-c) as well as the tetratopic (4-c) connectivity of the Cu_2 paddlewheel complex. Consequently, the n**bo** topology is a ditopic (3,4-c) topology. Going along the other direction by starting from a known topology and construct a network through assembly of the geometry matching building units is what is called the reverse topological approach.

By following this description, crystal structure can be simplified and classified according to the underlying network. The simple net derived in this way, however, is abstract and loses chemical information. Indeed, the above discussion pointed out that a network is merely an arrangement of nodes. However, in the description of networks the different vertices and edges are positioned on coordinates with maximum site symmetry. This approach permits to create a more realistic representation of an abstract mathematical object (a graph). This is referred to an embedding.[173]

The deconstruction concept of a given MOF structure into its underlying network can also be used to design materials based on a given topology by connection of suitable building block, this concept is called reverse topological approach,[108, 185, 188, 232] where the embedding of a given topology is used as a blueprint for the targeted synthesis of a new material (Figure 58 and 59). So far, the nodes and edges of a network were regarded as simple points, however, from a chemical point of view they are not simple points. The local symmetry of the vertex has a profound influence on the outcome of the synthesis of a new MOF material, as small differences in the angles of connection will lead to

differing arrangements (compare e.g. the **dia**, **nbo** and **lvt** topology). Consequently, to render the assignment and the design of new framework materials correctly, further descriptors are needed. These descriptors are tilings, transitivity and face symbols.[233, 234] An in-depth discussion of these concepts at this point is beyond the topic of an introduction, also because there are many different other terms that are used to characterize nets and the reader is referred to the relevant literature (see the end of the paragraph). However, I will shortly discuss the concept of transitivity.

Transitivity is described by a four letter code, *pqrs* (*p* = number of topological distinct vertices; *q* = number of topological distinct edges; *r* = number of topological distinct faces or rings in the tiling; *s* = number of tiles). 3-periodic nets with a transitivity of 1111 are called regular nets (**bcu**, **dia**, **nbo**, **pcu** and **srs**), 3-periodic nets with transitivity of 1122 are called quasiregular nets (**fcu**) and those with transitivity of 11rs are semiregular nets (**lvt**, **sod**, **lcs**, **lcv**, **qtz**, **hxg**, **lcy**, **crs**, **bcs**, **acs**, **reo**, **thp**, **rhr** and **ana**).[187] Interestingly, these three groups of networks have been shown to be the ones that most likely form, when on type of edge is linked by one type vertex (one type of SBU is reticulated with a ditopic linker).[187, 230] All nets that consist of one type of vertex and one type of edge are referred to as uninodal edge-transitive nets (edge-transitive = meaning that all edges in a structure are equivalent). These networks are the most likely products to be formed in reticular synthesis. Therefore, networks that are edge-transitive and binodal are of great importance in reticular chemistry (spoken the reaction of an organic ligand holding higher connectivity (3,4,…) with any inorganic SBU of higher coordination number (CN $\geq$ 3)). This class is called binodal, bipartite edge-transitive networks.[173] Aside of the before mentioned, reticular chemistry and topology is a very rich and broad research field, consequently an extensive overview cannot be given here. The above considerations were extracted in parts from excellent literature about topology and reticular chemistry.[173, 181, 185, 187, 188, 230, 231, 233-235]

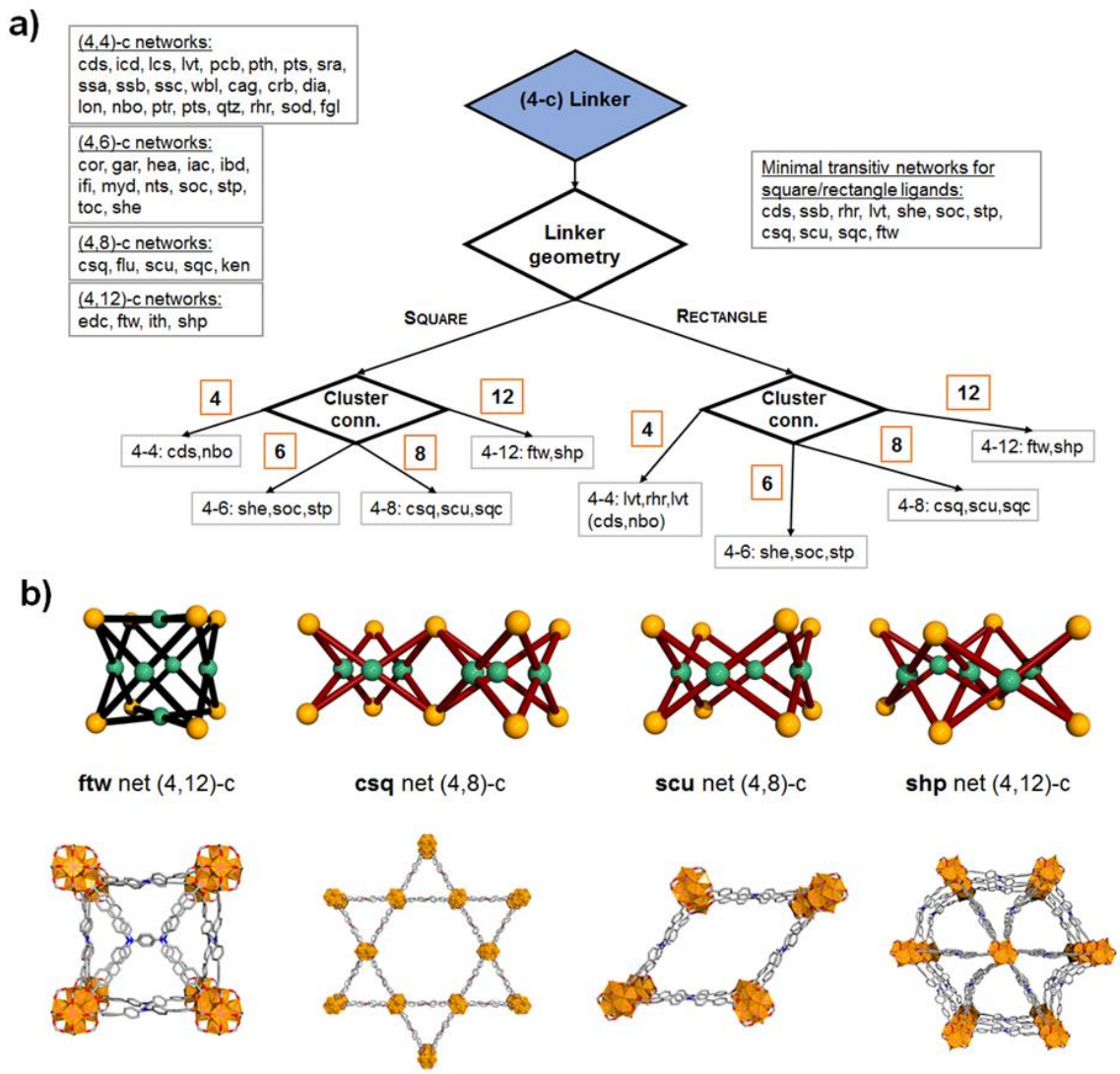

Figure 59. a) A topology analysis of tetratopic (4-c) ligand molecules, showing all possible topologies in the space of bipartite, edge-transitive networks b) A series of ditopic networks as often found in the chemistry of zirconium based MOFs (**ftw**, **csq**, **scu**, **shp**). The subjacent structures have been assembled following the topological information, using the ligand H_4TPBD and the respective Zr_6-oxo clusters with the help of the software materials studio (Version 5.0) in a reverse topological approach.

4.5 Photophysics in CPs and MOFs

Photoactive MOFs have been in the limelight of research in recent years. The work on CPs as optical materials encompasses the use of CPs and MOFs as phosphors in lightning applications (e.g. LMOFs = luminescent MOFs in white-light emission or biological fluorescence imaging),[236-238] luminescent sensing (e.g. sensing of aromatics, optical thermometers, pH-sensing, sensing of ions or gases),[238, 239] light-upconversion (e.g. lanthanide-based upconverson, triplet-

triplet annihilation upconversion),[240-243] non-linear optics (e.g. second-harmonic generation, MPA)[12, 69] photoswitching (e.g. photomodulated switching of MOFs for gas separation),[244] photocatalysis[245] or stimulated emission[28] and lasing (e.g. two-photon pumped lasing in MOFs containing hemicyanine dyes),[246, 247] to name a few.

Important photophysical process occurring in CPs and MOFs, which are recently under investigations, are exciton formation upon optical absorption (light harvesting),[83, 248-251] energy transfer phenomena (exciton migration e.g. Förster-type singlet ET, Dexter-type triplet ET)[248, 252, 253] and photocatalytic processes.[245, 254]

In the following section, I will summarize the fundamental photophysical processes of MOFs with an emphasis on mechanistic aspects within the recent literature of CPs and MOFs. The latter will mainly comprise the nature of the excited state and exciton migration processes. There have already been many great reviews on luminescent CPs and MOFs,[39] as well as summaries on photoswitching[244] or photochemistry.[254] However, there are little systematic and detailed investigations of photophysical properties in CPs and MOFs, compared to, for example, the field of organic crystals.[255] Consequently, laying the focus on mechanistic aspects of the photophysics of MOFs is of immense interest, as such properties in MOF structures are frequently observed and little effort has been investigated to gain a complete understanding of excited state processes.[86] Furthermore, in the frame of MPA, the excited state properties are of immense importance, as they will, on the bottom line, define the non-linear response of the system (compare the theory part of non-linear optics). From a more general point of view, the nature of the excited state in a molecular assembly (let’s regard a CP as a crystalline, periodic molecular assembly, to a first approximation) will be governed by geometrical aspects. The latter means that the type of intermolecular interactions is a function of the chromophore arrangement. However, in CPs and MOFs, this can be rationalized within the tools of reticular chemistry. Consequently, following this line of thought, the nature of the excited state of a CP can be “engineered” in a manner, that defined intermolecular interactions might be accessed by targeted synthesis with clear design principles. Compared to organic crystals, which are formed by

rather weak van-der-Waals interactions, CPs provide a richer synthetic pool, as crystallization is determined by a plethora of differing interactions between the building units (ionic and van-der-Waals interactions, solvation effects etc.).

4.5.1 Excited state properties of MOFs

For studying photophysical properties of CPs and MOFs, classical spectroscopically characterization techniques are used, such as absorption, reflection, emission and excitation spectroscopy (static and dynamic, polarization dependent or independent) either at defined wavelengths or spectrally resolved. The quantities of interest are the optical band gap, the spectral emission range and the corresponding luminescence maximum, the emission lifetimes and quantum yields. Furthermore, information about the number of participating states (e.g. from excitation spectroscopy, or transient absorption and emission spectroscopy), the absorption range or vibronic fine-structure are of highly interest. Measurements are conducted on crystalline powders, powders dispersed in differing organic solvents, on MOF-polymer composites or on MOF-thin films.[29, 30, 256]

The measured photoresponse is interpreted using established excited state theories, at differing levels. Depending on the energetic levels of the frontier orbitals of the organic ligand, used to assemble a CP or MOF, either the photophysics will mainly be characterized by the ligand (to a first approximation ligand-centered (LC) emission), or orbital interactions between the metal node and the ligand will be present (metal-to-ligand (ML) or ligand-to-metal (LM) charge transfer type interactions), as found in the ubiquitous MOF-5.[71, 256, 257] Furthermore, “through-space” interactions between ligands are described in the context of ligand-to-ligand charge transfer excitations,[258] excimers (excited dimer)[259] or excitonic resonance interactions.[124] As these conceptualities are used in various ways, I will shortly discuss the underlying physics and point towards similarities.

A ligand-to-ligand charge-transfer (LLCT) excitation is an excited state often discussed in conjunction with organometallic complexes and initially originates from inorganic spectroscopy. The term was introduced by Vogler et. al.. The first studies of LLCT in organometallic compounds goes back to Coates and

Green, Koester, Gouterman et. al. and Miller and Dance.[260] In its initial definition, a LLCT state is defined as a charge-transfer excitation between reduzing and oxidizing ligands coupled by coordination to a metal center. Also, in the absence of an intervening metal center, LLCT states can be observed, provided that the ligands are electronically coupled to each other, as for example found in donor-acceptor organic co-crystals. In a LLCT excitation, the excited state is located at a single optical active compound, e.g an organometallic complex or an organic charge transfer complex.

Excimers are dimers with associated excited electronic states, holding a dissociative ground state and a structureless emission spectra.[259] Excimer interaction is attributable to configurational mixing of exciton and charge transfer interactions. Excimer emission is found in noble and other monoatomic gases as well as in aromatic molecules (in fluid solutions, liquids, crystals, polymers and crystal defects) and excimer formation can also be understood as a self-trapping of (monomeric) excitons. In organic crystals such as e.g. naphthalene or pyrene, excimer states can migrate over the crystal[261] during their lifetimes (~ 100 ns), which has been proofed by incorporation of guest molecules, which act as traps (sensitized fluorescence). When the excimer is formed from different elements (different atoms or molecules), this is often called an exciplex.

The term resonance interaction originates from exciton theory, which has been introduced in chapter 4.1.1. Excitonic resonance states are locally excited states (the electron and hole remain on one molecule) with associated excited states, which interact with each other via dipole-dipole interaction.[81] This type of interaction is found in molecular dimers (monomeric or different molecules), in aggregates and in crystals. Upon excitation, energy associated with the excited states is resonantly spread over the complete aggregate (in the perfect case) between the excitonically coupled states. In the weak coupling limit (chromophore-chromophore distances $>$ 10 Å, incoherent coupling) energy transfer will occur via diffusive hopping mechanism, this is the so-called Förster-limit.[80]

The similarities between the above excitation types are reflected in the fact that they all describe excited states in molecular assemblies (dimeric structures

and higher). The excited wavefunctions of the associated electronically excited states, however, will differ by the grade of charge resonance within the respective parts of configurational mixing to form the delocalized states as well as by the number of molecules contributing to the excited state. In organic crystals or aggregates with higher number of interacting organic molecules the excited states can coherently be coupled and thus a description using the concepts of Frenkel exciton theory is more meaningful.

The experimental literature on photophysical properties of CPs and MOFs largely outweighs the computational studies.[86] The main problem in theoretical treatment of photophysical properties of MOFs is the system size together with the need of *ad hoc* exchange-correlation functionals, large basis sets and computationally extensive electronic structure methods (e.g TD-DFT) to correctly treat many-body dispersion interactions and excited state properties. Furthermore, to correctly simulate excitonic interactions in periodic calculations, higher required levels of theory (e.g. GW + Bethe-Salpeter method) are needed, which take many-body effects correctly into account (excitons are quasi-particles).[262, 263] However, treating CPs or MOFs with such methods is often simply not possible due to computational limitations.

Douhal et. al. conducted a number of spectroscopic studies on zirconium and cerium based MOFs incorporating naphthalene and pyrene based ligand molecules (Figure 60). For naphthalene carboxylate and aminonaphtalene carboxylate based Zr-MOFs, they spectroscopically revealed the existence of charge-seperated states (ligand-to-cluster charge transfer =LCCT) with a lifetime of ~ 170 fs (in DCM), besides the existence of excimer states between two adjacent naphthalene molecules (~ 840 ps in DCM). Furthermore, they proofed energy transfer from naphthalene molecules to aminonaphtalene within ~ 1.2 ps.[264, 265] The photobehaviors of Ce-NU-1000 and Ce-CAU-24-TBAPy, two MOFs formed from a pyrene based ligand (4,4',4'',4'''-(pyrene-1,3,6,8-tetrayl)tetrabenzoic acid = TBAPy), also revealed the existence of LCCT states in ~ 100 fs (for Ce-NU-1000) and ~ 70 fs (for CE-CAU-24-TBAPy). The formed charge-separated states recombined in ranges of ~ 0.5-15 ns. Furthermore, they also found excimer formation in 50 ps with a lifetime of ~ 14 ns in Ce-NU-1000, however, no excimer states were formed upon excitation of the TBAPy

ligand in Ce-CAU-24-TBAPy. The authors claimed that the lack of excimer formation in Ce-CAU-24-TBAPy is due to topological restriction. In both MOFs they found an ultrafast intramolecular charge-transfer state located at the TBAPy ligand (~ 160 fs). All measurements conducted in this works were done on MOF powders dispersed either in DMF or DCM solutions. The authors recorded steady-state absorption, fluorescence and excitation spectra of all investigated compounds. The photodynamics of the photosystems were examined using ps-time resolved emission spectroscopy employing time-correlated-single-photon counting (TCSPC) systems. Furthermore, femtosecond UV-Vis-NIR transient absorption measurements were conducted using a chirped-pulse amplification setup.[266]

Deria and co-workers investigated porphyrin and pyrene based In and Zr-MOFs, to be more precise they looked into the photobehavior of NU-902, MOF-525, NU-901, NU-1000 and ROD-7 (partly depicted in Figure 60).[29, 30, 98, 251] Starting with the porphyrin based MOFs, they measured steady-state extinction and emission spectra as well as time-resolved emission spectra (TRES) and transient fluorescence spectra of the compounds, incorporating either the free-base or the zinc-metallated form of the porphyrin ligand (TCPP = 4,4',4'',4'''-(porphyrin-5,10,15,20-tetrayl)tetrabenzoic acid). They suggested that the difference in the spectral shapes (red-shifts in the extinction and emission spectra, as well as differences in the vibronic $Q_{0,0}$ and $Q_{0,1}$ features) originate most probably from the difference in exciton coupling of the Q-bands, a direct consequence of the different ligand orientation within the MOFs. They found enhanced emission lifetimes compared to the sole ligands (MOF-525: ~ 5.4 ns, NU-901: ~ 4.6 ns, TCPP: ~ 9 ns). Furthermore, differences in the TRES and the stead-state emission spectra for the metallated MOFs point towards differences in the emissive state decay rate to the vibrational ν_0 and ν_1 levels. The authors suggested that an enhanced chromophore symmetry within the constraint framework geometries may influence the Franc-Condon overlap between the vibrational levels of emissive and ground state. Their work suggests that the excited state in these porphyrin containing MOFs is spread at least over two molecular moieties via dipole-dipole coupling. Emission quenching experiments (amplified emissive quenching) using ferrocene based quenchers and a Stern-Volmer analysis, revealed exciton hopping times of 0.65

ps (NU-901-H) and 0.13 (NU-901-Zn), corresponding to 170 (NU-901-H) and 114 (NU-901-Zn) chromophores an exciton visits within its lifetime.[98] They further expanded their investigations to the photophysical properties of zirconium and indium based pyrene-MOFs, NU-901, NU-1000 and ROD-7, where the authors showed the existence of long-living excimer states (6.27 ns for ROD-7, 4.68 ns for NU-901 and 3.78 for NU-1000) using again time-resolved emission spectroscopy. They further explained the differences in the excited state properties of these MOFs as a function of the chromophore distances, orientation and concentration, which is directly associated to the underlying topology of each framework compound. They intensified their investigations on the NU-901/NU-1000 systems, as these MOFs are polymorphic structures, thus are similar in their chemical compositions but show different spatial alignment of their building units. Transient femtosecond absorption spectroscopy revealed the existence of an intense $S_1 \rightarrow S_n$ excited state absorption (ESA), which diminishes with the emergence of a broad induced absorption feature origin from excimers (formation time: ~ 2.0 ps). This spectral feature was not found for the NU-1000 compound, which was the first clear observation of fast excimer formation in MOFs. Furthermore, excited state calculations on the level of TD-DFT predicted a delocalized wavefunction over TBAPy chromophores, with an exciton sized of ~ 1.7 nm.[29, 30] The measurements conducted in these works were either done on MOF powder dispersions (in DMF) or MOF samples were mixed with polystyrene and drop-casted on quartz substrates. The TRES measurements were conducted using a picosecond time-correlated single-photon counting spectrophotometer, transient absorption spectra were collected using standard pump-probe methods or the randomly interleaved pulse train method (picTAS).

Wöll and co-workers intensively investigated photophysical properties of a number of surface-supported metal-organic framework (SURMOF) type-2 thin-films, assembled from anthracene, and naphtalenediimide ligands. In the case of the anthracene based SURFMOF film they proofed the existence of excimer-related excited states by using time-resolved emission spectroscopy with the help of a streak camera (excimer lifetime of ~ 4 ns).[267] In the case of naphtelendiimide based SURMOF-2 films, they revealed an intensive fluorescence quenching of the films compared to the singe ligand moiety.

Furthermore, transient absorption spectroscopy on the films showed the excistence of dark states with a pronounced shorter absorption lifetime and a negative TA signal. The authors suggested the formation of H-type aggregation in these films.[82] They further showed that these non-emissive H-type aggregates can be transferred to thin-films with an enhanced emissive rate and quantum yield (J-type behavior). This fact was accompanied by side-position substitution of the naphthalene-core, which finally leads to a less planar chromophore arrangement within the SURMOF film due to steric hindrance. The preferred head-to-tail arrangement revealed a negative excitonic coupling (according to TD-DFT calculations), a photoluminescence lifetime of ~ 6.2 ns as well as an enhanced quantum yield.[83]

Pan et. al. showed that excimer formation in MOFs can be tailored by exfoliation of MOF bulk materials to ultrathin MOF sheets. They synthesized a calcium based MOF incorporating a aminoterphenyl based ligand (2'-amino-[1,1':4',1''-terphenyl]-4,4''-dicarboxylic acid). Excitation dependent emission spectroscopy revealed different contributions in the photoluminescence signal. The latter changed massively upon exfoliation of the bulk material, where the photoluminescence of the formed ultrathin 2D-MOF plates showed only a ligand located emission signal. The authors hypothesized that the red-edge contribution of the emission spectra could be attributed to excimer emission, which was lost during the exfoliation procedure due to diminished intermolecular contacts of the MOF ligands. Within this study they used exclusively static spectroscopy (excitation and emission spectroscopy). Measurements were directly conducted on powdered samples sealed in a glass cuvette.[268]

Belov and co-workers conducted static polarization-dependent absorption and emission measurements on single-crystals of van-der-Waals 2D-MOFs assembled from the pyrene based linker TBAPy and zinc-paddlewheel building units (Figure 60). The single-crystal absorption spectrum shows a pronounced absorption band near the absorption edge, which the authors assigned to the formation of two types of excitons, one exciton within one 2D sheet (intralayer exciton) and one between 2D-MOF sheets (interlayer exciton). Photoluminescence measurements revealed ligand-centered emission signals (~ 4 ns), alongside with a blueshifted emission signal (~ 0.8 ns), which the

authors claimed to originate from exciton recombination. Based on there measurements, Belov et. al. gave an exciton radius of ~ 9.5 Å for the intralayer exciton (0.20 eV binding energy) and ~ 4.8 Å for the interlayer exciton (0.45 eV binding energy).[269] Interestingly, Shelykh et. al. conducted a theoretical investigation of the examined MOF system of Belov et. al. The findings of Shelykh and co-workers showed, that they were able to fully reproduce the peak-shape of the absorption spectrum by only taking single-particle excitations based on TD-DFT calculations into account. Furthermore, they analyzed the effective masses in the band diagram of the van-der-Waals Zn-TBAPy MOF and showed, that only dark excitations have excitonic signature. They argued, that the assignment of interlayer and intralayer excitons in this special type of van-der-Waals MOF conducted by Belov et. al. might be misguided by an incorrect assignment (precisely single-particle excitations between π-π^* states of the ligand instead of exciton formation).[270]

Zhao and Du et. al. designed a number of pyridinethiomethylbenzene (1,2-bis((pyridin-4-ylthio)methyl)benzene) based 2D-Zn-MOFs, with the help of differing co-ligands. The spectroscopic analysis by excitation-dependent-emission -and transient emission spectroscopy showed the existence of a rich photophysical behavior, revealing a double-channel-emission pathway. The authors assigned the different emission peaks to the formation of an 2D-intralayer exciton and an excimer interaction between pyridinethiomethylbenzene ligands. They supported their arguments by a thorough analysis of the MOF structures and exfoliation experiments of the bulk materials to thin 2D-plates, where the formed plates finally showed a vanishing excimer emission signal. All measurements within this study was conducted directly on MOF powders.[271]

In closing, Samokhvalov and Grinnell used solid-state synchronous fluorescence spectroscopy to study the photoexcitation and recombination pathways of MIL-53(Al) in detail. They could show that the use of synchronous fluorescence spectroscopy on powdered MOFs samples is superior to common emission spectroscopy, as the latter suffers of pronounced line broadening. By using synchronous fluorescence spectroscopy, they found a plethora of different peaks in their emission signal, which they assigned to vibronic fine-structure of

the ligand (ligand-centered emission), band-gap recombination and the formation of LLCT states (excimers) between adjacent benzyl groups of the terephtalic acid molecules.[272]

In summarizing, the above presented work should serve to provide a picture about how researchers investigate the photobehavior of CPs and MOFs, what type of spectroscopic measurements are conducted, respectively, what theories researcher use to interpret the collected data.

As a basic characterization tool, static absorption and emission spectroscopy is conducted either directly on powders using quartz plates or cuvettes, on powder dispersion in organic solvents (e.g. DMF, DCM, toluene, etc.) or on polymer composites. Exceedingly few measurements are done on single crystals. Specified quantities are often the absorption and emission wavelength ranges and quantum yields. Furthermore, studies are pursued by the help of excitation spectroscopy. Less measurements are conducted using polarization dependent light sources. In dynamic spectroscopy, frequently photoluminescence lifetimes are measured using common measurement techniques (streak camera, TCPSC) and excited state properties are analyzed by the help of transient absorption spectroscopy (e.g. pump-prope, setup). The excited state properties are interpreted within the framework of molecular-orbital theory (ligand centered excited states, ligand-to-ligand charge transfer states), molecular exciton theory (as introduced by Kasha)[30] and also in the initial form of excitons from solid-state physics (electron-hole quasi-particle).[269]

The above presented analysis provides a basic view on the photoresponse of MOFs and CPs. Therefore, the photobehavior of MOFs can be positioned in a spectrum between the categories of molecular excitons localized on a single ligand or classical Frenkel type excitons localized within a unit cell.

The first category is defined by a small interchromophore coupling term caused by disorder and large spatial separations. In the case of a molecular exciton, the latter can be regarded as a molecular excited state localized on a single entity. In molecular solids the energetic levels of the molecule will be affected by the dielectric environment, leading to a distribution of energy levels (depending on the local symmetry). This distribution is Gaussian and leads to severe line broadening effects.

In Frenkel type excitons the delocalization of an optical excitation over the monomers of an aggregate is limited to one or two unit-cells, where oscillator strength of each molecule is distributed over more than one subunit (compare the introductory part of exciton theory).[273]

Based upon the optical studies conducted on MOFs and CPs so far (in part presented above), most of the work indicate that in this material class there are ligand-ligand intermolecular interactions of the second category. Commonly, the authors describe them as an excimer interaction located on small dimeric structures in the expanded MOF crystal, with a redshifted emission in the PL spectra. Taking this into account, the light-matter interactions of MOFs can be characterized in the best way by the formation of tightly bound Frenkel excitons. However, depending mainly on the interchromophore distance, the type of electronic excitation of the single chomophores and the spatial alignment of a chromophore linker with regard to each other (e.g. in highly porous, extended MOF structures, where the chromophores show distances $>$ 10 Å), the dipole-dipole coupling term becomes small, such as that excited state interactions in MOFs vanishes.

Besides ligand-ligand interactions, spectroscopic characterizations of MOFs and CPs as well as theoretical calculations reveal the existence of ligand-to-metal charge transfer interactions upon photoexcitation. This fact was shown to be dependent on the energy levels of the contributing orbitals of the ligand and the metal-oxo-clusters, which opens the possibility to specifically fine-tune the band-gap of these materials.[274, 275]

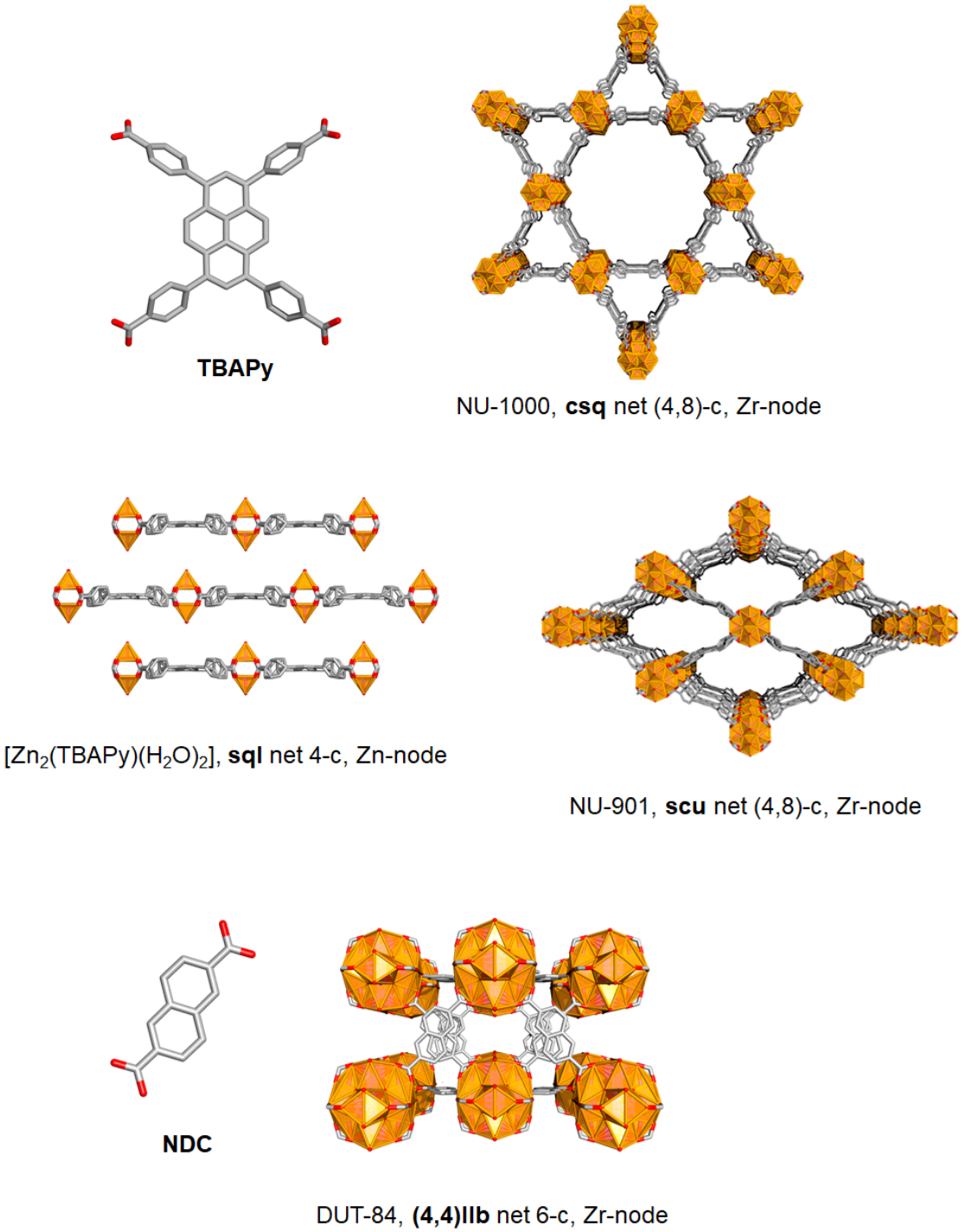

Figure 60. A selection of the investigated MOFs based on pyrene and naphthalene comprising MOFs (3D and 2D systems).

In summary, the simple idea of a single band-gap between valence and conduction bands, which is commonly used to describe the electronic structure situation of semiconductor materials, will fail to capture the complexity of electronic states in MOFs and CPs, due to the diverse chemistry of this material class, defined by the metal node, the organic ligand and the interface of the

organic and inorganic region. In reality, MOFs or CPs can thought of as having at least two band-gaps, corresponding to excitonic interactions (singlet Frenkel exciton band, triplet Frenkel exciton band, CT-exciton band etc.) and the inherent electronic band-gap formed of the electrons in the system (electronic bands), each of these bands having its own energy, bandwidth and photophysical properties.[130] However, it should be stated that the band diagrams of MOFs and CPs normally show flat electronic bands, due to weak electronic interactions (large effective masses for electrons and holes). Thus, the real physical situation in MOFs and CPs is better depicted by smaller aggregate-states with a limited number of interacting moieties (e.g. three interacting chromophores, or one ligand-cluster interaction), which are distributed over a single MOF crystal.

As MOFs and CPs are highly ordered materials the photoexcited exciton states hold the ability to diffuse over the material (exciton migration). This provides the basis for many useful properties (e.g. in photovoltaics). In the following chapter, I will give a short overview about exciton migration and energy transfer phenomena encountered in MOFs and CPs.

4.5.2 Energy transfer in MOFs

Light harvesting and energy transfer have a great potential for significantly enhancing the energy utilization efficiency, especially in photovoltaics. Studying these effects in crystalline hybrid scaffolds have advanced from a hypothetical to a developing area of research, within the last years. However, the current understanding of structural and mechanistic aspects of a directing ET process in a predesigned pathway is still rudimentary. Due to their tunability, versatility and modularity, MOFs and CPs represent an interesting platform to model and study energy transfer processes. MOFs have several advantages as model systems for energy transfer processes: (1) Systematic tuning of ligand design and/or synthetic conditions allow to render the photophysical properties (dimensionality and alignments of chromophores incorporated in MOF allow to tune the spectral overlap between acceptor and donor ligand). (2) The crystalline nature of MOFs allows for determining the distances between chromophore linker and the mutual chromophore alignment via structural

analysis techniques. This opens the possibilities to study long ET-ranges in detail. (3) As MOF synthesis is a self-assembly process it allows for a hierarchical self-organization of hundreds of chromophores found e.g. in the natural photosystem.[223, 276, 277]

In MOFs and CPs two main mechanism are discussed for energy transfer, which are based on Coulomb coupling or intermolecular orbital overlap interactions, the Förster resonance energy transfer (FRET) mechanism[278] and the Dexter mechanism.[279] In principle, exciton motion can be understood in terms of incoherent hopping between individual chromophores within the assembly. Förster was the first to treat resonance excitation transfer using a rigorous model from classical and quantum mechanical treatments of dipole-dipole interaction between donor and acceptor molecules in solution. The Förster transfer rate can be summarized as:[280]

$$k_{RET} = \frac{1}{\tau_0}\left(\frac{Q_D 3ln10}{64\pi^5 N_A n^4}\right)\left(\frac{1}{r^6}\right)\int_0^\infty F_D(\lambda)\,\lambda^4 d\lambda = \frac{1}{\tau_0}\left(\frac{R_0}{r}\right)^6 \qquad (4.35)$$

Where τ_0 is the fluorescence lifetime of the donor molecule in absence of an acceptor, Q_D is the donor quantum efficiency, N_A is the Avogadro's constant, n is the medium refractive index, r is the distance between donor and acceptor molecules, $\int_0^\infty F_D(\lambda)\,\lambda^4 d\lambda$ is the spectral overlap between the emission spectra of the donor and the absorption spectra of the acceptor molecule, which can be further summarized to the so-called Förster radius R_0. Based on this equation a diffusion constant for exciton migration on a lattice of chromophores can be derived as:[130]

$$D = \eta\left(\frac{4\pi C}{3}\right)^{\frac{4}{3}}\frac{{R_0}^6}{\tau_0} \qquad L_D = \sqrt{6D\tau_0} = \sqrt{6\eta}\left(\frac{4\pi C}{3}\right)^{\frac{2}{3}} R_0^3 \qquad (4.36)$$

With D is the diffusion constant, η is a pre-factor, accounting for the molecular details of the system (normally ranges between 0.32 and 0.56), C is the number density of the chromohores, and L_D is the diffusion lengths of the exciton. Equation 4.36 suggest that optimizing of certain system parameters (the Förster radius R_0, the number density C and the donor fluorescence lifetime τ_0) will increase the diffusion length of the exciton. Assuming reasonable values for these quantities (C = 1 molecule/nm^3, R_0 = 5 nm, τ_0 = 4 ns, r = 12 Å) gives a diffusion length of ~ 100 nm associated with an transfer rate of k_{RET} = 1.30 ps^{-1}. However, since most of the materials have way smaller diffusion lengths and greater transfer rates, the simple model by Förster breaks down (for MOFs diffusion lengths of ~ 40 nm and k_{RET} of ~ 50 ns^{-1} have been discussed).[252] The most obvious problem is that high chromophore densities open new ways for non-radiative decay pathways (low-energy nonradiative aggregate states act as traps). Furthermore, the simple dipole-dipole approximation used by Förster breaks down at small chromophore separations. It should be noted, (and has already been said before) that within the molecular exciton theory, exciton migration via resonance energy transfer between adjacent chromophores is a diffusive hopping process. It assumes weak excitonic coupling (weak-coupling limit), which is often found in semi-to-disordered systems (Förster-limit). In the strong coupling region, however, transfer of excitation energy will be happening in a more “wave-like” manner.[80]

A quantum mechanical treatment of energy transfer phenomena directly provides information about the distance and angle dependency of the donor and acceptor moieties, included in the energy transfer process. The interaction between donor and acceptor molecules (expecting that only two electrons are involved in the D-A transition) leads to a coupling matrix element U:

$$U = \langle \Psi_i | \hat{V} | \Psi_f \rangle \qquad (4.37)$$

Where Ψ_i and Ψ_f are the properly symmetrized ground-state and excited wavefunction, respectively, and $\hat{V}$ is the perturbation operator. The coupling matrix can be separated into two terms U_C and U_{ex}, where the former describes

coulomb coupling and the latter describes interactions due to electron exchange. Expanding the coulombic term into a sum of multipole-multipole interactions gives:

$$U_C = \frac{\overrightarrow{\mu_D} \circ \overrightarrow{\mu_A}}{r^3} - \frac{(\overrightarrow{\mu_A} \circ \vec{r})(\overrightarrow{\mu_D} \circ \vec{r})}{r^5} \tag{4.38}$$

Please note that the transition dipole moments are treated as vectors. Simplifying the scalar products gives:

$$U_C = 5.04 \frac{|\overrightarrow{\mu_D}||\overrightarrow{\mu_A}|}{r^3}(cos\theta_{DA} - 3cos\theta_D cos\theta_A) \tag{4.39}$$

On the contrary, for the exchange term U_{ex} one finds:

$$U_C = \left\langle \phi_D^*(1)\phi_A(2) \middle| \frac{e^2}{r_{12}} \middle| \phi_D(2)\phi_A^*(1) \right\rangle \tag{4.40}$$

Where e is the charge of an electron and the ϕ's depict the spin-function of the respective ground and excited state wavefunctions (they build as a linearcombination of donor and acceptor contribution). A rate equation can be accessed by incorporation of the above equations into *Fermi's* golden rule.

$$k_T = \frac{2\pi}{\hbar}|U|^2\rho \tag{4.41}$$

Here ρ denotes the density of the interacting ground and final states and is a related to the overlap integral $\int_0^\infty F_D(\lambda)\,\lambda^4 d\lambda$. In the case of long range energy

transfer ($r > 10$ Å) by dipole-dipole interaction, the final rate equation can be accessed by incorporation of equation 4.39 into 4.41.[281]

One immediately finds that the energy transfer rate is depending on the distance of the chromophores (power 6 dependency) and the mutual alignment of the donor and acceptor partners. However, in the case of low range interactions ($r < 10$ Å), electronic coupling needs to be taken into account. Inserting equation 4.40 into equation 4.41 and integrating over the spin coordinates gives a rate equation, initially described by Dexter.[279] In Dexter transfer processes the overall spin of the donor-acceptor pair is recovered. Furthermore, in case of optically forbidden acceptor excitations, dipole-dipole interactions may be negligible. Thus in triplet-triplet energy transfer processes, Dexter transfer will be dominant.[282] An important results is, that the rate of Dexter transfer processes decreases exponentially with the donor-acceptor separation (A transfer needs contact of donor-acceptor electron density, which decreases exponentially outside the boundaries).

$$k_T = \frac{2\pi}{h} K^2 e^{\left(\frac{-2r}{L}\right)} \rho \qquad (4.42)$$

With K is related to the electronic coupling and L is the sum of the van-der-Waals radii.

Energy transfer phenomena in porphyrinic MOFs have been extensively studied by Hupp et. al. They synthesized pillar-layered MOFs, incorporating BODIPY based dipyridine co-ligands as well as porphyrin ligands, so called BOB-MOFs. Upon excitation of the BODIPY co-ligands they encountered resonance energy transfer to the porphyrin moiety, measured as an emission signal depending on the type of BODIPY ligands.[250] They further expanded their studies to investigate the energy transport properties of porphyrin based MOFs, Zn_2(TCPB)(F-ZnP) and Zn_2(TCPB)(DA-ZnP), (TCPB = 1,2,4,5-tetrakis(4-carboxyphenyl)benzene, F-ZnP = = [5,15-di(4-pyridyl)-10,20-bis(pentafluorophenyl)porphinato]-zinc(II), DA-ZnP = [5,15-bis[(4-pyridyl)ethynyl]-10,20-diphenylporphinato]zinc(II)). These MOF adopt also a

pillar-layered MOF structure with the porphyrin derived ligands at the pillar positions. By using fluorescence quenching experiments and a Stern-Volmer analysis, they encountered exciton migration lengths of up to 60 nm. These studies further suggested that energy transfer in these types of MOFs is anisotropic, with intralayer rates being faster than interlayer rates.[283, 284] Hupp and co-workers expanded their work on porphyrin based SURMOFs, decorating the SURMOF thin-films with squaraine chromophores. Photophysical studies showed, that the porphyrin emission signal was completely quenched in a 50-cycle film, which suggest for very fast exciton migration over the porphyrin assembly.[285] Recently, the same group reported about a “MOF-like” film assemblage built from perylenediimide (PDI) and squaraine containing molecules. They synthesized a layer-by-layer assembly, following the absorption behavior of the single building molecules (from the blue to red) in a cascade manner. Excitation in the blue (PDI-Cl) followed in an almost complete transport of the formed exciton along the energy pathway to the squaraine ligand (for the smallest films: ~ 20 nm). They could show that aligned, multicomponent films can act as antenna-type light harvesters, with a directed transport pathway to an energetic sink.[285]

One of the first examples for metal-to-metal energy transfer was reported by Lin and Meyer in 2010. They synthesized a phosphorescent MOF, $Zn(L_M)\cdot 2DMF\cdot 4H_2O$, with L_M = $[M[4,4'\text{-}(HO_2C_2)\text{-}bpy]_2(2,2'\text{-}bpy)_2]$, M = Ru, Os. Upon photoexcitation, the materials showed a long lasting phosphorescence, approaching several hundreds of nanoseconds, due to the M^1LCT state of the L_{Ru} ligand (followed by ISC to a M^3LCT). Doping osmium to the ruthenium based MOFs followed in a strong quenching of the M^3LCT Ru excited state, indicative Ru-to-Ru excited state migration and a Ru-to-Os energy transfer. As Förster type transfers are forbidden in such systems, a site-by-site hopping mechanism based on Dexter transfer was initially proposed.[253, 276] Using a one-dimensional random-walk-model to describe the energy transfer map across the framework, revealed slower energy transfer rates than the one measured, suggesting cooperative or long-range effects. Further examples for triplet-triplet energy transfer in MOFs are given by Wöll et. al. They synthesized SURMOF type 2 thin-films incorporating a palladium-porphyrin ligand 5,15-bis(4-carboxyphenyl)-10,20-diphenylporphyrinato)palladium(II) and could show that

energy transfer processes follows a Dexter mechanism, with a transfer rate of 10^{10} s^{-1}. They further revealed that excitonic coupled chromophores (J-type aggregates) contribute significantly to the transfer rates and that the diffusion length is dominated by the domain size of the polycrystalline films.[248]

A detailed analysis of Förster energy transport in MOFs was conducted by Lin and Wang et. al. They synthesized two different MOFs, truMOF-1 and truMOF-2, built from truxene based ligands with different underlying topologies, which leads to differing mutual chromophore alignments in the structures. The exciton migration properties of these two MOFs were investigated by using coumarin as emission observer, which was incorporated into the MOFs at different doping levels. Thus photoexcited excitons migrate over the framework by ligand-to-ligand energy transfer until they meet a coumarin molecule, giving rise to coumarin centered photoluminescence. The ratios of the measured ligand photoluminescence lifetime and the coumarin photoluminescence lifetime served a sensitive measure of the exciton migration lifetime. The authors consequently found exciton diffusivities on truMOF-1 and truMOF-2 to be 1.8 x 10^{-2} cm^2/s and 2.3 x 10^{-2} cm^2/s with exciton diffusion length of 43 and 48 nm, respectively. Simulation of the energy transfer rates in these systems by using classical Förster theory in a random-walk-model with site-by-site interactions significantly underestimated the measured energy transfer rates. The authors further integrated beyond-nearest-neighbor interactions into their simulations and solved the kinetics by a master-equation ansatz. Regarding only nearest neighbor interactions in the fitting of the simulations underestimated the kinetics, however, incorporating jumping-beyond-nearest-neighbor interaction increased the diffusion lengths dramatically. They consequently found that beyond-nearest-neighbor jumping accounts for 67% of energy transfer rates in these systems.[252]

The authors expanded their works on singlet resonance energy transfer in MOFs and beyond-nearest-neighbor interactions by looking into the energy transfer properties of two MOFs based on hafnium oxo-cluster and a benzenetriyltrisethynenebenzoate based ligand as well as a nitro-substituted ligand variant acting as an energy trap. Lin and co-workers quantified resonance energy transfer in the 2D and 3D Hf-MOFs by quenching studies, but

also decomposed the single energy transfer contributions in these systems (exciton migration and donor-to-acceptor transfer). They showed that the lower dimensional 2D-MOF holds slower exciton migration with an overall lower energy transfer compared to the 3D-MOF. However, PL quenching experiments with an external emission quencher revealed that the excitons formed in the 2D-MOF can more easily be accessed from the surface, which is an important fact in the development of e.g. new photocatalyst or sensing devices.[286, 287]

4.6 Non-linear optics in MOFs

Non-linear optical effects occur upon exposure of materials to high intensity laser light and constitute a highly interesting photophysical behavior. As has already been stated, the term NLO describes the non-linear relationship between the dielectric polarization $\boldsymbol{P}$ of a material and the electric field $\boldsymbol{E}$ in an optical media. NLO is a cornerstone of emerging fields ranging from photonics and optoelectronics to biomedicine, with a main contribution of NLO in frequency modulation and photo-upconversion, e.g. NLO effects permit the use of bio-safe infrared-photons instead of higher energy ones.

NLO applications have significantly been studied in many material classes, among others a vast variety of dye molecules, organometallic dyes, organic polymers, organic semiconductor crystals, inorganic (nano)particles or inorganic semiconductors.[2, 7, 8, 288-290] Besides their intrinsic advantages, these materials, however, suffer from several practical problems. Organic and organometallic dyes, although showing sizeable NLO properties over a wide range of wavelengths, hold low photo -and thermal stability. Furthermore, since they are mostly used in diluted solutions the NLO response is limited by concentration quenching phenomena. On the other hand, inorganic materials (quantum dots, plasmonic particles, lanthanide doped nanoparticles etc.) show greater photostability, but are limited by factors such as insufficient performance, low wavelength tunability, toxicity and processability, to name only a few.[12]

CPs and MOFs consequently appear to be a highly promising material class for NLO applications, as they naturally combine advantages stemming from organic and inorganic building blocks, as well as a high degree of structural

tunability due to the underlying reticular chemistry concepts.[19] With respect to photophysical properties, the coordination of an organic chromophore to a metal often results in an enhanced response as non-radiative energy decay mechanism are suppressed (e.g. energy dissipation by rotation of phenyl rings). Furthermore, the choice of the secondary building units can influence the grade of ligand polarizability (electron deficient metals, differing metal oxidation states) and the nature of the underlying photo active states. The alignment of the organic building units within a CP has a profound influence on the nature of its excited state as intermolecular interactions between organic ligands can promote different types of interplays between the building units (excitonic interactions, charge-transfer interactions etc.) and therefore on its optical response. This fact is of highly interest, as CPs and MOFs constitute a unique possibility to control, or at least, influence (depending on the system) the assembly process during crystallization.[104] The crystalline character of MOFs furthermore allows for a detailed analysis of structure property relations upon the molecular interplays on NLO effects. It should be noted, that the influence of intermolecular interactions on the NLO response of condensed material is not well understood and investigations on such systems have only a few experimental realizations.[51] Finally, the potentially added planarization of the organic ligand when incorporated in a crystalline coordination network can lead to a more efficient charge localization over the organic scaffold during photo excitation. In other words, defining the molecular environment (surrounding molecules in the crystal lattice) can enhance the through-bond charge delocalization by enforcing planarity.[12]

To date, NLO studies on CPs and MOFs have mostly been focusing on second harmonic generation. Only a view number of explorations are looking into higher-order NLO effects, such as third-harmonic generation or MPA. This fact, among many others, nicely illustrates the need of a proper examination of the underlying higher-order non-linear photophysics of these hybrid material class. From a photo physical point of view, understanding of high-order NLO effects is of great importance for the tailored design of optically smart materials (OSMs).[2]

4.6.1 Second harmonic generation in MOFs

One of the most common NLO responses is second-harmonic generation (SHG). In SHG, an NLO material mediates a frequency doubling as two interacting photons are combined to form a new photon with twice the energy of the incoming photons. The SHG process can be described as a formal absorption of two photons followed by the emission of one photon, however, this process is not an emission process in the sense that the SHG mechanism is not dependent of the energy levels of the NLO active material (note that two-photon excited fluorescence is an incoherent process). In fact, the SHG process is a coherent process and proceeds via virtual states of the system (no energy levels are involved). The physical origin of SHG can be understood to a first approximation as an inharmonic deviation of atom centered electron clouds due to interaction with the passing light field.[3, 150, 152] SHG can be quantitatively described by the second-order non-linear optical susceptibility $\chi^{(2)}$, which is a third-rank tensor with 27 components.[3] The prerequisite for a material showing SHG intensity is an inequality of $\chi^{(2)}$ to zero. This condition is only achieved in anisotropic substances, which lack a center of inversion. Therefore, only crystals in non-centrosymmetric crystal classes can have non-vanishing $\chi^{(2)}$.[291] Furthermore, crystals in the non-centrosymmetric classes 422, 622 and 432 probably will show vanishing second-order NLO responses, due to structural symmetry as well as Kleinman's symmetry.[292] Important SHG active materials to date are KDP and DKDP (KH_2PO_4, KD_2PO_4), lithium niobate ($LiNbO_3$) or barium sodium niobate ($Ba_2NaNb_5O_{15}$).[293] These materials have already found widespread use in laser industry and optoelectronic devices. Several methods have been developed to determine absolute or relative $\chi^{(2)}$ values (parametric fluorescence, Raman scattering, Maker fringe method, etc.).[69] The Kurtz-Perry method allows to determine NLO properties of polycrystalline compounds in relation to a SHG standard (α-quartz, note SHG of $LiNbO_3$ ~ 600 x α-quartz) and is the standard technique for SHG characterization so far.[294]

SHG generation was one of the first function that was rationally designed on structural considerations in CPs and MOFs, as unlike in organic crystals or inorganic compounds, non-centrosymmetric structures can rationally be

synthesized with concepts of reticular chemistry, taking advantage of well-defined organic linker structures and metal nodes.[69]

There have different strategies been developed to access and refine the synthesis of non-centrosymmetric MOFs, among others (1) the breakage of inversions centers in diamondoid networks by using unsymmetric bridged ligands (e.g. *para*-pyridinecarboxylate and derivatives), (2) the reticular enhancement of unsymmetric ligands to access higher odd-numbered interpenetrated diamond networks, (3) the use of different metal nodes in the construction of a diamond net, (4) the targeted synthesis of 2D-CPs with **sql** topology and unsymmetric bridged ligands which gives the material the opportunity to crystallize in rhombohedral spacegroups and (5) MOFs built from achiral ligands. These strategies all have in common, that inversion symmetry is tried to circumvent, while enabling a rational assembly of the network.A comprehensive summary of work, coping with SHG effects in CPs and MOFs, is given by W. Lin and co-workers (summary to 2012)[69] as well as by A. V. Vinogradov and E. Hey-Hawkings et. al. (summary to 2016).[228]

4.6.2 MPA in MOFs

In the introduction chapter of non-linear optics, it has already been stated that NLO effects are a very important class of light-matter interactions and that the impact of non-linear optics on science is widely understood and accepted (at least by those in the field). In the following paragraph I will motivate NLO properties from the viewpoint of their impact on everyday life. These remarks are thought to create an understanding about the fact, why the synthesis, characterization and understanding of non-linear absorbing materials is important, initially outlined by Garmire.[4]

Generally, NLO provides benefits to some very important applications in commercial lasers, telecommunications, sensors, environmental monitoring, medicine, manufacturing and materials processing, military and scientific instrumentation. NLO has made possible a diversity of advanced lasers and coherent sources, has employed micromachining, offered high-resolution spectroscopy, new materials analysis tools and high-capacity telecommunications. For example, daily life without NLO would miss the high-

quality fiber-optics that power internet, technology that enables advanced medical devices, important laser-based tools for medicinal diagnosis, characterization of new materials, monitoring pollution in water and air…and green laser pointers. From this viewpoint, MPA contributes to effects such as saturable absorption, multi-photon filament formation, optical limiting and Q-switching, microfabrication, 3D-data storage, bioimaging and laser up-conversion.[8] Arguably, these applications having its greatest impact to science (but not exclusively), however, they also hold promise for possible technologies not yet to come. An example would be optical processing, were past effort has not led to practicality (meanwhile the future seems to be bright for quantum computing) and materials with optical limiting capabilities would be of high importance in this regard.[4] In general, the use of photons as chemical reagents in medicine or photovoltaics, as data deliverer in the fields of optical communication and imaging or as energy deliverer in machining and surgery is progressively increasing. In this regard, the control of luminous radiation has extremely important applications for modern and future technologies. Thus, control about the features of energy, intensity, direction of propagation and duration of the radiation is needed, and along with that opportune materials which enable to modulate the stated properties.[2]

In terms of MPA, the quantity to engineer is the MPA cross-section σ_M and the overall question is how to enhance the MPA response of optically smart systems. When it comes to applications of MPA such as bioimaging or biosensing, another crucial factor of merit is the MPA action cross-section, also called multi-photon brightness, the product of the quantum yield and the MPA cross-section, $\varphi\sigma_M$. It determines to what extend the absorbed laser light can be reemitted in an upconverted fashion.

Our group recently reviewed the field of MPA in MOFs. In the following part I will summarize these findings and further cover the missing parts from 2017-2019.

An early overview of TPA properties of CPs and MOFs revealed about 50 papers in a period of 2001-2016. These works mainly deal with low-dimensional (1D or 2D) CPs formed from rather small ligands (pyridine, aromatic acids, dicyanamide, amine etc.). Metals used to construct these CPs were Ag^{+}, Co^{2+},

Ni^{2+}, Cu^{2+}, Cu^{+}, Pb^{4+}, Mn^{2+} or Cu/W/S and Cu/Mo/S clusters. NLO characterization on these materials were conducted by measurements of third-order hyperpolarizabilities $\chi^{(3)}$ or non-linear absorption coefficients β with the help of degenerate-four-wave-mixing or Z-scan measurements. These data, however, are of limited value as the majority of the measurements were conducted in strongly coordinating solvents (DMF, DMSO, DMAc), which probably led to the dissolution of the CPs (please note that dispersion of CPs and MOFs in Z-scan determination of NLO quantities is not possible, due to excessive scattering). In principal, these studies did not answer the question of the chemical species present in the obtained solutions after solubilization procedure of the CPs (most likely oligomers of the CPs, free ligands and metal-ions). Furthermore, most of the measured values were obtained at single wavelength excitation, with the use of long-pulsed lasers. Such measurements are usually dominated by excited-state-absorption (ESA), which most probably interfered the NLO characterizations.[12]

The first multi-photon absorbing (2, 3, 4) metal-organic framework was reported by Vittal and co-workers in 2015. They synthesized a pillar-layer MOF structure of the form $[Zn_2(sdc)_2(An2Py)]$ (sdc = *trans, trans*-4,4'-stilbenedicarboxylicacid, An2Py = *trans, trans*-9,10-bis(4-pyridylethenyl)anthracene), where zinc-paddlewheel complexes are connected by the sdc ligands, which are further bridged by the An2Py ligands to from a 3D-framework structure. The ligand An2Py is a great exemplification of the above and below introduced design criteria for enhancing nonlinearity of MOF ligands. First, An2Py has a quadrupolar A-π-D-π-A structure (pyridyl groups serve as acceptors), secondly the ground-state of this molecule holds open-shell character, which is also transported to the MOF, as evidenced by EPR spectroscopy. They reported nonlinear absorption properties of the compound in form of two-, three-, and four-photon absorption action cross-sections using the multi-photon excited fluorescence method. The respective maxima were located at 800 nm ($\varphi\sigma_2$ = 7.2 GM) at 950 nm ($\varphi\sigma_3$ = 3.9 x 10^{-79} cm^6s^2) and at 1450 nm ($\varphi\sigma_4$ = 5.7 x 10^{-110} cm^8s^3). Furthermore, they incorporated naphthalene and perylene molecules into the MOF, which finally led to an enhancement MPA properties, which was attributed to the enhanced quantum yield of the compounds as well as the interaction of the guest molecules with

the framework via π-π^* stacking (elucidated by single-crystal Xray-diffraction analysis). The enhanced NLO response was explained in terms of Förster resonance energy transfer. By using the same compound, $[Zn_2(sdc)_2(An2Py)]$, Vittal and co-workers also investigated the coherent upconversion process of third-harmonic generation (THG). They showed, that the pillar-layered MOF, besides its multi-photon absorbing properties, is also suitable in THG, with signals peaking at 400 (1200 nm excitation), 433 (1300 nm excitation), 466 (1400 nm excitation), 500 (1500 nm excitation) and 533 nm (1600 nm excitation). They evaluated THG efficiencies in the form of an effective $\chi^{(3)}$ value (1.5 - 0.8 x 10^{-11} esu @ 1600 nm), three order of magnitude higher than α-quartz.[15, 17]

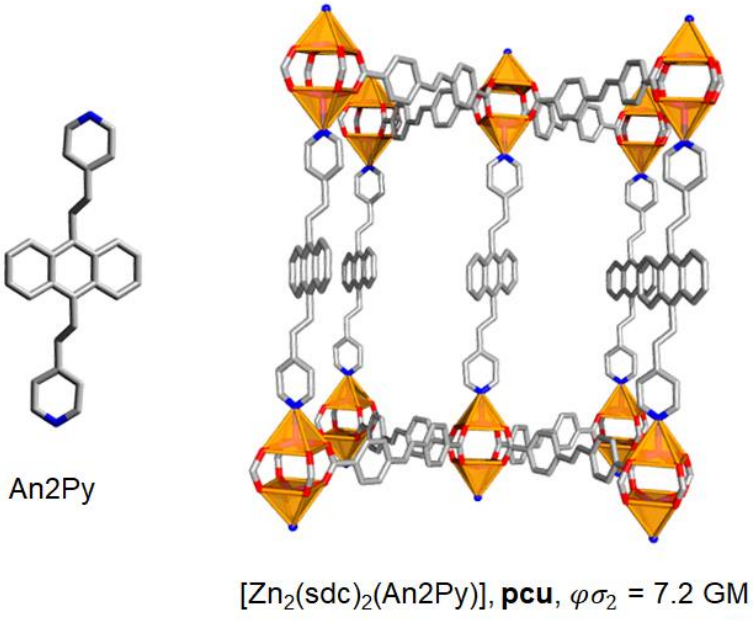

Figure 61. A section of the single crystal structure of $[Zn_2(sdc)_2(An2Py)]$ revealing its **pcu** topology. The left side shows the quadrupolar and open-shell donor-acceptor pillar An2Py.

Following their work, Vittal et. al recently published a 1D-CP constructed from An2Py and benzoic acid, $[Zn_2(benzoate)_4(An2Py)_2]$, which form a ladder-type CP, where the Zn^{2+} based SBU is formed of two zinc atoms coordinated by four benzoic acid groups to form a zinc dimer, which is further coordinated by two parallel aligned An2Py ligands. This compound crystallizes in the $P\bar{1}$ space group with Z=1. Interestingly, $[Zn_2(benzoate)_4(An2Py)_2]$ shows SHG, THG and MPA properties, with an effective $\chi^{(3)}$ value of 8 x 10^{-11} esu @ 1500 nm, an

second-order nonlinearity of d_{eff} of 6 pm V^{-1}, a two-photon cross-section of 890 GM @ 800 nm and a three-photon absorption cross-section of 3.1 x 10^{-78} cm^6s^2. Looking at the space group of $[Zn_2(benzoate)_4(An2Py)_2]$, one would assume that the material should not be SHG active, since it is centrosymmetric. However, the measured SHG signal was attributed to point defects associated with the benzoate ligands, which break the local centrosymmetry and thus give rise of SHG (exemplified by measurements of polarization dependent SHG efficiencies).[14] Note that a similar effect was earlier described for a structural similar MOF composed of Zn^{2+} ions, benzoate ligands and 4-styrilpyridine.[16] Furthermore, the authors showed that, by taken the excellent non-linear absorption properties of $[Zn_2(benzoate)_4(An2Py)_2]$ into account, the material is capable of two-photon pumped random lasing.[13]

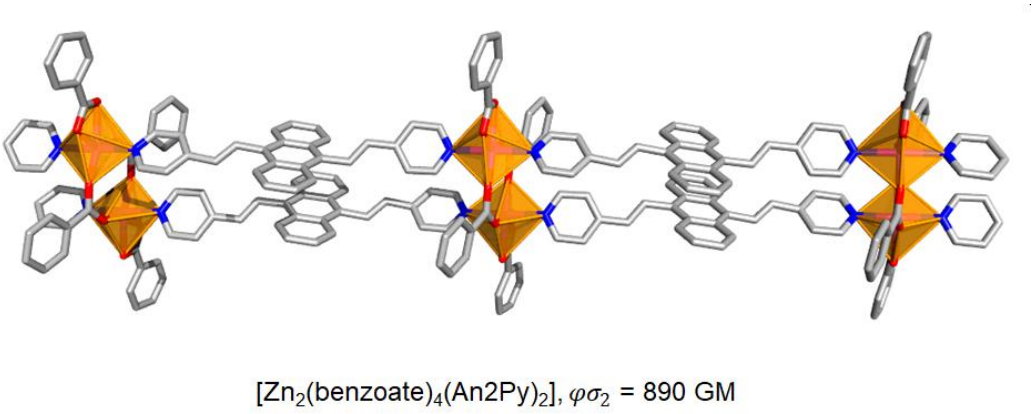

Figure 62. A section of the single crystal structure of $[Zn_2(benzoate)_4(An2Py)_2]$ showing the ladder type structure of the CP.

Based on their preliminary works, the group of Vittal and co-workers were the first to present a systematic study in which they gained to reveal the topological dependence of TPA on the MOF structure.[18] They synthesized and characterized a series of 9 MOFs composed of quadrupolar A-π-D-π-A linkers, using the same construction principle as in An2Py (pyridine groups as electron accepting groups, AnEPy = *trans, trans*-9,10-bis(4-pyridylethynyl)anthracene, BPEB = 1,4-bis[2-(4'-pyridyl)ethenyl]-benzene).

The reaction of these bipyridine pillar with Zn^{2+} salts and co-ligands (BDC = benzene dicarboxylic acid, BPDC = biphenyl dicarbocylic acid, BTC = benzene tricarboxylic acid, SDC = *trans, trans*-4,4'-stilbenedicarboxylicacid) gave the

following compounds: **1** = [Zn_2(SDC)(An2Py)], **2** = [Zn_2(BPDC)(An2Py)], **3** = [Zn_2(BDC)(An2Py)] (= An2Py block); **4** = [Zn_2(SDC)(AnEPy)], **5** = [Zn_2(BPDC)(AnEPy)], **6** = [Zn_2(BDC)(AnEPy)] (= AnEPy block); **7** = [Zn(BTC-H)(An2Py)], **8** = [Zn(BTC-H)(BPEP)] (=BTC block); **9** = [$ZnSiF_6$(An2Py)].

Structural analysis revealed a rich structural composition. Summarizing the findings, all compounds despite MOF **9** show pillar-layered MOF structures. Compounds **1**, **2**, **4** and **5** are isoreticular (**pcu** topology) and show the same grade of interpenetration (4-fold). Furthermore, they are composed of zinc paddle-wheel units, the respective organic acids and bipyridine pillars. The compounds **1** and **2** are isomorphous to **4**. Compounds **3** and **6** are structural analogues, with a **pcu** topology (isoreticular to **1**, **2**, **4** and **5**) and a two-fold interpenetration. They are composed of the respective organic acis, Zn^{2+} ions and a double-pillar structure (no classical paddle-wheel SBU). Compounds **7** and **8** are assembled with benzenetricarboxylic acid and show a similar structure. They are isoreticular (**hms** topology) and both are two-fold interpenetrated. The last compound, **9**, crystallizes in a tetragonal space group. Each Zn^{2+} ion is coordinated by four pillar-ligands in a square planar fashion. The so formed grids are further connected by the SiF_6^{2-} ions to form a 3D framework in **pcu** topology (two-fold interpenetrated).

The structural findings showed that by shortening the organic acid (from SDC to BDC), there is no change in the overall topology, packing and interpenetration (same trend for An2Py and AnEPy). When changing from a ditopic ligand motif to a tritopic ligand (BTC) the underlying toplogy **pcu** changed to **hms**, for both ligands An2Py and BPEP. Changing to an inorganic building unit (SiF_6^{2-} ion) the underlying packing motif changed from a pillar-layered structure to a structure comprised of single 6-coordinated Zn^{2+} ions, however, still holding a **pcu** topology. Compare figure 63 for an overview of the compounds.

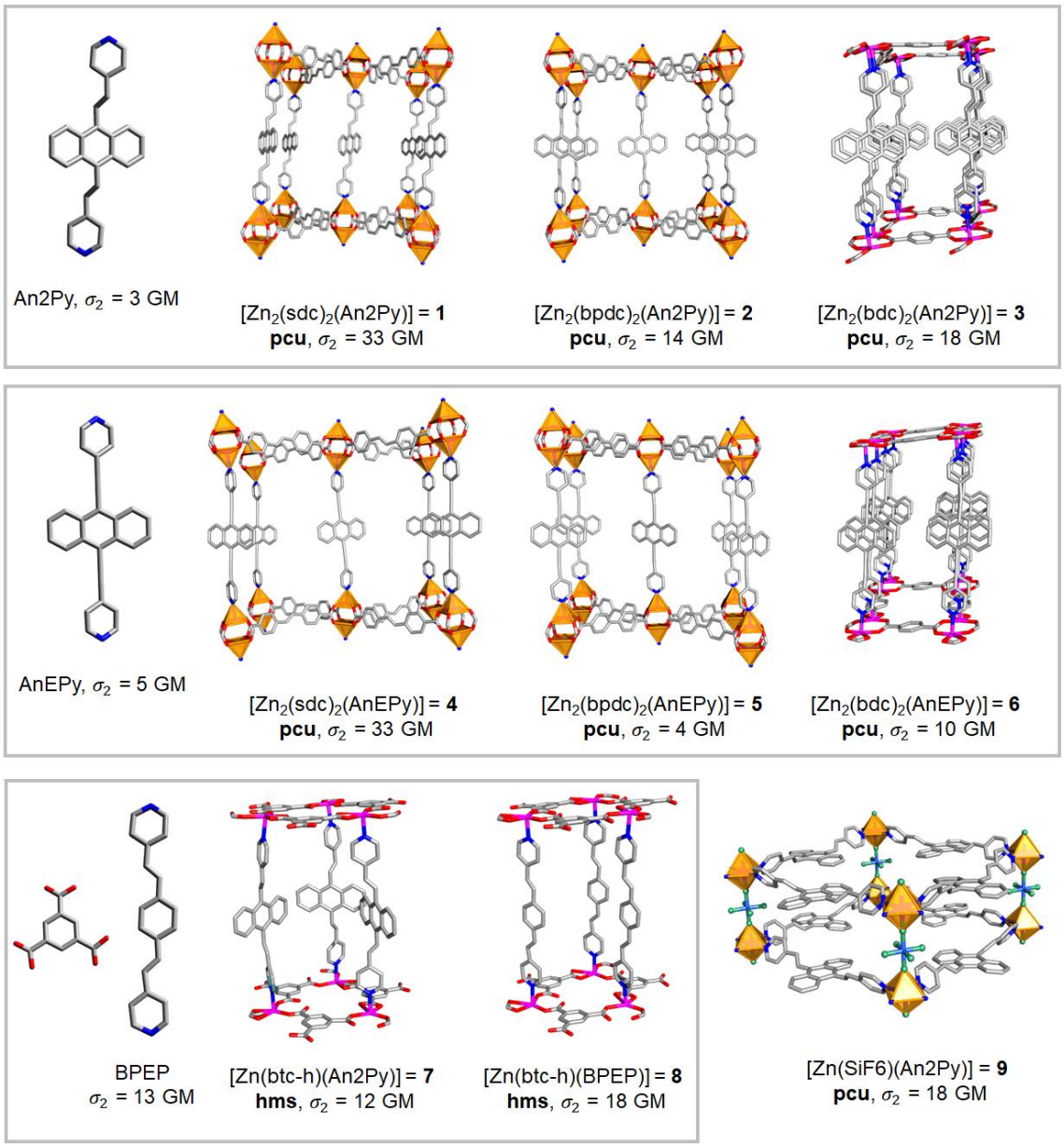

Figure 63. An overview of the pillar-layered MOF structures investigated towards their TPA properties by Vittal and co-workers. The picture shows the divers structures, their topology, TPA cross-sections and the structuring, two-photon active ligand. From top to down, An2Py based MOFs (**1**, **2**, **3**), AnEPy based MOFs (**4**, **5**, **6**) and the btc series (**7**, **8**) as well as the SiF_6^{2-} variant.

Based on the structural analysis and if the main contributing factor should be the underlying structure, one would expect that the TPA properties are dictated by structural trends. The TPA cross-section were measured at 800 nm excitation (no full spectrum) using the two-photon excited fluorescence method with perylene as internal standard. They revealed cross-section values σ_2 of: 33 (**1**), 14 (**2**), 18 (**3**), 4 (**4**), 7 (**5**), 10 (**6**), 12 (**7**), 18 (**8**), 18 (**9**), 3 (An2Py), 5 (AnEPy) and 13 (BPEP, Figure 63).

An analysis of the collected two-photon responses showed a trend, not at all affected by the underlying structures. Although MOFs **1** to **3** are isostructural to MOFs **4** to **6**, the σ_2 values showed not the same trend within one series, nor the cross-section values reflected the trend as found for the structuring ligands (σ_2 of An2Py < AnEPy and σ_2 of **1** to **3** > **4** to **6**). Furthermore, even though the MOFs **7** and **9** showed a different packing topology and interpenetration from MOFs **1** to **3**, this did not seem to affect the cross-section values in a significant manner. However, the measured σ_2 values for the MOFs **7** and **8** were shown to follow the trend of their structuring ligands. To sum up, structural aspects did not dictate the TPA behavior in this series of compounds, but rather effects from the different ligands caused by interpenetration and packing were shown to be critical in imbuing the measured values. In the end, the designed MOF series showed a couple of interplaying factors (conjugation degree of the ligands, ligand rotation within the framework, possible void space), which the authors did not allow to draw an detailed conclusion about structural influences on the TPA properties.

Our group (Fischer et. al.) started to work in the field of multi-photon absorbing MOFs with the synthesis and characterization of highly fluorescent MOFs based on aggregation-induced-emission dyes comprised of tetraphenylethylene (TPE) cores.[28] The reaction of H_4TCPE (= tetrakis[4-((4-carboxylato)phenyl)phenyl]ethylene) with indium and zinc salts gave two non-linear optically active, anionic MOFs, [Zn(HTCPE)](DMA) and [In(TCPE)](DMA] (DMA = dimethylammoniumcation, Figure 64). The non-linear absorption was measured in the form of two-photon action cross-section, $\varphi\sigma_2$, with record-high values of 3072 GM for [In(TCPE)](DMA) and 1053 GM for [Zn(HTCPE)](DMA) (excitation maxima at 800 nm). The presence of the AIE active chromophore linker, its coordination to the metal nodes, alongside with the relatively strong and dense packing arrangement of the framework structure, was discussed for the strong enhancement of the non-linear absorption compared to the sole ligand (H_4TCPE: 55 GM @ 800 nm). [In(TCPE)](DMA) was shown to be vulnerable against external forces such as solvent removal upon activation or grinding. Amorphization by grinding and subsequent analysis of the TPA properties revealed a drop in the cross-section values to 1111 GM, which supported the argument that in the pristine material the high non-linear

response is due to the specific arrangement and ordering of the TCPE molecules.

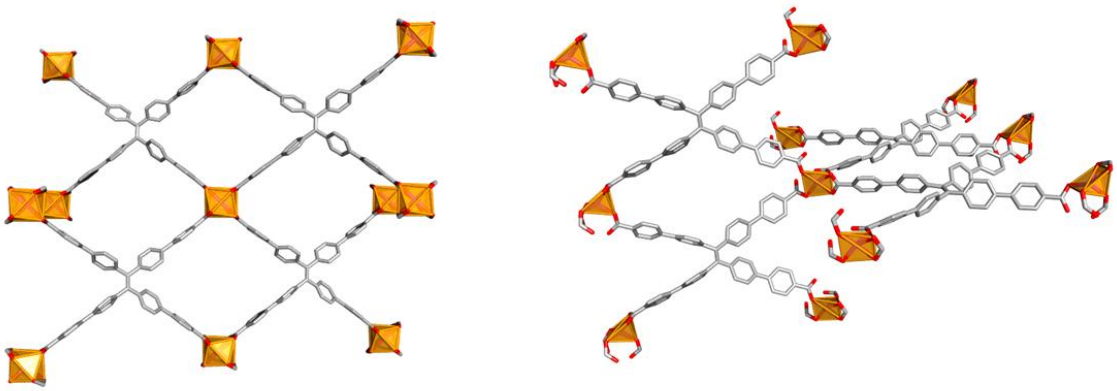

[In(TCPE)](DMA)], $\varphi\sigma_2$ = 3072 GM [Zn(HTCPE)](DMA)], $\varphi\sigma_2$ = 1053 GM

Figure 64. A section of the crystal structure of [In(TCPE)](DMA) (left) and [Zn(HTCPE)](DMA) (right).

Based on our findings of record high TPA action cross-sections of MOFs comprised of AIE dyes, we conducted a follow-up study. In this investigation, we synthesized 6 MOFs based on H_4TCPE and zirconium- and hafnium-oxo clusters, PCN-128, PCN-94, PCN-128-Hf, PCN-94-Hf.[19] The materials were systematically designed to decrease the parameter space for a detailed analysis of potentially structure-property relations in multi-photon absorbing MOFs. Firstly, we used no co-ligands, only H_4TCPE as a framework structuring unit. Thus, comparing measured $\varphi\sigma_2$ between the different structures will not be affected by other molecules, as the building blocks used to assemble the MOFs are similar. Secondly, PCN-94 and PCN-128 are representatives, where the crystal structure, respectively the orientation and alignment of chromophoric ligands follow the highest-symmetry embedding of the underlying topology (PCN-94 crystalllizes in the *P*m$\bar{3}$m space group with an underlying **ftw** topology; Symmetry of **ftw** is *P*m$\bar{3}$m; PCN-128 crystallizes in the *P*6/mmm space group with an underlying **csq** topology; Symmetry of **sql** is *P*6/mmm). Thirdly, we used a post-synthetic exchange reaction (PSE) to replace trifluoroacetic acid (TFA) molecules by OH-groups, which coordinate to the metal-oxo cluster during synthesis (TFA is used as a modulator). By doing so, we could

specifically tune the electron-withdrawing capacities of the metal-oxo clusters and consequently the ligand electron density.

Summing up, the measured TPA cross-sections $\varphi\sigma_2$ amount to: 1035 GM (PCN-94), 292 GM (PCN-94-Hf), 3582 GM (PCN-128^{TFA}), 2590 GM (PCN-128), 1984 GM (PCN-128-Hf^{TFA}), 1823 GM (PCN-128-Hf) and 55 GM (H_4TCPE). Three-photon absorption action-cross-sections were measured as: 131, 60, 1495, 931, 443, 168 x 10^{-80} cm^6s^2 (for PCN-94, PCN-94-Hf, PCN-128^{TFA}, PCN-128, PCN-128-Hf^{TFA} and PCN-128-Hf). Four-photon absorption action cross-sections were determined as: 109, 70, 400, 235, 120, 38 x 10^{-110} cm^6s^2 (for PCN-94, PCN-94-Hf, PCN-128^{TFA}, PCN-128, PCN-128-Hf^{TFA} and PCN-128-Hf).

The data impressively showed a very clear trend (consistently for all $\varphi\sigma_n, n =$ 2,3,4), such as that the cubic MOFs throughout hold the lowest non-linear absorption compared to the hexagonal counterparts. Furthermore, the TFA modified MOF variants showed the higher values compared to the OH-variants, in accordance with theoretical concepts. This trend appeared for both material classes, the zirconium -and hafnium-based variants. Intensive electronic structure calculations on the level of DFT and TD-DFT were used to calculate TPA tensors of the TCPE molecule (neutral as well as positively charged $TCPE^+$ to mimic the enhanced electron polarization of the TFA variants), as a function of ligand distortion. The calculations could reproduce the trend of the non-linear characterizations and revealed that indeed the higher grade of ligand distortion in PCN-128, the greater ligand electron polarization in the TFA variants of the MOFs and the enhancement of the unit-cell TPA tensor elements in PCN-128, are responsible for the found TPA increase in the hexagonal MOFs compared to the cubic variant.

By using a MOF class, which structurally followed the topological restraints, (no interpenetration, high symmetry), the study could demonstrate that there might be evidence of a structure-property relation in MPA. The results further revealed that the non-linear response might be controllable by topological guidelines.

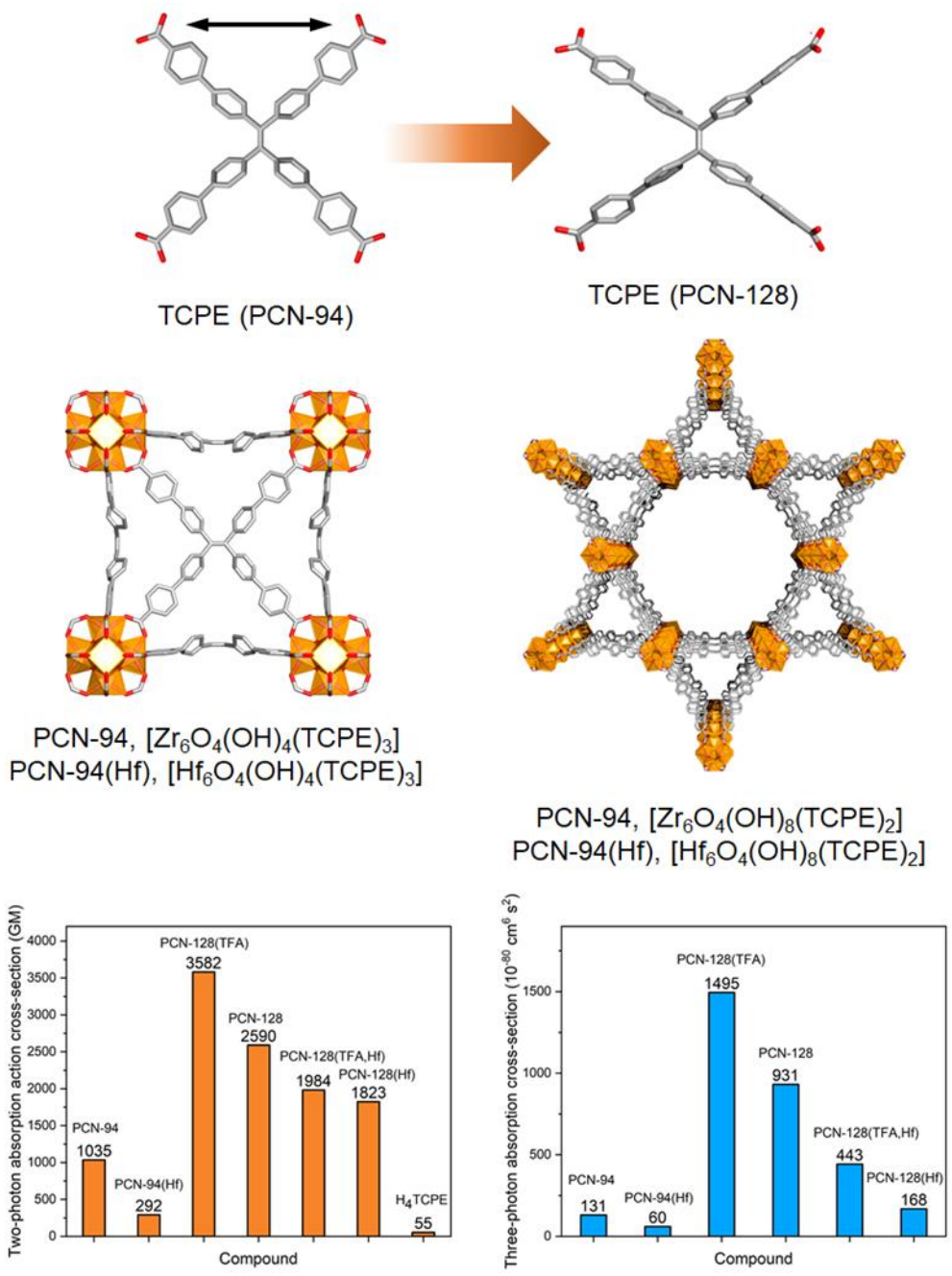

Figure 65. The local TCPE conformation in the MOFs PCN-94 and PCN-128, demonstrating the ligand distortion upon incorporation into the framework structures (top). A section of the crystal structures of PCN-94 and PCN-128 (middle). The TPA action cross-section values and the three-photon absorption cross-section values of the investigated series of MOFs revealing the higher values for the hexagonal structures.

The work of MPA in TCPE based Zr-MOFs was taken further by the group of Su and Pan et. al., which synthesized five MOFs, PCN-94, PCN-128, LIFM-66, LIFM-114, LIFM-223, and measured there two -and three photon excited fluorescence as a function of external stimuli.[295] The presented MOFs are all

composed of TCPE and zirconium-oxo-clusters besides LIFM-66, which used 5'-(4-carboxyphenyl)-[1,1':3',1''-terphenyl]-4,4''-dicarboxylic acid (named BTB in the paper) as a co-ligand. The MOFs possess different underlying topology, due to possibility of the zirconium-oxo-cluster as an SBU to tolerate different connectivities. Accordingly, PCN-94 (**ftw,** 12-c node), PCN-128 (**sqc**, 8-c node), LIFM-66 (not defined in the paper), LIFM-114 (**scu**, 8-c node, 2-fold interpenetrated), LIFM-223 (**shp,** 12-c node). Single-photon analysis of the MOFs revealed a pressure-induced red-shift in the emission maxima for all compounds, compared between the pristine and pressed materials.

It is a well-known fact, that the flexible ligand TCPE can be subject of deformation upon external pressure and thus MOFs incorporating TCPE as a ligand can undergo pressure-induced phase transitions. For PCN-128, such a phase transitions was described by Zhou et. al. as a reduction of the c-axis, leading to an overall squeezing of the MOF along its hexagonal channels. This new phase formed upon pressuring and staid stable when the external pressure stimuli was released (as demonstrated by extensive Pawley fitting and Rietveld refinement of synchrotron PXRD data of the pressed PCN-128 structure, PCN-128-p).[296]

Based on their single-photon characterization, Su and Pan et. al. claimed a similar mechanism for the other compounds (PCN-94, LIFM-66, LIFM-114, and LIFM-223). Non-linear absorption of the pristine and pressed MOF samples were measured in the form of TPA action cross-section in a range from 780 to 950 nm ($\varphi\sigma_2$ @ 780 nm in GM, pristine/pressed): 266/453 (PCN-94), 153/1897 (PCN-128), 31/229 (LIFM-66), 210/2177 (LIFM-114), 1383/2200 (LIFM-223). The collected non-linear absorption throughout showed higher values for the potentially pressure-induced transformed MOF structures. It should be noted that the not fully solved issue of a detailed structure analysis (the authors present Le Bail fits of low quality and claim a reduction of the c-axis) of the pressured MOF samples (What exactly happens to the MOFs PCN-94, LIFM-66, LIFM-114, LIFM-223 after pressing and returning it to the external pressure again?) leads to MPA values of rather limited value. However, the presented structures and its pressed variants point towards the fact, that indeed and alongside with our results, the local structure distortion of the TCPE moiety

inside the MOFs seems to hold a supporting influence on the non-linear response of this material class.

The non-linear absorption properties of zeolithic imidazolate frameworks, ZIFs, were first characterized by Samoć et. al.[297] Based on work bei van der Veen and co-workers,[298] which showed the two-photon excited fluorescence properties of ZIF-8 nano -and microparticles, Samoć and co-workers used femtosecond Z-scan measurements to reveal the TPA cross-section of ZIF-8 nanoparticle (in suspension) to be lower than 18 GM (@550 nm). Introduction of Co^{2+} ions into the ZIF-8 structure (up to doping levels of 50 %) gave a hybrid material formerly rooted between ZIF-8 and ZIF-67. The very strong linear d-d transition of the tetrahedrally coordinated Co^{2+} ion did not, however, translate into the non-linear regime ($\sigma_2 < 9$ GM @ 950 nm). The authors justified the low TPA cross-section values in ZIF-8 and similar compound to the lack of a charge transfer process within the framework (small π-electron system of the 2-methylimidazole).

They further investigated the non-linear response of Prussian-blue nanoparticles as suspension in D_2O. Z-scan studies revealed a strong three-photon absorption response in the 1350 - 1750 nm region, owing to the strong metal-to-metal charge transfer process of Prussian-blue ($\sigma_3 = 4.5 \times 10^{-78}$ cm^6s^2 @ 1375 nm). Looking into the origin of the measured signal, the authors conducted degenerated pump-probe spectroscopy of the non-linear absorption, which revealed that the observed three-photon absorption is cascade process of TPA followed by ESA.[299]

Very recently the group around Samoć presented that Gd-CPs constructed from the 1,3,5-benzenetricarboxylic acid, $Gd(NO_3)_3$ and phenanthroline doped with certain levels of Tb^{3+} or Eu^{2+} are capable of a three-photon absorption induced thermoresponse. They introduced three-photon absorption as an interesting process to realize NIR-to-Vis thermometry using CPs constructed from suitable building blocks to be used in biological thermometry. With the presented CPs and their developed method, the authors were able to access a sensitivity of 2.91% K^{-1}.[300]

A comprehensive analysis of the published literature of MPA shows some conformities in the data. However, it is of great importance to state, that the

insufficient data situation (small number of studies, uncertainties in the material characterization and differences in the collections of non-linear optical data), does not allow to compare the collected MPA characteristics to each other. Thus, drawing general conclusions so far is not possible here. Nevertheless, (1) all published studies showed an enhancement of the MPA response of the CPs/MOFs compared to their structuring ligands, (2) CPs/MOFs constructed from ligands structured according to push-pull design criteria show an higher MPA response than MOFs with small, molecular building units (3) ligands with AIE characteristics have a superior influence on the multi-photon brightness and (4) the changes in the local ligand geometry (sterically as well as electronically) have a profound influence on the non-linear absorption characteristics.

4.6.3 Ligand design concepts for MPA in MOFs

In the theory part of MPA, I already stated that over the last years a great deal of effort has been expended in the search of design principles for high multi-photon active chromophores. It could be shown that the dimensionality of the charge-transfer network, its length of conjugation and grade of planarity, and the strength and places of donor-acceptor groups are of fundamental importance (on a microscopic level) to enhance the MPA response of an organic molecule.[7] Low lying charge transfer states, giving rise to charge separation upon photoexcitation are therefore crucial factors. This fact led to the development of organic push-pull molecules, which could be categorized according to the number of electron donating and accepting groups and the shape and number of connections among them.[54] Considering the last two points, multi-photon active molecules are classified into different groups: dipolar push-pull chromophores (A-π-D), quadrupolar push-push or pull-pull chromophores (A-π-A, D-π-D), quadrupolar push-pull chromophores (A-π-D-π-A, D-π-A-π-D) or octupolar systems, respectively, branched systems.[51] It could be shown that the highest MPA response originates from quadrupolar push-pull chromophores or octupolar and branched systems. Consequently, the ligand design of MPA active MOF ligands should focus on quadrupolar or branched push-pull systems. The principles of MOF synthesis, however, generate some restraints to typically used building blocks in the assembly of MPA

chromophores. For example, strong withdrawing groups (-NO_2, -SO_2R, -SO_2CF_3) show low coordination abilities. The nitrile group (-CN), extensively used as electron accepting moiety can undergo hydrolysis under hydrothermal conditions, etc. By far, the most utilized ligand groups in the construction of MOFs is the carboxylic acid group (other oxygen-based linkers in use are the phosphonic and sulfonic acid groups), followed by N-heterocyclic groups (pyridines, imidazoles, pyrazoles, triazoles). These groups are electron withdrawing and consequently the majority of MOF ligands can be classified as A-π-A types.[12] They consequently lack an electron donating group, which has been stated as the prerequisite for large MPA activity. On the contrary, the presence of electron donating groups in MOF ligands is much less common. However, many MOF ligands possess extended polarizable π-electron cores (anthracene, perylene, pyrene), which could be prospective in accordance with push-pull design principles introduced above. Furthermore, it should be stated that the need of big and extended π-electron systems[7] (scales with the dimensionality of the charge-network) is an inherent contradiction to the need of rather small and rigid building units for MOF synthesis.[301] Thus, there will be a natural limitation of ligand size and shape given by the ability for incorporation in a framework compound. Also, one should distinguish, if the coordinating unit in the construction of a MOF (e.g. carboxylic or the pyridine group) is part of the push-pull system, meaning that the acceptor group in an A-π-D-π-A designed ligand is simultaneously coordinating to the metal node, or that the coordinating unit is not part of the push-pull system and only acting as a “hook” for the position of the ligand in the network, like in a D-π-A-π-D arrangement (this becomes important in the influence of the metal node).

Now the question arises, how in the frame of the push-pull design principles a systematic approach for the synthesis of MPA MOF ligands can be accessed? In the light of the above explanations, an A-π-D-π-A or D-π-A-π-D arrangements should be the choice. Firstly, due the superior MPA activity compared to other types of push-pull chromophores. Secondly, because the donating groups in an MOF ligand are normally located in the periphery of the ligand and most of the donating groups hold electron accepting properties (carboxylic or pyridinic groups are electron withdrawing). Thirdly, an A-π-D-π-A or D-π-A-π-D

arrangement should enable the synthesis of ligand molecules, which are suitable in size and shape to be incorporated in a framework compound.

The assembly of appropriate molecular building blocks according to the building block scheme of the push-pull arrangement with suitable acceptor and donor moieties under the restraints of MOF practicability, gives access to MPA active MOF ligands.[54, 155] Interesting molecular building blocks can be accessed by literature screening. Note that the presented ansatz would give rise for an extensive computer screening approach, which could be helpful in the finding of MPA ligands (calculation of MPA descriptors such as the TPA cross-section or the second-order non-linear hyperpolarizability as a function of the molecular structure).

Valuable accepting building blocks obviously seems to be carboxylic and pyridine groups as well as pyrazoles, triazoles, imidazoles, as sulfonyldibenzene, dibenzothiophene-dioxide, squaraine, benzothiazolium or triazines. Appropriate donor building blocks would be triphenyl amines derived compounds, moieties based on carbazoles, phenoxazines, phenothiazines and acridines. Suitable π-systems for bridging the acceptor and donor units are phenyl bridges, vinylene linkages or ethylene bridges. These building blocks form a pool, which can be used to generate different MPA active MOF ligands. Furthermore, by including topological restraints in form of intended ligand connectivities (e.g. 2-c, 3-c, 4-c etc.) or ligand geometries, one can design ligand motifs to be used in a reverse-topological-approach for MOF synthesis.

An overview of meaningful building units for the assembly of push-pull ligands under considerations of suitable MOF synthesis and an example for ligand formation gives figure 66 and table 6. The presented building units have been collected by a literature screening of push-pull ligands and two-photon active molecules.

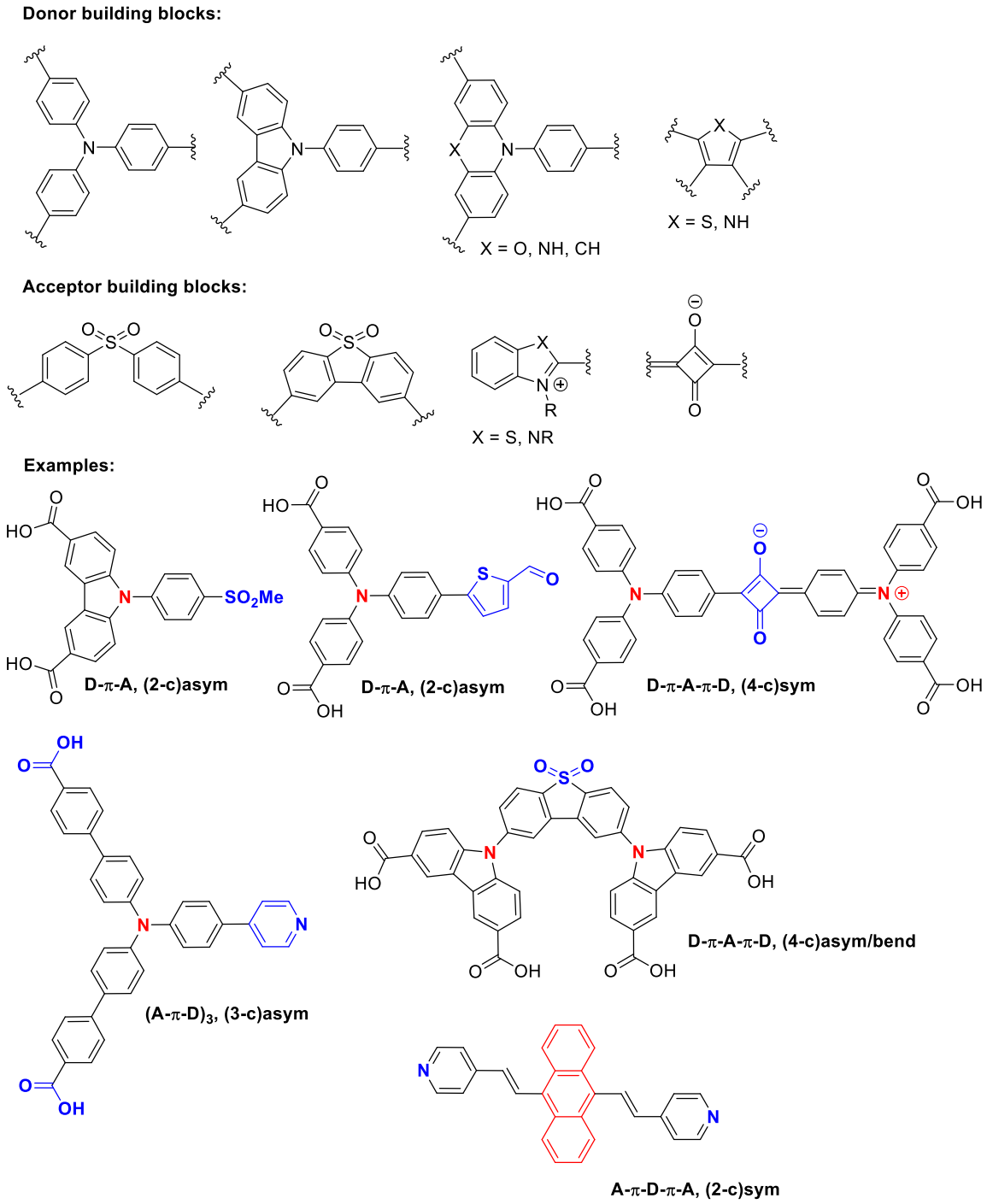

Figure 66. A summary of interesting building units for the development of push-pull chromophores under considerations of MOF synthesis (blue: acceptor group, red: donor group). The examples reveal the different levels of complexity. First, the choice of donor and acceptor types. Second, the grade of connectivity (here are (2-c), (3-c) and (4-c) ligands shown). Third, the geometry of the ligand and its symmetry (symmetric, asymmetric, linear, bend). Fourth, the acceptor/donor groups forming the charge transfer network as coordinating unit to the metal or as only anchoring parts (e.g. compare the carbazole based D-π-A-π-D chromophores with the anthracene based pillar-ligand). Fifth, the differences in the donor/acceptor arrangements (ditopic D-π-A, quadrupolar D-π-A-π-D or A-π-D-π-A, branched systems $(A-\pi-D)_3$).

Table 6. Electronic properties of selected donor and acceptor substituents used as A/D parts in push-pull chromophores and their respective Hammett (σ^i) and Pytela (σ_p) constants. The presented data rationalize, why most MOF ligands can be regarded as A-π-A type chromophores (compare the values of COOH and pyridine-4-yl). Furthermore, the given values of NHPh or NPh_2 show, why these building units are perfect candidates for design of MPA-MOF ligands.

Acceptor			**Donor**		
Subst.	σ_p	σ^i	**Subst.**	σ_p	σ^i
NO_2	0.78	0.606	NMe_2	-0.83	0.089
CN	0.66	0.525	NHMe	-0.70	0.094
CHO	0.42	0.385	NH_2	-0.66	0.089
COMe	0.50	0.286	NHPh	-0.56	-
COPh	0.43	-	NPh_2	-0.22	-
COOH	0.45	0.264	OH	-0.37	0.157
COOMe	0.45	0.274	OMe	-0.27	0.220
CF_3	0.54	0.372	OPh	-0.03	0.278
$COCF_3$	0.80	-	SMe	0.00	0.217
C_6F_5	0.27	-	2-Thienyl	0.05	-
SO_2Me	0.72	0.551	Fc	-0.18	-
SO_2CN	1.26	-			
SO_2CF_3	0.96	-			
SF_5	0.68	-			
Pyridin-4-yl	0.44	-			
Benzooxazol-2-yl	0.33	-			
Benzothiazol-2-yl	0.29	-			

4.6.4 Considerations in SBU choice for MPA-MOFs

The choice of metal nodes for the assembly of multi-photon absorbing MOFs is mainly influencing two areas, structure chemistry and photophysics. Regarding the first point, the choice of the used metal is affecting the coordination number of the metal-node, the formed coordination geometry and thus the underlying topology of the framework. For accessing different structure types, different connectivity combinations of the ligand and the SBU are essential, or rather, if one wants to target a specific topology the metal node has to provide the connectivity needed.[173]

In this regard, zirconium and hafnium-oxo-clusters has been proven to show a rich structure chemistry in the synthesis of MOFs, as they potentially can provide coordination numbers ranging from 6-12 (4,6,8,12).[102] Zinc and cadmium have tetrahedral or pseudotetrahedral coordination extensions and they can also form clusters with various coordination ligands leading to the

formation of 1D to 3D MOFs (e.g. zinc paddle-wheel complexes or basic zinc carboxylate).[69] Main group metals such as indium or lead have already been used in the construction of non-linear optical active MOFs. Indium specifically is of interest here, as it tends to form so-called ROD MOFs.[180] In such MOFs the metal node is an infinitely strand of metal-oxo clusters connected via one or more sharing oxygen atoms. This fact often leads to a low chromophore distance, which could trigger strong intermolecular interactions between the chromophoric ligands. Earth alkali metals, such as magnesium, calcium or strontium are also very interesting in this regard, as these materials tend to stabilize high coordination numbers and thus preferentially form extended oxo-clusters during MOF synthesis, often leading to interesting structure motifs.[302]

From the optical point of view, the role of the metal ions is rather not to provide a MPA response by themselves, as d-d transition show very low MPA cross-section values, but they act as modifiers for the ligand electron density.[12] As it is known from classical coordination chemistry, absorption characteristics of metal-ligand systems are not the sum of the individual components, but owing to the formation of coordination bonds, energy levels of the ligands and metal ions mixing. In the case of transition metals, for example, d-p orbital mixing is oven overriding d-d selection rules, given rise of intense LMCT or MLCT transitions. These charge transfer states or simple the polarization of ligand electron density due to electron push/pull effects of the metal can render high NLO responses. To avoid optical losses and to simplify data collection, the material should be transparent in the regarded working frequency range (~ 200-1400 nm), thus often d^0, d^5 and d^{10} transition metals are used in the construction of MPA-MOFs, such as Zn^{2+}, Cd^{2+}, Zr^{4+}, Hf^{4+} or Mn^{2+}. Further metals or metal combinations found are Ag^{+}, Co^{2+}, Ni^{2+}, Cu^{2+}, Cu^{+}, Pb^{4+}, Cu^{+}/W^{6+}, Cu^{+}/Mo^{6+}. Apart from the above considerations, another value of metal centers can arise from additional functionalities they bring. From the viewpoint of optical properties are luminescence effects of heavy transition metals, with accessible triplet states via spin-orbit coupling or f-f transitions of lanthanides. Another aspect could be the use of metals with unpaired d-electrons to impart redox, magnetic and magneto-optical properties. Such functionalities in MOFs have already been recognized and are a valid on their own, however, conjugation of these effects with NLO excitation still remains to be realized.

4.6.5 MPA theory in MOFs

In principle, the mechanisms of MPA in MOFs are poorly understood, as this area is a relatively young field of research. Interestingly, this fact accounts not only for CPs and related compounds, but also for a general understanding of non-linear absorption in condensed materials (organic crystals or molecular aggregates; So far, there is no coherent theory describing the TPA properties of periodic systems in three dimensions).[303] Investigations of such systems have only a few experimentally realizations,[304] which arises from the complexity of non-linear optical characterizations of solid-state systems (compare the last part of the following chapter) and the design of the respective experiments. It should be noted, that NLO effects are not strongly pronounced by nature (depending on the regarded system) and consequently the measured responses are highly depending on the experimental treatment. Theoretical considerations of TPA in excitonic coupled aggregates predict a strong non-linear optical response promoted by the large oscillator strengths of few excited states.[51] These effects, for example, were experimentally investigated by Z-scan measurements on J-aggregates of porphyrin chromophores,[305-307] however, up to now only a few investigations have been devoted to understand how intermolecular investigations influence the MPA behavior.

Regarding what has been introduced in the theoretical background part and the general photophysics part of MOFs and CPs, the MPA properties of this material class can best be described by either the semi-classical theory of non-linear optics or by an excited state theory in the framework of exciton theory. These theories enable the deviation of preliminary principles for an understanding of MPA in MOFs. The semi-classical theory of NLO can give an insight into structure-property relations of MPA in MOFs and thus potential topological control, as this theory contains geometrical transformations of single-molecule properties according to the underlying symmetry constrains of the structure. Seminal work in this direction has been conducted by Seidler and Champagne[308, 309] or by Macchi and co-workers.[310] In general, if a crystal can be partitioned into building blocks, the crystal tensor quantity may be approximated as:

$$Y_{cryst} = \sum_{i} R_i Y_{BB} R_i^T \qquad (4.43)$$

Where Y_{cryst} is the crystal quantity, Y_{BB} is the molecular quantity of the respective building block and R_i is the rotation matrix according to the symmetry operation i when the building block coincide with the asymmetric unit (our group used a similar ansatz for the calculation of TPA tensor elements of the MOFs PCN-94 and PCN-128).[19] For optical properties, molecular descriptors could be polarizabilities, hyperpolarizabilites or MPA tensor elements. A simple summation of building blocks properties calculated in isolation leads to the so-called oriented gas model, which does not account for any intermolecular interactions. There are approaches to recover such interactions, for example a cluster approach as introduced by Bishop and Champagne.[311] The underlying theory of equation 4.43 may allow to work out the influences of the geometrical transformations as dictated by the topological structure on the non-linear response and could give a first idea about potential topological control of MPA. The theory may further constitute a first basis for rationalizing the intricate interplay between molecular properties and the symmetry transformation of charge distribution in the unit cell as the governing effects of topological dependency in the higher NLO properties.

Exciton theory in the frame of state interaction as introduced by Kasha connected with essential-state models constitute a more direct approach to understand the effects of intermolecular interaction between chromophoric ligands on the MPA behavior of CPs or MOFs. Considering the excited state properties of CPs, the photophysics are mainly determined by aggregate-states of small clusters within the MOF crystal comprising of a low number of participating molecules. The cluster-approach opens the opportunity to model the photo-response of the system on different levels. Within the exciton theory, for example, the knowledge of the exact adjustment of chromophore ligands inside the MOF (assuming nearest neighbor interaction) from structure analysis together with the knowledge of the location of the coupling transition dipole moments (from TD-DFT calculations or polarization dependent absorption spectroscopy) gives access to exciton coupling elements.[83] Furthermore, using

electronic structure calculations suitable for computational demanding systems (e.g. TD-DFT) in conjunction with well-established tools for the analysis of excited states of aggregates opens the feasibility to study the photophysics in greater detail (influence of the metal node, exciton size and localization, etc.). This knowledge can help to draw a more general picture of the excited state situation of the investigated materials and the results of such calculations can be used to parametrize essential-state-models giving access to e.g. TPA spectra. Such examinations have already been conducted on squaraine and curcumin based aggregates by Sissa et. al.,[50] which showed that the TPA property of the theoretical investigated aggregates can be enhanced by a face-to-face or a brickwork alignment (as found in traditional J-type aggregates), alongside with seminal work by Spano and Mukamel,[52, 129] Collini[51] or Isborn[312] and co-workers. However, it should be stressed that these results are not providing evidence for rationalizing structure-property relationships in MPA of MOFs or CPs. Nevertheless, the theoretical considerations show that for specific chromophore alignments, the MPA response can be enhanced and such orientations can be generated in MOFs. Consequently, when intermolecular effects are anticipated as an underlying mechanism for MPA enhancement, rather densely packed framework compounds should be anticipated (chromophore distances $<$ 10 Å, no co-planar chromophore alignment, preferentially head-to-tail, ladder or brickwork orientations).

Cooperative enhancement effects are described by size-scaling laws. Depending on the respective non-linear optical experiment, the size-enhancement of TPA has been shown to scale with a $\sim N^2$ behavior, which is directly related to the two-exciton transition. TPA in the one-exciton band will lead to a linear scaling of the cross-section with approximately $\sim(N+1)$ behavior (compare the chapter about size-scaling part in MPA above). Such laws can give a first insight into the existence of potential excitonic effects in the measured non-linear response. The complete N dependency of the TPA properties in coupled aggregates will result from a combination of enhanced transition dipole moments, superradiant damping rates, homogeneous dephasing rates and laser detuning and must be analyzed for every experiment.[51] However, taken these things into account a scaling behavior of up

to $\sim N^6$ is theoretically predictive. This fact enlightens the enormous potential of self-assembled systems in improvement of TPA systems.

To sum up, the structural complexity and tailorability of CPs allows for the impartment of intermolecular phenomena on the structure, which can contribute to the overall non-linear optical response. Excitonic effects can play an important effect, however, nature and magnitude of the underlying effects needs to be analyzed for every experiment separately. A clear structural design principle for the integration of intermolecular interactions in MOFs or CPs at the present point, however, cannot be derived based on the actual data situation. There is a strong need to expand experimentally and theoretical studies on the higher-order non-linear optical properties of CPs.

4.6.6 Measurement techniques for MPA in MOFs

The two main techniques for MPA cross-sections MOFs and CPs are known as Z-scan and multi-photon excited fluorescence (MPEF). The Z-scan technique is currently one of the most widely used techniques for the characterization of third order non-linear properties (non-linear absorption and non-linear refraction), due to its relative simplicity and the broad variety of information, one can extract from these measurements.[313] In this technique a sample is moved along the axis of a focused laser beam (z-axis). Consequently, the sample experiences a gradual increase in the intensity up to the focal point (z = 0), and subsequently a decrease in intensity when it leaves that region. Essentially, in such measurements very high laser intensities are needed (50 – 250 GW/cm^2). Intensity caused changes of the real part of the refractive index, results in lensing properties of the sample (when the real part of n is positive, the sample will behave as an focusing lens and vice versa). Now, measuring sample induced changes in the beam profile as a change in the intensity of transmitted light by putting an aperture before the detector (closed-aperture Z-scan technique = CA Z-scan), give rise of the characterization of non-linear refraction of the sample. When a beam splitter is put between the moving sample and the aperture (open-aperture Z-scan technique = OA Z-scan), changes in the measured light absorbance are attributed to the non-linear absorption (the decrease of transmittance in an open-aperture Z-scan trace is

diagnostic for non-linear absorption). The amplitudes or the shapes of CA or OA Z-scan signals can be used to quantify the magnitudes of non-linear refraction and absorption.[12] However, this requires the exact knowledge of the light intensity, meaning the laser pulse shape and the beam profile. Alternatively, one can carry out measurements in a relative manner, using well characterized references. The analysis of Z-scan traces is done by a fitting-procedure derived by Sheikh-Bahae et. al.[313] This yields the non-linear absorption coefficient β which can be used by regarding the density of absorbers (e.g. the concentration of a sample) to calculate σ_2. Results of Z-scan measurements can be influenced by factors such as molecular reorientation, non-linear scattering, nonlinearities by local heating of the sample and excited state absorption. The optimal laser sources provides pulses on the femto-second lifetime with low repetition rate, with the latter ensuring that all excited states have been relaxed to the ground state before another photon is arriving and that heat is dispersed.[314] From the point of view of non-linear optical characterizations of CPs and MOFs, there is a limitation for the need of non-scattering samples. The great majority of MOFs are obtained in the form of insoluble polycrystalline powders and dispersions of such materials would mostly yield turbid samples. Additionally, sedimentation would lead to a change in the degree of scattering and local concentration with time. Consequently, Z-scan techniques are most suitable for CPs and MOFs that can be accessed in the form of nanoparticles, giving rise of non-scattering nanoparticle dispersions.[12, 297, 299] This accounts in general for other techniques which are based on measurements of transmission (e.g. transient absorption etc.).

The second experiment most widely used for the determination of MPA cross-section values, is the multi-photon excited fluorescence technique (MPEF), which was initially introduced by Xu and Webb.[315] Typically, such measurements are carried out in a relative way. In the considered wavelength range at every point the measured MPEF signal is compared with a reference for which the wavelength dependence of the cross-

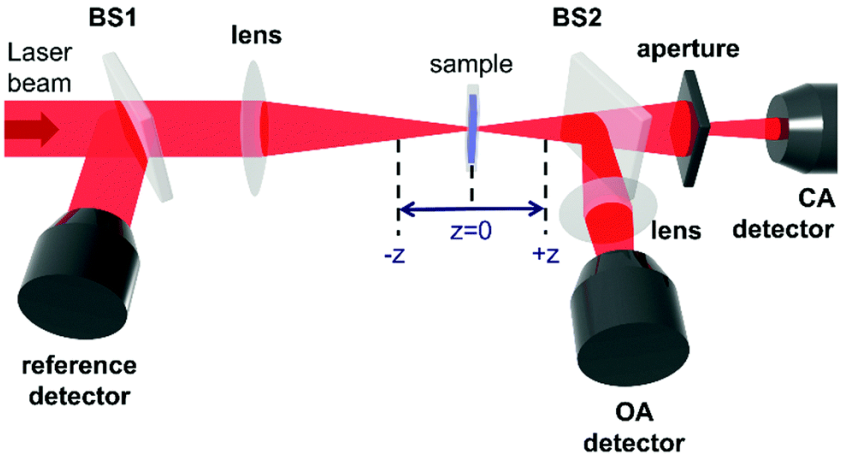

Figure 67. Experimental setup of a typical Z-scan experiment.

section is precisely known (there are numbers for standard dyes for e.g. σ_2 values in the whole Vis-NIR range by Makarov et. al.).[316]

Regarding a two-photon excited fluorescence process (TPEF), the intensity is given by the following equation:

$$A_{TPEF} = cI^2n^2\sigma_2\varphi F_{col} \tag{4.44}$$

With A_{TPEF} the integral area of the emission peak, I^2 the squared intensity of the laser beam, c the concentration of the two-photon absorber, n the refractive index of the medium, φ the quantum yield of the absorber and F_{col} a phenomenological factor, which accounts for setup related parameters (optical path, sensitivity of the collector, apertures, collection angles, light scattering processes etc.). In the standard TPEF procedure (diluted samples with an optical density of $\leq$ 0.1), the σ_2 is calculated from the ratios of fluorescence intensities:

$$\frac{A_{TPEF}^{sam}}{A_{TPEF}^{ref}} \rightarrow \sigma_{2(sam)} = \frac{A_{sam}c_{ref}\sigma_{2(ref)}\varphi_{ref}}{A_{ref}c_{sam}\varphi_{sam}} \tag{4.45}$$

Assuming similar experimental conditions and the same solvents for reference and sample the collection factor, the refractive index and the intensity of the laser radiation are cancelled.[315] In the case of CPs and MOFs, the above presented procedure of simple comparing TPEF signals is influenced by the fact, that the collection factor F_{col} can be significantly different between the reference and the regard framework material. However, modifications of the standard MPEF methods can help to circumvent the issue of e.g. scattering.

The internal-standard MPEF method (ISMPEF) comprises of measuring the multi-photon excited emission of a CP or a MOF suspended in a solution of a MP standard dye (e.g. Rhodamine B). Since the emission signal of both, the CP and the solution experience a similar degree of scattering under such conditions, it can be assumed that the collection factor term F_{col} cancels out. However, the fact that for the deviation of the signals a deconvolution procedure has to be applied and the possible presence of the laser excitation spectrum in the measured fluorescence spectrum (especially for excitation wavelengths close to the emission of the sample or reference) bring additionally uncertainty in the measured cross-section values. Furthermore, the characterized MOF material should be stable in the used solvents.[12, 19]

The MPA cross-sections of CPs and MOFs can also be determined on solid samples (solid-state multi-photon excited fluorescence = SSMPEF). In this technique, the MPEF signal is obtained via laser radiation of microcrystalline samples of a CP and a solid multi-photon standard (in the case of SSTPEF e.g. crystalline perylene). Concerns regarding F_{col} involve differences in the grain sizes of the regarded compounds as well as in the refractive indexes of the standard and the CP. A step towards an alleviation of these problems is to sieve the samples into the same particle size range (as routinely been done in SHG measurements). In the SSMPEF method, equation 4.45 needs to be modified (for TPA).

$$\sigma_{2(sam)} = \frac{A_{sam} d_{ref} \sigma_{2(ref)} \varphi_{ref} M_{sam} n_{ref}^2}{A_{ref} d_{sam} \varphi_{sam} M_{ref} n_{sam}^2} \qquad (4.46)$$

Where d is the crystal density, M is the molar mass of the molecular weight of the formula unit (or other repeating units) and n is the refractive index. The concentration c as occurring in equations 4.44 and 4.45 are interpreted as the ratio of the crystal density and the molar mass of a repeating unit, $\frac{d}{M}$. Equation 4.46 needs some remarks. Firstly, the crystal density as an output of a single crystal structure analysis is defined as the product of the number of atoms in the unit cell and their corresponding molar mass, divided by the unit-cell volume and the Avogadro constant. It should be noted that the number of atoms in the unit cell will change, when disordered solvent molecules are removed by the SQUEEZE routine. Since this is often done by default in the crystal structure analysis of CPs and MOFs,[114] the crystal density values in crystallographic information files will be affected by data post processing. Secondly, the refractive indexes of the CPs/MOFs and the used reference compounds are assumed to lay in the same ranges (most studies concerning the determination of refractive indexes of MOFs show values of about $\sim$ 1.5).[94, 317, 318] Consequently, the quantities will be cancelled out and not further regarded. The SSMPEF method is particular useful for CPs, which decompose in solvents and are therefore not accessible by the ISMPEF method. An essential drawback of this method is the fact, the great majority of cross-section numbers of reference substances have been determined in solutions, as well as the underlying approximations of equation 4.46.

Finally, experimental challenges in the non-linear optical characterization of CPs and MOFs (the same accounts also for optical characterizations of solid state materials in general), will have a couple of issues, which should be considered. These issues evolve around the chemical composition of the sample, distinguishing between effects arising from the intrinsic (excitonic) properties of the sample or from macroscopic optical properties, or aspects when analyzing laser experiments.[130]

Regarding aspects of chemical composition in solid-state samples, the effect of an impurity can be amplified due to its ability to react with neighboring molecules. Furthermore, defects which influence the long-range order of an assembly will influence the coupling between adjacent molecules and consequently affect the size and propagation of excited states. The main

problem with CPs and MOFs here is found in the fact, that these compounds crystallize during the synthesis procedure and therefore by nature are prone for the incorporation of defective sides (missing linker and node defects).[319] Due to that reason, CPs and MOFs escape of post-synthetic purification procedures. An important point is, that the type of required sample purity is depending on the quantity being measured. The emission lifetime of a singlet exciton lays in the nanosecond range, consequently the exciton will not have enough time to explore a large region of the sample before it decays.

The second issue is to distinguish between microscopic properties of the sample and optical properties that arise from the macroscopic sample. For example, most single crystals are absorbing so much light that simple transmission measurements become almost impossible. In emission measurements, one must account for self-absorption, waveguiding from total internal reflections, stimulated back scattering, depolarization due to crystal birefringence or non-linear cascading effects.

A last aspect, when working with laser radiation, is the formation of a high density of excitons. This enhances the probability that two of such states meet during a diffusion process and consequently annihilate (exciton-exciton annihilating). This type of interaction can produce a rapid decay. Since in non-linear optical characterizations, high fluence levels are commonly used, such phenomena are very probable and consequently, the non-linear response should be measured over a wider range of laser-powers (changes at least in one order of magnitude).

5 Experimental section

5.1 General materials and methods

All chemicals were purchased from commercial suppliers (Sigma-Aldrich, ABCR, Acros, Tokyo Chemical Industry and others) and used without further purification. Common organic solvents such as *n*-hexane, toluene, tetrahydrofurane, diethyl ether and so on, were dried using a MBraun solvent purification system (SPS), in which solvents were passed through consecutive filter columns containing suitable adsorbents by application of argon pressure gradients. All other solvents were dried using standard purification procedures e.g. by passing through a column of activated alumina under inert atmosphere or by using suitable activated molecular sieves. Such treated solvents exhibit a purity above 99 % and water contents below 5 ppm, as verified by Karl-Fischer titration. Solvents were degassed by freeze-pump-thaw cycles and subsequent saturation of argon. Deuterated solvents for NMR spectroscopy were dried above activated molecular sieves.

Manipulation of air and moisture-sensitive compounds was performed under an atmosphere of purified argon using conventional Schlenk and glovebox techniques. All glassware was flame dried in vacuum prior to usage, where needed. Air and moisture sensitive chemicals were stored in a glovebox. MOF synthesis was carried out in 5 cm standard short glass thread vial with a maximum volume of 4 mL with polypropylene caps and Teflon inlays. Further, for higher volumes, glass scintillation vials (maxima 20 mL volume) equipped with open top caps and Teflon septa were used. All MOF reactions were conducted in standard laboratory ovens equipped with a programmable heating unit (Memmert UN55).

5.1.1 Nuclear magnetic resonance (NMR) spectroscopy

Standard NMR spectroscopic measurements were performed on a Bruker Advance III AV400 US spectrometer operating at the appropriate frequencies. Variable temperature NMR experiments were conducted on a Bruker DRX400

spectrometer. ^{13}C-NMR measurements were conducted in fully proton decoupled modes. All spectra are referenced relative to the residual solvent signals (^{1}H: DMSO-d_6 2.50 ppm, DMF-d_7 2.74/2.91/8.02 ppm, $CDCl_3$ 7.26 ppm, D_2O 4.79 ppm; ^{13}C: DMSO-d_6 39.52 ppm, DMF-d_7 30.01/35.2/162.5 ppm, $CDCl_3$ 77.16 ppm). Organic samples were measured in DMSO-d_6, DMF-d_7 and CD_3Cl. Furthermore, digested MOFs were measured in DCl/D_2O/DMSO-d_6 mixtures. The spectra were processed and analyzed using the MestreNova (Mestrelab Research S. L.) software, version 9.0.1.

Solid state NMR spectroscopic characterizations were conducted in ZrO_2 rotors (2.5 mm probehead, spinning frequency of 30 kHz) using a Bruker Advance 300 spectrometer operating at the appropriate frequency range. ^{13}C spectra were recorded using the cross-polarization/magic angle spinning (CPMAS) technique. Spectra were referenced to the external standard adamantane (^{13}C: 29.47 ppm).

In the following chemical shifts are given in ppm (parts per million) and consecutively denoted as position, relative integral, multiplicity, coupling constant (in Hz) and assignment. Multiplicities are abbreviates as s = singlet, d = doublet, t = triplet, sept = septet and m = multiplet.

5.1.2 Infrared spectroscopy (IR)

IR spectra were measured on a Bruker Alpha FT-IR and a Frontier FT-IR spectrometer with an attenuated total reflection (ATR) geometry, using a diamond ATR unit under argon and on air. Spectral data were processed with the supplier software and further analyzed using OriginPro 8 (OriginLab Corporation). Absorption bands are consecutively reported as position (wavenumber in cm^{-1}) and relative bands (vs = very strong, s = strong, m = medium, w = weak).

5.1.3 Raman spectroscopy

Raman spectra were collected on a Renishaw inVia Raman Microscope at an excitation wavelength of 785 nm in scan range from 0 to 3200 cm^{-1} on powdered samples on air. For activated samples, the materials were filled in a

capillary in a glovebox and subsequently fused under argon atmosphere. Spectral data were processed with the supplier software and further analyzed using OriginPro 8 (OriginLab Corporation). Absorption bands are consecutively reported as position (wavenumber in cm^{-1}) and relative bands (vs = very strong, s = strong, m = medium, w = weak).

5.1.4 Mass spectrometry

Mass spectrometric measurements were performed on a Thermo Scientific LCQ/Fleet spectrometer by Thermo Fisher Scientific equipped with an ESI ionization source. Spectrometric data was analyzed using the supplier software and MS results are given in m/z.

5.1.5 Elemental analysis

Elemental analysis was performed at the Micranalytical Laboratory of the Technical University, Germany on a HEKAtech Euro EA CHNSO-Analyzer.

5.1.6 Thermogravimetric analysis (TGA)

TGA measurements were performed on a TGA/DSC device from Mettler Toledo Stare Default DB V.14.00 at a heating rate of 10 K min^{-1} in a temperature range from 30 – 1200 °C at ambient pressure and synthetic air (gas flow 25 mL min^{-1}, samples masses of approx.. 5 mg). Activated samples were prepared in aluminum oxide crucibles in a glovebox.

5.1.7 Power X-ray diffraction (PXRD)

PXRD patterns were recorded on a PANalytical Empyrean equipped with an X-ray generator (Cu-K_α1 radiation, λ = 1.54056 Å) and a one-dimensional PIXCel^{1D} strip detector or a STOE Stadi P diffractometer equipped with a Ge(111) monochromator (Cu-K_α1 radiation, λ = 1.54056 Å) equipped with a Dectris MYTHEN DCS 1K solid-state detector. Measurements were conducted in Bragg-Brentano geometry ($\theta - \theta$ mode) or in Debye-Scherrer geometry in 2θ ranges from 5° - 50° or 2° - 50°, respectively 2° - 90°. Grinded powders were

either packed in capillaries (ϕ = 0.5 mm) or put on a silicon flatbed sample holder. Samples of dried and activated materials were packed in a glovebox under Ar atmosphere in capillaries. Silicon was employed as external standard. Patterns were normalized to the highest intensity reflection. Indexation, cell parameter refinement and Rietveld refinement have been performed with TOPAS 6 (Bruker, academic version).

5.1.8 Single-crystal X-ray diffraction (SCXRD)

Single crystal X-ray diffraction data for all compounds were collected on a Bruker X-ray single crystal diffractometer equipped with a CMOS detector (Bruker Photon-100) a TXS rotating anode (Mo-K_α1 radiation, λ = 0.71073 Å) and a Helios mirror optic. Diffraction data was acquired and processes with the APEX-III program package. In a routine experiment, suitable single crystals for SCXRD were collected under a microscope using a microsampler and perfluoropolyether and subsequently mounted in a cooled nitrogen stream (100 $\pm$ 5 K) on the diffractometer. Lattice parameters were determined with initial matrix scans. Reflections were merged and corrected for Lorenz and polarization effects, as well as background using SAINT. Absorption correction was performed with SADABS. Structures were solved by intrinsic phasing using SHELXS[320] and refined against F^2 on all data by full-matrix least squares with SHELXL[321] in conjunction with SHELXLE. Disordering of phenyl rings in most structures was accounted by several restraints during the refinement process. Highly disorder solvent molecules were treated with the SQUEEZE routine of the Platon program package.[41] Compare the following sections for detailed crystallographic descriptions at each compound.

5.1.9 Sorption measurements

N_2 and CO_2 sorption measurements were performed on outgassed samples (120 °C for minimum 12 h *in vacuo*, sample mass between 20 and 100 mg) using a 3Flex Physisorption Instrument from Micromeritics Instrument Corp. The latter uses the volumetric method to determine the amount of adsorbed gas and an equilibrated gas pressure. All samples were further activated on a SmartVacPrep sample preparation station after initial activation on a standard

Schlenk line. Dead volume of sample tubes was determined prior to adsorption measurements using He. Purity of the used gases was at 99.999 vol%. The sample cells were cooled with a liquid nitrogen bath (77 K) or an iso-propanol/dry ice bath (195 K). Adsorption data were processed using the 3Flex Software Version 5.01 of Micromeritics Instrument Corp.

5.1.10 Scanning electron microscopy (SEM)

SEM images are obtained with a Jeol JSM - 7500F field emission scanning electron microscope in Gentle Beam mode. Pictures are analyzed with the supplier software.

5.1.11 UV-Vis spectroscopy

UV-Vis spectra were recorded on a Cary 60 UV-Vis spectrophotometer from Agilent in differing organic solvents at a range from 800 to 200 nm in quartz cuvettes. The concentration of the respective solutions showed a concentration of roughly 0.01 mmol/L. The reflection spectra of solid materials were measured on a SHIMADZU UV-3600 plus UV-Vis-NIR spectrophotometer equipped with a $BaSO_4$ coated integrating sphere detector. Samples were put between two quartz glass slides for measurements. Spectral data were processed with the supplier software and further analyzed using OriginPro 8 (OriginLab Corporation).

5.1.12 PL and PLE spectroscopy

Photoluminescence (PL) and photoluminescence excitation (PLE) spectra for $[Zn_2(TPBD)(DMAc)_2]$ and $[Cd_2(TPBD)(H_2O)_4]$ were recorded with a Horiba Jobin Yvon Fluorolog-3 FL3-22 spectrometer equipped with a water-cooled Horiba R928 photomultiplier tube mounted at 90° angle. A monochromated 450 W Xe-lamp was used for excitation. The signals were corrected for the spectral sensitivity of the detector and divided by the corrected excitation intensity. PL, PLE and emission lifetime measurements for H_4TPBD were collected on a spectrofluorometer from FS5 from Edinburgh Instruments. PL spectra for compounds $[Zn_2(TCPE)(bpy)]$, $[Zn_2(TCPE\text{-}F)(bpy)]$,

[Zn_2(TCPE)(bpy)]-contr, [Zn_2(TCPE-F)(bpy)]-contr, H_4TCPE and H_4TCPE-F were collected with a fiber-coupled Ocean Optics 2000 CCD spectrograph, upon excitation with a picosecond 377 nm laser diode (BDL-377-SMC). The integration time of one-photon fluorescence spectra was set from 2,000 ms to 5,000 ms. Solution samples were measured in a quartz cuvette. Solid samples were deposited on quartz glass slides for characterization.

5.1.13 Spectrally-resolved time-correlated single photon counting emission lifetime measurements

Emission lifetime measurements (TCSPC measurements) for [Zn_2(TCPE)(bpy)], [Zn_2(TCPE-F)(bpy)], [Zn_2(TCPE)(bpy)]-contr, [Zn_2(TCPE-F)(bpy)]-contr, H_4TCPE and H_4TCPE-F were performed using a Becker & Hickl system that includes a TCSPC module (SPC-130-EM), a hybrid PMT detector (HPM-100-06) with detector control card (DCC 100) mounted on a Princeton Instruments Spectrograph (Acton SpectraPro-2300i), and excitation was delivered by a picosecond 377 nm laser diode (BDL-377-SMC).

5.1.14 Non-linear optical characterization

TPA characterization was conducted by the solid-state two-photon excited fluorescence method (SSTPEF, compare the theoretical background section for detailed description of the method). For the compounds [Zn_2(TPBD)$(DMAc)_2$] and [Cd_2(TPBD)$(H_2O)_4$] TPEF measurements were conducted at room-temperature using a 800 nm femtosecond pulsed laser with a pulse width of 100 fs and a repetition rate of 1kHz (Coherent Inc.). The excitation laser was directed into the solid samples deposited on quartz glass substrates, while the PL was collected at different excitation intensities in the backward direction of the laser beam. Integration time of the signals ranged from 5 s to 60 s. The signal was collected using a fiber-coupled CCD spectrometer and processed with the supplier software. Analysis of the data was performed by OriginPro 8 (OriginLab Corporation).

The compounds [Zn_2(TCPE)(bpy)], [Zn_2(TCPE-F)(bpy)], [Zn_2(TCPE)(bpy)]-contr, [Zn_2(TCPE-F)(bpy)]-contr, H_4TCPE and H_4TCPE-F were studied with the

use of a laser system consisting of a Quantronix Integra-C regenerative amplifier operator as an 800 nm pump and a Quatronix-Palitra-FS BIBO crystal-based OPA. The system delivers wavelength tunable pulses of roughly 130 fs length and operates at a repetition rate of 1kHz. The output from the femtosecond optical parameter amplifier is tunable in the range of 460 nm to 2000 nm. The materials were characterized with regard to an external TPA standard (BDPAS = bis(4-diphenylamino) stilbene). All solid-state materials were deposited between quartz glass substrates, horizontally placed on an adjustable holder and excited at 45° angle, while a set of collimating lensed was placed perpendicular to the plane of the sample to collect the TPEF by a glass optical fiber coupled to a CCD spectrometer. Scattered exciting radiation was removed with the use of either a 700 nm or a 650 nm short pass dielectric filter. Integration times ranged from 10 s to 30 s. The collected signals were processed with the supplier software and analyzed by OriginPro 8 (OriginLab Corporation).

Two samples of the same material but different grain size can emit signals of significantly different intensity, which might lead to different conclusions in strength of their NLO response. To minimize errors connected with the sample preparation, prior to all SSTPEF measurements the solid samples and reference compounds were sieved through a mini-sieve set (Aldrich) to access grain size smaller than approximately 60 µm, accounting for effects from scattering. Note that this is the same procedure as one used in Kurtz-Perry-type SHG measurements, and it is crucial for the reproducibility of results.

5.1.15 Computational methods

Quantum chemical calculations on H_4TCPE, H_4TCPE-F, [Zn_2(TCPE)(bpy)] and [Zn_2(TCPE-F)(bpy)] were performed by the group of Prof. R. Zaleśny, in particular by M. Cholui from the Department of Physical and Quantum Chemisty, Faculty of Chemistry, Wroclaw University of Science and Technology, Poland. For more detailed information, please refer to R. Zaleśny directly. All other calculations were conducted by the author of this thesis.

All quantum chemical calculations for H_4TPBD, [Zn_2(TPBD)$(DMAc)_2$] and [Cd_2(TPBD)$(H_2O)_4$] were performed using the Gaussian16[322] software package

on the level of density functional theory (DFT) and time-dependent density functional theory (TD-DFT). Different long-range corrected functionals among others ωB97X-D, LC-ωHPBE and the cam-B3LYP functional were tested. The latter showed the best compliance with the measured spectra and consequently the coulomb-attenuating long-range corrected functional was used for all calculations. As basis set, def2-TZVP and def2-SVP were employed as implemented in this software. The basis-set qualities showed a good balance between computational costs and quality of the resulting energies, in particular concerning the calculation of the excited state geometry of H_4TPBD and the different TPBD-clusters. Starting geometries for the optimization of H_4TPBD were obtained from the respective single-crystal structure of Me_4TPBD, where the methyl group was replaced by hydrogen. The ground state geometries were optimized using camB3LYP/def2TZVP on the level of DFT. Calculations of the vibrational frequencies were used to determine the nature of the stationary points (no negative eigenfrequencies for minima). All quantum chemical calculations were conducted in the gas phase. To obtain information about the symmetry of the excited states, H_4TPBD was constrained to D_{2h} symmetry during geometry optimization. Vertical absorption energies were computed via TD-DFT by single-point TD calculations on the DFT optimized structures using 20 excited states. To gain information about the excited stated dipole moment and the high Stokes shift of the compound, the molecular geometry of the molecule was fully TD-DFT optimized and further analyzed for structural differences with the DFT derived ground state molecular structure. For the TD-DFT optimization an ultra-fine grid was used, to ensure proper convergence.

To get insights into the photo-physical response of $[Zn_2(TPBD)(DMAc)_2]$ and $[Cd_2(TPBD)(H_2O)_4]$ different cluster models constructed from various small crystallographic segments were extracted from the DFT optimized single crystal structures. For the latter, the Quantum Espresso software was used.[323] The structures were periodically optimized (plane-wave DFT) at the GGA approximation using periodic boundary conditions. The Kohn-Sham states were expanded in projected-augmented wave (PAW) pseudopotentials utilizing a kinetic cut-off energy of 60 Ry and 480 Ry for the density. ($C[2S^2 2P^2]$, $H[1S^1]$, $O[2S^2 2P^4]$, $N[2S^2 2P^3]$, $Zn[4S^2 4P^{0.3} 3D^{9.7}]$, $Cd[5S^2 5P^{0.5} 4D^{9.5}]$) Structures were optimized at the Γ-point. To stay within the crystallographic situation, only

atomic positions were optimized using the PBE functional and a Grimme D3 dispersion correction. The k-point sampling for the calculations of the density of states and the projected density of states was done on a 3x3x3 k-point mesh. From the so obtained structures, different crystallographic TPBD-cluster were extracted, which were saturated with Hydrogen atoms to enable charge neutrality. These clusters were treated within the TD-DFT level of theory (cam-B3LYP/def2-SVP, 20 excited states). Based on the TD-DFT calculation, fragmented transition density matrices were calculated using the MultiWfn software[324] (for the fragmentation scheme, see the respective chapter of this thesis).

TPA cross-section of H_4TCPE, H_4TCPE-F, [Zn_2(TCPE)(bpy)] and [Zn_2(TCPE-F)(bpy)] were calculated in the frame of sum-over-state formalism using the long-range corrected cam-B3LYP functional and the 6-31+G(d) basis set with the GAMESS US.[325] Results from the TD-DFT calculations (transition dipole moments from ground to excited states and between excited states) were used to parametrize the SOS expression, which finally gave two-photon absorption strength. The latter was converted to TPA cross-section values according to literature procedure. Input geometries for all calculations were directly taken from the respective single-crystal structure and further geometry optimized. TPA stenghts for H_4TPBD were calculated using the cam-B3LYP functional and the 6-31+G(d) basis set within a generalized three state model using an in-house code written in PYTHON. The parameters were extracted from TD-DFT calculations using GAMESS US.[325]

Finally, force-field calculations of the respective Zr^{IV}-TPBD MOFs were conducted using the universal force field in the Material Studio software 5.0. The calculations were based on crystal structures of similar MOFs, where the ligands were replaced by TPBD. Consequently, higher symmetry settings were adjusted and the geometries were optimized (atomic positions, unit cell parameters) using the smart algorithm and the ultra-fine settings as implemented in this software.

5.2 Synthetic procedures and characterization details

5.2.1 N^1,N^1,N^4,N^4-tetrakis(4-bromophenyl)benzene-1,4-diamine

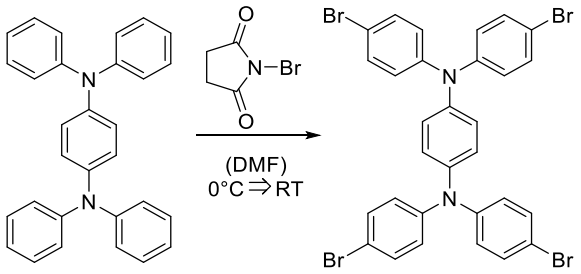

Scheme 8. Reaction scheme for the synthesis of N^1,N^1,N^4,N^4-tetrakis(4-bromophenyl)benzene-1,4-diamine.

The compound was synthesized following a slightly modified literature procedure. N^1,N^1,N^4,N^4-tetraphenylbenzene-1,4-diamine (1.00 g, 2.42 mmol, 1 equiv.) was suspended in 40 mL DMF and cooled to 0 °C using an ice-bath. N-bromosuccinimide (1.94 g, 10.8 mmol, 4.5 equiv.) in 20 mL DMF was slowly added to the N^1,N^1,N^4,N^4-tetraphenylbenzene-1,4-diamine solution over the course of 30 min using a syringe pump. After complete addition, the reaction mixture was stirred for 10 min at 0 °C and afterwards warmed up to room temperature. The green suspension was stirred overnight and subsequently poured onto water (500 mL). The formed precipitate was collected via filtration and recrystallized in chloroform (200 mL). N^1,N^1,N^4,N^4-tetrakis(4-bromophenyl)benzene-1,4-diamine was isolated by filtration as a white powder, washed three times with chloroform and dried *in vacuo* (1.48 g, 84 %). ^{1}H-NMR (400.13 MHz, $CDCl_3$): δ (ppm) = 7.35 (d, ^2J = 8.51 Hz, 8H, Ar-H), 6.94 (m, 12H, Ar-H). $^{13}C\{^1H\}$-NMR (100.62 MHz, $CDCl_3$): δ (ppm) = 132.3, 125.5, 125.2. MS-ESI (m/z): 727.64 (**M**-H^+). Elemental Analysis (%) calc. for $C_{30}H_{20}Br_4N_2$: C 49.49 H 2.77 N 3.85; found C 49.18 H 2.73 N 3.84.

5.2.2 *Tetramethyl-N¹,N¹,N⁴,N⁴-tetrakis[(1,1'-biphenyl)-4-carboxylate]-1,4-benzene diamine*

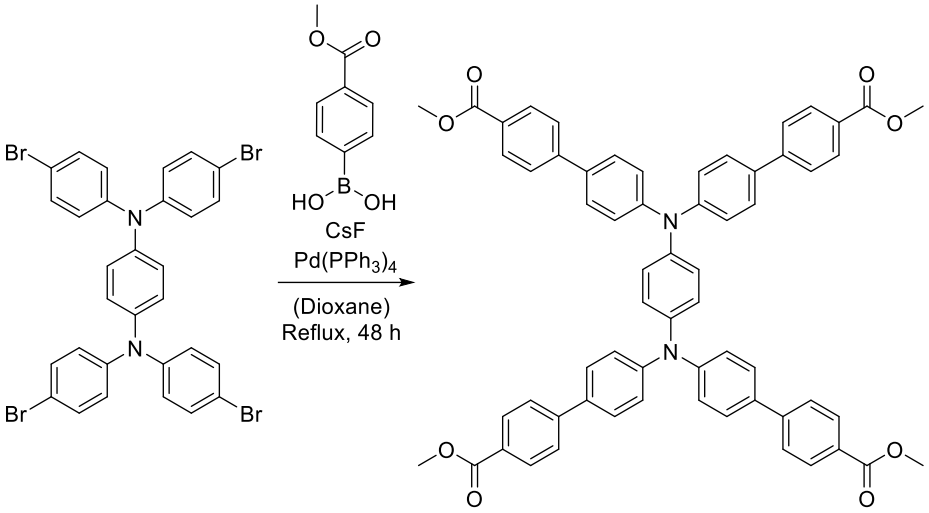

Scheme 9. Reaction scheme for the synthesis of tetramethyl-N^1,N^1,N^4,N^4-tetrakis[(1,1'-biphenyl)-4-carboxylate]-1,4-benzene diamine.

The compound was synthesized following a slightly modified literature procedure. N^1,N^1,N^4,N^4-tetrakis(4-bromophenyl)benzene-1,4-diamine (500 mg, 0.686 mmol, 1 equiv.), 4-methoxycarbonylboronic acid (734 mg, 4.08 mmol, 6 equiv.) and cesium fluoride (1.34 g, 8.84 mol, 13 equiv.) were suspended in dry dioxane. An argon flow was directed through the solution for one hour to degas the reaction mixture. Subsequently, tetrakis(triphenylphosphine)palladium (0) (62.1 mg, 0.05 mmol, 0.08 equiv.) was added and the reaction mixture was refluxed for 3 days. After the reaction mixture was cooled down to room temperature, dioxane was evaporated, the yellow crude product suspended in chloroform (50 mL) and washed with water (3 x 20 mL). The organic phase was dried with magnesium sulfate. After removal of chloroform, the solid was recrystallized from dichloromethane (100 mL), collected and dried *in vacuo* to get a bright, yellow product in a yield of 55 % (358 mg). ^{1}H-NMR (400.13 MHz, $CDCl_3$): δ (ppm) = 8.10 (d, ^{2}J = 8.01 Hz, 8H, Ar-H), 7.65 (d, ^{2}J = 8.01 Hz, 8H, Ar-H), 7.59 ($s_{\{broad\}}$, 8H, Ar-H), 7.24 ($s_{\{broad\}}$, 8H, Ar-H), 7.12 ($s_{\{broad\}}$, 4H, Ar-H), 3.94 (s, 12H, CH_3). $^{13}C\{^1H\}$ NMR (100.62 MHz, $CDCl_3$): δ (ppm) = 166.7, 147.2, 144.9, 133.7,129.8, 128.1, 127.4, 126.2, 125.8, 123.6, 51.83. MS-ESI (m/z): 947.25 (**M**-H^+). Elemental Analysis (%) calc. for $C_{62}H_{48}N_2O_8$: C 78.46 H 5.10 N 2.95; found C 78.12 H 5.14 N 3.07.

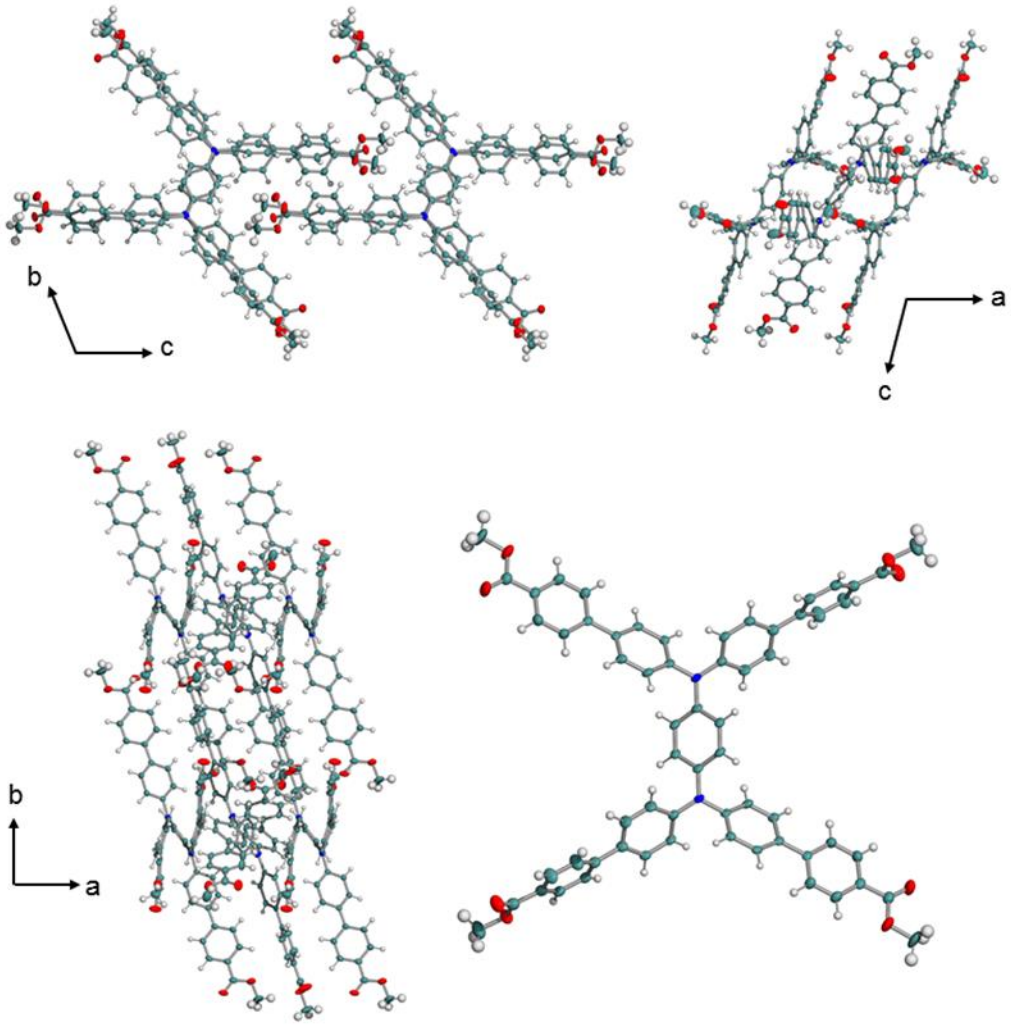

Figure 68. The crystal structure and molecular structure of Tetramethyl-N^1,N^1,N^4,N^4-tetrakis[(1,1‘-biphenyl)-4-carboxylate]-1,4-benzene diamine with packing along the crystallographic a, b and c axis. Displacement ellipsoids are given at the 50% probability level. Grey, blue, white and red spheres correspond to carbon, nitrogen, hydrogen and oxygen, respectively.

Table 7. Crystal structure data of $Me_4TPBD \cdot 3C_5H_{12} \cdot CHCl_3$

Compound	**$Me_4TPBD \cdot 3C_5H_{12} \cdot CHCl_3$**
CCDC	1910857
Formula	$C_{70}H_{66.5}N_2O_8Cl_{1.5}$
Formula weight	1116.98
Temperature (K)	100(2)
Wavelength (Å)	0.7103 (Mo-K_α)
Crystal system	Triclinic
Space group	*P*-1
Z	2
a (Å)	10.0386(7)
b (Å)	16.5446(11)
c (Å)	17.6418(10)
α (°)	100.011(2)
β (°)	104.223(2)
γ (°)	90.103(2)
Volume (Å^3)	2793.93
μ (mm^{-1})	0.155
d_{calc} (g/cm^3)	1.328
F (000)	996
Crystal size (mm^3)	0.067 x 0.098 x 0.140
Theta range	2.14 to 25.35°
Index range	-12 ≤ h ≤ 12 -19 ≤ k ≤ 19 -21 ≤ l ≤ 21
Refl. collected	150558
Independent reflections	10215 (R_{int} = 0.0674)
Data/restraints/parameters	10215 / 0 / 654
GOF on F^2	1.018
R_1/wR_2[a] [$I \geq 2\sigma(I)$][b]	0.0497 / 0.1214
R_1/wR_2 [all data]	0.0688 / 0.1323
Largest diff. peak and hole	0.366 and -0.287 eÅ^{-3}

a: $w = 1/[\sigma^2(F_o^2) + (0.0532P)^2 + 2.4824P]$ where $P = (F_o^2 + 2F_c^2)/3$

b: $R_1 = \sum \frac{||F_o| - |F_c||}{\sum |F_o|}$; $wR_2 = \{\sum[w(F_o^2 - F_c^2)^2] / \sum[w(F_o^2)^2]\}^{\frac{1}{2}}$

Suitable single crystals for single crystal X-ray structure determination (SCXRD) were grown by slow diffusion of pentane into a chloroform solution of Me_4TPBD. The compound crystallizes in small bright yellow needles with an approximate shape of 0.067 x 0.098 x 0.140 mm. X-ray intensity data were collected at 100(2)K using a Bruker D8 Venture diffractometer equipped with a Helios optic monochromator, a Photon 100 CMOS detector and a Mo TXS rotating anode source (Mo-K_α radiation). The raw area detector data frames were reduced and corrected for absorption effects using the SAINT and

SADABS programs with multi-scan absorption correction. Final unit cell parameters were determined by least-squares refinement of 102015 independent reflections taken from the data sets. The structure was solved by intrinsic phasing with SHELXT. Subsequent difference Fourier calculations and full-matrix least-squares refinement against F^2 were performed by SHELXL-2014/7 (Sheldrick, 2014).

The compound crystallizes in the triclinic crystal system in the space group $P\bar{1}$. The asymmetric unit consists of one molecule. All non-hydrogen atoms were refined with anisotropic displacement parameters. Hydrogen atoms could not be located in the Fourier difference maps and were calculated in ideal positions using a riding model (d(C-H) = 0.95 Å, $U_{iso}(H) = 1.2U_{eq}(C)$). The unit cell contained 3 molecules of pentane and one molecule of chloroform from the crystallization process. The disordered solvent molecules could not properly be refined and were treated as diffuse contribution to the overall scattering without specific positions using the SQUEEZE routine of PLATON (solvent accessible volume (SAV) = 542 $Å^3$, electrons found in SAV = 174). The largest residual electron density peak in the final difference map is 0.366 e/$Å^3$.

5.2.3 *N^1,N^1,N^4,N^4-tetrakis[(1,1‘-biphenyl)-4-carboxylic acid]-1,4-benzene diamine*

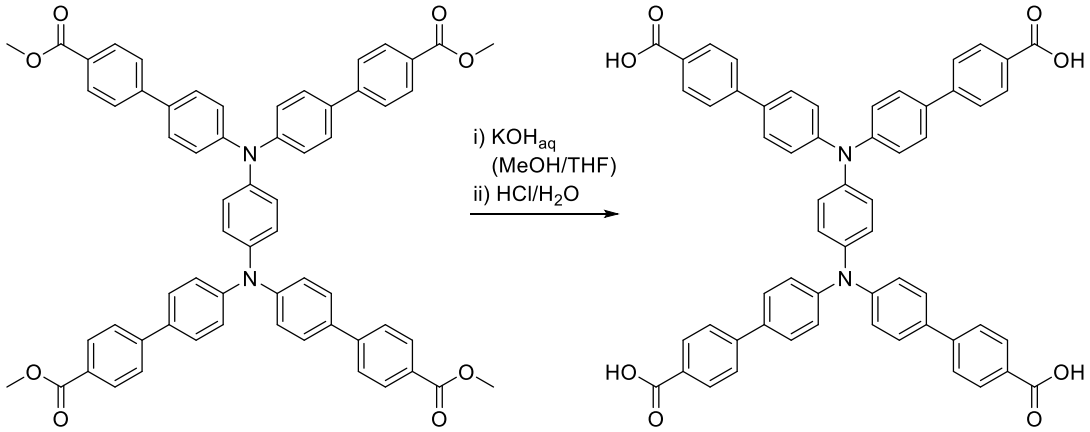

Scheme 10. Reaction scheme for the synthesis of N^1,N^1,N^4,N^4-tetrakis[(1,1‘-biphenyl)-4-carboxylic acid]-1,4-benzene diamine.

Tetramethyl N^1,N^1,N^4,N^4-tetrakis[(1,1‘-biphenyl)-4-carboxylate]-1,4-benzene diamine (500 mg, 0.524 mmol, 1 equiv.) was suspended in a mixture of methanol (15 mL) and tetryhydrofurane (30 mL). Aqueous 3 molar KOH solution (30 mL) was added and the reaction mixture refluxed for 24 h. The organic solvents were evaporated and HCl was added until a bright, green solid precipitated, which was thoroughly washed with excess water and dried *in vacuo*. H_4TPBD was obtained as green solid (450 mg, 96 %). ^{1}H-NMR (400.13 MHz, DMSO-d^6): δ (ppm) = 8.00 (d, ^{2}J = 8.00 Hz, 8H, Ar-H), 7.80 (d, ^{2}J = 8.00 Hz, 8H, Ar-H), 7.74 (d, ^{2}J = 7.98 Hz, 8H, Ar-H), 7.20 (d, ^{2}J = 8.00 Hz, 8H, Ar-H), 7.17 (s, 4H, Ar-H). ^{13}C{^{1}H} NMR (100.62 MHz, DMSO-d^6): δ (ppm) = 164.5, 145.7, 141.1, 132.2, 128.2, 127.4, 126.2, 124.1, 121.9. MS-ESI (m/z): 891.2 (**M**-H^+). Elemental Analysis (%) calc. for ($C_{58}H_{40}N_2O_8$) · 0.5 H_2O: C 76.93 H 4.61 N 3.09 O 15.37; found C 76.41 H 4.60 N 3.06 O 14.87. IR (ATR, neat, cm^{-1}): 3200-2200 (OH, broad), 1708 (m), 1667 (s), 1592 (m), 1521 (w), 1489 (s), 1436 (w), 1381 (m), 1309 (s), 1273 (s), 1200 (m), 1179 (m), 1098 (s), 1003 (m), 866 (w), 827 (m), 799 (w), 774 (s), 718 (s), 701 (s), 669 (m).

5.2.4 Dimethyl 4,4'-(9H-carbazole-3,6-diyl)dibenzoate

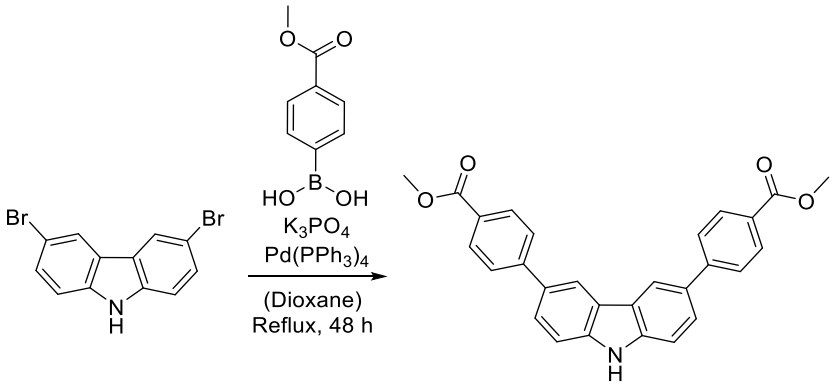

Scheme 11. Reaction scheme for the synthesis of dimethyl 4,4'-(9H-carbazole-3,6-diyl)dibenzoate.

1.00 g (3.08 mmol, 1.00 equiv.) 3,6-dibromo-9*H*-carbazole, 1.38 g (5.55 mmol, 1.80 equiv.) (4-(methoxycarbonyl) phenyl)boronic acid and 10.6 g (7.69 mmol, 2.50 equiv.) K_3PO_4 were suspended in 100 ml Dioxane and degassed for 1h with Argon. 81.8 mg (0.07 mmol, 0.02 eq.) $Pd(PPh_3)_4$ were added to the reaction mixture and refluxed at 120°C for 48h. The solvent was removed under vacuum and the precipitate was washed three times with H_20 and CH_2Cl_2, respectively. Recrystallization from CH_3OH yielded dimethyl 4,4'-(9*H*-carbazole-3,6-diyl)dibenzoate (344 mg, 0.78 mmol, 26%) as a light brown powder. ^{1}H-NMR (400 MHz, 298 K, DMSO-d_6) δ (ppm) = 11.57 (s, 1H, N-H), 8.75 (s, 2H, Ar-H), 8.07 (d, *J* = 8.5 Hz, 4H, Ar-H), 7.98 (d, *J* = 8.5 Hz, 4H, Ar-H), 7.85 (dd, *J* = 8.5, 1.9 Hz, 2H, Ar-H), 7.62 (d, *J* = 8.5 Hz, 2H, Ar-H), 3.89 (s, 6H, C*H*$_3$). ^{13}C-NMR (101 MHz, 298K, DMSO-d_6) δ (ppm) = 145.94, 140.61, 130.03, 126.81, 111.96, 52.29. MS-ESI (m/z): 409.3 (**M**-H$^+$).

5.2.5 4-Di(9H-carbazol-9-yl)benzene

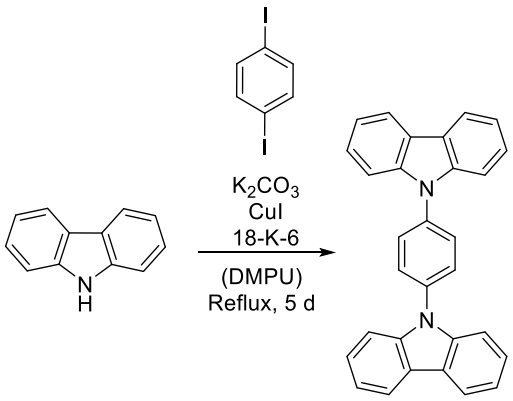

Scheme 12. Reaction scheme for the synthesis of 4-di(9H-carbazol-9-yl)benzene.

1.50 g (8.97 mmol, 1.00 eq.) 9*H*-carbazole, 1.48 g (4.47 mmol, 0.50 eq.) 1,4-diiodobenzene, 2.48 g (17.9 mmol, 2.00 eq.) K_2CO_3, 78.0 mg (0.24 mmol, 0.03 eq.) 18-Crown-6 and 85.7 mg (0.45 mmol, 0.05 eq.) CuI were suspended in 9 ml DMPU and refluxed at 155°C for five days. 40 ml of saturated NH_4Cl solution were added to the reaction mixture and washed three times with CH_2Cl_2. The organic phases were combined and concentrated in vacuum until a brown oil was received. A white solid was precipitated of the brown oil by the addition of acetonitrile. The precipitate was washed with acetonitrile and diethyl ether before it was dried on air. The yield of 1,4-di(9*H*-carbazol-9-yl)benzene was 1.01 g (2.47 mmol, 55%). ^{1}H-NMR (400 MHz, 298K, $CDCl_3$) δ (ppm) = 8.20 (dd, *J* = 7.8, 1.0 Hz, 4H, Ar-H), 7.83 (s, 1H, Ar-H), 7.58 (dd, *J* = 8.2, 1.0 Hz, 1H, Ar-H), 7.49 (ddd, *J* = 8.2, 7.1, 1.2 Hz, 1H, Ar-H), 7.35 (ddd, *J* = 7.5, 1.0 Hz, 1H, Ar-H). MS-ESI (m/z): 408.11 (**M**-H^+). Elemental Analysis (%) calc. for ($C_{30}H_{20}N_2$) : C 88.21 H 4.94 N 6.86; found C 87.14 H 4.83 N 6.81.

5.2.6 1,4-Bis(3,6-dibromo-9H-carbazol-9-yl)benzene

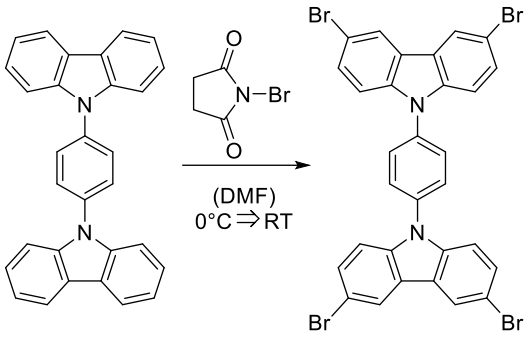

Scheme 13. Reaction scheme for the synthesis of 1,4-bis(3,6-dibromo-9H-carbazol-9-yl)benzene.

To a stirring suspension of 500 mg (1.22 mmol, 1.00 eq.) 4-di(9H-carbazol-9-yl)benzene in 20 ml DMF a solution of 981 mg (5.51 mmol, 4.50 eq.) *N*-Bromosuccinimide in 20 ml DMF was added over 20 min at 0°C. The reaction mixture was stirred for further 10 min at 0°C until it was allowed to warm up to room temperature, where it was further stirred for 18 h. The reaction mixture was poured into 600 ml H_2O and a white solid precipitated. The precipitate was filtered of and washed three times with H_2O. The white solid was recrystallized from THF before it was dried *in vacuo* to yield 380 mg of 1,4-bis(3,6-dibromo-9*H*-carbazol-9-yl)benzene (0.53 mmol, 53%). ^{1}H-NMR (400 MHz, 298K, THF-d_8) δ (ppm) = 8.39 (d, *J* = 2.1 Hz, 4H, Ar-H), 7.88 (s, 4H, Ar-H), 7.55 (dd, *J* = 8.8, 2.2 Hz, 4H, Ar-H), 7.46 (d, *J* = 8.9 Hz, 4H, Ar-H).

5.2.7 1,1,2,2-Tetrakis(4-bromophenyl)ethene

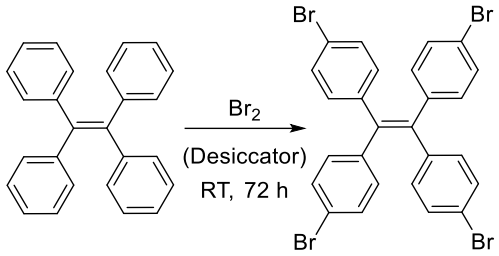

Scheme 14. Reaction scheme for the synthesis of 1,1,2,2-tetrakis(4-bromophenyl)ethene.

Powdered tetraphenylene (4.00 g, 12.0 mmol) is reacted with bromine vapour under room temperature for four days. The resulting solid is recrystallized from acetone to yield a white powder (5.4 g, 8.4 mmol, 70 % yield). %). ^{1}H-NMR (400 MHz, 298K, $CDCl_3$) δ (ppm) = 7.62 (d, *J* = 8.0 Hz, 8H, Ar-H), 7.19 (d, *J* = 8.0 Hz, 8H, Ar-H).

5.2.8 *4',4''',4'''',4''''''-(Ethene-1,1,2,2-tetrayl)tetrakis(([1,1'-biphenyl]-4-carboxylic acid))*

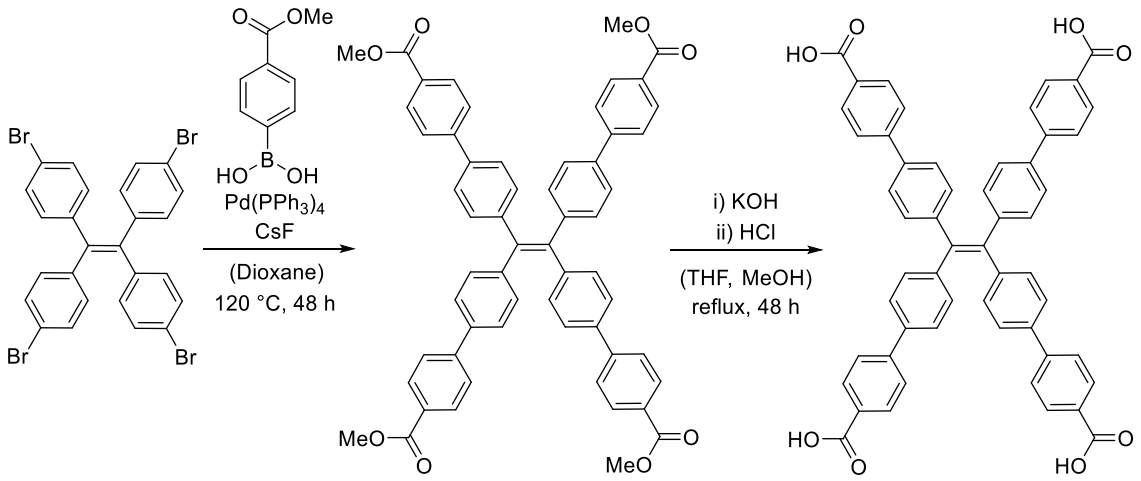

Scheme 15. Reaction scheme for the synthesis of 4',4''',4'''',4''''''-(ethene-1,1,2,2-tetrayl)tetrakis(([1,1'-biphenyl]-4-carboxylic acid)).

4',4''',4'''',4''''''-(Ethene-1,1,2,2-tetrayl)tetrakis(([1,1'-biphenyl]-4-carboxylic acid)) is synthesized according to literature procedure. Tetrakis(4-bromophenyl)ethene (1.50 g, 2.30 mmol, 1.0 equiv.) is refluxed with 4-methoxycarbonylphenylboronic acid (2.50 g, 13.9 mmol, 6.0 equiv.), cesium fluoride (4.40 g, 29.0 mmol, 12.6 equiv.) and tetrakis(triphenylphosphine)palladium (0.20 g, 0.17 mmol, 0.07 equiv.) in degassed and dried dioxane (150 mL) under argon atmosphere for two days. After cooling to room temperature, dioxane is removed in vacuum and the residue solved in dichloromethane. The bright yellow solution is washed with water (3 x 75 mL) and the aqueous phase extracted with dichloromethane. The organic phase is dried with anhydrous $MgSO_4$. After removing the solvent, the raw product is separated by column chromatography (silica gel, dichloromethane/hexane: 1:9). The corresponding methyl ester is dissolved in tetrahydrofuran/methanol (50/25 mL) and aqueous solution of 3 M KOH (25 mL) is added to the reaction mixture, which is refluxed overnight. Afterwards, the solution is concentrated under reduced pressure and acidified with 3M HCl to yield a bright yellow product. The product is collected by centrifugation and washed with excess water (1.0 g, 1.23 mmol, 53 % referred to tetrakis(4-bromophenyl)ethene over two steps): ^{1}H-NMR (400 MHz, DMSO-d_6, 298 K) δ

(ppm) = 7.97 (d, J = 8.1 Hz, 8H, Ar-H), 7.77 (d, J = 8.1 Hz, 8H, Ar-H), 7.62 (d, J = 8.1 Hz, 8H, Ar-H), 7.19 (d, J = 8.0 Hz, 8H, Ar-H). Elemental Analysis (%) calc. for $(C_{54}H_{36}O_8)\cdot 2(H_2O)$: C 77.06 H 4.69; found C 76.98 H 4.56. IR (ATR, neat, cm^{-1}): 3200-2400 (OH, broad), 1622 (s), 1573 (w), 1522 (w), 1492 (w), 1416 (m), 1392 (m), 1313 (w), 1269 (m), 1228 (m), 1175 (m), 1103 (m), 1005 (m), 855 (w), 828 (w), 763 (s), 744 (w), 736 (w), 699 (w).

5.2.9 *4',4''',4'''''',4''''''''-(Ethene-1,1,2,2-tetrayl)tetrakis(3-fluoro-[1,1'-biphenyl]-4-carboxylic acid)*

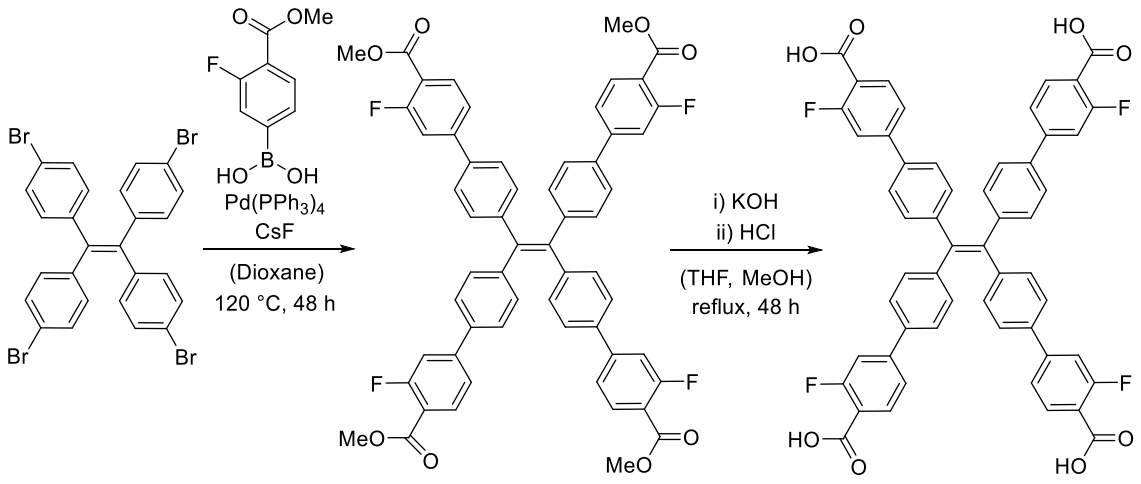

Scheme 16. Reaction scheme for the synthesis of 4',4''',4'''''',4''''''''-(ethene-1,1,2,2-tetrayl)tetrakis(3-fluoro-[1,1'-biphenyl]-4-carboxylic acid).

Tetrakis(4-bromophenyl)ethene (1.50 g, 2.30 mmol, 1.0 equiv.) is refluxed with (2-fluoro-4-(methoxycarbonyl)phenyl)boronic acid (2.75 g, 13.9 mmol, 6.0 equiv.), cesium fluoride (4.40 g, 29.0 mmol, 12.6 equiv.) and tetrakis(triphenylphosphine)palladium (0.20 g, 0.17 mmol, 0.07 equiv.) in degassed and dried dioxane (150 mL) under argon atmosphere for two days. After cooling to room temperature, dioxane is removed in vacuum and the residue is solved in dichloromethane. The bright yellow solution is washed with water (3 x 75 mL) and the aqueous phase extracted with dichloromethane. The organic phase is dried with anhydrous $MgSO_4$. After removing the solvent, the raw product is separated by column chromatography (silica gel, dichloromethane/hexane: 1:9). The corresponding methyl ester is dissolved in tetrahydrofuran/methanol (50/25 mL) and aqueous solution of 3 M KOH (25 mL) is added to the reaction mixture, which is refluxed overnight. Afterwards, the solution is cooled and concentrated under reduced pressure and acidified with 3M HCl to yield a bright yellow product. The compound is collected by centrifugation and washed with excess water (890 mg, 0.994 mmol, 43 % referred to tetrakis(4-bromophenyl)ethene over two steps): ^{1}H-NMR (400 MHz, DMSO-d_6, 298 K) δ (ppm) = 7.89 (t, J = 8.2 Hz, 4H, Ar-H), 7.71 – 7.56 (m, 16H, Ar-H), 7.18 (d, J = 8.1 Hz, 8H, Ar-H). Elemental Analysis (%) calc. for

$C_{54}H_{32}F_4O_8)\cdot 1(H_2O)$: C 72.2 H 3.76; found C 72.2 H 3.76. IR (ATR, neat, cm^{-1}): 3200-2400 (broad, OH), 1698 (s), 1619 (s), 1575 (w), 1548 (w), 1523 (w), 1489 (w), 1433 (m), 1395 (m), 1262 (s), 1232 (w), 1194 (m), 1069 (broad, s), 902 (s), 801 (s), 775 (m), 750 (w), 695 (w).

5.2.10 1,3,6,8-Tetrakis(benzoic acid)pyrene

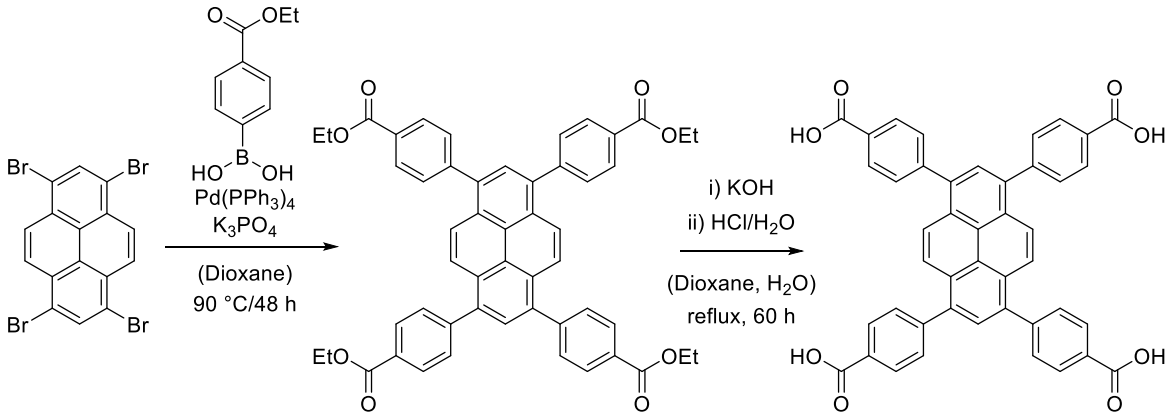

Scheme 17. Reaction scheme for the synthesis of 1,3,6,8-tetrakis(benzoic acid)pyrene.

Tetrabromopyrene (2.850 g, 5.50 mmol, 1.0 equiv.) is refluxed with 4-ethoxycarbonylphenylboronic acid (6.0 g, 32.9 mmol, 6.0 equiv.), basic potassium phosphate (5 g, 23.5 mmol, 4.5 equiv.) and tetrakis(triphenylphosphine)palladium (0) (0.10 g, 0.09 mmol, 0.016 equiv.) in degassed and dried dioxane (50 mL) under argon atmosphere for two days. After cooling to room temperature, dioxane is removed in vacuum and the residue solved in chloroform. The bright yellow solution is washed with water (3 x 75 mL) and the aqueous phase extracted with chloroform. The organic phase is dried with anhydrous $MgSO_4$. After removing the solvent, the raw product is subject to Soxhlet extraction using chloroform for 24 h. The bright yellowish solution is reduced to give a yellow powder with an overall yield of 85 % of 1,3,6,8-tetrakis(4-(ethoxycarbonylphenyl)pyene) (3.44 g, 4.6 mmol). 1 g of the latter is refluxed in a mixture of THF/dioxane (90 mL, 2/1) and 30 ml 3M aqueous KOH solution for 60 h. The organic solvents are evaporated and water is added to the residue. Hydrochloric acid (3 mol/L) is put to the clear yellow solution until no further precipitate is formed. The latter is separated by centrifugation and thoroughly washed with excess water several times. Drying under *vacuo* yields the final product in a yield of 0.88 g (97 %). ^{1}H-NMR (400 MHz, DMSO-d_6, 298 K) δ (ppm) = 13.1 (s, 4H, COOH), 8.81 (s, 4H, Ar-H), 8.14 (d, J = 8.2 Hz, 8H, Ar-H), 8.04 (s, 4H, Ar-H), 7.83 (d, J = 8.2 Hz, 8H, Ar-H).

5.2.11 [Zn_2(TPBD)$(DMAc)_2$]

$Zn(NO_3)_2 \cdot 4H_2O$ (9.00 mg, 0.0336 mmol, 3 equiv.) and H_4TPBD (10.0 mg, 0.0111 mmol, 1 equiv.) were dissolved in 2 mL dimethylacetamide (DMAc) in a 4 mL glass vial by ultrasonication (10 min). MeOH (0.5 mL) was added to the clear bright green solution and the reaction mixture was heated to 100 °C for 48 h and subsequently cooled to room temperature with a rate of 0.2 K/min. Bright yellow crystals were collected via filtration and washed with excess DMAc to give [Zn_2(TPBD)$(DMAc)_2$] (9.4 mg, 23 % based on Zn). Elemental Analysis (%) calc. for $C_{66}H_{54}N_4O_{10}Zn_2$: C 66.4 H 4.56 N 4.69; found C 65.89 H 4.57 N 4.19.

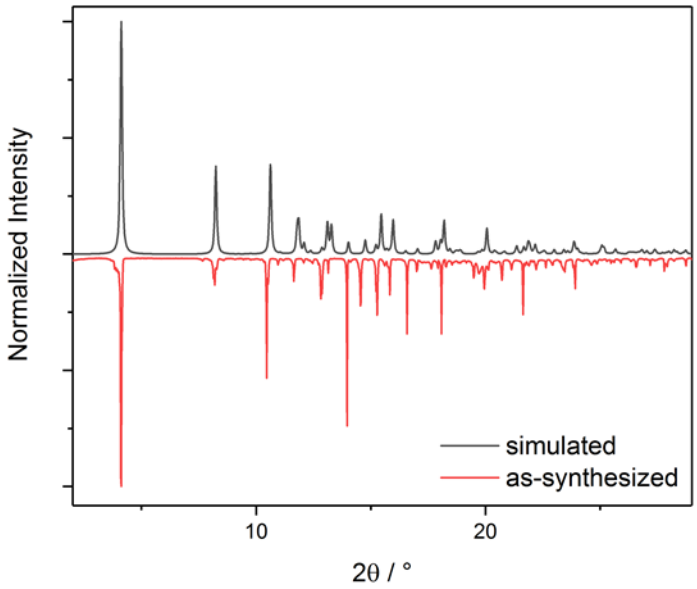

Figure 69. Simulated and as-synthesized PXRD data of [Zn_2(TPBD)$(DMAc)_2$] in a range of 2° to 30°.

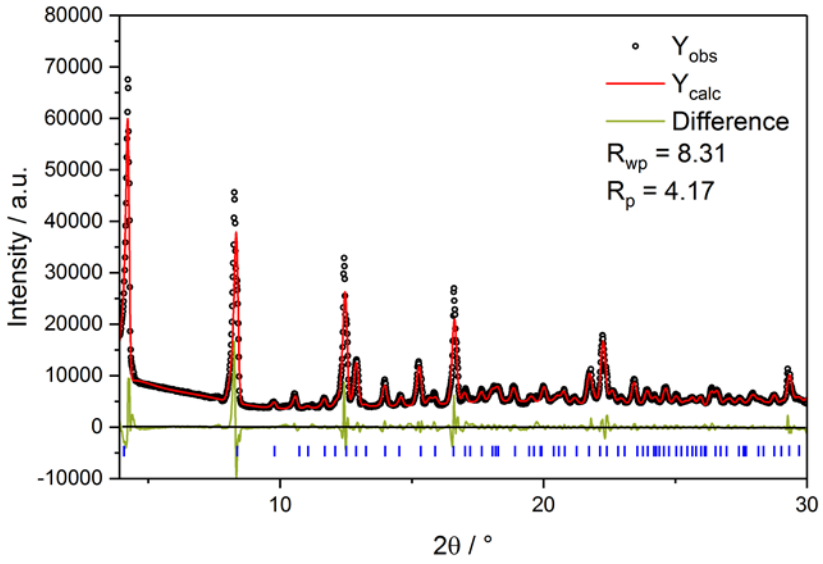

Figure 70. Pawley refinement of $[Zn_2(TPBD)(DMAc)_2]$ in a range of 4° to 30°.

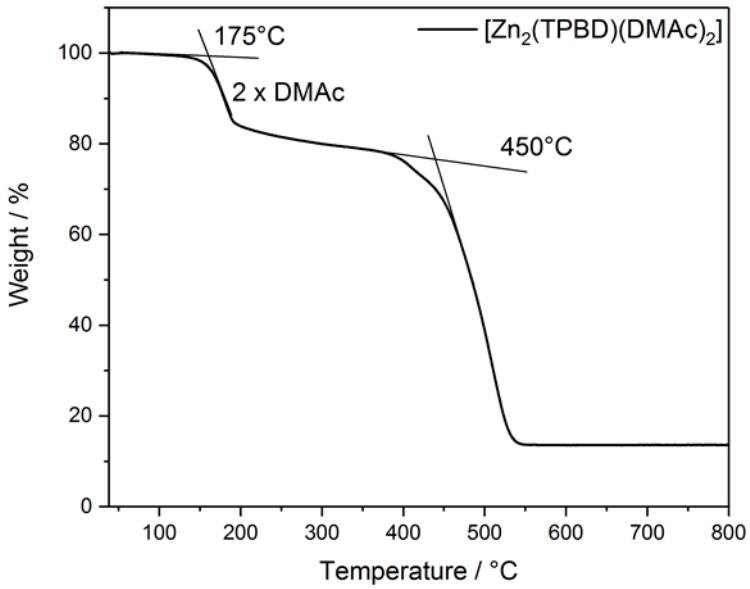

Figure 71. TGA traces of $[Zn_2(TPBD)(DMAc)_2]$ in a range of 35 °C to 800 °C.

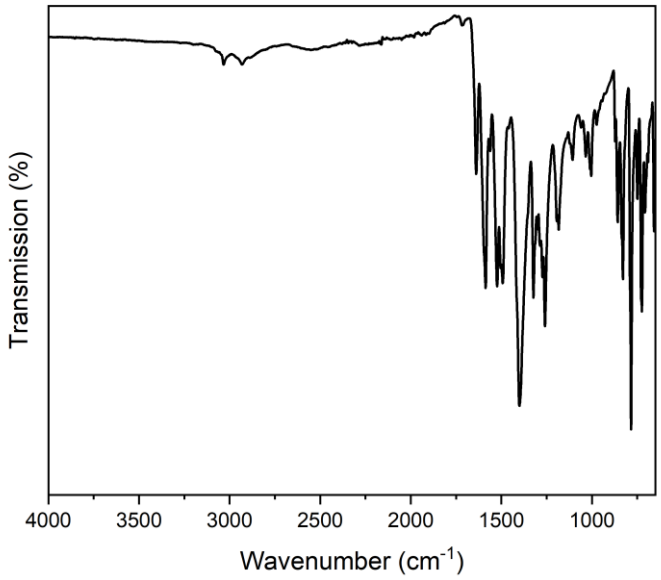

Figure 72. IR-spectra of $[Zn_2(TPBD)(DMAc)_2]$.

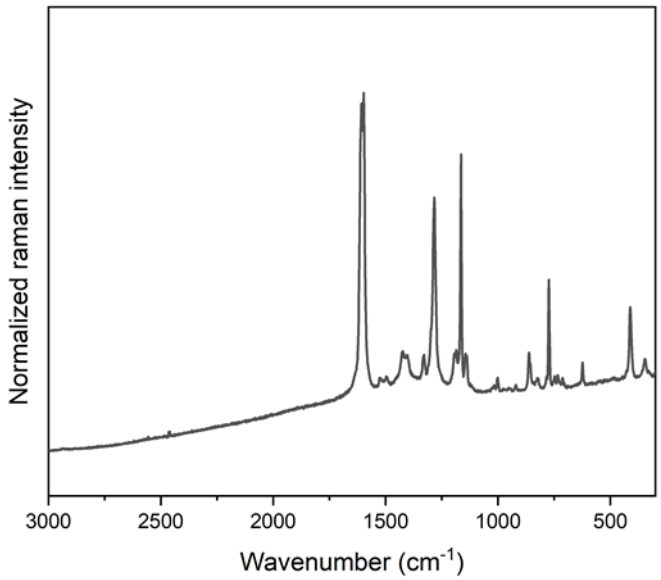

Figure 73. Raman spectra of $[Zn_2(TPBD)(DMAc)_2]$.

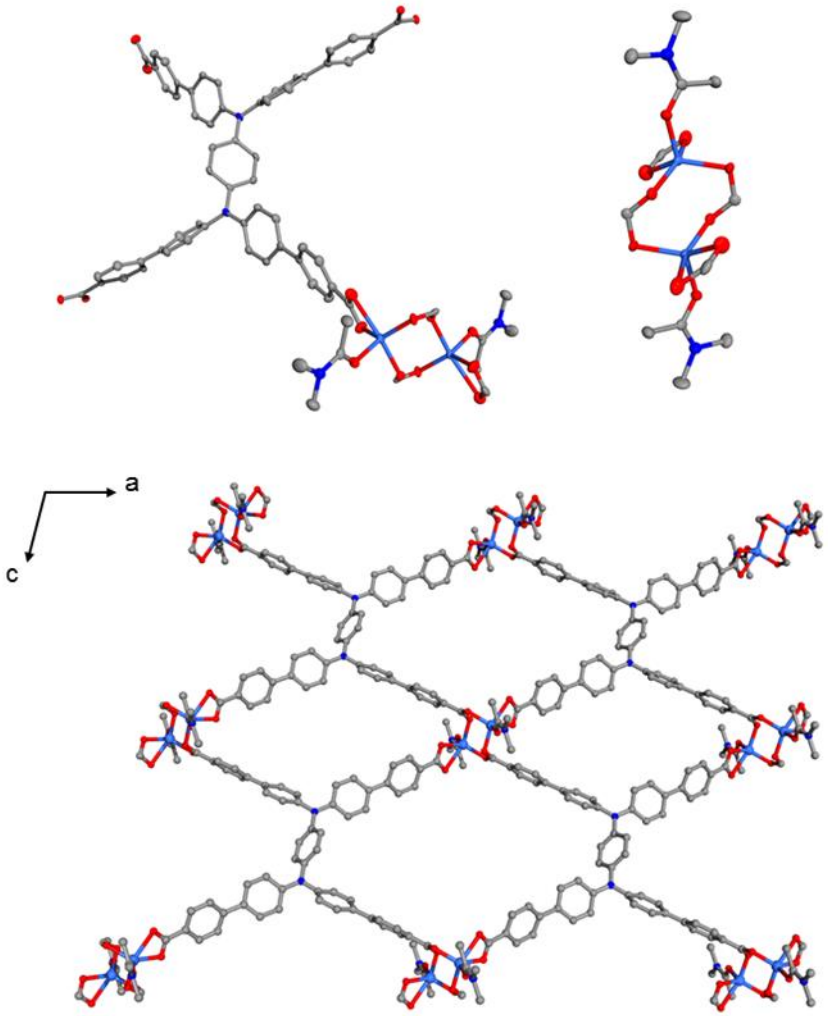

Figure 74. A section of the crystal structure of $[Zn_2(TPBD)(DMAc)_2]$ and the corresponding secondary building unit (SBU, top); Assembly of the linker TPBD and the SBU in $[Zn_2(TPBD)(DMAc)_2]$ (bottom). Displacement ellipsoids are given at the 50% probability level. Hydrogen atoms have been removed, for reasons of clarity. Grey, blue, red and turquoise spheres correspond to carbon, nitrogen, oxygen and zinc, respectively.

Table 8. Crystal structure data of $[Zn_2(TPBD)(DMAc)_2] \cdot 4DMAc$

Compound	**$[Zn_2(TPBD)(DMAc)_2] \cdot 4DMAc$**
CCDC	1910856
Formula	$C_{74}H_{72}N_6O_{12}Zn_2$
Formula weight	1368.18
Temperature (K)	100(2)
Wavelength (Å)	0.7103 (Mo-K_α)
Crystal system	monoclinic
Space group	$P2_1/c$
Z	2
a (Å)	21.714(2)
b (Å)	10.0036(10)
c (Å)	15.1820(16)
α (°)	90
β (°)	99.158(3)
γ (°)	90
Volume (Å^3)	3255.77
μ (mm^{-1})	0.806
d_{calc} (g/cm^3)	1.396
F (000)	1236
Crystal size (mm^3)	0.040 x 0.215 x 0.457
Theta range	2.45 to 25.35°
Index range	-26 ≤ h ≤ 26 -11 ≤ k ≤ 12 -18 ≤ l ≤ 18
Refl. collected	64259
Independent reflections	5955 (R_{int} = 0.0446)
Data/restraints/parameters	5955 / 0 / 376
GOF on F^2	1.058
R_1/wR_2[a] [I ≥ 2σ(I)][b]	0.0300 / 0.0721
R_1/wR_2 [all data]	0.0392 / 0.0768
Largest diff. peak and hole	0.365 and -0.385 eÅ^{-3}

a: $w = 1/[\sigma^2(F_o^2) + (0.0306P)^2 + 3.5043P]$ where $P = (F_o^2 + 2F_c^2)/3$

b: $R_1 = \sum||F_o|-|F_c||/\sum|F_o|$; $wR_2 = \{\sum[w(F_o^2 - F_c^2)^2]/\sum[w(F_o^2)^2]\}^{1/2}$

Single crystals of $[Zn_2(TPBD)(DMAc)_2]$ suitable for SCXRD were directly taken from the reaction solutions. The crystals grow as clear, bright-yellow plates with defined facets with an approximately size of 0.040 x 0.215 x 0.457 mm. X-ray intensity data were collected at 100(2)K using a Bruker D8 Venture diffractometer equipped with a Helios optic monochromator, a Photon 100 CMOS detector and a Mo TXS rotating anode source (Mo-K_α radiation). The raw area detector data frames were reduced and corrected for absorption effects using the SAINT and SADABS programs with multi-scan absorption correction.

Final unit cell parameters were determined by least-squares refinement of 5955 independent reflections take from the data sets. The structure was solved by intrinsic phasing with SHELXT. Difference Fourier calculations and full-matrix least-squares refinement against F^2 were performed by SHELXL-2014/7 (Sheldrick, 2014).

The compound crystallizes in the monoclinic crystal system. The pattern of systematic absences in the intensity data was consistent with the $P2_1/c$ space group, which was confirmed by structure solution. The asymmetric unit consists of one crystallographic independent zinc atom, a bisected molecule fragment of TPBD ($C_{17}H_{18}O_4N$ specimen) and one molecule dimethylacetamide (DMAc). All non-hydrogen atoms were refined with anisotropic displacement parameters. Hydrogen atoms could not be located in the Fourier difference maps and were calculated in ideal positions using a riding model (d(C-H) = 0.95 Å, $U_{iso}(H) = 1.2U_{eq}(C)$). The unit cell contains 4 molecules of dimethylacetamide. The disordered solvent molecules could not properly be refined and were treated as diffuse contribution to the overall scattering without specific positions using the SQUEEZE routine of PLATON (solvent accessible volume (SAV) = 730 $Å^3$, electrons found in SAV = 186). The largest residual electron density peak in the final difference map is 0.365 e/ $Å^3$.

5.2.12 [$Cd_2(TPBD)(H_2O)_4$]

$Cd(NO_3)_2 \cdot 4H_2O$ (6.90 mg, 0.0223 mmol, 2 equiv.) and H_4TPBD (10.0 mg, 0.0111 mmol, 1 equiv.) were dissolved in 1 mL dimethylformamide (DMF), 0.5 mL EtOH and 0.125 mL H_2O in a 4 mL glass vial by ultrasonication (10 min). The bright green reaction mixture was heated to 100 °C for 48 h and subsequently cooled to room temperature with a rate of 0.2 K/min. Bright yellow crystals were collected via filtration and washed with excess DMF to give [$Cd_2(TPBD)(H_2O)_4$] (8.7 mg, 32 % based on Cd). Elemental Analysis (%) calc. for $C_{58}H_{40}N_2O_{10}Cd_2 \cdot 2\ C_3H_7NO \cdot 2\ H_2O$: C 57.8 H 4.33 N 4.04; found C 57.56 H 4.10 N 4.13.

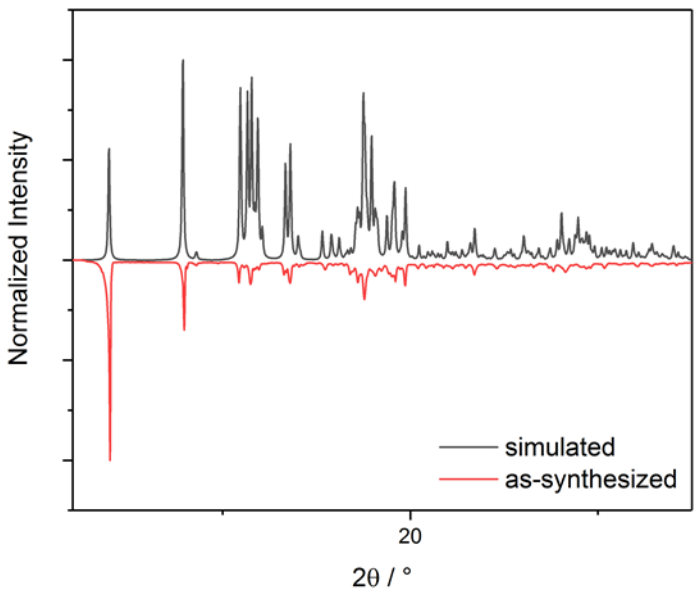

Figure 75. Simulated and as-synthesized PXRD data of [$Cd_2(TPBD)(H_2O)_4$] in a range of 2° to 30°.

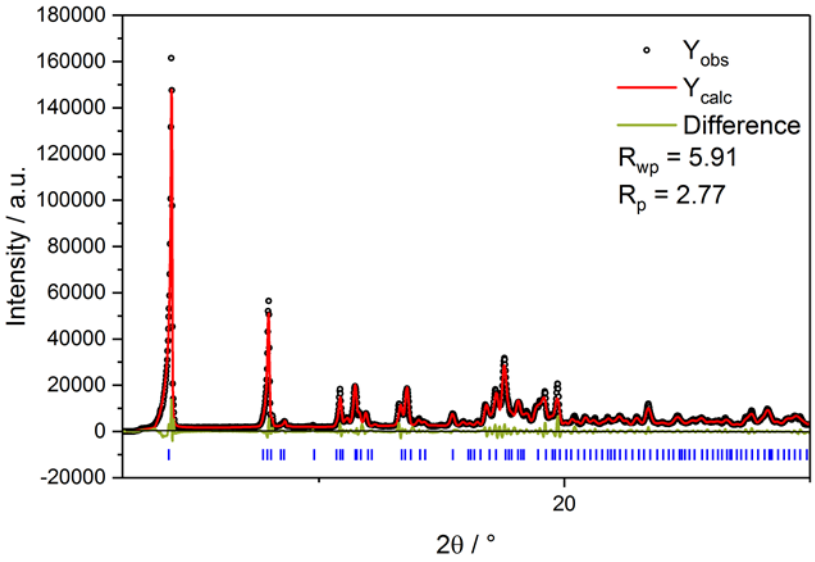

Figure 76. Pawley refinement of $[Cd_2(TPBD)(H_2O)_4]$ in a range of 4° to 30°.

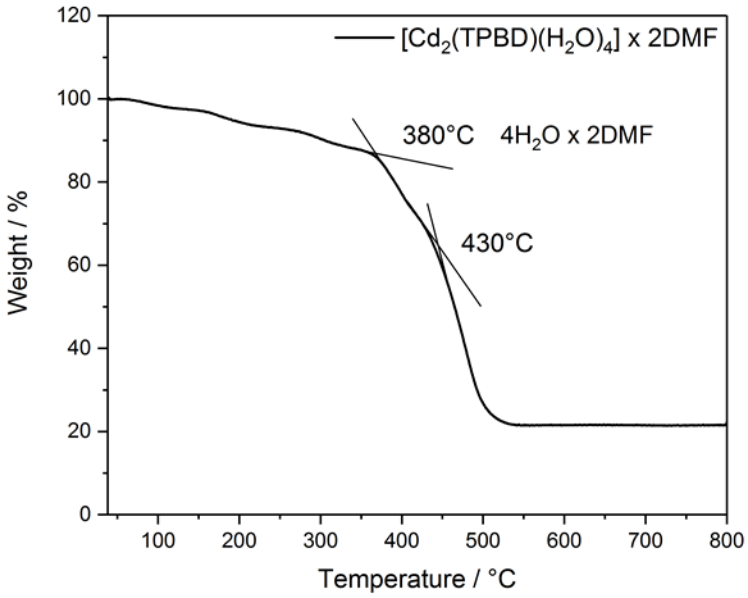

Figure 77. TGA traces of $[Cd_2(TPBD)(H_2O)_4]$ in a range of 35 °C to 800 °C.

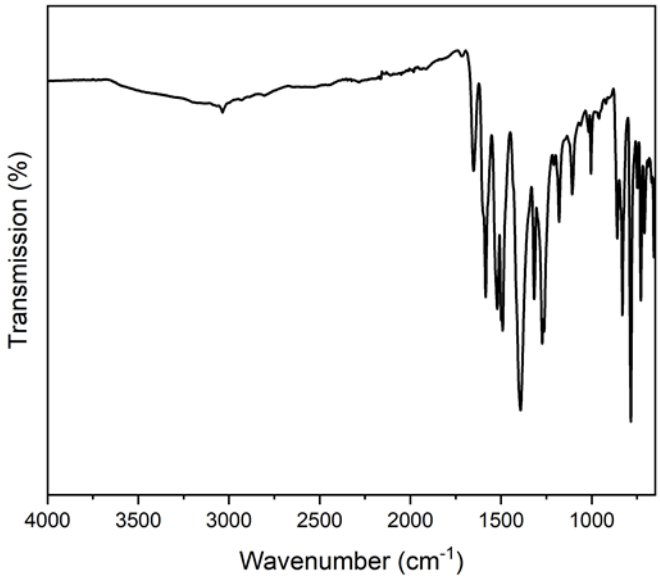

Figure 78. IR-spectra of $[Cd_2(TPBD)(H_2O)_4]$.

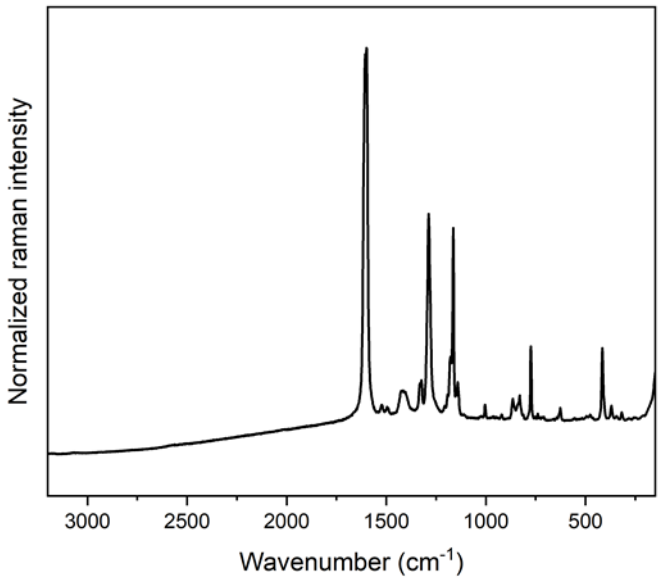

Figure 79. Raman spectra of $[Cd_2(TPBD)(H_2O)_4]$.

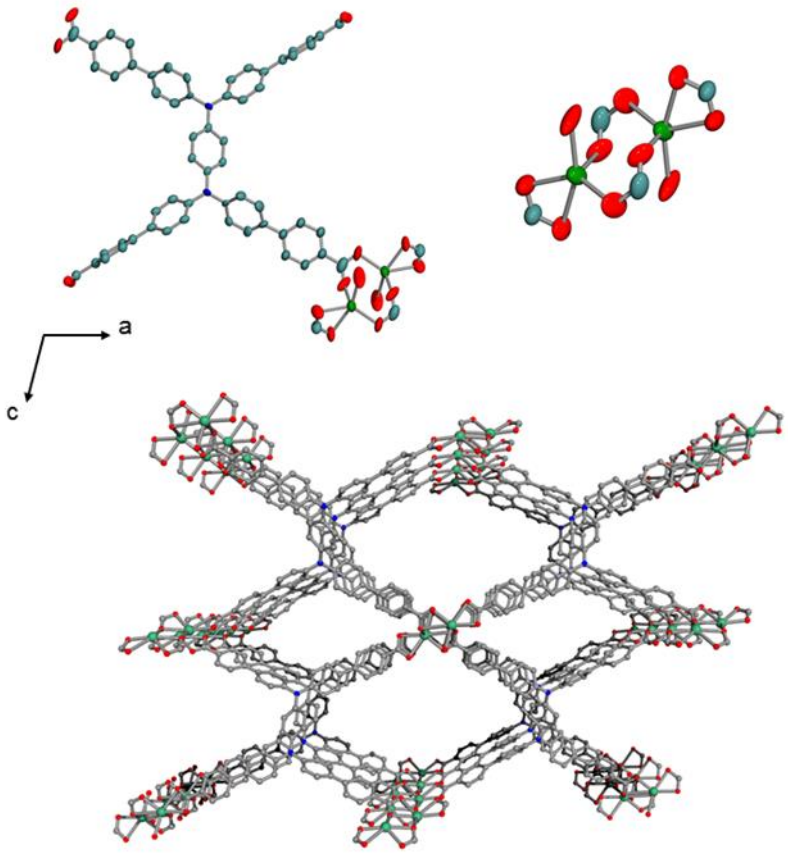

Figure 80. A section of the crystal structure of $[Cd_2(TPBD)(H_2O)_4]$ and the corresponding secondary building unit (SBU, top); Assembly of the linker TPBD and the SBU in $[Cd_2(TPBD)(H_2O)_4]$ (bottom). Displacement ellipsoids are given at the 50% probability level. Hydrogen atoms have been removed, for reasons of clarity. Grey, blue, red and green spheres correspond to carbon, nitrogen, oxygen and cadmium, respectively.

Table 9. Crystal structure data of $[Cd_2(TPBD)(H_2O)_2] \cdot 2DMF \cdot 2H_2O$

Compound	**$[Cd_2(TPBD)(H_2O)_2] \cdot 2DMF \cdot 2H_2O$**
CCDC	1910855
Formula	$C_{61}H_{44}N_3O_{11}Cd_2$
Formula weight	1219.83
Temperature (K)	293(2)
Wavelength (Å)	0.7103 (Mo-K_α)
Crystal system	Triclinic
Space group	*P*-1
Z	2
a (Å)	11.072(10)
b (Å)	11.414(10)
c (Å)	22.31(2)
α (°)	91.12(4)
β (°)	92.52(7)
γ (°)	93.32(4)
Volume (Å^3)	2811.5
μ (mm^{-1})	0.819
d_{calc} (g/cm^3)	1.441
F (000)	1132
Crystal size (mm^3)	0.062 x 0.096 x 0.159
Theta range	1.83° to 23.26°
Index range	-11 ≤ h ≤ 11 -12 ≤ k ≤ 12 -24 ≤ l ≤ 24
Refl. collected	15082
Independent reflections	7266 (R_{int} = 0.1408)
Data/restraints/parameters	7266 / 349 / 804
GOF on F^2	0.972
R_1/wR_2[a]	0.0955 / 0.2665
[I ≥ 2σ(I)][b]	
R_1/wR_2	0.2001 / 0.3306
[all data]	
Largest diff. peak and hole	2.099 and -0.784 eÅ^{-3}

a: $w = 1/[\sigma^2(F_o^2) + (0.20000P)^2]$ where $P = (F_o^2 + 2F_c^2)/3$

b: $R_1 = \sum||F_o|-|F_c||/\sum|F_o|$; $wR_2 = \{\sum[w(F_o^2 - F_c^2)^2]/\sum[w(F_o^2)^2]\}^{1/2}$

Crystals of $[Cd_2(TPBD)(H_2O)_4]$ grow as tiny light yellow plates and were used for SCXRD analysis directly from the reaction solution. The very small and thin crystallizes of the 3D Cd-MOF tend to form overlapping single-crystals with more than one domain, which complicated the structure analysis considerable. Also, upon cooling of the material to 100 K significant decomposition of the crystalline sample and the formation of side-phases or possible twinning was observed. The material thus was measured at room-temperature to circumvent the above problems. By using a small and thin plate in the approximate size of 0.062 x 0.096 x 0.159 it was able to solve and refine the collected data to a

reasonable good structure model (R_1/wR_2 = 0.0955 / 0.2665). Due to the size of the used crystals, it showed only low diffraction with a resolution of 23.26 ° (sin(Θ)/λ = 0.5556) even using high intensity X-ray radiation (Mo TXS rotating anode source) and long exposure time (60 s/frame). The small resolution was accessed during refinement of the collected and reduced data by the SHELX *SHEL* command. Furthermore, the biphenyl carboxy groups showed great disordering and consequently the disordered phenyl groups were restrained to lie in a common plane by SHELX *FLAT* and the total site population was constrained to one. Molecular geometries of the disordered compounds were restrained to be similar using SHELX *SAME* commands and the U_{ij} of neighboring atoms were restrained to be similar by SHELX *SIMU*. In total, 349 restraints had been used in disorder modeling. X-ray intensity data were collected at 293(2)K using a Bruker D8 Venture diffractometer equipped with a Helios optic monochromator, a Photon 100 CMOS detector and a Mo TXS rotating anode source (Mo-K_α radiation). The raw area detector data frames were reduced and corrected for absorption effects using the SAINT and SADABS programs with multi-scan absorption correction. Final unit cell parameters were determined by least-squares refinement of 7266 independent reflections take from the data sets. The structure was solved by intrinsic phasing with SHELXT. Difference Fourier calculations and full-matrix least-squares refinement against F^2 were performed by SHELXL-2014/7 (Sheldrick, 2014). The compound crystallizes in the triclinic crystal system in the space group *P*-1. The asymmetric unit consists of one molecule TPBD and two cadmium atoms. All non-hydrogen atoms were refined with anisotropic displacement parameters. Hydrogen atoms could not be located in the Fourier difference maps and were calculated in ideal positions using a riding model (d(C-H) = 0.95 Å, $U_{iso}(H) = 1.2U_{eq}(C)$). The unit cell contains 3 molecules of dimethylformamide from the crystallization process. The disordered solvent molecules could not properly be refined and were treated as diffuse contribution to the overall scattering without specific positions using the SQUEEZE routine of PLATON (solvent accessible volume (SAV) = 553 $Å^3$, electrons found in SAV = 133). The largest residual electron density peak in the final difference map is 2.099 e/ $Å^3$ and is located in vicinity of the Cd1 atom, which either is due to abort effects of the Fourier series near the heavy atom or unaccounted

twinning. Checking the crystal data by the PLATON Twin-Rot-Mat procedure did not give any signs for twinning. Furthermore, detailed analysis of the collected raw-data did not show any indications, however, due to the low intensity signals for reflections at higher resolutions we a twinned structure fraction cannot fully be excluded.

5.2.13 [Cd_2(TPBD)(DMF)]

$Cd(NO_3)_2 \cdot 4H_2O$ (6.90 mg, 0.0223 mmol, 2 equiv.) and H_4TPBD (10.0 mg, 0.0111 mmol, 1 equiv.) were dissolved in 1 mL dimethylformamide (DMF) and 0.5 mL EtOH in a 4 mL glass vial by ultrasonication (10 min). The bright green reaction mixture was heated to 100 °C for 48 h and subsequently cooled to room temperature with a rate of 0.2 K/min. Bright yellow cubic crystals were obtained besides polycrystalline powder, as inspected by eye under microscope. The material was suitable for SCXRD analysis. Various other experiments with the aim to reproduce the material failed. Note that [Cd_2(TPBD)(DMF)] is a solvate structure of [Cd_2(TPBD)(H_2O)$_4$].

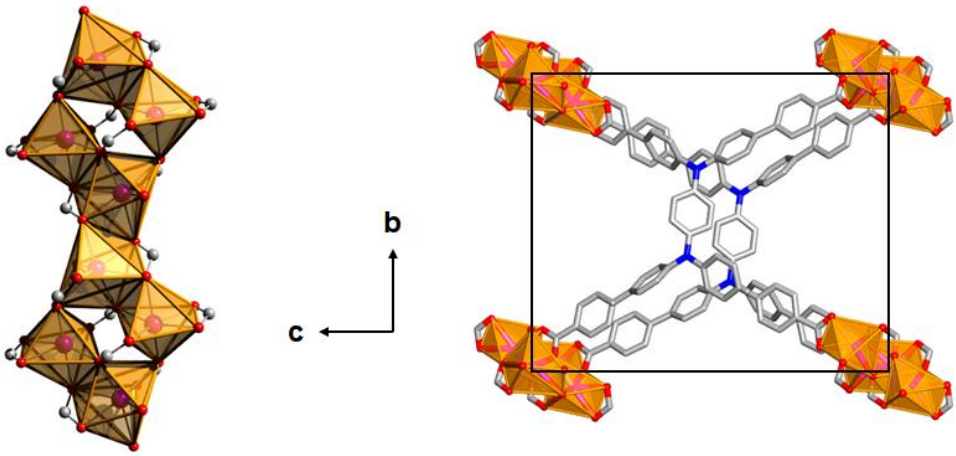

Figure 81. A section of the crystal structure of [Cd_2(TPBD)(DMF)] and the corresponding secondary rod building unit (SBU, left); Assembly of the linker TPBD and the SBU in [Cd_2(TPBD)(DMF)] (right). Hydrogen atoms have been removed, for reasons of clarity. Grey, blue, red and purple spheres correspond to carbon, nitrogen, oxygen and cadmium, respectively.

Table 10. Crystal structure data of [Cd_2(TPBD)(DMF)].

Compound	**[Cd_2(TPBD)(DMF)]**
Formula	$C_{61}H_{41}O_9N_3Cd_2$
Formula weight	1168.77
Temperature (K)	296(2)
Wavelength (Å)	0.7103 (Mo-K_α)
Crystal system	Triclinic
Space group	*P*-1
Z	2
a (Å)	9.7803(1)
b (Å)	17.9362(1)
c (Å)	21.2134(2)
α (°)	89.575(4)
β (°)	86.320(7)
γ (°)	79.169(4)
Volume (Å^3)	3721.5
μ (mm^{-1})	0.624
d_{calc} (g/cm^3)	1.062
F (000)	1132
Crystal size (mm^3)	0.205 x 0.365 x 0.159
Theta range	2.45 to 25.35°
Index range	-11 ≤ h ≤ 11
	-21 ≤ k ≤ 21
	-24 ≤ l ≤ 24
Refl. collected	12583
Independent reflections	8592 (R_{int} = 0.1021)
Data/restraints/parameters	8592 / 0 / 677
GOF on F^2	1.604
R_1/wR_2[a]	0.0720 / 0.2373
[I ≥ 2σ(I)][b]	
R_1/wR_2	0.1009 / 0.2567
[all data]	
Largest diff. peak and hole	3.030 and -0.078 eÅ^{-3}

a: $w = 1/[\sigma^2(F_o^2) + (0.10000P)^2]$ where $P = (F_o^2 + 2F_c^2)/3$

b: $R_1 = \sum||F_o|-|F_c||/\sum|F_o|$; $wR_2 = \{\sum[w(F_o^2 - F_c^2)^2]/\sum[w(F_o^2)^2]\}^{1/2}$

Single crystals of [Cd_2(TPBD)(DMF)] suitable for SCXRD were directly taken from the reaction solutions. The crystals grow as clear, bright-yellow blocks with defined facets with an approximately size of 0.205 x 0.365 x 0.159 mm. X-ray intensity data were collected at 296(2)K using a Bruker D8 Venture diffractometer equipped with a Helios optic monochromator, a Photon 100 CMOS detector and a Mo TXS rotating anode source (Mo-K_α radiation). The raw area detector data frames were reduced and corrected for absorption effects using the SAINT and SADABS programs with multi-scan absorption correction. Final unit cell parameters were determined by least-squares refinement of 8592

independent reflections taken from the data sets. The structure was solved by intrinsic phasing with SHELXT. Difference Fourier calculations and full-matrix least-squares refinement against F^2 were performed by SHELXL-2014/7 (Sheldrick, 2014).

The compound crystallizes in the triclinic crystal system. The asymmetric unit consists of two crystallographic independent cadmium atoms, molecule fragment of TPBD and one molecule dimethylformamide (DMF). All non-hydrogen atoms were refined with anisotropic displacement parameters. Hydrogen atoms could not be located in the Fourier difference maps and were calculated in ideal positions using a riding model (d(C-H) = 0.95 Å, U_{iso}(H) = 1.2U_{eq}(C)). Disordered solvent molecules could not properly be refined and were treated as diffuse contribution to the overall scattering without specific positions using the SQUEEZE routine of PLATON (solvent accessible volume (SAV) = 730 Å^3, electrons found in SAV = 186). The largest residual electron density peak in the final difference map is 3.030 e/Å^3.

5.2.14 [Zn_2(TPBD)(DMF)$_2$(Tol)]

$Zn(NO_3)_2 \cdot 4H_2O$ (13.3 mg, 0.050 mmol, 5 equiv.) was dissolved in a mixture of 3 mL MeOH and toluene (3 mL). Furthermore, H_4TPBD (10.0 mg, 0.0100 mmol, 1 equiv.) was dissolved in a mixture of 2 mL dimethylformamide (DMF) and 5 mL of MeOH. Subsequently, the H_4TPBD solution was smoothly overlaid with the $Zn(NO_3)_2$ solution in a small, thin Schlenk tube (0.8 cm diameter) and the solutions were allowed to diffuse to each other over the period of 6 months. It turned out that small, clear yellow blocks formed, which were suitable for SCXRD analysis. However, the small amount of formed material and the long time-frame of the reaction hampered the reproducibility of the material. Please note, that [Zn_2(TPBD)(DMF)$_2$(Tol)] is a solvate of [Zn_2(TPBD)(DMAc)$_2$].

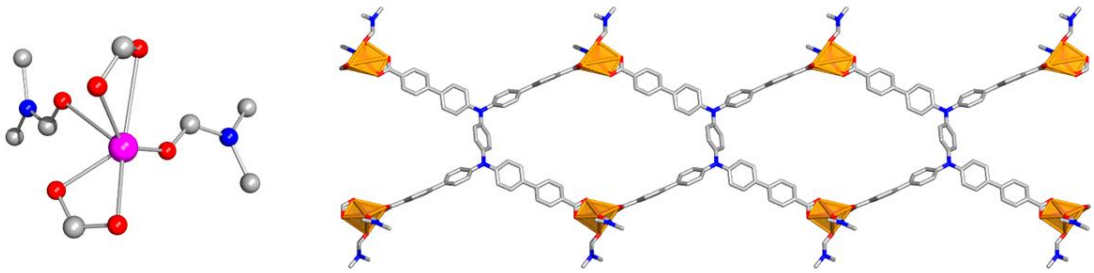

Figure 82. A section of the crystal structure of [Zn_2(TPBD)(DMF)$_2$(Tol)] and the corresponding secondary rod building unit (SBU, left); Assembly of the linker TPBD and the SBU in [Zn_2(TPBD)(DMF)$_2$(Tol)] (right). Hydrogen atoms have been removed, for reasons of clarity. Grey, blue, red and purple spheres correspond to carbon, nitrogen, oxygen and zinc, respectively.

Table 11. Crystal structure data of $[Zn_2(TPBD)(DMF)_2(Tol)]$

Compound	**$[Zn_2(TPBD)(DMF)_2(Tol)]$**
Formula	$C_{42}N_4O_7H_{44}Zn$
Formula weight	738.18
Temperature (K)	100(2)
Wavelength (Å)	0.7103 (Mo-K_α)
Crystal system	monoclinic
Space group	*P*-1
Z	4
a (Å)	22.6786(8)
b (Å)	9.4544(14)
c (Å)	18.6152(6)
α (°)	90
β (°)	102.8630(10)
γ (°)	90
Volume ($Å^3$)	3891.2(2)
μ (mm^{-1})	0.674
d_{calc} (g/cm^3)	1.260
F (000)	1548
Crystal size (mm^3)	0.065 x 0.251 x 0.159
Theta range	2.343° to 25.34°
Index range	-26 ≤ h ≤ 27
	-11 ≤ k ≤ 9
	-22 ≤ l ≤ 18
Refl. collected	23767
Independent reflections	7056 (R_{int} = 0.1408)
Data/restraints/parameters	7056 / 0 / 487
GOF on F^2	1.058
R_1/wR_2[a]	0.0300 / 0.0721
[I ≥ 2σ(I)][b]	
R_1/wR_2	0.0392 / 0.0768
[all data]	
Largest diff. peak and hole	0.365 and -0.385 eÅ^{-3}

a: $w = 1/[\sigma^2(F_o^2) + (0.10000P)^2]$ where $P = (F_o^2 + 2F_c^2)/3$

b: $R_1 = \sum||F_o|-|F_c||/\sum|F_o|$; $wR_2 = \{\sum[w(F_o^2 - F_c^2)^2]/\sum[w(F_o^2)^2]\}^{1/2}$

Single crystals of $[Zn_2(TPBD)(DMF)_2(Tol)]$ suitable for SCXRD were directly taken from the reaction solutions. The crystals grow as clear, bright-yellow plates with defined facets with an approximately size of 0.065 x 0.251 x 0.159 mm. X-ray intensity data were collected at 100(2)K using a Bruker D8 Venture diffractometer equipped with a Helios optic monochromator, a Photon 100 CMOS detector and a Mo TXS rotating anode source (Mo-K_α radiation). The raw area detector data frames were reduced and corrected for absorption effects using the SAINT and SADABS programs with multi-scan absorption correction. Final unit cell parameters were determined by least-squares refinement of 7056

independent reflections take from the data sets. The structure was solved by intrinsic phasing with SHELXT. Difference Fourier calculations and full-matrix least-squares refinement against F^2 were performed by SHELXL-2014/7 (Sheldrick, 2014).

The compound crystallizes in the monoclinic crystal system. The pattern of systematic absences in the intensity data was consistent with the $P2_1/c$ space group, which was confirmed by structure solution. The asymmetric unit consists of one crystallographic independent zinc atom, a bisected molecule fragment of TPBD ($C_{17}H_{18}O_4N$ specimen) three molecules dimethylformamide (DMF) and one molecule toluene. All non-hydrogen atoms were refined with anisotropic displacement parameters. Hydrogen atoms could not be located in the Fourier difference maps and were calculated in ideal positions using a riding model (d(C-H) = 0.95 Å, $U_{iso}(H) = 1.2U_{eq}(C)$). The largest residual electron density peak in the final difference map is 0.365 e/ Å^3.

5.2.15 [$Zr_6O_4(OH)_4(TPBD)_3$]

$ZrCl_4$ (26.1 mg, 0.111 mmol, 1.0 equiv.) and 614 mg benzoic acid (6.71 mmol, 45 equiv.) were dissolved in 5 mL dry dimethylformamide. The reaction mixture was reacted at 100 °C for 2 h and subsequently cooled to room temperature. 20 mg of H_4TPBD (0.022 mmol, 0.2 equiv.) in 3 mL dimethylformamide is put to the reaction mixture and further reacted at 100 °C for 24 h. Bright, yellow cubic crystals were collected via filtration and subsequently washed with DMF (3 x 20 mL) to give [$Zr_6O_4(OH)_4(TPBD)_3$] (25 mg, 31 % yield calculated on H_4TPBD). Elemental Analysis (%) calc. for ($C_{174}H_{112}N_6O_{32}Zr_6$) · 8 CH_2Cl_2: C 54.5 H 3.04 N 2.08; found C 54.4 H 3.21 N 2.09. (Note that EA was conducted on washed and solvent-exchanged material, to ensure no impurities of inorganic and organic rest chemicals).

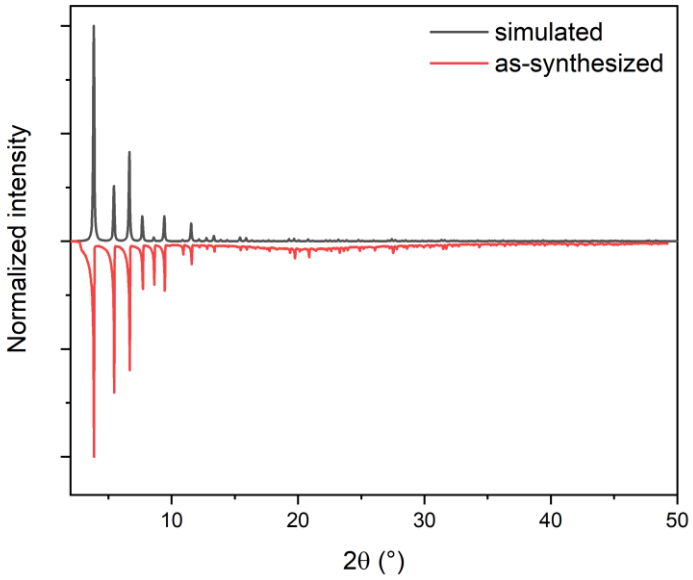

Figure 83. Simulated and as-synthesized PXRD data of $[Zr_6O_4(OH)_4(TPBD)_3]$ in a range of 2° to 50°.

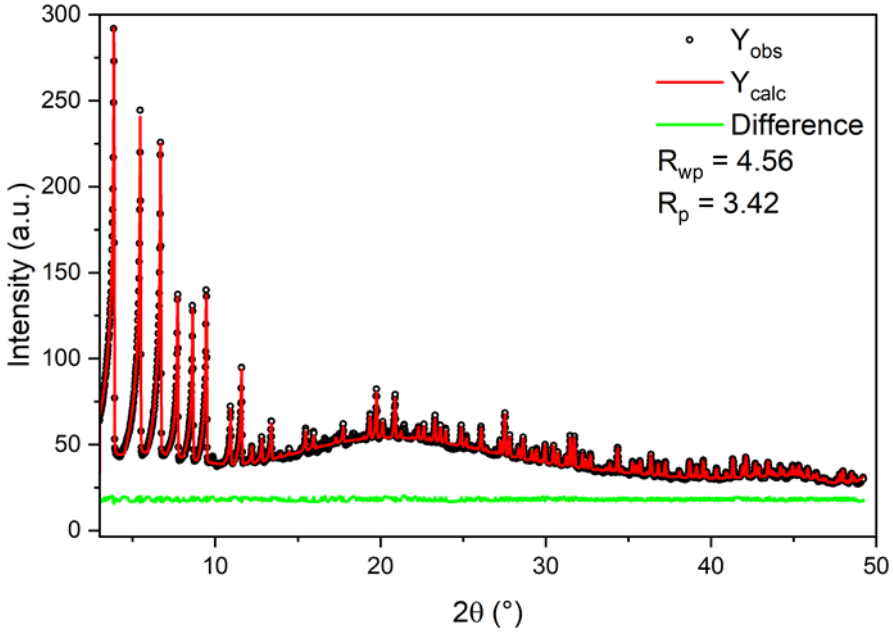

Figure 84. Pawley refinement of $[Zr_6O_4(OH)_4(TPBD)_3]$ in a range of 3° to 50°.

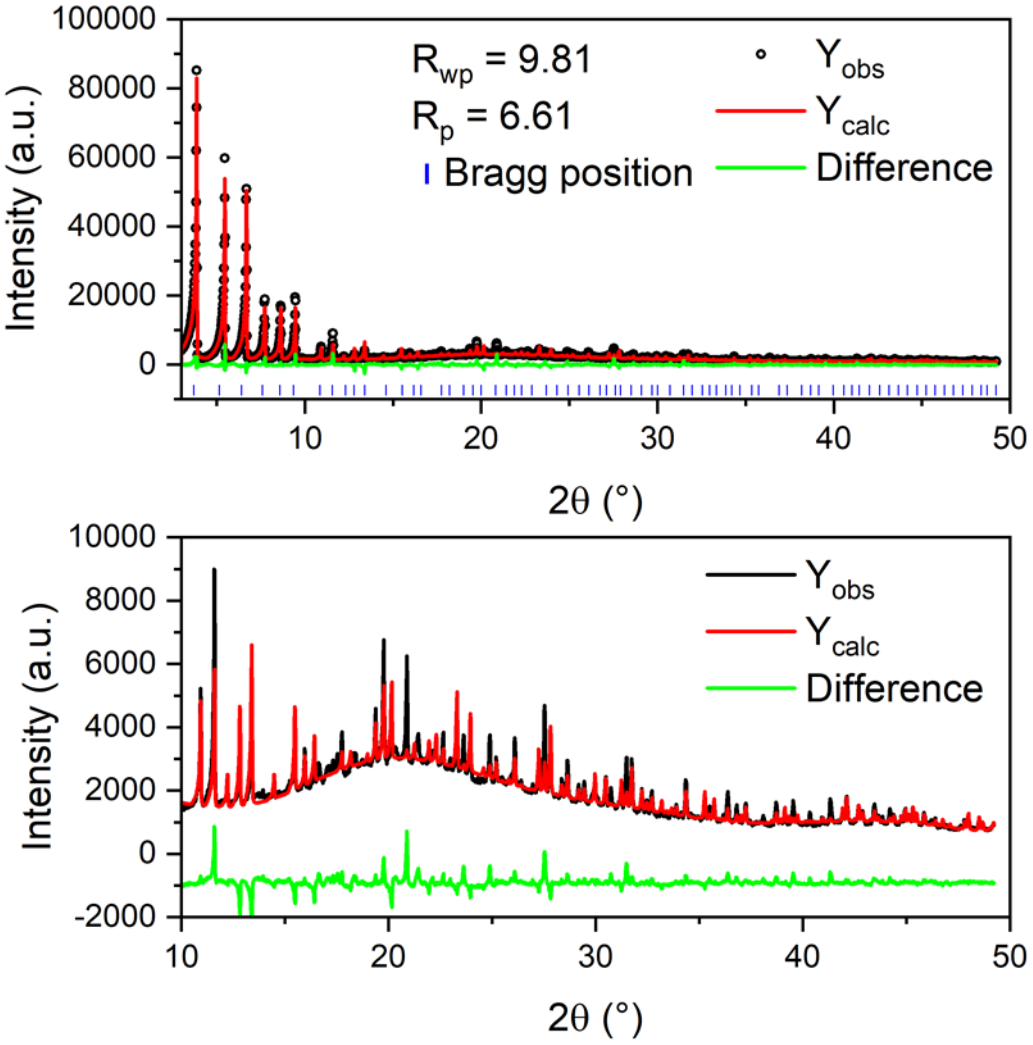

Figure 85. Rietveld refinement of $[Zr_6O_4(OH)_4(TPBD)_3]$ in a range of 3° to 50° (upper panel) and a zoom in to the 10°-50° region (lower panel).

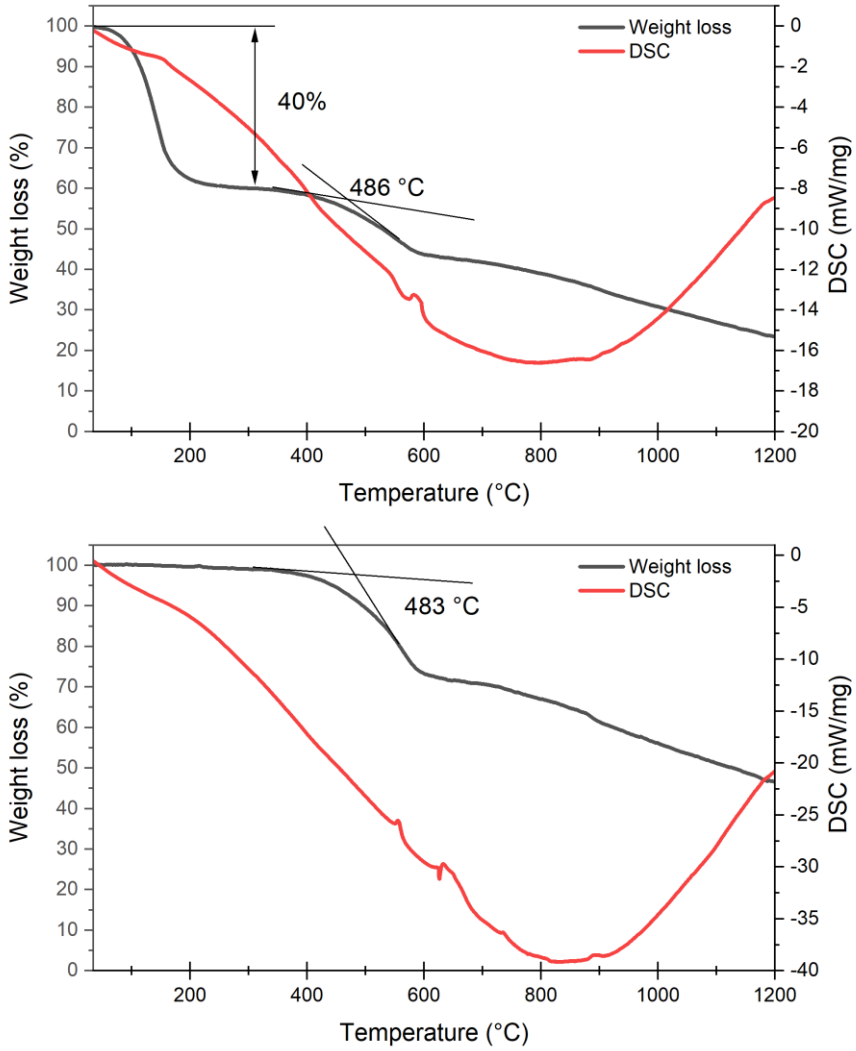

Figure 86. TGA traces of $[Zr_6O_4(OH)_4(TPBD)_3]$ in a range of 35 °C to 1200 °C.

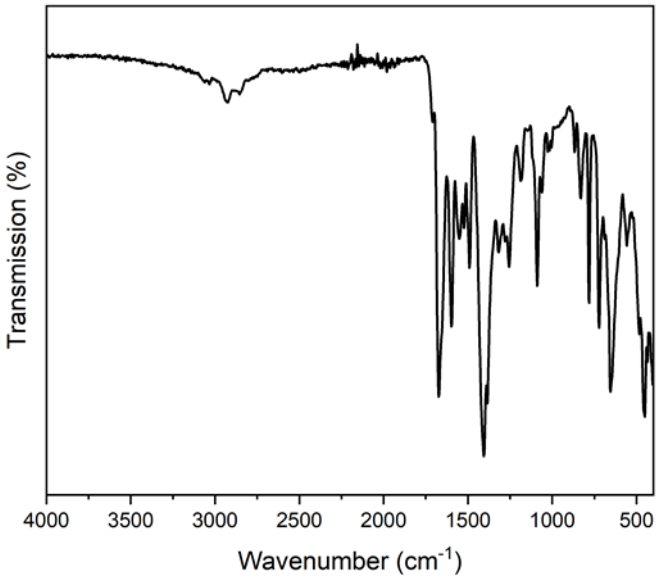

Figure 87. IR-spectra of $[Zr_6O_4(OH)_4(TPBD)_3]$ (as-synthesized).

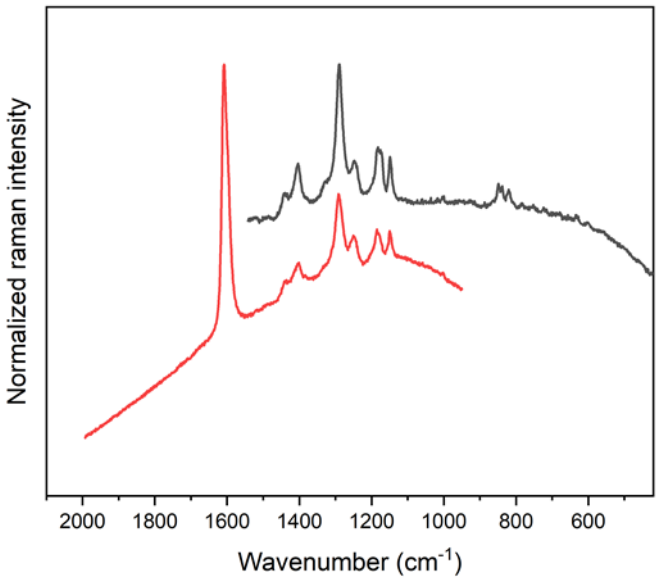

Figure 88. Raman spectra of $[Zr_6O_4(OH)_4(TPBD)_3]$ (as-synthesized).

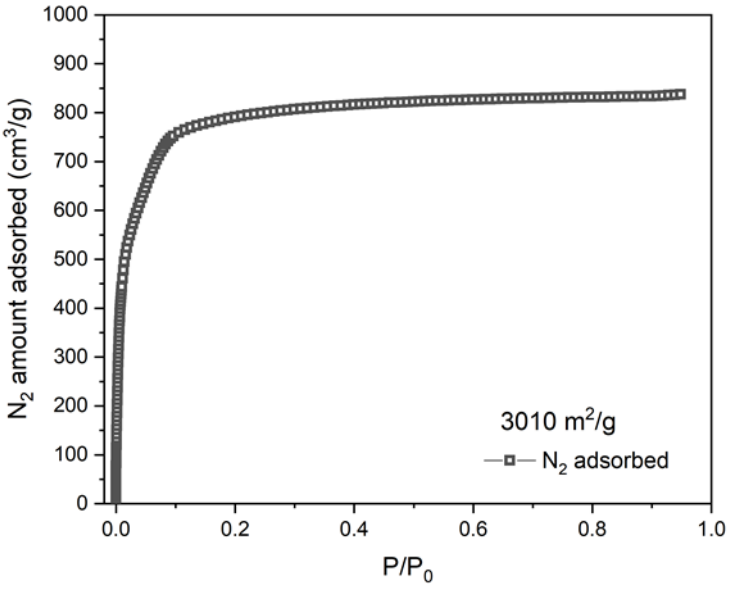

Figure 89. N_2 adsorption isotherm of activated $[Zr_6O_4(OH)_4(TPBD)_3]$.

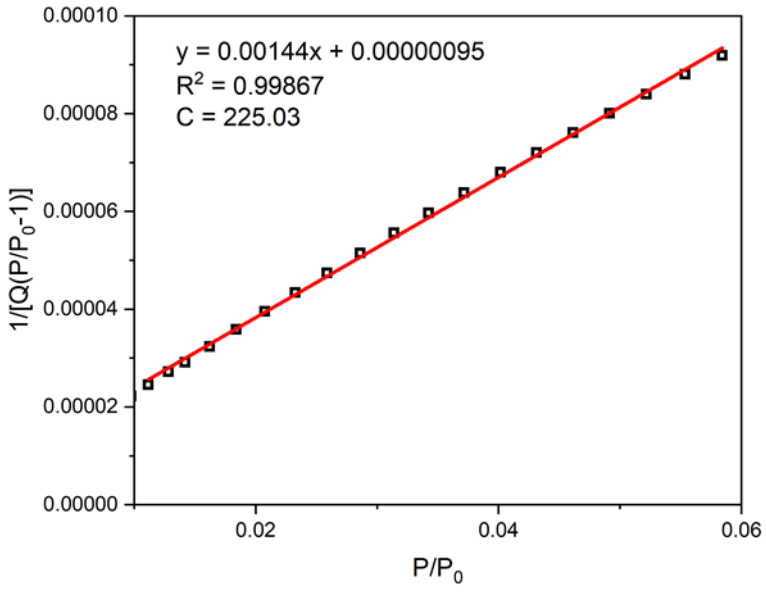

Figure 90. BET surface area plot of activated $[Zr_6O_4(OH)_4(TPBD)_3]$.

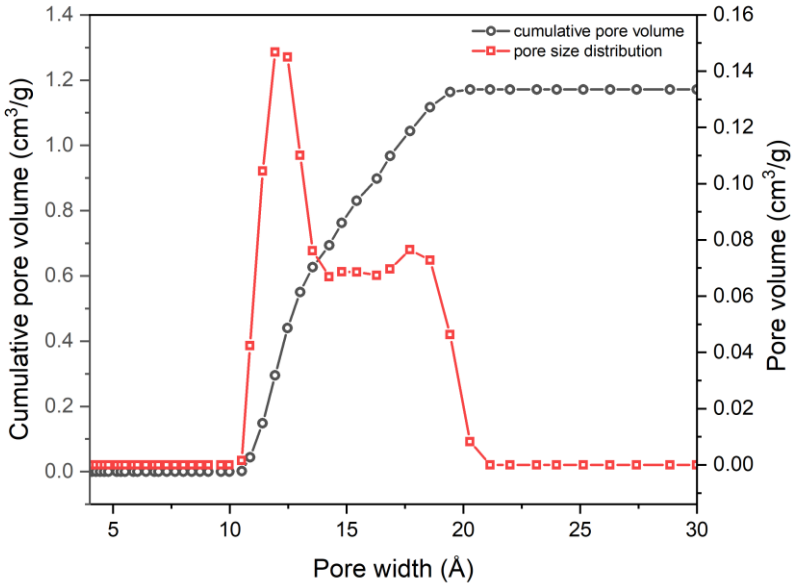

Figure 91. Pore size distribution and cumulative pore volume of $[Zr_6O_4(OH)_4(TPBD)_3]$.

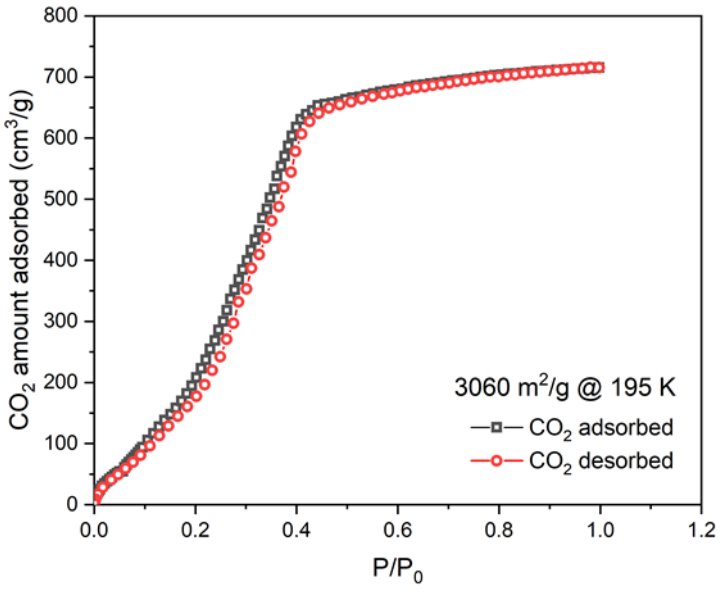

Figure 92. CO_2 adsorption and desorption isotherm of activated $[Zr_6O_4(OH)_4(TPBD)_3]$.

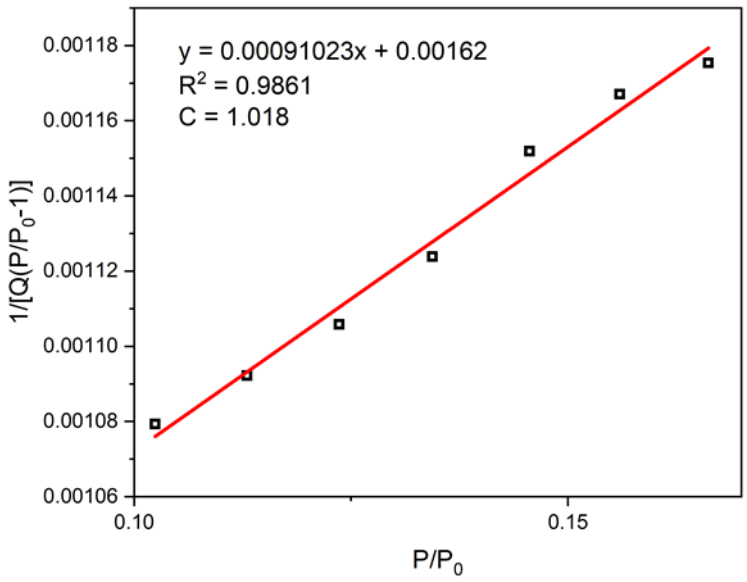

Figure 93. BET surface area plot of activated $[Zr_6O_4(OH)_4(TPBD)_3]$.

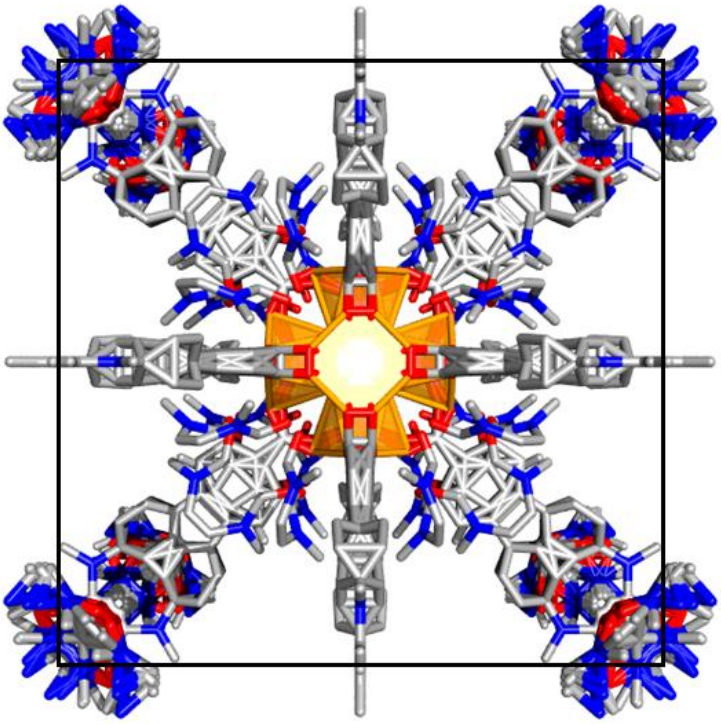

Figure 94. Results of the Rietveld refinement. Structure of $[Zr_6O_4(OH)_4(TPBD)_3]$ in cubic space group.

Table 12. Crystal data of $[Zr_6O_4(OH)_4(TPBD)_3]$ x 2 DMF.

Compound	**$[Zr_6O_4(OH)_4(TPBD)_3]$ x 2 DMF**
Formula	$C_{174}H_{112}N_6O_{32}Zr_6\,(C_3H_7NO)_2$
Formula weight	3345.2
Temperature (K)	295
Wavelength (Å)	1.54056 (Cu-K_α)
Crystal system	cubic
Space group	*Pm-3m*
a (Å)	22.8928
b (Å)	22.8928
c (Å)	22.8928
α (°)	90
β (°)	90
γ (°)	90
Volume (Å^3)	11997.76
2-Theta range	3.86° to 48.5°

Zr1	6	0.5 0.5 0.5	1
O1	8	0.54898 0.54898 0.54898	1
O2	48	1.410528 -0.332588 0.477814	0.25
O3	48	1.354012 -0.416667 0.479768	0.25
N1	24	1.0 -0.122502 0.500078	0.5
C1	24	1.0 -0.060557 0.500078	0.5
C2	48	1.052511 -0.03024 0.500078	0.5
C3	48	1.053646 0.15363 0.500078	0.5
C4	48	1.103065 0.137591 0.531335	0.25
C5	48	1.153323 0.171349 0.52801	0.25
C6	48	1.154162 0.221147 0.493426	0.25
C7	48	1.104742 0.237187 0.462169	0.25
C8	48	1.054485 0.203428 0.465494	0.25
C9	48	1.204419 0.254906 0.490101	0.25
C10	48	1.200235 0.315345 0.48762	0.25
C11	48	1.250492 0.349104 0.484295	0.25
C12	48	1.304935 0.322423 0.48344	0.25
C13	48	1.30912 0.261984 0.4859299	0.25
C14	48	1.258862 0.228225 0.489255	0.25
C15	48	1.358198 0.3582 0.479924	0.5
C1a	48	-0.09756979 0.05000121 -0.05332722	0.1514497
C2a	48	-0.107932 -0.06009719 -0.0805108	0.1514497
C3a	48	-0.1766319 -0.01612338 -0.004905031	0.1514497
N1a	48	-0.1278365 -0.009643496 -0.04613877	0.1514497
O1a	48	-0.1141839 0.0921146 -0.0246371	0.1514497
C1b	48	-0.3237143 0.2583083 0.3748763	0.3959126
C2b	48	-0.2304518 0.1934338 0.3670411	0.3959126
C3b	48	-0.31638 0.1578723 0.428044	0.3959126
N1b	48	-0.2896662 0.2023571 0.3902196	0.3959126
O1b	48	-0.3731401 0.2657565 0.3942232	0.3959126

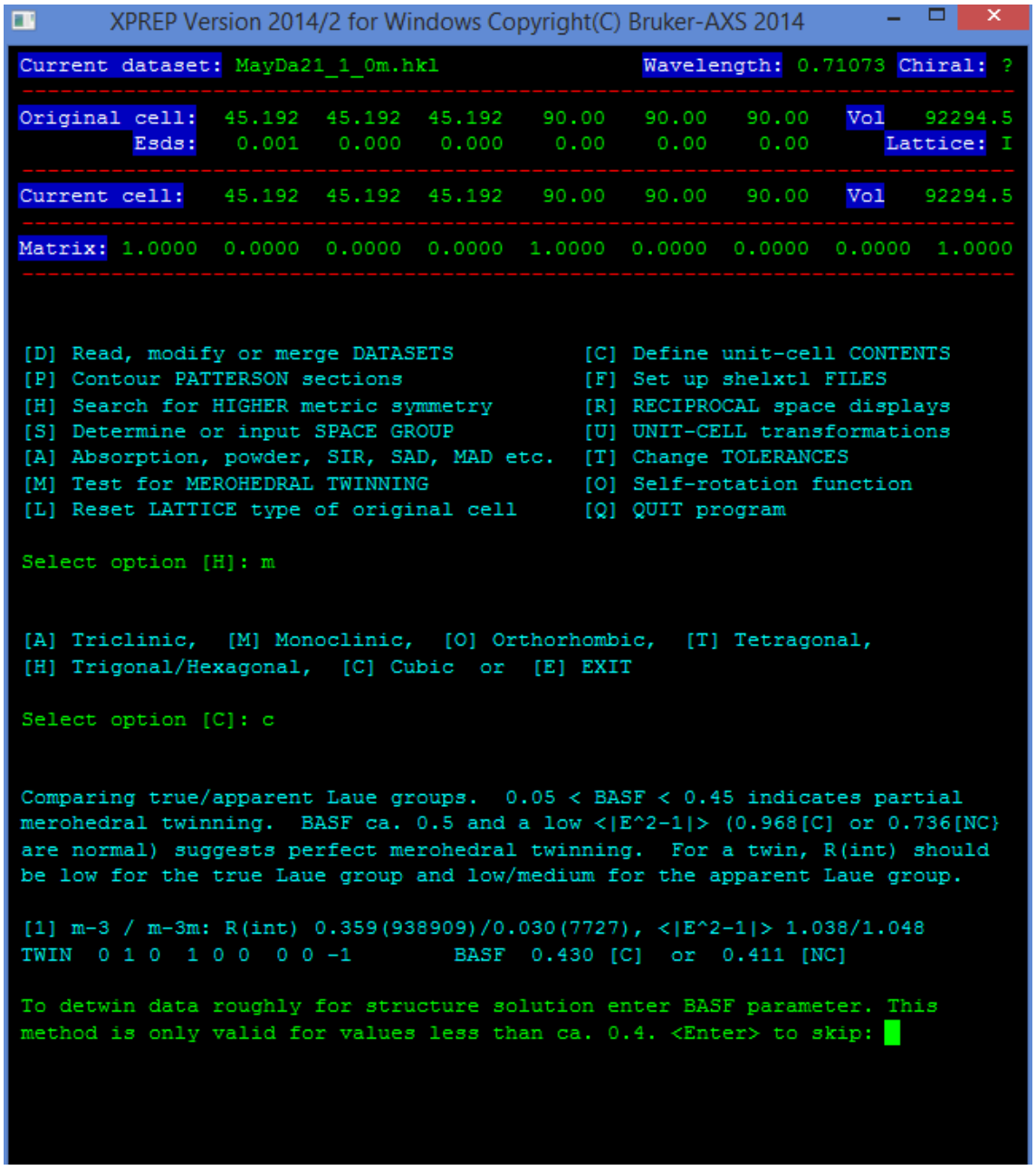

Figure 95. Output of XPREP checking for merohedral twinning option of SCXRD data of $[Zr_6O_4(OH)_4(TPBD)_3]$.

5.2.16 [Zn_2(TCPE)(bpy)]

$Zn(NO_3)_2 \cdot 4H_2O$ (10.5 mg, 0.04 mmol, 1.00 equiv.) and 16.3 mg H_4TCPE (0.019 mmol, 4.75 eqivl.) are dissolved in 2 mL of N,N-dimethylformamide (DMF) to form a light yellow clear solution in a 4 ml glass vial. 6.2 mg of 4,4-bipyridine (0.039 mmol, 9.75 equiv.) are dissolved in 0.5 mL of methanol (MeOH). The DMF solution is slowly covered with the methanolic bpy solution. The glass vials are tightly capped and handled with care to ensure the separation of the two phases. The reaction mixture is placed in an oven at 100 °C for 24h and directly transferred to the laboratory bench to be allowed to cool at room temperature after the reaction is finalized. Light yellow block crystals are collected via filtration and washed with 10 mL DMF for five times to give 21 mg of [Zn_2(TCPE)(bpy)] (yield: 20 % based on TCPE) ^{1}H-NMR (400 MHz, DCl/DMSO-d_6, 298 K) δ (ppm) = 8.97 (m, 4H, Ar-H, *4,4'-bpy*), 8.51 (m, 4H, Ar-H, *4,4'-bpy*), 7.81 (d, ^{2}J = 8.1 Hz, 8H, Ar-H, *TCPE*), 7.57 (d, ^{2}J = 8.4 Hz, 8H, Ar-H, *TCPE*), 7.41 (d, ^{2}J = 8.3 Hz, 8H, Ar-H, *TCPE*), 7.07 (d, ^{2}J = 8.3 Hz, 8H, Ar-H, *TCPE*). Elemental analysis (%) calc. for $(C_{64}H_{40}N_2O_8Zn_2)\cdot 4(C_3H_7NO)\cdot 7(C_3HO)$: C 62.17 H 5.90 N 5.06; found: C 61.39 H 5.12 N 5.80.

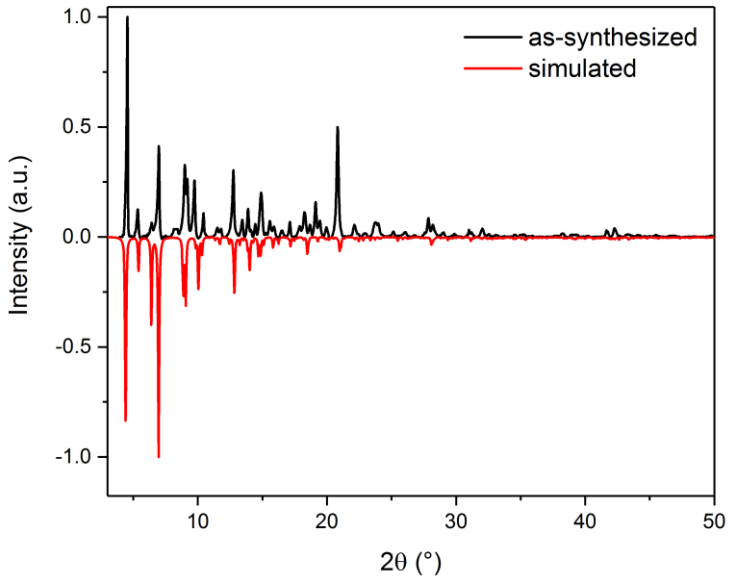

Figure 96. Simulated and as-synthesized PXRD data of [Zn_2(TCPE)(bpy)] in a range of 2° to 50°.

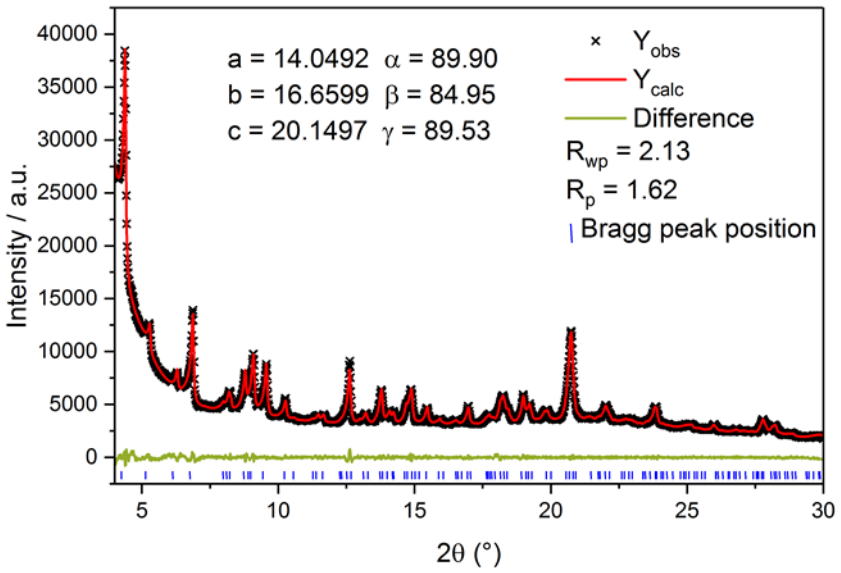

Figure 97. Pawley refinement of [Zn_2(TCPE)(bpy)] in a range of 4° to 30°.

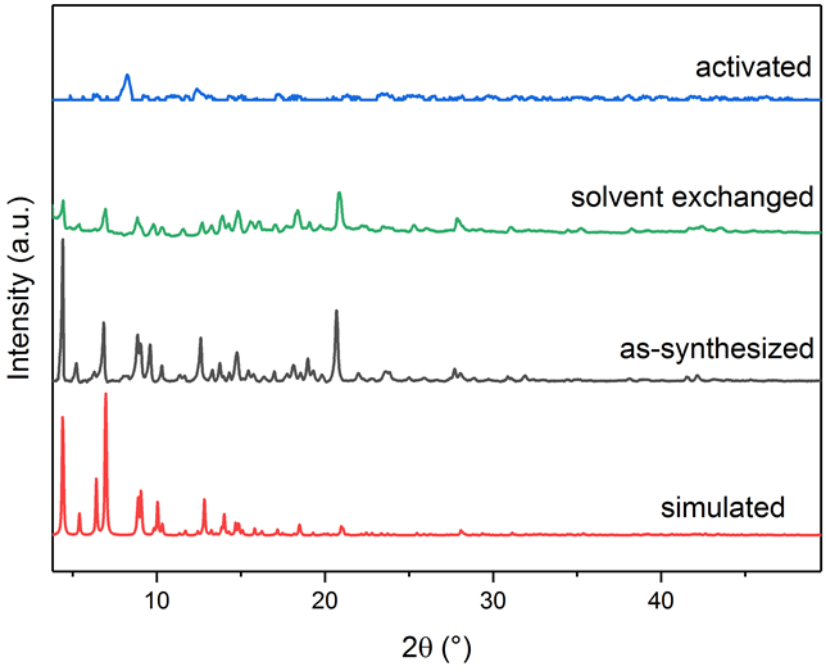

Figure 98. PXRDs of simulated, as-synthesized, solvent exchange and activated forms of [Zn_2(TCPE)(bpy)] in a range of 4° to 50°.

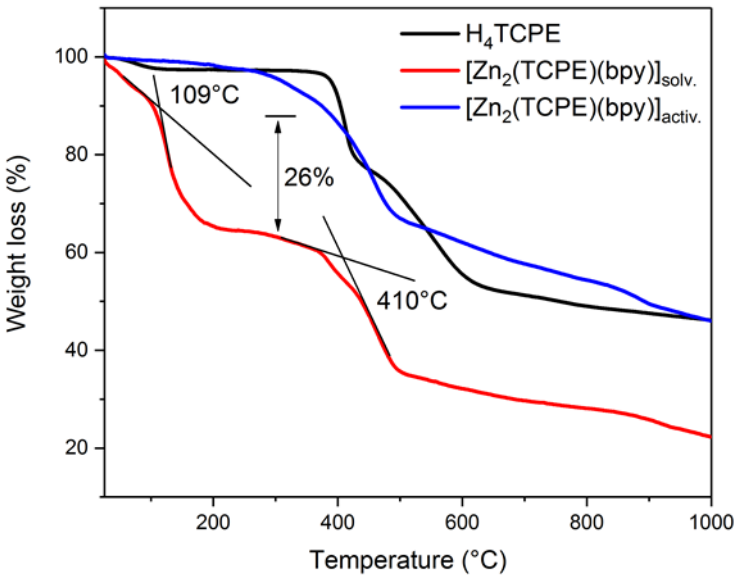

Figure 99. TGA traces of [Zn_2(TCPE)(bpy)] (as-synthesized), [Zn_2(TCPE)(bpy)] (activated) and H_4TCPE in a range of 35 °C to 1000 °C.

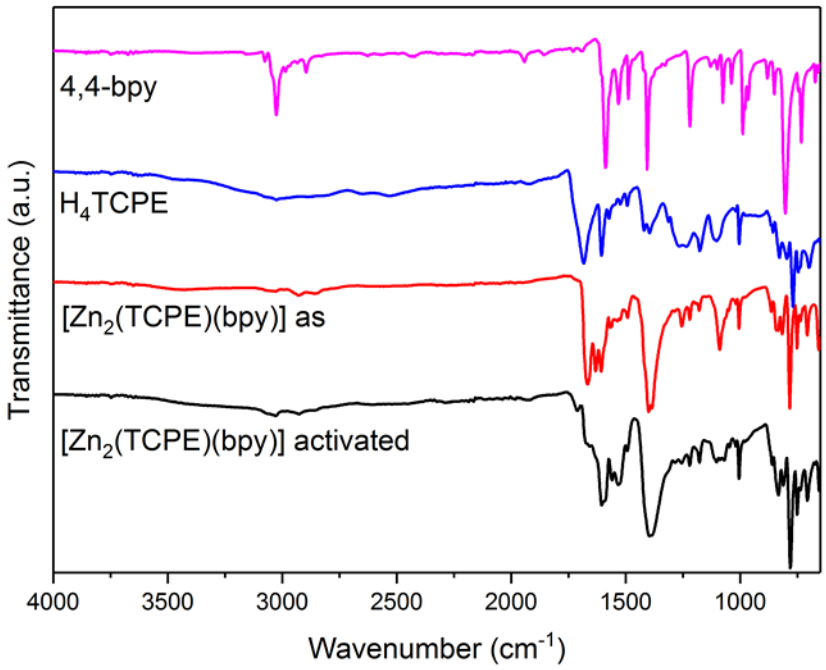

Figure 100. IR spectra of [Zn_2(TCPE)(bpy)] (as-synthesized), [Zn_2(TCPE)(bpy)] (activated), H_4TCPE and 4,4-bpy.

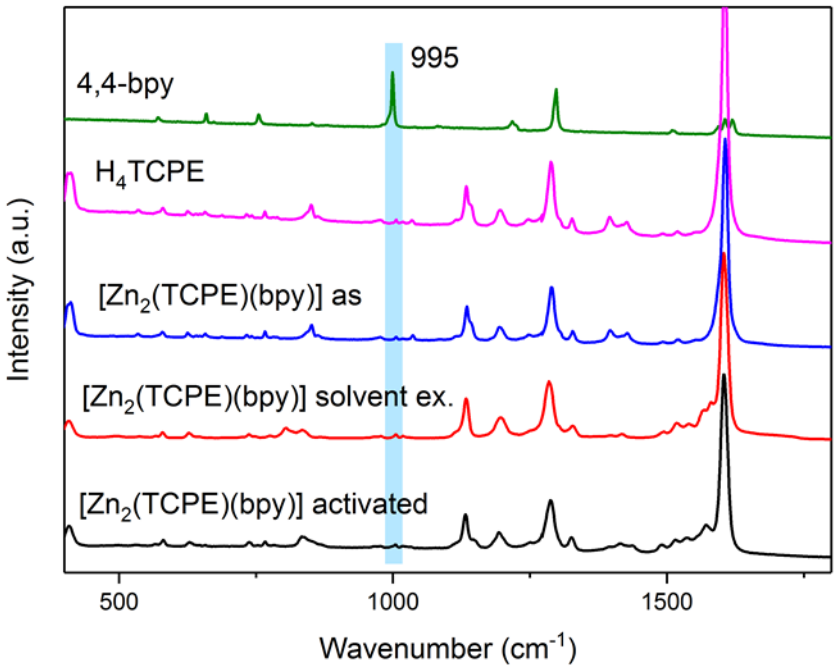

Figure 101. Raman spectra of [Zn_2(TCPE)(bpy)] (as-synthesized), [Zn_2(TCPE)(bpy)] (activated), H_4TCPE and 4,4-bpy. The blue blar indicates the characteristic A_1 ring breathing mode of pyridine.

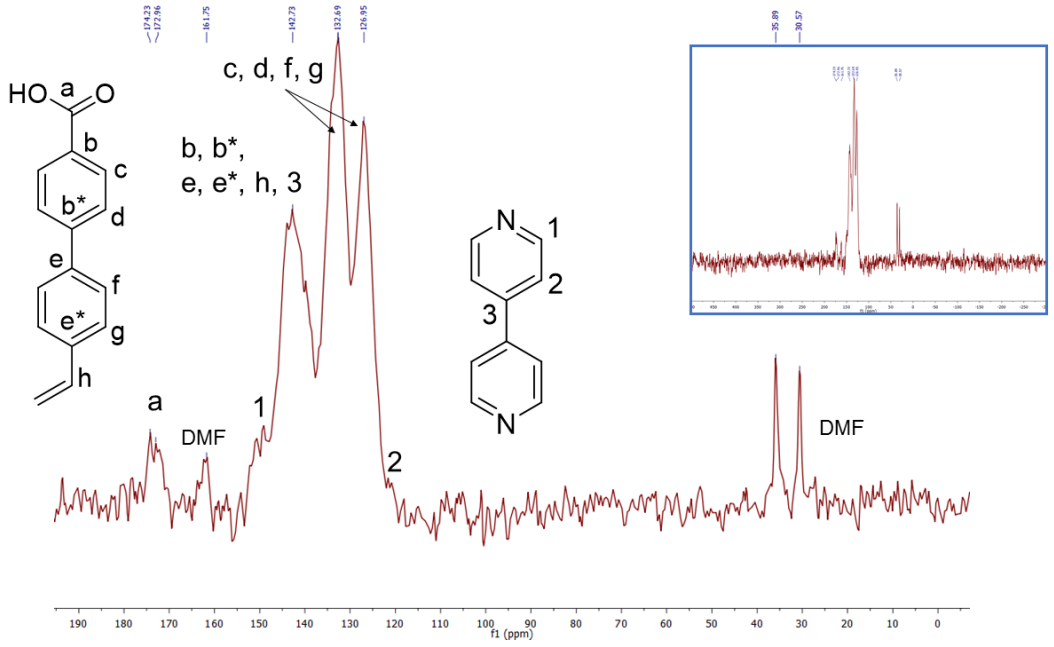

Figure 102. CP-MAS ^{13}C SS-NMR spectrum of [Zn_2(TCPE)(bpy)] (as-synthesized) and the peak assignment.

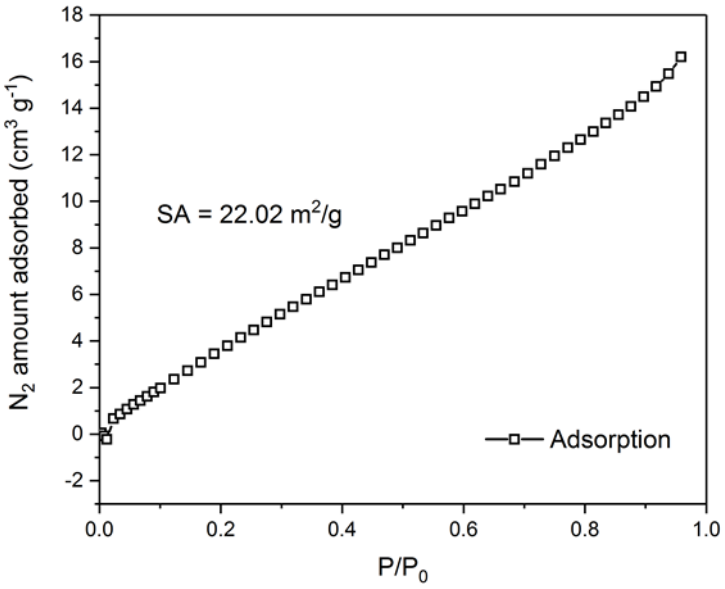

Figure 103. N_2 adsorption isotherm of [Zn_2(TCPE)(bpy)] (thermal activated and collapsed) and the respective surface area (SA).

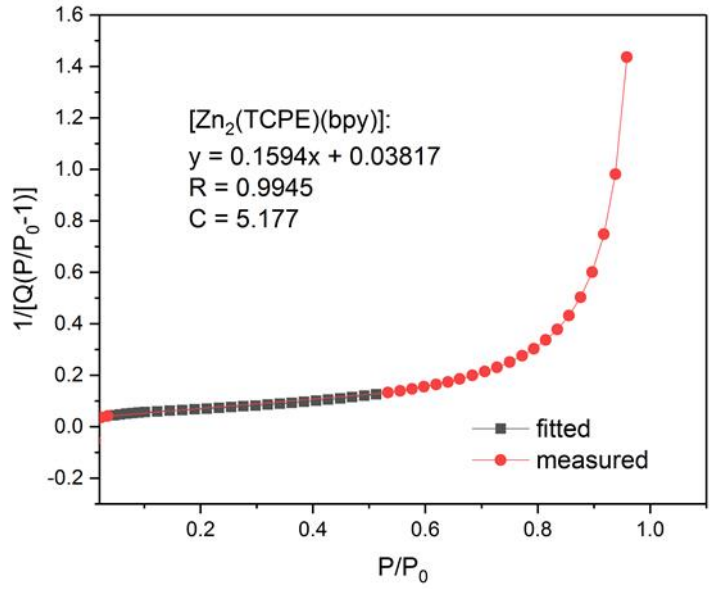

Figure 104. BET surface area plot of activated [Zn_2(TCPE)(bpy)] (measured and fitted range).

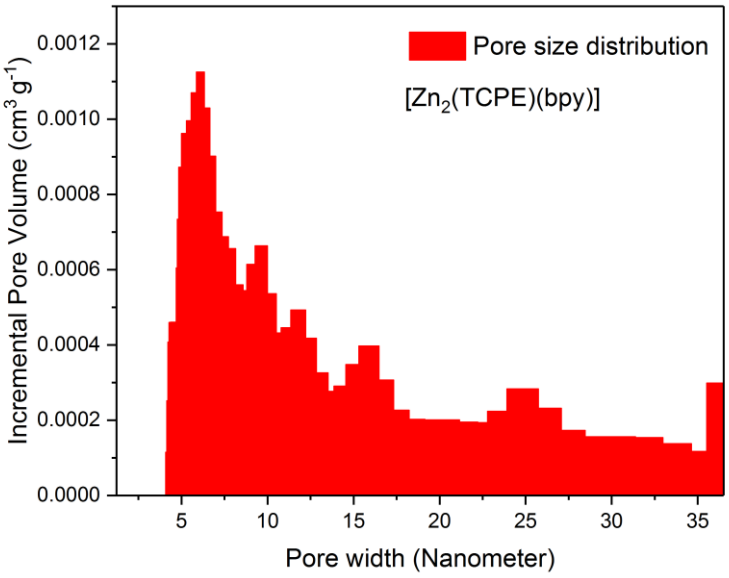

Figure 105. Pore-size distribution of activated [Zn_2(TCPE)(bpy)].

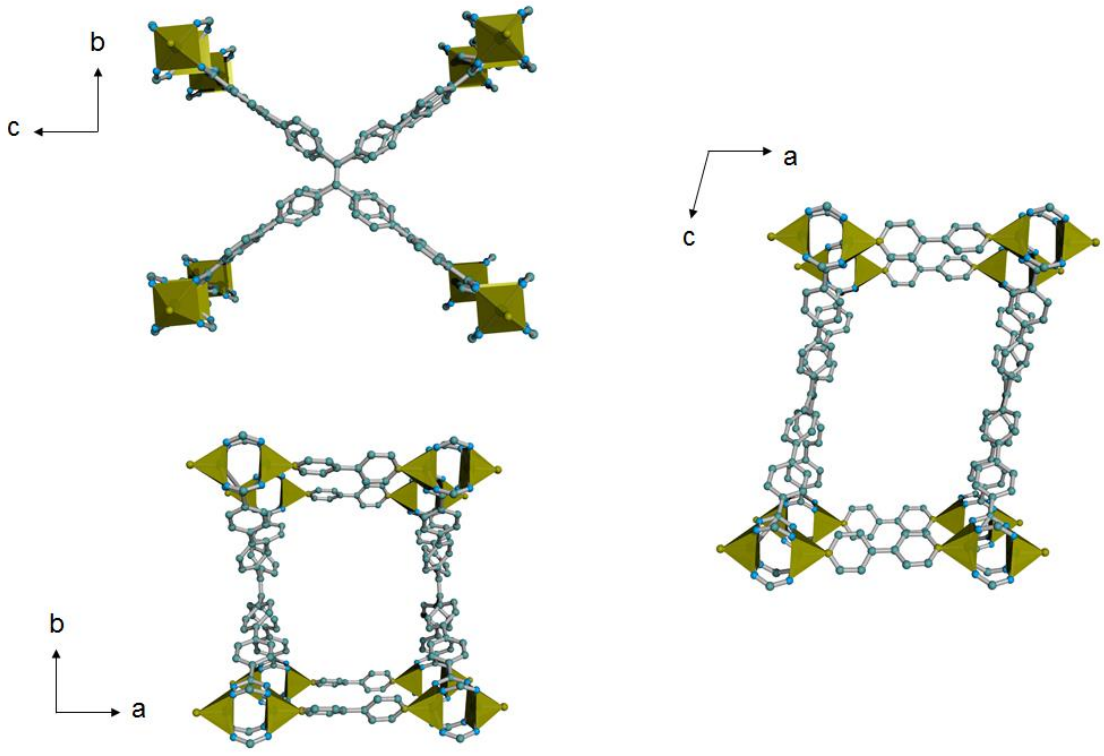

Figure 106. Single crystal structure of non-interpenetrated [Zn_2(TCPE)(bpy)]. Note that the second network and hydrogen atoms have been removed for clarity reasons (zinc = black, oxygen = blue, nitrogen = green, carbon = grey).

Table 13. Crystal structure data of $[Zn_2(TCPE)(bpy)]$

Compound	**$[Zn_2(TCPE)(bpy)]$**
Formula	$C_{64}H_{40}N_2O_8Zn_2$
Formula weight	1095.76
Temperature (K)	100(2)
Wavelength (Å)	0.7103 (Mo-K_α)
Crystal system	Triclinic
Space group	*P*-1
Z	2
a (Å)	13.9758(7)
b (Å)	16.3474(8)
c (Å)	20.298(1)
α (°)	90.064(2)
β (°)	99.260(2)
γ (°)	91.467(2)
Volume ($Å^3$)	4575.5(4)
μ (mm^{-1})	0.559
d_{calc} (g/cm^3)	0.795
F (000)	1124
Crystal size (mm^3)	0.286 x 0.223 x 0.170
Theta range	2.27° to 25.35°
Index range	-16 ≤ h ≤ 16
	-19 ≤ k ≤ 19
	-24 ≤ l ≤ 24
Refl. collected	215172
Independent reflections	16754 (R_{int} = 0.0684)
Data/restraints/parameters	16754 / 1015 / 576
GOF on F^2	1.035
R_1/wR_2[a]	0.0356 / 0.1045
[I ≥ 2σ(I)][b]	
R_1/wR_2	0.0479 / 0.1106
[all data]	
Largest diff. peak and hole	0.356 and -0.279 eÅ^{-3}

a: $w = 1/[\sigma^2(F_o^2) + (0.0620P)^2 + 2.1244P]$ where $P = (F_o^2 + 2F_c^2)/3$

b: $R_1 = \sum||F_o|-|F_c||/\sum|F_o|$; $wR_2 = \{\sum[w(F_o^2 - F_c^2)^2]/\sum[w(F_o^2)^2]\}^{1/2}$

Single crystals of $[Zn_2(TCPE)(bpy)]$ suitable for SCXRD were directly taken from the reaction solutions. The crystals grow as clear, bright-yellow fragments with defined facets and an approximately size of 0.286 x 0.223 x 0.170 mm. X-ray intensity data were collected at 100(2)K using a Bruker D8 Venture diffractometer equipped with a Helios optic monochromator, a Photon 100 CMOS detector and a Mo TXS rotating anode source (Mo-K_α radiation). The raw area detector data frames were reduced and corrected for absorption effects using the SAINT and SADABS programs with multi-scan absorption correction. Final unit cell parameters were determined by least-squares refinement of

16754 independent reflections take from the data sets. The structure was solved by intrinsic phasing with SHELXT. Difference Fourier calculations and full-matrix least-squares refinement against F^2 were performed by SHELXL-2014/7 (Sheldrick, 2014).

The compound crystallizes in the triclinic crystal system. The pattern of systematic absences in the intensity data was consistent with the $P\bar{1}$ space group, which was confirmed by structure solution. The asymmetric unit consists of two crystallographic independent zinc atoms, a molecule of TCPE and one molecule bipyridine. All non-hydrogen atoms were refined with anisotropic displacement parameters. Hydrogen atoms could not be located in the Fourier difference maps and were calculated in ideal positions using a riding model (d(C-H) = 0.95 Å, U_{iso}(H) = 1.2U_{eq}(C)). The unit cell contains a considerable amounts of disorder solvent molecules from the reaction solution. The latter could not properly be refined and were treated as diffuse contribution to the overall scattering without specific positions using the SQUEEZE routine of PLATON (solvent accessible volume (SAV) = 730 Å^3, electrons found in SAV = 186). The largest residual electron density peak in the final difference map is 0.356 e/ Å^3.

5.6.17 [Zn_2(TCPE-F)(bpy)]

$Zn(NO_3)_2 \cdot 4H_2O$ (10.5 mg, 0.04 mmol, 1.00 equiv.) and 16.3 mg H_4TCPE-F (0.018 mmol, 4.50 equiv.) are dissolved in 2 mL of N,N-dimethylformamide (DMF) to form a light yellow clear solution in a 4 ml glass vial. 6.2 mg of 4,4-bipyridine (0.039 mmol, 9.75 eqiv.) are dissolved in 0.5 mL of methanol (MeOH). The DMF solution is slowly covered with the methanolic bpy solution. The glass vials are tightly capped and handled with care to ensure the separation of the two phases. The reaction mixture is placed in an oven at 100 °C for 24h and directly transferred to the laboratory bench to be allowed to cool at room temperature after the reaction is finalized. Light yellow block crystals are collected via filtration and washed with 10 mL DMF for five times. Yield: 19 mg (18 % based on TCPE-F). ^{1}H-NMR (400 MHz, DCl/DMSO-d_6, 298 K) δ (ppm) = 9.27 (m, 4H, Ar-H, *4,4'-bpy*), 8.80 (m, 4H, Ar-H, *4,4'-bpy*), 7.98 (t, ^{2}J = 8.0 Hz, 8.1 Hz, 8H, Ar-H, *TCPE-F*), 7.61 (m, 12H, Ar-H, *TCPE-F*), 7.52 (d, ^{2}J = 8.3 Hz, 8H, Ar-H, *TCPE-F*), 7.27 (d, ^{2}J = 8.1 Hz, 8H, Ar-H, *TCPE*). Elemental analysis (%) calc. for $(C_{64}H_{36}F_4N_2O_8Zn_2)\cdot 4(C_3H_7NO)\cdot 7(C_3HO)$: C 59.1 H 5.55 N, 5.18; found: C 58.3 H 4.74 N 5.96.

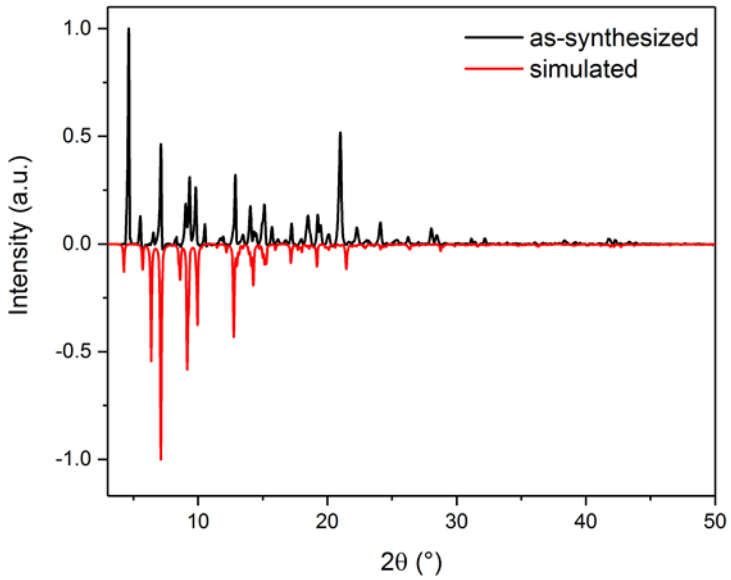

Figure 107. Simulated and as-synthesized PXRD data of [Zn_2(TCPE-F)(bpy)] in a range of 2° to 50°.

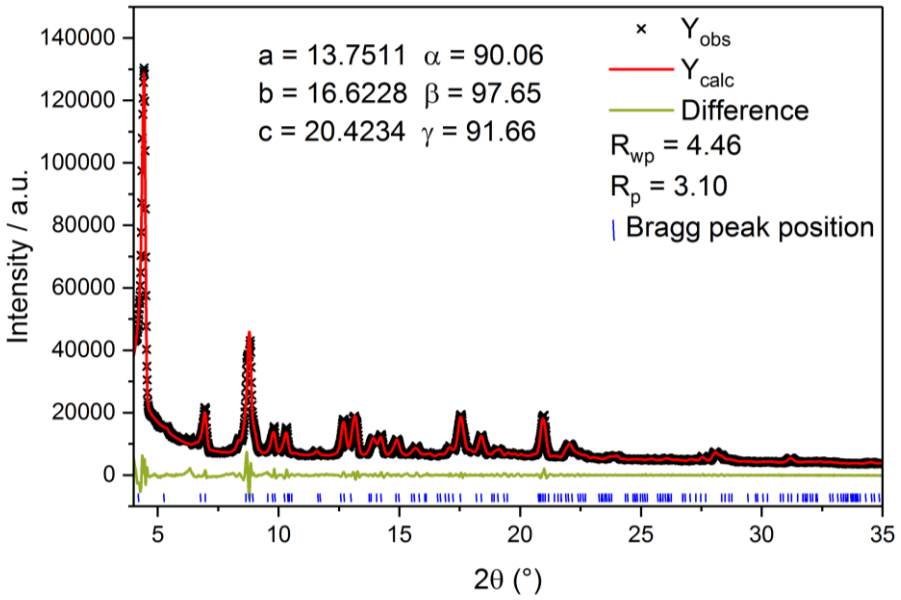

Figure 108. Pawley refinement of as-synthesized [Zn_2(TCPE-F)(bpy)] in a range of 4° to 35°.

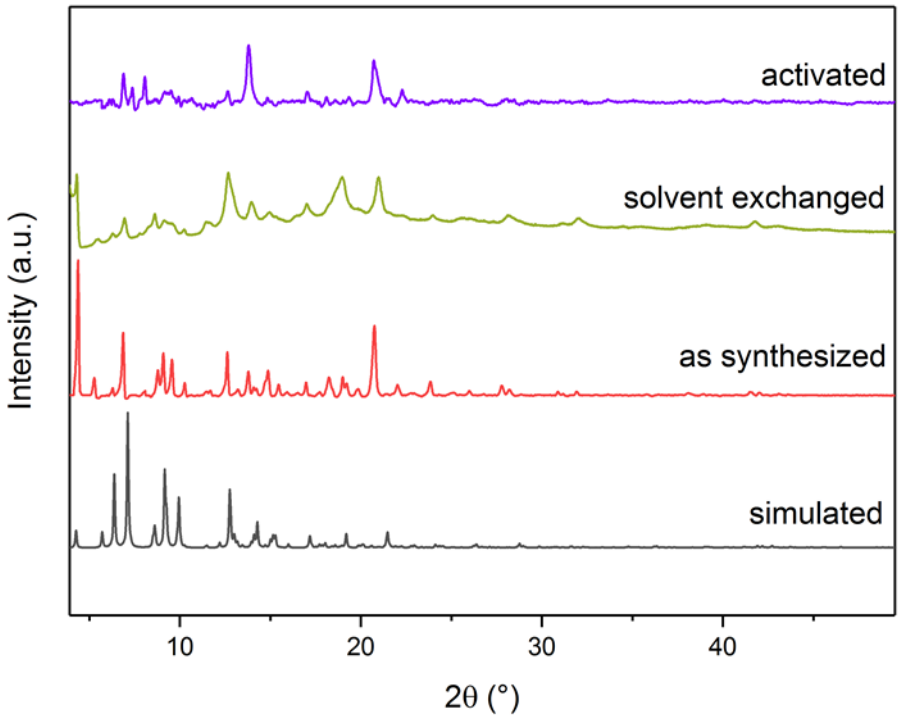

Figure 109. PXRDs of simulated, as-synthesized, solvent exchange and activated forms of [Zn_2(TCPE-F)(bpy)] in a range of 4° to 50°.

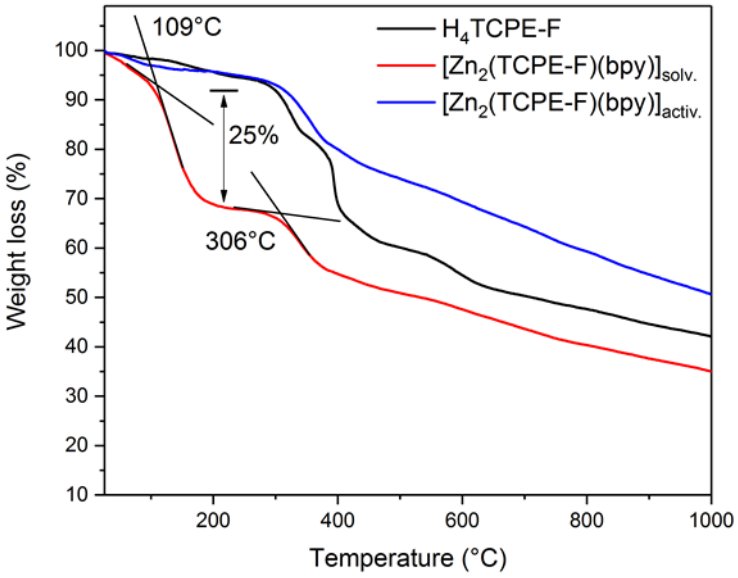

Figure 110. TGA traces of [Zn_2(TCPE-F)(bpy)] (as-synthesized), [Zn_2(TCPE-F)(bpy)] (activated) and H_4TCPE-F in a range of 35 °C to 1000 °C.

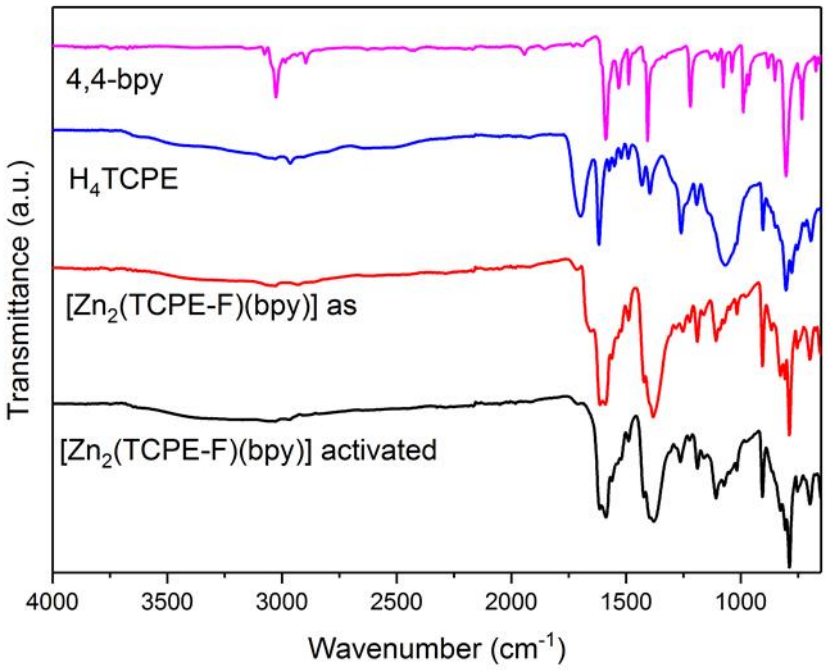

Figure 111. IR spectra of [Zn_2(TCPE-F)(bpy)] (as-synthesized), [Zn_2(TCPE-F)(bpy)] (activated), H_4TCPE-F and 4,4-bpy.

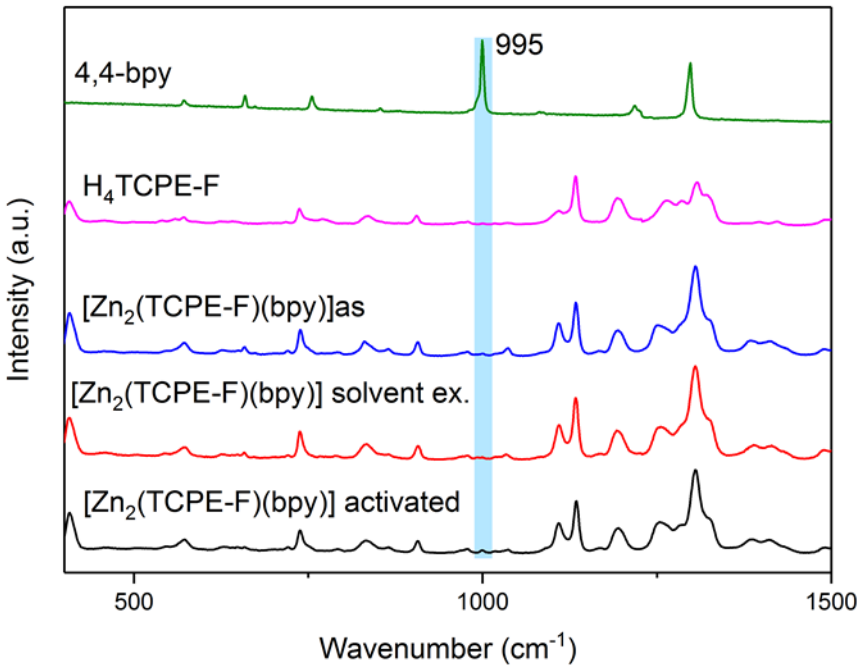

Figure 112. Raman spectra of [Zn_2(TCPE-F)(bpy)] (as-synthesized), [Zn_2(TCPE-F)(bpy)] (activated), H_4TCPE-F and 4,4-bpy. The blue blar indicates the characteristic A_1 ring breathing mode of pyridine.

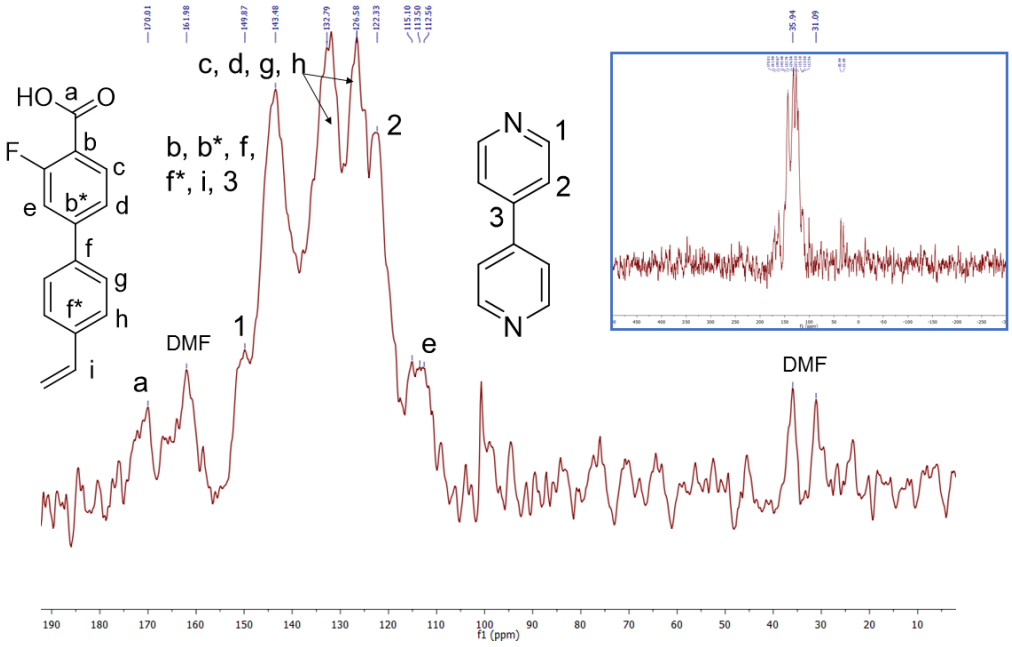

Figure 113. CP-MAS ^{13}C SS-NMR spectrum of [Zn_2(TCPE-F)(bpy)] (as-synthesized) and the peak assignment.

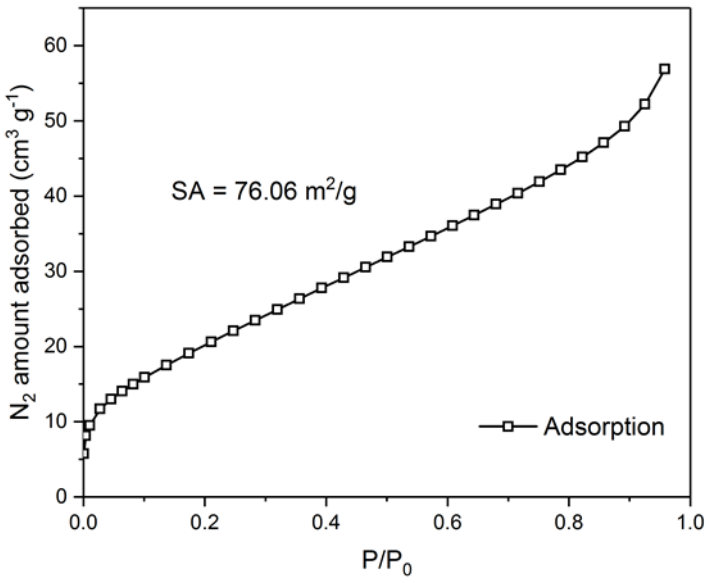

Figure 114. N_2 adsorption isotherm of thermally activated and collapsed [Zn_2(TCPE-F)(bpy)].

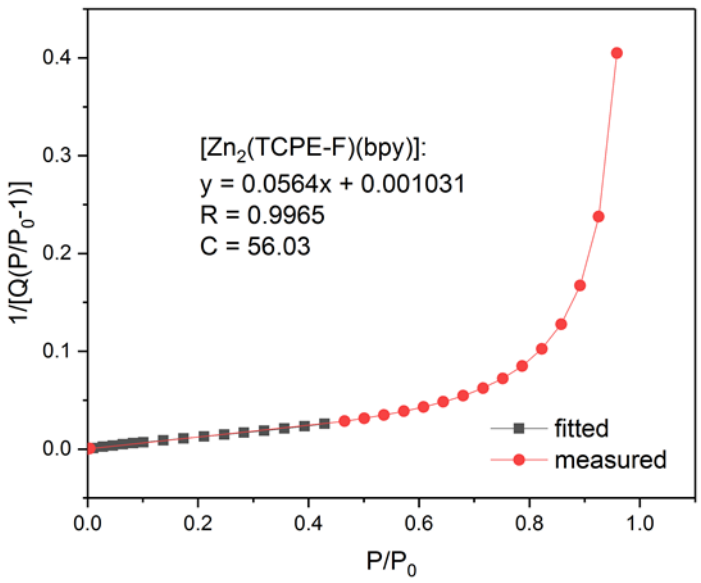

Figure 115. BET surface area plot of activated [Zn_2(TCPE-F)(bpy)] (measured and fitted range).

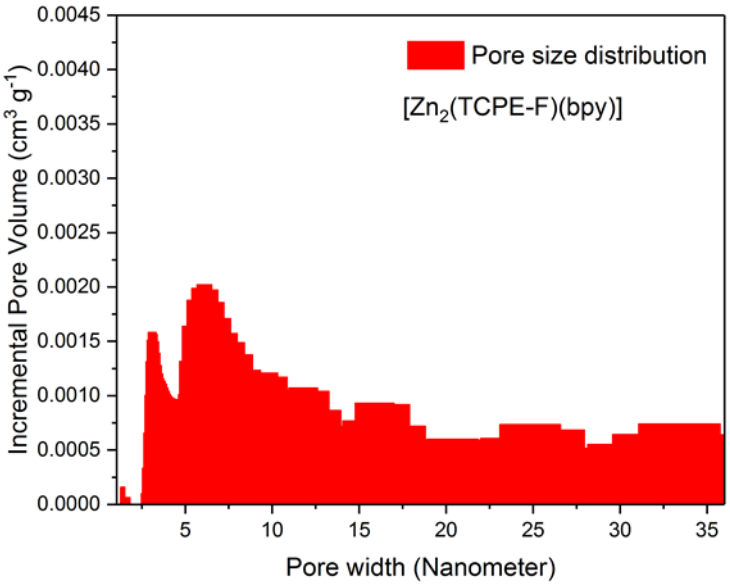

Figure 116. Pore size distribution of [Zn_2(TCPE-F)(bpy)].

5.6.18 Pillar-layered MOFs of the form [Zn_2(TCPE)(X)]: X = bpee, bpea, azpy

Reaction attempts for the synthesis of further pillar-layered MOF structures with different pyridine pillars followed the procedure as described for *[Zn_2(TCPE)(bpy)]* and *[Zn_2(TCPE-F)(bpy)]*. In short, $Zn(NO_3)_2 \cdot 4H_2O$ (10.5 mg, 0.04 mmol, 1.00 equiv.) and 16.3 mg H_4TCPE (0.019 mmol, 4.75 equiv.) were dissolved in 2 mL of N,N-dimethylformamide (DMF) to form a light yellow clear solution in a 4 ml glass vial. 10 equivalents of the respective bipyridine (1,2-di(pyridin-4-yl)ethene, 1,2-di(pyridin-4-yl)ethane**,** 1,2-di(pyridin-4-yl)diazene) where dissolved in 0.5 mL of methanol (MeOH). The DMF solution was slowly covered with the methanolic bipyridine solution and the glass vials were tightly capped. The reaction mixture was placed in a pre-warmed oven at 100 °C for 24 h and directly transferred to the laboratory bench to cool to room temperature. Following this procedure revealed the formation of partly polycrystalline material alongside with amorphous parts. The powder was pervaded by single crystals suitable for SCXRD analysis. Attempts for obtaining phase-pure bulk materials of the single MOFs, however, failed. Crystal structures are discussed in detail in chapter 2.1 of this thesis.

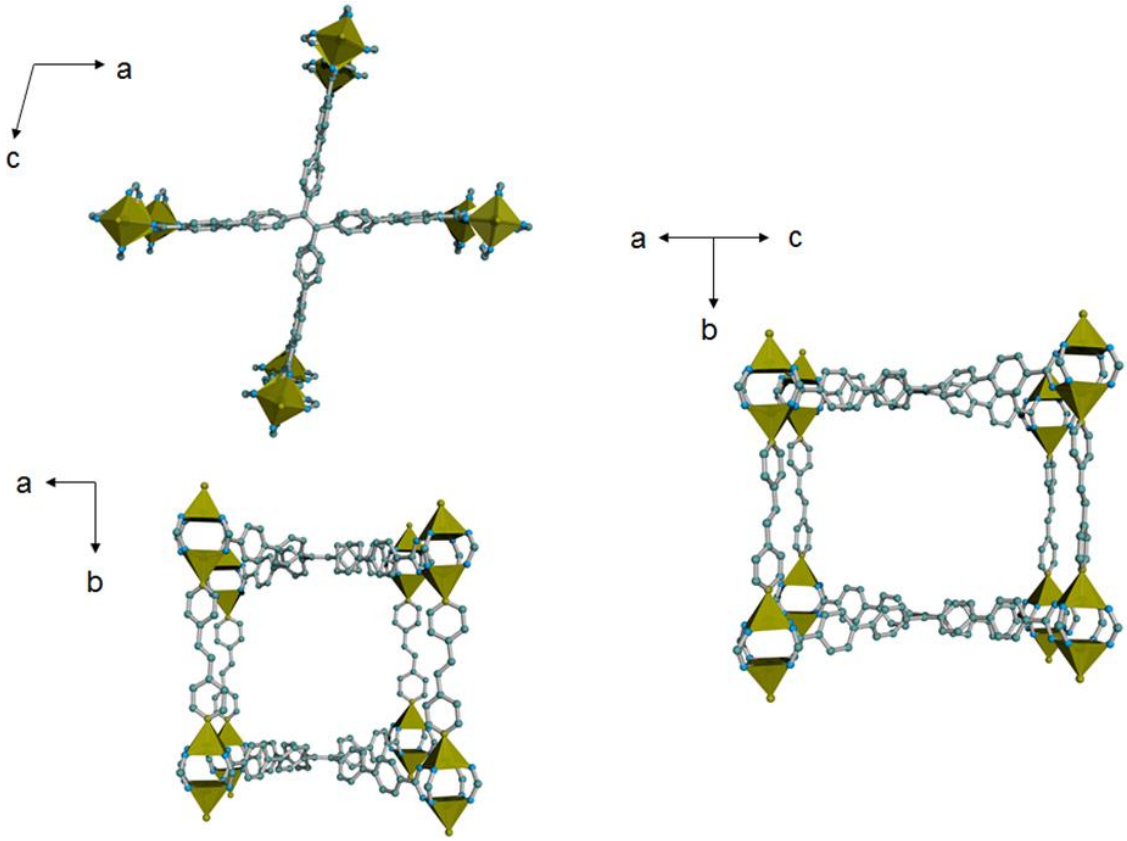

Figure 117. Single crystal structure of non-interpenetrated [Zn_2(TCPE)(bpee)]. Note that the second network and hydrogen atoms have been removed for clarity reasons (zinc = black, oxygen = blue, nitrogen = green, carbon = grey).

Table 14. Crystal structure data of $[Zn_2(TCPE)(bpee)] \cdot 2$ dimethylacetamide.

Compound	**$[Zn_2(TCPE)(bpee)] \cdot 2$ dimethylacetamide**
Formula	$C_{66}H_{42}N_2O_8Zn_2\ 2(C_4H_9NO)$
Formula weight	1296.04
Temperature (K)	100(2)
Wavelength (Å)	0.7103 (Mo-K_α)
Crystal system	Monoclinic
Space group	*P* 21/n
Z	4
a (Å)	26.0056(15)
b (Å)	16.2711(10)
c (Å)	26.1129(17)
α (°)	90
β (°)	99.392(2)
γ (°)	90
Volume (Å^3)	10901.3(12)
μ (mm^{-1})	0.477
d_{calc} (g/cm^3)	0.790
F (000)	2688
Crystal size (mm^3)	0.372 x 0.232 x 0.118
Theta range	2.23° to 25.35°
Index range	-31 ≤ h ≤ 31 -19 ≤ k ≤ 19 -31 ≤ l ≤ 31
Refl. collected	431764
Independent reflections	19929 (R_{int} = 0.0671)
Data/restraints/parameters	19929 / 99 / 849
GOF on F^2	1.027
R_1/wR_2[a] [$I \geq 2\sigma(I)$][b]	0.0658 / 0.1888
R_1/wR_2 [all data]	0.0776 / 0.1968
Largest diff. peak and hole	1.144 and -0.756 eÅ^{-3}

a: $w = 1/[\sigma^2(F_o^2) + (0.0902P)^2 + 41.3352P]$ where $P = (F_o^2 + 2F_c^2)/3$

b: $R_1 = \sum||F_o|-|F_c||/\sum|F_o|$; $wR_2 = \{\sum[w(F_o^2 - F_c^2)^2]/\sum[w(F_o^2)^2]\}^{1/2}$

Single crystals of $[Zn_2(TCPE)(bpee)]$ suitable for SCXRD were directly taken from the reaction solutions. The crystals grow as clear, bright-yellow fragments with defined facets and an approximately size of 0.372 x 0.232 x 0.118 mm. X-ray intensity data were collected at 100(2)K using a Bruker D8 Venture diffractometer equipped with a Helios optic monochromator, a Photon 100 CMOS detector and a Mo TXS rotating anode source (Mo-K_α radiation). The raw area detector data frames were reduced and corrected for absorption effects using the SAINT and SADABS programs with multi-scan absorption correction.

Final unit cell parameters were determined by least-squares refinement of 19929 independent reflections take from the data sets. The structure was solved by intrinsic phasing with SHELXT. Difference Fourier calculations and full-matrix least-squares refinement against F^2 were performed by SHELXL-2014/7 (Sheldrick, 2014).

The compound crystallizes in the monoclinic crystal system. The pattern of systematic absences in the intensity data was consistent with the *P21/n* space group, which was confirmed by structure solution. The asymmetric unit consists of one crystallographic independent zinc atom, a bisected molecule of TCPE, a half molecule bpee and one molecule DMAc. All non-hydrogen atoms were refined with anisotropic displacement parameters. Hydrogen atoms could not be located in the Fourier difference maps and were calculated in ideal positions using a riding model (d(C-H) = 0.95 Å, $U_{iso}(H) = 1.2U_{eq}(C)$). The unit cell contains a considerable amounts of disorder solvent molecules from the reaction solution. From the high amount of disordered molecules, two DMAc molecules could be refined, however, the remaining solvent molecules could not properly be refined and were treated as diffuse contribution to the overall scattering without specific positions using the SQUEEZE routine of PLATON (solvent accessible volume (SAV) = 730 $Å^3$, electrons found in SAV = 186). The largest residual electron density peak in the final difference map is 1.144 e/ $Å^3$.

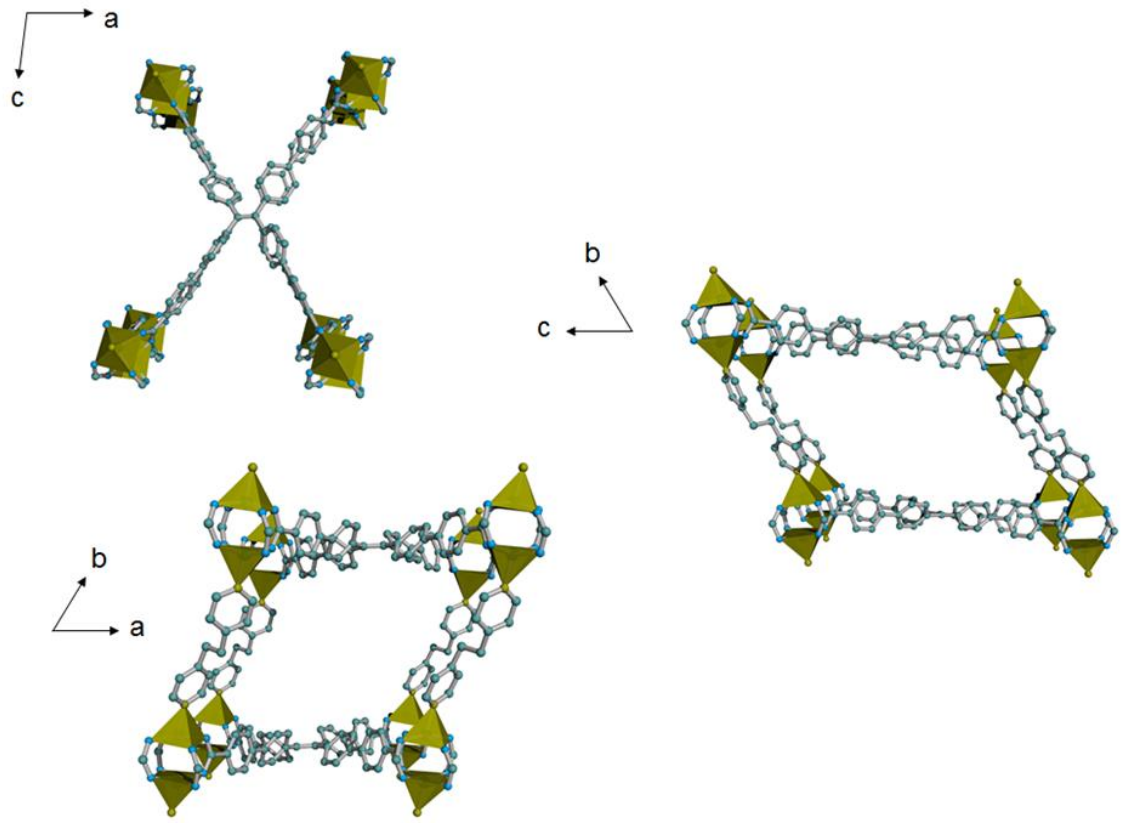

Figure 118. Single crystal structure of non-interpenetrated [Zn_2(TCPE)(bpea)]. Note that the second network and hydrogen atoms have been removed for clarity reasons (zinc = black, oxygen = blue, nitrogen = green, carbon = grey).

Table 15. Crystal structure data of $[Zn_2(TCPE)(bpea)]$

Compound	**$[Zn_2(TCPE)(bpea)]$**
Formula	$C_{66}H_{44}N_2O_8Zn_2$
Formula weight	1219.83
Temperature (K)	100(2)
Wavelength (Å)	0.7103 (Mo-K_α)
Crystal system	Triclinic
Space group	*P*-1
Z	2
a (Å)	15.4106(9)
b (Å)	15.6148(9)
c (Å)	20.8962(11)
α (°)	68.426(2)
β (°)	89.997(2)
γ (°)	72.703(2)
Volume ($Å^3$)	4430.7(4)
μ (mm^{-1})	0.578
d_{calc} (g/cm^3)	0.842
F (000)	1156
Crystal size (mm^3)	0.088 x 0.184 x 0.513
Theta range	2.19° to 25.35°
Index range	-18 ≤ h ≤ 18 -18 ≤ k ≤ 18 -25 ≤ l ≤ 25
Refl. collected	173820
Independent reflections	16210 (R_{int} = 0.0548)
Data/restraints/parameters	16210 / 90 / 760
GOF on F^2	1.046
R_1/wR_2[a]	0.0373 / 0.1043
[I ≥ 2σ(I)][b]	
R_1/wR_2	0.0481 / 0.1098
[all data]	
Largest diff. peak and hole	0.472 and -0.326 eÅ^{-3}

a: $w = 1/[\sigma^2(F_o^2) + (0.0553P)^2 + 3.980P]$ where $P = (F_o^2 + 2F_c^2)/3$

b: $R_1 = \sum||F_o|-|F_c||/\sum|F_o|$; $wR_2 = \{\sum[w(F_o^2 - F_c^2)^2]/\sum[w(F_o^2)^2]\}^{1/2}$

Single crystals of $[Zn_2(TCPE)(bpea)]$ suitable for SCXRD were directly taken from the reaction solutions. The crystals grow as clear, bright-yellow plates with defined facets and an approximately size of 0.088 x 0.184 x 0.513 mm. X-ray intensity data were collected at 100(2)K using a Bruker D8 Venture diffractometer equipped with a Helios optic monochromator, a Photon 100 CMOS detector and a Mo TXS rotating anode source (Mo-K_α radiation). The raw area detector data frames were reduced and corrected for absorption effects using the SAINT and SADABS programs with multi-scan absorption correction.

Final unit cell parameters were determined by least-squares refinement of 16210 independent reflections take from the data sets. The structure was solved by intrinsic phasing with SHELXT. Difference Fourier calculations and full-matrix least-squares refinement against F^2 were performed by SHELXL-2014/7 (Sheldrick, 2014).

The compound crystallizes in the triclinic crystal system. The pattern of systematic absences in the intensity data was consistent with the $P\bar{1}$ space group, which was confirmed by structure solution. The asymmetric unit consists of two crystallographic independent zinc atoms, a molecule of TCPE and one molecule bpea. All non-hydrogen atoms were refined with anisotropic displacement parameters. Hydrogen atoms could not be located in the Fourier difference maps and were calculated in ideal positions using a riding model (d(C-H) = 0.95 Å, U_{iso}(H) = 1.2U_{eq}(C)). The unit cell contains a considerable amounts of disorder solvent molecules from the reaction solution. The latter could not properly be refined and were treated as diffuse contribution to the overall scattering without specific positions using the SQUEEZE routine of PLATON (solvent accessible volume (SAV) = 730 Å^3, electrons found in SAV = 186). The largest residual electron density peak in the final difference map is 0.472 e/ Å^3.

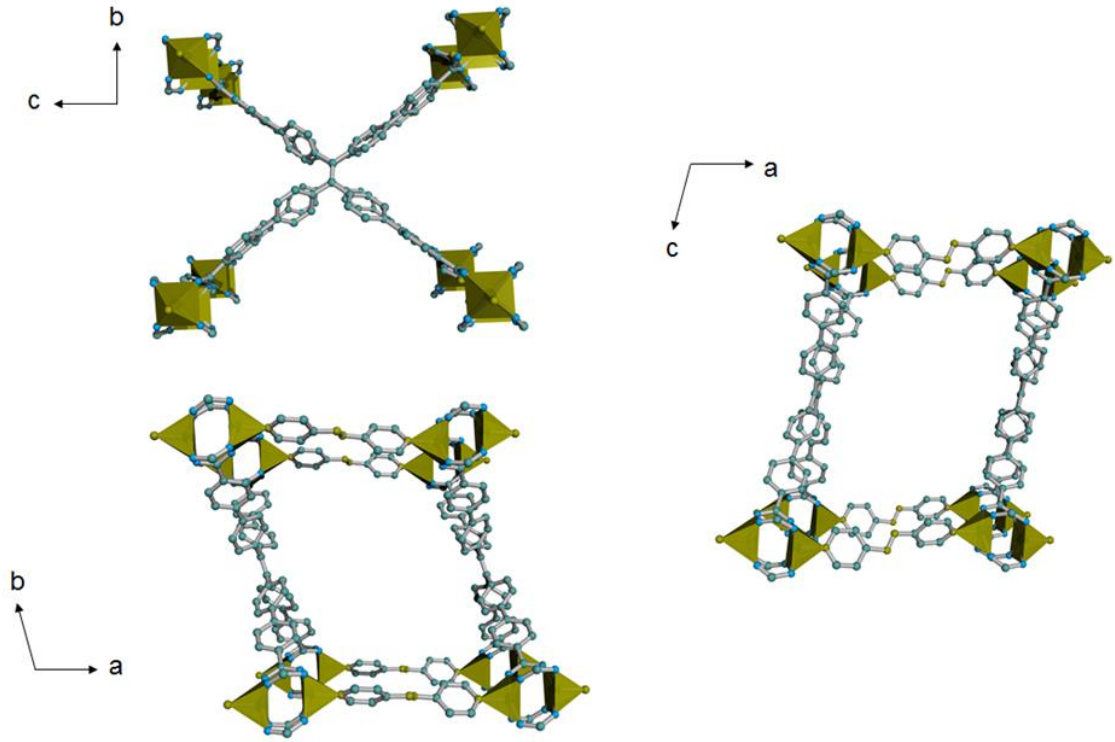

Figure 119. Single crystal structure of non-interpenetrated [Zn_2(TCPE)(azpy)]. Note that the second network and hydrogen atoms have been removed for clarity reasons (zinc = black, oxygen = blue, nitrogen = green, carbon = grey).

Compound	$[Zn_2(TCPE)(azpy)]$
Formula	$C_{64}H_{40}N_4O_8Zn_2$
Formula weight	1123.78
Temperature (K)	100(2)
Wavelength (Å)	0.7103 (Mo-K_α)
Crystal system	Triclinic
Space group	*P*-1
Z	2
a (Å)	15.7595(11)
b (Å)	16.9308(12)
c (Å)	19.8682(13)
α (°)	90.166(2)
β (°)	101.182(2)
γ (°)	104.966(2)
Volume ($Å^3$)	5016.4(6)
μ (mm^{-1})	0.511
d_{calc} (g/cm^3)	0.744
F (000)	1152
Crystal size (mm^3)	0.044 x 0.131 x 0.179
Theta range	2.26° to 25.35°
Index range	-18 ≤ h ≤ 18 -20 ≤ k ≤ 20 -23 ≤ l ≤ 23
Refl. collected	133604
Independent reflections	18313 (R_{int} = 0.0633)
Data/restraints/parameters	18313 / 100 / 767
GOF on F^2	1.032
R_1/wR_2[a] [$I \geq 2\sigma(I)$][b]	0.0409 / 0.1192
R_1/wR_2 [all data]	0.0545 / 0.1267
Largest diff. peak and hole	0.504 and -0.584 eÅ^{-3}

a: $w = 1/[\sigma^2(F_o^2) + (0.0703P)^2 + 3.2466P]$ where $P = (F_o^2 + 2F_c^2)/3$

b: $R_1 = \sum||F_o|-|F_c||/\sum|F_o|$; $wR_2 = \{\sum[w(F_o^2 - F_c^2)^2]/\sum[w(F_o^2)^2]\}^{1/2}$

Single crystals of $[Zn_2(TCPE)(bpy)]$ suitable for SCXRD were directly taken from the reaction solutions. The crystals grow as clear, bright-red plates with defined facets and an approximately size of 0.286 x 0.223 x 0.170 mm. X-ray intensity data were collected at 100(2)K using a Bruker D8 Venture diffractometer equipped with a Helios optic monochromator, a Photon 100 CMOS detector and a Mo TXS rotating anode source (Mo-K_α radiation). The raw area detector data frames were reduced and corrected for absorption effects using the SAINT and SADABS programs with multi-scan absorption correction. Final unit cell parameters were determined by least-squares refinement of 18313 independent reflections take from the data sets. The structure was

solved by intrinsic phasing with SHELXT. Difference Fourier calculations and full-matrix least-squares refinement against F^2 were performed by SHELXL-2014/7 (Sheldrick, 2014).

The compound crystallizes in the triclinic crystal system. The pattern of systematic absences in the intensity data was consistent with the $P\bar{1}$ space group, which was confirmed by structure solution. The asymmetric unit consists of two crystallographic independent zinc atoms, a molecule of TCPE and one molecule bipyridine. All non-hydrogen atoms were refined with anisotropic displacement parameters. Hydrogen atoms could not be located in the Fourier difference maps and were calculated in ideal positions using a riding model (d(C-H) = 0.95 Å, U_{iso}(H) = 1.2U_{eq}(C)). The unit cell contains a considerable amounts of disorder solvent molecules from the reaction solution. The latter could not properly be refined and were treated as diffuse contribution to the overall scattering without specific positions using the SQUEEZE routine of PLATON (solvent accessible volume (SAV) = 730 Å^3, electrons found in SAV = 186). The largest residual electron density peak in the final difference map is 0.584 e/ Å^3.

*5.1.19 NU-1000 and NU-901 (= [$Zr_6O_4(OH)_8(H_2O)_4(TBAPy)_2$]): Two polymorphic structures with **csq** and **scu** network.*

5.1.19.1 General remarks

NU-1000 is a robust mesoporous MOF with a hexazirconium-oxo-node $[Zr_6O_{16}H_{16}]^{8+}$ and two pyrene base $TBAPy^{4-}$ ligands.[26] Normally, the MOF is synthesized by reaction of a solution of $ZrOCl_2 \cdot 8H_2O$, H_4TBAPy and benzoic acid as modulator in DMF at elevated temperatures. The resulting material following that synthesis route, however, has shown to hold a phase impurity up to 25% percent and was recognized as a polymorphic structure of NU-1000, NU-901.[111, 326] The phase pure synthesis of the two polymorphs has been subject of intensive research, as NU-1000 is a very promising MOF material in areas like (photo)-catalysis, gas adsorption or post-synthetic modifications (e.g. SALI, SIM or AIM). The phase impurity in NU-1000 was shown to not only pertain in the bulk material, but even pass to single crystallites. Both MOFs hold 8-connected zirconium nodes and the resulting polymorphism stems from differences in the ligand alignments, as was shown by Truhlar and co-workers (precisely the relatively alignment of the C_2-axis of TBAPy along the nodes).[327] A couple of different groups investigated the influence of different modulators on the formation of phase pure NU-1000. Among other, Farha and co-workers showed that the usage of trifluoroacetic acid delivers nearly phase-pure NU-1000, which they hypothesized is due to a formation/re-solvation procedure by virtue of the strong acidic TFA modulator.[26] Further, the group around Penn and co-workers followed a structural approach, by using a steric demanding biphenyl carboxylic acid modulator in the synthesis of NU-1000.[326] The biphenyl carboxylic acid is coordinating to the zirconium node and consequently enhances the steric bulk in the surrounding of the latter, finally preventing the formation of NU-901.

NU-901 shows similar problems in its synthesis, as obviously NU-1000 can form as a side product in the reaction. The NU-1000 formation in the synthesis of NU-901 was shown to be suppressed by using non-halogenated zirconium salts ($Zr(acac)_2$) and aminobenzoic acid as modulator, as demonstrated recently by Farha and co-workers.[109]

The three state-of-the art characterization tools for the differentiation of NU-1000/NU-901 pairs in the synthesis of the latter has shown to be PXRD, N_2-sorption measurements and SEM. PXRD is helpful to distinguish NU-1000 from NU-901, as NU-1000 will show a very characteristic (100) reflex at 2.5°. Furthermore, NU-901 shows a type I isotherm without a mesoporous step and characteristic total pore volume. The latter can be used to distinguish NU-901 impurities in NU-1000 synthesis (characteristic pore volume of 1.366 cc/g and N_2-uptake of roughly 1000 cm^3/g). Finally, both MOFs show a characteristic crystal morphology apparent in SEM. NU-1000 can be described as rod-shaped hexagonal crystals, NU-901 shows an egg-shaped morphology.[26, 109, 111, 326]

The two structures are highly promising for non-linear optical characterizations, as they are polymorphic structures and thus the non-linear response should be only a pure function of the chromophore alignments (assuming other effects not contributing to the measurements).[29, 98, 266] So far no MPA characterization was conducted on the materials. The aim of the here presented study is to provide a proven synthetic protocol based on adjusted literature work for further NLO measurements. Within this work, several published procedures were tested in the synthesis of phase pure MOFs NU-1000 and NU-901. Finally, the published procedure by Penn et. al. showed to yield excellent NU-1000 material, however, with a wide-ranging crystal size distribution (2 – 20 µm).[326] The NU-901 phase could be synthesized by an adjusted procedure following Farha et. al., however, in lower yields than in the original procedure.[109] The materials were characterized by PXRD measurements, N_2-sorption measurements and SEM characterization, proving the phase purity of the materials.

5.1.19.2 NU-1000: [$Zr_6O_4(OH)_8(H_2O)_4(TBAPy)_2$]

Zirconyl chloride octahydrate ($ZrOCl_2 \cdot 8H_2O$, 0.388 g, 1.20 mmol, 1.00 equiv.) and biphenyl-4-carboxylic acid (17.574 g, 88.40 mmol, 74.0 equiv.) were dissolved in 32 mL of DMF in a Schott glass and further heated to 100 °C for 1 h in an oven. Note the biphenyl-4-carboxylic acid will not solve in DMF at RT, however, going to higher temperature will dissolve the modulator extremely well. During heating phase, the ingredients were smoothly mixed by careful shaking of the Schott glass. The reaction mixture was allowed to cool to RT to yield 40 mL of node-solution. Meanwhile, in a 20 mL scintillation vile H_4TBAPy (50.0 mg, 0.0732 mmol) were dissolved in 3 mL of DMF. Note that H_4TBAPy shows a rather low solubility in DMF and is tending to precipitate. Therefore, the mixture needs to be warmed to 100 °C (either with the help of an oven or via an aluminum heating block) to ensure complete solution of the ligand. 10 mL of a pre-warmed (100 °C) node-solution was put to the hot ligand solution and the reaction was held at 100 °C for 24 h using an aluminum heating block and a standard laboratory heating plate. The bright yellow product was isolated via centrifugation and extensively washed with DMF and acetone. (yield = 52 mg). The yellow powder was further suspended in 12 ml DMF and 0.5 mL of 8 M aqueous HC was added. The suspension was heated in an oven for 100 °C for 18 h. After cooling to room temperature, the powder was isolated by centrifugation and extensively washed with DMF and acetone. Activation of the particles was conducted by extended soaking of the raw material in dry acetone and subsequently heating at 120 °C under static vacuum.

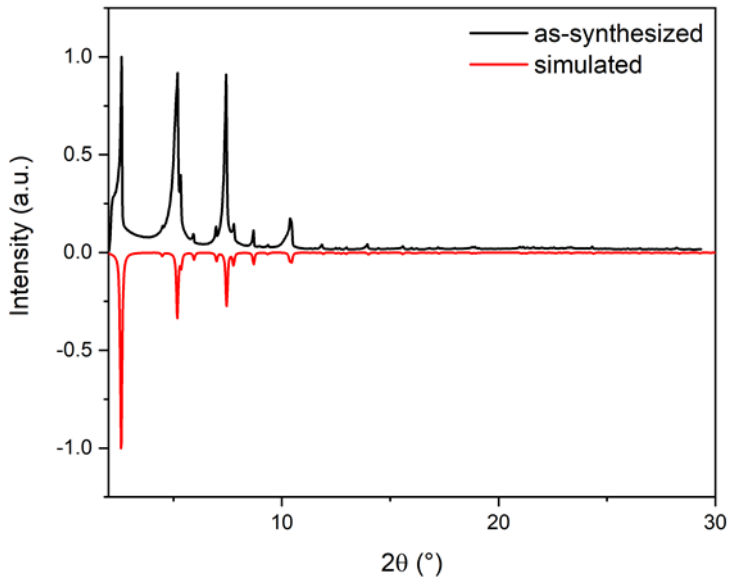

Figure 120. PXRD data of NU-1000 of as-synthesized MOF material. Note the characteristic (100) reflex at 2.5°.

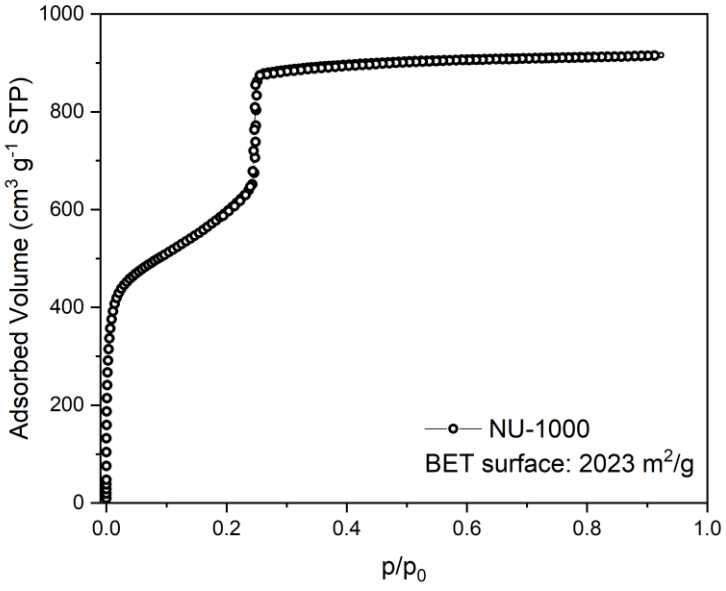

Figure 121. N_2-adsorption isotherm of NU-1000 with the characteristic mesoporous step (type II isotherm), the amount of total adsorbed volume (950 cm^3/g) and BET surface (2023 m^2/g).

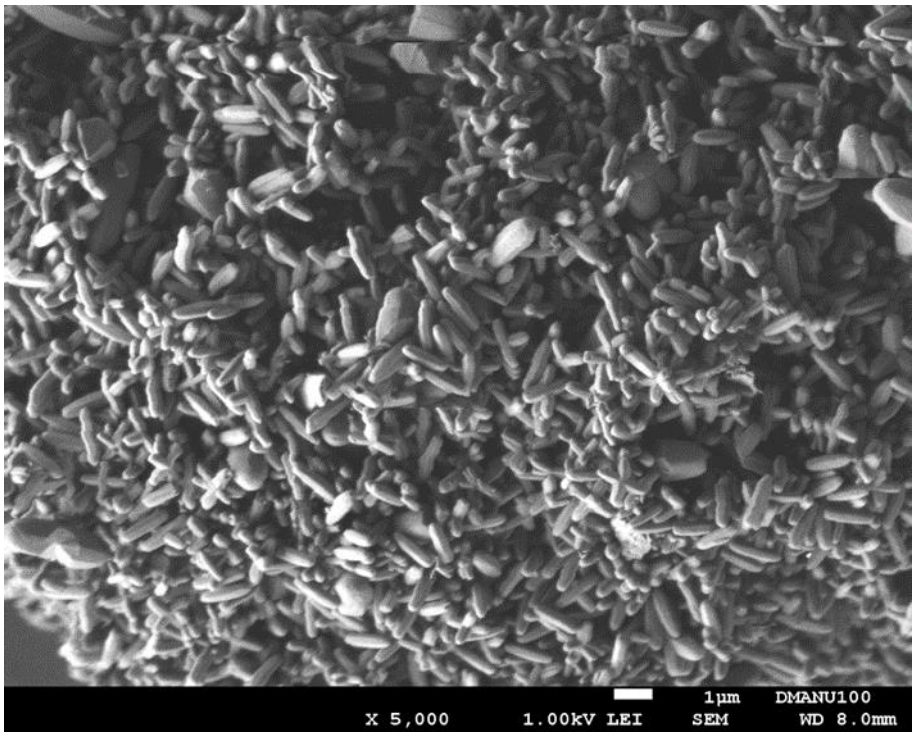

Figure 122. SEM picture of as-synthesized NU-1000 showing the characteristic rod-shaped hexagonal crystals with a crystal size distribution of 1 to 20 µm.

5.1.19.3 NU-901: $[Zr_6O_4(OH)_8(H_2O)_4(TBAPy)_2]$

$Zr(acac)_2$ (97 mg, 0.2 mmol) and 4-aminobenzoic acid (3.02 mg, 22 mmol) were mixed in 8 mL of dry DMF in a 20 mL scintillation vial and heated to 100 °C. The reaction mixture was shaken from time to time to ensure full solvation of all reaction ingredients. The solution was hold at 100 °C for 1 h and allowed to cool to room temperature, afterwards. A solution of H_4TBAPy (40 mg, 0.06 mmol) in 2 ml of dry DMF was prepared and heated to 100 °C to ensure full solvation of the ligand. The node-solution was heated to 100 °C and both reaction solutions were put together. This solution was held at 100 °C for further 18 h yielding in a polycrystalline material. The latter was isolated by centrifugation and subsequently extended washed by DMF and acetone. The yellow powder was further suspended in 12 ml DMF and 0.5 mL of 8 M aqueous HC was added. The suspension was heated in an oven for 100 °C for 18 h. After cooling to room temperature, the powder was isolated by centrifugation and extensively washed with DMF and acetone. Activation of the material was conducted by soaking in dry acetone for several days as well as thermal activation (120 °C) for 24 h in vacuum. Yield = 32 mg).

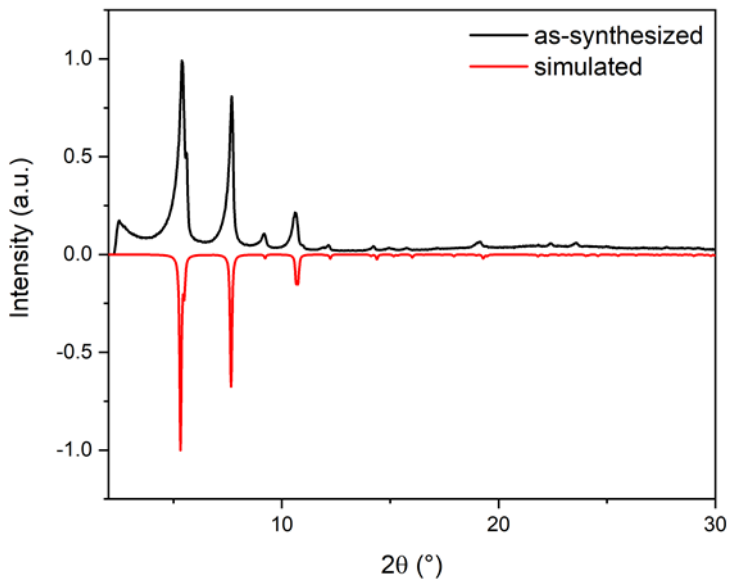

Figure 123. PXRD data of as-synthesized NU-901. Note the missing reflex at 2.5°, proofing the absence of NU-1000 side-phase.

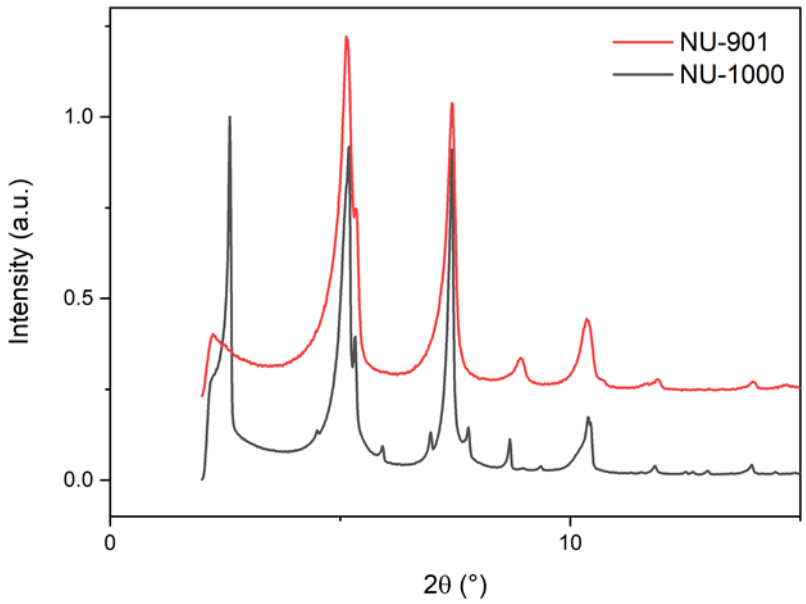

Figure 124. PXRD of NU-901 and NU-1000 phases measured at the same diffractometer under similar conditions to assure the absence of 2.5 ° (001) reflex.

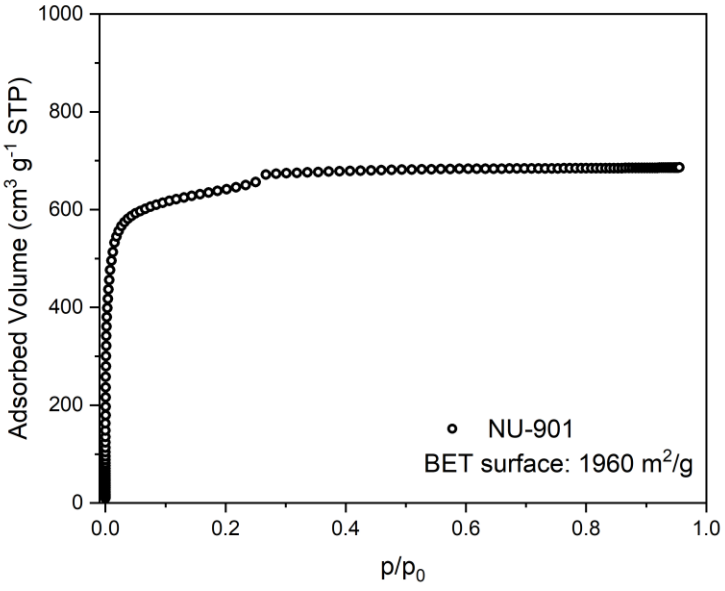

Figure 125. N_2-adsorption isotherm of NU-901. The small step at 0.3 p/p_0 could be attributed to small NU-1000 impurities, however, regarding the PXRD characterization, is most probably due to the presence of defects in the sample. The BET characterization reveals a characteristic BET surface of 1960 m^2/g and a total adsorbed volume of 686 cm^3/g (literature value of ~ 650 cm^3/g) in excellent accordance with literature values.

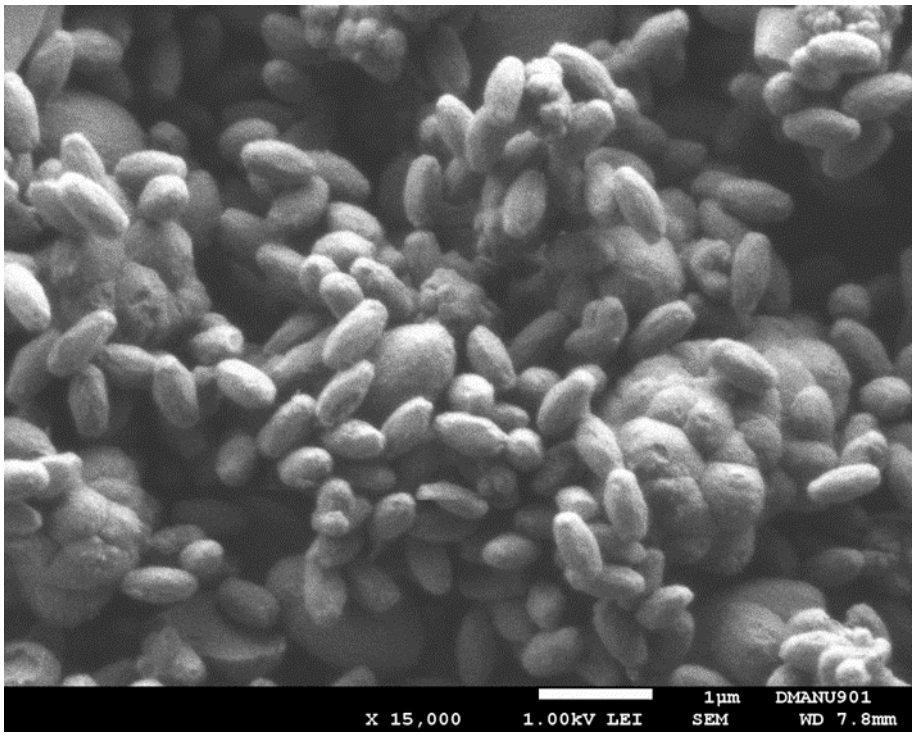

Figure 126. SEM picture of as-synthesized NU-901 showing the characteristic oval crystals with a narrow crystal size distribution of 0.1 to 1 µm.

5.3 Optical characterization details

The following chapters contain details about the optical characterization of the synthesized materials in this thesis. The spectra were collected with the experimental setup described in chapter 4.1. Measurements on powders were conducted on pressed materials between quartz glass slides. To ensure a homogeneous crystal size distribution, all materials were sieved through a set of microsieves measurements (Aldrich). Measurements on solutions were conducted in different type of quartz glass cuvettes (standard 4 mL cuvettes or different other geometries) in spectroscopic quality solvents (toluene, THF, MeOH, EtOH, acetone, DMF) at differing concentrations (0.1 to 1 mmol/L). Titration experiments were conducted via subsequent titration of defined amounts of water to chromophore solutions at the respectively depicted concentrations and solvents.

Linear and non-linear optical characterizations on compounds H_4TCPE, H_4TCPE-F, [Zn_2(TCPE)(bpy)] and [Zn_2(TCPE-F)(bpy)] were in parts conducted by J. K. Zareba from the Advanced Materials and Engineering and Modelling Group, Faculty of Chemistry, Wroclaw University of Science and Technology, Poland (UV-Vis, PL and titration experiments of the ligands; PL and PL lifetime, SS-TPEF of the MOFs) and the author of this thesis (sold-state absorbance and reflectance spectra).

Linear and non-linear optical characterization on compounds H_4TPBD, [Zn_2(TPBD)(DMAc)$_2$] and [Cd_2(TPBD)(H_2O)$_4$] were conducted by the author of this thesis (UV-Vis and PL of the ligand, quantum yields of the CPs) in cooperation with Dr. A. Manzi (PL and excitation spectra of the CPs, SS-TPEF of the CPs) from the chair of photonics and optoelectronics, nano-institute munich, department of physics and CeNS, Ludwigs-Maximilians-Universität, munich. Furthermore, optical characterization of H_4TPBD and aggregates at higher concentrations were conducted by the author of this thesis together with Dr. Thyrhaug from the chair of dynamic spectroscopy, department of chemistry, technical university of munich. Dr. Thyrhaug did the data analysis and interpretation.

5.3.1 H_4TCPE, H_4TCPE-F, [Zn_2(TCPE)(bpy)], [Zn_2(TCPE-F)(bpy)]

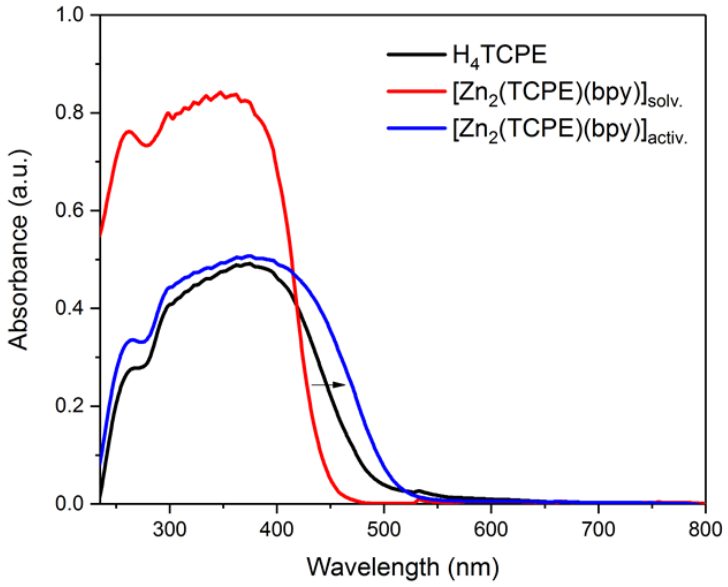

Figure 127. Solid state absorption spectra of H_4TCPE, [Zn_2(TCPE)(bpy)] (solvated = as synthesized form) and activated MOF.

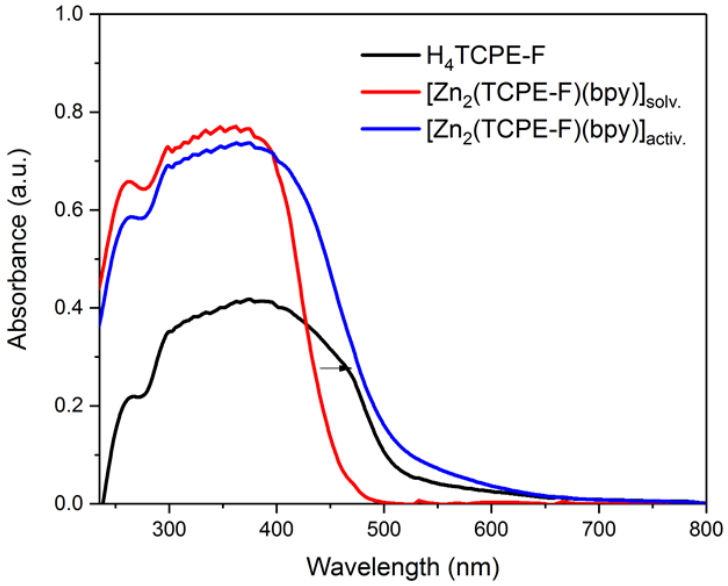

Figure 128. Solid state absorption spectra of H_4TCPE-F, [Zn_2(TCPE-F)(bpy)] (solvated = as synthesized form) and the activated MOF.

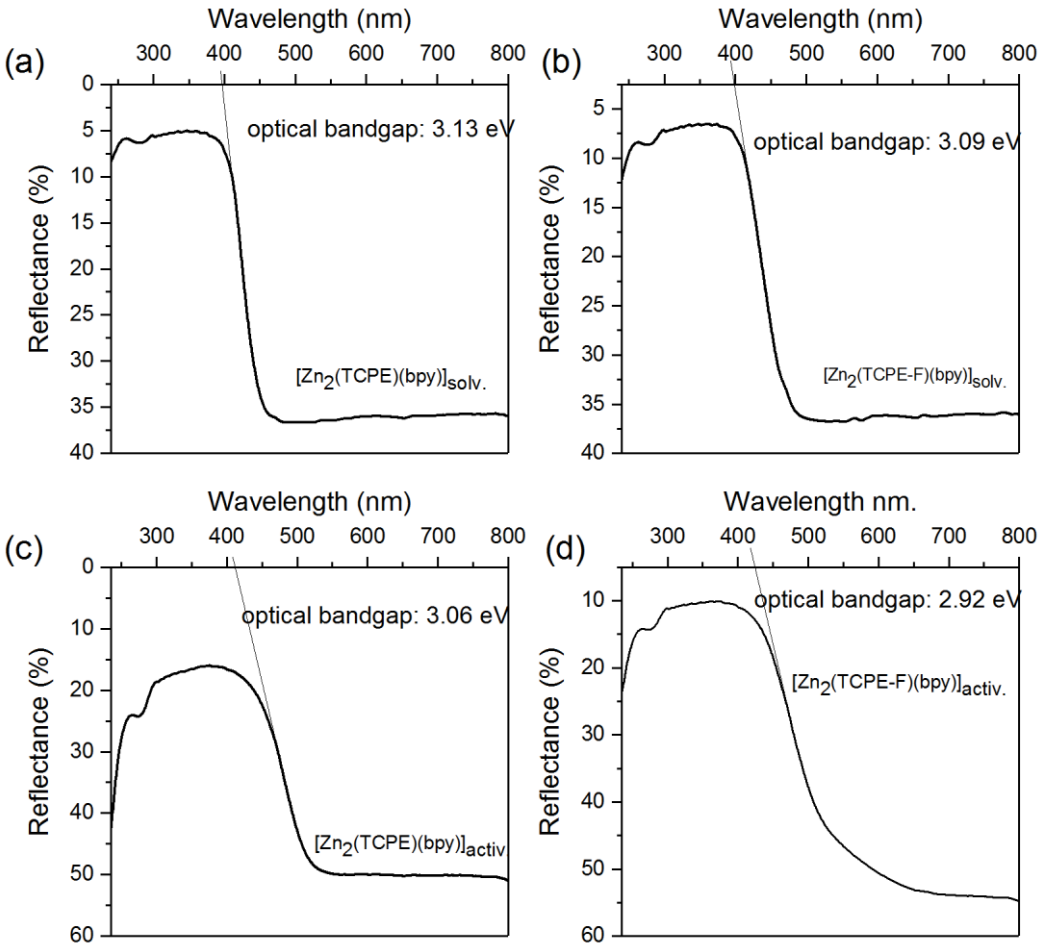

Figure 129. Solid state reflectance spectra of as synthesized and activated MOFs ([Zn_2(TCPE)(bpy)] (a, c), [Zn_2(TCPE-F)(bpy)] (b, d)).

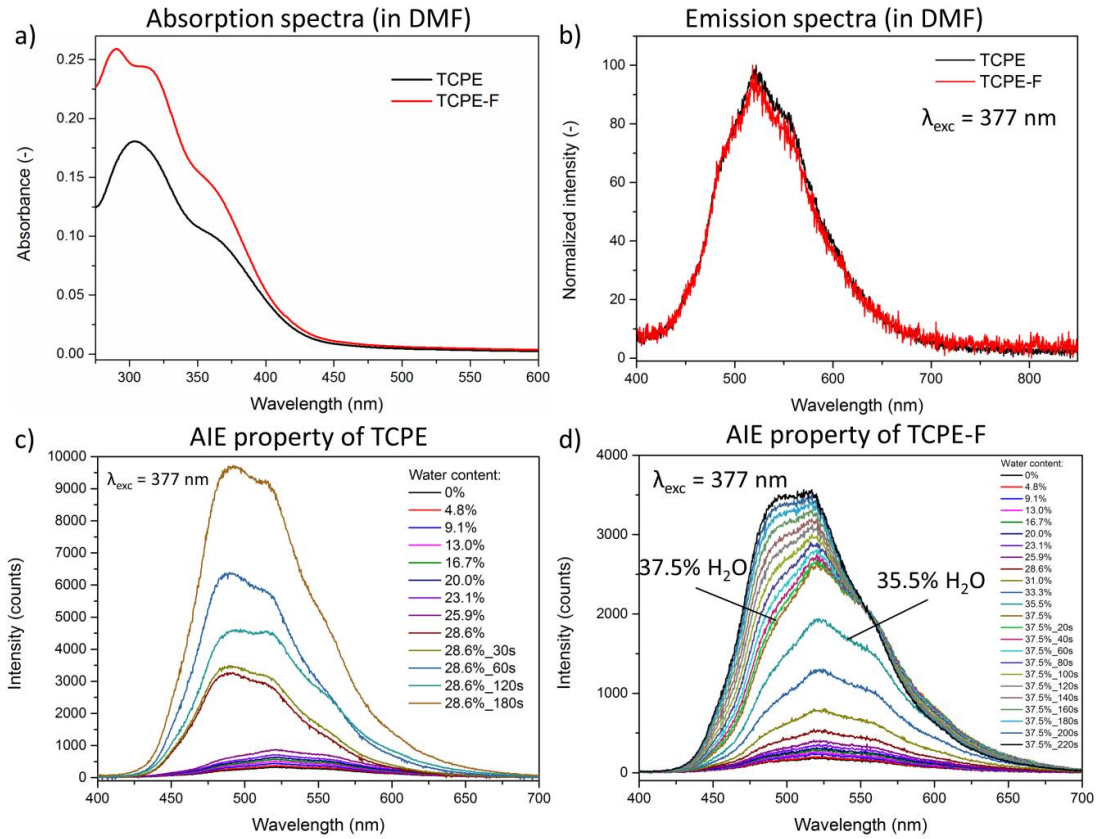

Figure 130. a) Absorption spectra of TCPE and TCPE-F in DMF solution; b) Emission spectra of H_4TCPE and H_4TCPE-F in DMF solution. (c, d) Titration experiment of H_4TCPE and H_4TCPE-F in DMF solution.

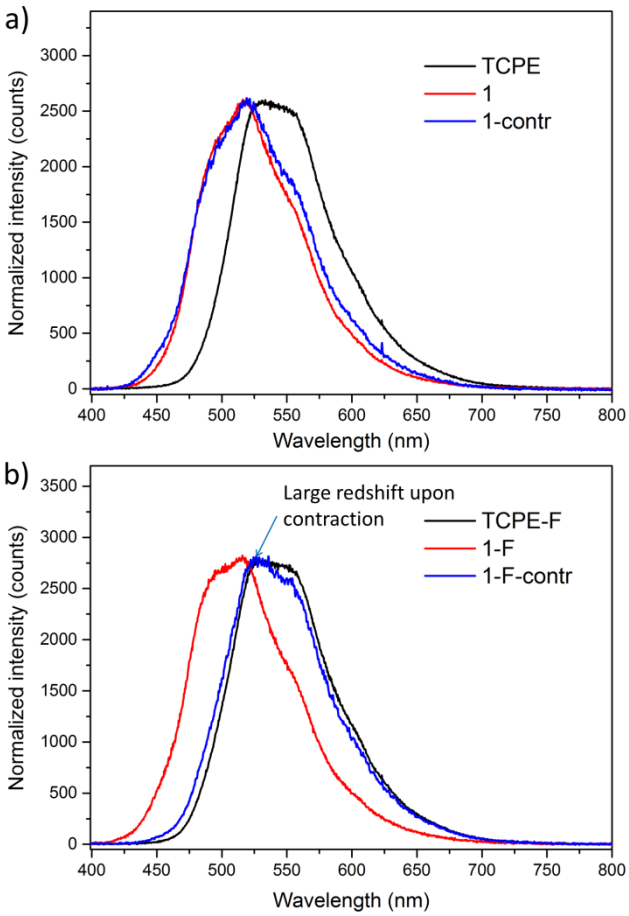

Figure 131. Normalized emission spectra (λ_{exc} = 377 nm) of solid state samples of H_4TCPE, H_4TCPE-F, [Zn_2(TCPE)(bpy)], [Zn_2(TCPE-F)(bpy)] and the contracted frameworks (a: H_4TCPE, [Zn_2(TCPE)(bpy)], [Zn_2(TCPE)(bpy)]-contr; b: H_4TCPE-F, [Zn_2(TCPE-F)(bpy)], [Zn_2(TCPE-F)(bpy)]-contr)

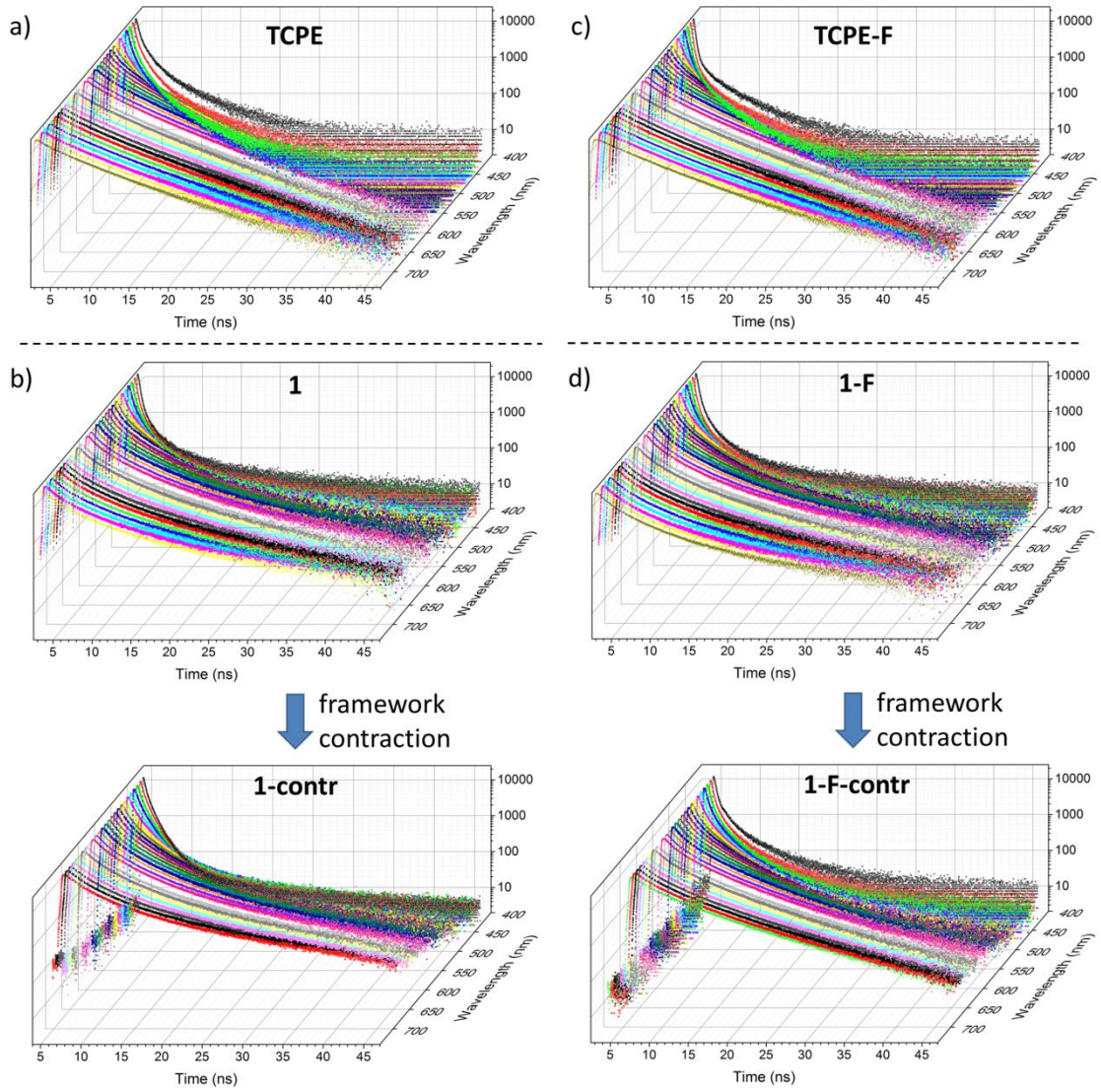

Figure 132. Fluorescence decay curves plotted in the function of probed wavelength for H_4TCPE, H_4TCPE-F (a,b), [Zn_2(TCPE)(bpy)], [Zn_2(TCPE-F)(bpy)] and the contracted frameworks (b,d).

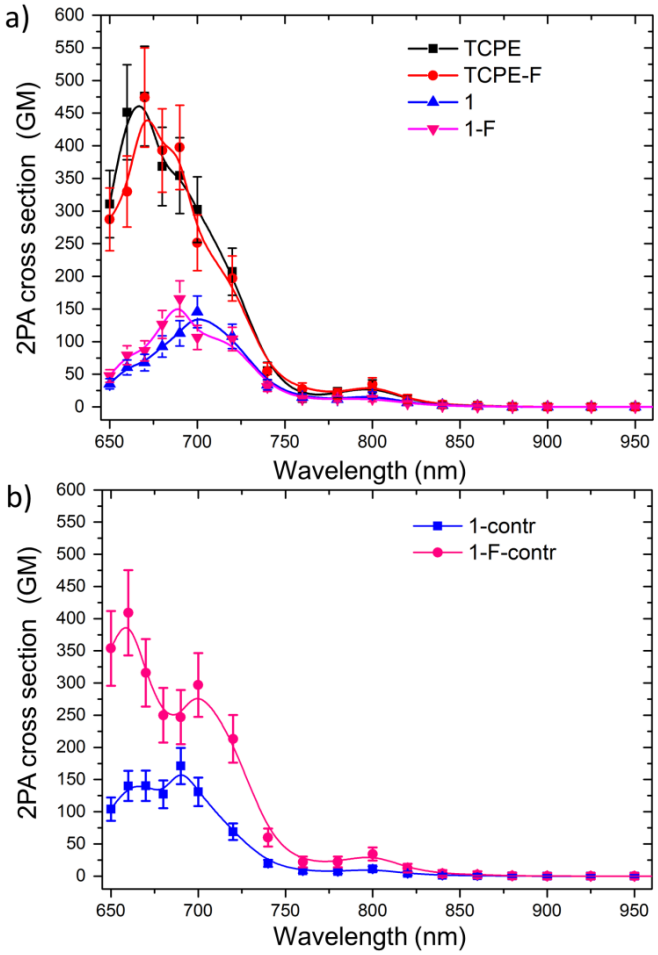

Figure 133. a) TPA spectra of H_4TCPE, H_4TCPE-F, [Zn_2(TCPE)(bpy)] and [Zn_2(TCPE-F)(bpy)]. b) TPA spectrum of [Zn_2(TCPE)(bpy)]-contr and [Zn_2(TCPE-F)(bpy)]-contr.

5.3.2 H_4TPBD, [Zn_2(TPBD)(DMAc)$_2$], [Cd_2(TPBD)(H_2O)$_4$]

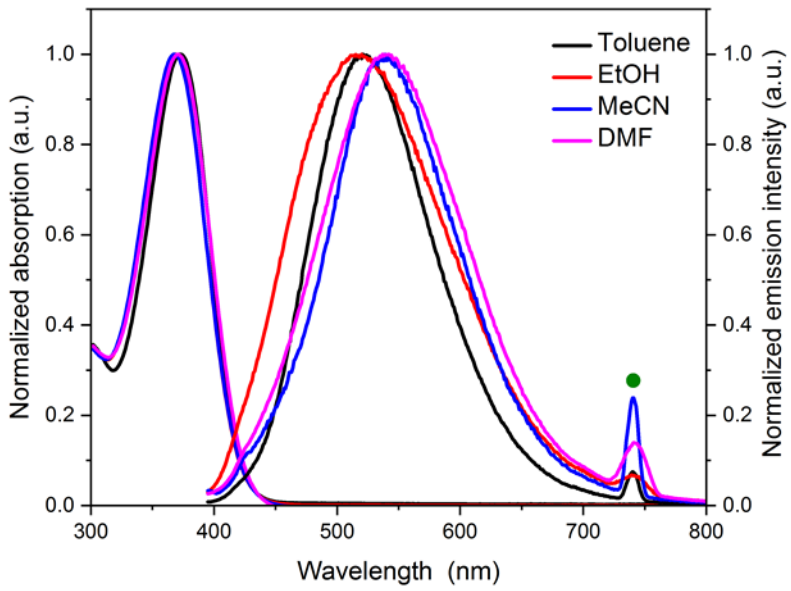

Figure 134. Absorption and emission spectra of H_4TPBD in organic solvents of differing polarity.

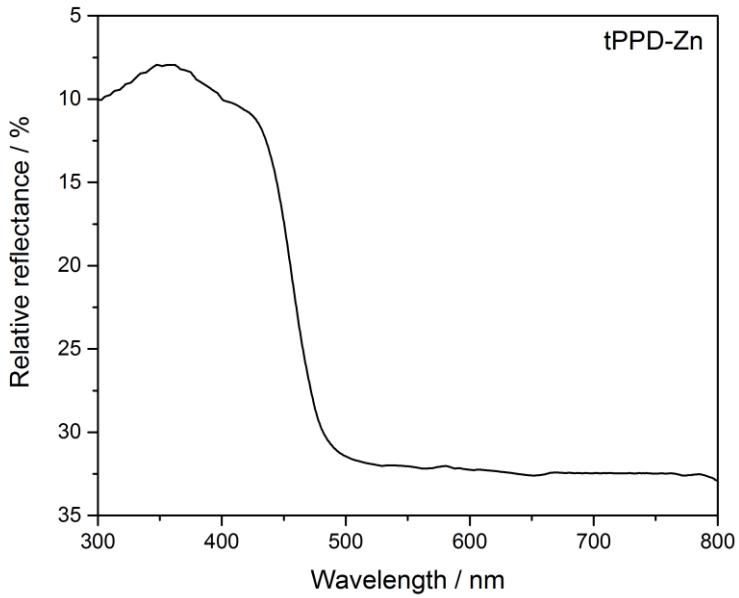

Figure 135. Reflectance spectra of [Zn(TPBD)(DMAc)$_2$].

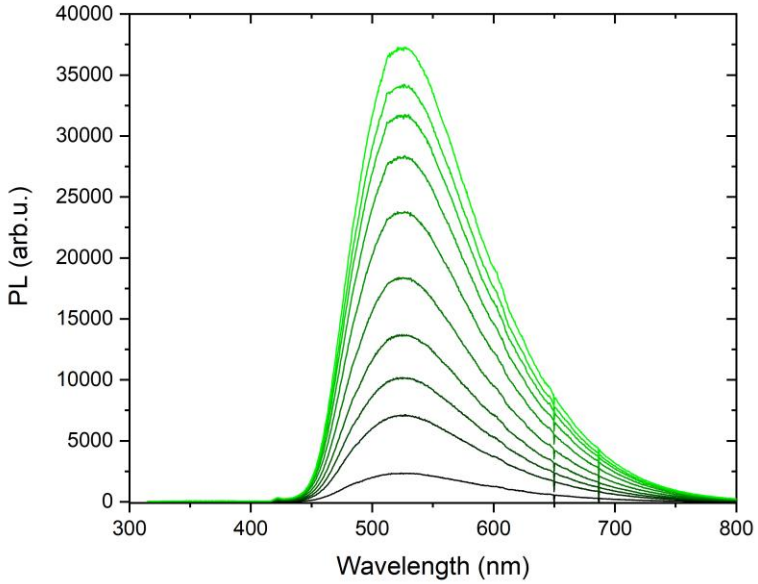

Figure 136. Solid-state PL spectra of [Zn_2(TPBD)(DMAc)$_2$].

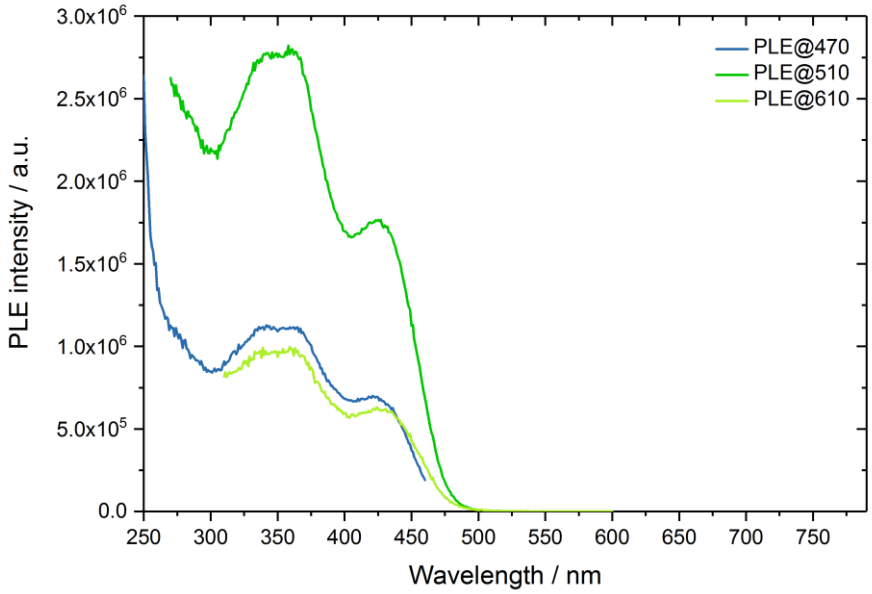

Figure 137. Photoluminescence excitation spectra of [Zn_2(TPBD)(DMAc)$_2$].

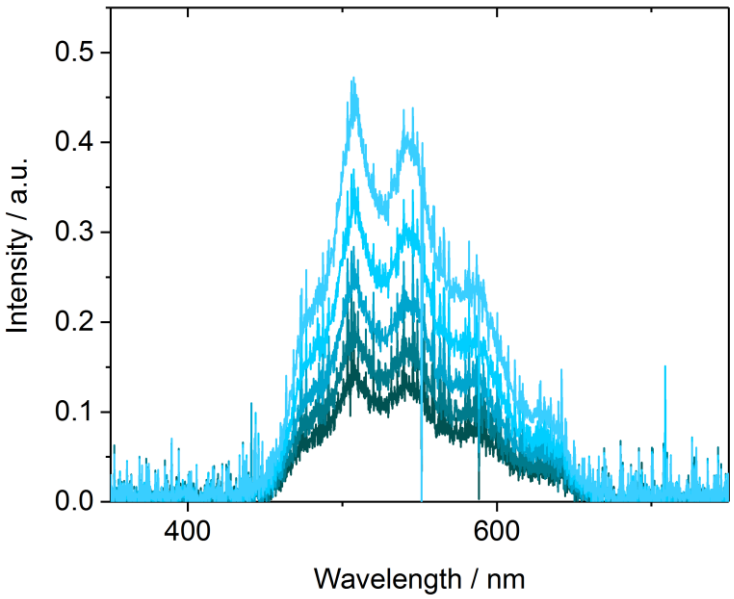

Figure 138. TPEF spectra of [Zn_2(TPBD)$(DMAc)_2$] excited at 800 nm (100 fs-laser, 1kHz repetition rate, integration time 60 s).

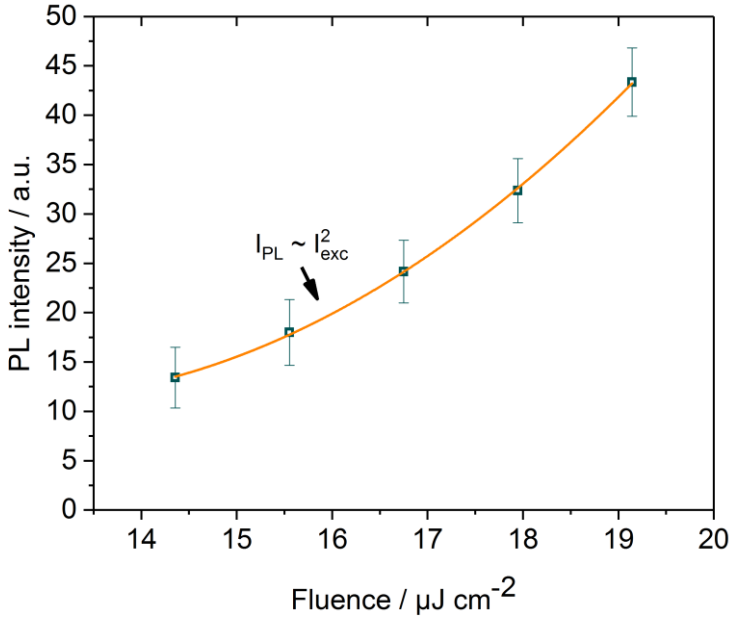

Figure 139. Power-dependent two-photon excited fluorescence areas of [Zn_2(TPBD)$(DMAc)_2$]. The integrated areas show a quadratic behavior in the fluence, thus proofing two-photon absorption.

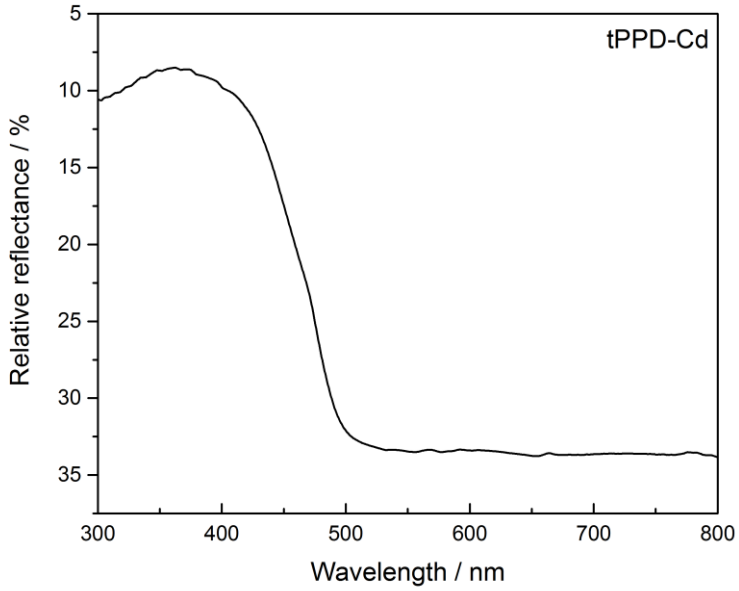

Figure 140. Reflectance spectra of [Cd(TPBD)(H_2O)$_4$].

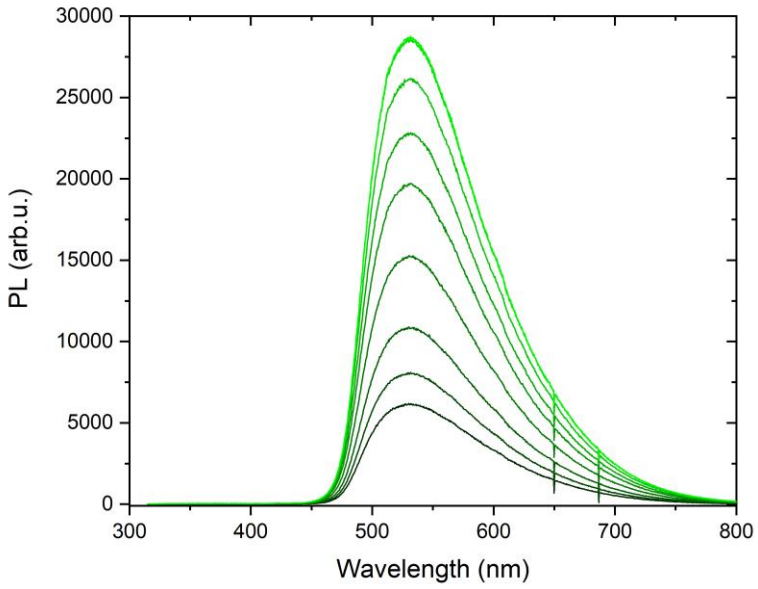

Figure 141. Solid-state PL spectra of [Cd(TPBD)(H_2O)$_4$].

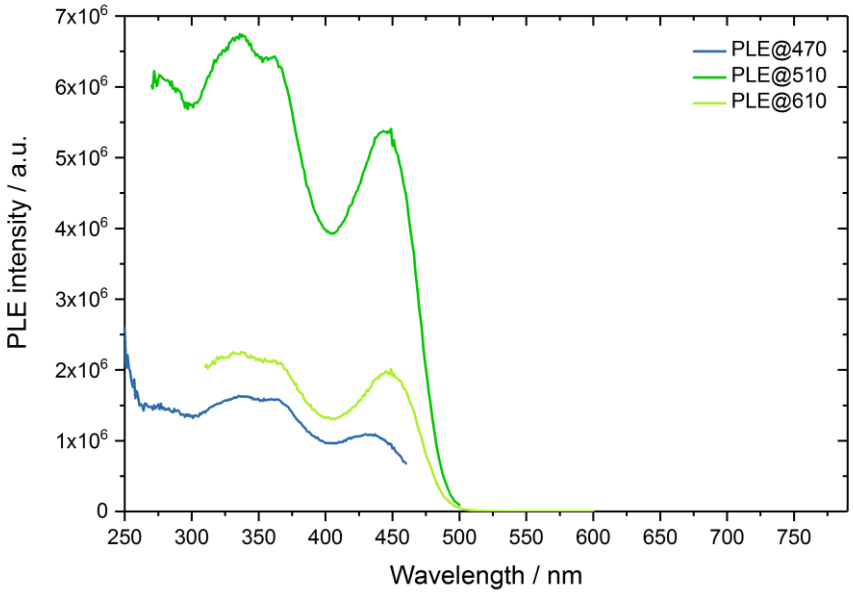

Figure 142. Photoluminescence excitation spectra of [Cd(TPBD)(H_2O)$_4$].

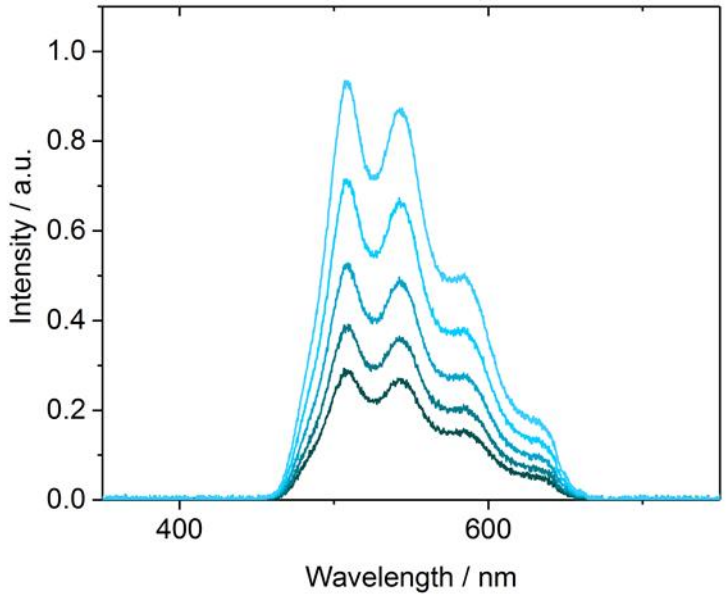

Figure 143. TPEF spectra of [Cd_2(TPBD)(H_2O)$_4$] excited at 800 nm (100 fs-laser, 1kHz repetition rate, integration time 5 s).

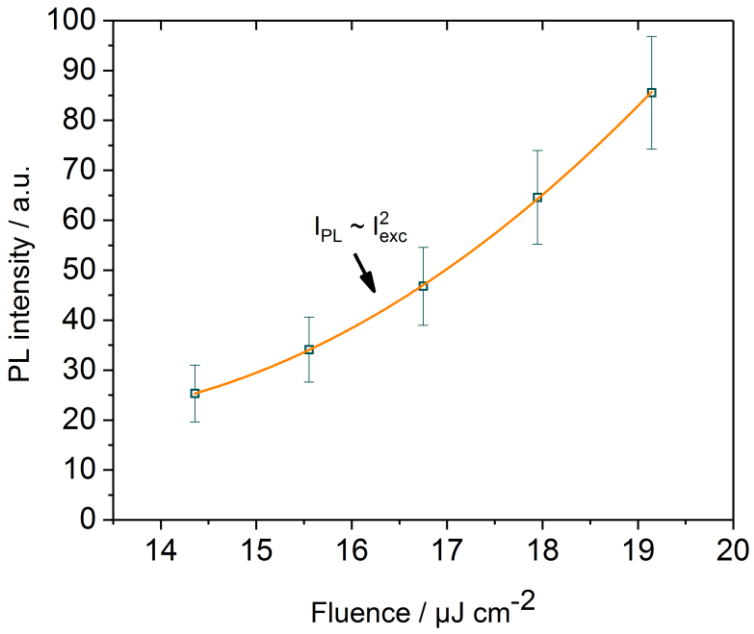

Figure 144. Power-dependent two-photon excited fluorescence areas of $[Cd_2(TPBD)(H_2O)_4]$. The integrated areas show a quadratic behavior in the fluence, thus proofing two-photon absorption.

Table 16. Photophysical characterization details of $[Zn_2(TPBD)(DMAc)_2]$ and $[Cd_2(TPBD)(H_2O)_4]$.

	H_4TPBD	**$[Zn_2(TPBD)(DMAc)_2]$**	**$[Cd_2(TPBD)(H_2O)_4]$**
λ_{em}^{max} [nm]	573[a]	520	521
λ_{abs}^{max} [nm]	371[a]	494[b]	515[b]
$\Delta\lambda^{Stokes}$	202	26	6
EQY [%]	25	25	52
d^{chrom} [mol/dm^3]		1.00	1.19
$\langle\xi\rangle$		1.00	9.38
λ_{em}^{max} (2PA) [nm]		519	520
		F $[\frac{Intensity \cdot nm}{Integration\ time}]$	
14.3 [µJ/cm^2]		0.223	5.06
15.5 [µJ/cm^2]		0.299	6.82
16.7 [µJ/cm^2]		0.402	9.35
17.9 [µJ/cm^2]		0.534	12.9
19.1 [µJ/cm^2]		0.723	17.1

[a]in DMF solution; [b]Absorption edge;

5.3.3 Determination of NLO properties with the SSMPEF method – methodological background and operational specifics

The most frequently utilized method for determination of TPA cross-sections of CPs and MOFs is a modification of the standard TPEF technique. The SS-MPEF technique is in parts already discussed in the background section. Consequently, here operational specifics concerning the characterized materials will be discussed.

In principal, there are two experimental solutions to this technique. Either multi-photon excited fluorescence is collected via a microscope setup, using emission from single microcrystallites of CPs and MOFs, or powdered bulk, sieved material is mounted between glass samples and further characterized. The registration of MPEF is performed with the use of an optical fibre-coupled CCD spectrograph.

In the SS-MPEF technique the considered samples are powdered solids. Therefore, one needs to employ the molar concentration of selected repeating units, in the case here for both compounds, the reference and the CP or MOF. The concentration can be defined as the crystal density divided by the molar mass of selected repeating units of the CP, whereas for the dye standard normally the crystal density is divided by the molar mass of the compound.

There are several approximations that lie behind the methodology of SS-MPEF. Firstly, the scattering has an immense role when fluorescence properties of the samples are considered. That means, that two samples of the same materials but of different grain size can emit signals of significantly different intensity, which can lead to varying conclusions of strength of their NLO response. To minimize such errors, all samples in this thesis were sieved through a set of microsieves before NLO characterization (~ 60 - 100 µm size). Secondly, experimental errors imparted from different spectral dispersion of refractive indices of CPs and reference substance were assume to be approximately equal and are cancelled out. The is assumed for experimental errors accompanied by the experimental setup etc. The above facts lead to an overall error estimation of 15 % to 20 % (compare also the background section).

In general for all considered samples within this thesis, the materials were placed between microscope glass slides and fixed. The focal point of the excitation laser was put onto the powders materials and the MPEF signal was collected by a set of collimating lenses, mounted to the glass optical fiber. Scattered exciting radiation was removed with suitable short and long pass filters. Integration times of the signal ranged between 5 s to 60 s.

In the case of H_4TCPE, H_4TCPE-F, [Zn_2(TCPE)(bpy)] and [Zn_2(TCPE-F)(bpy)] glass slides were horizontally placed on an adjustable holder. Next, the beam from the optical parametric amplifier was directed onto samples at about 45° while the set of collimating lenses, mounted to the glass optical fiber, was placed perpendicular to the plane of the sample. As a TPA reference crystalline bis(4-diphenylamino)stilbene was used.

In the case of [Zn_2(TPBD)$(DMAc)_2$] and [Cd_2(TPBD)$(H_2O)_4$] the beam from the excitation laser was directed onto the samples and the TPEF signals were collected in the backward direction of the laser using an optical fiber coupled CCD spectrograph and collimating lenses. Power-dependent TPEF measurements in the excitation fluence region of mJ/cm^2 revealed considerable photosaturation of the compounds. Consequently, the TPEF signals were then collected at the µJ/cm^2 region. However, changing to a three order of magnitude lower excitation energy, most of the used TPA references (e.g. crystalline perylene) showed no measurable TPEF signal, which circumvents the determination of absolute cross-section numbers. Consequently, the TPEF signals of the compounds were compared between each other, using the similar approach as for comparison with a TPA reference. Following, an enhancement factor can be deduced, phenomenological describing the structure related TPA enhancement in the materials.

5.4 Computational details

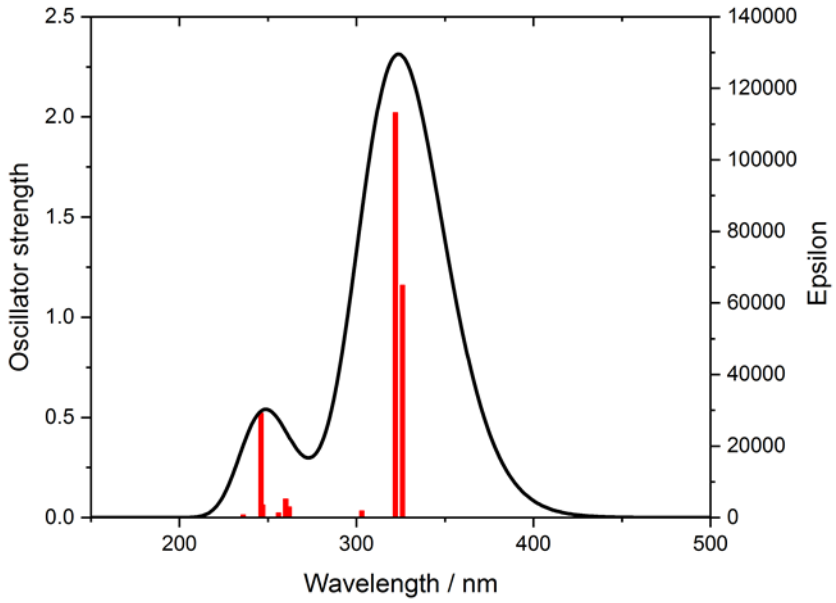

Figure 145. Theoretical UV/Vis spectra of H_4TPBD on the level of TD-DFT(camB3LYP/def2SVP), 20 excited states. The maximum absorption was predicted at 330 nm (compare to 372 nm experimental maximum in DMF solution).

Ground state optimized structure of H_4TPBD in C_i point group

Symbol	X	Y	Z
	Nimag = 0		
O	-8.2294230	-9.4483670	0.1102980
O	-6.2315770	-10.4313090	-0.0037170
O	-9.0928560	8.2944830	-1.0981130
O	-8.6905850	8.6541480	1.0651440
N	-2.8158740	-0.2599370	-0.0129140
C	-6.8887140	-9.4234250	0.0437410
C	-6.3284690	-8.0470940	0.0356100
C	-7.1383940	-6.9107070	0.0926740
H	-8.2216830	-7.0253050	0.1369390
C	-6.5651980	-5.6461540	0.0814430
H	-7.2111610	-4.7667030	0.1008770
C	-5.1741430	-5.4813900	0.0153400
C	-4.3739900	-6.6324890	-0.0405900
H	-3.2875510	-6.5328580	-0.0671230
C	-4.9417620	-7.8978920	-0.0315940
H	-4.3220820	-8.7952730	-0.0674870
C	-4.5660870	-4.1287480	0.0057230
C	-5.1198870	-3.0762940	0.7463020
H	-5.9991450	-3.2579690	1.3673530
C	-4.5484170	-1.8117090	0.7499290
H	-4.9887390	-1.0191800	1.3563660
C	-3.4022250	-1.5442880	-0.0096380
C	-2.8460780	-2.5874530	-0.7606930
H	-1.9622270	-2.3975090	-1.3709750

C	-3.4144060	-3.8534580	-0.7427140
H	-2.9698340	-4.6390030	-1.3567790
C	-3.6240820	0.8989950	-0.0076990
C	-4.7896780	0.9674810	-0.7810320
H	-5.0805210	0.1122790	-1.3924600
C	-5.5799970	2.1084200	-0.7690100
H	-6.4933470	2.1229940	-1.3668170
C	-5.2377950	3.2283460	-0.0002460
C	-4.0659410	3.1528460	0.7630440
H	-3.7562580	4.0107730	1.3628590
C	-3.2751580	2.0120140	0.7668740
H	-2.3691560	1.9812100	1.3734670
C	-6.0836890	4.4473410	0.0061330
C	-6.7360470	4.8786990	-1.1576660
H	-6.6011250	4.3234820	-2.0875310
C	-7.5287750	6.0186400	-1.1551490
H	-8.0245850	6.3483510	-2.0684130
C	-7.6874210	6.7583180	0.0188410
C	-7.0432750	6.3403710	1.1850780
H	-7.1836720	6.9245400	2.0958880
C	-6.2532190	5.2004510	1.1774970
H	-5.7758130	4.8728150	2.1025780
C	-8.5233730	7.9856140	0.0777380
C	-1.4037760	-0.1304580	-0.0067000
C	-0.6178360	-0.8982460	0.8594260
H	-1.1005280	-1.5970750	1.5443960
C	0.7646390	-0.7697030	0.8659750
H	1.3616410	-1.3682520	1.5558850
O	8.2294120	9.4483730	-0.1104050
O	6.2315660	10.4313130	0.0036410
O	9.0928450	-8.2944930	1.0981230
O	8.6905880	-8.6541490	-1.0651380
N	2.8158770	0.2599370	0.0129180
C	6.8887100	9.4234280	-0.0437140
C	6.3284660	8.0470970	-0.0355920
C	7.1383920	6.9107100	-0.0926630
H	8.2216810	7.0253090	-0.1369280
C	6.5651970	5.6461570	-0.0814320
H	7.2111610	4.7667070	-0.1008700
C	5.1741420	5.4813920	-0.0153280
C	4.3739890	6.6324900	0.0406070
H	3.2875490	6.5328580	0.0671430
C	4.9417590	7.8978930	0.0316130
H	4.3220780	8.7952740	0.0675110
C	4.5660870	4.1287490	-0.0057130
C	5.1198870	3.0762970	-0.7462950
H	5.9991420	3.2579740	-1.3673470
C	4.5484180	1.8117120	-0.7499240
H	4.9887390	1.0191840	-1.3563650
C	3.4022280	1.5442870	0.0096440
C	2.8460810	2.5874510	0.7607030
H	1.9622310	2.3975040	1.3709860
C	3.4144080	3.8534550	0.7427260
H	2.9698370	4.6389990	1.3567940
C	3.6240850	-0.8989950	0.0077020
C	4.7896790	-0.9674830	0.7810380
H	5.0805200	-0.1122820	1.3924690
C	5.5799990	-2.1084210	0.7690160
H	6.4933460	-2.1229960	1.3668270
C	5.2377980	-3.2283460	0.0002480
C	4.0659480	-3.1528440	-0.7630450
H	3.7562670	-4.0107700	-1.3628630

C	3.2751640	-2.0120130	-0.7668750
H	2.3691640	-1.9812070	-1.3734710
C	6.0836930	-4.4473420	-0.0061300
C	6.7360440	-4.8787040	1.1576720
H	6.6011170	-4.3234890	2.0875380
C	7.5287710	-6.0186460	1.1551560
H	8.0245740	-6.3483600	2.0684220
C	7.6874220	-6.7583200	-0.0188360
C	7.0432830	-6.3403690	-1.1850740
H	7.1836840	-6.9245360	-2.0958850
C	6.2532280	-5.2004480	-1.1774940
H	5.7758270	-4.8728100	-2.1025770
C	8.5233710	-7.9856180	-0.0777310
C	1.4037790	0.1304570	0.0067020
C	0.6178390	0.8982450	-0.8594240
H	1.1005310	1.5970740	-1.5443930
C	-0.7646360	0.7697020	-0.8659720
H	-1.3616380	1.3682510	-1.5558820
H	-8.4879710	-10.3836730	0.1091610
H	9.6091680	-9.1027170	0.9504120
H	-9.6091800	9.1027060	-0.9504010
H	8.4879540	10.3836800	-0.1093470

Ground state optimized structure of H_4TPBD in C_{2h} point group

Symbol	X	Y	Z
	Nimag = 0		
O	9.8078080	0.0439740	7.1814400
O	8.6405450	-0.0847240	9.0766000
O	-9.8078080	-0.0439740	7.1814400
O	-8.6405450	0.0847240	9.0766000
O	-9.8078080	-0.0439740	-7.1814400
O	-8.6405450	0.0847240	-9.0766000
O	9.8078080	0.0439740	-7.1814400
O	8.6405450	-0.0847240	-9.0766000
N	0.0000000	0.0000000	2.8278610
N	0.0000000	0.0000000	-2.8278610
C	8.7425570	-0.0136980	7.7397930
C	-7.4255160	0.0146580	-7.0514230
C	-8.7425570	0.0136980	-7.7397930
C	-0.8375210	0.8623860	-0.6942180
C	-0.8375210	0.8623860	0.6942180
C	0.0000000	0.0000000	1.4098040
C	6.2017150	0.0566460	4.9720400
C	7.4077870	0.0555860	5.6569740
C	7.4255160	-0.0146580	7.0514230
C	6.2181790	-0.0830360	7.7501500
C	5.0135070	-0.0797810	7.0598990
C	4.9806900	-0.0105170	5.6596950
C	2.3114290	0.7591500	3.0751630
C	3.5194300	0.7454180	3.7584970
C	3.6913310	-0.0080470	4.9268160
C	2.5974770	-0.7596250	5.3757550
C	1.3915370	-0.7673340	4.6892460
C	1.2262420	-0.0012010	3.5283680
C	-3.5194300	-0.7454180	3.7584970
C	-2.3114290	-0.7591500	3.0751630
C	-1.2262420	0.0012010	3.5283680
C	-1.3915370	0.7673340	4.6892460

C	-2.5974770	0.7596250	5.3757550
C	-3.6913310	0.0080470	4.9268160
C	-7.4077870	-0.0555860	5.6569740
C	-6.2017150	-0.0566460	4.9720400
C	-4.9806900	0.0105170	5.6596950
C	-5.0135070	0.0797810	7.0598990
C	-6.2181790	0.0830360	7.7501500
C	-7.4255160	0.0146580	7.0514230
C	-8.7425570	0.0136980	7.7397930
C	0.8375210	-0.8623860	0.6942180
C	0.8375210	-0.8623860	-0.6942180
C	0.0000000	0.0000000	-1.4098040
C	-5.0135070	0.0797810	-7.0598990
C	-6.2181790	0.0830360	-7.7501500
C	-7.4077870	-0.0555860	-5.6569740
C	-6.2017150	-0.0566460	-4.9720400
C	-4.9806900	0.0105170	-5.6596950
C	-2.3114290	-0.7591500	-3.0751630
C	-3.5194300	-0.7454180	-3.7584970
C	-3.6913310	0.0080470	-4.9268160
C	-2.5974770	0.7596250	-5.3757550
C	-1.3915370	0.7673340	-4.6892460
C	-1.2262420	0.0012010	-3.5283680
C	3.5194300	0.7454180	-3.7584970
C	2.3114290	0.7591500	-3.0751630
C	1.2262420	-0.0012010	-3.5283680
C	1.3915370	-0.7673340	-4.6892460
C	2.5974770	-0.7596250	-5.3757550
C	3.6913310	-0.0080470	-4.9268160
C	7.4077870	0.0555860	-5.6569740
C	6.2017150	0.0566460	-4.9720400
C	4.9806900	-0.0105170	-5.6596950
C	5.0135070	-0.0797810	-7.0598990
C	6.2181790	-0.0830360	-7.7501500
C	7.4255160	-0.0146580	-7.0514230
C	8.7425570	-0.0136980	-7.7397930
H	-9.5470170	0.0773970	9.4228490
H	-9.5470170	0.0773970	-9.4228490
H	9.5470170	-0.0773970	9.4228490
H	9.5470170	-0.0773970	-9.4228490
H	-1.4889370	1.5496320	-1.2363530
H	-1.4889370	1.5496320	1.2363530
H	6.2046990	0.0860050	3.8811300
H	8.3595430	0.1002780	5.1252460
H	6.2303610	-0.1297630	8.8393010
H	4.0769400	-0.1077300	7.6194410
H	2.1999230	1.3736780	2.1809200
H	4.3387180	1.3671750	3.3923800
H	2.7013340	-1.3852150	6.2644000
H	0.5655300	-1.3815770	5.0500560
H	-4.3387180	-1.3671750	3.3923800
H	-2.1999230	-1.3736780	2.1809200
H	-0.5655300	1.3815770	5.0500560
H	-2.7013340	1.3852150	6.2644000
H	-8.3595430	-0.1002780	5.1252460
H	-6.2046990	-0.0860050	3.8811300
H	-4.0769400	0.1077300	7.6194410
H	-6.2303610	0.1297630	8.8393010
H	1.4889370	-1.5496320	1.2363530
H	1.4889370	-1.5496320	-1.2363530
H	-4.0769400	0.1077300	-7.6194410
H	-6.2303610	0.1297630	-8.8393010

H	-8.3595430	-0.1002780	-5.1252460
H	-6.2046990	-0.0860050	-3.8811300
H	-2.1999230	-1.3736780	-2.1809200
H	-4.3387180	-1.3671750	-3.3923800
H	-2.7013340	1.3852150	-6.2644000
H	-0.5655300	1.3815770	-5.0500560
H	4.3387180	1.3671750	-3.3923800
H	2.1999230	1.3736780	-2.1809200
H	0.5655300	-1.3815770	-5.0500560
H	2.7013340	-1.3852150	-6.2644000
H	8.3595430	0.1002780	-5.1252460
H	6.2046990	0.0860050	-3.8811300
H	4.0769400	-0.1077300	-7.6194410
H	6.2303610	-0.1297630	-8.8393010

First excited state geometry of H_4TPBD

Symbol	X	Y	Z
	Nimag = 0		
O	8.7473770	-9.0857470	-0.3598380
O	6.8401900	-10.1852360	-0.0023390
O	8.9001200	8.4003720	1.2766630
O	8.6699280	8.6759950	-0.9244920
N	2.7975190	-0.2505080	0.0227060
C	7.4229120	-9.1430420	-0.1539420
C	6.7759570	-7.8038260	-0.1352840
C	7.4996470	-6.6234980	-0.3171450
H	8.5777480	-6.6731550	-0.4710700
C	6.8484660	-5.3973790	-0.2909530
H	7.4296360	-4.4812980	-0.4095530
C	5.4641790	-5.3185520	-0.0837330
C	4.7505730	-6.5124420	0.0973170
H	3.6684970	-6.4795070	0.2356480
C	5.3968040	-7.7395280	0.0720730
H	4.8454390	-8.6717310	0.2042220
C	4.7720450	-4.0067110	-0.0563560
C	5.1708260	-2.9578660	-0.8960430
H	5.9867210	-3.1142590	-1.6038630
C	4.5217270	-1.7313970	-0.8790050
H	4.8375860	-0.9356480	-1.5551610
C	3.4526710	-1.5094350	-0.0050780
C	3.0520420	-2.5437460	0.8471620
H	2.2351000	-2.3756400	1.5505550
C	3.6977420	-3.7718020	0.8124020
H	3.3826250	-4.5547720	1.5044190
C	3.5911150	0.9273640	0.0375460
C	4.6913240	1.0277310	0.8952240
H	4.9359840	0.1955270	1.5569060
C	5.4734520	2.1741180	0.9013420
H	6.3380340	2.2203380	1.5657240
C	5.1844320	3.2601750	0.0639560
C	4.0789740	3.1460670	-0.7903380
H	3.8159010	3.9766990	-1.4474690
C	3.2970160	1.9998520	-0.8111680
H	2.4443070	1.9340800	-1.4886110
C	6.0197620	4.4861120	0.0791050
C	6.5765480	4.9626400	1.2743740
H	6.3741650	4.4396610	2.2106710
C	7.3576990	6.1103880	1.2927900

H	7.7783020	6.4771830	2.2292880
C	7.6010830	6.8099610	0.1089700
C	7.0529500	6.3460370	-1.0884020
H	7.2587910	6.9004260	-2.0053220
C	6.2724650	5.1996200	-1.1018750
H	5.8698250	4.8371730	-2.0492890
C	8.4302030	8.0440600	0.0714900
C	1.4062740	-0.1721400	0.0382700
C	0.6152190	-1.1598470	-0.5910250
H	1.1008770	-1.9824730	-1.1158220
C	-0.7597710	-1.0790930	-0.5846330
H	-1.3450630	-1.8324140	-1.1124210
O	-8.0065910	9.4174210	0.7387160
O	-6.6971030	10.0947130	-0.9362730
O	-9.4669600	-8.1355570	-1.0252210
O	-8.9645250	-8.5936790	1.0990390
N	-2.8077160	0.1108220	0.0264590
C	-7.0237410	9.2160160	-0.1688960
C	-6.4368330	7.8746900	-0.1092590
C	-6.8607200	6.8943180	0.8074420
H	-7.6585780	7.1357710	1.5106960
C	-6.2794520	5.6451860	0.8270760
H	-6.6371310	4.9270290	1.5641140
C	-5.2305430	5.2842680	-0.0690480
C	-4.8204080	6.2960160	-0.9875010
H	-4.0319940	6.0890980	-1.7103720
C	-5.4029580	7.5428940	-1.0046750
H	-5.0768680	8.3018990	-1.7179120
C	-4.6207310	3.9763730	-0.0464310
C	-5.0832270	2.9319300	0.8196550
H	-5.9216990	3.1185580	1.4886160
C	-4.5073990	1.6877670	0.8460650
H	-4.8861210	0.9265680	1.5307440
C	-3.4035870	1.3841440	0.0068700
C	-2.9280810	2.3965880	-0.8692170
H	-2.1017650	2.1745360	-1.5470720
C	-3.5167440	3.6352870	-0.8903340
H	-3.1213340	4.3746210	-1.5850740
C	-3.6325870	-1.0310130	0.0129970
C	-4.8130110	-1.0388690	-0.7488510
H	-5.0669250	-0.1655020	-1.3497920
C	-5.6414190	-2.1473920	-0.7382170
H	-6.5555300	-2.1240050	-1.3333170
C	-5.3465930	-3.2806750	0.0385090
C	-4.1721070	-3.2503090	0.8105850
H	-3.9064480	-4.1135260	1.4227430
C	-3.3301680	-2.1523850	0.8046730
H	-2.4337830	-2.1481170	1.4259700
C	-6.2411570	-4.4584570	0.0498180
C	-6.9724430	-4.8206330	-1.0927780
H	-6.8635680	-4.2408040	-2.0106440
C	-7.8099380	-5.9268740	-1.0877350
H	-8.3649120	-6.2025410	-1.9846830
C	-7.9400350	-6.7025280	0.0670970
C	-7.2199410	-6.3534810	1.2120200
H	-7.3400500	-6.9632170	2.1088290
C	-6.3828500	-5.2487960	1.2025170
H	-5.8501200	-4.9762460	2.1148760
C	-8.8232210	-7.8959930	0.1278350
C	-1.4210830	-0.0052530	0.051474H0
C	-0.6314350	0.9885110	0.6707790
H	-1.1241000	1.8149850	1.1823480

C	0.7443900	0.8996670	0.6711660
H	1.3286370	1.6628790	1.1851500
H	9.0695050	-10.0012270	-0.3538580
H	-10.0107960	-8.9260370	-0.8798370
H	9.4194880	9.2094080	1.1440490
H	-8.3063860	10.3283330	0.5972990

Table 17. TD-DFT results of H_4TPBD, first 20 excited states.

State	Energy [eV] ([nm])	Oscillator strengths	TDM [D][a]	Symmetry[b]
S_1	3.8018 (326.12)	1.1623	12.4794	A_u
S_2	3.8108 (325.35)	0.0000	0.0000	B_g
S_3	3.8432 (322.61)	2.0220	21.4749	B_u
S_4	4.0853 (303.49)	0.0325	0.3249	B_u
S_5	4.3900 (282.42)	0.0000	0.0000	B_g
S_6	4.4203 (280.49)	0.0000	0.0000	A_g
S_7	4.7239 (262.46)	0.0531	0.4591	B_u
S_8	4.7636 (260.27)	0.0920	0.7886	A_u
S_9	4.7753 (259.63)	0.0000	0.0000	A_g
S_{10}	4.8368 (256.34)	0.0233	0.1970	A_u
S_{11}	4.9620 (249.87)	0.0000	0.0000	A_g
S_{12}	5.0116 (247.39)	0.0000	0.0000	B_g
S_{13}	5.0124 (247.36)	0.0626	0.5098	B_u
S_{14}	5.0159 (247.18)	0.0000	0.0000	B_g
S_{15}	5.0169 (247.13)	0.0561	0.4566	A_u
S_{16}	5.0203 (246.96)	0.0000	0.0000	A_g
S_{17}	5.0269 (246.64)	0.5024	4.0794	B_u
S_{18}	5.2432 (236.47)	0.0000	0.0000	B_g
S_{19}	5.2439 (236.43)	0.0132	0.1026	B_u
S_{20}	5.2462 (236.33)	0.0000	0.0000	B_g

[a]TDM = Transition dipole moment; [b]Symmetry according to C_{2h} point group

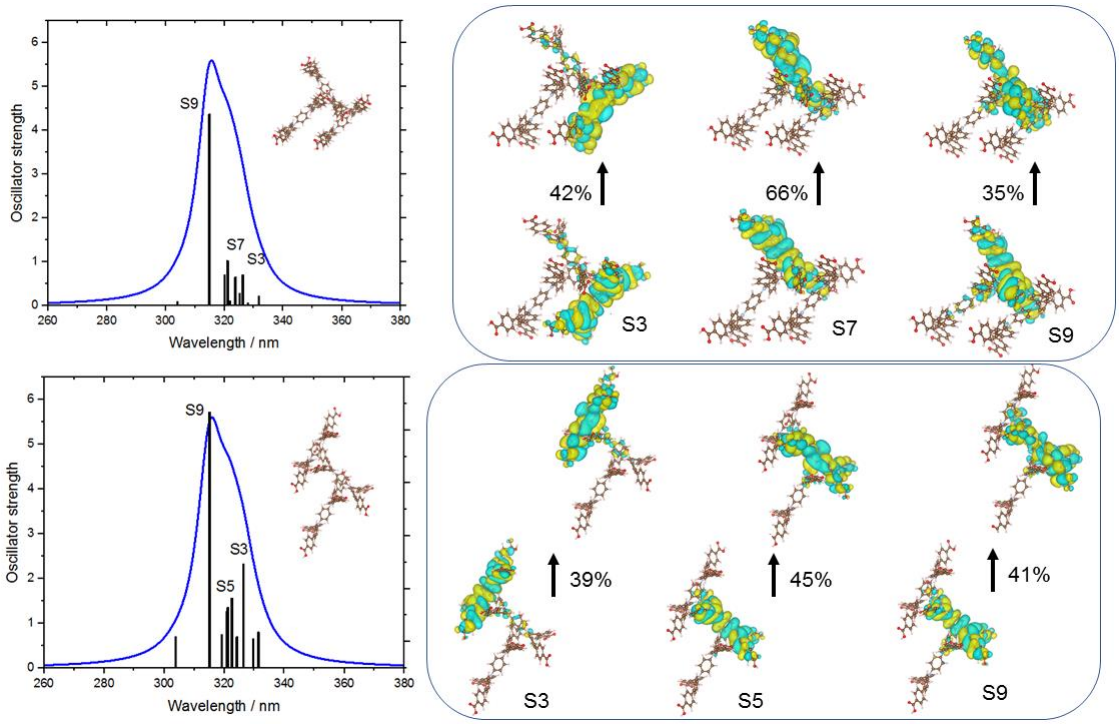

Figure 146. Electronic absorption spectra (camB3LYP/def2SVP level) and respective NTOs of $[Zn_2(TPBD)(DMAc)_2]$ trimer structures (above = along b-axis, down = along c-axis).

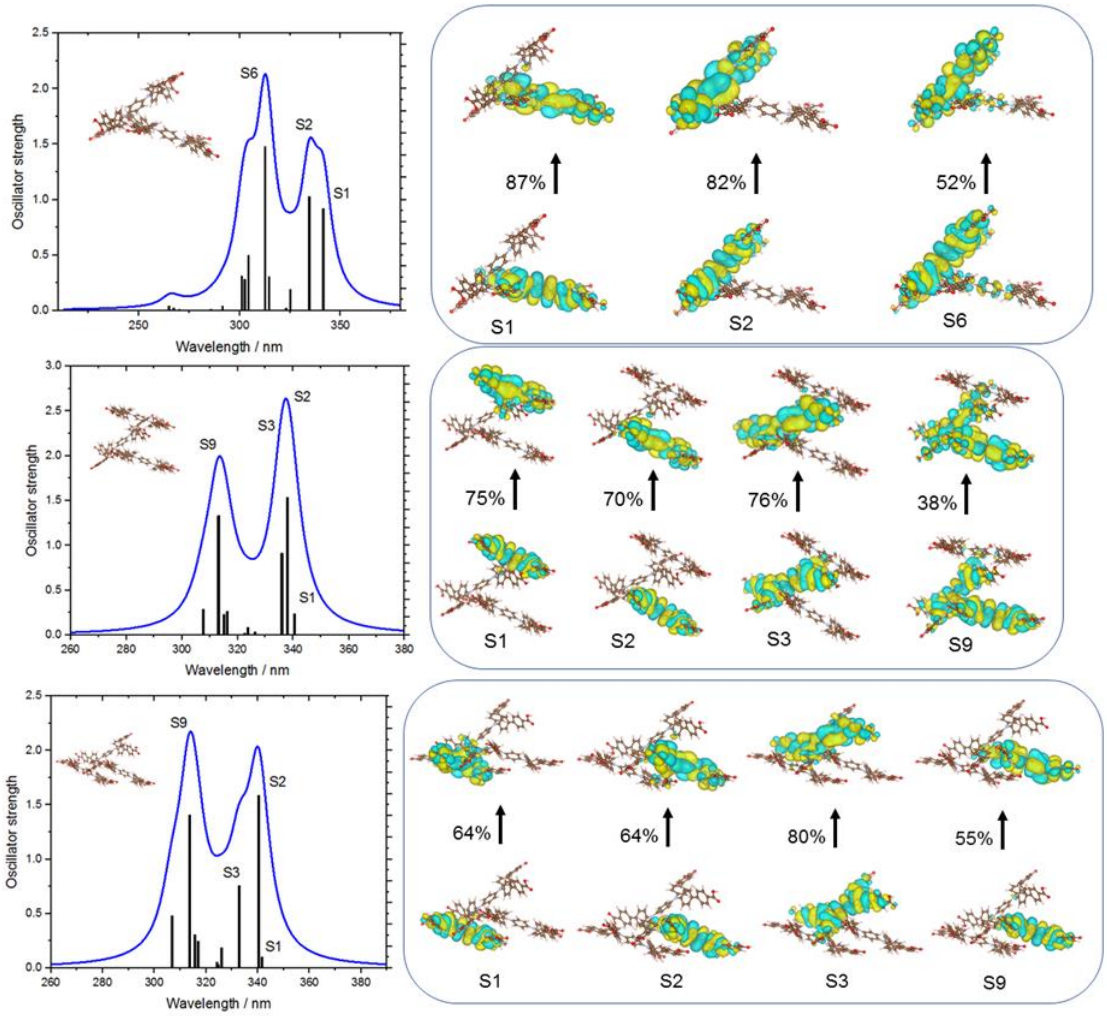

Figure 147. Electronic absorption spectra (camB3LYP/def2SVP level) and respective NTOs of $[Cd_2(TPBD)(H_2O)_4]$ herringbone dimer structure (above) and trimer structure (middle = along a-axis, down = along b-axis).

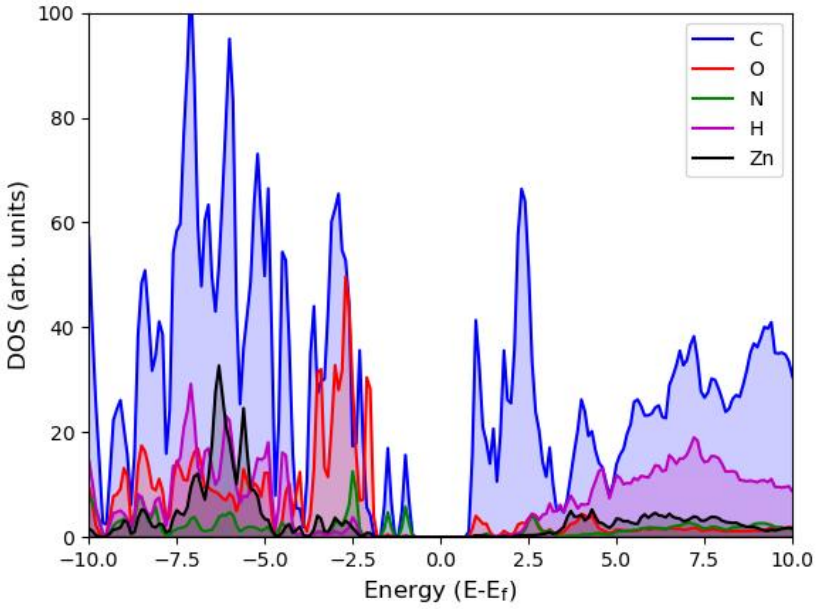

Figure 148. Projected density of states of $[Zn_2(TPBD)(DMAc)_2]$.

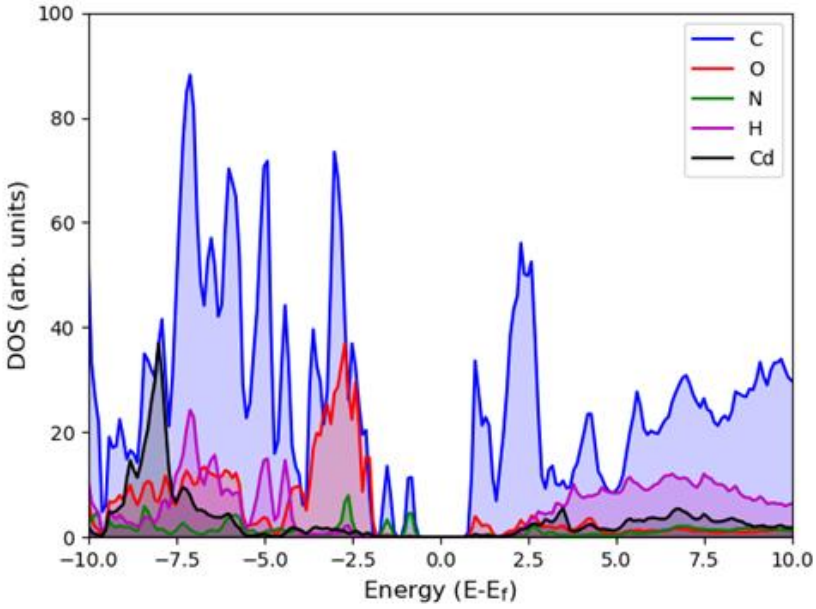

Figure 149. Projected density of states of $[Cd_2(TPBD)(H_2O)_4]$.

Optimized geometry of [Zn_2(TPBD)(DMAc)$_2$]

_cell_length_a		21.71400			
_cell_length_b		10.00360			
_cell_length_c		15.18200			
_cell_angle_alpha		90			
_cell_angle_beta		99.15800			
_cell_angle_gamma		90			
	Zn	1.0	0.960330	0.644732	0.056424
	Zn	1.0	0.039575	0.144485	0.443526
	Zn	1.0	0.039670	0.355268	0.943576
	Zn	1.0	0.960425	0.855515	0.556474
	C	1.0	0.066101	0.499822	0.110677
	C	1.0	0.933863	0.999653	0.389278
	C	1.0	0.933899	0.500178	0.889323
	C	1.0	0.066137	0.000347	0.610722
	O	1.0	0.884794	0.542743	0.068255
	O	1.0	0.115165	0.042661	0.431740
	O	1.0	0.115206	0.457257	0.931745
	O	1.0	0.884835	0.957339	0.568260
	O	1.0	0.915942	0.616007	0.208089
	O	1.0	0.084039	0.116358	0.292009
	O	1.0	0.084058	0.383993	0.791911
	O	1.0	0.915961	0.883642	0.707991
	C	1.0	0.131258	0.464042	0.148128
	C	1.0	0.868729	0.963702	0.351846
	C	1.0	0.868742	0.535958	0.851872
	C	1.0	0.131271	0.036298	0.648154
	O	1.0	0.030146	0.410654	0.069777
	O	1.0	0.969876	0.910589	0.430194
	O	1.0	0.969854	0.589346	0.930223
	O	1.0	0.030124	0.089411	0.569806

C	1.0	0.173134	0.556763	0.194215
C	1.0	0.826841	0.056367	0.305725
C	1.0	0.826866	0.443237	0.805785
C	1.0	0.173159	0.943633	0.694275
H	1.0	0.157515	0.658618	0.203714
H	1.0	0.842450	0.158215	0.296180
H	1.0	0.842485	0.341382	0.796286
H	1.0	0.157550	0.841785	0.703820
O	1.0	0.047015	0.619520	0.121189
O	1.0	0.952889	0.119396	0.378755
O	1.0	0.952985	0.380480	0.878811
O	1.0	0.047111	0.880604	0.621245
C	1.0	0.233973	0.518481	0.228124
C	1.0	0.766008	0.018036	0.271850
C	1.0	0.766027	0.481519	0.771877
C	1.0	0.233992	0.981964	0.728150
H	1.0	0.265731	0.590483	0.265235
H	1.0	0.734236	0.089982	0.234711
H	1.0	0.734269	0.409517	0.734765
H	1.0	0.265764	0.910018	0.765289
C	1.0	0.254472	0.387029	0.216717
C	1.0	0.745530	0.886588	0.283328
C	1.0	0.745528	0.612971	0.783283
C	1.0	0.254470	0.113412	0.716672
O	1.0	0.945240	0.840560	0.040723
O	1.0	0.054673	0.340252	0.459317
O	1.0	0.054760	0.159440	0.959277
O	1.0	0.945327	0.659748	0.540683
C	1.0	0.151560	0.333125	0.136111
C	1.0	0.848457	0.832774	0.363926
C	1.0	0.848440	0.666875	0.863889

C	1.0	0.151543	0.167226	0.636074
H	1.0	0.119217	0.261184	0.100221
H	1.0	0.880814	0.760898	0.399862
H	1.0	0.880783	0.738816	0.899779
H	1.0	0.119186	0.239102	0.600138
C	1.0	0.212238	0.295982	0.169162
C	1.0	0.787781	0.795576	0.330894
C	1.0	0.787762	0.704018	0.830838
C	1.0	0.212219	0.204424	0.669106
H	1.0	0.227600	0.194655	0.157999
H	1.0	0.772432	0.694247	0.342090
H	1.0	0.772400	0.805345	0.842001
H	1.0	0.227568	0.305753	0.657910
N	1.0	0.496694	0.188264	0.360469
N	1.0	0.503257	0.688212	0.139535
N	1.0	0.503306	0.811736	0.639531
N	1.0	0.496743	0.311788	0.860465
N	1.0	0.935123	0.056597	0.078282
N	1.0	0.064905	0.556279	0.421884
N	1.0	0.064877	0.943403	0.921718
N	1.0	0.935095	0.443721	0.578116
C	1.0	0.385031	0.157620	0.315211
C	1.0	0.614892	0.657330	0.184892
C	1.0	0.614969	0.842380	0.684789
C	1.0	0.385108	0.342670	0.815108
H	1.0	0.390444	0.053548	0.335702
H	1.0	0.609427	0.553258	0.164414
H	1.0	0.609556	0.946452	0.664298
H	1.0	0.390573	0.446742	0.835586
C	1.0	0.437544	0.241171	0.323450
C	1.0	0.562420	0.740999	0.176600

C	1.0	0.562456	0.758829	0.676550
C	1.0	0.437580	0.259001	0.823400
C	1.0	0.429578	0.375712	0.297448
C	1.0	0.570434	0.875526	0.202593
C	1.0	0.570422	0.624288	0.702552
C	1.0	0.429566	0.124474	0.797407
H	1.0	0.469908	0.441988	0.303903
H	1.0	0.530132	0.941883	0.196109
H	1.0	0.530092	0.558012	0.696097
H	1.0	0.469868	0.058117	0.803891
C	1.0	0.370407	0.424445	0.263218
C	1.0	0.629621	0.924153	0.236832
C	1.0	0.629593	0.575555	0.736782
C	1.0	0.370379	0.075847	0.763168
H	1.0	0.365334	0.528935	0.242553
H	1.0	0.634741	0.028646	0.257470
H	1.0	0.634666	0.471065	0.757447
H	1.0	0.365259	0.971354	0.742530
C	1.0	0.317633	0.340883	0.254298
C	1.0	0.682359	0.840475	0.245791
C	1.0	0.682367	0.659117	0.745702
C	1.0	0.317641	0.159525	0.754209
C	1.0	0.326365	0.206977	0.281939
C	1.0	0.673576	0.706555	0.218200
C	1.0	0.673635	0.793023	0.718061
C	1.0	0.326424	0.293445	0.781800
H	1.0	0.286383	0.140152	0.277946
H	1.0	0.713527	0.639633	0.222237
H	1.0	0.713617	0.859848	0.722054
H	1.0	0.286473	0.360367	0.777763
C	1.0	0.551479	0.224107	0.327917

C	1.0	0.448474	0.724191	0.172038
C	1.0	0.448521	0.775893	0.672083
C	1.0	0.551526	0.275809	0.827962
C	1.0	0.609600	0.222444	0.384449
C	1.0	0.390364	0.722669	0.115477
C	1.0	0.390400	0.777556	0.615551
C	1.0	0.609636	0.277331	0.884523
H	1.0	0.612120	0.189908	0.453409
H	1.0	0.387849	0.690099	0.046525
H	1.0	0.387880	0.810092	0.546591
H	1.0	0.612151	0.309901	0.953475
C	1.0	0.663435	0.261650	0.353144
C	1.0	0.336543	0.762073	0.146749
C	1.0	0.336565	0.738350	0.646856
C	1.0	0.663457	0.237927	0.853251
H	1.0	0.707626	0.257411	0.398611
H	1.0	0.292354	0.757955	0.101267
H	1.0	0.292374	0.742589	0.601389
H	1.0	0.707646	0.242045	0.898733
C	1.0	0.662327	0.305784	0.264756
C	1.0	0.337655	0.806194	0.235141
C	1.0	0.337673	0.694216	0.735244
C	1.0	0.662345	0.193806	0.764859
C	1.0	0.604319	0.302062	0.208074
C	1.0	0.395646	0.802267	0.291857
C	1.0	0.395681	0.697938	0.791925
C	1.0	0.604353	0.197733	0.708143
H	1.0	0.600770	0.333901	0.138722
H	1.0	0.399200	0.834082	0.361215
H	1.0	0.399230	0.666099	0.861278
H	1.0	0.600800	0.165918	0.638785

C	1.0	0.550096	0.262012	0.238389
C	1.0	0.449856	0.762094	0.261566
C	1.0	0.449904	0.737988	0.761611
C	1.0	0.550144	0.237906	0.738434
H	1.0	0.505953	0.262610	0.192856
H	1.0	0.493990	0.762556	0.307119
H	1.0	0.494047	0.737390	0.807144
H	1.0	0.506010	0.237444	0.692881
C	1.0	0.718761	0.359509	0.234936
C	1.0	0.281245	0.860020	0.264966
C	1.0	0.281239	0.640491	0.765064
C	1.0	0.718755	0.139980	0.735034
C	1.0	0.767235	0.414626	0.297198
C	1.0	0.232802	0.915315	0.202737
C	1.0	0.232765	0.585374	0.702802
C	1.0	0.767198	0.084685	0.797263
H	1.0	0.763119	0.415611	0.367845
H	1.0	0.236939	0.916443	0.132097
H	1.0	0.236881	0.584389	0.632155
H	1.0	0.763061	0.083557	0.867903
C	1.0	0.818772	0.474317	0.269866
C	1.0	0.181272	0.974990	0.230103
C	1.0	0.181228	0.525683	0.730134
C	1.0	0.818728	0.025010	0.769897
H	1.0	0.855191	0.520549	0.317819
H	1.0	0.144865	0.021339	0.182185
H	1.0	0.144809	0.479451	0.682181
H	1.0	0.855135	0.978661	0.817815
C	1.0	0.824147	0.480757	0.179229
C	1.0	0.175880	0.981229	0.320742
C	1.0	0.175853	0.519243	0.820771

C	1.0	0.824120	0.018771	0.679258
C	1.0	0.777212	0.422965	0.116601
C	1.0	0.222810	0.923364	0.383340
C	1.0	0.222788	0.577035	0.883399
C	1.0	0.777190	0.076636	0.616660
H	1.0	0.781799	0.427136	0.046149
H	1.0	0.218211	0.927403	0.453789
H	1.0	0.218201	0.572864	0.953851
H	1.0	0.781789	0.072597	0.546211
C	1.0	0.725472	0.363362	0.144121
C	1.0	0.274537	0.863768	0.355784
C	1.0	0.274528	0.636638	0.855879
C	1.0	0.725464	0.136232	0.644216
H	1.0	0.689530	0.318810	0.094341
H	1.0	0.310458	0.819077	0.405530
H	1.0	0.310470	0.681190	0.905659
H	1.0	0.689542	0.180923	0.594470
C	1.0	0.878803	0.551751	0.151813
C	1.0	0.121193	0.052001	0.348213
C	1.0	0.121197	0.448249	0.848187
C	1.0	0.878807	0.947999	0.651787
C	1.0	0.499110	0.094120	0.430998
C	1.0	0.500847	0.594081	0.068999
C	1.0	0.500890	0.905880	0.569002
C	1.0	0.499153	0.405919	0.931001
C	1.0	0.464846	0.116491	0.500630
C	1.0	0.535079	0.616586	-0.000652
C	1.0	0.535154	0.883509	0.499370
C	1.0	0.464921	0.383414	1.000652
H	1.0	0.437315	0.207619	0.500598
H	1.0	0.562532	0.707823	-0.000634

H	1.0	0.562685	0.792381	0.499402
H	1.0	0.437468	0.292177	1.000634
C	1.0	0.465641	0.023495	0.568826
C	1.0	0.534330	0.523625	0.931143
C	1.0	0.534359	0.976505	0.431174
C	1.0	0.465670	0.476375	0.068857
H	1.0	0.439301	0.042252	0.623034
H	1.0	0.560633	0.542465	0.876905
H	1.0	0.560699	0.957748	0.376966
H	1.0	0.439367	0.457535	0.123095
C	1.0	0.981999	0.898448	0.194610
C	1.0	0.018009	0.398383	0.305432
C	1.0	0.018001	0.101552	0.805390
C	1.0	0.981991	0.601617	0.694568
H	1.0	0.945137	0.867151	0.232262
H	1.0	0.054896	0.367404	0.267732
H	1.0	0.054863	0.132849	0.767738
H	1.0	0.945104	0.632596	0.732268
H	1.0	0.008627	0.981535	0.228919
H	1.0	0.991313	0.481475	0.271239
H	1.0	0.991373	0.018465	0.771081
H	1.0	0.008687	0.518525	0.728761
H	1.0	0.012770	0.812110	0.192697
H	1.0	0.987316	0.311892	0.307227
H	1.0	0.987230	0.187890	0.807303
H	1.0	0.012684	0.688108	0.692773
C	1.0	0.953082	0.931262	0.100822
C	1.0	0.046899	0.431005	0.399260
C	1.0	0.046918	0.068738	0.899178
C	1.0	0.953101	0.568995	0.600740
C	1.0	0.936903	0.168358	0.141058

C	1.0	0.063169	0.668086	0.359162
C	1.0	0.063097	0.831642	0.858942
C	1.0	0.936831	0.331914	0.640838
H	1.0	0.946723	0.134203	0.210229
H	1.0	0.053396	0.633977	0.289976
H	1.0	0.053277	0.865797	0.789771
H	1.0	0.946604	0.366022	0.710024
H	1.0	0.891037	0.217832	0.130167
H	1.0	0.109032	0.717567	0.370131
H	1.0	0.108963	0.782168	0.869833
H	1.0	0.890968	0.282433	0.629869
H	1.0	0.972264	0.241419	0.128353
H	1.0	0.027792	0.741136	0.371831
H	1.0	0.027736	0.758581	0.871647
H	1.0	0.972208	0.258864	0.628169
C	1.0	0.908779	0.089099	0.986068
C	1.0	0.091235	0.588610	0.514129
C	1.0	0.091221	0.910901	0.013932
C	1.0	0.908765	0.411390	0.485871
H	1.0	0.922888	0.190807	0.970984
H	1.0	0.077153	0.690307	0.529287
H	1.0	0.077112	0.809193	0.029016
H	1.0	0.922847	0.309693	0.470713
H	1.0	0.857443	0.084592	0.976821
H	1.0	0.142570	0.584025	0.523400
H	1.0	0.142557	0.915408	0.023179
H	1.0	0.857430	0.415975	0.476600
H	1.0	0.925579	1.017875	0.940611
H	1.0	0.074395	0.517322	0.559511
H	1.0	0.074421	-0.017875	0.059389
H	1.0	0.925605	0.482678	0.440489

Optimized geometry of [Cd_2(TPBD)(H_2O)$_4$]

_cell_length_a	10.94400
_cell_length_b	11.56770
_cell_length_c	22.44416
_cell_angle_alpha	90.34900
_cell_angle_beta	92.11000
_cell_angle_gamma	91.97800

Cd	1.0	0.430057	0.415486	0.440616
Cd	1.0	0.569943	0.584514	0.559384
N	1.0	0.781613	0.866310	0.018466
N	1.0	0.218387	0.133690	0.981534
O	1.0	0.575216	0.570657	0.458917
O	1.0	0.424784	0.429343	0.541083
C	1.0	0.681325	0.604293	0.439169
C	1.0	0.318675	0.395707	0.560831
Cd	1.0	0.075469	0.882930	0.556173
Cd	1.0	0.924531	0.117070	0.443827
N	1.0	0.291423	0.634392	0.013210
N	1.0	0.708577	0.365608	0.986790
O	1.0	0.773754	0.617499	0.474255
O	1.0	0.226246	0.382501	0.525745
C	1.0	0.690684	0.628578	0.374395
C	1.0	0.309315	0.371422	0.625605
O	1.0	0.241241	0.771650	0.608604
O	1.0	0.758759	0.228350	0.391396
C	1.0	0.589799	0.614994	0.334111
C	1.0	0.410201	0.385006	0.665889
H	1.0	0.501688	0.584343	0.349712
H	1.0	0.498312	0.415657	0.650288
C	1.0	0.600625	0.642591	0.274175
C	1.0	0.399375	0.357409	0.725825

H	1.0	0.520872	0.633115	0.243656
H	1.0	0.479128	0.366885	0.756344
O	1.0	0.116031	0.881693	0.657820
O	1.0	0.883969	0.118307	0.342180
C	1.0	0.670379	0.676697	0.140729
C	1.0	0.329621	0.323303	0.859271
H	1.0	0.618644	0.595026	0.144891
H	1.0	0.381356	0.404974	0.855109
O	1.0	0.581145	0.294014	0.457444
O	1.0	0.418855	0.705986	0.542556
O	1.0	0.024538	0.943470	0.439957
O	1.0	0.975462	0.056530	0.560043
C	1.0	0.812831	0.699178	0.293528
C	1.0	0.187169	0.300822	0.706472
H	1.0	0.900458	0.731830	0.277897
H	1.0	0.099542	0.268170	0.722103
C	1.0	0.711449	0.688404	0.253091
C	1.0	0.288551	0.311596	0.746909
O	1.0	0.133282	0.793355	0.468226
O	1.0	0.866718	0.206645	0.531774
O	1.0	0.723787	0.721466	0.615212
O	1.0	0.276213	0.278534	0.384788
C	1.0	0.722630	0.732123	0.191865
C	1.0	0.277370	0.267877	0.808135
C	1.0	0.803150	0.669191	0.352956
C	1.0	0.196850	0.330809	0.647044
H	1.0	0.882404	0.678034	0.383670
H	1.0	0.117596	0.321966	0.616330
O	1.0	0.635602	0.562630	0.652163
O	1.0	0.364398	0.437370	0.347837
C	1.0	0.492327	0.851688	0.925075

C	1.0	0.507673	0.148312	0.074925
H	1.0	0.395580	0.867234	0.930358
H	1.0	0.604420	0.132766	0.069642
C	1.0	0.093942	0.862251	0.427391
C	1.0	0.906058	0.137749	0.572609
C	1.0	0.211643	0.820970	0.656746
C	1.0	0.788357	0.179030	0.343254
C	1.0	0.131717	0.844234	0.364941
C	1.0	0.868283	0.155766	0.635059
C	1.0	0.063837	0.891734	0.317366
C	1.0	0.936163	0.108266	0.682634
H	1.0	0.986952	0.945632	0.326776
H	1.0	0.013048	0.054368	0.673224
C	1.0	0.093363	0.868031	0.258871
C	1.0	0.906637	0.131969	0.741129
H	1.0	0.039068	0.903058	0.221912
H	1.0	0.960932	0.096942	0.778088
C	1.0	0.192649	0.798985	0.246264
C	1.0	0.807351	0.201015	0.753736
C	1.0	0.264439	0.757749	0.294289
C	1.0	0.735561	0.242251	0.705711
H	1.0	0.342592	0.705005	0.285557
H	1.0	0.657408	0.294995	0.714443
C	1.0	0.233631	0.778678	0.352786
C	1.0	0.766369	0.221322	0.647214
H	1.0	0.288230	0.742756	0.389209
H	1.0	0.711770	0.257244	0.610791
C	1.0	0.218175	0.765133	0.184745
C	1.0	0.781825	0.234867	0.815255
C	1.0	0.122614	0.728108	0.144889
C	1.0	0.877386	0.271892	0.855111

H	1.0	0.028544	0.728364	0.159576
H	1.0	0.971456	0.271636	0.840424
C	1.0	0.145471	0.685764	0.088316
C	1.0	0.854529	0.314236	0.911684
H	1.0	0.070229	0.653343	0.059010
H	1.0	0.929771	0.346657	0.940990
C	1.0	0.265967	0.681901	0.069160
C	1.0	0.734033	0.318099	0.930840
C	1.0	0.361876	0.723731	0.107818
C	1.0	0.638124	0.276269	0.892182
H	1.0	0.455431	0.723929	0.093027
H	1.0	0.544569	0.276071	0.906973
C	1.0	0.338503	0.762646	0.164721
C	1.0	0.661497	0.237354	0.835279
H	1.0	0.414512	0.794178	0.193924
H	1.0	0.585488	0.205822	0.806076
C	1.0	0.205723	0.642334	0.964384
C	1.0	0.794277	0.357666	0.035616
C	1.0	0.161404	0.749535	0.946717
C	1.0	0.838596	0.250465	0.053283
H	1.0	0.191546	0.827283	0.971329
H	1.0	0.808454	0.172717	0.028671
C	1.0	0.078095	0.756452	0.898563
C	1.0	0.921905	0.243548	0.101437
H	1.0	0.043742	0.840627	0.885941
H	1.0	0.956258	0.159373	0.114059
C	1.0	0.036480	0.656905	0.866632
C	1.0	0.963520	0.343095	0.133368
C	1.0	0.082371	0.550013	0.884832
C	1.0	0.917629	0.449987	0.115168
H	1.0	0.053526	0.471695	0.860201

H	1.0	0.946474	0.528305	0.139799
C	1.0	0.165242	0.542483	0.932856
C	1.0	0.834758	0.457517	0.067144
H	1.0	0.200263	0.459084	0.945886
H	1.0	0.799737	0.540916	0.054114
C	1.0	0.395499	0.566491	0.006808
C	1.0	0.604501	0.433509	0.993192
C	1.0	0.439070	0.496626	0.053401
C	1.0	0.560930	0.503374	0.946599
H	1.0	0.390705	0.492235	0.094912
H	1.0	0.609295	0.507765	0.905088
C	1.0	0.542280	0.431764	0.046791
C	1.0	0.457720	0.568236	0.953209
H	1.0	0.573940	0.377051	0.083056
H	1.0	0.426060	0.622949	0.916944
C	1.0	0.948699	0.661252	0.815310
C	1.0	0.051301	0.338748	0.184690
C	1.0	0.950520	0.753341	0.774691
C	1.0	0.049480	0.246659	0.225309
H	1.0	0.017732	0.824421	0.781216
H	1.0	0.982268	0.175579	0.218784
C	1.0	0.873103	0.751423	0.723991
C	1.0	0.126897	0.248577	0.276009
H	1.0	0.878850	0.821589	0.691986
H	1.0	0.121150	0.178411	0.308014
C	1.0	0.790771	0.657428	0.712910
C	1.0	0.209229	0.342572	0.287090
C	1.0	0.785587	0.567018	0.754338
C	1.0	0.214413	0.432982	0.245662
H	1.0	0.721582	0.494157	0.745727
H	1.0	0.278418	0.505843	0.254273

C	1.0	0.863057	0.569029	0.804675
C	1.0	0.136943	0.430971	0.195325
H	1.0	0.858111	0.497814	0.836139
H	1.0	0.141889	0.502186	0.163861
C	1.0	0.713382	0.648578	0.657086
C	1.0	0.286618	0.351422	0.342914
O	1.0	0.259414	0.595786	0.466731
O	1.0	0.740586	0.404214	0.533269
C	1.0	0.687411	0.720929	0.083802
C	1.0	0.312589	0.279071	0.916198
H	1.0	0.648165	0.673816	0.044993
H	1.0	0.351835	0.326184	0.955007
C	1.0	0.756437	0.824327	0.075847
C	1.0	0.243563	0.175673	0.924153
C	1.0	0.802661	0.883649	0.127328
C	1.0	0.197339	0.116351	0.872672
H	1.0	0.851925	0.966335	0.122899
H	1.0	0.148075	0.033665	0.877101
O	1.0	0.230982	0.021381	0.532383
O	1.0	0.769018	0.978619	0.467617
C	1.0	0.787973	0.837244	0.183450
C	1.0	0.212027	0.162756	0.816550
H	1.0	0.824851	0.884517	0.222563
H	1.0	0.175149	0.115483	0.777437
O	1.0	0.875926	0.805830	0.537380
O	1.0	0.124074	0.194170	0.462620
C	1.0	0.998450	0.915616	0.043009
C	1.0	0.001550	0.084384	0.956991
H	1.0	0.999558	0.848622	0.076518
H	1.0	0.000442	0.151378	0.923482
C	1.0	0.890723	0.932807	0.008784

C	1.0	0.109277	0.067193	0.991216
C	1.0	0.894725	0.018825	0.964990
C	1.0	0.105275	0.981175	0.035010
H	1.0	0.813494	0.036513	0.937420
H	1.0	0.186506	0.963487	0.062580
C	1.0	0.572333	0.865254	0.974451
C	1.0	0.427667	0.134746	0.025549
H	1.0	0.538458	0.892989	0.017127
H	1.0	0.461542	0.107011	0.982873
C	1.0	0.697163	0.844710	0.969413
C	1.0	0.302837	0.155290	0.030587
C	1.0	0.532870	0.817587	0.868932
C	1.0	0.467130	0.182413	0.131068
C	1.0	0.657759	0.793505	0.865206
C	1.0	0.342241	0.206495	0.134794
H	1.0	0.693672	0.766365	0.822847
H	1.0	0.306328	0.233635	0.177153
C	1.0	0.738276	0.806347	0.914451
C	1.0	0.261724	0.193653	0.085549
H	1.0	0.834771	0.788524	0.910237
H	1.0	0.165229	0.211476	0.089763
C	1.0	0.448265	0.810894	0.815910
C	1.0	0.551735	0.189106	0.184090
C	1.0	0.391626	0.740027	0.715551
C	1.0	0.608374	0.259973	0.284449
H	1.0	0.410210	0.684417	0.677826
H	1.0	0.589790	0.315583	0.322174
C	1.0	0.290525	0.811632	0.712316
C	1.0	0.709475	0.188368	0.287684
C	1.0	0.267967	0.880440	0.762080
C	1.0	0.732033	0.119560	0.237920

H	1.0	0.190225	0.936659	0.759503
H	1.0	0.809775	0.063341	0.240497
C	1.0	0.345190	0.880508	0.812583
C	1.0	0.654810	0.119492	0.187417
H	1.0	0.328048	0.939226	0.849183
H	1.0	0.671952	0.060774	0.150817
C	1.0	0.468690	0.739368	0.766406
C	1.0	0.531310	0.260632	0.233594
H	1.0	0.546406	0.682754	0.767366
H	1.0	0.453594	0.317246	0.232634
H	1.0	0.364371	0.731111	0.574781
H	1.0	0.635629	0.268889	0.425219
H	1.0	0.360611	0.665140	0.513063
H	1.0	0.639389	0.334860	0.486937
H	1.0	0.798845	0.340065	0.537405
H	1.0	0.201156	0.659935	0.462595
H	1.0	0.781093	0.468989	0.512841
H	1.0	0.218906	0.531011	0.487159
H	1.0	0.173175	0.218486	0.427627
H	1.0	0.826825	0.781514	0.572373
H	1.0	0.138984	0.259523	0.490924
H	1.0	0.861016	0.740477	0.509076
H	1.0	0.194280	0.079215	0.505121
H	1.0	0.805720	0.920785	0.494879
H	1.0	0.293366	-0.016147	0.510238
H	1.0	0.706634	1.016147	0.489762

5.5 Further applied methods

5.5.1 Theoretical calculation of surface areas in [Zn$_2$(TCPE)(bpy)] and [Zn$_2$(TCPE-F)(bpy)]

Theoretical surface areas of [Zn$_2$(TCPE)(bpy)] and [Zn$_2$(TCPE-F)(bpy)] were calculated based on the solvent accessible surface area (SASA) per unit cell (by Material Studios 5.0), as well as the density and cell volume from single crystal structures.

$$Surface\ Area\ (m^2\ g^{-1}) = \frac{Surface\ Area\ per\ Cell\ (\text{Å}^2)}{Density\ (g\ cm^{-3})\ \times Cell\ Volume\ (\text{Å}^3)} \times 10^4 \qquad (5.13)$$

Table 18. Calculated solvent accessible surface area, cell volume, crystal densities and corresponding theoretical surface areas for [Zn$_2$(TCPE)(bpy)] and [Zn$_2$(TCPE-F)(bpy)].

	SASA [Å^2]	**crystal density** [$g\ cm^{-3}$]	**cell volume** [Å^3]	**SA** [$m^2\ g^{-1}$]
[Zn$_2$(TCPE)(bpy)]	848.38	0.656	4575.33	2332.3
[Zn$_2$(TCPE-F)(bpy)]	845.95	0.689	4484.07	2330.4

5.5.2 Calculated spectra of [Zn$_2$(TPBD)(DMAc)$_2$] using exciton theory

Within the Frankel exciton picture, for coherently coupled dimers of identical chromophores two new one-exciton eigenstates will form via resonance interaction, which can be described as follows:

$$\psi_{Dimer} = {}^{1}/_{\sqrt{2}}(\psi_{1,e}\psi_{2,g} \pm \psi_{1,e}\psi_{2,g}) \qquad (5.2)$$

where ψ_{Dimer} represents the wavefunction of the dimer, $\psi_{1/2}$ represent the wavefunction of the monomer 1 respectively 2, and e and g stand for excited and ground state. By specifying the coupling elements of the two monomer

units, one can deduce the total excited state Hamiltonian. Assuming one vibrational degree of freedom for every chromophore subunit, the Hamiltonian is built as follows:

$$H_e^{Dimer} = \begin{pmatrix} H_{e1}^D(q_1, q_2) & J(R, \beta, \alpha_1, \alpha_2) \\ J(R, \beta, \alpha_1, \alpha_2) & H_{e2}^D(q_1, q_2) \end{pmatrix} \quad (5.3)$$

where q_1 and q_2 depict a scaled coordinate describing the equilibrium distance displacement, R is the center of mass distance and α, β describe geometrical quantities. Solving the respective Hamiltonian one obtains the optical transition energies for a dimer as:

$$\Delta E_{Dimer} = \Delta E_{Mono} + \Delta W \pm |J| \quad (5.4)$$

J here represents the exciton coupling strength, which can be expressed within the dipole-dipole approximation:

$$J = \frac{\mu_1 \mu_2}{4\pi\varepsilon_0 R^3} - \frac{3(\mu_1 R) \cdot (\mu_2 R)}{4\pi\varepsilon_0 R^5} \quad (5.5)$$

with μ as the corresponding transition dipole moments and R as the distance vector between the monomer centers. Introducing geometric quantities, J can be deduced to:

$$J = \frac{\mu_1 \mu_2}{4\pi\varepsilon_0 R^3} [\cos(\beta) - 3\cos(\alpha_1)\cos(\alpha_2)] \quad (5.6)$$

where β is the angle between the chromophores and α describes the orientation of μ with respect to the distance vectors R.

Excitonic coupling constants were derived from dimeric structures of the underlying crystal packing motifs along the crystallographic axis based on transition charges with the help of TD-DFT calculations. The following table summarizes the results. Note that only the transition dipole moment of the lowest lying S_1 state was considered in the calculation of optical absorption spectra. The Frenkel exciton of equation 5.3 was diagonalized in the nearest

neighbor coupling approximation, however, using four coupled chromophores (equation 5.3 shows the procedure for a dimer structure).

Table 19. Exciton coupling constant calculated by the transition charge method using TD-DFT calculations.

Coupling constant	$J_{1/2\ 1/2}$ **[eV]**	$J_{1\ 0}$ **[eV]**	$J_{0\ 1}$ **[eV]**
$[Zn_2(TPBD)(DMAc)_2]$	(-)0.107	(-)0.032	(+)0.019
$[Cd_2(TPBD)(H_2O)_4]$	(-)0.091	(-)0.028	(+)0.043

Oscillator strengths, which give access to theoretical absorption spectra were calculated following a procedure by Isborn and co-workers.[328] Figure 150 exemplarily shows the calculated absorption spectra of $[Zn_2(TPBD)(DMAc)_2]$ in comparison with experimentally measured UV-Vis data. The gas-to-crystal shift was extracted from the experimental data (difference between linker and MOF absorption onset). The inlet shows the used classification for the calculated coupling constants in table 19. Similar results can be obtained with the procedure described above also for $[Cd_2(TPBD)(H_2O)_4]$. The results suggest, that the near band edge states of the respective CPs bear pronounced excitonic character with delocalized states up to four coupled ligands.

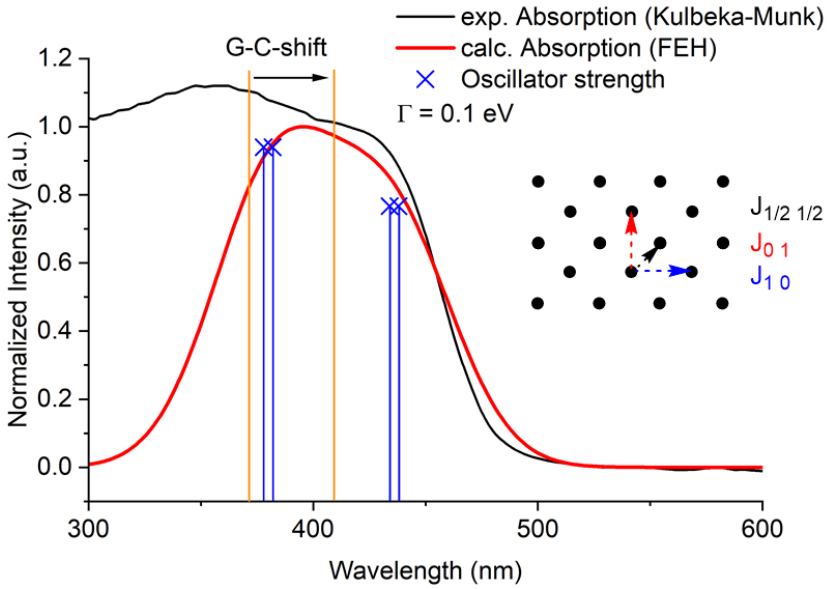

Figure 150. Theoretical absorption spectra using exciton theory for $[Zn_2(TPBD)(DMAc)_2]$ with four coupled chromophores. The blue bars show the oscillator strength of the respective exciton states. The orange bars lines represent the gas-to-crystal shift. The inlet shows the herringbone packing motif with the respective exciton couplings taken into account when diagonalizing the Frenkel exciton Hamiltonian.

6. List of publications

The following list shows a summary of publications of the author of this thesis (sorted by date). The entries marked with an asterisk are results of the above presented work. Various paragraphs and figures of this thesis have been published in peer-reviewed journals. The articles are reproduced in part with the permission of the related publishers.

Work of this thesis:

*1. **Mayer, D. C.**; Manzi, A.; Medishetty, R.; Winkler, B.; Schneider, C.; Kieslich, G.; Pöthig, A.; Feldmann, J.; Fischer, R. A., Controlling Multiphoton Absorption Efficiency by Chromophore Packing in Metal–Organic Frameworks. *Journal of the American Chemical Society* **2019,** *141* (29), 11594-11602.

*2. **Mayer**, **D. C.**, Zareba, J. K.; Raudschl-Sieber, G.; Pöthig, A.; Choluj, M.; Zaleśny, R.; Samoć, M.; Fischer, R. A., Post-Synthetic Framework Contraction Enhances the Two-Photon Absorption Properties of Pillar-Layered Metal-Organic Frameworks. *Chemistry of Materials* **2020**, *32* (13), 5682 – 5690.

Review articles:

*1. Medishetty, R.; Zaręba, J. K.; **Mayer, D.**; Samoć, M.; Fischer, R. A., Nonlinear optical properties, upconversion and lasing in metal–organic frameworks. *Chemical Society Reviews* **2017,** *46* (16), 4976-5004.

Contributions to other projects:

1. Zhong, R.; Pöthig, A.; **Mayer, D. C.**; Jandl, C.; Altmann, P. J.; Herrmann, W. A.; Kühn, F. E., Spectroscopic and Structural Properties of Bridge-Functionalized Dinuclear Coinage-Metal (Cu, Ag, and Au) NHC Complexes: A Comparative Study. *Organometallics* **2015,** *34* (11), 2573-2579.

2. Rieb, J.; Dominelli, B.; **Mayer, D.**; Jandl, C.; Drechsel, J.; Heydenreuter, W.; Sieber, S. A.; Kühn, F. E., Influence of wing-tip substituents and reaction conditions on the structure, properties and cytotoxicity of Ag(i)– and Au(i)–bis(NHC) complexes. *Dalton Transactions* **2017,** *46* (8), 2722-2735.

3. Jandl, C.; **Mayer, D. C.**; Pöthig, A., The Ambivalent Nature of Halogenated Tropone Derivatives: Dihalocycloheptatriene vs. Halotropylium Halide. *European Journal of Organic Chemistry* **2017,** *2017* (29), 4255-4259.

4. Medishetty, R.; Nalla, V.; Nemec, L.; Henke, S.; **Mayer, D.**; Sun, H.; Reuter, K.; Fischer, R. A., A New Class of Lasing Materials: Intrinsic Stimulated Emission from Nonlinear Optically Active Metal–Organic Frameworks. *Advanced Materials* **2017,** *29* (17), 1605637.

5. Weger, M.; Grötsch, R. K.; Knaus, M. G.; Giuman, M. M.; **Mayer, D. C.**; Altmann, P. J.; Mossou, E.; Dittrich, B.; Pöthig, A.; Rieger, B., Non-Innocent Methylene Linker in Bridged Lewis Pair Initiators. *Angewandte Chemie International Edition* **2019,** *58* (29), 9797-9801.

6. Weishäupl, S.; **Mayer, C. D.**; Thyrhaug, E.; Hauer, J.; Pöthig, A.; Fischer, R. A., A Nitrophenyl-Carbazole based Push-Pull Linker as a Building Block for Non-Linear Optical Active Coordination Polymers: A Structural and Photophysical Study. *Dyes and Pigments* **2020**, https://doi.org/10.1016/j.dyepig.2020.109012.

Overview of the author contribution to work in this thesis:

Chapter 2.1:

- Synthesis and characterization of all organic linker molecules
- Single crystal structure determination of the compound Me_4TPBD

Chapter 2.2:

- Synthesis and characterization of all MOF compounds and organic linkers
- Single crystal structure determination of all MOF compounds
- Linear and non-linear optical characterizations were conducted by J. Zareba and M. Samoć
- Electronic structure calculations were performed by M. Choluj and R. Zaleśny

Chapter 2.3:

- Synthesis and characterization of all MOF compounds and organic linkers
- Single crystal structure determination of all MOF compounds
- Electronic structure calculations
- Linear and non-linear optical characterization were conducted by A. Manzi and J. Feldmann

Chapter 2.4:

- Synthesis and characterization of all MOF compounds and organic linkers
- Single crystal structure determination of MOF compounds
- Structure simulation using FF
- Rietveld Refinement of collected powder data

7. List of presentations

Oral presentation

“Multiphoton Absorption in Metal-Organic Frameworks”, Symposium on Porous Coordination Polymers and Metal-Organic Frameworks docMOF, Raitenhaslach, Germany, May 2018.

Poster presentations

D. C. Mayer, R. A. Fischer, “Multiphoton Absorption in Pillar-layered Metal-Organic Frameworks”, 2nd European Conference on Metal-Organic Frameworks & Porous Polymers, Delft, Netherlands, November 2017.

D. C. Mayer, A. Manzi, R. Medishetty, B. Winkler, C. Schneider, Kieslich, A. Pöthig, J. Feldmann, R. A. Fischer, “Controlling Multiphoton Absorption Efficiency by Chromophore Packing in Metal–Organic Frameworks”, 6th International Conference on Metal-Organic Frameworks, MOF 2018, Auckland, New Zealand, December 2018.

8. Curriculum vitae

Personal data:

Name	David Christian Mayer
Date of birth	02.01.1989
Place of birth	München (Germany)
Citizenship	Germany
Marital status	unmarried
Children	two (one son, Moritz Benedikt; one daughter, Jule Malea)

Education:

11/2016 – 12/2020	Dr. rer. nat. at the Chair of Inorganic and Metal-organic Chemistry, Technical University Munich Team assistant at the DFG priority program “SPP1928 COORNETs”
10/2014 – 09/2016	Master of Science in Chemistry with focus on inorganic and physical chemistry at the Technical University Munich. Title of Master thesis: “Synthesis and Characterization of novel macrocyclic NHC Complexes and Scanning Tunneling Microscopy Studies on their surface behavior”
10/2011 – 09/2014	Bachelor of Science in Chemistry at the Technical University Munich. Title of Bachelor thesis: “Coinage Metal Complexes bearing Hydroxymethyl-functionalized *Bis*(NHC) Ligands: Synthesis and Characterization”
07/2010 – 09/2011	Education and work as a paramedic during civil service at the Bavarian Red Cross.
09/2008 – 07/2010	High School Education (allgemeine Abitur) and Vocational Education (Fachhochschul-Reife) at the Hans-Leipelt Berufsoberschule Donauwörth
09/2005 – 09/2008	Apprenticeship and work as galvanizer (Ausbildung zum Galvaniseur) at Airbus Helicopters Donauwörth, formerly Eurocopter.
09/1999 – 09/2005	Junior High School Education (Mittlere Reife) at the Staatliche Realschule Rain am Lech.

9. References

1. Diamanti, M. V., Special Issue: Novel Photoactive Materials. *Materials Chemistry Frontiers* **2018,** *11*, 2553.
2. Dini, D.; Calvete, M. J. F.; Hanack, M., Nonlinear Optical Materials for the Smart Filtering of Optical Radiation. *Chemical Reviews* **2016,** *116* (22), 13043-13233.
3. Boyd, R. W., *Nonlinear Optics (Third Edition)*. Academic Press: Burlington, 2008.
4. Garmire, E., Nonlinear optics in daily life. *Opt. Express* **2013,** *21* (25), 30532-30544.
5. Göppert-Mayer, M., Elementary processes with two quantum transitions. *Annalen der Physik* **2009,** *18* (7-8), 466-479.
6. Kaiser, W.; Garrett, C. G. B., Two-Photon Excitation in CaF_2: Eu^{2+}. *Physical Review Letters* **1961,** *7* (6), 229-231.
7. Pawlicki, M.; Collins, H. A.; Denning, R. G.; Anderson, H. L., Two-Photon Absorption and the Design of Two-Photon Dyes. *Angewandte Chemie International Edition* **2009,** *48* (18), 3244-3266.
8. He, G. S.; Tan, L.-S.; Zheng, Q.; Prasad, P. N., Multiphoton Absorbing Materials: Molecular Designs, Characterizations, and Applications. *Chemical Reviews* **2008,** *108* (4), 1245-1330.
9. Li, L.; Shang, X.; Wang, S.; Dong, N.; Ji, C.; Chen, X.; Zhao, S.; Wang, J.; Sun, Z.; Hong, M.; Luo, J., Bilayered Hybrid Perovskite Ferroelectric with Giant Two-Photon Absorption. *Journal of the American Chemical Society* **2018,** *140* (22), 6806-6809.
10. Saouma, F. O.; Park, D. Y.; Kim, S. H.; Jeong, M. S.; Jang, J. I., Multiphoton Absorption Coefficients of Organic–Inorganic Lead Halide Perovskites $CH_3NH_3PbX_3$ (X = Cl, Br, I) Single Crystals. *Chemistry of Materials* **2017,** *29* (16), 6876-6882.
11. Liu, W.; Xing, J.; Zhao, J.; Wen, X.; Wang, K.; Lu, P.; Xiong, Q., Giant Two-Photon Absorption and Its Saturation in 2D Organic–Inorganic Perovskite. *Advanced Optical Materials* **2017,** *5* (7), 1601045.
12. Medishetty, R.; Zaręba, J. K.; Mayer, D.; Samoć, M.; Fischer, R. A., Nonlinear optical properties, upconversion and lasing in metal–organic frameworks. *Chemical Society Reviews* **2017,** *46* (16), 4976-5004.
13. Liu, M.; Quah, H. S.; Wen, S.; Li, Y.; Vittal, J. J.; Ji, W., Multiphoton Absorption and Two-Photon-Pumped Random Lasing in Crystallites of a Coordination Polymer. *The Journal of Physical Chemistry C* **2018,** *122* (1), 777-781.
14. Liu, M.; Quah, H. S.; Wen, S.; Wang, J.; Kumar, P. S.; Eda, G.; Vittal, J. J.; Ji, W., Nonlinear optical properties of a one-dimensional coordination polymer. *Journal of Materials Chemistry C* **2017,** *5* (11), 2936-2941.
15. Liu, M.; Quah, H. S.; Wen, S.; Yu, Z.; Vittal, J. J.; Ji, W., Efficient Third Harmonic Generation in a Metal–Organic Framework. *Chemistry of Materials* **2016,** *28* (10), 3385-3390.
16. Nalla, V.; Medishetty, R.; Wang, M.; Bai, Z.; Sun, H.; Wei, J.; Vittal, J., Second harmonic generation from the 'Centrosymmetric' crystals. *IUCrJ* **2015,** *2*, 317-321.

17. Quah, H. S.; Chen, W.; Schreyer, M. K.; Yang, H.; Wong, M. W.; Ji, W.; Vittal, J. J., Multiphoton harvesting metal–organic frameworks. *Nature Communications* **2015,** *6* (1), 7954.
18. Quah, H. S.; Nalla, V.; Zheng, K.; Lee, C. A.; Liu, X.; Vittal, J. J., Tuning Two-Photon Absorption Cross Section in Metal Organic Frameworks. *Chemistry of Materials* **2017,** *29* (17), 7424-7430.
19. Medishetty, R.; Nemec, L.; Nalla, V.; Henke, S.; Samoć, M.; Reuter, K.; Fischer, R. A., Multi-Photon Absorption in Metal–Organic Frameworks. *Angewandte Chemie International Edition* **2017,** *56* (46), 14743-14748.
20. Mayer, D. C.; Manzi, A.; Medishetty, R.; Winkler, B.; Schneider, C.; Kieslich, G.; Pöthig, A.; Feldmann, J.; Fischer, R. A., Controlling Multiphoton Absorption Efficiency by Chromophore Packing in Metal–Organic Frameworks. *Journal of the American Chemical Society* **2019,** *141* (29), 11594-11602.
21. Wei, Z.; Gu, Z.-Y.; Arvapally, R. K.; Chen, Y.-P.; McDougald, R. N.; Ivy, J. F.; Yakovenko, A. A.; Feng, D.; Omary, M. A.; Zhou, H.-C., Rigidifying Fluorescent Linkers by Metal–Organic Framework Formation for Fluorescence Blue Shift and Quantum Yield Enhancement. *Journal of the American Chemical Society* **2014,** *136* (23), 8269-8276.
22. Stylianou, K. C.; Heck, R.; Chong, S. Y.; Bacsa, J.; Jones, J. T. A.; Khimyak, Y. Z.; Bradshaw, D.; Rosseinsky, M. J., A Guest-Responsive Fluorescent 3D Microporous Metal−Organic Framework Derived from a Long-Lifetime Pyrene Core. *Journal of the American Chemical Society* **2010,** *132* (12), 4119-4130.
23. Biffis, A.; Centomo, P.; Del Zotto, A.; Zecca, M., Pd Metal Catalysts for Cross-Couplings and Related Reactions in the 21st Century: A Critical Review. *Chemical Reviews* **2018,** *118* (4), 2249-2295.
24. Hooshmand, S. E.; Heidari, B.; Sedghi, R.; Varma, R. S., Recent advances in the Suzuki–Miyaura cross-coupling reaction using efficient catalysts in eco-friendly media. *Green Chemistry* **2019,** *21* (3), 381-405.
25. Yin, Q.; Zhao, P.; Sa, R.-J.; Chen, G.-C.; Lü, J.; Liu, T.-F.; Cao, R., An Ultra-Robust and Crystalline Redeemable Hydrogen-Bonded Organic Framework for Synergistic Chemo-Photodynamic Therapy. *Angewandte Chemie International Edition* **2018,** *57* (26), 7691-7696.
26. Wang, T. C.; Vermeulen, N. A.; Kim, I. S.; Martinson, A. B. F.; Stoddart, J. F.; Hupp, J. T.; Farha, O. K., Scalable synthesis and post-modification of a mesoporous metal-organic framework called NU-1000. *Nature Protocols* **2016,** *11* (1), 149-162.
27. Wang, F.; Liu, W.; Teat, S. J.; Xu, F.; Wang, H.; Wang, X.; An, L.; Li, J., Chromophore-immobilized luminescent metal–organic frameworks as potential lighting phosphors and chemical sensors. *Chemical Communications* **2016,** *52* (67), 10249-10252.
28. Medishetty, R.; Nalla, V.; Nemec, L.; Henke, S.; Mayer, D.; Sun, H.; Reuter, K.; Fischer, R. A., A New Class of Lasing Materials: Intrinsic Stimulated Emission from Nonlinear Optically Active Metal–Organic Frameworks. *Advanced Materials* **2017,** *29* (17), 1605637.
29. Deria, P.; Yu, J.; Smith, T.; Balaraman, R. P., Ground-State versus Excited-State Interchromophoric Interaction: Topology Dependent Excimer Contribution in Metal–Organic Framework Photophysics. *Journal of the American Chemical Society* **2017,** *139* (16), 5973-5983.
30. Yu, J.; Park, J.; Van Wyk, A.; Rumbles, G.; Deria, P., Excited-State Electronic Properties in Zr-Based Metal–Organic Frameworks as a Function of

a Topological Network. *Journal of the American Chemical Society* **2018,** *140* (33), 10488-10496.
31. Hong, Y.; Lam, J. W. Y.; Tang, B. Z., Aggregation-induced emission. *Chemical Society Reviews* **2011,** *40* (11), 5361-5388.
32. Ding, D.; Li, K.; Liu, B.; Tang, B. Z., Bioprobes Based on AIE Fluorogens. *Accounts of Chemical Research* **2013,** *46* (11), 2441-2453.
33. Mei, J.; Leung, N. L. C.; Kwok, R. T. K.; Lam, J. W. Y.; Tang, B. Z., Aggregation-Induced Emission: Together We Shine, United We Soar! *Chemical Reviews* **2015,** *115* (21), 11718-11940.
34. Qin, W.; Ding, D.; Liu, J.; Yuan, W. Z.; Hu, Y.; Liu, B.; Tang, B. Z., Biocompatible Nanoparticles with Aggregation-Induced Emission Characteristics as Far-Red/Near-Infrared Fluorescent Bioprobes for In Vitro and In Vivo Imaging Applications. *Advanced Functional Materials* **2012,** *22* (4), 771-779.
35. Prlj, A.; Došlić, N.; Corminboeuf, C., How does tetraphenylethylene relax from its excited states? *Physical Chemistry Chemical Physics* **2016,** *18* (17), 11606-11609.
36. Zhao, Z.; Lam, J. W. Y.; Tang, B. Z., Tetraphenylethene: a versatile AIE building block for the construction of efficient luminescent materials for organic light-emitting diodes. *Journal of Materials Chemistry* **2012,** *22* (45), 23726-23740.
37. Shustova, N. B.; McCarthy, B. D.; Dincă, M., Turn-On Fluorescence in Tetraphenylethylene-Based Metal–Organic Frameworks: An Alternative to Aggregation-Induced Emission. *Journal of the American Chemical Society* **2011,** *133* (50), 20126-20129.
38. Shustova, N. B.; Ong, T.-C.; Cozzolino, A. F.; Michaelis, V. K.; Griffin, R. G.; Dincă, M., Phenyl Ring Dynamics in a Tetraphenylethylene-Bridged Metal–Organic Framework: Implications for the Mechanism of Aggregation-Induced Emission. *Journal of the American Chemical Society* **2012,** *134* (36), 15061-15070.
39. Thao, Ch.; Ying, Y.; Wang, H.; Chen, B.; Zhu, G.; Song, Y.; Liu, X.; Zhao, Z.; Shen, L.; Tang, B. Z., Nonwoven fabric coated with a tetraphenylethene-based luminescent metal-organic framework for selective and sensitive sensing of nitrobenzene and ammonia. *J. Mater. Chem. C* **2018,** *6* (45), 12371-12376.
40. Guillerm, V.; Maspoch, D., Geometry Mismatch and Reticular Chemistry: Strategies To Assemble Metal–Organic Frameworks with Non-default Topologies. *Journal of the American Chemical Society* **2019,** *141* (42), 16517-16538.
41. Spek, A., Single-crystal structure validation with the program PLATON. *Journal of Applied Crystallography* **2003,** *36* (1), 7-13.
42. Cheetham, A. K.; Kieslich, G.; Yeung, H. H. M., Thermodynamic and Kinetic Effects in the Crystallization of Metal–Organic Frameworks. *Accounts of Chemical Research* **2018,** *51* (3), 659-667.
43. Shustova, N. B.; Cozzolino, A. F.; Dincă, M., Conformational Locking by Design: Relating Strain Energy with Luminescence and Stability in Rigid Metal–Organic Frameworks. *Journal of the American Chemical Society* **2012,** *134* (48), 19596-19599.
44. Yanai, T.; Tew, D. P.; Handy, N. C., A new hybrid exchange–correlation functional using the Coulomb-attenuating method (CAM-B3LYP). *Chemical Physics Letters* **2004,** *393* (1), 51-57.

45. Ditchfield, R.; Hehre, W. J.; Pople, J. A., Self-Consistent Molecular-Orbital Methods. IX. An Extended Gaussian-Type Basis for Molecular-Orbital Studies of Organic Molecules. *The Journal of Chemical Physics* **1971,** *54* (2), 724-728.
46. Papadopoulos, M. G. S., A. J.; Leszczynski J., *Non-Linear Optical Properties of Matter: from molecules to condensed phases*. Springer: Springer Netherlands, 2006.
47. Rabin, H.; Tang, C. L., *Quantum electronics: A treatise. Volume 1 - Nonlinear Optics. Part A*. Academic Press: 1975.
48. Beerepoot, M. T. P.; Friese, D. H.; List, N. H.; Kongsted, J.; Ruud, K., Benchmarking two-photon absorption cross sections: performance of CC2 and CAM-B3LYP. *Physical Chemistry Chemical Physics* **2015,** *17* (29), 19306-19314.
49. Cronstrand, P.; Luo, Y.; Ågren, H., Generalized few-state models for two-photon absorption of conjugated molecules. *Chemical Physics Letters* **2002,** *352* (3), 262-269.
50. Sanyal, S.; Painelli, A.; Pati, S. K.; Terenziani, F.; Sissa, C., Aggregates of quadrupolar dyes for two-photon absorption: the role of intermolecular interactions. *Physical Chemistry Chemical Physics* **2016,** *18* (40), 28198-28208.
51. Collini, E., Cooperative effects to enhance two-photon absorption efficiency: intra- versus inter-molecular approach. *Physical Chemistry Chemical Physics* **2012,** *14* (11), 3725-3736.
52. Spano, F. C.; Mukamel, S., Cooperative nonlinear optical response of molecular aggregates: Crossover to bulk behavior. *Physical Review Letters* **1991,** *66* (9), 1197-1200.
53. Davydov, A. S.; Kasha, M.; Oppenheimer, M. J., *Theory of molecular excitons*. McGraw-Hill: New York (N.Y.), 1962.
54. Bureš, F., Fundamental aspects of property tuning in push–pull molecules. *RSC Advances* **2014,** *4* (102), 58826-58851.
55. Aumiler, D.; Wang, S.; Chen, X.; Xia, A., Excited State Localization and Delocalization of Internal Charge Transfer in Branched Push−Pull Chromophores Studied by Single-Molecule Spectroscopy. *Journal of the American Chemical Society* **2009,** *131* (16), 5742-5743.
56. Li, Y.; Zhou, M.; Niu, Y.; Guo, Q.; Xia, A., Solvent-dependent intramolecular charge transfer delocalization/localization in multibranched push-pull chromophores. *The Journal of Chemical Physics* **2015,** *143* (3), 034309.
57. Haberhauer, G., Planarized and Twisted Intramolecular Charge Transfer: A Concept for Fluorophores Showing Two Independent Rotations in Excited State. *Chemistry – A European Journal* **2017,** *23* (39), 9288-9296.
58. Katan, C.; Terenziani, F.; Mongin, O.; Werts, M. H. V.; Porrès, L.; Pons, T.; Mertz, J.; Tretiak, S.; Blanchard-Desce, M., Effects of (Multi)branching of Dipolar Chromophores on Photophysical Properties and Two-Photon Absorption. *The Journal of Physical Chemistry A* **2005,** *109* (13), 3024-3037.
59. Yan, L.; Chen, X.; He, Q.; Wang, Y.; Wang, X.; Guo, Q.; Bai, F.; Xia, A.; Aumiler, D.; Vdović, S.; Lin, S., Localized Emitting State and Energy Transfer Properties of Quadrupolar Chromophores and (Multi)Branched Derivatives. *The Journal of Physical Chemistry A* **2012,** *116* (34), 8693-8705.
60. Li, Y.; Hu, J.; He, G.; Zhu, H.; Wang, X.; Guo, Q.; Xia, A.; Lin, Y.; Wang, J.; Zhan, X., Influence of Thiophene Moiety on the Excited State

Properties of Push–Pull Chromophores. *The Journal of Physical Chemistry C* **2016,** *120* (26), 13922-13930.
61. Li, W.; Pan, Y.; Yao, L.; Liu, H.; Zhang, S.; Wang, C.; Shen, F.; Lu, P.; Yang, B.; Ma, Y., A Hybridized Local and Charge-Transfer Excited State for Highly Efficient Fluorescent OLEDs: Molecular Design, Spectral Character, and Full Exciton Utilization. *Advanced Optical Materials* **2014,** *2* (9), 892-901.
62. Terenziani, F.; Sissa, C.; Painelli, A., Symmetry Breaking in Octupolar Chromophores: Solvatochromism and Electroabsorption. *The Journal of Physical Chemistry B* **2008,** *112* (16), 5079-5087.
63. Terenziani, F.; Painelli, A.; Katan, C.; Charlot, M.; Blanchard-Desce, M., Charge Instability in Quadrupolar Chromophores: Symmetry Breaking and Solvatochromism. *Journal of the American Chemical Society* **2006,** *128* (49), 15742-15755.
64. Wang, Y.; He, G. S.; Prasad, P. N.; Goodson, T., Ultrafast Dynamics in Multibranched Structures with Enhanced Two-Photon Absorption. *Journal of the American Chemical Society* **2005,** *127* (29), 10128-10129.
65. Klikar, M.; Kityk, I. V.; Kulwas, D.; Mikysek, T.; Pytela, O.; Bureš, F., Multipodal arrangement of push–pull chromophores: a fundamental parameter affecting their electronic and optical properties. *New Journal of Chemistry* **2017,** *41* (4), 1459-1472.
66. Kournoutas, F.; Seintis, K.; Karakostas, N.; Tydlitát, J.; Achelle, S.; Pistolis, G.; Bureš, F.; Fakis, M., Photophysical and Protonation Time Resolved Studies of Donor–Acceptor Branched Systems With Pyridine Acceptors. *The Journal of Physical Chemistry A* **2019,** *123* (2), 417-428.
67. Weigend, F.; Ahlrichs, R., Balanced basis sets of split valence, triple zeta valence and quadruple zeta valence quality for H to Rn: Design and assessment of accuracy. *Physical Chemistry Chemical Physics* **2005,** *7* (18), 3297-3305.
68. Reiffers, A.; Torres Ziegenbein, C.; Schubert, L.; Diekmann, J.; Thom, K. A.; Kühnemuth, R.; Griesbeck, A.; Weingart, O.; Gilch, P., On the large apparent Stokes shift of phthalimides. *Physical Chemistry Chemical Physics* **2019,** *21* (9), 4839-4853.
69. Wang, C.; Zhang, T.; Lin, W., Rational Synthesis of Noncentrosymmetric Metal–Organic Frameworks for Second-Order Nonlinear Optics. *Chemical Reviews* **2012,** *112* (2), 1084-1104.
70. Allendorf, M. D.; Bauer, C. A.; Bhakta, R. K.; Houk, R. J. T., Luminescent metal–organic frameworks. *Chemical Society Reviews* **2009,** *38* (5), 1330-1352.
71. Ji, M.; Lan, X.; Han, Z.; Hao, C.; Qiu, J., Luminescent Properties of Metal–Organic Framework MOF-5: Relativistic Time-Dependent Density Functional Theory Investigations. *Inorganic Chemistry* **2012,** *51* (22), 12389-12394.
72. Blatov, V. A.; Shevchenko, A. P.; Proserpio, D. M., Applied Topological Analysis of Crystal Structures with the Program Package ToposPro. *Crystal Growth & Design* **2014,** *14* (7), 3576-3586.
73. Taghizadeh, A.; Pedersen, T. G., Nonlinear optical selection rules of excitons in monolayer transition metal dichalcogenides. *Physical Review B* **2019,** *99* (23), 235433.
74. Ji, W. In *Third-Order and Fifth-Order Optical Nonlinearities by Two-Dimensional Excitonics*, Nonlinear Optics (NLO), Waikoloa Beach, Hawaii,

2019/07/15; Optical Society of America: Waikoloa Beach, Hawaii, 2019; p NM3A.1.
75. Johnson, J. C.; Li, Z.; Ndione, P. F.; Zhu, K., Third-order nonlinear optical properties of methylammonium lead halide perovskite films. *Journal of Materials Chemistry C* **2016,** *4* (22), 4847-4852.
76. Liu, Y.; Zhang, C.; Zhang, H.; Wang, R.; Hua, Z.; Wang, X.; Zhang, J.; Xiao, M., Broadband Optical Non-linearity Induced by Charge-Transfer Excitons in Type-II CdSe/ZnTe Nanocrystals. *Advanced Materials* **2013,** *25* (32), 4397-4402.
77. Ohara, K.; Yamada, T.; Tahara, H.; Aharen, T.; Hirori, H.; Suzuura, H.; Kanemitsu, Y., Excitonic enhancement of optical nonlinearities in perovskite $CH_3NH_3PbCl_3$ single crystals. *Physical Review Materials* **2019,** *3* (11), 111601.
78. Saouma, F. O.; Stoumpos, C. C.; Wong, J.; Kanatzidis, M. G.; Jang, J. I., Selective enhancement of optical nonlinearity in two-dimensional organic-inorganic lead iodide perovskites. *Nature Communications* **2017,** *8* (1), 742.
79. Larsen, J. K.; Li, S.-Y.; Scragg, J. J. S.; Ren, Y.; Hägglund, C.; Heinemann, M. D.; Kretzschmar, S.; Unold, T.; Platzer-Björkman, C., Interference effects in photoluminescence spectra of Cu_2ZnSnS_4 and $Cu(In,Ga)Se_2$ thin films. *Journal of Applied Physics* **2015,** *118* (3), 035307.
80. Brixner, T.; Hildner, R.; Köhler, J.; Lambert, C.; Würthner, F., Exciton Transport in Molecular Aggregates – From Natural Antennas to Synthetic Chromophore Systems. *Advanced Energy Materials* **2017,** *7* (16), 1700236.
81. Kasha, M., Molecular Excitons in Small Aggregates. In *Spectroscopy of the Excited State*, Di Bartolo, B.; Pacheco, D.; Goldberg, V., Eds. Springer US: Boston, MA, 1976; pp 337-363.
82. Haldar, R.; Mazel, A.; Joseph, R.; Adams, M.; Howard, I. A.; Richards, B. S.; Tsotsalas, M.; Redel, E.; Diring, S.; Odobel, F.; Wöll, C., Excitonically Coupled States in Crystalline Coordination Networks. *Chemistry – A European Journal* **2017,** *23* (57), 14316-14322.
83. Haldar, R.; Mazel, A.; Krstić, M.; Zhang, Q.; Jakoby, M.; Howard, I. A.; Richards, B. S.; Jung, N.; Jacquemin, D.; Diring, S.; Wenzel, W.; Odobel, F.; Wöll, C., A de novo strategy for predictive crystal engineering to tune excitonic coupling. *Nature Communications* **2019,** *10* (1), 2048.
84. Jacquemin, D.; Duchemin, I.; Blase, X., Benchmarking the Bethe–Salpeter Formalism on a Standard Organic Molecular Set. *Journal of Chemical Theory and Computation* **2015,** *11* (7), 3290-3304.
85. Wilbraham, L.; Adamo, C.; Labat, F.; Ciofini, I., Electrostatic Embedding To Model the Impact of Environment on Photophysical Properties of Molecular Crystals: A Self-Consistent Charge Adjustment Procedure. *Journal of Chemical Theory and Computation* **2016,** *12* (7), 3316-3324.
86. Wilbraham, L.; Coudert, F.-X.; Ciofini, I., Modelling photophysical properties of metal–organic frameworks: a density functional theory based approach. *Physical Chemistry Chemical Physics* **2016,** *18* (36), 25176-25182.
87. Plasser, F.; Bäppler, S. A.; Wormit, M.; Dreuw, A., New tools for the systematic analysis and visualization of electronic excitations. II. Applications. *The Journal of Chemical Physics* **2014,** *141* (2), 024107.
88. Kimber, P.; Plasser, F., Toward an understanding of electronic excitation energies beyond the molecular orbital picture. *Physical Chemistry Chemical Physics* **2020,** *22*, 6058-6080.

89. Plasser, F.; Lischka, H., Analysis of Excitonic and Charge Transfer Interactions from Quantum Chemical Calculations. *Journal of Chemical Theory and Computation* **2012,** *8* (8), 2777-2789.
90. Bäppler, S. A.; Plasser, F.; Wormit, M.; Dreuw, A., Exciton analysis of many-body wave functions: Bridging the gap between the quasiparticle and molecular orbital pictures. *Physical Review A* **2014,** *90* (5), 052521.
91. Mewes, S. A.; Plasser, F.; Dreuw, A., Communication: Exciton analysis in time-dependent density functional theory: How functionals shape excited-state characters. *The Journal of Chemical Physics* **2015,** *143* (17), 171101.
92. Mewes, S. A.; Plasser, F.; Krylov, A.; Dreuw, A., Benchmarking Excited-State Calculations Using Exciton Properties. *Journal of Chemical Theory and Computation* **2018,** *14* (2), 710-725.
93. Mewes, S. A.; Dreuw, A., Density-based descriptors and exciton analyses for visualizing and understanding the electronic structure of excited states. *Physical Chemistry Chemical Physics* **2019,** *21* (6), 2843-2856.
94. Haldar, R.; Heinke, L.; Wöll, C., Advanced Photoresponsive Materials Using the Metal–Organic Framework Approach. *Advanced Materials*, 1905227.
95. Nangia, A., Pseudopolymorph: Retain This Widely Accepted Term. *Crystal Growth & Design* **2006,** *6* (1), 2-4.
96. Bernstein, J., ...And Another Comment on Pseudopolymorphism. *Crystal Growth & Design* **2005,** *5* (5), 1661-1662.
97. Xie, L. S.; Alexandrov, E. V.; Skorupskii, G.; Proserpio, D. M.; Dincă, M., Diverse π–π stacking motifs modulate electrical conductivity in tetrathiafulvalene-based metal–organic frameworks. *Chemical Science* **2019,** *10* (37), 8558-8565.
98. Deria, P.; Yu, J.; Balaraman, R. P.; Mashni, J.; White, S. N., Topology-dependent emissive properties of zirconium-based porphyrin MOFs. *Chemical Communications* **2016,** *52* (88), 13031-13034.
99. Gong, X.; Noh, H.; Gianneschi, N. C.; Farha, O. K., Interrogating Kinetic versus Thermodynamic Topologies of Metal–Organic Frameworks via Combined Transmission Electron Microscopy and X-ray Diffraction Analysis. *Journal of the American Chemical Society* **2019,** *141* (15), 6146-6151.
100. Pang, J.; Yuan, S.; Qin, J.; Liu, C.; Lollar, C.; Wu, M.; Yuan, D.; Zhou, H.-C.; Hong, M., Control the Structure of Zr-Tetracarboxylate Frameworks through Steric Tuning. *Journal of the American Chemical Society* **2017,** *139* (46), 16939-16945.
101. Chen, Z.; Hanna, S. L.; Redfern, L. R.; Alezi, D.; Islamoglu, T.; Farha, O. K., Reticular chemistry in the rational synthesis of functional zirconium cluster-based MOFs. *Coordination Chemistry Reviews* **2019,** *386*, 32-49.
102. Bai, Y.; Dou, Y.; Xie, L.-H.; Rutledge, W.; Li, J.-R.; Zhou, H.-C., Zr-based metal–organic frameworks: design, synthesis, structure, and applications. *Chemical Society Reviews* **2016,** *45* (8), 2327-2367.
103. Wang, H.; Dong, X.; Lin, J.; Teat, S. J.; Jensen, S.; Cure, J.; Alexandrov, E. V.; Xia, Q.; Tan, K.; Wang, Q.; Olson, D. H.; Proserpio, D. M.; Chabal, Y. J.; Thonhauser, T.; Sun, J.; Han, Y.; Li, J., Topologically guided tuning of Zr-MOF pore structures for highly selective separation of C6 alkane isomers. *Nature Communications* **2018,** *9* (1), 1745.
104. Shaikh, S. M.; Usov, P. M.; Zhu, J.; Cai, M.; Alatis, J.; Morris, A. J., Synthesis and Defect Characterization of Phase-Pure Zr-MOFs Based on Meso-tetracarboxyphenylporphyrin. *Inorganic Chemistry* **2019,** *58* (8), 5145-5153.

105. Lyu, J.; Gong, X.; Lee, S.-J.; Gnanasekaran, K.; Zhang, X.; Wasson, M. C.; Wang, X.; Bai, P.; Guo, X.; Gianneschi, N. C.; Farha, O. K., Phase Transitions in Metal–Organic Frameworks Directly Monitored through In Situ Variable Temperature Liquid-Cell Transmission Electron Microscopy and In Situ X-ray Diffraction. *Journal of the American Chemical Society* **2020,** *142* (10), 4609-4615.
106. Karadeniz, B.; Žilić, D.; Huskić, I.; Germann, L. S.; Fidelli, A. M.; Muratović, S.; Lončarić, I.; Etter, M.; Dinnebier, R. E.; Barišić, D.; Cindro, N.; Islamoglu, T.; Farha, O. K.; Friščić, T.; Užarević, K., Controlling the Polymorphism and Topology Transformation in Porphyrinic Zirconium Metal–Organic Frameworks via Mechanochemistry. *Journal of the American Chemical Society* **2019,** *141* (49), 19214-19220.
107. Hong, S. W.; Paik, J. W.; Seo, D.; Oh, J.-M.; Jeong, Y. K.; Park, J. K., Substrate templated synthesis of single-phase and uniform Zr-porphyrin-based metal–organic frameworks. *Inorganic Chemistry Frontiers* **2020,** *7* (1), 221-231.
108. Bureekaew, S.; Balwani, V.; Amirjalayer, S.; Schmid, R., Isoreticular isomerism in 4,4-connected paddle-wheel metal–organic frameworks: structural prediction by the reverse topological approach. *CrystEngComm* **2015,** *17* (2), 344-352.
109. Garibay, S. J.; Iordanov, I.; Islamoglu, T.; DeCoste, J. B.; Farha, O. K., Synthesis and functionalization of phase-pure NU-901 for enhanced CO2 adsorption: the influence of a zirconium salt and modulator on the topology and phase purity. *CrystEngComm* **2018,** *20* (44), 7066-7070.
110. Kelty, M. L.; Morris, W.; Gallagher, A. T.; Anderson, J. S.; Brown, K. A.; Mirkin, C. A.; Harris, T. D., High-throughput synthesis and characterization of nanocrystalline porphyrinic zirconium metal–organic frameworks. *Chemical Communications* **2016,** *52* (50), 7854-7857.
111. Islamoglu, T.; Otake, K.-i.; Li, P.; Buru, C. T.; Peters, A. W.; Akpinar, I.; Garibay, S. J.; Farha, O. K., Revisiting the structural homogeneity of NU-1000, a Zr-based metal–organic framework. *CrystEngComm* **2018,** *20* (39), 5913-5918.
112. Ma, J.; Tran, L. D.; Matzger, A. J., Toward Topology Prediction in Zr-Based Microporous Coordination Polymers: The Role of Linker Geometry and Flexibility. *Crystal Growth & Design* **2016,** *16* (7), 4148-4153.
113. Gómez-Gualdrón, D. A.; Wang, T. C.; García-Holley, P.; Sawelewa, R. M.; Argueta, E.; Snurr, R. Q.; Hupp, J. T.; Yildirim, T.; Farha, O. K., Understanding Volumetric and Gravimetric Hydrogen Adsorption Trade-off in Metal–Organic Frameworks. *ACS Applied Materials & Interfaces* **2017,** *9* (39), 33419-33428.
114. Øien-Ødegaard, S.; Shearer, G. C.; Wragg, D. S.; Lillerud, K. P., Pitfalls in metal–organic framework crystallography: towards more accurate crystal structures. *Chemical Society Reviews* **2017,** *46* (16), 4867-4876.
115. Gutov, O. V.; Bury, W.; Gomez-Gualdron, D. A.; Krungleviciute, V.; Fairen-Jimenez, D.; Mondloch, J. E.; Sarjeant, A. A.; Al-Juaid, S. S.; Snurr, R. Q.; Hupp, J. T.; Yildirim, T.; Farha, O. K., Water-Stable Zirconium-Based Metal–Organic Framework Material with High-Surface Area and Gas-Storage Capacities. *Chemistry – A European Journal* **2014,** *20* (39), 12389-12393.
116. Kalidindi, S. B.; Nayak, S.; Briggs, M. E.; Jansat, S.; Katsoulidis, A. P.; Miller, G. J.; Warren, J. E.; Antypov, D.; Corà, F.; Slater, B.; Prestly, M. R.; Martí-Gastaldo, C.; Rosseinsky, M. J., Chemical and Structural Stability of Zirconium-based Metal–Organic Frameworks with Large Three-Dimensional

Pores by Linker Engineering. *Angewandte Chemie International Edition* **2015,** *54* (1), 221-226.
117. Morris, W.; Volosskiy, B.; Demir, S.; Gándara, F.; McGrier, P. L.; Furukawa, H.; Cascio, D.; Stoddart, J. F.; Yaghi, O. M., Synthesis, Structure, and Metalation of Two New Highly Porous Zirconium Metal–Organic Frameworks. *Inorganic Chemistry* **2012,** *51* (12), 6443-6445.
118. Wang, T. C.; Bury, W.; Gómez-Gualdrón, D. A.; Vermeulen, N. A.; Mondloch, J. E.; Deria, P.; Zhang, K.; Moghadam, P. Z.; Sarjeant, A. A.; Snurr, R. Q.; Stoddart, J. F.; Hupp, J. T.; Farha, O. K., Ultrahigh Surface Area Zirconium MOFs and Insights into the Applicability of the BET Theory. *Journal of the American Chemical Society* **2015,** *137* (10), 3585-3591.
119. Jablonski, A., Efficiency of Anti-Stokes Fluorescence in Dyes. *Nature* **1933,** *131* (3319), 839-840.
120. Ostroverkhova, O., Organic Optoelectronic Materials: Mechanisms and Applications. *Chemical Reviews* **2016,** *116* (22), 13279-13412.
121. Mewes, J. M. Development and Application of Methods for the Description of Photochemical Processes in Condensed Phase. *Doctoral Thesis*, 2015.
122. Kasha, M., Characterization of electronic transitions in complex molecules. *Discussions of the Faraday Society* **1950,** *9* (0), 14-19.
123. Mewes, S. A.; Mewes, J.-M.; Dreuw, A.; Plasser, F., Excitons in poly(para phenylene vinylene): a quantum-chemical perspective based on high-level ab initio calculations. *Physical Chemistry Chemical Physics* **2016,** *18* (4), 2548-2563.
124. Kasha, M., Energy Transfer Mechanisms and the Molecular Exciton Model for Molecular Aggregates. *Radiation Research* **1963,** *20* (1), 55-70.
125. Frenkel, J., On the Transformation of Light into Heat in Solids. II. *Physical Review* **1931,** *37* (10), 1276-1294.
126. Kasha, M.; Rawls, H.; El-Bayoumi, M., The exciton model in molecular spectroscopy, Pure Appl. Chem.11, 371-392. *Pure and Applied Chemistry - PURE APPL CHEM* **1965,** *11*, 371-392.
127. Hestand, N. J.; Spano, F. C., Expanded Theory of H- and J-Molecular Aggregates: The Effects of Vibronic Coupling and Intermolecular Charge Transfer. *Chemical Reviews* **2018,** *118* (15), 7069-7163.
128. Potma, E. O.; Wiersma, D. A., Exciton superradiance in aggregates: The effect of disorder, higher order exciton-phonon coupling and dimensionality. *The Journal of Chemical Physics* **1998,** *108* (12), 4894-4903.
129. Spano, F. C.; Mukamel, S. E. D., Excitons in confined geometries: Size scaling of nonlinear susceptibilities. *The Journal of Chemical Physics* **1991,** *95*, 7526-7540.
130. Bardeen, C. J., The Structure and Dynamics of Molecular Excitons. *Annual Review of Physical Chemistry* **2014,** *65* (1), 127-148.
131. Reynolds, D. C.; Collins, T. C., Chapter 2 - Theory of Excitons. In *Excitons*, Reynolds, D. C.; Collins, T. C., Eds. Academic Press: 1981; pp 20-41.
132. Leng, X.; Jin, F.; Wei, M.; Ma, Y., GW method and Bethe–Salpeter equation for calculating electronic excitations. *WIREs Computational Molecular Science* **2016,** *6* (5), 532-550.
133. Mewes, S. A. Exciton analysis tools for quantum-chemical investigation of molecular photochemistry *Doctoral Thesis*, 2018.
134. Egri, I., A simple model for the unified treatment of Wannier and Frenkel excitons. *Journal of Physics C: Solid State Physics* **1979,** *12* (10), 1843-1854.

135. Jelley, E. E., Spectral Absorption and Fluorescence of Dyes in the Molecular State. *Nature* **1936,** *138* (3502), 1009-1010.
136. Würthner, F.; Kaiser, T. E.; Saha-Möller, C. R., J-Aggregates: From Serendipitous Discovery to Supramolecular Engineering of Functional Dye Materials. *Angewandte Chemie International Edition* **2011,** *50* (15), 3376-3410.
137. Hohenberg, P.; Kohn, W., Inhomogeneous Electron Gas. *Physical Review* **1964,** *136* (3B), B864-B871.
138. Runge, E.; Gross, E. K. U., Density-Functional Theory for Time-Dependent Systems. *Physical Review Letters* **1984,** *52* (12), 997-1000.
139. Martin, R. M., *Electronic Structure: Basic Theory and Practical Methods*. Cambridge University Press: Cambridge, 2004.
140. Koch, W., Holthausen, M. C., *A Chemist's Guide to Density Functional Theory*. Wiley-VCH: Weinheim, 2001.
141. Kohn, W.; Sham, L. J., Self-Consistent Equations Including Exchange and Correlation Effects. *Physical Review* **1965,** *140* (4A), A1133-A1138.
142. Yu, H. S.; Li, S. L.; Truhlar, D. G., Perspective: Kohn-Sham density functional theory descending a staircase. *The Journal of Chemical Physics* **2016,** *145* (13), 130901.
143. Cohen, A. J.; Mori-Sánchez, P.; Yang, W., Challenges for Density Functional Theory. *Chemical Reviews* **2012,** *112* (1), 289-320.
144. Adamo, C.; Jacquemin, D., The calculations of excited-state properties with Time-Dependent Density Functional Theory. *Chemical Society Reviews* **2013,** *42* (3), 845-856.
145. Kuzyk, M. G.; Singer, K. D.; Stegeman, G. I., Theory of Molecular Nonlinear Optics. *Adv. Opt. Photon.* **2013,** *5* (1), 4-82.
146. Lytel, R.; Mossman, S.; Crowell, E.; Kuzyk, M. G., Exact Fundamental Limits of the First and Second Hyperpolarizabilities. *Physical Review Letters* **2017,** *119* (7), 073902.
147. Kuzyk, M. G., Fundamental limits on two-photon absorption cross sections. *The Journal of Chemical Physics* **2003,** *119* (16), 8327-8334.
148. Boyd, R. W.; Maki, J. J.; Sipe, J. E., Local field effects in enhancing the nonlinear susceptibility of optical materials. In *Nonlinear Optics*, Miyata, S., Ed. Elsevier: Amsterdam, 1992; pp 63-76.
149. Bennett, K.; Mukamel, S., Cascading and local-field effects in non-linear optics revisited: A quantum-field picture based on exchange of photons. *The Journal of Chemical Physics* **2014,** *140* (4), 044313.
150. Sutherland, R. L., *Handbook of Nonlinear Optics*. Marcel Dekker: New York, 1998.
151. Swofford R. L.; Albrecht, A. C., Nonlinear Spectroscopy. *Annual Review of Physical Chemistry* **1978,** *29* (1), 421-440.
152. Bloembergen, N., Nonlinear optics and spectroscopy. *Reviews of Modern Physics* **1982,** *54* (3), 685-695.
153. Alam, M. M.; Chattopadhyaya, M.; Chakrabarti, S.; Ruud, K., Chemical Control of Channel Interference in Two-Photon Absorption Processes. *Accounts of Chemical Research* **2014,** *47* (5), 1604-1612.
154. Reinhardt, B. A.; Brott, L. L.; Clarson, S. J.; Dillard, A. G.; Bhatt, J. C.; Kannan, R.; Yuan, L.; He, G. S.; Prasad, P. N., Highly Active Two-Photon Dyes: Design, Synthesis, and Characterization toward Application. *Chemistry of Materials* **1998,** *10* (7), 1863-1874.
155. Morales, A. R.; Frazer, A.; Woodward, A. W.; Ahn-White, H.-Y.; Fonari, A.; Tongwa, P.; Timofeeva, T.; Belfield, K. D., Design, Synthesis, and

Structural and Spectroscopic Studies of Push–Pull Two-Photon Absorbing Chromophores with Acceptor Groups of Varying Strength. *The Journal of Organic Chemistry* **2013,** *78* (3), 1014-1025.
156. Hrobárik, P.; Hrobáriková, V.; Sigmundová, I.; Zahradník, P.; Fakis, M.; Polyzos, I.; Persephonis, P., Benzothiazoles with Tunable Electron-Withdrawing Strength and Reverse Polarity: A Route to Triphenylamine-Based Chromophores with Enhanced Two-Photon Absorption. *The Journal of Organic Chemistry* **2011,** *76* (21), 8726-8736.
157. Katan, C.; Charlot, M.; Mongin, O.; Le Droumaguet, C.; Jouikov, V.; Terenziani, F.; Badaeva, E.; Tretiak, S.; Blanchard-Desce, M., Simultaneous Control of Emission Localization and Two-Photon Absorption Efficiency in Dissymmetrical Chromophores. *The Journal of Physical Chemistry B* **2010,** *114* (9), 3152-3169.
158. Pucher, N.; Rosspeintner, A.; Satzinger, V.; Schmidt, V.; Gescheidt, G.; Stampfl, J.; Liska, R., Structure−Activity Relationship in D-π-A-π-D-Based Photoinitiators for the Two-Photon-Induced Photopolymerization Process. *Macromolecules* **2009,** *42* (17), 6519-6528.
159. Fang, Z.; Teo, T.-L.; Cai, L.; Lai, Y.-H.; Samoc, A.; Samoc, M., Bridged Triphenylamine-Based Dendrimers: Tuning Enhanced Two-Photon Absorption Performance with Locked Molecular Planarity. *Organic Letters* **2009,** *11* (1), 1-4.
160. Bordeau, G.; Lartia, R.; Metge, G.; Fiorini-Debuisschert, C.; Charra, F.; Teulade-Fichou, M.-P., Trinaphthylamines as Robust Organic Materials for Two-Photon-Induced Fluorescence. *Journal of the American Chemical Society* **2008,** *130* (50), 16836-16837.
161. Samoc, M.; Matczyszyn, K.; Nyk, M.; Olesiak-Banska, J.; Wawrzynczyk, D.; Hanczyc, P.; Szeremeta, J.; Wielgus, M.; Gordel, M.; Mazur, L.; Kolkowski, R.; Straszak, B.; Cifuentes, M.; Humphrey, M., *Nonlinear absorption and nonlinear refraction: maximizing the merit factors*. SPIE: 2012; Vol. 8258.
162. Mikhaylov, A.; Kondratuk, D. V.; Cnossen, A.; Anderson, H. L.; Drobizhev, M.; Rebane, A., Cooperative Enhancement of Two-Photon Absorption in Self-Assembled Zinc-Porphyrin Nanostructures. *The Journal of Physical Chemistry C* **2016,** *120* (21), 11663-11670.
163. Walther, V.; Johne, R.; Pohl, T., Giant optical nonlinearities from Rydberg excitons in semiconductor microcavities. *Nature Communications* **2018,** *9* (1), 1309.
164. Hanamura, E., Rapid radiative decay and enhanced optical nonlinearity of excitons in a quantum well. *Physical Review B* **1988,** *38* (2), 1228-1234.
165. Wang, Y., Resonant third-order optical nonlinearity of molecular aggregates with low-dimensional excitons. *J. Opt. Soc. Am. B* **1991,** *8* (5), 981-985.
166. Yoneda, K.; Nakano, M.; Fukuda, K.; Matsui, H.; Takamuku, S.; Hirosaki, Y.; Kubo, T.; Kamada, K.; Champagne, B., Third-Order Nonlinear Optical Properties of One-Dimensional Open-Shell Molecular Aggregates Composed of Phenalenyl Radicals. *Chemistry – A European Journal* **2014,** *20* (35), 11129-11136.
167. Wang, C.; Yuan, Y., The influence of aggregation on the third-order nonlinear optical property of π-conjugated chromophores: the case of cyanine dyes. *Physical Chemistry Chemical Physics* **2018,** *20* (24), 16777-16785.

168. Markov, R.; Plekhanov, A.; Shelkovnikov, V., *Observation of optical nonlinearity size enhancement in one-dimensional molecular aggregates*. SPIE: 2002; Vol. 4751.
169. Wang, X.; Yang, P.; Li, B.; Jiang, W.; Huang, W.; Qian, S.; Tao, X.; Jiang, M., Two-photon absorption of new multibranched chromophore with dibenzothiophene core. *Chemical Physics Letters* **2006,** *424* (4), 333-339.
170. Burgel, M. v.; Wiersma, D. A.; Duppen, K., The dynamics of one-dimensional excitons in liquids. *The Journal of Chemical Physics* **1995,** *102* (1), 20-33.
171. Drobizhev, M.; Karotki, A.; Dzenis, Y.; Rebane, A.; Suo, Z.; Spangler, C. W., Strong Cooperative Enhancement of Two-Photon Absorption in Dendrimers. *The Journal of Physical Chemistry B* **2003,** *107* (31), 7540-7543.
172. Ceymann, H.; Rosspeintner, A.; Schreck, M. H.; Mützel, C.; Stoy, A.; Vauthey, E.; Lambert, C., Cooperative enhancement versus additivity of two-photon-absorption cross sections in linear and branched squaraine superchromophores. *Physical Chemistry Chemical Physics* **2016,** *18* (24), 16404-16413.
173. Yaghi, O. M., Kalmutzki, M. J., Diercks, C. S., *Introduction to Reticular Chemistry*. Wiley-VCH: Weinheim, 2019.
174. Yaghi, O. M., Reticular Chemistry in All Dimensions. *ACS Central Science* **2019,** *5* (8), 1295-1300.
175. Cordova, K. E.; Yaghi, O. M., The 'folklore' and reality of reticular chemistry. *Materials Chemistry Frontiers* **2017,** *1* (7), 1304-1309.
176. Kalmutzki, M. J.; Hanikel, N.; Yaghi, O. M., Secondary building units as the turning point in the development of the reticular chemistry of MOFs. *Science Advances* **2018,** *4* (10), eaat9180.
177. Li, M.; Li, D.; O'Keeffe, M.; Yaghi, O. M., Topological Analysis of Metal–Organic Frameworks with Polytopic Linkers and/or Multiple Building Units and the Minimal Transitivity Principle. *Chemical Reviews* **2014,** *114* (2), 1343-1370.
178. O'Keeffe, M., Nets, tiles, and metal-organic frameworks. *APL Materials* **2014,** *2* (12), 124106.
179. D.Evans, J.; Garai, B.; Reinsch, H.; Li, W.; Dissegna, S.; Bon, V.; Senkovska, I.; Fischer, R.; Kaskel, S.; Stock, N.; Volkmer, D., Metal-Organic Frameworks in Germany: from Synthesis to Function. *Coordination Chemistry Reviews* **2018,** *380*, 378-418.
180. Schoedel, A.; Li, M.; Li, D.; O'Keeffe, M.; Yaghi, O. M., Structures of Metal–Organic Frameworks with Rod Secondary Building Units. *Chemical Reviews* **2016,** *116* (19), 12466-12535.
181. Hoffmann, F., Fröba, M., Network Topology. In *The Chemistry of Metal–Organic Frameworks*, Kaskel, S., Ed. 2016; pp 5-40.
182. O'Keeffe, M.; Yaghi, O. M., Deconstructing the Crystal Structures of Metal–Organic Frameworks and Related Materials into Their Underlying Nets. *Chemical Reviews* **2012,** *112* (2), 675-702.
183. Zhou, H.-C.; Long, J. R.; Yaghi, O. M., Introduction to Metal–Organic Frameworks. *Chemical Reviews* **2012,** *112* (2), 673-674.
184. Furukawa, H.; Cordova, K. E.; O'Keeffe, M.; Yaghi, O. M., The Chemistry and Applications of Metal-Organic Frameworks. *Science* **2013,** *341* (6149), 1230444.
185. Yaghi, O. M.; O'Keeffe, M.; Ockwig, N. W.; Chae, H. K.; Eddaoudi, M.; Kim, J., Reticular synthesis and the design of new materials. *Nature* **2003,** *423* (6941), 705-714.

186. Diercks, C. S.; Yaghi, O. M., The atom, the molecule, and the covalent organic framework. *Science* **2017,** *355* (6328), eaal1585.
187. Delgado-Friedrichs, O.; O'Keeffe, M.; Yaghi, O. M., Taxonomy of periodic nets and the design of materials. *Physical Chemistry Chemical Physics* **2007,** *9* (9), 1035-1043.
188. Ockwig, N. W.; Delgado-Friedrichs, O.; O'Keeffe, M.; Yaghi, O. M., Reticular Chemistry: Occurrence and Taxonomy of Nets and Grammar for the Design of Frameworks. *Accounts of Chemical Research* **2005,** *38* (3), 176-182.
189. Batten, S. R.; Champness, N. R.; Chen, X.-M.; Garcia-Martinez, J.; Kitagawa, S.; Öhrström, L.; O'Keeffe, M.; Suh, M. P.; Reedijk, J., Coordination polymers, metal–organic frameworks and the need for terminology guidelines. *CrystEngComm* **2012,** *14* (9), 3001-3004.
190. Batten Stuart, R.; Champness Neil, R.; Chen, X.-M.; Garcia-Martinez, J.; Kitagawa, S.; Öhrström, L.; O'Keeffe, M.; Paik Suh, M.; Reedijk, J., Terminology of metal–organic frameworks and coordination polymers (IUPAC Recommendations 2013). In *Pure and Applied Chemistry*, 2013; Vol. 85, p 1715.
191. Coudert, F.-X., Soft Porous Crystals: Extraordinary Responses to Stimulation. *Bulletin of Japan Society of Coordination Chemistry* **2019,** *73*, 15-23.
192. Coudert, F.-X., Responsive Metal–Organic Frameworks and Framework Materials: Under Pressure, Taking the Heat, in the Spotlight, with Friends. *Chemistry of Materials* **2015,** *27* (6), 1905-1916.
193. Schneemann, A.; Bon, V.; Schwedler, I.; Senkovska, I.; Kaskel, S.; Fischer, R. A., Flexible metal–organic frameworks. *Chemical Society Reviews* **2014,** *43* (16), 6062-6096.
194. Gandara, F.; Bennett, T., Crystallography of metal–organic frameworks. *IUCrJ* **2014,** *1*, 563-570.
195. Horike, S.; Shimomura, S.; Kitagawa, S., Soft porous crystals. *Nature Chemistry* **2009,** *1* (9), 695-704.
196. Werner, A., Beitrag zur Konstitution anorganischer Verbindungen. *Zeitschrift für anorganische Chemie* **1893,** *3* (1), 267-330.
197. Hofmann, K. A.; Küspert, F., Verbindungen von Kohlenwasserstoffen mit Metallsalzen. *Zeitschrift für anorganische Chemie* **1897,** *15* (1), 204-207.
198. Yukio, K.; Ikuo, M.; Taiichi, H.; Yoshihiko, S., The Crystal Structure of Bis(adiponitrilo)copper(I) Nitrate. *Bulletin of the Chemical Society of Japan* **1959,** *32* (11), 1221-1226.
199. Kinoshita, Y.; Matsubara, I.; Higuchi, T.; Saito, Y., The Crystal Structure of Bis(adiponitrilo)copper(I) Nitrate. *Bulletin of the Chemical Society of Japan* **1959,** *32* (11), 1221-1226.
200. Yukio, K.; Ikuo, M.; Yoshihiko, S., The Crystal Structure of Bis(glutaronitrilo)copper(I) Nitrate. *Bulletin of the Chemical Society of Japan* **1959,** *32* (11), 1216-1221.
201. Wells, A., The geometrical basis of crystal chemistry. Part 1. *Acta Crystallographica* **1954,** *7* (8-9), 535-544.
202. Hoskins, B. F.; Robson, R., Infinite polymeric frameworks consisting of three dimensionally linked rod-like segments. *Journal of the American Chemical Society* **1989,** *111* (15), 5962-5964.
203. Hoskins, B. F.; Robson, R., Design and construction of a new class of scaffolding-like materials comprising infinite polymeric frameworks of 3D-linked molecular rods. A reappraisal of the zinc cyanide and cadmium cyanide

structures and the synthesis and structure of the diamond-related frameworks [N(CH3)4][CuIZnII(CN)4] and CuI[4,4',4'',4'''-tetracyanotetraphenylmethane]BF4.xC6H5NO2. *Journal of the American Chemical Society* **1990,** *112* (4), 1546-1554.
204. Yaghi, O. M.; Li, H., Hydrothermal Synthesis of a Metal-Organic Framework Containing Large Rectangular Channels. *Journal of the American Chemical Society* **1995,** *117* (41), 10401-10402.
205. Li, H.; Eddaoudi, M.; Groy, T. L.; Yaghi, O. M., Establishing Microporosity in Open Metal−Organic Frameworks: Gas Sorption Isotherms for Zn(BDC) (BDC = 1,4-Benzenedicarboxylate). *Journal of the American Chemical Society* **1998,** *120* (33), 8571-8572.
206. Li, H.; Eddaoudi, M.; O'Keeffe, M.; Yaghi, O. M., Design and synthesis of an exceptionally stable and highly porous metal-organic framework. *Nature* **1999,** *402* (6759), 276-279.
207. Moghadam, P. Z.; Li, A.; Wiggin, S. B.; Tao, A.; Maloney, A. G. P.; Wood, P. A.; Ward, S. C.; Fairen-Jimenez, D., Development of a Cambridge Structural Database Subset: A Collection of Metal–Organic Frameworks for Past, Present, and Future. *Chemistry of Materials* **2017,** *29* (7), 2618-2625.
208. Nangia, A. K.; Desiraju, G. R., Crystal Engineering: An Outlook for the Future. *Angewandte Chemie International Edition* **2019,** *58* (13), 4100-4107.
209. Stock, N.; Biswas, S., Synthesis of Metal-Organic Frameworks (MOFs): Routes to Various MOF Topologies, Morphologies, and Composites. *Chemical Reviews* **2012,** *112* (2), 933-969.
210. Biemmi, E.; Christian, S.; Stock, N.; Bein, T., High-throughput screening of synthesis parameters in the formation of the metal-organic frameworks MOF-5 and HKUST-1. *Microporous and Mesoporous Materials* **2009,** *117* (1), 111-117.
211. Van Vleet, M. J.; Weng, T.; Li, X.; Schmidt, J. R., In Situ, Time-Resolved, and Mechanistic Studies of Metal–Organic Framework Nucleation and Growth. *Chemical Reviews* **2018,** *118* (7), 3681-3721.
212. Gandara, F.; Bennett, T. D., Crystallography of metal-organic frameworks. *IUCrJ* **2014,** *1* (6), 563-570.
213. Cavka, J. H.; Jakobsen, S.; Olsbye, U.; Guillou, N.; Lamberti, C.; Bordiga, S.; Lillerud, K. P., A New Zirconium Inorganic Building Brick Forming Metal Organic Frameworks with Exceptional Stability. *Journal of the American Chemical Society* **2008,** *130* (42), 13850-13851.
214. Maurin, G., Role of molecular simulations in the structure exploration of Metal-Organic Frameworks: Illustrations through recent advances in the field. *Comptes Rendus Chimie* **2016,** *19* (1), 207-215.
215. Chui, S. S.-Y.; Lo, S. M.-F.; Charmant, J. P. H.; Orpen, A. G.; Williams, I. D., A Chemically Functionalizable Nanoporous Material $[Cu_3(TMA)_2(H_2O)_3]_n$. *Science* **1999,** *283* (5405), 1148-1150.
216. Loiseau, T.; Serre, C.; Huguenard, C.; Fink, G.; Taulelle, F.; Henry, M.; Bataille, T.; Férey, G., A Rationale for the Large Breathing of the Porous Aluminum Terephthalate (MIL-53) Upon Hydration. *Chemistry – A European Journal* **2004,** *10* (6), 1373-1382.
217. Serre, C.; Millange, F.; Thouvenot, C.; Noguès, M.; Marsolier, G.; Louër, D.; Férey, G., Very Large Breathing Effect in the First Nanoporous Chromium(III)-Based Solids: MIL-53 or $CrIII(OH)\cdot\{O_2C-C_6H_4-CO_2\}\cdot\{HO_2C-C_6H_4-CO_2H\}_x\cdot H_2O_y$. *Journal of the American Chemical Society* **2002,** *124* (45), 13519-13526.

218. Barthelet, K.; Marrot, J.; Riou, D.; Férey, G., A Breathing Hybrid Organic–Inorganic Solid with Very Large Pores and High Magnetic Characteristics. *Angewandte Chemie International Edition* **2002,** *41* (2), 281-284.
219. ZareKarizi, F.; Joharian, M.; Morsali, A., Pillar-layered MOFs: functionality, interpenetration, flexibility and applications. *Journal of Materials Chemistry A* **2018,** *6* (40), 19288-19329.
220. Chen, B.; Yang, Z.; Zhu, Y.; Xia, Y., Zeolitic imidazolate framework materials: recent progress in synthesis and applications. *Journal of Materials Chemistry A* **2014,** *2* (40), 16811-16831.
221. Hönicke, I. M.; Senkovska, I.; Bon, V.; Baburin, I. A.; Bönisch, N.; Raschke, S.; Evans, J. D.; Kaskel, S., Balancing Mechanical Stability and Ultrahigh Porosity in Crystalline Framework Materials. *Angewandte Chemie International Edition* **2018,** *57* (42), 13780-13783.
222. Krishtab, M.; Stassen, I.; Stassin, T.; Cruz, A. J.; Okudur, O. O.; Armini, S.; Wilson, C.; De Gendt, S.; Ameloot, R., Vapor-deposited zeolitic imidazolate frameworks as gap-filling ultra-low-k dielectrics. *Nature Communications* **2019,** *10* (1), 3729.
223. Dolgopolova, E. A.; Rice, A. M.; Martin, C. R.; Shustova, N. B., Photochemistry and photophysics of MOFs: steps towards MOF-based sensing enhancements. *Chemical Society Reviews* **2018,** *47* (13), 4710-4728.
224. Mínguez Espallargas, G.; Coronado, E., Magnetic functionalities in MOFs: from the framework to the pore. *Chemical Society Reviews* **2018,** *47* (2), 533-557.
225. Hendon, C. H.; Tiana, D.; Walsh, A., Conductive metal–organic frameworks and networks: fact or fantasy? *Physical Chemistry Chemical Physics* **2012,** *14* (38), 13120-13132.
226. Kumar, P.; Deep, A.; Kim, K.-H., Metal organic frameworks for sensing applications. *TrAC Trends in Analytical Chemistry* **2015,** *73*, 39-53.
227. Yu, J.; Cui, Y.; Wu, C.-D.; Yang, Y.; Chen, B.; Qian, G., Two-Photon Responsive Metal–Organic Framework. *Journal of the American Chemical Society* **2015,** *137* (12), 4026-4029.
228. Mingabudinova, L. R.; Vinogradov, V. V.; Milichko, V. A.; Hey-Hawkins, E.; Vinogradov, A. V., Metal–organic frameworks as competitive materials for non-linear optics. *Chemical Society Reviews* **2016,** *45* (19), 5408-5431.
229. Öhrström, L., Designing, Describing and Disseminating New Materials by using the Network Topology Approach. *Chemistry – A European Journal* **2016,** *22* (39), 13758-13763.
230. O'Keeffe, M.; Peskov, M. A.; Ramsden, S. J.; Yaghi, O. M., The Reticular Chemistry Structure Resource (RCSR) Database of, and Symbols for, Crystal Nets. *Accounts of Chemical Research* **2008,** *41* (12), 1782-1789.
231. Delgado-Friedrichs, O.; O'Keeffe, M., Crystal nets as graphs: Terminology and definitions. *Journal of Solid State Chemistry* **2005,** *178*, 2480-2485.
232. Bureekaew, S.; Schmid, R., Hypothetical 3D-periodic covalent organic frameworks: exploring the possibilities by a first principles derived force field. *CrystEngComm* **2013,** *15* (8), 1551-1562.
233. Blatov, V. A.; Delgado-Friedrichs, O.; O'Keeffe, M.; Proserpio, D. M., Three-periodic nets and tilings: natural tilings for nets. *Acta Crystallographica Section A* **2007,** *63* (5), 418-425.

234. Delgado Friedrichs, O.; O'Keeffe, M.; Yaghi, O. M., Three-periodic nets and tilings: regular and quasiregular nets. *Acta Crystallographica Section A* **2003,** *59* (1), 22-27.
235. Delgado-Friedrichs, O.; Foster, M. D.; O'Keeffe, M.; Proserpio, D. M.; Treacy, M. M. J.; Yaghi, O. M., What do we know about three-periodic nets? *Journal of Solid State Chemistry* **2005,** *178* (8), 2533-2554.
236. Cornelio, J.; Zhou, T.-Y.; Alkaş, A.; Telfer, S. G., Systematic Tuning of the Luminescence Output of Multicomponent Metal–Organic Frameworks. *Journal of the American Chemical Society* **2018,** *140* (45), 15470-15476.
237. Gao, X.; Cui, R.; Ji, G.; Liu, Z., Size and surface controllable metal–organic frameworks (MOFs) for fluorescence imaging and cancer therapy. *Nanoscale* **2018,** *10* (13), 6205-6211.
238. Liu, Y.; Xie, X.-Y.; Cheng, C.; Shao, Z.-S.; Wang, H.-S., Strategies to fabricate metal–organic framework (MOF)-based luminescent sensing platforms. *Journal of Materials Chemistry C* **2019,** *7* (35), 10743-10763.
239. Diamantis, S. A.; Margariti, A.; Pournara, A. D.; Papaefstathiou, G. S.; Manos, M. J.; Lazarides, T., Luminescent metal–organic frameworks as chemical sensors: common pitfalls and proposed best practices. *Inorganic Chemistry Frontiers* **2018,** *5* (7), 1493-1511.
240. Yuan, Z.; Zhang, L.; Li, S.; Zhang, W.; Lu, M.; Pan, Y.; Xie, X.; Huang, L.; Huang, W., Paving Metal–Organic Frameworks with Upconversion Nanoparticles via Self-Assembly. *Journal of the American Chemical Society* **2018,** *140* (45), 15507-15515.
241. Li, M.; Gul, S.; Tian, D.; Zhou, E.; Wang, Y.; Han, Y.; Yin, L.; Huang, L., Erbium(iii)-based metal–organic frameworks with tunable upconversion emissions. *Dalton Transactions* **2018,** *47* (37), 12868-12872.
242. Gharaati, S.; Wang, C.; Förster, C.; Weigert, F.; Resch-Genger, U.; Heinze, K., Triplet–Triplet Annihilation Upconversion in a MOF with Acceptor-Filled Channels. *Chemistry – A European Journal* **2020,** *26* (5), 1003-1007.
243. Oldenburg, M.; Turshatov, A.; Busko, D.; Wollgarten, S.; Adams, M.; Baroni, N.; Welle, A.; Redel, E.; Wöll, C.; Richards, B. S.; Howard, I. A., Photon Upconversion at Crystalline Organic–Organic Heterojunctions. *Advanced Materials* **2016,** *28* (38), 8477-8482.
244. Rice, A. M.; Martin, C. R.; Galitskiy, V. A.; Berseneva, A. A.; Leith, G. A.; Shustova, N. B., Photophysics Modulation in Photoswitchable Metal–Organic Frameworks. *Chemical Reviews* **2019**.
245. Xiao, J.-D.; Jiang, H.-L., Metal–Organic Frameworks for Photocatalysis and Photothermal Catalysis. *Accounts of Chemical Research* **2019,** *52* (2), 356-366.
246. Lv, Y.; Xiong, Z.; Dong, H.; Wei, C.; Yang, Y.; Ren, A.; Yao, Z.; Li, Y.; Xiang, S.; Zhang, Z.; Zhao, Y. S., Pure Metal–Organic Framework Microlasers with Controlled Cavity Shapes. *Nano Letters* **2020**.
247. Yu, J.; Cui, Y.; Xu, H.; Yang, Y.; Wang, Z.; Chen, B.; Qian, G., Confinement of pyridinium hemicyanine dye within an anionic metal-organic framework for two-photon-pumped lasing. *Nature Communications* **2013,** *4*, 2719.
248. Adams, M.; Kozlowska, M.; Baroni, N.; Oldenburg, M.; Ma, R.; Busko, D.; Turshatov, A.; Emandi, G.; Senge, M. O.; Haldar, R.; Wöll, C.; Nienhaus, G. U.; Richards, B. S.; Howard, I. A., Highly Efficient One-Dimensional Triplet Exciton Transport in a Palladium–Porphyrin-Based Surface-Anchored Metal–

Organic Framework. *ACS Applied Materials & Interfaces* **2019,** *11* (17), 15688-15697.
249. Foster, M. E.; Azoulay, J. D.; Wong, B. M.; Allendorf, M. D., Novel metal–organic framework linkers for light harvesting applications. *Chemical Science* **2014,** *5* (5), 2081-2090.
250. Lee, C. Y.; Farha, O. K.; Hong, B. J.; Sarjeant, A. A.; Nguyen, S. T.; Hupp, J. T., Light-Harvesting Metal–Organic Frameworks (MOFs): Efficient Strut-to-Strut Energy Transfer in Bodipy and Porphyrin-Based MOFs. *Journal of the American Chemical Society* **2011,** *133* (40), 15858-15861.
251. Yu, J.; Li, X.; Deria, P., Light-Harvesting in Porous Crystalline Compositions: Where We Stand toward Robust Metal–Organic Frameworks. *ACS Sustainable Chemistry & Engineering* **2019,** *7* (2), 1841-1854.
252. Zhang, Q.; Zhang, C.; Cao, L.; Wang, Z.; An, B.; Lin, Z.; Huang, R.; Zhang, Z.; Wang, C.; Lin, W., Förster Energy Transport in Metal–Organic Frameworks Is Beyond Step-by-Step Hopping. *Journal of the American Chemical Society* **2016,** *138* (16), 5308-5315.
253. Lin, J.; Hu, X.; Zhang, P.; Van Rynbach, A.; Beratan, D. N.; Kent, C. A.; Mehl, B. P.; Papanikolas, J. M.; Meyer, T. J.; Lin, W.; Skourtis, S. S.; Constantinou, M., Triplet Excitation Energy Dynamics in Metal–Organic Frameworks. *The Journal of Physical Chemistry C* **2013,** *117* (43), 22250-22259.
254. Dhakshinamoorthy, A.; Li, Z.; Garcia, H., Catalysis and photocatalysis by metal organic frameworks. *Chemical Society Reviews* **2018,** *47* (22), 8134-8172.
255. Wang, C.; Dong, H.; Jiang, L.; Hu, W., Organic semiconductor crystals. *Chemical Society Reviews* **2018,** *47* (2), 422-500.
256. Rodríguez, N. A.; Parra, R.; Grela, M. A., Structural characterization, optical properties and photocatalytic activity of MOF-5 and its hydrolysis products: implications on their excitation mechanism. *RSC Advances* **2015,** *5* (89), 73112-73118.
257. Tachikawa, T.; Choi, J. R.; Fujitsuka, M.; Majima, T., Photoinduced Charge-Transfer Processes on MOF-5 Nanoparticles: Elucidating Differences between Metal-Organic Frameworks and Semiconductor Metal Oxides. *The Journal of Physical Chemistry C* **2008,** *112* (36), 14090-14101.
258. Vogler, A.; Kunkely, H., Optical Ligand to Ligand Charge Transfer of Metal Complexes Including Ligand-Based Mixed-Valence Systems. *Comments on Inorganic Chemistry* **1990,** *9* (3-4), 201-220.
259. Birks, J. B., Excimers. *Reports on Progress in Physics* **1975,** *38* (8), 903-974.
260. Kunkely, H., Ligand-to-ligand and intraligand charge transfer and their relation to charge transfer interactions in organic zwitterions. *Coordination Chemistry Reviews* **2007,** *251*, 577-583.
261. Kaufmann, C.; Kim, W.; Nowak-Król, A.; Hong, Y.; Kim, D.; Würthner, F., Ultrafast Exciton Delocalization, Localization, and Excimer Formation Dynamics in a Highly Defined Perylene Bisimide Quadruple π-Stack. *Journal of the American Chemical Society* **2018,** *140* (12), 4253-4258.
262. Skelton, J. M.; Lora da Silva, E.; Crespo-Otero, R.; Hatcher, L. E.; Raithby, P. R.; Parker, S. C.; Walsh, A., Electronic excitations in molecular solids: bridging theory and experiment. *Faraday Discussions* **2015,** *177* (0), 181-202.

263. Elliott, J. D.; Colonna, N.; Marsili, M.; Marzari, N.; Umari, P., Koopmans Meets Bethe–Salpeter: Excitonic Optical Spectra without GW. *Journal of Chemical Theory and Computation* **2019,** *15* (6), 3710-3720.
264. Gutiérrez, M.; Sánchez, F.; Douhal, A., Spectral and dynamical properties of a Zr-based MOF. *Physical Chemistry Chemical Physics* **2016,** *18* (7), 5112-5120.
265. Gutierrez, M.; Cohen, B.; Sánchez, F.; Douhal, A., Photochemistry of Zr-based MOFs: ligand-to-cluster charge transfer, energy transfer and excimer formation, what else is there? *Physical Chemistry Chemical Physics* **2016,** *18* (40), 27761-27774.
266. Caballero-Mancebo, E.; Cohen, B.; Smolders, S.; De Vos, D. E.; Douhal, A., Unravelling Why and to What Extent the Topology of Similar Ce-Based MOFs Conditions their Photodynamic: Relevance to Photocatalysis and Photonics. *Advanced Science* **2019,** *6* (19), 1901020.
267. Haldar, R.; Jakoby, M.; Mazel, A.; Zhang, Q.; Welle, A.; Mohamed, T.; Krolla, P.; Wenzel, W.; Diring, S.; Odobel, F.; Richards, B. S.; Howard, I. A.; Wöll, C., Anisotropic energy transfer in crystalline chromophore assemblies. *Nature Communications* **2018,** *9* (1), 4332.
268. Liao, W.-M.; Zhang, J.-H.; Yin, S.-Y.; Lin, H.; Zhang, X.; Wang, J.; Wang, H.-P.; Wu, K.; Wang, Z.; Fan, Y.-N.; Pan, M.; Su, C.-Y., Tailoring exciton and excimer emission in an exfoliated ultrathin 2D metal-organic framework. *Nature Communications* **2018,** *9* (1), 2401.
269. Milichko, V. A.; Makarov, S. V.; Yulin, A. V.; Vinogradov, A. V.; Krasilin, A. A.; Ushakova, E.; Dzyuba, V. P.; Hey-Hawkins, E.; Pidko, E. A.; Belov, P. A., van der Waals Metal-Organic Framework as an Excitonic Material for Advanced Photonics. *Advanced Materials* **2017,** *29* (12), 1606034.
270. Vrubel, I. I.; Senkevich, N. Y.; Khramenkova, E. V.; Polozkov, R. G.; Shelykh, I. A., Electronic Structure and Optical Response of Zn-Based Metal–Organic Frameworks. *Advanced Theory and Simulations* **2018,** *1* (9), 1800049.
271. Yan, T.; Zhou, J.; Zhu, R.-R.; Zhao, Y.-R.; Xue, Z.; Jia, L.; Wang, Q.; Du, L.; Zhao, Q.-H., Two-Dimensional Excitonic Metal–Organic Framework: Design, Synthesis, Regulation, and Properties. *Inorganic Chemistry* **2019,** *58* (5), 3145-3155.
272. Grinnell, C.; Samokhvalov, A., Exploring the electronic structure of aluminum metal–organic framework Basolite A100: solid-state synchronous fluorescence spectroscopy reveals new charge excitation/relaxation pathways. *Physical Chemistry Chemical Physics* **2018,** *20* (42), 26947-26956.
273. Böer, K. W.; Pohl, U. W., Excitons. In *Semiconductor Physics*, Springer International Publishing: Cham, 2014; pp 1-41.
274. Pham, H. Q.; Mai, T.; Pham-Tran, N.-N.; Kawazoe, Y.; Mizuseki, H.; Nguyen-Manh, D., Engineering of Band Gap in Metal–Organic Frameworks by Functionalizing Organic Linker: A Systematic Density Functional Theory Investigation. *The Journal of Physical Chemistry C* **2014,** *118* (9), 4567-4577.
275. Lin, C.-K.; Zhao, D.; Gao, W.-Y.; Yang, Z.; Ye, J.; Ge, Q.; Ma, S.; Liu, D.-J., Tunability of Band Gaps in Metal-Organic Frameworks. *Inorganic chemistry* **2012,** *51*, 9039-44.
276. Kent, C. A.; Mehl, B. P.; Ma, L.; Papanikolas, J. M.; Meyer, T. J.; Lin, W., Energy Transfer Dynamics in Metal−Organic Frameworks. *Journal of the American Chemical Society* **2010,** *132* (37), 12767-12769.

277. Williams, D. E.; Shustova, N. B., Metal–Organic Frameworks as a Versatile Tool To Study and Model Energy Transfer Processes. *Chemistry – A European Journal* **2015,** *21* (44), 15474-15479.
278. Förster, T., Zwischenmolekulare Energiewanderung und Fluoreszenz. *Annalen der Physik* **1948,** *437* (1-2), 55-75.
279. Dexter, D. L., A Theory of Sensitized Luminescence in Solids. *Journal of Chemical Physics* **1953,** *21*, 836.
280. Lakowicz, J. R., *Principles of fluorescence spectroscopy*. Kluwer Academic/Plenum: New York, 1999.
281. Jang, S., Generalization of the Forster resonance energy transfer theory for quantum mechanical modulation of the donor-acceptor coupling. *The Journal of chemical physics* **2007,** *127*, 174710.
282. You, Z.-Q.; Hsu, C.-P.; Fleming, G. R., Triplet-triplet energy-transfer coupling: Theory and calculation. *The Journal of Chemical Physics* **2006,** *124* (4), 044506.
283. So, M.; Wiederrecht, G.; Mondloch, J.; Hupp, J.; Farha, O., Metal–organic framework materials for light-harvesting and energy transfer. *Chemical communications* **2015,** *51*.
284. Son, H.-J.; Jin, S.; Patwardhan, S.; Wezenberg, S. J.; Jeong, N. C.; So, M.; Wilmer, C. E.; Sarjeant, A. A.; Schatz, G. C.; Snurr, R. Q.; Farha, O. K.; Wiederrecht, G. P.; Hupp, J. T., Light-Harvesting and Ultrafast Energy Migration in Porphyrin-Based Metal–Organic Frameworks. *Journal of the American Chemical Society* **2013,** *135* (2), 862-869.
285. Park, H. J.; So, M. C.; Gosztola, D.; Wiederrecht, G. P.; Emery, J. D.; Martinson, A. B. F.; Er, S.; Wilmer, C. E.; Vermeulen, N. A.; Aspuru-Guzik, A.; Stoddart, J. F.; Farha, O. K.; Hupp, J. T., Layer-by-Layer Assembled Films of Perylene Diimide- and Squaraine-Containing Metal–Organic Framework-like Materials: Solar Energy Capture and Directional Energy Transfer. *ACS Applied Materials & Interfaces* **2016,** *8* (38), 24983-24988.
286. Wang, Z.; Liu, Y.; Wang, Z.; Cao, L.; Zhao, Y.; Wang, C.; Lin, W., Through-space Förster-type energy transfer in isostructural zirconium and hafnium-based metal–organic layers. *Chemical Communications* **2017,** *53* (67), 9356-9359.
287. Cao, L.; Lin, Z.; Shi, W.; Wang, Z.; Zhang, C.; Hu, X.; Wang, C.; Lin, W., Exciton Migration and Amplified Quenching on Two-Dimensional Metal–Organic Layers. *Journal of the American Chemical Society* **2017,** *139* (20), 7020-7029.
288. Wu, K.; Pan, S., A review on structure-performance relationship toward the optimal design of infrared nonlinear optical materials with balanced performances. *Coordination Chemistry Reviews* **2018,** *377*, 191-208.
289. Marder, S. R., Organic nonlinear optical materials: where we have been and where we are going. *Chemical Communications* **2006,** (2), 131-134.
290. Yang, G.; Wu, K., Two-dimensional nonlinear optical materials predicted by network visualization. *Molecular Systems Design & Engineering* **2019,** *4* (3), 586-596.
291. Dobson, P., Physical Properties of Crystals – Their Representation by Tensors and Matrices. *Physics Bulletin* **1985,** *36*, 506-506.
292. Kleinman, D. A., Nonlinear Dielectric Polarization in Optical Media. *Physical Review* **1962,** *126* (6), 1977-1979.
293. Paras, N. P., Williams, D. J., *Introduction to nonlinear optical effects in molecules and polymers*. John Wiley & Sons: New York, 1991.

294. Kurtz, S. K.; Perry, T. T., A Powder Technique for the Evaluation of Nonlinear Optical Materials. *Journal of Applied Physics* **1968,** *39* (8), 3798-3813.
295. Chen, C.-X.; Yin, S.-Y.; Wei, Z.-W.; Qiu, Q.-F.; Zhu, N.-X.; Fan, Y.-N.; Pan, M.; Su, C.-Y., Pressure-Induced Multiphoton Excited Fluorochromic Metal–Organic Frameworks for Improving MPEF Properties. *Angewandte Chemie International Edition* **2019,** *58* (40), 14379-14385.
296. Zhang, Q.; Su, J.; Feng, D.; Wei, Z.; Zou, X.; Zhou, H.-C., Piezofluorochromic Metal–Organic Framework: A Microscissor Lift. *Journal of the American Chemical Society* **2015,** *137* (32), 10064-10067.
297. Zaręba, J.; Nyk, M.; Samoc, M., Co/ZIF-8 heterometallic nanoparticles: control of the nanocrystal size and properties by mixed-metal approach. *Crystal Growth & Design* **2016,** *16*.
298. Van Cleuvenbergen, S.; Stassen, I.; Gobechiya, E.; Zhang, Y.; Markey, K.; De Vos, D. E.; Kirschhock, C.; Champagne, B.; Verbiest, T.; van der Veen, M. A., ZIF-8 as Nonlinear Optical Material: Influence of Structure and Synthesis. *Chemistry of Materials* **2016,** *28* (9), 3203-3209.
299. Zaręba, J. K.; Szeremeta, J.; Waszkielewicz, M.; Nyk, M.; Samoć, M., Nonlinear-Optical Response of Prussian Blue: Strong Three-Photon Absorption in the IR Region. *Inorganic Chemistry* **2016,** *55* (19), 9501-9504.
300. Zaręba, J. K.; Nyk, M.; Janczak, J.; Samoć, M., Three-Photon Absorption of Coordination Polymer Transforms UV-to-VIS Thermometry into NIR-to-VIS Thermometry. *ACS Applied Materials & Interfaces* **2019,** *11* (11), 10435-10441.
301. Lu, W.; Wei, Z.; Gu, Z.-Y.; Liu, T.-F.; Park, J.; Park, J.; Tian, J.; Zhang, M.; Zhang, Q.; Gentle Iii, T.; Bosch, M.; Zhou, H.-C., Tuning the structure and function of metal–organic frameworks via linker design. *Chemical Society Reviews* **2014,** *43* (16), 5561-5593.
302. Alkaline Earth Metal-Based Metal–Organic Frameworks: Synthesis, Properties, and Applications. In *The Chemistry of Metal–Organic Frameworks*, pp 73-103.
303. Kobayashi, T., *J-Aggregates*. World Scientific: 1996.
304. Hu, H.; Fishman, D. A.; Gerasov, A. O.; Przhonska, O. V.; Webster, S.; Padilha, L. A.; Peceli, D.; Shandura, M.; Kovtun, Y. P.; Kachkovski, A. D.; Nayyar, I. H.; Masunov, A. E.; Tongwa, P.; Timofeeva, T. V.; Hagan, D. J.; Van Stryland, E. W., Two-Photon Absorption Spectrum of a Single Crystal Cyanine-like Dye. *The Journal of Physical Chemistry Letters* **2012,** *3* (9), 1222-1228.
305. Biswas, S.; Ahn, H.-Y.; Bondar, M. V.; Belfield, K. D., Two-Photon Absorption Enhancement of Polymer-Templated Porphyrin-Based J-Aggregates. *Langmuir* **2012,** *28* (2), 1515-1522.
306. Zhang, Y.; Kim, B.; Yao, S.; Bondar, M. V.; Belfield, K. D., Controlled Aggregation and Enhanced Two-Photon Absorption of a Water-Soluble Squaraine Dye with a Poly(acrylic acid) Template. *Langmuir* **2013,** *29* (35), 11005-11012.
307. Belfield, K. D.; Bondar, M. V.; Hernandez, F. E.; Przhonska, O. V.; Yao, S., Two-photon absorption of a supramolecular pseudoisocyanine J-aggregate assembly. *Chemical Physics* **2006,** *320* (2), 118-124.
308. Seidler, T.; Stadnicka, K.; Champagne, B., Second-order Nonlinear Optical Susceptibilities and Refractive Indices of Organic Crystals from a

Multiscale Numerical Simulation Approach. *Advanced Optical Materials* **2014,** *2* (10), 1000-1006.
309. Seidler, T.; Champagne, B., Second-Order Nonlinear Optical Susceptibilities of Metal–Organic Frameworks Using a Combined Local Field Theory/Charge Embedding Electrostatic Scheme. *The Journal of Physical Chemistry C* **2016,** *120* (12), 6741-6749.
310. Ernst, M.; Dos Santos, L. H. R.; Macchi, P., Optical properties of metal–organic networks from distributed atomic polarizabilities. *CrystEngComm* **2016,** *18* (38), 7339-7346.
311. Champagne, B.; Bishop, D., Calculations of Nonlinear Optical Properties for the Solid State. *Advances in Chemical Physics* **2003,** *126*, 41-92.
312. Kocherzhenko, A. A.; Shedge, S. V.; Sosa Vazquez, X.; Maat, J.; Wilmer, J.; Tillack, A. F.; Johnson, L. E.; Isborn, C. M., Unraveling Excitonic Effects for the First Hyperpolarizabilities of Chromophore Aggregates. *The Journal of Physical Chemistry C* **2019,** *123* (22), 13818-13836.
313. Sheik-Bahae, M.; Said, A. A.; Wei, T.-H.; Hagan, D. J.; van Stryland, E. W., Sensitive measurement of optical nonlinearities using a single beam. *IEEE Journal of Quantum Electronics* **1990,** *26*, 760.
314. He, G. S.; Swiatkiewicz, J.; Jiang, Y.; Prasad, P. N.; Reinhardt, B. A.; Tan, L.-S.; Kannan, R., Two-Photon Excitation and Optical Spatial-Profile Reshaping via a Nonlinear Absorbing Medium. *The Journal of Physical Chemistry A* **2000,** *104* (20), 4805-4810.
315. Xu, C.; Webb, W. W., Measurement of two-photon excitation cross sections of molecular fluorophores with data from 690 to 1050 nm. *J. Opt. Soc. Am. B* **1996,** *13* (3), 481-491.
316. Makarov, N. S.; Drobizhev, M.; Rebane, A., Two-photon absorption standards in the 550–1600 nm excitation wavelength range. *Opt. Express* **2008,** *16* (6), 4029-4047.
317. Zhang, Z.; Müller, K.; Heidrich, S.; Koenig, M.; Hashem, T.; Schlöder, T.; Bléger, D.; Wenzel, W.; Heinke, L., Light-Switchable One-Dimensional Photonic Crystals Based on MOFs with Photomodulatable Refractive Index. *The Journal of Physical Chemistry Letters* **2019,** *10* (21), 6626-6633.
318. Ryder, M.; Zeng, Z.; Sun, Y.; Flyagina, I.; Titov, K.; E. M, M.; Bennett, T.; Civalleri, B.; Kelley, C.; Frogley, M.; Cinque, G.; Tan, J.-C., Dielectric Properties of Metal-Organic Frameworks Probed via Synchrotron Infrared Reflectivity. **2018**. arXiv:180206702
319. Dissegna, S.; Epp, K.; Heinz, W. R.; Kieslich, G.; Fischer, R. A., Defective Metal-Organic Frameworks. *Advanced Materials* **2018,** *30* (37), 1704501.
320. Sheldrick, G., A short history of SHELX. *Acta Crystallographica Section A* **2008,** *64* (1), 112-122.
321. Sheldrick, G., Crystal structure refinement with SHELXL. *Acta Crystallographica Section C* **2015,** *71* (1), 3-8.
322. Frisch, M. J.; Trucks, G. W.; Schlegel, H. B.; Scuseria, G. E.; Robb, M. A.; Cheeseman, J. R.; Scalmani, G.; Barone, V.; Petersson, G. A.; Nakatsuji, H.; Li, X.; Caricato, M.; Marenich, A. V.; Bloino, J.; Janesko, B. G.; Gomperts, R.; Mennucci, B.; Hratchian, H. P.; Ortiz, J. V.; Izmaylov, A. F.; Sonnenberg, J. L.; Williams; Ding, F.; Lipparini, F.; Egidi, F.; Goings, J.; Peng, B.; Petrone, A.; Henderson, T.; Ranasinghe, D.; Zakrzewski, V. G.; Gao, J.; Rega, N.; Zheng, G.; Liang, W.; Hada, M.; Ehara, M.; Toyota, K.; Fukuda, R.; Hasegawa, J.; Ishida, M.; Nakajima, T.; Honda, Y.; Kitao, O.;

Nakai, H.; Vreven, T.; Throssell, K.; Montgomery Jr., J. A.; Peralta, J. E.; Ogliaro, F.; Bearpark, M. J.; Heyd, J. J.; Brothers, E. N.; Kudin, K. N.; Staroverov, V. N.; Keith, T. A.; Kobayashi, R.; Normand, J.; Raghavachari, K.; Rendell, A. P.; Burant, J. C.; Iyengar, S. S.; Tomasi, J.; Cossi, M.; Millam, J. M.; Klene, M.; Adamo, C.; Cammi, R.; Ochterski, J. W.; Martin, R. L.; Morokuma, K.; Farkas, O.; Foresman, J. B.; Fox, D. J. *Gaussian 16 Rev. C.01*, Wallingford, CT, 2016.

323. Giannozzi, P.; Andreussi, O.; Brumme, T.; Bunau, O.; Buongiorno Nardelli, M.; Calandra, M.; Car, R.; Cavazzoni, C.; Ceresoli, D.; Cococcioni, M.; Colonna, N.; Carnimeo, I.; Dal Corso, A.; de Gironcoli, S.; Delugas, P.; DiStasio, R. A.; Ferretti, A.; Floris, A.; Fratesi, G.; Fugallo, G.; Gebauer, R.; Gerstmann, U.; Giustino, F.; Gorni, T.; Jia, J.; Kawamura, M.; Ko, H. Y.; Kokalj, A.; Küçükbenli, E.; Lazzeri, M.; Marsili, M.; Marzari, N.; Mauri, F.; Nguyen, N. L.; Nguyen, H. V.; Otero-de-la-Roza, A.; Paulatto, L.; Poncé, S.; Rocca, D.; Sabatini, R.; Santra, B.; Schlipf, M.; Seitsonen, A. P.; Smogunov, A.; Timrov, I.; Thonhauser, T.; Umari, P.; Vast, N.; Wu, X.; Baroni, S., Advanced capabilities for materials modelling with Quantum ESPRESSO. *Journal of Physics: Condensed Matter* **2017,** *29* (46), 465901.

324. Lu, T.; Chen, F., Multiwfn: A multifunctional wavefunction analyzer. *Journal of Computational Chemistry* **2012,** *33* (5), 580-592.

325. Schmidt, M. W.; Baldridge, K. K.; Boatz, J. A.; Elbert, S. T.; Gordon, M. S.; Jensen, J. H.; Koseki, S.; Matsunaga, N.; Nguyen, K. A.; Su, S.; Windus, T. L.; Dupuis, M.; Montgomery Jr, J. A., General atomic and molecular electronic structure system. *Journal of Computational Chemistry* **1993,** *14* (11), 1347-1363.

326. Webber, T. E.; Liu, W.-G.; Desai, S. P.; Lu, C. C.; Truhlar, D. G.; Penn, R. L., Role of a Modulator in the Synthesis of Phase-Pure NU-1000. *ACS Applied Materials & Interfaces* **2017,** *9* (45), 39342-39346.

327. Liu, W.-G.; Truhlar, D. G., Computational Linker Design for Highly Crystalline Metal–Organic Framework NU-1000. *Chemistry of Materials* **2017,** *29* (19), 8073-8081.

328. Kocherzhenko, A. A.; Sosa Vazquez, X. A.; Milanese, J. M.; Isborn, C. M., Absorption Spectra for Disordered Aggregates of Chromophores Using the Exciton Model. *Journal of Chemical Theory and Computation* **2017,** *13* (8), 3787-3801.